PHYSICAL CHEMISTRY 2024

17th International Conference
on Fundamental and Applied Aspects of
Physical Chemistry

Proceedings
Volume I



This conference is dedicated to the 100th anniversary of the birth of Professor Slobodanka Caca Veljković

September 23-27, 2024
Belgrade, Serbia



PHYSICAL CHEMISTRY 2024

17th International Conference
on Fundamental and Applied Aspects of
Physical Chemistry

Proceedings
Volume I

This conference is dedicated to the 100th anniversary of the birth of Professor Slobodanka Caca Veljković

September 23-27, 2024
Belgrade, Serbia

Title: PHYSICAL CHEMISTRY 2024, 17th International Conference on Fundamental and Applied Aspects of Physical Chemistry (Proceedings) ISBN-978-86-82475-44-6
Volume I: ISBN-978-86-82475-45-3
Editors: Željko Čupić, Slobodan Anić and Ana Ivanović-Šašić
Published by: Society of Physical Chemists of Serbia, Studentski Trg 12-16, 11158, Belgrade, Serbia
Publisher: Society of Physical Chemists of Serbia
For Publisher: S. Anić, President of Society of Physical Chemists of Serbia
Printed by: ″Jovan″, <Printing and Publishing Company, Ilije Đuričića 19, Belgrade, 50 Copies
Number of pages: 12+402, Format A4, printing finished in December 2024.

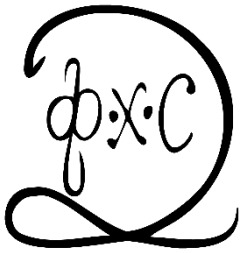
Text and Layout: ″Jovan″

Neither this book nor any part may be reproduced or transmitted in any form or by any means, including photocopying, or by any information storage and retrieval system, without permission in writing from the publisher.

50- *Copy printing*

CONTENT

Volume I
Organizer IV
Comittes V
Sponsors VI
Plenary Lecture 1
Chemical Thermodynamic 37
Spectroscopy, Molecular Structure, Physical Chemistry of Plasma 43
Kinetics, Catalysis 57
Nonlinear Dynamics, Oscillatory Reactions, Chaos 105
Electrochemistry 171
Biophysical Chemistry, EPR investigations of Bio-systems 211
Organic Physical Chemistry 247
Material Science 273



PHYSICAL CHEMISTRY 2024

17th International Conference on
Fundamental and Applied Aspects of
Physical Chemistry

Organized by

The Society of Physical Chemists of
Serbia

in co-operation with

Institute of Catalysis, Bulgarian Academy of Sciences

and

Boreskov Institute of Catalysis, Siberian Branch of
Russian Academy of Sciences

and

University of Belgrade, Serbia:

Faculty of Physical Chemistry
Institute of Chemistry, Technology and Metallurgy
Vinča Institute of Nuclear Sciences
Faculty of Pharmacy

and

Institute of General and Physical Chemistry, Belgrade, Serbia

International Organizing Committee

Chairman: S. Anić (Serbia)
Vice-chairman: Z. Petkova Cherkezova-Zheleva (Bulgaria)
Oleg N. Martyanov (Russia)
S. N. Blagojević (Serbia)
Members: N. Cvjetićanin (Serbia), S. M. Blagojević (Serbia), M. Daković (Serbia), J. Dimitrić-Marković (Serbia), T. Grozdić (Serbia), Lj. Ignjatović (Serbia), A. Ivanović-Šašić (Serbia), D. Jovanović (Serbia), N. Jović-Jovičić (Serbia), M. Kuzmanović (Serbia), S. Maćešić (Serbia), D. Marković (Serbia), B. Milosavljević (USA), M. Mojović (Serbia), N. Pejić (Serbia), M. Petković (Serbia), A. Popović Bijelić (Serbia), B. Simonović (Serbia), B. Šljukić (Serbia), G. Tasić (Serbia), S. Veličković (Serbia), N. Vukelić (Serbia)

International Scientific Committee

Chairman: Ž. Čupić (Serbia)
Vice-chairman: V. Bukhtiyarov (Russia)
S. Minkovska-Dodova (Bulgaria)
B. Adnađević (Serbia)
Members: S. Anić (Serbia), A. Antić-Jovanović (Serbia), A. Clayton (Australia), P. Banković (Serbia), M. Fronczak (Poland), Lj. Gavrilovic (Norway), M. Jeremić (Serbia), E. Kiš (Serbia), A.V. Knyazev (Russia), L.I. László (Hungary), G. Lente (Hungary), S. Macura (USA), Z. Marković (Serbia), K. Novaković (UK), V. Parmon (Russia), D. Peddis (Italy), M.B. Plavšić (Serbia), L. J. Prins (Italy), J. Savović (Serbia), G. Schmitz (Belgium), I. Schreiber (Czech), L. Schreiberova (Czech), D. Stanisavljev (Serbia), N. Stepanov (Russia), Z. Šaponjić (Serbia), S. Tosti (Italy) Á. Tóth (Hungary), N. Vasilyeva (Russia), V. Vukojević (Sweden), A. De Wit (Belgium), A. Yüksel (Türkiye), M. Žabić (Bosnia and Herzegovina)

Local Executive Committee

Chairman: S. N. Blagojević
Vice-chairman: A. Ivanović-Šašić
Members: M. Ajduković, S. Bulatović, J. Dostanić, J. Đuričić-Milanković, M. Jelić, S. Jovanović, Z. Jovanović, N. Jović-Jovičić, B. Marković, J. Maksimović, S. Maćešić, S. Marinović, D. Milenković, T. Mudrinić, N. Nedić, M. Pagnacco, B. Stanković, I. Stefanović, T. Tadić, J. Parlić, M. Pejčić, G. Stevanović, H. Šalipur

SPONSORS

Ministry of Science, Technological Development and Innovation of the Republic of Serbia

Institute of General and Physical Chemistry, Belgrade

University of Belgrade, Institute of Chemistry, Technology and Metallurgy, National Institute of Republic of Serbia, Belgrade

University of Belgrade, Faculty of Physical Chemistry, Belgrade

J. Serb. Chem. Soc. 59(7)403-407(1994)

Professor Slobodanka R. Veljković (1924 – 1989)

HOMAGE TO A GREAT TEACHER



Dr. S. Veljković in Oxford, 1956. It is a curious fact that this is the only photograph found in the files left after her death.

A group of former students and colleagues of the late Professor Slobodanka Veljković decided to mark her 70th brithday by issuing a small collection of scientific papers which should show a cross section of her educational and scientific heritage.

Slobodanka Veljković was born in a small town in central Serbia, Aranđelovac, a picturesque spa. Her father, Radomir, was a high school teacher, teaching chemistry and physics. Her mother, Jelka (maiden name Krunić), died two years after the birth of her only child.

Slobodanka Veljković finished elementary and high school in her place of birth. She studied chemistry at the Faculty of Science of Belgrade University. During her studies she had to work to support herself and her father who was jobless at the time. She graduated in 1950 with flying colours. After graduation she worked for a short while for the pharmaceutial company Galenika, to be sent by decree (as the employment was managed at this time) to the Boris Kidrič Institute of Nuclear

Sciences in Vinča near Belgrade.

In the Chemistry Department, in close collaboration with Professor Pavle Savić, the head of the Department, she worked actively up to 1957, to be elected assistant professor to the Chair of Physical Chemistry of the Faculty of Science, University of Belgrade.* (In many of the following years close collaboration with the Institute was maintained). She was elected to associate professor in 1966 and to full professor in 1973. She served two terms as director of the Institute of Physical Chemistry of the Faculty of Science. She retired in 1983.

Scientific activities

She spent the period of 1954 to 1956 at the University of Oxford, England, working with professor E. J. Bowen. This stay ended with a degree of Doctor of Philosophy. The thesis was entitled "Studies in Fluorescence". She was very proud of the fact that a member of the examining committee was the Nobel Prize holder Sir C. N. Hinshelwood.

The year between 1961 and 1962 was spent fruitfully working with Dr. Garman Harbottle in the field of hot atom chemistry at the Brookhaven National Laboratory, Upton, L. I., New York.

Professor Veljković published a comparatively small number of scientific papers (listed in the Appendix). She was obviously immune to the publish-or-perish spirit. Each paper was being composed seriously and with love. She was also a unique example of a research worker who declined receiving government grants in the last years of scientific acitivity.

As can be seen from the list of papers in the Appendix, they cover chemical kinetics of reactions in homogeneous systems (liquids and solids) and heterogeneous systems (solid – liquid, solid – gas). Generally, changes were studied in relatively simple systems: inorganic salts, oxides and metals, induced by thermal, particulate or radiational stresses. She also initiated investigations of oscillatory chemical reactions, resulting later in a number of papers of the former students. On the low energy side, membrane transport was investigated. At the time of publication, the results were often of a pioneering character, but belonged mostly to the realm of pure science. An unexpected result, which led to a straightforward and very effective practical application (Refs. 7 – 9), was the production of pure and carrier-free phosphorus-32. The developed procedure found applications in many isotope-producing centres in the world.

In 1961 Professor Veljković received the "Award of the 7th of July" given by the Republic of Serbia to its most outstanding intellectuals. She was also decorated in 1987 with the "Order of Labour with the Silver Wreath", a rather high-ranking decoration.

Educational activities

Following her arrival at the Institute of Physical Chemistry Professor Veljković taught Radiochemistry for a short while. The main subject of her interest was chemical

---

* Her father, Radomir, held the position of instructor of the same institution during the periods 1919 to 1923 and 1931 to 1934.

kinetics. She devoted most of her activities to this work and wrote the first textbook on this subject (two editions), which is still in full use by the students of Physical Chemistry.

Professor Veljković founded the Chair on Molecular Structures. She felt the acute deficiency of theoretical subjects in the curriculum. Even though she had no adequate training in the theoretical field, she prepared and organised the sending of talented students to foreign scientific institutions and universities to acquire the lacking knowledge. As time passed, new subjects emerged in the curriculum: Chemical Reactivity, Statistical Thermodynamics, Non-Equilibrium Thermodynamics, Quantum Chemistry, Theory of Nucleation, Catalysis, Computer Programming, *etc.* The students enthusiastically accepted these courses. (Some results of this effort can be directly seen in some of the articles written for this issue of the *Journal*).

A number of her students later developed into research workers with 25 Master and ten Doctoral degrees all supervised by Prof. Veljković.

Private life

Slobodanka was tall and slender, somehow stiff looking. When communicating with colleagues she always kept a certain distance, if nothing by maintaining the formal address "vi" (the equivalent of the French "vous").* (By the way, this was also her relationship to her own father!). This psychological guard could, however, not hide an inner warmth, a love for the people surrounding her. She was an extraordinarily honest person.

Professor Veljković had no children of her own. The longing for offspring transformed into a great affection for her students whom she always called "my children".

She died of cancer in 1989. It turned out that she had no relatives at all and only her former students were caring for her to the very end. In her will she bequeathed all her property to the Serbian Orthodox Church.

S. R. Anić, V. Dondur, S. V. Ribnikar

Appendix

List of published papers

1. S. Veljković: The photolysis of $Co[(NH_3)_6(NO_3)_3]$, *Rec. Trav. Inst. Rech. Struct. Matière* **2** (1953) 93
2. S. Veljković: Kinetics of the photolysis of $Co[(NH_3)_6(NO_3)_3]$, *Bull. Inst. Boris Kidrich* **4** (1954) 63
3. E. J. Bowen, S. Veljković: The enhancement of the fluorescence of vapours, *Proc. Roy. Soc.* **236A** (1956) 1
4. S. Veljković: Red shifts in the spectra of anthracene derivatives, *Trans. Faraday Soc.* **53** (1957) 1181
5. S. Veljković: The influence of the environment on the process of deactivation of excited molecules. *Studies of Fluorescence*, University of Oxford, St. Anne's College, Trinity Term, 1956 (D. Phil. Thesis)
6. S. Veljković: Kinetics of the reactions of radiobromine activated by $^{81}Br(n,gamma)^{82}Br$ process in aryl bromides. *Bull. Inst. Boris Kidrich* **7** (1957) 65

---

* The third undersigned, S. V. R., was one of the very few persons who could address her with the informal "ti" (like the French "tu").

7. S. Veljković, S. Milenković: Concentration in carrier-free radioisotopes by adsorption on alumina. *Second UN Conference on Peaceful Uses of Atomic Energy*, Proceedings, Vol. 20, p. 46, Geneva 1958
8. S. Veljković, S. Milenković: Concentration of carrier-free phosphorus by adsorption on alumina. *Bull. Inst. Boris Kidrich* **10** (1960) 61
9. S. Veljković, S. Milenković: Separation of P-32 from S-35 and some other anions on MgO. *Bull. Inst. Boris Kidrich* **10** (1960) 71
10. S. Veljković, J. Stevović: Stabilization of the colloidal Au-198, *Bull. Inst. Boris Kidrich* **10** (1960) 75
11. S. Veljković, S. Milenković, O. Mićić: Activated exchange in inorganic crystals, *Chemical Effects of Nuclear Transformations*, IAEA, Vienna 1961, p. 465
12. S. Veljković, G. Harbottle: Low temperature investigations of the Szilard-Chalmers reactions in potassium permanganate. *J. Inorg. Nucl. Chem* **23** (1961) 159
13. S. Veljković, G. Harbottle: Recoil-atom reactions at low temperature, *Nature* **191** (1961) 1287
14. G. Harbottle, S. Veljković, Low temperature studies of recoil reactions, *J. Inorg. Nucl. Chem.* **24** (1962) 1517
15. S. Veljković, N. Milašin: Radiation damage in molybdenum and tungsten in high neutron fluxes, *Bull. Inst. Boris Kidrich* **15** (1964) 63
16. J. Stevović, Lj. Jaćimović, S. Veljković: The behavior of radioiodine in TeO_2, *J. Inorg. Nucl. Chem.* **27** (1965) 29
17. S. Veljković, S. Milenković, M. Ratković: The behavior of recoil Cr-51 in chromates deposited on MgO, *J. Inorg. Nucl. Chem.* **27** (1965) 266
18. Lj. Jaćimović, J. Stevović, S. Veljković: Post-irradiation behavior of I-131 in TeO_2, *Chemical Effects of Nuclear Reactions and Radioactive Transformations*, Vol. 2, IAEA, Vienna, 1965, p. 523
19. S. Veljković, S. Milenković, M. Ratković: Recoil processes of Cr-51 in mixed inorganic systems, *ibid.* p. 267
20. S. Milenković, S. Veljković: Recoil processes of chromium-51 in K_2CrO_4 mixed with alkali chlorides, *Radiochim. Acta* **8** (1967) 146
21. Lj. Jaćimović, J. Stevanović, S. Veljković, N. Ajdačić: Adsorption of phosphates on alumina irradiated by neutrons and gamma-rays, *Radiochim. Acta.* **12** (1969) 49
22. S. Stanković, S. Veljković: Upotreba kompleksirajućih jedinjenja kao zaštitnih sredstava pri kontaminaciji organskih membrana, *Acta Veterinaria* **18** (1968) 203
23. E. Bogdanović, S. Veljković: L'analyse radiochimique des composées du zinc après l'irradiation en pile, *Radiochim. Acta* **11** (1969) 94
24. S. Veljković, A. Šćepanović, V. Stefanović: Radiation damage in steel with medium and high carbon content, *Bull. Inst. Boris Kidrich* **17** (1966) 77
25. M. Schara, M. Šentjurc, S. Milenković, S. Veljković: ESR measurements of irradiated anion doped potassium chromate, *J. Inorg. Nucl. Chem.* **32** (1970) 369
26. S. Veljković: The annealing kinetics of recoil atoms in solids, *Phil. Mag.* **21** (1970) 627
27. S. Milenković, S. Bingulac, S. Veljković: Reaction models for the annealing of recoil atoms in solids, *J. Inorg. Nucl. Chem* **33** (1971) 1187
28. S. Kapor, Lj. Anić, A. Žeželj, U. Mioč, S. Veljković: Gas adsorption chromatography of the organic vapours on inorganic salts modified alumina, *Ber. Bunsen Ges. Phys. Chem.* **75** (1971) 1127
29. Lj. Jaćimović, J. Stevović, S. Veljković: Kinetics of adsorption of mineral acids on alumina, *J. Phys. Chem.* **76** (1972) 3625
30. S. Milenković, S. Veljković: ESR and chemical behavior of anion doped potassium chromate, *J. Inorg. Nucl. Chem.* **36** (1974) 683
31. Lj. Jaćimović, J. Stevović, S. Veljković, M. Galonja: Adsorption of mineral acids on alumina irradiated in the nuclear reactor, *Isotopenpraxis* **10** (1974) 224
32. Lj. Kolar-Anić, S. Veljković, S. Kapor, B. Dubljević: The Weibull distribution and kinetics of heterogeneous processes, *J. Chem. Phys.* **63** (1975) 663
33. Lj. Kolar-Anić, S. Veljković: Statistical foundations of heterogeneous kinetics, *J. Chem. Phys.* **63** (1975) 669
34. S. Veljković, P. Bibović: Growth and composition of Al clusters on NaCl, *Vacuum* **27** (1977) 141
35. L. Mihovilović, S. Veljković: Kinetički aspekti rastvaranja Al_2O_3 u kiselinama, *Glasnik Hem. društva Beograd* **43** (1978) 449
36. S. Veljković, L. Mihovilović, P. Tufegdžić: Specifičnosti u kinetici rastvaranja TiO, *Glasnik Hem. društva Beograd* **44** (1979) 587

37. S. Veljković: Nuclear transformations and correlation effects in solids, *Glasnik Hem. društva Beograd* **45**(1980) 131
38. M. Mladenović, S. Veljković: Tok hemijske reakcije na primeru monomolekulskih reakcija, *Glasnik Hem. društva Beograd* **45** (1980) 461
39. S. Veljković: Heterogeneity and rate modifications of the Bray-Liebhafsky reaction, *Glasnik Hem. društva Beograd* **46** (1981) 711.

(*Text is reproduced with permission from J Serb Chem Soc*)

PL *– Plenary lectures*

TOWARDS ACTIVE MATTER: DRIVING CHEMICAL SYSTEMS AWAY FROM EQUILIBRIUM

L. J. Prins

University of Padova, Department of Chemical Sciences, Via Marzolo 1, 35131 Padova, Italy (leonard.prins@unipd.it)

DOI: https://doi.org/10.46793/Phys.Chem24I.003P

ABSTRACT

The development of synthetic active matter requires the ability to rationally design materials capable of harnessing energy from a source to carry out work.[1,2] Nature achieves this using metabolic cycles in which energy released from an exergonic chemical reaction, e.g. ATP hydrolysis, is used to drive endergonic biochemical processes. Extensive theoretical and experimental studies on synthetic molecular machinery have demonstrated that energy and information ratchet mechanisms play an essential role in transferring energy from the energy source to the system.[3, 4] Recently, it has been understood that these mechanisms can also be exploited for the development of active matter [5, 6]. Here, we report our progress made on the use of energy and information ratchet mechanisms for the synthesis of high-energy molecular structures [8, 9].

Acknowledgment

Funding from MUR (2022TSB8P7 and P2022ANCEK) and the University of Padova (P-DiSC #CASA-BIRD2022-UNIPD) is acknowledged.

REFERENCES

[1] C. Cheng, P.R. McGonigal, J.F. Stoddart, R.D. Astumian, ACS Nano 9 (2015) 8672–8688.
[2] A. Walther, Adv. Mater. 32 (2020) 1–10.
[3] E.R. Kay, D.A. Leigh, F. Zerbetto, Chem. Int. Ed., 46 (2007) 72-191.
[4] Y. Feng, M. Ovalle, J.S.W. Seale, C.K. Lee, D.J. Kim, R.D. Astumian, J.F. Stoddart, J. Am. Chem. Soc., 143 (2021) 5569–5591.
[5] G. Ragazzon, L.J. Prins, Nat. Nanotechnol., 13 (2018) 882–889.
[6] K. Das, L. Gabrielli, L.J. Prins, Angew. Chem. Int. Ed., 60 (2021) 20120-20143.
[7] T. Marchetti, D. Frezzato, L. Gabrielli, L.J. Prins, Angew.Chem.Int.Ed. 2023, e202307530
[8] (+) T. Marchetti, (+) B.W.M. Roberts, D. Frezzato, L.J. Prins, Angew.Chem.Int.Ed 2024, e202402965. (+) both authors contributed equally.

ANALYTICAL SOLUTION FOR MULTISTEP SCHEMES IN REACTION KINETICS

G. Lente

University of Pécs, Institute of Chemistry,
Ifjúság útja 6, H-7624, Hungary. (lenteg@gamma.pte.ttk.hu)

DOI: https://doi.org/10.46793/Phys.Chem24I.005L

ABSTRACT

Exact analytical solutions of a number of multistep kinetic schemes are presented for cases when at least one of the reactions in a sequence is not a simple first order process. These solutions, given by closed formulas, are superior to the commonly used numerical solutions in any system but sometimes necessitate the knowledge of some special functions, which usually appear in the theory of second order ordinary differential equations, e.g. exponential integral function, hypergeometric function, Legendre function, incomplete gamma function. The systems for which these analytical solutions are available usually do not include any reversible elements, with the exception of systems with a reversible reaction that is first order in both directions.

INTRODUCTION

The solution of systems of ordinary differential equations describing the time dependence of all concentration is a scheme is a central problem in chemical kinetics. Whilst analytical formulas are available for basically all single-step schemes [1-3], even if the reaction is reversible, multi-step schemes that are important in a huge number of practical problems [4-16] seldom have routinely used symbolic solutions. The only exception is when a reaction network features solely first order processes (reversible or unidirectional), a case for which a general solution, basically comprising suitable combinations of exponential functions, has been known for quite some time [2,17-20].

This contribution shows analytical solutions for a number of two-step schemes, which involve at least one process that is not first order [21-23]. The systems dealt with here will be limited to those that contain the combinations of first and second order elementary reactions only, and the solutions will be stated for a minimal number of components from which all the others can be given using the law of mass conservation. Some mathematical results involving zeroth order and third order processes are available [21-25], but these are less common in the practice of chemical kinetics.

RESULTS AND DISCUSSION

The **first system** to be handled is when the first step is a second order process, which is followed by a first order second reaction. The kinetic scheme has the following form:

$$2\mathrm{A} \xrightarrow{k_1} \mathrm{B} \xrightarrow{k_2} \mathrm{C}$$

The simultaneous differential equations for the concentrations are as follows:

$$\frac{\mathrm{d[A]}}{\mathrm{d}t} = -2k_1[\mathrm{A}]^2$$

$$\frac{\mathrm{d[B]}}{\mathrm{d}t} = k_1[\mathrm{A}]^2 - k_2[\mathrm{B}]$$

$$\frac{\mathrm{d[C]}}{\mathrm{d}t} = k_2[\mathrm{B}]$$

The solution for the independent components is:

$$[\mathrm{A}](t) = \frac{[\mathrm{A}]_0}{1 + 2k_1[\mathrm{A}]_0 t}$$

$$[\mathrm{B}](t) = \frac{4k_1[\mathrm{B}]_0 + 2k_1[\mathrm{A}]_0 - k_2 \mathrm{e}^{-k_2/(2k_1[\mathrm{A}]_0)}\,\mathrm{Ei}\left(\frac{k_2}{2k_1[\mathrm{A}]_0}\right)}{4k_1}\mathrm{e}^{-k_2 t} + \frac{-2k_1[\mathrm{A}]_0 + k_2 \mathrm{e}^{-k_2 t - k_2/(2k_1[\mathrm{A}]_0)}(1 + 2k_1[\mathrm{A}]_0 t)\,\mathrm{Ei}\left(k_2 t + \frac{k_2}{2k_1[\mathrm{A}]_0}\right)}{4k_1(1 + 2k_1[\mathrm{A}]_0 t)}$$

In this equation, Ei denotes the exponential integral function, which is defined for real numbers as follows:

$$\mathrm{Ei}(a) = -\int_{-a}^{\infty} \frac{\mathrm{e}^{-\tau}}{\tau}\mathrm{d}\tau$$

The **second system** displayed here is when a mixed second order process is followed by a first order decay. A mixed second order step is one in which two different molecules (rather than two identical molecules in the 'normal' second order case) react to give some sort of a product. So a mixed second order step followed by a first order reaction is represented by the following scheme:

$$\mathrm{A}_1 + \mathrm{A}_2 \xrightarrow{k_1} \mathrm{B} \xrightarrow{k_2} \mathrm{C}$$

This is probably the most important two-stage consecutive schemes of all, as the underlying concept is that two different reactants (A_1 and A_2) give final product C through the intervention of intermediate B. In this case, four concentrations are involved and the differential equations are as follows:

$$\frac{\mathrm{d}[\mathrm{A}_1]}{\mathrm{d}t} = -k_1[\mathrm{A}_1][\mathrm{A}_2]$$

$$\frac{\mathrm{d}[\mathrm{A}_2]}{\mathrm{d}t} = -k_1[\mathrm{A}_1][\mathrm{A}_2]$$

$$\frac{\mathrm{d}[\mathrm{B}]}{\mathrm{d}t} = k_1 k_1[\mathrm{A}_1][\mathrm{A}_2] - k_2[\mathrm{B}]$$

$$\frac{\mathrm{d}[\mathrm{C}]}{\mathrm{d}t} = k_2[\mathrm{B}]$$

Again, the solutions are only given for $[A_1]$ and [B], the rest can be calculated from simple conservation equations:

$$[\mathrm{A}_1](t) = \frac{([\mathrm{A}_2]_0 - [\mathrm{A}_1]_0)[\mathrm{A}_1]_0}{[\mathrm{A}_2]_0 \mathrm{e}^{([\mathrm{A}_2]_0 - [\mathrm{A}_1]_0)k_1 t} - [\mathrm{A}_1]_0}$$

$$[\mathrm{B}](t) = [\mathrm{B}]_0 \mathrm{e}^{-k_2 t} + [\mathrm{A}_1]_0 \mathrm{e}^{-k_2 t} - \frac{k_2[\mathrm{A}_1]_0([\mathrm{A}_2]_0 - [\mathrm{A}_1]_0)\,H(0)}{[\mathrm{A}_2]_0(k_1[\mathrm{A}_1]_0 - k_1[\mathrm{A}_2]_0 + k_2)}\mathrm{e}^{-k_2 t} + \frac{[\mathrm{A}_1]_0([\mathrm{A}_2]_0 - [\mathrm{A}_1]_0)\mathrm{e}^{([\mathrm{A}_1]_0 - [\mathrm{A}_2]_0)k_1 t}}{[\mathrm{A}_1]_0 \mathrm{e}^{([\mathrm{A}_1]_0 - [\mathrm{A}_2]_0)k_1 t} - [\mathrm{A}_2]_0} + \frac{k_2[\mathrm{A}_1]_0([\mathrm{A}_2]_0 - [\mathrm{A}_1]_0)\mathrm{e}^{([\mathrm{A}_1]_0 - [\mathrm{A}_2]_0)k_1 t}\,H(t)}{[\mathrm{A}_2]_0(k_1[\mathrm{A}_1]_0 - k_1[\mathrm{A}_2]_0 + k_2)}$$

$$H(t) = {}_2F_1\left(1,\ 1+\frac{k_2}{k_1([A_1]_0-[A_2]_0)},\ 2+\frac{k_2}{k_1([A_1]_0-[A_2]_0)},\ \frac{[A_1]_0}{[A_2]_0}e^{([A_1]_0-[A_2]_0)k_1t}\right)$$

The notation ${}_2F_1$ means the first hypergeometric function, which is primarily known from the theory of second-order ordinary differential equations. There is a notable singular case here where the above stated solution cannot be used, this is when $k_2 = ik_1([A_2]_0 - [A_1]_0)$ (i is a positive integer). This special case is analyzed in an earlier publication [21].

The **third system** to be analyzed here is when the first step is first order, whereas the second one is second order. The scheme is described as follows:

$$A \xrightarrow{k_1} B$$
$$2B \xrightarrow{k_2} C$$

The simultaneous differential equations based on this scheme can be given as:

$$\frac{d[A]}{dt} = -k_1[A]$$
$$\frac{d[B]}{dt} = k_1[A] - 2k_2[B]^2$$
$$\frac{d[C]}{dt} = k_2[B]^2$$

The first equation in this series is a well-known first order rate equation, the solution of which is available in almost any textbook on chemical kinetics [1, 21]:

$$[A] = [A]_0e^{-k_1t}$$

$$[B] = \sqrt{\frac{k_1[A]_0e^{-k_1t}}{2k_2}}\frac{2K_1\left(\sqrt{8k_2[A]_0e^{-k_1t}/k_1}\right) - \omega I_1\left(\sqrt{8k_2[A]_0e^{-k_1t}/k_1}\right)}{2K_0\left(\sqrt{8k_2[A]_0e^{-k_1t}/k_1}\right) + \omega I_0\left(\sqrt{8k_2[A]_0e^{-k_1t}/k_1}\right)}$$
$$\omega = \frac{\sqrt{8[A]_0/(k_2/k_1)}K_1\left(\sqrt{8(k_2/k_1)[A]_0}\right) - 4[B]_0K_0\left(\sqrt{8(k_2/k_1)[A]_0}\right)}{\sqrt{2[A]_0/(k_2/k_1)}I_1\left(\sqrt{8(k_2/k_1)[A]_0}\right) + 2[B]_0I_0\left(\sqrt{8(k_2/k_1)[A]_0}\right)}$$

In these equations, I_1 and I_0 are modified Bessel functions of the first kind, whereas K_1 and K_0 are modified Bessel function of the second kind.

In the **fourth system** of interest, a second order process is followed by a second order process. The scheme is, therefore:

$$2A \xrightarrow{k_1} B$$
$$2B \xrightarrow{k_2} C$$

The simultaneous differential equations that can be written based on this scheme take the following form:

$$\frac{d[A]}{dt} = -2k_1[A]^2$$
$$\frac{d[B]}{dt} = k_1[A]^2 - 2k_2[B]^2$$
$$\frac{d[C]}{dt} = k_2[B]^2$$

The solution for the concentration of A and B is as follows:

$$[A] = \frac{[A]_0}{1 + 2k_1[A]_0t}$$

$$[\mathrm{B}] = \frac{k_1[\mathrm{A}]_0}{2k_2} \frac{(1+\alpha)(\sqrt{1+2k_1[\mathrm{A}]_0 t})^{-1+\alpha} + \omega(1-\alpha)(\sqrt{1+2k_1[\mathrm{A}]_0 t})^{-1-\alpha}}{(\sqrt{1+2k_1[\mathrm{A}]_0 t})^{1+\alpha} + \omega(\sqrt{1+2k_1[\mathrm{A}]_0 t})^{1-\alpha}}$$

$$\omega = \frac{1+\alpha-(\alpha-1)(\alpha+1)[\mathrm{B}]_0/[\mathrm{A}]_0}{(\alpha-1)(\alpha+1)[\mathrm{B}]_0/[\mathrm{A}]_0 + \alpha - 1}$$

In the **fifth system**, a mixed second order first step precedes a second order process:

$$\mathrm{A_1} + \mathrm{A_2} \xrightarrow{k_1} \mathrm{B}$$

$$2\mathrm{B} \xrightarrow{k_2} \mathrm{C}$$

The rate equations are given as follows:

$$\frac{\mathrm{d}[\mathrm{A_1}]}{\mathrm{d}t} = -k_1[\mathrm{A_1}][\mathrm{A_2}]$$

$$\frac{\mathrm{d}[\mathrm{A_2}]}{\mathrm{d}t} = -k_1[\mathrm{A_1}][\mathrm{A_2}]$$

$$\frac{\mathrm{d}[\mathrm{B}]}{\mathrm{d}t} = k_1[\mathrm{A_1}][\mathrm{A_2}] - 2k_2[\mathrm{B}]^2$$

$$\frac{\mathrm{d}[\mathrm{C}]}{\mathrm{d}t} = k_2[\mathrm{B}]^2$$

The solution for the independent concentrations is given as:

$$\Delta = [\mathrm{A_2}]_0 - [\mathrm{A_1}]_0$$

$$[\mathrm{A_1}] = \frac{\Delta[\mathrm{A_1}]_0}{[\mathrm{A_2}]_0 \mathrm{e}^{\Delta k_1 t} - [\mathrm{A_1}]_0}$$

$$[\mathrm{B}] = \frac{\Delta + 2[\mathrm{A_1}]}{2\alpha} - \frac{\Delta\omega P_{\alpha+1}\left(1+\frac{2[\mathrm{A_1}]}{\Delta}\right) + \Delta Q^0_{\alpha+1}\left(1+\frac{2[\mathrm{A_1}]}{\Delta}\right)}{2\alpha\omega P_\alpha\left(1+\frac{2[\mathrm{A_1}]}{\Delta}\right) + 2\alpha Q^0_\alpha\left(1+\frac{2[\mathrm{A_1}]}{\Delta}\right)}$$

$$\omega = \frac{\Delta Q^0_{\alpha+1}(x_0) - \Delta x_0 Q^0_\alpha(x_0) + 2[\mathrm{B}]_0 \alpha Q^0_\alpha(x_0)}{\Delta x_0 P_\alpha(x_0) - \Delta P_{\alpha+1}(x_0) - 2[\mathrm{B}]_0 \alpha P_\alpha(x_0)} \qquad \alpha = \frac{\sqrt{8\left(\frac{k_2}{k_1}\right)+1}-1}{2} \qquad x_0 = 1 + \frac{2[\mathrm{A_1}]_0}{\Delta}$$

In these formulas, $P_\alpha(x)$ represents the Legendre function of the first kind, whereas $Q_\alpha{}^0(x)$ is the associated Legendre function of the second kind type 3. An obvious special case here is $\Delta = 0$ (i.e. $[\mathrm{A_2}]_0 = [\mathrm{A_1}]_0$), which leads back directly to the solution of the fourth case [22].

In the **sixth system**, a first order reaction is followed by a mixed second order process:

$$\mathrm{A} \xrightarrow{k_1} \mathrm{B_1}$$

$$\mathrm{B_1} + \mathrm{B_2} \xrightarrow{k_2} \mathrm{C}$$

The relevant system of differential equations looks like this:

$$\frac{\mathrm{d}[\mathrm{A}]}{\mathrm{d}t} = -k_1[\mathrm{A}]$$

$$\frac{\mathrm{d}[\mathrm{B_1}]}{\mathrm{d}t} = k_1[\mathrm{A}] - k_2[\mathrm{B_1}][\mathrm{B_2}]$$

$$\frac{\mathrm{d}[\mathrm{B_2}]}{\mathrm{d}t} = -k_2[\mathrm{B_1}][\mathrm{B_2}]$$

$$\frac{\mathrm{d}[\mathrm{C}]}{\mathrm{d}t} = k_2[\mathrm{B_1}][\mathrm{B_2}]$$

The solutions is as follows:

$$[\mathrm{A}] = [\mathrm{A}]_0 \mathrm{e}^{-k_1 t}$$

$$\Delta = [\mathrm{A}]_0 + [\mathrm{B}_1]_0 - [\mathrm{B}_2]_0$$

$$[B_2] = \frac{[\mathrm{B}_2]_0 \mathrm{e}^{-k_2 \Delta t - k_2 [\mathrm{A}]_0 (\mathrm{e}^{-k_1 t} - 1)/k_1}}{1 + [\mathrm{B}_2]_0 [\mathrm{A}]_0^{-k_2 \Delta / k_1} \mathrm{e}^{k_2 [\mathrm{A}]_0 / k_1} (k_2/k_1)^{1 - k_2 \Delta / k_1} G_1(t)}$$

$$G_1(t) = \Gamma(k_2 \Delta / k_1, k_2 [\mathrm{A}]_0 \mathrm{e}^{-k_1 t}/k_1) - \Gamma(k_2 \Delta / k_1, k_2 [\mathrm{A}]_0 / k_1)$$

Here Γ denotes the upper incomplete gamma function, which is defined as follows:

$$\Gamma(\alpha, x) = \int_x^\infty \tau^{\alpha - 1} \mathrm{e}^{-\tau} \mathrm{d}\tau$$

In the **seventh system**, a second order step is the first, whereas a mixed second order step is the second:

$$2\mathrm{A} \xrightarrow{k_1} \mathrm{B}_1$$

$$\mathrm{B}_1 + \mathrm{B}_2 \xrightarrow{k_2} \mathrm{C}$$

The differential equation for the individual concentrations are:

$$\frac{\mathrm{d}[\mathrm{A}]}{\mathrm{d}t} = -2k_1 [\mathrm{A}]^2$$

$$\frac{\mathrm{d}[\mathrm{B}_1]}{\mathrm{d}t} = k_1 [\mathrm{A}]^2 - k_2 [\mathrm{B}_1][\mathrm{B}_2]$$

$$\frac{\mathrm{d}[\mathrm{B}_2]}{\mathrm{d}t} = -k_2 [\mathrm{B}_1][\mathrm{B}_2]$$

$$\frac{\mathrm{d}[\mathrm{C}]}{\mathrm{d}t} = k_2 [\mathrm{B}_1][\mathrm{B}_2]$$

The solutions is given by the following formulas:

$$[\mathrm{A}] = \frac{[\mathrm{A}]_0}{1 + 2k_1 [\mathrm{A}]_0 t}$$

$$\Delta = [\mathrm{A}]_0/2 + [\mathrm{B}_1]_0 - [\mathrm{B}_2]_0$$

$$[\mathrm{B}_2] = \frac{[\mathrm{B}_2]_0 (1 + 2k_1 [\mathrm{A}]_0 t)^{k_2/(4k_1)} \mathrm{e}^{-k_2 \Delta t}}{1 + [\mathrm{B}_2]_0 \Delta^{-1 - k_2/(4k_1)} [\mathrm{A}]_0^{k_2/(4k_1)} (k_2/2k_1)^{-k_2/(4k_1)} \mathrm{e}^{k_2 \Delta/(2k_1 [\mathrm{A}]_0)} G_2(t)}$$

$$G_2(t) = \Gamma\left(\frac{k_2}{4k_1} + 1, \frac{k_2 \Delta}{2k_1 [\mathrm{A}]_0}\right) - \Gamma\left(\frac{k_2}{4k_1} + 1, \frac{k_2 \Delta}{2k_1 [\mathrm{A}]_0} + k_2 \Delta t\right)$$

In the **eighth system**, two mixed second order reactions are combined:

$$\mathrm{A}_1 + \mathrm{A}_2 \xrightarrow{k_1} \mathrm{B}_1$$

$$\mathrm{B}_1 + \mathrm{B}_2 \xrightarrow{k_2} \mathrm{C}$$

The ordinary differential equation characterizing this system are given as:

$$\frac{\mathrm{d}[\mathrm{A}_1]}{\mathrm{d}t} = -k_1 [\mathrm{A}_1][\mathrm{A}_2]$$

$$\frac{\mathrm{d}[\mathrm{A}_2]}{\mathrm{d}t} = -k_1 [\mathrm{A}_1][\mathrm{A}_2]$$

$$\frac{\mathrm{d[B_1]}}{\mathrm{d}t} = k_1[\mathrm{A_1}][\mathrm{A_2}] - k_2[\mathrm{B_1}][\mathrm{B_2}]$$
$$\frac{\mathrm{d[B_2]}}{\mathrm{d}t} = -k_2[\mathrm{B_1}][\mathrm{B_2}]$$
$$\frac{\mathrm{d[C]}}{\mathrm{d}t} = k_2[\mathrm{B_1}][\mathrm{B_2}]$$

Here the solutions for the independent concentrations are given by the following formulas:

$$\Omega = [\mathrm{A_2}]_0 - [\mathrm{A_1}]_0$$
$$[\mathrm{A_1}] = \frac{\Omega[\mathrm{A_1}]_0}{([\mathrm{A_1}]_0 + \Omega)\mathrm{e}^{\Omega k_1 t} - [\mathrm{A_1}]_0}$$
$$\Delta = [\mathrm{A_1}]_0 + [\mathrm{B_1}]_0 - [\mathrm{B_2}]_0$$
$$[\mathrm{B_2}] = \frac{[\mathrm{B_2}]_0 \left(\frac{\Omega}{S}\right)^{\alpha} \left(\frac{S}{\Omega \mathrm{e}^{k_1 \Omega t}}\right)^{\alpha+\beta}}{1 + \frac{[\mathrm{B_2}]_0}{\Delta}\left(\frac{[\mathrm{A_1}]_0 + \Omega}{\Omega}\right)^{\alpha+\beta} G_3(t)}$$
$$G_3(t) = {}_2F_1\left(\alpha, \alpha+\beta+1, \alpha+1, -\frac{[\mathrm{A_1}]_0}{\Omega}\right) - \left(\frac{\Omega}{S}\right)^{\alpha} {}_2F_1\left(\alpha, \alpha+\beta+1, \alpha+1, -\frac{[\mathrm{A_1}]_0}{S}\right)$$
$$S = ([\mathrm{A_1}]_0 + \Omega)\mathrm{e}^{k_1 \Omega t} - [\mathrm{A_1}]_0 \qquad \alpha = k_2\Delta/(k_1\Omega) \qquad \beta = k_2/k_1$$

The function ${}_2F_1$ in is the hypergeometric function again. This type of two-step scheme has some interesting stoichiometric variations, which are fully analyzed in an earlier article [23].

The **ninth system** is the first one to include an element a reversibility: a second order process feeds its product into a reversible first order reaction. The scheme is:

$$\mathrm{C} \xrightarrow{k_2} \mathrm{A} \underset{k_{-1}}{\overset{k_1}{\rightleftharpoons}} \mathrm{B}$$

The ordinary differential equations are:

$$\frac{\mathrm{d[A]}}{\mathrm{d}t} = -k_1[\mathrm{A}] + k_{-1}[\mathrm{B}] + k_2[\mathrm{C}]^2$$
$$\frac{\mathrm{d[B]}}{\mathrm{d}t} = k_1[\mathrm{A}] - k_{-1}[\mathrm{B}]$$
$$\frac{\mathrm{d[C]}}{\mathrm{d}t} = -2k_2[\mathrm{C}]^2$$

The solution for the two independent concentrations is:

$$[\mathrm{C}] = \frac{[\mathrm{C}]_0}{1 + 2k_2[\mathrm{C}]_0 t}$$
$$[\mathrm{A}] = \frac{k_1[\mathrm{A}]_0 - k_{-1}[\mathrm{B}]_0 + k_1\frac{[\mathrm{C}]_0}{2}}{k_1 + k_{-1}} \mathrm{e}^{-(k_1+k_{-1})t} - \frac{[\mathrm{C}]_0}{2 + 4k_2[\mathrm{C}]_0 t} +$$
$$\frac{k_1}{4k_2} \mathrm{e}^{-(k_1+k_{-1})\left(t + \frac{1}{2k_2[\mathrm{C}]_0}\right)} \left[\mathrm{Ei}\left(\frac{(k_1+k_{-1})(1+2k_2[\mathrm{C}]_0 t)}{2k_2[\mathrm{C}]_0}\right) - \mathrm{Ei}\left(\frac{k_1+k_{-1}}{2k_2[\mathrm{C}]_0}\right)\right]$$
$$+ \frac{k_{-1}}{k_1 + k_{-1}}\left([\mathrm{A}]_0 + [\mathrm{B}]_0 + \frac{[\mathrm{C}]_0}{2}\right)$$

Here Ei means the exponential integral function, as defined earlier.

The **tenth** and final **system** is when a mixed second order process feeds its product into a reversible first order reaction:

$$\mathrm{C{+}D} \xrightarrow{k_2} \mathrm{A} \underset{k_{-1}}{\overset{k_1}{\rightleftharpoons}} \mathrm{B}$$

The ordinary differential equations take the following form:

$$\frac{d[A]}{dt} = -k_1[A] + k_{-1}[B] + k_2[C][D]$$

$$\frac{d[B]}{dt} = k_1[A] - k_{-1}[B]$$

$$\frac{d[C]}{dt} = -k_2[C][D]$$

$$\frac{d[D]}{dt} = -k_2[C][D]$$

The solution for the independent concentrations is:

$$[C] = \frac{([D]_0 - [C]_0)[C]_0}{[D]_0 e^{([D]_0 - [C]_0)k_2 t} - [C]_0}$$

CONCLUSION

To our knowledge, we are the first to report changes in the expression of synapse-located proteins in rats following chronic oral d-gal treatment. Our results represent valuable data guiding us into further research on region-specific modulation of NMDA receptors in the aging brain.

Acknowledgment

The research was funded by project no. RRF-2.3.1-21-2022-00009, titled National Laboratory for Renewable Energy, which has been implemented with the support provided by the Recovery and Resilience Facility of the European Union within the framework of Programme Széchenyi Plan Plus.

REFERENCES

[1] Z. Szabó in: Comprehensive Chemical Kinetics, Vol. 2, C. H. Bamford, C. F. H Tipper (Eds.), Elsevier, Amsterdam, 1969.
[2] P. Érdi, J. Tóth, Mathematical Models of Chemical Reactions, Manchester University Press, Manchester, 1989.
[3] J. H. Espenson, Chemical Kinetics and Reaction Mechanisms, 2nd ed, McGraw-Hill, New York, 1995.
[4] G. Lente, I. Fábián, Inorg. Chem., 37 (1998) 4204.
[5] G. Lente, I. Fábián, Inorg. Chem., 38 (1999) 603.
[6] J. Jacob, G. Lente, I. A. Guzei, J. H. Espenson, Inorg. Chem., 38 (1999) 376
[7] G. Lente, J. H. Espenson, Inorg. Chem., 39 (2000) 4809.
[8] G. Lente, J. H. Espenson, Chem. Commun., (2003) 1162.
[9] M. Galajda, G. Lente, I. Fábián, J. Am. Chem. Soc., 129 (2007) 603.
[10] M. Gombár, É. Józsa, M. Braun, K. Ősz, Photochem. Photobiol. Sci., 11 (2012) 1592.
[11] T. Lehóczki, É. Józsa, K. Ősz, J. Photochem. Photobiol. A Chem., 251 (2013) 63.
[12] V. Kiss, G. Lehoczki, K. Ősz, Photochem. Photobiol. Sci., 16 (2017) 519.
[13] V. Kiss, K. Ősz, Int. J. Chem. Kinet., 49 (2017) 602.
[14] É. Józsa, V. Kiss, K. Ősz, J. Photochem. Photobiol. A Chem., 360 (2018) 166.
[15] J. Michnyóckzy, V. Kiss, K. Ősz, J. Photochem. Photobiol. A Chem., 408 (2021) 113110.
[16] É. Józsa, L. B. Jenei, T: Kégl, K. Ősz, J. Mol. Struc., 1261 (2022) 132916.
[17] J. Z. Hearon, Bull. Math. Biophys., 15 (1953) 121.
[18] J. Radcliffe, P. J. Staff, J. Appl. Probab., 6 (1969) 186.
[19] J. A. Jacquez, C. P. Simon, SIAM Review, 35 (1993) 43.

[20] R. Tóbiás, L. L. Stacho, G. Tasi, J. Math. Chem., 54 (2016) 1863.
[21] G. Lente, J. Math. Chem., 53 (2015) 1179.
[22] G. Lente, J. Math. Chem., 53 (2015) 1759.
[23] G. Lente, J. Math. Chem., 55 (2017) 832.
[24] A. P. Paz, ChemRxiv, (2024) 10.26434/chemrxiv-2024-6kdjr.
[25] A. P. Paz, ChemRxiv, (2024) 10.26434/chemrxiv-2024-pt550.

TARGETING OXIDATIVE STRESS IN DISEASE: A PHYSICOCHEMICAL PERSPECTIVE

J. Dimitrić Marković

University of Belgrade, Faculty of Physical Chemistry Studentski trg 12-16, 11000 Belgrade, Serbia (markovich@ffh.bg.ac.rs)

DOI: https://doi.org/10.46793/Phys.Chem24I.013DM

ABSTRACT

Oxidative stress is caused by an imbalance between the production of reactive radical species and a biological system's ability to detoxify the reactive intermediates or easily repair the resulting damage. Chronic exposure to stressors can lead to disturbances of the psychological balance, immunosuppression, and an increase in the likelihood of many diseases, such as cardiovascular, neurodegenerative, and inflammatory diseases, allergies, immune system dysfunctions, diabetes, aging, and cancer [1,2].

As most human diseases are very complex, multifactorial, and oxidative stress-related it is of high importance to create new types of biologically active compounds, which may be suitable for the treatment of different diseases or used as adjuvants with conventional therapeutic regimens [3].

Cancer is among the most prominent causes of death worldwide and nowadays there is an increased interest in new drug discovery, to adequately promote the survival rate against it. The innovative approach to the issue is reflected in a multidisciplinary, experimental, and theoretical, access to the problem that is solved by engaging scientists with qualifications and expertise in different scientific areas, and by applying many sophisticated and contemporary methods of analysis.

The clinical usefulness of platinum(II) drugs, which have been successfully used in clinical practice for decades, has frequently been limited by severe side effects and the development of resistance. These drawbacks along with promising characteristics of other transition metal complexes have motivated alternative chemotherapeutic strategies and further development of novel metal-based chemotherapy agents. What gives an additional advantage to transition metal complexes over conventional organic compounds are the numerous possible structural modifications, diversity in chemical and redox properties, as well as the unique interactions they enter with biologically relevant molecules. All this represents a significant advance in the development of structurally different compounds with potential anticancer properties [4-6].

Besides scientifically sound experiments which provide a substantial amount of new information a very important approach in modern drug design is based on theoretically optimized drug structures before the experimental tests themselves (*Structure-Based Drug Design*, SBDD). The SBDD is in expansion thanks to the rapid development of algorithms for complex theoretical calculations in an acceptable time frame that can give a realistic picture of biological systems and the processes within. Classical molecular dynamics simulations and related methods such as molecular docking are routine computational tools in modern drug design that allow the implementation of SBDD strategies and take into account the structural flexibility of the model drug-target system and the influence of the solvent, thus providing a unique insight into intermolecular interactions. Furthermore, the definition of the types of interactions between small molecules, ligands, and receptors, most often protein structures, and the assessment of the basic

thermodynamic parameters in the bioactive conformation are the basis for determining the strength of drug-receptor binding and understanding molecular recognition [7-9].

Based on this framework, this presentation will focus on the design, synthesis, structural characterization, and biological activity evaluation of the new ruthenium(II) complexes, and an explanation of the molecular basis of their biological activities [10-13].

Acknowledgment

The author acknowledges the financial support of the Ministry of Science, Technological Development and Innovation, Serbia, Grant No 451-03-65/2024-03/200146**.**

REFERENCES

[1] G. Pizzino, N. Irrera, M. Cucinotta, G. Pallio, F. Mannino, V. Arcoraci, F. Squadrito, D. Altavilla, A. Bitto, Oxid. Med. Cell. Longev, Volume 2017, Article ID 8416763.

[2] B. Halliwell, Understanding mechanisms of antioxidant action in health and disease, Nat. Rev. Mol. Cell. Bio., 25 (2024) 13.

[3] C.R. Reczek, N.S. Chandel, Annu. Rev. Cancer Biol, 1:4 (2017) 1–4.2.

[4] C.C. Konkankit, S.C. Marker, K.M. Knopf, J.J .Wilson, Dalton Trans., 47 (2018) 9934.

[5] H. Hu, Q. Xu, Z. Mo, Xi Hu, Q. He, Z. Zhang, Z Xu, J. Nanobiotechnology, 20 (2022) 457.

[6] Y. Liu, Yi Wang, S. Song, H. Zhang, Chem. Sci., 12 (2021) 12234.

[7] M. Batool, B. Ahmad, S. Choi, Int. J. Mol. Sci., 20 (2019) 2783.

[8] R. Özçelik, D van Tilborg, J. Jiménez-Luna, F. Grisoni, Chem.Bio.Chem, 24 (2023) e2022007.

[9] Y. Tang, R. Moretti, J Meiler, J. Chem. Inf. Model., 64 (2024) 1794.

[10]D.S. Dimić, Z.S. Marković, L. Saso, E.H. Avdović, J.R. Đorović, I.P. Petrović, D.D Stanisavljević, M.J. Stevanović, I. Potočňák, E. Samoľová, S.R. Trifunović, J.M. Dimitrić Marković, Oxid. Med. Cell. Longev, Volume 2019, Article ID 2069250.

[11]D.S. Dimić, G.N. Kaluđerović, E.H. Avdović, D.A. Milenković, M.N. Živanović, I. Potočnak, E. Samol'ová, M.S. Dimitrijević, L. Saso, Z.S. Marković, J.M. Dimitrić Marković, Int. J. Mol. Sci, 23 (2022) 1001.

[12]T. Eichhorn, F. Kolbe, S. Mišić, D. Dimić, I. Morgan, M. Saoud, D. Milenković, Z. Marković, T. Rüffer, J. Dimitrić Marković, G.N. Kaluđerović, Int. J. Mol. Sci, 24 (2023) 689.

[13]T. Eichhorn, M. Đošić, D. Dimić, I. Morgan, D. Milenković, R. Rennert, A. Amić, Z. Marković, G.N. Kaluđerović, J. Dimitrić Marković**,** Eur. J. Inorg. Chem., (2024) e202300683.

AMMONIA AS A HYDROGEN CARRIER – BENCHMARK CATALYSTS FOR AMMONIA CRACKING

Lj.Gavrilovic', J. P. Pinheiro, S. S. Kazi and J. Meyer

Institute for Energy Technology, 2007 Kjeller, Norway (ljubisa.gavrilovic@ife.no)

DOI: https://doi.org/10.46793/Phys.Chem24I.015G

ABSTRACT

Currently, H_2 is overwhelmingly produced from fossil fuels, mainly from natural gas without CCS (grey H_2). The global annual emissions from this practice amount to about 900 Mt CO_2. This is comparable to the global emissions from air traffic or shipping. Such a practice cannot continue in a world targeting net zero emissions by 2050. There is an urgent need to retrofit grey H_2 production with CCS and replace it with green H_2 where possible. In addition, massive scale-up of clean H_2 and H_2-based energy carriers such as ammonia (NH_3) are crucial for reaching the climate targets set by the Paris Agreement. Targets that were confirmed and strengthened at the COP26 in Glasgow. By 2030, the global market must increase from 90 to 200 MtH_2/year if we are to reach IEA's Net Zero Emissions by 2050 Scenario. If all planned H_2-production projects are implemented, the global production will reach only 105 MtH_2/year. A rapid ramp-up of production and end use in several sectors will require clean H_2 from different sources.

Integrating NH_3 into the H_2 value chain can increase flexibility and reduce emissions. Furthermore, commercially applied catalytic NH_3 decomposition is fast at 700–900°C. The equilibrium conversion is 99% at 400°C, but slow reaction kinetics limit implementation. Commercially available NH_3 crackers convert up to 2.5 tons/day, delivering H_2 for industrial applications. For maritime and gas-turbine applications, a variable conversion rate in the range of 100 tons/day is needed. Therefore, NH_3 crackers and advanced reactors need to be developed with improved load flexibility and increased efficiency. Currently, NH_3 is not produced for energy purposes. The market for in the energy/fuel sector could become substantial.

The aim of the present paper is to investigate ammonia cracking reaction using novel low-temperature catalysts synthesized from non-noble precursors, studied using advanced characterization techniques, kinetic studies for model development, and benchmarked at industry-relevant operating conditions against state-of-the-art reference materials. Different catalyst promoters, metal loadings will be investigated. The effect of temperature, pressure, GHSV on catalytic performance is also part of the study. Special attention will be on catalyst stability.

Acknowledgment

This publication has been produced with support from the HYDROGENi Research Centre (hydrogeni.no), performed under the Norwegian research program FMETEKN. The authors acknowledge the industry partners in HYDROGENi for their contributions and the Research Council of Norway (**333118**).

THE STABILITY AND EVOLUTION OF HEAVY OIL SYSTEMS STUDIED VIA ADVANCED METHODS IN SITU

O.N. Martyanov[1], S.N. Trukhan[1], E.V. Morozov[2,3] and A.M. Chibiryaev[1]

[1]Federal Research Center Boreskov Institute of Catalysis, Lavrentiev Ave. 5, Novosibirsk, 630090, Russia (oleg@catalysis.ru)
[2]Institute of Chemistry and Chemical Technology, Federal Research Center "Krasnoyarsk Science Center of Siberian Branch of the Russian Academy of Sciences", Akademgorodok 50/24, Krasnoyarsk 660036, Russia
[3]Federal Research Center "Krasnoyarsk Science Center of Siberian Branch of the Russian Academy of Sciences", Akademgorodok 50, Krasnoyarsk 660036, Russia

DOI: https://doi.org/10.46793/Phys.Chem24I.017M

ABSTRACT

Heavy crude oil, which is essentially a dispersed system (ODS), is comparable in complexity to biological objects. While the sizes of the molecules found in ODS are inferior to those of proteins, RNA, and DNA, the diversity of the chemical structure of molecules and "medium-size" chemical compounds in ODS is undoubtedly greater [1]. In terms of structural organization, ODS are simpler than biological systems, but the variations in the supramolecular structures of asphaltene aggregates, are greater than the diversity of objects of similar size in living organisms. The diverse structure of heavy oil molecules presents a significant challenge even for systematization [1, 2].

As a result of the accumulation of a huge amount of data on the structure and processes occurring in heavy oils under various conditions, it became clear that the properties of SDS fundamentally depend not only on its composition, but also on intermolecular interactions of various types, including hydrogen bonds, pi-pi stacking, interactions of molecules with different polarities, etc. There are no universal models describing the behavior of stress-strain states taking into account such interactions, which is primarily due to the lack of consistent experimental data on the behavior of multicomponent dispersed petroleum systems.

The listed features create fundamental problems that arise at every stage of extraction, transportation and processing of heavy oils using catalytic processes. In this context, one of the most intractable problems is the loss of phase stability of oil dispersed system [1,2], which leads to a decrease in the efficiency of oil refining processes due to significant losses of energy and raw materials. Thus, an important prerequisite for the development of effective processes for the extraction and processing of heavy oils is an understanding of the key factors that determine the aggregative behavior and stability of dispersed oil systems, taking into account the chemical transformations of their components under various external conditions [3]. A key factor influencing the aggregation and precipitation of asphaltenes is their local environment, which determines the nature of the intermolecular interactions. Therefore, predicting the stability of crude oil and asphaltene-containing disperse systems requires fundamental knowledge of the nature of the intermolecular interactions of asphaltenes not only with each other, but also with other components of heavy oil in the local environment.

At present, the structure and properties of heavy oils and oil residues are studied using highly informative and sophisticated physico-chemical methods. [4,5]. The description and analysis of the results obtained using each method can take hundreds of pages. However, it should be recognized that the data obtained by even the most advanced methods in ex situ mode do not reflect the processes occurring in crude oil under real conditions and therefore cannot always unambiguously predict the behavior of various oils and determine the limits of their stability and aggregation stability and/or the

formation of asphaltene-containing deposits. The use of advanced physical methods in situ at the atomic-molecular level is a fundamental step towards identifying the factors that determine the stability of petroleum dispersed systems and elucidating the mechanisms of aggregation and disaggregation of high-molecular components of heavy oils. In this case, it is important to use not one, even a unique approach, but a set of complementary research methods that will allow one to obtain information about the system at various spatial and temporal scales in situ [6-8].

The present report analyzes the potential of advanced physical methods for studying phase stability and physicochemical processes occurring in heavy oils in situ, taking into account possible chemical transformations of heavy components. The basic principles of using in situ methods are outlined and the capabilities and limitations of each approach are discussed. Special attention is paid to the chemical visualization of the asphaltene aggregation process using the method of Fourier transform infrared spectroscopy (microscopy) in different modes providing spatial resolution with array detection [9-13], magnetic resonance imaging (MRI) [14-17], nuclear magnetic resonance (NMR) and electron paramagnetic resonance (EPR) in situ [18-23]. These methods provide complementary information on the properties and behavior of dispersed petroleum systems, including information on the mobility of individual asphaltene molecules, the dynamics of their local environment, changes in the size and shape of aggregates, and their chemical transformations.

Acknowledgment

This work was supported by the Russian Science Foundation (grant no 24-13-00208, https://rscf.ru/project/24-13-00208).

REFERENCES

[1] Y. Zhang, Energy & Fuels, 35 (2021) 14422.
[2] J. C. Law, T. F. Headen, G. Jiménez-Serratos, E. S. Boek, J. Murgich, E. A. Müller, Energy & Fuels, 33 (2019) 9779.
[3] L. Chen, A., Bertolini et al., Energy & Fuels, 34 (2020) 14074.
[4] P. Chen, Y. V. Joshi, J. N. Metz, N. Yao, and Y. Zhang, Energy & Fuels, 34 (2020)12135.
[5] He Bian, Fang Xu, Aiting Kan, Shengchao Wei, Huiming Zhang, Shiguo Zhang, Lijun Zhu, Daohong Xia, J. Molecular Liquids, 343 (2021) 117576.
[6] A. G. Marshall, R. P. Rodgers, Proceedings of the National Academy of Sciences of the United States of America (PNAS) 105 (2008) 18090.
[7] E. V. Morozov, S. N. Trukhan, et al. Proceedings of 248th National Meeting of the American Chemical Society. San Francisco. CA. 2014, 531.
[8] O. N. Martyanov, Yu. V. Larichev, E. V. Morozov, S. N. Trukhan, S. G. Kazarian, Russ. Chem. Rev., 86 (2017) 999.
[9] A. A. Gabrienko, V. Subramani, et al., Adsorpt. Sci. Technol., 32 (2014) 243.
[10] A. A. Gabrienko, O. N. Martyanov, S. G. Kazarian, Energy & Fuels, 29 (2015) 7114.
[11] A. A. Gabrienko, E. V. Morozov, et al., J. Phys. Chem. C, 119 (2015) 2646.
[12] A. A. Gabrienko, O. N. Martyanov, S. G. Kazarian, Energy & Fuels, 30 (2016) 4750.
[13] A. S. Shalygin, I. V. Kozhevnikov, et al., J. Pet. Sci. Eng., 181 (2019) 106205.
[14] E. V. Morozov, O. V. Falaleev, O. N. Martyanov, Energy & Fuels, 30 (2016) 9003.
[15] E. V. Morozov, O. N. Martyanov, Appl. Magn. Reson., 47 (2016) 223.
[16] E. V. Morozov, O. N. Martyanov, Energy & Fuels, 31 (2017) 10639.
[17] E. V. Morozov, P. V. Yushmanov, O. N. Martyanov, Energy & Fuels, 33 (2019) 6934.
[18] S. N. Trukhan, V. F. Yudanov, et al., Energy & Fuels, 28 (2014) 6315.
[19] S. N. Trukhan, S. G. Kazarian, O. N. Martyanov, Energy & Fuels, 31 (2017) 387.
[20] E. V. Morozov, P. V. Nizovtseva, O. N. Martyanov, Energy & Fuels 36 (2022) 14696.

[21] S. N. Trukhan, S. S. Yakushkin, O. N. Martyanov, J. Phys. Chem. C 126 (2022) 10729.
[22] E. M. Morozov, S. N. Trukhan, I. V. Kozhevnikov, I. V. Peterson, O. N. Martyanov, Energy & Fuels. 37 (2023) 17215.
[23] S. N. Trukhan, E. V. Morozov, O. N.Martyanov, Energy & Fuels 37 (2023) 11797.

QUANTITATIVE NUCLEAR MAGNETIC RESONANCE

S. Macura

Department of Biochemistry and Molecular Biology, Mayo Clinic, Rochester, MN 55905, USA.

DOI: https://doi.org/10.46793/Phys.Chem24I.021M

ABSTRACT

The analytical potential of nuclear magnetic resonance (NMR) spectroscopy has been recognized since the early days of NMR. It is well known that the NMR signal is linear (proportional to the spin concentration), specific (spin groups have characteristic chemical shifts), and nondestructive (signal recording does not affect the sample). The last aspect is particularly important for biomedical studies, which culminated in NMR imaging (MRI) becoming an indispensable diagnostic tool. The broad application of the quantitative aspect of NMR only started after the development of NMR technology (magnets, electronics, and computers), which, in addition to selectivity, enabled the reproducibility and repeatability of data collection, even in biological systems.

In this presentation, quantitative NMR microscopy and NMR spectroscopy will be illustrated by examples from studies of biological systems (live mice, fixed tissue, and body fluids). For instance, it will be shown how NMR spectroscopy can be used to quantify total proteins in biological fluids, irrespective of the protein composition, without the need for method calibration.

SUPERSPIN GLASS: A USELESS PIECE OF MATERIALS

D. Peddis

Dipartimento di Chimica e Chimica Industriale, Università degli Studi di Genova, 1-16146 Genova, Italy (davide.peddis@unige.it)
Istituto di Struttura della Materia-CNR, 00015 Monterotondo Scalo (RM), Italy

DOI: https://doi.org/10.46793/Phys.Chem24I.023P

ABSTRACT

In a magnetic nanoparticles the thermal evolution of the magnetization dynamics depends on the particle concentration and the nature of the inter-particle interactions[1]. In sufficiently concentrated nanoparticle systems, strong dipolar interaction combined with random orientation of anisotropy axes determine a competition between different moment alignments leading to a collective freezing of particle moments in a disordered magnetic state, known as superspin glass (SSG), below a characteristic glass temperature (T_g).[2] SSG exhibits slow dynamics which is qualitatively indistinguishable from that observed in atomic spin glasses, and typical properties of an ordinary SG, such as aging, memory and rejuvenation are observed. This talk focus on the non-equilibrium magnetization dynamics of two different SSG systems: concentrated $MnFe_2O_4$ nanoparticles (<D> ≅ 2 nm), a model of SSG, and a dilute, really peculiar system, of Co particles (<D> ≅ 2 nm) embedded in an antiferromagnetic Mn matrix with a volume fraction of 4.7 % (Co@Mn 4.7%). Non-equilibrium dynamics of these system has been studied by memory and rejuvenation effects using different protocols (TRM; ZFC, IRM), showing the validity of the principle of superpositon for a SSG system Co@Mn 4.7% represent a very interesting example of SSG behaviour in a dilute system. Generally, for such particle dilution in diamagnetic matrix (e.g. Co embedded in Ag matrix), dipolar interactions are weak and an ordinary blocking process is observed. In Co@Mn 4.7% non-equilibrium dynamics typical of SSG is observed. This is due to a strong interface exchange coupling between Co nanoparticle and Mn matrix, which transmits an effective long range interparticle correlation giving rise to a SSG freezing at low temperature.[3–5] By memory and rejuvenation experiments and Monte Carlo simulations we showed that the memory effects increase with the concentration and that both the interface exchange coupling and the dipolar interparticle interactions contribute to the observed dynamical behavior. In particular, the interface exchange interaction provides an additive source for the frustration of the system resulting in an enhancement of the memory effect. In 2001 J.P. Bouchand[6] claim that lthough (super) spin glasses are totally useless pieces of material, they constitute an exceptionally convenient laboratory frame for theoretical and experimental investigations define. In this perspective the importance of these materials has been clearly demonstrated buy the physics Nobel Prize in 2021.

REFERENCES

[1] New Trends in Nanoparticle Magnetism. vol. 308 (Springer International Publishing, Cham, 2021).
[2] D. Peddis, et al, Scientific Report 11, (2021).
[3] D. Fiorani, & D. Peddis, Journal of Physics: Conference Series 521 (2014) 12006.
[4] D. Peddis, M. Hudl, C. Binns, D. Fiorani, & P. Nordblad. J. Phys.: Conf. Ser. 200 (2010) 072074.
[5] G. Margaris, G. et al. Nanotechnolgy 28(2017). 035701.
[6] J. P. Bouchaud, V. Dupuis, J. Hammann, J. & E. Vincent, Phys. Rev. B 65 (2001) 024439.

FROM CLASSICAL TO SOFT MATTER SCALING: THERMODYNAMICS, KINETICS AND ENERGETICS

M.B. Plavsic [1, 2] and M.M. Plavsic [3,4]

[1] *University of Belgrade -TMF,*
Karnegijeva 4, 11000 Belgrade, Serbia. (plavsic@tmf.bg.ac.rs)
[2]*Engineering Science Academy of Serbia, Belgrade, Serbia*
[3] *The Academy of Applied Studies Polytechnic, Belgrade-Serbia (milankaplav@gmail.com)*
[4]*University of Niš- Faculty of Technology- Leskovac, Serbia*

DOI: https://doi.org/10.46793/Phys.Chem24I.025P

ABSTRACT
In parallel with review of modern concepts of scaling phenomena and papers of S. Veljkovic and Lj. Kolar-Anic connected to the field, is presented our **Theory on network grow scaling in cells and cell systems**, illustrating our experience within the field, and opinions on it. In short, all the spectra of problems discussed, can be presented by the following key words: the scope and importance of **scaling concept** and **theory** (in **thermodynamic** aspects) and the new approach from **kinetics** for bio-systems scaling, **energetics** as nominator they share, and **bio-thermodynamic** issues today, **molecular clock** as an example of opportunity for bridging over such difficulties.

1. INTRODUCTION

In this lecture we present our long time experience with, and some results on, the **integrative** and **comparative approaches** to the physical-chemistry problems (especially in Polymer science), very obvious by considering principles of The Scaling Theory [1-9] and that all also related to our visions of activities of Belgrade School of Physical-chemistry (BSPhChm) [10-20], to whose two distinguished members, Prof. Slobodanka Veljkovic and Prof. Ljiljana Kolar-Anic contributions, and in memory of them, is dedicated this conference.

The **specialization and integration of knowledge** are nothing new in sciences, but, new is the high nowadays arising rate of the specialized scientific disciplines, growing from just one part of physical chemistry (related to some biological systems phenomena). All those new disciplines have suffices “omics”, in their names (e.g. proteomics, viromics, genomics (not to confuse it with genetics!) etc..) and their number has grown over 30, just last years. But, we first have to remember how the integrative approaches started here, (about hundred years ago, when Serbia started to recover from hard wounds made in the Big War), and how The Department of Physical chemistry (DPhCh) was leading at Belgrade University that process. Of course, it was not new approach than, at Sorbonne in Paris, at Oxford and Cambridge universities, and also the University of Vienna and Free University of Brussels (ULB) and some others, but here was something specially, comparing that time customs for teaching in applicative (“die Fach Schule”) manner. So, 99 years ago, was founded the new “Eng. School-Module for Technology” (nowadays The Faculty of Technology and Metallurgy, (TMF), where we belong) at Belgrade University. It was than incorporated into School of Engineering, and in a occasion, one of the 3 founding professors of it, had been asked: ”But, what you mean with the Technology” (because only a few schools in the world have had than the name of that kind, (e.g. ETH in Switzerland, MIT and CALTEC in USA), so he answered (anecdotally) : “it will deal with engineering aspects of physical chemistry applications”. (In terms of modern aspect of Molecular engineering, Materials engineering, Cell engineering, Tissue engineering etc.) it was quite an advancing view, but many people have understood it in another

way: as a need to separate applicative and fundamental studies. But later, some of us at TMF have worked more on fundamental, and some people at Faculty of Physical Chemistry (PCF), worked more on applicative aspects, of the Science which we all serve. In the year when Prof. Kolar -Anic was born (and one of us was, in that year, as well) started organization and the building of "The institute of Matter" in Vica (suburb of Belgrade) what officially was opened next year, with members of BSPhCh, in the core of it. Prof Pavle Savic was heading it all, as the leading professor of physical chemistry at DPhCh and director of the new Institute, as well. One the favorite collaborators of him, was then Slobodanka Veljkovic. Later, she went, (on his advice), to make her PhD at Oxford, and later on, when she already was the professor at DPhCh, became Ljiljana Kolar-Anic the favorite assistant of hears. So later on, in a similar way, Ljiljana went for post-doc studies at ULB, dealing with problems of oscillatory kinetics [17] (she got interested for kinetics already during her work on master thesis here, and Prof Veljkovic got interested for oscillatory systems already at Oxford [15], in some general sense. In other words: the continuity in sharing ideas and methods is there obvious, as it is obvious in all entities, that we call "Schools of...(some special... knowledge on..)". Ljiljana had continued it later, for long time and very successfully, but that part of her work will be covered in some other talks at this symposium. Also later, the Institute changed its name, and also, started similar dilemma about the fundamental or applicative character of its activities, as mentioned for the previous period with TMF. (Of course, such specifications have determined later facilities supply. staff generating, character and levels of project etc., but moreover, the way and style of living of the local scientific community...). In short, the Institute was at that time, (and the Belgrade School (BSPhChm) as the core of it) one of the fourth or fifth largest scientific centers of that kind in the world. Naturally, that all has had the high impact to all our scientific population. It acted to the generation working in 1950es and the next generation as well, and so on, indirectly acting on several generations later [19,20], that also have been writing beautiful papers (all around the world). In short, the foundation of the Institute has had both, some good and some bed consequences. All of that is long and complex story (with a lot of interesting data now) but, to long for the lecture of an half of hour, at such meetings. So, when we have been invited to deliver this plenary lecture at the special occasion, we decided to talk (instead on historical data, and instead on their papers), about some silent aspects of sharing ideas, as described above as the characteristics of "Schools of knowledge". Now we will talk about some ideas and some intuitive visions in BSPhCh less known today, but related to very deep, fundamental problems.

Of course, such shearing efforts, is different from the common research practice, moreover because the data are coming from very different disciplines and about systems of very different kind, what needs some **integrative approach**. Also, should be pointed that rear tools providing such (very) special approach, are imbedded in **Scaling Theory**, in some straight, but also in some silent aspects of it [21-25]. For example, as his last contribution before retirement, Pavle Savic published (in several papers) the "Theory on behavior of materials under high pressure", (mainly in corporation with mathematician Prof. R. Kasanin) in 1961 [10]. It starts with considering the behavior of electron clouds of the material been under huge pressure, and goes through the also huge number of system size levels, as well (up to the level of our Planet and the Moon), trying to explain the generation of Earth magnetic field and rotation phenomena. But, the solution of such issues as Kondo problem and so on, was not possible at all, till K.G. Wilson published in 1975 at Cornel School, his final paper on Group renormalization method, for solving such problems by Scaling Theory [21]. Moreover, 30 years after Savic ideas, made Wang 1990-progress in high pressure scaling but then scaling methods were broadly accepted [11,12]. In the similar way S. Velkovic and Lj. Kolar-Anic offed 1975 some beautiful ideas for materials surface chemistry characterization by some scaling exponents [13], but fifteen years was needed till such scaling

parameters were accepted (from Pfeifer work) [14]. But such examples should not be understood as the slow rising ideas about scaling. Scaling Concept is very old, but sometimes complex in formulation or hard for interpretation. The eldest paper on scaling (saved in roman translation till now) is written by Archimedes, (written in ancient style as The Letter to King Galo II) but, there are some indications that it was discussed already in Pythagoras School - one so important "School of Knowledge" (as defined above)! With **Scaling Concept** had been dealing in last two thousand years also Galileo, Newton, Pascale etc., till the formulation of **Scaling Theory** (Fig.1) and nowadays at The Schools: Cornell, Stanford, CALTECK, Santa Fe, and some others, as well [21-30].

2. FOUNDATIONS OF THE SCALING THEORY

Less than ten months ago was exactly 200 years since Cagntard de la Tour discovered **Critical point** phenomenon, measuring transition temperature at high pressures (of course not in so high range we described in Part-1, but working with one soft matter system- just the same we are going to talk about here, the yeast cells, by fermentation). So the first **Critical temperature** (T_C) was determined for ethanol system. It also wasn't understood, and appreciated, appropriately than, but still encouraged T. Andrews to make detailed measurements of evaporation, and present it by charts of pressure-volume relations been called later **The Phase Diagrams**. In 1873 (50 years after De la Tour descovery) showed J.D. van der Waals, that Andrews diagrams can be explained theoretically, by the **Equation of State** and two years after, L Boltzmann showed how simple **model in form of the lattice,** can provide possibilities of derivation one of most powerful function in science (**The Partition Function**) and formula for **entropy**, and so further, the theoretical equation of state, etc. The same years W. Gibbs published his famous paper of 300 pages for precise definition of **system equilibration**. Still, besides this high success, the behavior of systems close to critical point staid mysterious, e.g. when closing to the critical point, the basic parameters of state, were observed to follow the **scaling lows**, with the same exponent for each kind of parameter, no matter what is the chemical structure of a liquid substance used, and then diverge. For example, the change of the heat capacity is described by this characteristic scaling form:

$$C_P \propto |T - T_C|^{-\alpha} \tag{2.1a}$$

The new approach to the problem, and also to unusual behavior of helium transitions, especially its superconductivity and magnetic properties, started Lev Landau in 1937. But for the magnetic properties, the fundamental influence has head also the theoretical model of Ising, published in 1924. He considered magnetic dipole moment orientation changes with the field, through magnetic spin vectors ***S*** orientation. Landau used both, Gibbs thermodynamics and Ising model for the start:

$$C_P = -T\left(\frac{\partial^2 G}{\partial T^2}\right)_P \tag{2.1b}$$

But, Landau assumed that Gibbs free energy density (g_s) change with spin ordering, what can be represented by power series of spin density field variable S (**X**), later called **The order parameter** with **X** representing the space coordinates [4]:

$$g_S(T, \mathscr{S}) = g_0 + a(T)\mathscr{S}^2 + \frac{1}{2}b(T)\mathscr{S}^4 + \ldots \tag{2.2a}$$

For thermodynamic equilibrium, Gibbs free energy tends to minimum, so:

$$\left(\frac{\partial g_S}{\partial \mathscr{S}}\right) = 2a(T)\mathscr{S} + 2b(T)\mathscr{S}^3 = 0 \tag{2.2b}$$

Likewise can be expended the parameter *a(T)* around the critical point: $a(T)=a_0\,(T-T_C)+\ldots$, so we obtain in the first approximation two solutions for the order parameter (the trivial S = 0) and relation:

$$\mathscr{S}_c^2 = -\frac{a}{b} = -\frac{a_0}{b_0}(T - T_C) \tag{2.2c}$$

This gives values for $C_P = (a^2_0 / b_0)\ T$ for $T<T_C$ and $C_P = 0$ for $T>T_C$ and results with scaling exponent $\alpha=0$. In addition it leads to scaling of order parameter that can be related for helium to magnetic susceptibility (what can be measured) and indicate the **change of particle ordering** as reason to special properties. In thermodynamics it is analogy to compressibility [30] and leads to introduction of a new kind of universal exponent, related to system ordering assigned β:

$$\mathscr{S}(T) \propto |T - T_C|^{\beta} = |T - T_C|^{1/2} \qquad (2.2d)$$

Landau continued work on those problems till 1953, collaborating with Ginsburg and they introduced, for better description of ordering a new kind of scaling described by **correlation length** ξ, very useful parameter to quantify cooperative coupling in the system, with the scaling exponent assigned $\boldsymbol{\nu_{scl}}$:

$$\xi \propto |T - T_C|^{-\nu_{scl}} \qquad (2.3)$$

In parallel with this foundation of scaling theory in the School of theoretical physics mentioned, but in the same period of time, came Paul Flory completely independently, (working in quite different field, and on the opposite side of the Planet), practically to the same scaling relation as Eq.2.3. This similarity was not observed for pretty long time, because Flory worked in Polymer science, developing his **Theory on interaction specificity in systems with long chain molecules**, called **Excluded volume theory** and his scaling relation describes micro-field of interactions, inside one polymer molecules, what is (in formal view), something quite different from phase transitions of macro-systems, described above. Flory found that the size of polymer molecule (i.e. the radius of coiled polymer chain $\boldsymbol{R}$ in unperturbed state (i.e. when the forces excluding other particles from a chain segment volume in the coil, are balanced with chain group attraction forces), and scales with number of chain links (segments) N_m , as [1, 5-9]:

$$R = (B_V a^2)^{1/5} N_m^{3/5} \qquad (2.4)$$

Now is explained that in both those cases, is considered scaling of cooperative coupling of particles (molecules, or flexible segments) in the interaction field, but at the start Flory and Landau with Ginsburg came to different values of the scaling exponents. Some authors than also opposed the excluding volume theory principles. Direct measurements of unperturbed dimensions of chain in bulk was impossible, all the time till neutron scattering method has been developed, so Flory developed his theory mainly studding interactions of polymers in solutions, under different physicochemical conditions. The exact solution of Ising model also didn't exist, all the time until Lars Onsager find analytical procedure for its solution in two dimensions (Ising model in 3D analytically nobody succeeded to solve, till now) but the way for understanding fundamental relations and their silent aspect (e.g. relations with mean field approach),was open. Both methods and appropriate experimental tests, confirmed Flory's value for $\boldsymbol{\nu_{scl}}$ as well as Flory's excluded volume theory. So was opened the way for fundamental interpretations of polymer chain space structure, and the reference state, for much easier interpretation of variations and deviations. Than almost all models in Polymer science had to be revisited, and Flory became the "leading authority of Polymer science", for the long time [12].In short, this research started with application of lattice model to polymer solutions, what had done Flory and Huggins, independently each of other, but Flory extended it later very much. According to Flory, the free energy of mixing, polymer and a solvent, with lattice fractions (ϕ_p) and (ϕ_s) and molecule numbers n_p and n_s respectively, and using van Laar parameter for heat of mixing ($\chi_{p\text{-}s}$) is:

$$\Delta G_{mix} = \Delta H_{mix} - T\Delta S_{mix} = k_B T[n_s \ln \phi_s + n_P \ln \phi_P + \chi_{s-p} n_S \phi_p] \qquad (2.5)$$

According to van Laar parameter χ is dimensionless quantity describing the difference in interaction solvent-solute molecules compared to interaction in pure substances $\chi = z\ \Delta w_{1\text{-}2}\ v_1 / (k_B T)$, where z is coordination number of lattice, $\Delta w_{1\text{-}2}$ the interaction energies difference, v_1 ,the volume of solvent molecule in lattice, k_B is Boltzmann constant. Differentiation of Eq.2.5 with respect to n_s brings us to the excess of solvent chemical potential in polymer solution, what is in the

first approximation proportional to χ i.e., $(\Delta\mu_s)_{exc} \sim (1/2 - \chi_{p\text{-}s})$. He extended the meaning of χ parameter, adding besides partial enthalpy also the partial entropic factors toit, $(1/2 - \chi) = (\Delta H_s / RT\, \nu_p^2)_{par} - (\Delta S_s / R\, \nu_p^2)_{par} = \kappa_s - \Psi_s$. So is defined the Flory temperature $\Theta_{FL} = T(\kappa_s / \Psi_s)$ giving $(1/2 - \chi) = \Psi_s (1 - \Theta_{FL}/T)$, and solvent excess chemical potential $(\Delta\mu_s)_{exc} = -RT\, \Psi_s (1 - \Theta_{FL}/T)\, \nu_p^2$, is zero for $T = \Theta_{FL}$, It can be understood as canceling attraction and repulsion forces betwee segments and solvent molecules giving the excess potential zero, so the deviation from ideal state vanish. The chain configuration is unperturbed. It can be described in the following way:

$$G_{coil} = U - TS = N_m k_B T B_{vir} \frac{N_m}{(4/3)(\pi R^3)} + \frac{3k_B T R^2}{2N_m a^2} \tag{2.6a}$$

here B_{vir} is thermodynamic second virial coefficient, and ***a*** describes link dimensions (all other as in Eq. 2.4)According to equilibration principles : $(\partial G_{coil} / \partial R) = 0$, so we obtain

$$-\frac{k_B T B_{vir} N_m^2}{R^4} + \frac{k_B T R}{N_m a^2} = 0 \tag{2.6b}$$

Solving Eq.2.6b for ***R*** gives Eq. 2.4 and the scaling low as described. Later Flory extended solution model of Eq. 2.5, (with majority of solvent molecules) to polymer gels (with majority of polymers in the system) working with Rehner, and further with Bob Orwoll [9] formulated new statistical c)mechanics model of polymer solution, introducing several new interaction parameters: relative temperature $T_{rel} = (T / T^*)$, where $T^* = \varepsilon^* / c k_B 0$. Later on Flory developed, working with Ken Dill spherical lattice model [25] able to describe the soft matter structures like micelles, vesicles and similar structure. The energetics aspects of the models are based on ε^*, representing energy interactions of one segment, at dense packing, with its degrees of freedom c_{df}, in partition functions of the form:

$$Z(T,V) = const.v^{*crN}\, ((\bar{v})^{1/3} - 1)3crN \cdot \exp(crN\rho / T_{rel}) \tag{2.7}$$

One of us (M.B.P) also contributed to those investigations, working with Prof. Flory on factors able to include conformational energy changes, into the interactions in those models, in particular, the dipole moment effects, what is important especially for bio-systems [7,8].

3. EXTENSIONS OF THE CRITICALITY CONCEPT AND SOME PAPERS OF BSPhChm

With early models described, the scaling theory was established in thermodynamics, but soon been extended to a number of other sciences. But here must be added, that the first ideas are very old, from ancient times, and the first paper saved (is roman translation) is written by Archimedes on sand clusters scaling and described by exponential calculus, what he discovered, on that occasion:

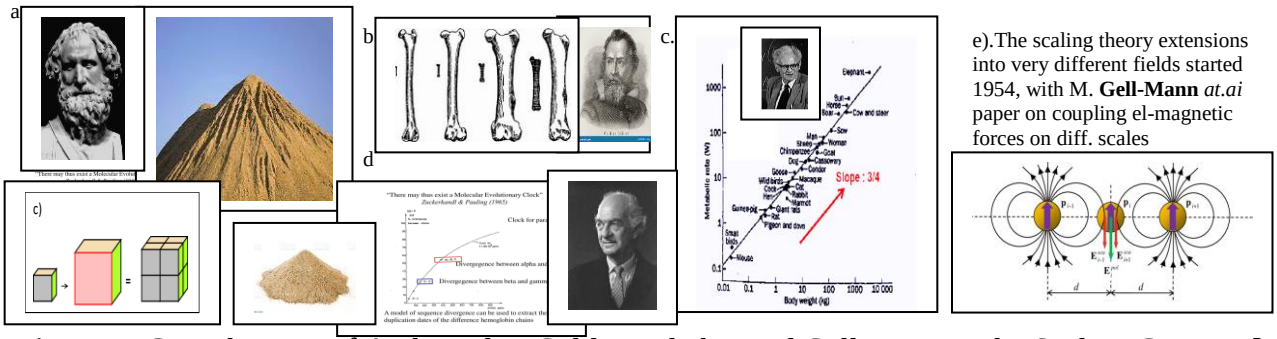


Figure 1. Contributions of Archimedes, Galileo, Kleiber and Gell-Mann to the Scaling Concept [12, 23,29]

Later, a number of authors were looking for physical meaning and possible generalizations of such phenomena: B. Windom, A. Patashinski, V. Pokrovsky, L. Kadanoff, and especially the

Cornell group: M. Fisher and K. Wilson mentioned [21]. So the research extended from classical to quantum electrodynamics and nuclear structure, all up to cosmology. Also Ljiljana with Prof. Velkovic and tater with Z. Cupic and groups at BSPhChm and IHTM, published very interesting ideas on possible characterisation systems by exponents from active point distribution [13, 18].

4. SOFT MATTER SCALING AND SOME BIOTHERMODYNAMIC ISSUES

The term "soft matter" introduced Pierre-Gilles de Gennes, for the group of systems with very similar physicochemical properties (especially those of importance for nowadays applications), in spite of their different chemical constitution [1]. There belong polymers, gels, bio-membranes, foams, colloids etc. but experience shows that for optimal properties are polymers the most useful and for further development of that theory, are bio-systems of the most importance. Of course those two aspects are related (because bio-polymers play the major roles in bio-systems). In aspects of the scaling theory, is very important, just for that interplay of polymers and bio-systems in soft matter approach the low, introduced by M. Kleiber in 1932, and illustrated by simple schema, in Fig.1c. He found [26] that the metabolic rate scales with mass of organisms, in the huge spectra, from birds up to human, with the same exponent (3/4) = 0.75 what A. Hemmingsen extended it in 1960 to unicellular eukaryotes and some prokaryotes [26], It has been understood as indication of some deep, kinetic or/and thermodynamic relations, governing all that organisms in spite of biological differences in that structure, but no explanation was found for the long time. Still it contributed to the field development, at least from three aspects: confirming usefulness of the (unusual) "approach of Soft matter science", confirming universality of scaling lows, and confirming the bio-thermodynamics integrative methods, relating properties from very different scales of organism structure into unified approach. (Of course, several theories are offered to explanation Kleiber's low, but they are still under discussion, what will require here more space, then available). Instead, we would pointed here to some bio-thermodynamic issues: In the same way as classical thermodynamics has united results from numerous different fields and methods of measurements (and theirs separate solutions, theoretical and practical) and transformed them into simple, but fundamental lows, providing much deeper understanding and manipulating of the phenomena, so nowadays also tries bio-thermodynamics with numerous data from specialized disciplines (especially those with -omics suffices, as mentioned) being at 3 levels: molecular, cell and cell-systems, and mainly studied separately. We believe that scaling concept application can help for it, very much. It seems simple e.g. considering mass scaling: proteins (*index*: PRT) make the most of the macromolecular number (or mass) inside cell (CL), and the number of such cells building a cluster (CLC), so one might write

$$C_{LC} = Cluster(m_1) \propto a_1 \sum_{1}^{N_{CL}} Cell(m_2) \propto a_1 {C_L}^{n_1}, \textbf{and}. C_L = Cell(m_2) \propto a_2 \sum_{1}^{N_{prt}} P_{RT}(m_3) \propto a_2 {P_{RT}}^{n_2}. \textbf{so}, C_{LC} \propto a_1 a_2^{n_1} (P_{RT})^{n \cdot n_{21}}. \quad (4.1)$$

But, such (formal) approach doesn't seem much useful. The space organization of those unites is much more interesting, because it reflects their structure and (some) functions that follows. The simplest approach to that is the volume scaling. Even more is of interest the volume scaling of cells and clusters during growth (in the course of cell division, -or tissue forming, wound healing but also tumour formation (e.g. cancer), cell engineering etc.(for support or prevention of the process)), but moreover for more fundamental understanding of life processes mechanisms. Nature used it in large spectra, but following the same (sometimes simple, but basic) scaling lows, as we have seen from the metabolism rate, above. Of course, the importance of that, have initiated numerous, and long-time investigation of the growing rate with other main factors of cell-systems e.g. metabolic rate (mainly articulated through the food supply). It was encouraged with the success of universal scaling low of Kleiber, as described above. But even before him, exactly 100 years ago, in 1923 Wertenbaker proposed also the simple rule for cell grow: "as larger the cell should be, so faster it

will grow". It was about 10 years before Flory and Carothers proved existence of macromolecules (and established the new field in physical chemistry), so no molecular-genetics interpretations were possible. But, a number of papers repeated that rule, and do it in the long period [23] so it was accepted broadly, until Talia found that some cells behave in just the opposite way (e.g. baker yeast) [22, 27]. In addition, the correlation of colony size with metabolic rate (food supply), was surprisingly poor [23]! But if cell volumes are included, the correlations become much better. Moreover, all those data come from cancer cell lines, and we now know that the cancer cell have significantly larger volumes, and divide much faster than normal cells. In addition, the volume change is obviously related more directly to the cell growing rate, then to the metabolism rate of cells. The importance of the field and contradictions observed, have induced our interest on the subject especially for the research on the volume change relations to the growth rate of a cell, and cell systems. So, we first revisited the phenomenology of cell system growth, but by considering normal cells, as yeast data. Baker yeast cells are among the most studied cell systems worldwide, with lot of data published on its wild strains behaviour, in normal standard way (but at some phys-chem. conditions also shows some special properties) [23]. In addition, the last years are applied for yeast characterisation, especially for studying its polymers, new sophisticated experimental technics (flow fluorescent cytometry etc.) So, yeast is here the appropriate experimental model to look for the structural link between two general, essential parameters of bio-system, for which we believe, exist some very important relations connecting the cell volume and its growing rate (as of cells so of cell systems), but they are not as simple, as proposed by Wertenbaker rule. We will illustrate it now, with brief overview of our **Theory on network growth scaling**, of cells, that follows.

5. NETWORK GROWTH SCALING THEORY OF CELLS AND CELL SYSTEMS

We have considered first the **phenomenology** of volume change, at all 3 levels *of systems*, for yeast cell cycle, as an example, and compared it with production of proteins (P_{RT}) in that cell (C_L), for the same time, and with its cluster (C_{LC}) growth, that we normalized appropriately (in Fig.2a-c).The protein production is presented in Fig.2d what can be described by Eq.5.1 with constants k_i for sub-

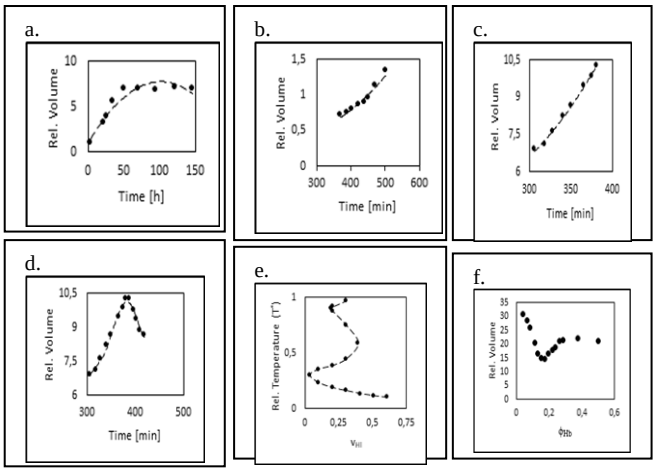


Figure 2. Cell-system properties scaling at 3 levels

substrate-$\mathscr{F}$) consumption, and P_{RT} production and conc. correction (for cell volume increase):

$$P_{RT} = (P_{RT})_0 + \mathscr{F}(k_1/(k_2+k_3-k_1)\left[e^{-(k_1-k-k_3)} - e^{-(k_2+k_3)}\right] \quad (5.1)$$

The scaling exponents from Fig.2a-c : 1.1, 2.0, 1.9, respectively, indicate different change pattern from Eq.4.1. But it says nothing about the structure change during the volume increase So we applied lattice model as described in Sc.2 using (virtual) mixing process, to define the system structure, staring with reference volume at "relaxed" yeast state-at stationary conditions. $\Delta G_{sys}=\Delta G_{mixSCL}+ \Delta G_{mixFr}\ \Delta G_{elstr} +\Delta G_{elec} +\Delta G_{HL}$

Here indexes indicate: cell skeleton polymers interactions with water, free-moving proteins with water,and holes (***HL***)-gel, respectively. The holes are introduced into the lattice to describe the free volume of polymer network necessarily for the cell growth by incorporation of the new proteins. The interaction schema indicated by mixing is:

$$\Delta G_{mix} = k_B T\{(n_w \ln\phi_w + n_{PlF} + \chi_{w-Pl}\phi_{PlF}) + (n_w \ln\phi_w + \chi_{w-Pl}\phi_{SCL}) + (n_{Hl} \ln\phi_{Hl} + \chi_{Hl-Pl}\phi_{SCL}) + \alpha_{elc} \ln_{Pl} + \beta_{Elast}\phi^{-2/3}\} \quad (5.2)$$

here are only polymer- holes interactions in focus because polymer steric hindrances require much more free volume. The increase of polymer content requires some **free volume** and its further

expansion to keep "stationary" conditions (or "stable non-equilibrium state"-in Prigogine terms) but will expand cell network and (temporary) changes pressure (ΔP) in correlation to volume increase, leading to formulation of equation of state in the form: $P=(1/V)(\partial \Delta G_{mix} / \partial n_{Hl})_{T,SCL,w}$. Applying it to Eq.5.2 with introduction of the temperature dependence using relation $(1/2-\chi)=(1-\Theta/T)$ and T^*_{rel}, (as described in Section 2) leads to the phase diagram presented in Fig.2e.(In other words, the increase of chemical potential, due to a new protein in the cell, with small expansion of the network and the water complement-supplied by the membrane proteins from the outside, bringing its free volume increment $\Delta\phi_{Hl}$, what further leads to equilibration, and repeats in series of successive states, with corresponding free volume complements, (required for the "cell stabile state") we can reduce those complicated relations only to continually increase of the necessary free volume represented with Δn_{Hl} lattice units. Further, the analysis can be even more simplified, to consider free energy density of the gal (as a unique entity), in relation to free volume:

$$g = (1/\phi_{gel})(1-\phi_{gel})\ln(1-\phi_{gel}) + \chi_{gel-Hl}(1-\phi_{gel}) + \alpha_{elct}\ln\phi_{gel} + \beta_{Elst}\phi^{-2/3} \tag{5.3}$$

It is not only theoretical supposition: experimental results last years indicate existence of such soft, but very compact polymer network, (solvated with tight water complement), imbuedding the cell and attracting and directing the free polymers: mass spectrometry of affinity enrichment proteins indicated for yeast cell the network of 3 927 proteins, 31 994 interactions, with 16 main interactions per particle [1.7,1.10,2.32] and interferometry scattering microscopy confirmed network shape organization of those components. It requires more space and time and will be described with some of our results, based on this theory, in another our paper at this Conference. But, here we will extend the Theory to possible criticality conditions, in analogy to Eq.2 as described in Sc. 2., using benefit properties of yeast carcass, mainly homogenously concentrated in a thin layer under membrane, so satisfying condition $|\phi/\phi_C - 1| \cong |v/\varsigma - 1| < 1$, for displacements ζ, and $\boldsymbol{v=1/\phi = V/(\phi_0 V_0)}$

$$g \cong (\chi - \chi_C)(1/v) + (\alpha_{elec} - \alpha_{C-elec})\ln v - 0.3\phi_C^6(v - v_C)^4 \tag{5.4}$$

The possible physical interpretations of critical values will be discussed later. For internal pressure

$$\Delta P \cong \phi_{oneHl}^{-1}\phi_{gel}^0 k_B T \phi_{gel}^2 \left[(\chi_C - \chi) + (\alpha_C - \alpha)v - 0.3\phi_C^6(v - v_C)^4 + ...\right] \tag{5.5}$$

for compensated increase of pressure, and expanding in series in analogy to Se.2, we obtain

$$(\chi_C - \chi) + (\alpha_C - \alpha)v_C = -(\alpha_C - \alpha)(v - v_C) + 0.3\phi_C^4(v - v_C)^3 + .. \tag{5.6}$$

Eq.5.6 express gel network interactions field in function of the cell volume expansion around some critical value, what can be pronounced as the **volume criticality of the cell.** Also, from Fig.2f we can see that gel network volume V diverge for both, very small and very high values of free volume in relation to hyperbola: $[1 - \Delta\phi/\Delta\phi]^2_{Hl}$ i.e. if the network is too dense for growth, or too expanded, so interactions are lost. The minimum would than correspond to percolation of interactions network, what recalculated to mass fractions corresponds to cell density about 1.1(g/cm^3), comp. also the range in Fig.2e. Indeed, it is reported: for budding yeast 1.08-1.10, for *E.coli* also 1.08-1.10, erythrocyte 1.1, human muscle 1.06 etc.[23].As supposed, ΔP vanishes by equilibration steps of cell: e.g. internal pressure of budding and fission yeast is 0.3 MPa for both, during growth. It follows: cell prefers to keep its pressure constant, so changes the volume. The theory can be easily extended to the cell colony: but with holes between cells, with water and its free volume increment. In some tissues even exists chemical network junctions e.g. desmosomes. May be that very similar density of soft tissues can be than understood as above? But, also some chemical reaction networks follow that all in parallel. In that approach is interesting Pauling idea on constant of cell polymers change: "the molecular clock" [24] From Fig.2d can be calculated $(\partial V/V\partial t)$,-relative volume increase being constant, and almost all the time. Also recently the Santa

Fe group [28] proposed that it “tickles” not with time, but with mass (like it metabolism rate does), but our results [30] indicate the tickling in terms of cell-systems-volume oscillations.

CONCLUSION

Instead of some formal conclusions, we would point here to our feelings of both, sorrow and excitement, by writing here, on the work and time that has passed: sorrow because so many of people mentioned above, are not more alive, but excitement, because their work still makes us hearing their words, ideas, even feelings with that work, like they are here, with us. This is the beauty, and power, of good papers...

REFERENCES

[1] P.G. De Gennes, Scaling Concept in Polymer Physics Cornell Univ. Ithaca-USA, 1979.
[2] P.G. De Gennes , Nobel Laureate lecture: Soft Matter, Publications of Nobel Foundation Stockholm, 1991.
[3] H. Reiss, Scaled particle methods in Fluid Statistical Mech. Ch.1 in Adv. Chm. Phys. Vol.IX, I. Prigogine (Ed.) Wiley, New York 1965.
[4] L.D. Landau, E.M. Lifschitz, Course of Theoretical Physics, Butterworth, Oxford, 1984.
[5] P.J. Flory, Principles of Polymer Chemistry, Cornell Un. Ithaca-USA, 1953.
[6] P.J. Flory, Nobel Laureate lecture: Spatial Configuration of Macromolecules, Nobel Found. Pub. Stockholm, 1974.
[7] P.J. Flory, M.B. Plavsic at al., J. Phys. Chem., 85 (1981) 3211.
[8] P.J. Flory, M.B. Plavsic at al., ACS Polym. Pb. 24(1983) 71.
[9] P.J. Flory, R.A. Orwall at al., J. Am. Chem. Soc. 86 (1964) 3515.
[10] P. Savic. Bull Sci. Math.-Natur. Acad. Serbe Sci, 20(1961)107.
[11] D. M. Wang at al., J. Phys. C21 (1988) 3585.
[12] H. Moravec, Polymers-Origin and Growth of Science, Wiley, NY, 1985.
[13] Lj. Kolar-Anic S. Veljkovic at. al., J.Chem. Phys. 63 (1975) 663-Part I, 669-Part II
[14] P. Pfeifer, D. Avnir, D. Farin, J. Chem Phys. 79 (1983) 3558-Part I, 3568-Part II.
[15] S. Veljkovic at al., Proc. Royal Soc.236 (1956) A1.
[16] S. Veljkovic at al., Nature 191 (1961) 1287.
[17] Lj. Kolar-Anic, Z.Cupic, Encyclopedia of Phys.Org.Chem, Z.Wang (Ed.) Wiley NY,2017.
[18] Lj. Kolar-Anic at al. Frontiers in Endocrinology 13 (2022) 1
[19] S. Ostoijc at al., Nature, 439 (2006) 828.
[20] S. Ostojic at al., Nature, Neuro. Sc. 25 (2022) 783.
[21] K.G. Wilson, Nobel Laureate lecture: The Renormalization Group and Critical Phenomena, Nobel Found. Pub., Stockholm,1982.
[22] A.C. Michselis at al., Nature., 624 (2023) 192.
[23] https://bionumbers.hms.harvard.edu and *references therein (Ref. in).*
[24] L.C. Pauling, E. Zuckerkandl, The Molecular Clock,in: Evolving Genes and Proteins, Bryson J.H. Vogel (Eds.) Academic Press NY..1965.
[25] P.J. Flory, K.A. Dill, Proc. Natl. Acad. Sci. USA 78(1981) 676.
[26] J.K.L. De Silva at al., Physics of Life Rev., 3(2996)229 *and Ref in.*
[27] S. Di Talia at al., Nature, 448 (2007) 947 *and Ref.in.*
[28] J.F. Gillooly at al. Science, 293 (2001) 2248.
[29] T. Suntola at al. History of Science, Society of Natural Philosophy, Helsinki,2018.
[30] M.M. Plavsic, M.B. Plavsic, (second paper at this Conf.) this Proceeding *and Ref.in*.

PHYLLOTACTIC STRUCTURES IN RADIALLY GROWING PATTERN FORMING SYSTEMS

G. Facchini*[2], M. Budroni*[1], G. Schuszter[3], F. Brau[2], and A. De Wit[1]

[1] *Nonlinear Physical Chemistry Unit, Université libre de Bruxelles (ULB), CP231, 1050 Brussels, Belgium. (anne.de.wit@ulb.be) *contributed equally to this work*
[2] *Dipartimento di Chimica e Farmacia, Universita degli Studi di Sassari, Via Vienna 2, Sassari 07100, Italy *contributed equally to this work*
[3] *Department of Physical Chemistry and Materials Science, University of Szeged, Rerrich Béla tér 1., Szeged, H-6720, Hungary*

DOI: https://doi.org/10.46793/Phys.Chem24I.035F

ABSTRACT
Phyllotactic patterns, i.e. regular arrangements of leaves or flowers around a plant stem, are beautiful and fascinating examples of regular complex structures encountered in Nature. In botany, their specific symmetries develop when a new primordium periodically grows in the largest gap left between the previous primordium and the apex [1]. Experiments using ferrofluid droplets have also shown that phyllotactic patterns spontaneously form when identical elements repulsing each other are periodically released at a given distance from an injection center and are advected radially at a constant speed [2]. A central issue in phyllotaxis is to understand whether other self-organized mechanisms can generate such patterns. We show that phyllotactic patterns can also develop in the large class of spatial symmetry-breaking systems giving spotted structures with an intrinsic wavelength in the case of radial growth. The constraint of maintaining a fixed wavelength between spots while expanding radially either diffusively or advectively generalizes the concept of successive release of repulsing agents in botany or ferrofluids to new classes of systems. We evidence this numerically on two different models describing reaction-driven phase transitions [3] and self-organized spatial Turing patterns [4], respectively. We further confirm it experimentally with phyllotactic patterns obtained within a radial flow using a precipitation reaction, similar to mineralization reactions important for CO_2 sequestration [5]. A generalized method for the construction of this new family of phyllotactic structures is presented. Revealing the genericity of the simple conditions needed to obtain such new phyllotactic arrangements paves the way to discover them in large classes of systems ranging from spinodal decomposition [3], chemical [6], biological [7] or optical [8] Turing structures, and ecological [9] or Liesegang [10] patterns, to name a few.

REFERENCES
[1] R.V. Jean, Phyllotaxis, (Cambridge University Press, 2010).
[2] S. Douady, & Y. Couder, Phys. Rev. Lett., 68 (1992) 2098
[3] J.W. Cahn & J.E. Hilliard, The Journal of Chemical Physics, 28 (1958) 258.
[4] A.Turing, Philos Trans R Soc Lond B. 237 (1952) 37.
[5] G. Schuszter, F. Brau, & A. De Wit, Environ. Sci. Technol. Lett. 3 (2016) 156.
[6] V. Castets, et al., Phys. Rev. Lett. 64 (1990) 2953.
[7] S. Kondo & Asai, Pomacanthus, Nature 376 (1995) 765.
[8] K. Staliunas. Phys. Rev. Lett. 81 (1998) 81.
[9] R. Lefever & O. Lejeune, Bull. Math. Biol. 59 (1997) 263.
[10] M. Dayeh, M. Ammar, and M. Al-Ghoul, RSC Adv. 4 (2014) 60034.

A *– Chemical Thermodynamics*

THERMODYNAMIC PROPERTIES OF THE AQUEOUS TRIS+TRIS·HCl SOLUTION AT A TEMPERATURE OF 298.15 K

D. Ž. Popović[1], T. G. Ivanović[2], J. M. Miladinović[3], Z. P. Miladinović[4] and J. Nikolić[3]

[1] *Innovation Centre Faculty of Technology and Metallurgy, University of Belgrade, Karnegijeva 4, 11 001 Belgrade, Serbia (*dpopovic@tmf.bg.ac.rs*)*
[2] *Institute for Multidisciplinary Research, University of Belgrade, Kneza Višeslava 1, 11 030 Belgrade, Serbia*
[3] *Faculty of Technology and Metallurgy, University of Belgrade, Karnegijeva 4, 11 001 Belgrade, Serbia*
[4] *Institute of General and Physical Chemistry, Studentski trg 12-16, 11 000 Belgrade, Serbia*

DOI: https://doi.org/10.46793/Phys.Chem24I.039P

ABSTRACT

The isopiestic method was used to experimentally estimate the values of the osmotic coefficient of an aqueous solution of a mixture of TRIS and TRIS·HCl, as part of a preliminary study of thermodynamic properties. There were no data available in the literature for this system. The values of the parameters of the extended Pitzer model were estimated by processing the experimental data of the osmotic coefficients of the mixed solution. The values of the mixing parameters were determined to be $\lambda_{\mathrm{TRIS,TRISH^+}}\left(m^0\right)^2 = 0.0241425$ and $\xi_{\mathrm{TRIS,TRISH^+,Cl^-}}\left(m^0\right)^3 = -0.0057747$ with a standard deviation of fit of the order of 10^{-3}.

INTRODUCTION

The substance TRIS and its conjugate acid $TRISH^+$, which dissociates in aqueous solutions according to the equation $TRISH^+ = TRIS + H^+$ with pK = 8.07 in pure water at a temperature of 298.15 K [1], make the mixture TRIS+TRIS·HCl suitable for the preparation of buffer solutions in the pH range 7–9. In artificial seawater, these buffers are used to determine the pK value of the indicator dye in spectrophotometric measurements [2] and to calibrate glass electrodes in potentiometric measurements [3, 4]. According to some sources [5] TRIS-buffer is used instead of saline in Pfizer-BioNTech's Covid-19 vaccine to obtain improved stability profile.

METHODS

The isopiestic method can be used to determine the values of the osmotic coefficients in electrolyte and non-electrolyte solutions. Scathard et al. [6] have described the procedure for carrying out this method in detail. Solutions that are in isopiestic equilibrium have the same solvent activity. The relation for isopiestic equilibrium, when the nonelectrolyte-electrolyte aqueous mixture {*x*TRIS+(1–*x*) TRIS-HCl}(aq) is involved, is:

$$\nu_{\mathrm{R}} m_{\mathrm{R}} \phi_{\mathrm{R}} = \left(m_{\mathrm{TRIS}} + 2m_{\mathrm{TRIS{\cdot}HCl}}\right)\phi \qquad (1)$$

where for the reference solution R, ν_{R} is the number of ions into which an electrolyte molecule completely dissociates, m_{R} is the stoichiometric molality and ϕ_{R} osmotic coefficient, while m_{TRIS}, $m_{\mathrm{TRIS{\cdot}HCl}}$ and ϕ are the molality of TRIS, of TRIS·HCl and osmotic coefficient of the mixture

{*x*TRIS+(1–*x*) TRIS·HCl }(aq), respectively. The TRIS(aq) stock solution was prepared in an inert nitrogen atmosphere, to exclude the presence of CO_2(g), using double-distilled, deionized water and Sigma-Aldrich chemical TRIS(s) with a mass fraction greater than 0.999. The molality of the TRIS(aq) solution was determined by potentiometric titration with a standard solution of 1M HCl(aq) without the presence of CO_2(g) with the indicator chlorophenol red until the pH of the solution was 4.7. The determined molality of the stock solution of TRIS(aq) is m_{TRIS} = (5.4657 ±0.0030) mol·kg^{-1}. The stock solution $CaCl_2$(aq) was prepared from $CaCl_2 \cdot 4H_2O$(s) (Merck suprapure grade, mass fraction 0.99995) and double-distilled deionized water. The molality of the solutions was determined gravimetrically by converting three mass aliquots into anhydrous $CaSO_4$(s) and the molality of the reference solution was m_R =(1.6545±0.0029) mol·kg^{-1}. The mixed solution {*x*TRIS+(1–*x*) TRIS·HCl}(aq) was prepared by mixing the aliquots of TRIS(aq) stock solution and HCl(aq) (Sigma Aldrich, mass fraction 0.37).

RESULTS AND DISCUSSION

Table 1. shows the experimental values of the molality of the reference solution, the tested solution and the osmotic coefficient of the system {*x*TRIS+(1-*x*) TRIS·HCl}(aq) at the temperature T = 298.15 K, where $x = m_{TRIS}/(m_{TRIS} + m_{TRIS\cdot HCl}) = 0.5141$.

Table 1. The experimental values of the stoichiometric molality of the reference solution $CaCl_2$(aq), m_R, isopiestic product for the reference solution, $\nu_R m_R \phi_R$, molality values of TRIS, m_{TRIS}, and of TRIS·HCl, $m_{TRIS\cdot HCl}$, with deviations from the mean value from triplicates in the system {*x*TRIS+(1-*x*)TRIS·HCl}(aq) and values of the osmotic coefficient, ϕ, determined by the isopiestic method, at the temperature T = 298.15 K.

m_R (mol·kg^{-1})	$\nu_R m_R \phi_R$	m_{TRIS} (mol·kg^{-1})	$m_{TRIS\cdot HCl}$ (mol·kg^{-1})	ϕ
$1.6674_3 \pm 0.0004$	$6.3123_4 \pm 0.0062$	$2.2638_0 \pm 0.0003$	$2.1394_0 \pm 0.0003$	0.9447 ± 0.0020
$1.5787_6 \pm 0.0007$	$5.8327_7 \pm 0.0059$	$2.0912_4 \pm 0.0005$	$1.9763_2 \pm 0.0005$	0.9454 ± 0.0021
$1.4834_1 \pm 0.0003$	$5.3380_3 \pm 0.0057$	$1.9177_8 \pm 0.0006$	$1.8123_9 \pm .0.0006$	0.9440 ± 0.0022
$1.4122_1 \pm 0.0007$	$4.9824_8 \pm 0.0055$	$1.7810_3 \pm 0.0006$	$1.6831_5 \pm 0.0005$	0.9491 ± 0.0023
$1.3323_3 \pm 0.0006$	$4.5975_4 \pm 0.0053$	$1.6685_7 \pm 0.0005$	$1.5768_7 \pm 0.0005$	0.9352 ± 0.0024
$1.2753_1 \pm 0.0006$	$4.3315_7 \pm 0.0052$	$1.5633_9 \pm 0.0005$	$1.4774_8 \pm 0.0005$	0.9407 ± 0.0025
$1.2155_2 \pm 0.0001$	$4.0604_2 \pm 0.0051$	$1.4667_3 \pm 0.0007$	$1.3861_3 \pm 0.0006$	0.9402 ± 0.0026
$1.1243_2 \pm 0.0007$	$3.6618_0 \pm 0.0048$	$1.3286_1 \pm 0.0004$	$1.2556_0 \pm 0.0004$	0.9366 ± 0.0028
$1.0416_0 \pm 0.0007$	$3.3154_6 \pm 0.0046$	$1.2041_8 \pm 0.0004$	$1.1380_1 \pm 0.0004$	0.9361 ± 0.0029
$0.9847_5 \pm 0.0005$	$3.0856_2 \pm 0.0045$	$1.1254_4 \pm 0.0004$	$1.0635_9 \pm 0.0003$	0.9325 ± 0.0031
$0.9546_8 \pm 0.0003$	$2.9666_7 \pm 0.0044$	$1.0622_0 \pm 0.0002$	$1.0038_3 \pm 0.0002$	0.9500 ± 0.0032

The treatment of the experimental results for the osmotic coefficients of the mixture {*x*TRIS+(1-*x*) TRIS-HCl}(aq) from Table 1. was performed by applying the Pitzer model for solutions containing electrolytes and non-electrolytes, Eqs.(2)-(4):

$$(\phi-1)=\left(2/\sum_{i} m_i\right)\left[-A_\phi I^{1.5}/\left(1+1.2I^{1/2}\right)+m_{\mathrm{TRISH^+}}m_{\mathrm{Cl^-}}\left(B^{\phi}_{\mathrm{TRIS\cdot HCl}}+ZC^{\phi}_{\mathrm{TRIS\cdot HCl}}\right)\right.$$
$$+m_{\mathrm{TRIS}}m_{\mathrm{TRISH^+}}\lambda_{\mathrm{TRIS,\,TRISH^+}}+m_{\mathrm{TRIS}}m_{\mathrm{TRISH^+}}m_{\mathrm{Cl^-}}\xi_{\mathrm{TRIS,\,TRISH^+,Cl^-}}$$
$$\left.+1/2m^2_{\mathrm{TRIS}}\lambda_{\mathrm{TRIS,TRIS}}+m^3_{\mathrm{TRIS}}\mu_{\mathrm{TRIS,TRIS,TRIS}}\right] \qquad (2)$$
$$B^{\phi}_{\mathrm{TRIS\cdot HCl}}=\beta^{(0)}_{\mathrm{TRIS\cdot HCl}}+\beta^{(1)}_{\mathrm{TRIS\cdot HCl}}\exp(-\alpha_{\mathrm{TRIS\cdot HCl}}I^{1/2}) \qquad (3)$$
$$C^{\phi}_{\mathrm{TRIS\cdot HCl}}=C^{(0)}_{\mathrm{TRIS\cdot HCl}}+C^{(1)}_{\mathrm{TRIS\cdot HCl}}\exp(-\omega_{\mathrm{TRIS\cdot HCl}}I^{1/2}) \qquad (4)$$

where m_{TRIS}, $m_{\mathrm{TRISH^+}}$ and $m_{\mathrm{Cl^-}}$ are the molalities of species in the mixed solution, function Z is defined as $Z=m_{\mathrm{TRISH^+}}+m_{\mathrm{Cl^-}}$, value A_ϕ = 0.391475 mol$^{-1/2}$·kg$^{1/2}$ represents Debye–Hückel limiting coefficient for the function of the osmotic coefficient, at T = 298.15 K and p=101.325 kPa [7] and ionic strength is defined as $I=m_{\mathrm{TRIS\cdot HCl}}$. Parameter values of $\beta^{(0)}_{\mathrm{TRIS\cdot HCl}}$, $\beta^{(1)}_{\mathrm{TRIS\cdot HCl}}$, $\alpha_{\mathrm{TRIS\cdot HCl}}$, $C^{(0)}_{\mathrm{TRIS\cdot HCl}}$, $C^{(1)}_{\mathrm{TRIS\cdot HCl}}$ and $\omega_{\mathrm{TRIS\cdot HCl}}$ of the TRIS·HCl(aq) solution with parameters $\lambda_{\mathrm{TRIS,TRIS}}$ and $\mu_{\mathrm{TRIS,TRIS,TRIS}}$ of the TRIS(aq) solution at T=298.15 K were obtained by treatment of isopiestic data of Robinson and Bower [6].

The nonlinear least squares method was used to determine the mixing parameters of TRIS and TRIS·HCl, the values are $\lambda_{\mathrm{TRIS,TRISH^+}}(m^0)^2$ = 0.0241425 and $\xi_{\mathrm{TRIS,TRISH^+,Cl^-}}(m^0)^3$ = – 0.0057747 with standard deviation σ (ϕ) = 0.0051 in the total molality range (1.6545 - 5.4657) mol·kg^{-1} at a mole fraction x = 0.5141.

Figure 1. shows the osmotic coefficients of the mixture {xTRIS+(1-x)TRIS·HCl}(aq) as a function of the total molality of the solution at T=298.15 K, together with calculated values of osmotic coefficients for the solution of TRIS(aq), TRIS·HCl(aq) and their mixture using Extended Pitzer's model and parameters $\lambda_{\mathrm{TRIS,TRISH^+}}$ and $\xi_{\mathrm{TRIS,TRISH^+,Cl^-}}$.

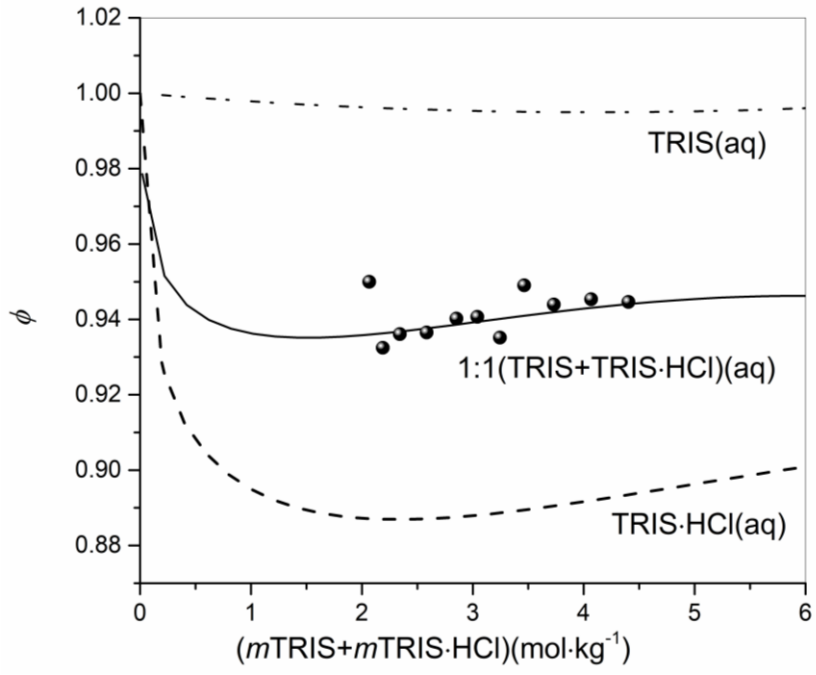


Figure 1. Dependence of the osmotic coefficients of the mixture {xTRIS+(1-x) TRIS·HCl}(aq) on the total molality of the solution: ●- experimental data from isopiestic measurements, ____ osmotic coefficients of the mixture calculated using the Pitzer model and mixing parameters, -·-·- calculated values of osmotic coefficients of a pure solution TRIS(aq) and - - - osmotic coefficients of TRIS·HCl(aq) solutions at the temperature 298,15 K.

CONCLUSION

The isopiestic method was used to determine the osmotic coefficients of the solution {*x*TRIS+(1-*x*) TRIS-HCl }(aq) in the total molality range (1.6545 - 5.4657) mol·kg^{-1} at a mole fraction x = 0.5141 with $CaCl_2$(aq) as reference solution. The experimental results were treated using the Extended Pitzer model for the aqueous mixture of electrolyte and nonelectrolyte. The values of the mixture parameters were determined to be $\lambda_{\mathrm{TRIS,TRISH^+}}\left(m^0\right)^2$ = 0.0241425 and $\xi_{\mathrm{TRIS,TRISH^+,Cl^-}}\left(m^0\right)^3$ = – 0.0057747, with a standard deviation of fit of the order of 10^{-3}. This preliminary investigation gives reason to study the thermodynamic properties for other compositions of the aqueous mixture of TRIS and TRIS·HCl.

ACKNOWLEDGEMENT

This work was supported by the Ministry of Science, Technological Development and Innovation of the Republic of Serbia (Contract No. 451-03-66/2024-03/200287, Contract No.451-03-65/2024-03/200135).

REFERENCES

[1] R. G. Bates, H. B. Hetzer, J. Phys. Chem. 65 (4) (1961) 667–671.
[2] B. Yang, M. C. Patsavas, R. H. Byrne, Mar. Chem. 160 (2014) 75–81.
[3] A. G. Dickson, *Mar. Chem*. 44 (2) (1993) 131–142.
[4] R. A. Durst and B. R. Staples, Clin. Chem., 18 (3) (1972) 206-208.
[5] Scatchard G., J. Chem. Eng. Data, 83 (1961) 2636-2640.
[6] Robinson R. A, Bower V. E., J. Chem. Eng. Data, **10** (1965) 246-247.
[7] S. L. Clegg, J. A. Rard, K. S. Pitzer, J. Chem. Soc. Faraday Trans., 90 (1994) 1875-1894.

B *– Spectroscopy, Molecular Structure, Physical Chemistry of Plasma*

THE EFFECT OF THE SURROUNDING GAS ON THE SPECTRA INTENSITY IN THE CHARACTERISATION OF THE ARCHEOLOGICAL COINS USING LIBS

M. Stoiljković, S. Veličković, I. Staičić, and F. Veljković

University of Belgrade, Vinča Institute of Nuclear Sciences, Dept. of Phys. Chem., Belgrade, Serbia, (missa@vinca.rs)

DOI: https://doi.org/10.46793/Phys.Chem24I.045S

ABSTRACT

The effect of helium as a surrounding gas on the abundance and intensity of the spectra in the laser-induced plasma was considered. A microsecond laser at 10.6 μm was used to induce the breakdown plasma and, the outcome is illustrated in the archaeological valued coins. The two distant past coins were considered and, with both, additional and distinctively intensive spectral lines were recorded compared to air. This is especially valid in the 200-300 nm range in which these spectral lines may be used to identify the main but specifically the trace elements. The sulfur case is pointed out here.

INTRODUCTION

Laser-induced breakdown spectroscopy (LIBS) is a long-established technique for determining the elemental composition of primarily solid samples. One of its dominant advantages is that a small amount of material is required for analysis, which implies micron-sized damage to the surface of the material being analyzed. This makes LIBS a preferred technique of culturally valuable object analysis, for example, metal coins [1]. Contrary to numerous advantages, LIBS captures the very local surface of the material being analyzed, so in cases where the material is metallurgically inhomogeneous by surface or by volume or has been subject to some chemical influence, the results should be carefully analyzed in conjunction with other characterization and diagnostic techniques [2, 3].

Also, the intensity of the emission spectrum of laser-induced plasma can be affected by various factors, including the reflectivity of the laser wavelength, surface roughness, as well as the pressure and composition of the atmosphere in which the plasma is generated.

This work demonstrates a simple approach for increasing the emission intensity and promoting extra lines of laser-induced plasma containing ablated material from coins of archaeological value, which involves the introduction of helium gas into the plasma.

METHODS

A CO_2 pulsed laser of a microsecond range at 10.6 μm and, an average power of 110 kW was used to induce the breakdown plasma on the coins sample [4]. The laser is focused on the coin using a ZnSe f/5.6 lens and the ablated material from the sample expand backward of the target forming the emitting plasma. A collimating lens-provided optic cable gathers the plasma optical emission into the monochromator (JY H25) equipped with an Andor iDus-BVF CCD camera giving a 5000 resolving power. A flow of helium 3.5 dm^3/min was directed at the point on the target where the laser was focused. Otherwise, the plasma was induced in the open air. The coins have not been pre-treated other than lightly wiped and, the LIBS spectra were recorded in the 200-500 nm range through three consecutive laser pulses. The focusing point on the coins was chosen randomly. The spectral lines are identified using Reference Data [5] and reference spectra [6].

RESULTS AND DISCUSSION

The two coins dated the end of the 18th century, Habsburg Monarchy Franz II, 1 Kreuzer, [7], and Constantine I, CONSTANTINOPOLIS BSIS, AD 334-335 [8] were examined. The first was classified as copper and the second as bronze. For both coins, it is shown that the spectrum intensity recorded in helium-supported plasma is about ten times higher compared to that recorded in air. Besides, the lines missing in the air emerge in helium as intensive enough for accurate identification and possible analytical use.

As an illustration, the spectra of Constantine I (C) coin in helium and air plasma are given in Figure 1. Since numerous extra lines emerge in helium, only a narrow spectral range is shown for clarity. In the same range, the C and F coins spectra in helium are shown in Figure 2. Several sulfur lines were identified which are not present in the air. By comparing the intensities at 196 nm, 198 nm, and 200 nm, the estimate is that the C coin contains about ten-fold more sulfur than F. Consideration of the origin of sulfur in the coins may be interesting. First, it could be the base material impurity. Both coins are copper-based so copper sulfate presence as an impurity is possible. As the F coin originates from a more recent historical period when obtaining and refining metal was at a higher technological level, one can expect lower impurities in the material. Also, the copper sulfate could have arisen on the surface due to exposing the coins to the atmosphere including the ground and moisture to which they were undoubtedly exposed. Both assumptions seem consistent with the fact that the C coin is 15 centuries older than the F and that by all accounts it should contain more sulfur regardless of its source.

For the case of copper as the base metal for both coins, the copper line intensity ratio at 194.5 nm shows about three times more copper in the F than in the C coin. Since C is declared as bronze, the above seems acceptable considering that the intensity ratio of tin lines, 238 nm, and 248 nm, shows that the C coin contains about 15 times more tin than F. It is well known that ancient bronzes can contain up to 30% tin and, if we assume that this is so, then the F coin could contain about 2% tin, which is close to the officially declared value [9].

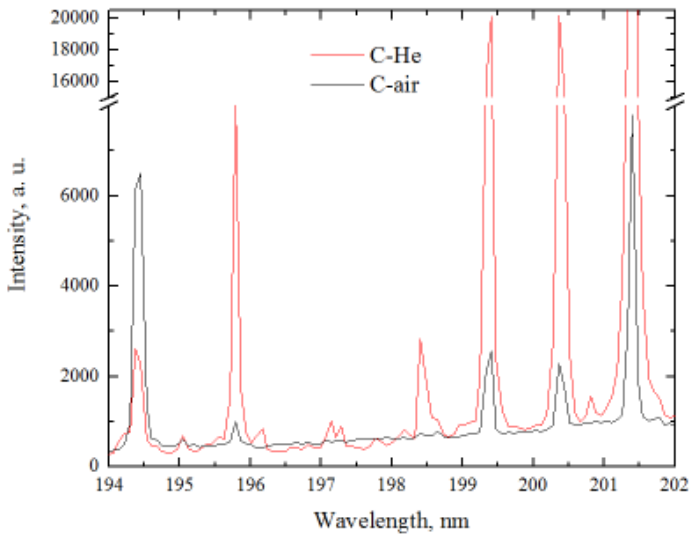


Figure 1. Comparison of the Constantine I (C) coin spectra intensity in helium and air.

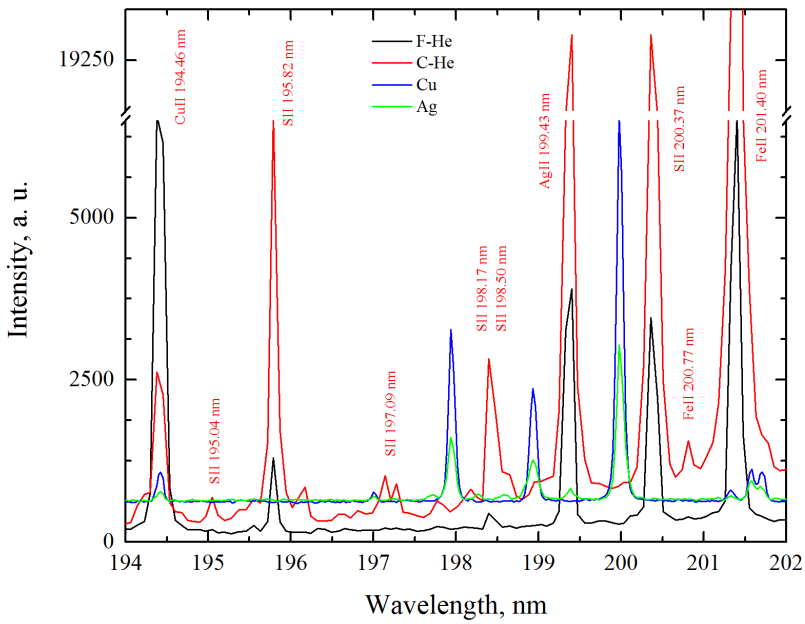


Figure 2. The spectral lines identified in the Constantine I (C) and Franz II (F) coins spectra in helium-rich plasma. The blue and green lines correspond to the Spectragryph spectral base. [5]

Finally, the contents of Fe and Ag in the C coin suggest that it is possible to consider them as a consequence of a technologically insufficiently developed material purification process used for coinage. As impurities, the C coin contains about 8.5 times more Fe and 5.5 times more Ag than the F coin, which can be a consequence of the composition of the ore or raw metals in the ancient period.

CONCLUSION

We demonstrated an effective and easy-to-apply way to increase significantly the intensity of the laser-induced breakdown plasma emission spectrum. That is illustrated through the qualitative chemical characterization and comparison of the two distant past coins that assume significantly different metal ore processing technologies. The results confirm the fact above since very intensive emission appears in helium-generated plasma with many extra lines enabling distinction of fine details in the content of the elements.

Acknowledgment

This work was supported by the Ministry of Education, Science and Technological Development of the Republic of Serbia (grant no 451-03-66/2024-03/200017).

REFERENCES

[1] R. A. Rezk, N.A. Abdel Ghany, A. M. Mostafa, Coatings, 1 (2022) 21548 https://doi.org/10.3390/coatings12101548.

[2] C.De Vito, M. Bernabale, C. Aurisicchio, F. Catalli, L. Medeghini, S. Mignardi, A. Maria Conte, T. de Caro, Heritage, 7 (2024) 412–426 https://doi.org/10.3390/heritage7010020.

[3] M. Di Fazio, A. candida Felici, F. Catalli, C. De Vito, Scientific Reports, 9 (2019) 12668.

[4] J. Savović, M. Stoiljković, M. Kuzmanović, M. Momčilović, J. Ciganović, D. Ranković, S. Živković, M. Trtica, Spectrochim Acta B 118 (2016) 127-136.

[5] https://physics.nist.gov/PhysRefData/ASD/lines_form.html.
[6] https://www.effemm2.de/spectragryph/.
[7] https://en.numista.com/catalogue/pieces7075.html\.
[8] https://en.numista.com/catalogue/pieces59270.html.
https://colnect.com/en/coins/coin/18767-6_Kreuzer_A_B_C_D_E_F_G_S-1792~1835_-_Habsburg_Monarchy_Franz_II_I-Austro-Hungarian_Monarchy.

OPTIMIZATION OF LASER-INDUCED PLASMA EMISSION FOR ELEMENTAL AND ISOTOPIC ANALYSIS OF HYDROGEN

I. Traparić[1], D. Ranković[2], D.B. Stankov[1], J. Savović[3], M. Kuzmanović[2] and M. Ivković[1]

[1]*Institute of Physics, University of Belgrade, Pregrevica 118, 11080 Belgrade, Serbia, (traparic@ipb.ac.rs)*
[2]*Faculty of Physical Chemistry, University of Belgrade, Studentski trg 12-16, 11000 Belgrade, Serbia*
[3]*Vinca Institute of Nuclear Sciences, University of Belgrade, Mike Petrovića Alasa 12-14, 11351 Vinča, Belgrade, Serbia*

DOI: https://doi.org/10.46793/Phys.Chem24I.049T

ABSTRACT
The LIBS technique based on the TEA CO2 laser is optimized for obtaining narrow and intense hydrogen Balmer lines, with the aim of application for quantitative and isotopic analysis of hydrogen. In the helium atmosphere under reduced pressure (below 10 mbar), for delay times longer than 5 μs, line widths of 0.04 nm were obtained, close to the instrumental width of the spectrograph. For optimal experimental conditions, plasma diagnostics were performed using optical emission spectroscopy methods: the electron concentration from 2.5 x 10^{21} m^{-3} to 2.7 x 10^{20} m^{-3}, and gas temperature from 5000 to 3500 K were obtained.

INTRODUCTION
Quantitative analysis of hydrogen is of great importance for many classes of materials, peculiarly for organic materials. Due to its unique analytical properties, Laser Induced Breakdown Spectroscopy (LIBS) technique is particularly suitable for rapid elemental analysis of solid samples, without or with minimal sample preparation [1]. The possibility of remote analysis is a feature of the LIBS technique that comes to the fore especially in health-hazardous environments, such as nuclear reactors. On the other hand, it is precisely in nuclear technology that the analysis of hydrogen and its isotopes is of key importance [2].

However, hydrogen analysis, especially isotopic analysis, is accompanied by several problems. Laser induced plasmas have significantly high values of electron number density and therefore all hydrogen lines in the optical region show a pronounced linear Stark effect: the lines of hydrogen are strongly broadened, that's why they overlap with the lines of other elements. This fact, along with the additional problem of background signal substitution, makes it difficult to analyze content of hydrogen with sufficient accuracy. The broadening of hydrogen spectral line profile is especially serious when there is a need to determine the isotopic composition of hydrogen: due to the very small isotopic effect on H lines, even high-resolution spectral instruments cannot resolve hydrogen isotope lines.

The goal of this work was to find the optimal conditions in the laser-induced plasma, as well as the optimal conditions for the detection of plasma emission, to obtain narrow and still sufficiently intensive lines of hydrogen, above all the Balmer alpha line, which is the narrowest of the optical lines of hydrogen. The conditions defined in this way actually mean that it is necessary to achieve conditions in the plasma with a low electron number density, while the excitation temperature is still high enough to excite spectral lines with a high excitation energy, such as the Balmer alpha line (excitation energy of 12.1 eV). We achieved such conditions by inducing plasma under reduced pressure, in a helium atmosphere, using a TEA CO2 laser, due to its extended pulse duration

compared to nanosecond Nd:YAG lasers. As a target suitable for controllable experiments with water and heavy water, we used pastille made from a mixture of graphite and silica gel.

METHODS

The LIBS setup was based on TEA CO_2 laser (Tachisto 215G) operated at 10.6 μm, with a repetition rate of 1 Hz. The duration of the main laser pulse (initial spike) was 80 ns with a tail lasting 2 μs (Fig. 3), with laser pulse energy in range of 230 - 420 mJ. The target (pastille obtained by pressing silica gel and graphite, with the addition of water) was placed within the vacuum chamber mounted on the x-y table. The chamber was vacuumed and filled with a continuous helium gas flow at the desired pressure.

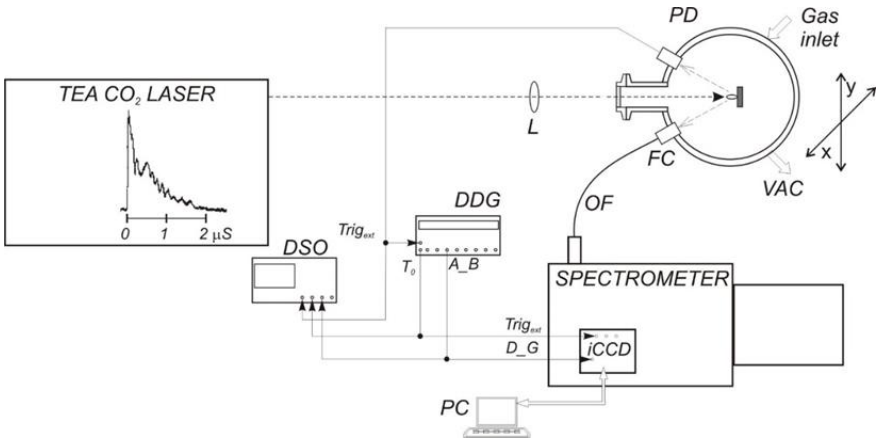


Figure 1. Experimental setup: L-lens, PD-photodiode, OF-optical fiber, FC-focusing collimator, VAC-vacuum outlet, DSO-digital storage oscilloscope and DDG-digital delay generator.

For spectra recording, a a spectrometer (Sol Instruments MS7504i) was employed, equipped with an iCCD camera (Andor Technology, model DH720I-18F-63, with matrix of 256 x 1024 pixels, pixel size of 26 x 26 μm and an 18 mm diameter intensifier). In order to position the acquisition time during the temporal evolution of the plasma, a pulse generator (DG-535, Stanford Research Systems, triggered optically by a fast photodiode) was used. The acquisition gate width was varied between 15 ns and 70 μs, and typical gate time of 5 μs. The instrumental width (diffraction grating with 1800 groves/mm and a 15 μm wide entrance slit of spectrometer) was determined to be 0.03 nm, by using low pressure Ne pen lamp.

RESULTS AND DISCUSSION

Due to the high ionization energy, the plasma induced in helium has a lower values of electron number density for a given temperature, compared to other gases. At lower pressures, the electron number density decreases, and the plasma temperature is still sufficient for intense emission. Figure 2a shows an example of the dependence of the width of the Hα line on the helium pressure, at low pressures lines of satisfactory width and intensity are obtained. The detection delay time in relation to the laser pulse is also a parameter that needs to be optimized: with the prolongation of the beginning of the exposure, the electron concentrations decrease, and thus the line widths, but the intensity also decreases. Figure 2b illustrates the effect of time delay on hydrogen emission detection. The exposure time (gate time) should be increased with an increase of the delay time, in order to increase the intensity, and consequently the signal-to-noise ratio.

The results of a systematic study of the dependence of the half-width of the Halfa line for different helium pressures and delay times are summarized in Fig. 2c. At lower pressures and longer delay times, spectral lines with a profile width of the order of 0.04 nm are obtained, which is only slightly

more than the instrumental profile in our measurements. Under these conditions, the quantitative analysis of hydrogen is much more precise and sensitive, compared to the conditions typical for the usual use of the LIBS (p=1000 mbar) technique. Bearing in mind that the isotopic shift between the Balmer alpha line of hydrogen and deuterium and deuterium and tritium is 0.18 nm and 0.05 nm respectively, the results shown in Figure 2 actually confirm that under optimal experimental conditions LIBS technique is also possible to perform isotopic analysis of hydrogen.

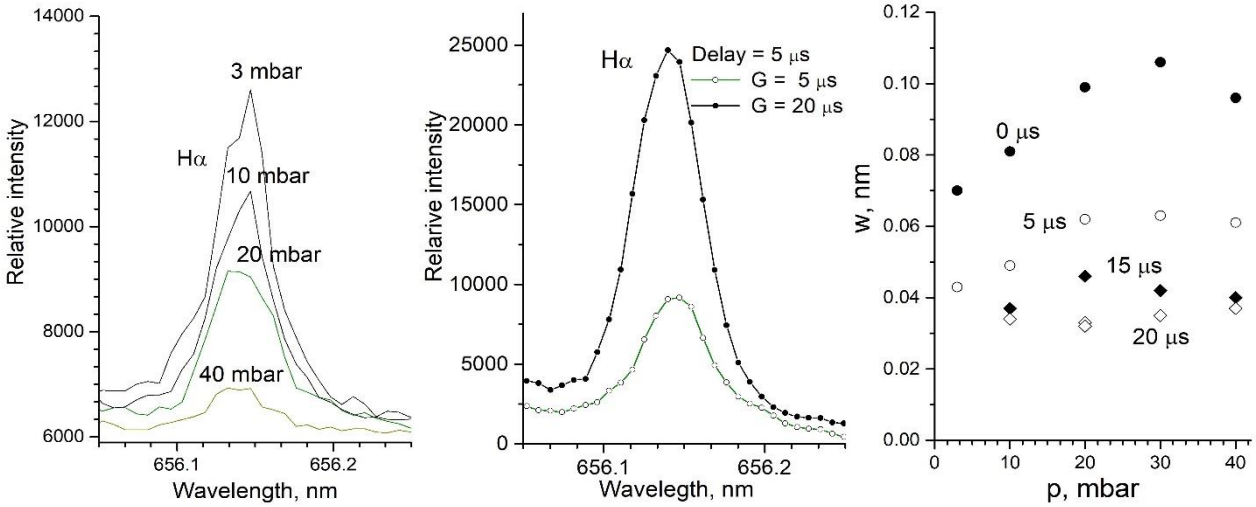


Figure 2. a) The influence of He pressure on H_α line shape, at a delay of 15 μs, gate of 5 μs and laser pulse energy of 260 mJ. b) The influence of gate time on spectra recorded in He at 10 mbar and pulse energy of 260 mJ. c) The influence of He pressure on the half-width of the Halfa line, for different values of delay time. Gate was 5 μs and pulse energy was 320 mJ.

In order to confirm the assumption about the optimal temperature and electron number density for quantitative and isotopic analysis of hydrogen, plasma diagnostics were performed under optimal conditions. The electron number density was estimated by using method based on the separation of the forbidden and allowed components of the He I line at 447.1 nm [3], figure 3a. For a helium pressure of 10 mbar, electron number density was 2.5 x 10^{21} m^{-3} for a delay time of 0.5 μs, and 2.7 x 10^{20} m^{-3} for 5.5 μs delay time. Similar results were obtained by applying the same diagnostic method to the components of the He I 492.2 nm spectral line.

The gas temperature was determined by comparing the synthetic and recorded spectra of the sequence $\Delta v = 0$ of the C2 molecule Swann system at 515 nm [4]. Figure 3b shows a part of the C2 molecule Swann system spectrum, between the band heads (0-0) and (1-1), obtained at pressure of 10 millibars. Spectra were captured for different delay times (5, 10, and 15 μs), with a gate of 5 μs. The instrumental profile of the spectrograph and the plasma parameters allow obtaining spectra with a well-developed rotational structure, where the lines of the R and P branches are well-separated. The band intensities obtained for different delay times decrease rapidly with increasing time, consistent with the temperature decreasing during extinguishing of plasma. By matching the experimental and synthesized spectra, the temperature was determined for different delay times: for a delay of 5 μs, a temperature value of 5 000 K was measured, with an error of 10%. With the delay time increase, a clear trend of temperature decrease was observed, from 4 500 K for a delay of 10 μs to a temperature of about 3 500 K for a delay of 20 μs. The estimated temperature is the rotational temperature (gas temperature).

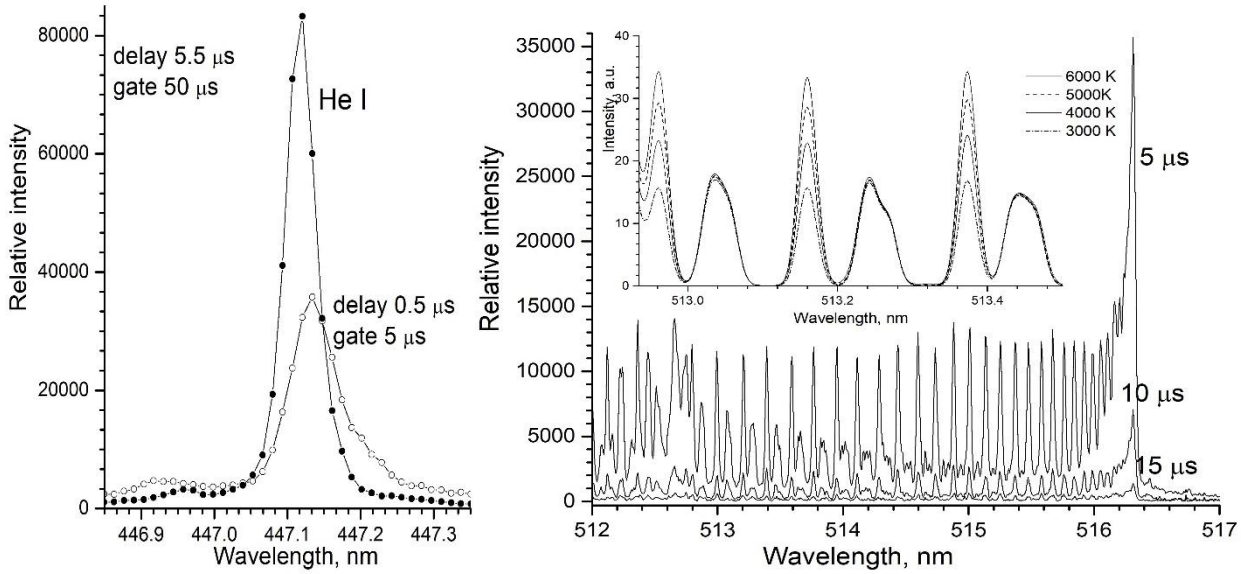


Figure 3. a) Profile of the He I line at 447.1 nm for different delay times. The He pressure and laser pulse energy were 10 mbar and 260 mJ respectively. b) Experimentally obtained spectrum of the Swan band ($\Delta v = 0$ sequence) for different delay times. The He pressure, laser pulse energy and gate were 10 mbar, 260 mJ and 5 μs respectively. The synthesized normalized spectra for different rotational temperatures (part of 0-0 band) were added as upper part of figure.

CONCLUSION

It has been demonstrated that by applying a carefully optimized LIBS technique, very narrow Balmer alpha lines can be obtained, suitable even for hydrogen isotopic analysis. Using a TEA CO2 laser with extended pulse duration, in a low-pressure helium atmosphere, under optimal experimental conditions, half-widths of the Halfa line with a width of about 0.04 nm were obtained. The measured values for electron number density and plasma temperature confirmed the assumption that the optimal conditions for obtaining narrow lines of hydrogen imply low electron concentrations and moderately low temperatures.

Acknowledgment

The research was funded by the Ministry of Science, Technological Development and Innovations of the Republic of Serbia, Contract numbers: 451-03-68/2022-14/200024 and 451-03-65/2024-03/200146, and supported by the Science Fund of the Republic Serbia, Grant no. 7753287 "NOVA2LIBS4fusion". This work was carried out under the project: "Laser induced breakdown spectroscopy for determination of LHD wall composition" (NIFS21KLPF087) within the agreement between NIFS and the University of Belgrade.

REFERENCES

[1] D.A. Cremers, L.J. Radziemski, Handbook of Laser-Induced Breakdown Spectroscopy, Wiley, Chichester, 2013.

[2] A.P. Zakharov, A.E. Gorodetsky, V.K. Alimov, S.L. Kanashenko, A.V. Markin, J. Nucl. Mater., 241–243 (1997) 52.

[3] M. Ivković, M.A. Gonzalez, S. Jovićević, M.A. Gigosos, N. Konjević, Spectrochim. Acta Part B At. Spectrosc. 65 (2010) 234.

[4] C.M. Western, J. Quant. Spectrosc. Radiat. Transf. 186 (2017) 221.

SYNTHESIS, SPECTROSCOPIC CHARACTERIZATION AND BSA INTERACTIONS OF 3-(1-((4-HYDROXY PENTYLAMINO)ETHYLIDENE)CHROMAN-2,4-DIONE

E. Avdović[1], S. Jovičić Milić[1], D. Simijonović[1], D. Stojković[1], D. Milenković[1], and Z. Marković[1,2]

[1] University of Kragujevac, Institute for Information Technologies, Department of Science, Jovana Cvijića bb, 34000 Kragujevac, Serbia (edina.avdovic@pmf.kg.ac.rs)
[2]Department of Natural Science and Mathematics, State University of Novi Pazar, Vuka Karadžića bb,36300 Novi Pazar, Serbia

DOI: https://doi.org/10.46793/Phys.Chem24I.053A

ABSTRACT
In this study, we synthesized a novel coumarin derivative, specifically 3-(1-((4-hydroxy pentylamino)ethylidene)cromane-2,4-dione by the reaction of 3-acetyl-4-hydroxycoumarin and 5-aminopentanol in methanol. The compound was obtained after 2 hours of reflux. The synthesized coumarin derivative was obtained in very good yield (80%) and characterized using elemental microanalysis, Uv-Vis, IR and NMR spectroscopy. Furthermore, the interaction of investigated compound with bovine serum albumin (BSA) was studied using fluorescence spectroscopy and the Stern-Volmer constant (Ksv), quenching rate constant (kq) and the number of binding sites (n) are determined. The obtained constants for the formed BSA-ligand complex indicate good quenching ability of BSA.

INTRODUCTION
Coumarin is a heterocyclic aromatic chemical compound, widely distributed in nature. It consists of fused benzene and α-pyrone ring, belonging structurally to the benzopyrone group of compounds. This structure allows six positions available for substitution. There are numerous known derivatives of coumarin, both natural and synthetic, which owe their significant biological activity to this structural diversity. These compounds are known for their broad range of biological activities. They demonstrate cytotoxic effects against various human tumor cell lines [1,2], as well as spasmolytic, antiarrhythmic, cardiotonic, photodynamic, and antioxidant properties [3,4]. Additionally, they are utilized in flavoring foods and as fragrances in cosmetic products [5]. Research has also explored the anticoagulant [6] and antitumor activities of metal complexes derived from coumarins [7]. In this work, we have reported synthesis of new coumarin derivative, 3-(1-((4-hydroxypentylamino)ethylidene)cromane-2,4-dione, as well as the characterization of the synthesized compound by elemental microanalysis, UV-Vis, IR and NMR spectroscopy. Fluorescence spectroscopy was used to investigate the structural changes in the BSA molecule caused by the addition of the newly coumarin derivative and at the same time to determine the binding constant and the number of binding sites.

METHODS
Elemental microanalyses for C, H and N were done by standard methods at the Institute for Information Technologies, University of Kragujevac, Serbia. UV-Vis spectrum of the investigated compound was measured in the range between 200 and 500 nm in methanol at PerkinElmer, Lambda 365 UV/Vis Spectrophotometer. Infrared spectra were recorded by Perkin-Elmer Spectrum One FT-IR spectrometer using the KBr pellet technique (4000-400 cm^{-1}); ^{1}H and ^{13}C NMR spectra were

recorded by Varian Gemini-2000 (200 MHz) spectrometer in $CDCl_3$ using tetramethylsilane as an internal standard. The interactions of the new coumarin derivative with BSA were monitored using Shimadzu, RF-6000 Spectro fluorophotometer.

Synthesis and characterization of the compound

The reaction mixture containing 0.500 g (0.002 mol) of 3-acetyl-4-hydroxycoumarin and 0.206 g (0.002 mol) of 5-aminopentanol in 50 mL of methanol was heated for 2 hours to reflux (**Figure 1**). The progress of the reaction was monitored using TLC (toluene:acetone = 4:1). When the reaction was complete, the volume of solvent was reduced by half via evaporation. Upon addition of 5 mL of water, a white precipitate was formed, which was subsequently filtered, dried, and washed with 96% ethanol. Yield: 80%. $C_{16}H_{19}NO_4$ (FW = 289.32): C, 66.42; N, 4.84; H, 6.62%; found: C, 66.38; N, 5.03; H, 6.58%. ^{1}HNMR (200 MHz, $CDCl_3$): 1.61 (m, 2H, C3"–H), 1.83 (m, 4H, C2"–H, C4"–H), 2.74 (s, 3H, CH_3), 3.56 (t, 2H, C1"–H), 3.69 (t, 2H, C5"–H), 4.69 (s, 1H, -OH), 7.22 (m, 1H, C6–H), 7.53 (m, 2H, C7–H, C8–H), 8.04 (dd, H, C5–H), 14.26 (s, 1H, NH). ^{13}C NMR (50 MHz, $CDCl_3$): 18.57 (C2'), 23.15 (C3"), 28.78 (C2"), 44.33 (C1"), 32.03 (C4"), 62.29 (C5"), 97.07 (C3), 116.53 (C5, C8), 120.63 (C6), 123.51 (C10), 125.94 (C7), 133.72 (C9), 153.65 (C2), 173.59 (C1'), 176.37 (C4). IR (KBr, cm^{-1}): 3449 (NH and OH), 2943, 2861 (CH), 1701(C=O), 1608, 1565, 1487 (C=C), 1053 (C–O).

Interactions of new coumarin derivative with BSA – fluorescence spectroscopy

To study the interaction of a novel coumarin derivative with bovine serum albumin (BSA) the fluorescence spectroscopy was used. This experiment was performed at a temperature of 296 K with constant concentration of BSA protein solution and different concentrations of investigation compound. The decrease of the emission intensity of the BSA solution was monitored at 337 nm. Fluorescence quenching data were obtained using the Stern-Volmer equation (Eq. 1):

$$\frac{I_0}{I} = 1 + k_q \tau_0 [Q] = 1 + K_{SV}[Q]. \quad (1)$$

Where: I_o and I represent BSA fluorescence intensities in the absence and in the presence of investigated compound, while K_{SV} and k_q are the quenching constant and the quenching rate constant of BSA, τ_o is the half-life of BSA without complex (10^{-8} s for BSA) and [Q] is the concentration of investigation compound. The binding constant between compound and BSA was calculated by the Hill equation (Eq. 2) [8]:

$$log\frac{I_0 - I}{I} = logK_b + nlog[Q]. \quad (2)$$

I_0 and I are BSA fluorescence intensities in the absence and in the presence of the compound, and K_b represent the binding constant, n is the number of binding sites and [Q] is the concentration of the quencher.

RESULTS AND DISCUSSION

Chemistry

The reaction for preparation of new coumarin derivative is presented in **Figure 1**. The reaction was performed by treatment of 3-acetyl-4-hydroxycoumarin with 5-aminopentanol in methanol, under reflux. After cooling and filtration of the reaction mixture, product was obtained in very good yield.

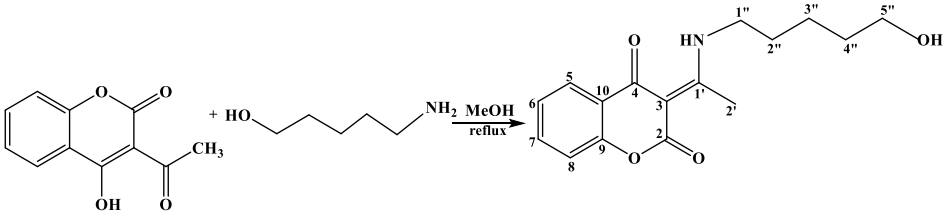


Figure 1. Synthesis of 3-(1-((4-hydroxy pentylamino)ethylidene)cromane-2,4-dione and numbering used for NMR data analysis.

The structure of the synthesized compound was confirmed based on the results of elemental microanalyses, as well as its UV-Vis, IR, and NMR (^{1}H and ^{13}C) spectra.
The results of elemental microanalysis showed that the found values for C, H, and N are in good agreement with the corresponding calculated values.

The experimental UV-Vis spectrum of the obtained coumarin derivative was recorded in methanol solution. This spectrum is shown in **Figure 2** and it can be seen that the tested compound exhibits two characteristic absorption maxima at around 245 and 320 nm. This type of absorption is found in similar coumarin derivatives [9].

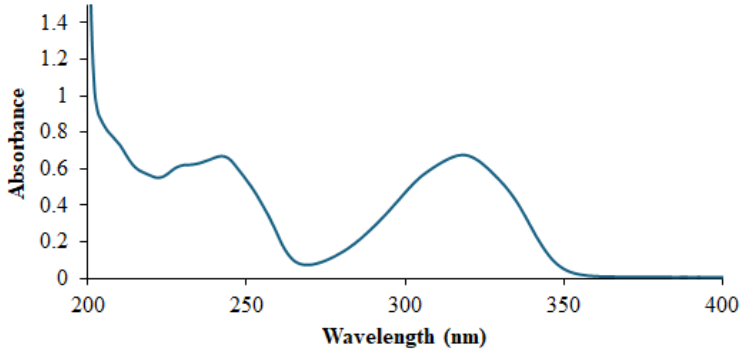


Figure 2. UV-Vis spectrum of new coumarin derivative.

In the IR spectrum, characteristic band at 3449cm^{-1} was attributed to vibrations of NH and OH groups. Stretching vibrations corresponding to the C=O group were observed at 1701 cm^{-1}, while vibrations corresponding to the C–O group were found at 1053 cm^{-1}.

In the ^{1}H NMR spectrum, the singlet assumed at 2.74 ppm originates from the proton from the CH_3 group. In the range from 7.22 to 8.04 ppm were observed protons from the phenyl group of coumarin part, while the protons of the aliphatic chain were detected as multiplets (at 1.61 and 1.83 ppm) and triplets (at 3.56 and 3.69 ppm). Also, the singlet from the amino NH group was observed at 14.26 ppm, and the signal from the hydroxyl group was detected at 4.69 ppm while carbon atoms in position 3 are at significantly lower chemical shifts.

Interactions of new coumarin derivative with BSA

For distribution drugs in blood, serum albumin plays an inportant role. Bovine serum albumin has been studied most often because of its structural homology with human serum albumin.

To get information on the binding constant and number of binding sites a spectrofluorimetric investigation was performed (done) by monitoring of decreasing in the intesity of the peaks as a result of adding the various concentrations of the tested compound to the BSA solution (**Figure 3**). This change in intensity is due to a change in the secondary structure of the protein in the environment of tryptophan due to the binding of the tested compound to BSA. The values of Stern-Volmer constant

(Ksv), quenching rate constant (kq), binding constant (K_b), and the number of binding sites are presented in **Table 1**.

Table 1. Quenching and binding parameters of BSA-coumarin derivative complex at 296 K.

Ksv (M^{-1})	**k_q (M^{-1})**	**K_b (M^{-1})**	**n (BSA)**
1.61×10^{4}	1.61×10^{12}	3.45×10^{5}	1.7

The obtained constants for the formed BSA-investigated compound complex discovered good quenching ability of BSA.

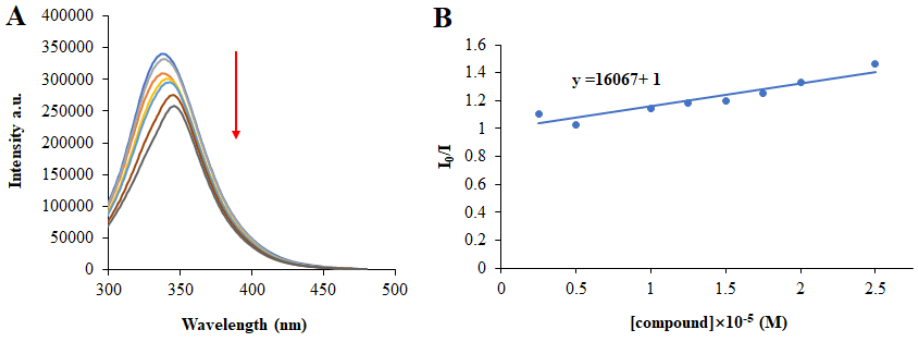


Figure 3. (**A**) Emission spectra of BSA in the presence of investigated compound. (**B**) Stern-Volmer graph used to calculate K_{SV} and quenching rate constant k_q at 296 K.

CONCLUSION

The new compound 3-(1-((4-hydroxypentyamino)ethylidene)cromane-2,4-dione was successfully synthesized and its structure was confirmed through a combination of elemental microanalysis, UV-Vis, IR and NMR spectroscopy. All experimental data obtained from these analyses corroborate the proposed chemical structure of the novel compound. The high value of the binding constant, K_b, and the Stern-Volmer quenching constant, K_{SV}, are the result of good binding of the investigated compound to BSA.

Acknowledgment

This research was funded by the Serbian Ministry of Science, Technological Development and Innovation (Agreements No. 451-03-66/2024-03/200378).

REFERENCES

[1] T. K. Joanna, H. Elzbieta, K. Hanna, W. Irena, M. Dorota, Eur. J. Med. Chem. 46 (2011) 2252.
[2] L. W. Wattenberg, L. K. T. Low, A. V. Fladmoe, Canc. Res. 39 (1979) 1651.
[3] I. Manolov, I. Kostova, T. Netzeva, S. Konstantinov, M. Karaivanova, Archiv. Pharm. Med. Chem. 333 (2000) 93.
[4] B. G. Lake, Food Chem. Toxicol. 37 (1999) 423.
[5] P. Manojkumar, T. K. Ravi, G. Subbuchettiar, Acta Pharm. 59 (2009) 159.
[6] R. Deng, J. Wu, L. Long, Bull. Soc. Chim. Belg. 101 (1992) 439.
[7] I. Kostova, I. Manolov, T. Netzeva, S. Konstantinov, M. Karaivanova, Eur. J. Med. Chem. 34 (1999) 63.
[8] M. Jiang, M.X. Xie, D. Zheng, Y. Liu, X.Y. Li, X. Chen, J. Mol. Struct. 692 (2004) 71-80.
[9] M. R. Antonijević, E. H. Avdović, D. Simijonović, Ž. Milanović, O. R. Klisurić, M. E. Alberto, N. Russo, R. Vojinović, Z. S. Marković, Polycycl. Aromat. Comp. (2024).
[10] C. Tan, J. Liu, H. Li, W. Zheng, S. Shi, L. Chen, L. Ji, J. Inorg. Biochem. 102 (2008) 347.

C *– Kinetics, Catalysis*

APPLICATION OF COLD PLASMA DEPOSITED MATERIALS FOR HYDROGEN PRODUCTION: ADVANCEMENTS IN PHOTOCATALYSIS

M. Fronczak*

Lodz University of Technology, Faculty of Process and Environmental Engineering, Department of Molecular Engineering
Wólczańska 213, 90-005 Lodz, Poland (maciej.fronczak@p.lodz.pl)

DOI*:* https://doi.org/10.46793/Phys.Chem24I.059F

ABSTRACT

Plasma is a state of matter in which positively charged ions and electrons are separated and move independently. Two types of plasma can be distinguished based on the kinetic energy of electrons and other components: (i) thermal plasma, where the energy of electrons and ions is the same, and (ii) cold plasma, where electrons exhibit much higher kinetic energy than ions [1]. Both types of plasma are utilized in current scientific practices for synthesizing nanomaterials or modifying the surfaces of various materials.

Within cold plasma methods, non-equilibrium plasma is particularly interesting. This method can be applied to obtain thin film materials on a variety of surfaces. For example, it can be used to produce catalysts for CO_2 conversion [2,3] or to develop hydrophobic surfaces on materials like goose down [4]. This technique is commonly known as plasma-enhanced chemical vapor deposition (PECVD) and has been identified as an ideal means of generating novel nanomaterials and modifying traditional material surfaces through molecular engineering. Researchers worldwide are exploring the development of PECVD methods. This technique enables the creation of a various range of materials in the form of thin films and allows for easy doping of the synthesized materials with metals or their compounds. Introducing precursors into the plasma environment under low pressure offers the possibility of designing materials at the atomic scale, tailoring their molecular and electronic structure to achieve desired properties.

Cold plasma methods are also applied for depositing thin-film carbon-nitrogen materials. These coatings are similar to bulk materials, known for their semiconductive and photocatalytic performance. Among various interesting applications, noteworthy ones include photocatalytic hydrogen production and the photodegradation of pollutants in aqueous solutions. Carbon-nitrogen materials deposited via cold plasma differ in structure and physicochemical properties from those obtained through conventional polymerization methods, marking a new category of innovative photocatalysts with potential applications in water splitting.

As an example, in performed studies, carbon-nitrogen thin films were produced using the PECVD method with acrylonitrile and acetonitrile. The primary objective was to apply these films in photocatalytic hydrogen production. The materials were deposited onto quartz plates (1cm x 1cm) with glow discharge assistance, ranging in power from 10 to 80 W. It was observed that discharge power is a key parameter for controlling the carbon-to-nitrogen ratio, with higher power resulting in a higher C/N ratio. The results demonstrated that thin-film carbon-nitrogen materials exhibit hydrogen production activity under UV-Vis irradiation, yielding a hydrogen production rate of approximately 32 $\mu mol \cdot h^{-1} \cdot cm^{-2}$ for acetonitrile-based samples and 66-82 $\mu mol \cdot h^{-1} \cdot cm^{-2}$ for acrylonitrile-based samples.

Acknowledgments
Dr. Maciej Fronczak acknowledges the financial support provided by the National Science Center within the Miniatura Program (grant no. 2021/05/X/ST8/00089) and by Lodz University of Technology within the program for support young researchers FU^{2}N (grant no. 503/9-9-4-3).

REFERENCES

[1] C. Roth, Nanoscale plasma surface modification of powders, ETH Zurich, 2012.
[2] M. Smolarek, H. Kierzkowska-Pawlak, R. Kapica, M. Fronczak, M. Sitarz, M. Leśniak, J. Tyczkowski, Catalysts, 11 (2021) 905.
[3] H. Kierzkowska-Pawlak, M. Ryba, M. Fronczak, R. Kapica, J. Sielski, M. Sitarz, P. Zając, K. Łyszczarz, J. Tyczkowski, Catalysts, 11 (2021) 883.
[4] R. Kapica, J. Markiewicz, E. Tyczkowska-Sieroń, M. Fronczak, J. Balcerzak, J. Sielski, J. Tyczkowski, Coatings, 10 (2020) 904.

SELECTIVE DEHYDROGENATION OF METHYLCYCLOHEXANE USING TIN-MODIFIED HIGH-LOADED NICKEL CATALYSTS

S.A. Stepanenko, A.P. Koskin and V.A. Yakovlev

Federal Research Center Boreskov Institute of Catalysis SB RAS,
Acad. Lavrentiev Ave. 5, 630090 Novosibirsk, Russia. (stepanenko@catalysys.ru)

DOI: https://doi.org/10.46793/Phys.Chem24I.061S

ABSTRACT

High-loaded nickel catalysts (HLNC) modified with tin were synthesized and evaluated for the dehydrogenation of methylcyclohexane (MCH), which serves as a liquid organic hydrogen carrier. By optimizing the catalyst composition and reduction temperature, a dehydrogenation selectivity of >99.0% was achieved at a MCH conversion rate of 92% and a WHSV of 6.0 h^{1}. The stability of the Sn-modified HLNC was confirmed through a long-term (100-hour) catalyst test. The genesis of the HLNC during Sn modification and reductive activation in hydrogen was investigated. It was found that activation at temperatures above 450°C resulted in a uniform distribution of Sn, primarily forming solid NiSn solutions with a crystal lattice similar to metallic nickel. The formation of these solid solutions decreased the adsorptive properties related to the reaction product, toluene, which consequently enhanced the selectivity of MCH dehydrogenation.

INTRODUCTION

The increasing demand for sustainable energy solutions has spurred significant research into efficient hydrogen storage and transportation methods. Liquid Organic Hydrogen Carriers (LOHCs) have emerged as a promising technology in this field, offering a safe and effective means to store and transport hydrogen [1].

Dehydrogenation of methylcyclohexane (MCH) to produce toluene and hydrogen is a critical step in the LOHC cycle. Nickel-based catalysts can serve as a good alternative to noble metals due to their high activity and cost-effectiveness. However, achieving high selectivity and stability in Ni-catalyzed dehydrogenation processes remains a challenge. The presence of by-products and catalyst deactivation over prolonged usage can significantly impact the efficiency and economic viability of the process.

Recent advances have demonstrated that modifying Ni catalysts with additional elements, such as copper [2], zinc [3,4] and tin [4,5], can enhance their performance. These modifications can lead to improved selectivity and stability by altering the catalyst's structural and electronic properties.

This paper explores the synthesis, optimization, and performance of Sn-modified HLNCs in the dehydrogenation of MCH. By examining the effects of catalyst composition, reduction temperature, and operational parameters, we aim to achieve high selectivity and conversion rates while maintaining long-term stability. Understanding the genesis of these catalysts during modification and activation provides insights into the mechanisms driving their enhanced performance. Our findings contribute to the development of more efficient and durable catalysts for LOHC systems, supporting the broader goal of advancing hydrogen-based energy solutions.

METHODS

Catalyst preparation

The heterophase sol-gel technique [6] was employed to prepare the high-loaded nickel catalyst (HLNC), referred to as "Ni100", with SiO_2 serving as a stabilizing agent. To begin, an appropriate

amount of Ni(II) carbonate basic hydrate was mixed with distilled water and an aqueous solution of ammonia (25% NH_3) under constant stirring. Subsequently, ethyl silicate (containing 32 wt% SiO_2) was added to the mixture. The resulting suspension was subjected to vigorous stirring, then dried in air for 12 hours at 120°C, followed by calcination for 4 hours at 400°C.

Tin (Sn) was introduced through wetness impregnation of the NiO-SiO_2 system using an ethanol solution of Sn(II) chloride. After drying at 120°C for 12 hours and calcination at 600°C for 4 hours in air, the Sn-modified HLNC oxide precursors, designated as "Sn(X)/Ni(Y)", where "X" and "Y" relate to the weight ratio of the corresponding metal.

Catalyst characterization

The structure of the initial and reduced Sn/Ni catalytic systems was investigated using a set of physicochemical methods (HRTEM, XRD, N_2 adsorption, CO chemisorption, temperature-programmed reduction by H_2, etc). For a more detailed study of the processes occurring during the reduction treatment of the modified Sn catalytic systems, in situ X-ray diffraction (XRD) analysis of the Sn20/Ni80 sample (H_2, 1 hour, 300-500°C) was conducted. Additionally, the samples reduced at 400°C and 500°C and passivated with ethanol were examined using high resolution transmission electron microscopy (HRTEM).

To study the adsorption properties of Ni and Ni:Sn systems, the toluene temperature-programmed desorption (TPD-Tol) experiments and DFT calculations were made.

Amount of carbon formed during dehydrogenation catalytic reaction was estimated by elemental CHNS analysis and the temperature-programmed oxidation (TPO).

Catalyst testing

The process was carried out in a fixed-bed continuous flow reactor at temperatures ranging from 250°C to 350°C under ambient pressure (0.1 MPa). Prior to the experiment, 0.5 g of the oxide precursor catalyst (0.25–0.5 mm fraction) was mixed with quartz sand of the same fraction at a volume ratio of 1:5 and loaded into the reactor. The catalyst was then reduced in situ under a constant hydrogen flow of 500 mL/min. After the reduction, the reactor was cooled down to 250°C. During the testing phase, an equimolar mixture of hydrogen and argon with a total flow rate of 24 nL/h and a liquid MCH flow rate of 12 mL/h was continuously supplied to the reactor, corresponding to a weight hourly space velocity (WHSV) of 18.5 h^{-1}.

RESULTS AND DISCUSSION

Catalyst testing demonstrated that the addition of tin enables high (>99%) selectivity for toluene while maintaining high MCH conversion (**Figure 1, Table 1**), with the optimal tin content of 20 wt.% and reduction temperature for tin-containing samples being 500°C. The specific surface area and chemisorption data are given in Table 1.

According to XRD data, the reduction process leads to the formation of Ni_3Sn and Ni_3Sn_2 intermetallics, with tin redistribution occurring at higher temperatures. The deviation of the metallic Ni lattice parameter (3.535 Å) from the standard value (3.523 Å; PDF 04-850) indicates the formation of Ni_xSn_{1-x} solid solutions with a cubic structure.

TEM analysis revealed that the samples consist of rounded submicron agglomerates, comprising a SiO_2 matrix embedding NiSn nanoparticles (5-10 nm). Examination of individual crystallites in the Sn20/Ni80-400 catalyst showed that Sn content generally increases from the center to the surface of the particles, while the sample reduced at 500°C (Sn20/Ni80-500) exhibited a more uniform Sn distribution.

The primary hypothesis for the increased selectivity of Sn-modified systems is the reduced adsorption energy of the reaction product, toluene, facilitating its rapid removal from the catalyst surface and preventing further decomposition. This hypothesis is supported by TPD experiments and theoretical calculations. Toluene TPD showed 3 peaks that correspond to evaporation of

physisorbed toluene, desorption of physisorbed toluene, and desorption of chemisorbed toluene. The Ni100-500 catalyst exhibited stronger chemisorption of toluene, with the proportion of chemisorbed toluene being 6.4% compared to 1.5% for the Sn20/Ni80-500 sample. According to theoretical calculations, the adsorption energy of toluene for the Ni100 system is -1.45 eV, while for the Sn20/Ni80 system it is -0.08 eV.

Table 1. Specific surface areas and CO chemisorption data of the reduced (H_2, 500°C) catalysts and comparison of catalytic properties (reaction temperature 350°C).

Catalyst	Specific surface area, m^2/g	CO uptake, μL/g	MCH conversion, %	TOL selectivity, %
Ni100	310	555	92.9	15.3
Sn5Ni95	273	501	78.8	75.1
Sn10Ni90	169	470	77.4	91.9
Sn20Ni80	167	350	53.9	99.9
Sn30Ni70	124	208	50.3	97.3

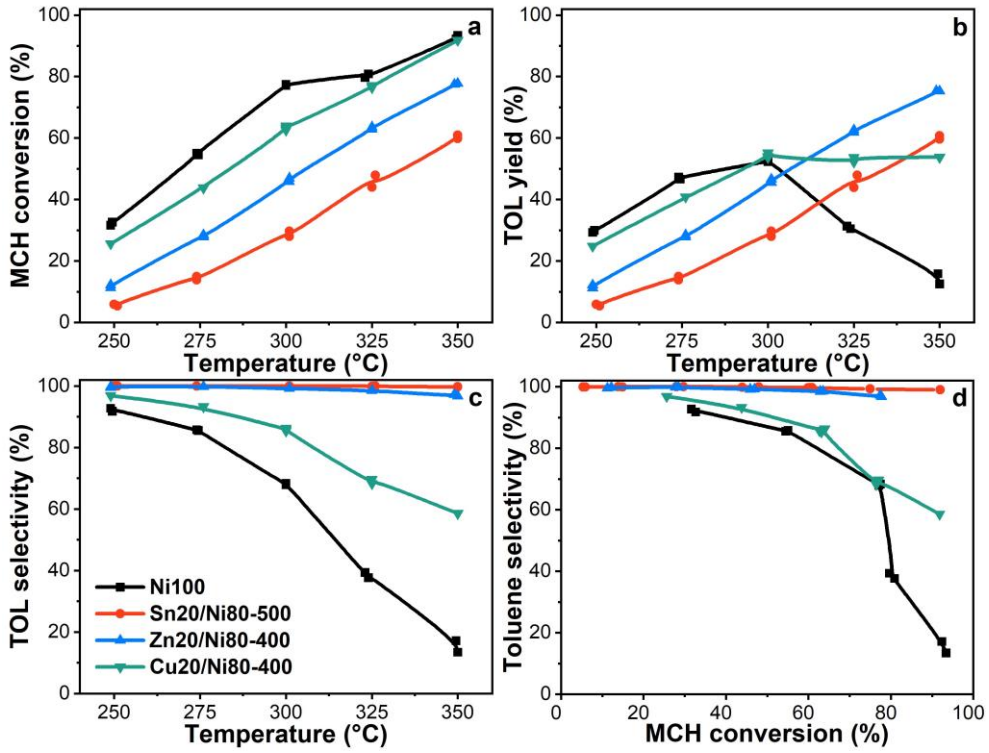


Figure 1. Comparison of the catalytic properties of the initial nickel catalyst (Ni100) and modified SnX/NiY-T systems (where X, Y are the mass ratios of metals; T is the reduction temperature (H_2, 1 hour, 500 mL/min)). Test conditions: T 250-350°C, 1 atm, 400 mL/min Ar/H_2 (1:1), 0.5 g of catalyst, WHSV 18.5 h^{-1}.

A long-term (120-hour) test of the Sn20/Ni80-500 catalyst showed stable selectivity throughout the cycle, with MCH conversion decreasing by no more than 5% (Fig. 4). Activity decreased more sharply with increased process temperature, likely due to the deposition of high-molecular-weight

organic compounds. CHNS analysis indicated that the carbon content in the spent catalyst sample was ~1 wt%, and TPO revealed that the oxidation of deposits occurred in the 300-400°C range.

Varying the contact time in tests of the Sn20/Ni80-500 sample showed that its selectivity was almost independent of reaction extent, unlike previously synthesized and studied catalytic systems (**Figure 1, Table 2**). It maintained a high selectivity (>99%) even at a conversion rate (92%) close to the thermodynamically possible limit (94%) under the test conditions (350°C; 0.1 MPa).

Table 2. Results of catalyst testing at various residence time.

WHSV, h^{-1}	MCH conversion, %	TOL selectivity, %
18.5	60.4	99.9
9.3	77.4	99.2
6.2	92.0	99.0

CONCLUSION

The Sn-modified high-loaded nickel catalyst with an optimal composition of Sn20/Ni80 (Ni:Sn atomic ratio of 4:1) reduced at 500°C achieved a dehydrogenation selectivity of 99.0% at an MCH conversion of 92% and a WHSV of 6.0 h¹. A selectivity of 99.9% was reached at a conversion of 60.4% and a WHSV of 18.5 h¹. The catalyst demonstrated high stability over a 100-hour test. A slight decrease in MCH conversion was attributed to the deposition of amorphous carbon or resins on the catalyst surface and minor enlargement of NiSn particles. This catalyst's selectivity surpasses that of previously studied Cu- and Zn-modified HLNC analogs and is comparable to Pt-based catalysts. The high selectivity is due to the formation of NiSn solid solutions, resulting in lower adsorption energy for the reaction product, toluene, which is quickly removed from the high-temperature reaction bed, preventing decomposition into benzene and methane.

Acknowledgment

This work was supported by the Ministry of Science and Higher Education of the Russian Federation within governmental order for Boreskov Institute of Catalysis SB RAS (projects FWUR-2024-0038, FWUR-2024-0043).

REFERENCES

[1] A. Lin, G. Bagnato, Int. J. Hydrogen Energy. 63 (2024) 315–329.
[2] Y. Gulyaeva, M. Alekseeva, O. Bulavchenko, A. Kremneva, A. Saraev, E. Gerasimov, S. Selishcheva, V. Kaichev, V. Yakovlev, Nanomaterials. 11 (2021).
[3] M. V. Alekseeva (Bykova), Y.K. Gulyaeva, O.A. Bulavchenko, A.A. Saraev, A.M. Kremneva, S.A. Stepanenko, A.P. Koskin, V. V. Kaichev, V.A. Yakovlev. Dalt. Trans. 51 (2022) 6068–6085.
[4] A.H. Al-Shaikhali, A. Jedidi, L. Cavallo, K. Takanabe. Chem. Commun. 51 (2015) 12931–12934.
[5] A.P. Koskin, S.A. Stepanenko, O.A. Alekseeva (Bykova), M.V. Bulavchenko, E.Y. Gerasimov, A.I. Lysikov, P.M. Yeletsky, V.V. Kaichev, V.A. Yakovlev. Chem. Eng. J. 476 (2023).
[6] M.A. Ermakova, D.Y. Ermakov. Appl. Catal. A Gen. 245 (2003) 277–288.

HEMATITE/GOETHITE COMPOSITE FORMATION WITH ENHANCED PHOTO-CATALYTIC ACTIVITY

T. Basuki [1], S.Permana[3] and S. Nakashima [2]

[1] *Research center for nuclear material and radioactive waste technology, National research and innovation agency (BRIN), Indonesia (triy019@brin.go.id)*
[2]*Graduate school of advanced science and engineering, Hiroshima University, Japan (snaka@hiroshima-u.ac.jp)*
[3]*Gunadarma University, Indonesia (sulaksana@yahoo.com)*

DOI: https://doi.org/10.46793/Phys.Chem24I.065B

ABSTRACT
Iron oxide and iron oxyhydroxide having narrow bandgap energy can efficiently utilize visible light and resulted in charge carriers for hetero-catalysis. The well-known rapid photoelectron-hole pair recombination of iron oxide species including iron oxyhydroxide is the drawback of these materials to be solved. In the present study, the production of hematite/goethite composite which improved its photo-catalytic activity is reported. Moreover, the ratio of hematite/goethite influenced the activity of the produced materials. The findings are valuable as an alternative to regulate the formation of composite with distinct properties.

INTRODUCTION
Iron oxide and iron oxyhydroxide are a class of semiconductor materials with narrow bandgap (2.0 – 2.5 eV) [1,2,3] which could efficiently utilize visible light and resulted in photo-induced electrons and holes important for hetero-catalysis, such as, photocatalyst of organic pollutant degradation with or without addition of H_2O_2.

Nevertheless, the rapid recombination of photoelectron-hole pair of iron oxide and iron oxyhydroxide is well-known drawback of these materials. The strategy to solve this problem has been a focus of many previous reports, such as by doping with other transition metals [3,4,5] and compositing iron oxide with other materials to form heterostructure. [6]

The magnetite/goethite composite with improved photo-catalytic activity has been previously reported. The different phase in the composite increases the surface area, enhances the visible light absorption and improves the electron-hole separation by forming heterojunction structure. [6]

We reported the production of a new hematite (α-Fe_2O_3)/goethite (α-FeO(OH)) nanocomposite to enhance photo-catalytic activity for the degradation of methylene blue (MB) using a facile hydrothermal synthesis. The temperature-dependent phase transformation of the material was analyzed with the finding that 120°C was the optimum temperature to produce the composite with the highest catalytic activity. The findings are valuable as an alternative to regulate the formation of composite with distinct properties.

METHODS
Chemicals
$FeCl_3 \cdot 6H_2O$ 99%, ethanol 99.5%, NH_3 10%, H_2O_2 30%, methylene blue (Wako chemicals) are reagent grades and used without further purification.

Synthesis procedure

Iron oxide was produced by hydrothermal synthesis method following to previous methods [1] with some modifications. $FeCl_3 \cdot 6H_2O$ (2 g) was dissolved in distilled H_2O (30 mL), then NH_3 (7.5 mL) was added dropwise and mixed for 30 minutes to form suspension. The suspension was transferred to 50 mL PTFE tube, then inserted into an autoclave reactor. It was heated in the oven furnace at some temperature ranges of 80, 100, 120, 140 and 200ºC for 6 hours. The product was washed by ethanol and dried in the oven at 60ºC for 24 h. The sample produced with temperature 80, 100, 120, 140 and 200ºC are denoted as S-80, S-100, S-120, S-140 and S-200, respectively.

Characterization of materials

The products were characterized by powder X-ray diffraction (PXRD) pattern analysis and Mössbauer spectroscopy.

Catalytic activity measurement

The catalytic activity of the produced materials was evaluated based on the photo-degradation of MB. The sample (6 mg) was added to 10 mL MB (20μM) and mixed by horizontal shaker (recipro shaker NR-1, Taitec) for 30 minutes to establish the MB adsorption and desorption equilibrium. The H_2O_2 (1M) 0.3 mL was added to the mixture just prior to the visible light irradiation (metal halide type lamp 100 W, Iwasaki, MT100FCE-W/S2, 20 cm lamp to sample distance in dark room). The 1 mL suspension was taken out at the designated time interval and centrifuged at 10,000 rpm to get the supernatant for analyzing the MB degradation based on the light absorbance decrease at λ 550 ~ 700 nm by JASCO V-650 UV/Vis spectrophotometer.

RESULTS AND DISCUSSION

Figure 1 shows the PXRD patterns of the synthesized materials. Sample produced at 200ºC (S-200) exhibited the patterns that was in a good agreement with the PXRD pattern of α-Fe_2O_3 (JCPDS-00-001-1053). Sample produced at 140ºC (S-140) shows the appearance of new diffraction peaks which corresponded to PXRD pattern of α-FeO(OH). This demonstrates the occurrence of two phases, namely, α-Fe_2O_3 and α-FeO(OH). The proportion of α-FeO(OH) in the composite increased with the decrease of synthesis temperature that related to the incomplete oxidation reaction at low-temperature.

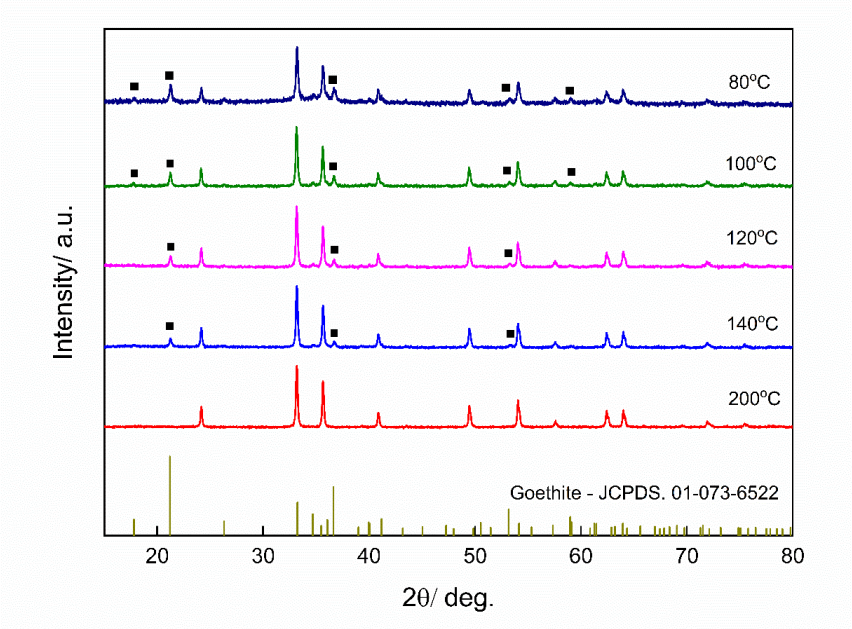


Figure 1. PXRD of the samples produced under different temperatures.

Table 1 presents the hyperfine parameters of the samples derived from the Mössbauer spectroscopy. It confirmed the presence of 100% hematite phase of S-200. The presence of hematite/goethite mixture was observed with ratio 86/14 and 81/19 for S-140 and S-120, respectively, analyzed at room temperature Mössbauer spectroscopy. Moreover, the presence of hematite/goethite mixture was also observed for S-100 and S-80 with the existence of unreacted Fe(III).

Table 1. Hyperfine parameters of the samples produced under different temperatures.

Samples	T/ K	IS[a)]/ mm s^{-1}	QS/ mm s^{-1}	B/ T	A/ %	Assignment
S-80	298	0.38	-0.20	51.4	45	Hematite
		0.38	-0.29	38.0	19	Goethite
		0.35	0.67	-	36	unreacted Fe(III)
	78	0.47	0.38	53.1	36	Hematite
		0.44	-0.20	48.9	22	Goethite
		0.42	0.70	-	42	unreacted Fe(III)
S-100	298	0.38	-0.20	51.5	72	Hematite
		0.37	-0.28	38.4	22	Goethite
		0.27	0.00	-	6	unreacted Fe(III)
	78	0.48	0.43	53.2	66	Hematite
		0.46	-0.18	49.1	22	Goethite
		0.19	1.61	-	12	unreacted Fe(III)
S-120	298	0.37	-0.21	51.1	81	Hematite
		0.36	-0.25	38.6	19	Goethite
	78	0.47	0.43	53.2	80	Hematite
		0.43	-0.17	48.8	20	Goethite
S-140	298	0.38	-0.21	51.5	86	Hematite
		0.38	-0.25	38.4	14	Goethite
	78	0.49	0.43	53.2	84	Hematite
		0.43	-0.16	49.1	16	Goethite
S-200	298	0.37	-0.22	51.7	100	Hematite
	78	0.48	0.42	53.4	100	Hematite

[a)] relative to iron foil

Figure 2 shows the K_{app} of the MB photo-degradation facilitated by the synthesized materials. S-120 surprisingly demonstrated the best photocatalytic activity among the samples. The coexistence of hematite/goethite synergistically improved their photocatalytic activity compared to pure hematite phase (S-200). Furthermore, the ratio of hematite/goethite was found to determine the activity of the samples. Activity of S-120 with 81/19 ratio was higher than that of S-140 with 86/14 ratio.

These findings probably implied to the formation of hematite/goethite heterostructure which could increase the surface area for better MB adsorption on catalyst surface to undergo photo-catalytic degradation and formed a hetero-junction structure for decelerating the recombination of charge carriers. Moreover, the importance of hematite/goethite ratio was probably an evidence of photo-induced electron transfer mechanism from conduction band of hematite to conduction band of goethite to undergo photo-Fenton reaction.

The presence of unreacted Fe(III) in S-100 and S-80 decreased their catalytic activity, although their catalytic activity of S-100 was still higher than that of S-200 (pure hematite). This was due to

the decrease of the photon-harvesting materials (hematite and goethite) which finally reduced the number of photo-induced electrons and holes.

CONCLUSION

We reported the production of new hematite/goethite composite using facile hydrothermal synthesis method. Temperature dependence of the iron oxide formation was analyzed to show the production of pure hematite at synthesis temperature of 200°C and hematite /goethite at synthesis temperature of 140°C and below. The S-120 showed a superior photo-catalytic activity to those of other produced samples which demonstrated the importance of hematite/goethite ratio. These findings are important for alternative strategy to improve the photo-catalytic activity of iron oxides.

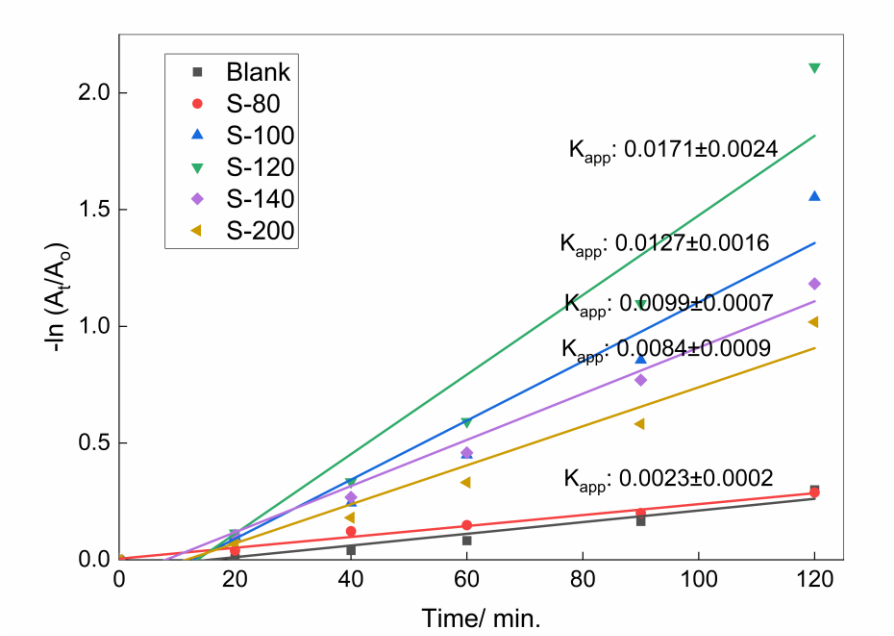


Figure 2. Apparent rate constant (K_{app}) of MB photodegradation by synthesized materials.

Acknowledgment

This work was supported by Hiroshima Universiy (JAPAN) and Indonesia National Research and Innovation Agency (BRIN). We are indebted to Ms. Naomi Kawata (N-BARD, Hiroshima University) for performing PXRD analysis

REFERENCES

[1] F. M Ali, M. Hmadeh, P.G. O'Brien, D.D. Perovic, G.A. Ozin, ChemNanoMat, 2(11) (2016) 1047–1054.
[2] Z. Huang, F. Han, M. Li, Z. Zhou, X. Guan, L. Guo, Comput Mater Sci, 169 (2019) 109110.
[3] A.H. Asif, S. Wang, H. Sun, Current Opinion in Green and Sustainable Chemistry, 28 (2021) 100447.
[4] X. Zhang, h. Li, S. Wang, F.R.F. Fan, A. Bard, Journal of Physical Chemistry C, 118 (30) (2014) 16842–16850.
[5] S. Rahim Pouran, A.A. Abdul Raman, W.M.A. Wan Daud, Journal of Cleaner Production, 64 (2014) 24–35.
[6] X. Huang, H. Zhou, X. Yue, S. Ran, J. Zhu, ACS Omega, 6(13) (2021) 9095–9103.

CATALYTIC OXIDATIVE DEGRADATION OF TEXTILE DYES USING COBALT-BASED ALUMINA CATALYSTS

S. Marinović, N. Jović-Jovičić, M. Ajduković, G. Stevanović, J. Parlić, P. Banković and T. Novaković

University of Belgrade, Institute of Chemistry, Technology and Metallurgy, Njegoševa 12, 11000 Belgrade, Serbia. (sanja.marinovic@ihtm.bg.ac.rs)

DOI: https://doi.org/10.46793/Phys.Chem24I.069M

ABSTRACT

Two cobalt-based aluminas calcined at 1000 °C and 1100 °C were investigated in catalytic oxidative degradation of Orange G, Methylene blue, Remazol brilliant blue R, and Basic blue 41 textile dyes. The catalysts were used to activate Oxone® to obtain reactive oxidative species from its active component, peroxymonosulfate. Apart from single dye degradation tests, both catalysts were employed in three binary dye systems containing Orange G and each blue dye. Catalysts were proven efficient both in single and binary dye systems. However, there were significant differences in their behavior in terms of their efficiency, as well as the obtained degradation profiles. It is dominantly the consequence of different cobalt phases formed at 1000 °C and 1100 °C, and to a lesser extent of the structural and textural properties of two catalysts.

INTRODUCTION

The textile industry is a major contributor to environmental pollution in many countries. Over 10,000 tons of synthetic dyes are annually used by the textile industry at various stages of the textile production process. The most commonly used textile dyes are: azo, direct, reactive, mordant, acid, basic, disperse, and sulfide dyes. Since textile dyes do not bind tightly to the fabric they get discharged as effluent into aquatic environments [1]. The discharge of industrial wastewater containing synthetic dyes has a severe negative impact on the environment when released into surface waters. Dyes in water can obstruct sunlight and negatively impact the photosynthesis of aquatic life. In addition, most of them are highly toxic and even carcinogenic [2].

For this reason, the treatment of textile wastewater is highly important to protect the environment and ecosystem. Many techniques were employed for the removal of synthetic dyes from effluents including adsorption, coagulation, chemical oxidation, membrane separation process, electrochemical and aerobic and anaerobic microbial degradation. All these methods suffer from many restrictions, so they are not very successful [3].

Advanced oxidation processes including Fenton-like processes are considered very effective in synthetic dye degradation. These processes include catalytic oxidative degradation using Oxone® as a source of reactive sulfate anion radicals. The self-decomposition of Oxone® is very slow and catalysts should be used to promote its activation. Cobalt-based heterogeneous catalysts were proven to be the most effective in Oxone® activation [4]. Different cobalt catalyst supports were reported in the literature such as metal oxides, layered double hydroxides, metal-organic frameworks, carbon composites, etc. [4, 5]. Alumina belongs to the group of surface-active metal oxides. Metal-doped alumina was reported as a good adsorbent and catalyst in wastewater treatments to remove different organic pollutants. [6]. Co-doped aluminas catalysts in the degradation of food dye Tartrazine in the presence of Oxone® were investigated for the first time by our research group [7].

In the present work two Co-based alumina catalysts were examined in different textile dye degradation using Oxone® as oxidant. Apart from single dye degradation, the degradation of the binary dye systems was also tested.

EXPERIMENTAL

Oxone® (potassium triple salt – $KHSO_5 \cdot 0.5 \cdot KHSO_4 \cdot 0.5 \cdot K_2SO_4$), Orange G (OG), Methylene blue (MB), Remazol brilliant blue R (RB), and Basic blue 41 (BB) were supplied by Sigma Aldrich and were used as received.

The catalysts were previously synthetized using sol-gel method, gelled and calcined at 1000 °C (CoA-1000) and 1100 °C (CoA-1100), fully characterized using X-ray powder diffraction (XRPD), temperature programmed reduction (TPR), and low-temperature N_2 physisorption analysis [7].

In all catalytic tests, 200 cm3 of aqueous solution of single dyes or binary dyes mixtures were added into the Julabo MC 4 thermostated Pyrex reactor. The initial dye concentration was always 20 mg dm-3. 1 cm3 of Oxone® solution containing 0.130 mmol of Oxone® was added to the dye solution and that was considered as 0 min of the reaction, after which 10 mg of catalyst was added. The aliquots were taken at predetermined periods after the reaction started. The reaction was monitored for 240 minutes using UV-Vis spectrophotometry (Thermo Scientific, Evolution 220 UV–Visible Spectrophotometer) by observing the decrease of the peak maxima at 478 nm, 665 nm, 592 nm, and 609 nm for OG, MB, RB, and BB respectively. The reaction temperature was 30 °C in all experiments.

RESULTS AND DISCUSSION

The investigated catalysts were previously characterized. XRPD confirmed the presence of γ-Al_2O_3 as a dominant aluminium phase in CoA-1000, and α-Al_2O_3 in CoA-1100. H_2-TPR was used to identify the type of Co phase. The presence of both Co_3O_4 and $CoAl_2O_4$ in CoA-1000 was determined. On the other hand, only Co-spinel $CoAl_2O_4$ was found in CoA-1100. Four times higher specific surface area (S_{BET} = 43 m^2 g^{-1}) for the CoA-1000 was confirmed using the N_2 physisorption technique. Total pore volume was $V_{0.98}$ = 0.122 cm^3 g^{-1}, and $V_{0.98}$ = 0.057 cm^3 g^{-1} for CoA-1000 and CoA-1100 respectively [7].

CoA-1000 and CoA-1100 were tested in Oxone® induced oxidative degradation of OG, MB, RB, and BB and in binary dye solutions of OG with each blue dye. The differences in the results obtained for CoA-1000 and CoA-1100 are very pronounced. The efficiency of CoA-1100 is much lower for the degradation of single dyes and binary dye mixtures, but also the degradation profiles are noticeably different compared to CoA-1000.

Figure 1 shows the degradation percentage of single dyes for both catalysts.

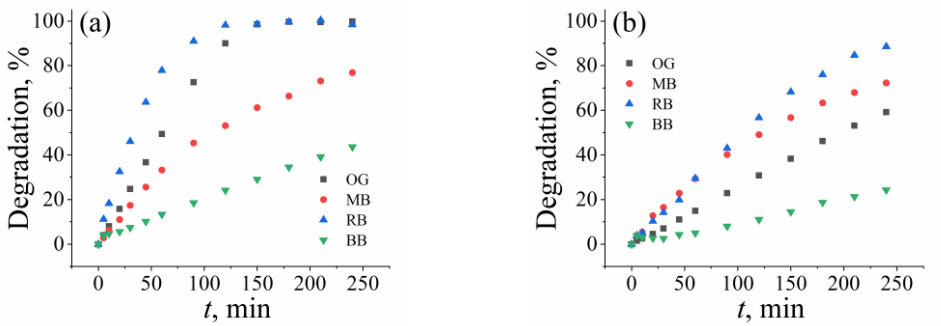


Figure 1. Degradation efficiency for single dyes for (a) CoA-1000 and (b) CoA-1100 ($C_{0,dye}$ = 20 mg dm^{-3}; $V_{dye\ solution}$ = 200 cm^3; $m_{Oxone®}$ = 40 mg; m_{cat} = 10 mg; T = 30 °C).

It is obvious from **Figure 1.** that complete degradation for the investigated experimental conditions was only achieved for OG and RB with CoA-1000. The peak maximum decay at 478 nm, corresponding to decolorization of OG, was completed after 150 minutes. The characteristic peak for RB at 592 nm disappeared after 120 minutes. During the investigated time with CoA-1000 as catalyst, 80% degradation of the MB and only approx. 40% degradation of BB was observed. With CoA-1100 catalyst, degradation was much slower for all dyes and neither of them was completely degraded within 240 minutes. However, the degradation efficiency of the investigated dyes showed a different order for this catalyst compared to CoA-1000. Although the highest efficiency was achieved for RB, as for CoA-1000, the degradation of MB was faster than for OG. The lowest degradation capacity was observed for BB and it was about 25%.

Determining the interactions between pollutants present in wastewater is crucial for effective wastewater treatment. This has great practical application in real wastewater, which always contains multiple pollutants. In order to examine how interaction between dyes affects the degradation efficiency, the simultaneous degradation of dyes should be investigated. **Figures 2**. and **3.** show the results obtained for the degradation of binary dye mixtures using CoA-1000 and CoA-1100, respectively.

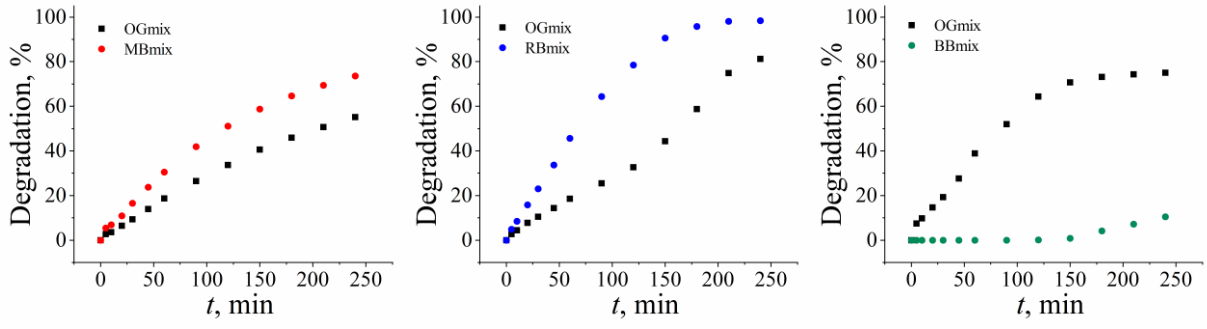


Figure 2. Degradation efficiency for binary dye mixtures for CoA-1000 ($C_{0,dye}$ = 20 mg dm^{-3}; $V_{dye\ solution}$ = 200 cm^3; $m_{Oxone®}$ = 40 mg; m_{cat} = 10 mg; T = 30 °C).

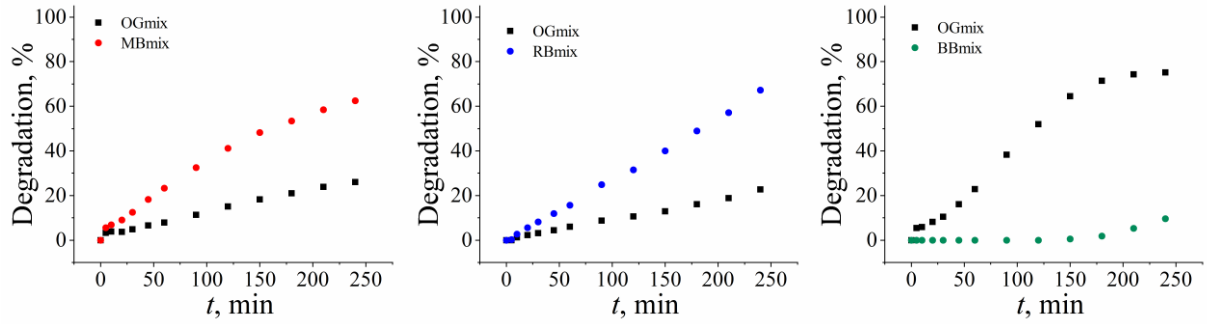


Figure 3. Degradation efficiency for binary dye mixtures for CoA-1100 ($C_{0,dye}$ = 20 mg dm^{-3}; $V_{dye\ solution}$ = 200 cm^3; $m_{Oxone®}$ = 40 mg; m_{cat} = 10 mg; T = 30 °C).

For OG and MB binary system, as well as for OG and RB combination of dyes, the dye degradation efficacy in the binary system (OG_{mix}, MB_{mix}, and RB_{mix}) dropped in comparison to single dye degradation. This phenomenon is much more pronounced for OG_{mix} than for the other two dyes. The same behaviour was observed for both catalysts, although with CoA-1000 the percent of the degradation of OG_{mix} was about twice as high as for CoA-1100. The effectiveness of the MB_{mix} degradation with CoA-1000 as a catalyst was very similar to MB degradation as single dye,

while for CoA-1100, degradation of the MB_{mix} was a bit lower. When it comes to the OG and RB binary system, the drop of RB_{mix} degradation is more pronounced then for MB_{mix} for both catalysts. However, it is much less than the drop of the OG_{mix}. Also, in the case of CoA-1000, degradation of OG_{mix} accelerates when the most of the amount of RB_{mix} was degraded. This was not observed for CoA-1100, but it might be due to slower reaction rate of both dyes degradation.

In the OG and BB combination of dyes the noticed behaviour was much different than for other two systems. Firstly, both investigated catalysts showed selective degradation of OG_{mix}. It was observed that the degradation of the BB_{mix} had not started before the degradation of the OG_{mix} was completed. After OG_{mix} degradation completion, the BB_{mix} degradation started and it was very slow for both catalysts. It is assumed that the interaction of OG and BB in a mixed dye system led to a significantly faster and selective degradation of OG_{mix}.

The difference in the molecular structure of the dyes and the presence of different cobalt phases in CoA-1000 and CoA-1100 likely contribute to the observed degradation efficiency for single dye degradation. Conversely, the degradation of a dye mixture involves interactions and competition between the dyes.

CONCLUSION

Two cobalt-based alumina catalysts (CoA-1000 and CoA-1100) were investigated in Orange G (OG), Methylene blue (MB), Remazol brilliant blue R (RB), and Basic blue 41 (BB) Fenton-like degradation with Oxone®. The degradation was followed in single dye system, as well in binary systems of OG and each of the blue dyes. It was noticed that CoA-1000 was much more effective in degradation of all investigated dyes, as well as in binary dye mixtures. This was attributed to the presence of Co_3O_4 and γ-Al_2O_3 in this catalyst, which are more active phases than those present in coA-1100. In binary dye systems, the dye degradation behaviour was different compared to single dye systems. It was explained by the interactions occurring between dyes.

Both investigated catalysts can be used in complex systems with more than one organic pollutant present in the wastewater.

Acknowledgment

This research was financially supported by the Ministry of Science, Technological Development and Innovation of Republic of Serbia (Contract No: 451-03-66/2024-03/200026).

REFERENCES

[1] R. Al-Tohamy, S.S. Ali, F. Li, K. M. Okasha, Y. A.-G. Mahmoud, T. Elsamahy, H. Jiao, Y. Fu, J. Sun, Ecotox. Environ. Safe., 231 (2022) 113160.
[2] V. Dulman, S. M. Cucu-Man, R. I. Olariu, R. Buhaceanu, Dyes Pigments., 95 (2012) 79-88.
[3] M. A. M. Salleh, D. K. Mahmoud, Wan Azlina W. A. W. A. Karim, A. Idris, Desalination., 280 (2011) 1–13.
[4] K-Y. A. Lin, T-Y. Lin, Water Air Soil Pollut., 229 (2018) 10.
[5] W. Zhao, Q. Shen, T. Nan, M. Zhou, Y. Xia, G. Hu, Q. Zheng, Y. Wu, T. Bian, T. Wei, C. Zhang, J. Alloy Compd., 958 (2023) 170370.
[6] A. K. Khattak, M. Afzal, M. Saleem, G. Yasmeen, R. Ahmad, Colloid Surf. A., 162 (2000) 99-106.
[7] S. Marinović, T. Mudrinić, B. Dojčinović, T. Barudžija, P. Banković, T. Novaković, J. Environ. Chem. Eng., 9 (2021) 106348.

PHOTOCATALYTIC DEGRADATION OF CIPROFLOXACIN WITH IRON-MODIFIED TITAN(IV) OXIDE

M. Kovačević, M. Simić, K. Stojanović, D. Aćimović, S. Živković,
T. Brdarić and D. Vasić Anićijević

University of Belgrade, Vinča Institute of Nuclear Sciences - National Institute of the Republic of Serbia, Mike Petrovića Alasa 12-14, Belgrade, Serbia
(marija.simic@vin.bg.ac.rs)

DOI: https://doi.org/10.46793/Phys.Chem24I.073K

ABSTRACT

Considering the increasing significance of emerging pollutants in the environment, this research investigates the photodegradation of ciprofloxacin, which ranks among the top three most detected antibiotics in aquatic ecosystems. Therefore, we synthesized TiO_2 modified with Fe in three different molar ratios (0.5, 1 and 2 %) and applied it to the photodegradation of the ciprofloxacin infusion solution. The photodegradation process was monitored by UV-Vis spectroscopy for over 240 minutes. The results have shown that the efficiency rate is around 50 % for all three photocatalysts. However, the degradation efficiency can't be precisely determined with UV-Vis spectroscopy because by-products that occurred in degradation have an absorbance maximum similar to the ciprofloxacin.

INTRODUCTION

Ciprofloxacin (CIP, Figure 1) is a synthetic fluoroquinolone derivative with a large usage scale for inflammatory treatment for animals and humans [1,2]. Ciprofloxacin is effective against both, gram-positive and gram-negative bacteria because it blocks their DNA synthesis [1,2].

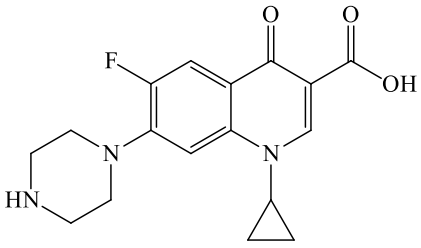


Figure 1. Structure of ciprofloxacin

The UV-based photodegradation with TiO_2 represents one of the most promising methods for antibiotic removal [3]. The main advantages of photocatalysis are low cost and energy saving, easy to operate, highly efficient and environmentally friendly process because it doesn't require additional chemicals [3,5,7]. On the other hand, TiO_2 photocatalytic performance is limited due to their tendance to agglomerate according to the high surface energy, large band gap (requires UV range light) and short recombination time of photogenerated electron–hole pairs [6,8]. To overcome these deficiencies, metal decoration of TiO_2 can be utilized [2]. The aim of this study is to modify TiO_2 by deposition of iron in different molar ratios (0.5, 1 and 2%) and apply it for photocatalytic degradation of ciprofloxacin.

METHODS

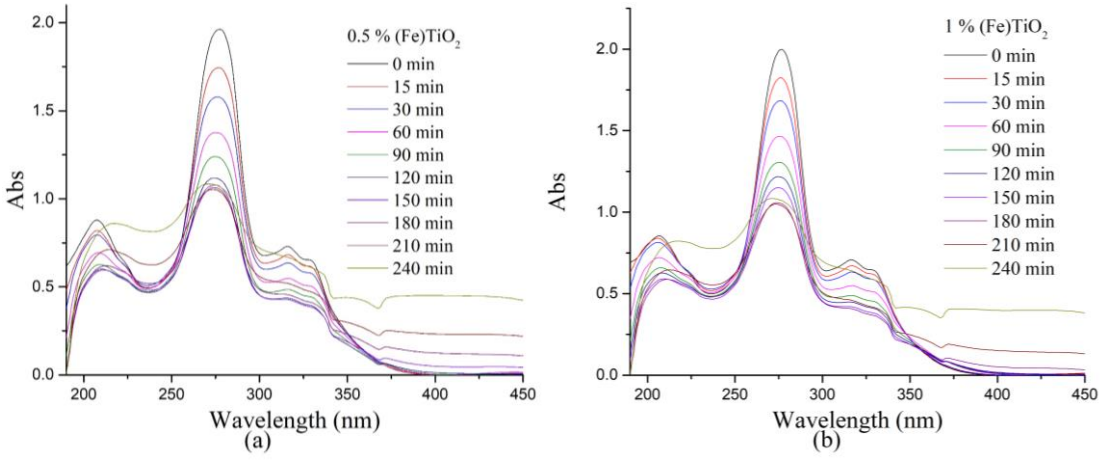
Synthesis of modified TiO_2 with Fe was carried out in the same way for all three molar ratios 0.5. 1 and 2 %. 500 mg of TiO_2 nanoparticles were added to 50 mL of deionized water and dispersed using an ultrasonic bath at 90 ºC for 30 minutes. Then required amounts (0.5, 1 and 2 % compared to TiO_2) of $FeC_6H_5O_7 \cdot 5H_2O$ (The British Drug House, London, England, 98 %) and 12.5 mg of solid NaOH (Hemos, Belgrade, Serbia 99.6 %) were added to the mixture and stirred for a couple of minutes. Next 5 mL (0.5, 1 and 2 g L^{-1} for 0.5, 1 and 2 % molar ratio respectively) $NaBH_4$ solution (The British Drug House, London, England, 95 %) was added dropwise to the reaction mixture and stirred at room temperature for 2 h. Next, the suspension was washed with deionized water, centrifuged and dried overnight in the dryer at 100 ºC [4].

The ciprofloxacin mixture was prepared from ciprofloxacin commercial solution for infusion (Marocen®, Hemofarm, Serbia), that contains 100 mg of the ciprofloxacin lactate in 10 mL of the solution. First, the commercial solution was dissolved in deionized water in a volumetric flask of 250 mL and then the 12.5 mL of this solution was dissolved in deionized water in another volumetric flask of 250 mL, with the final concentration of 4.75 $\cdot 10^{-4}$ M, 20 mg L^{-1} of ciprofloxacin.

The procedure of photodegradation was carried out with 30 mg of every catalyst for the ciprofloxacin commercial solution. The required mass of finely powdered catalyst nanoparticles was added into 50 mL of the ciprofloxacin solution (20 mg L^{-1} of ciprofloxacin). The reaction mixture was stirred for 30 minutes in the dark, alongside blank (solution ciprofloxacin without catalyst). Next, the blank and the reaction mixture were irradiated under UV light (Philips TUV 15W UVC Disinfection, Poland) for 4 hours. Aliquots were taken over after 0, 15, 30, 60, 120, 150, 180, 210 and 240 minutes for mixture and hourly for blank in a 4 mL quartz cuvette. The photodegradation process was monitored by UV-Vis spectrometry (LLG Labware, Detroit, USA), by recording the UV-Vis spectra in the wavelength range from 190 to 500 nm.

RESULTS AND DISCUSSION

The UV-Vis spectra for photocatalytic degradation of ciprofloxacin during 240 minutes of irradiation with UV light are presented in Figure 2. These spectra confirm that the characteristic absorption maximum of ciprofloxacin is at about 277 nm decreases with time, due to the photodegradation. The absorption maximum shift to the left with degradation process, as well as the existence of spectra overlapping region at about 200-270 nm, point to the formation of the degradation products structurally similar to ciprofloxacin.



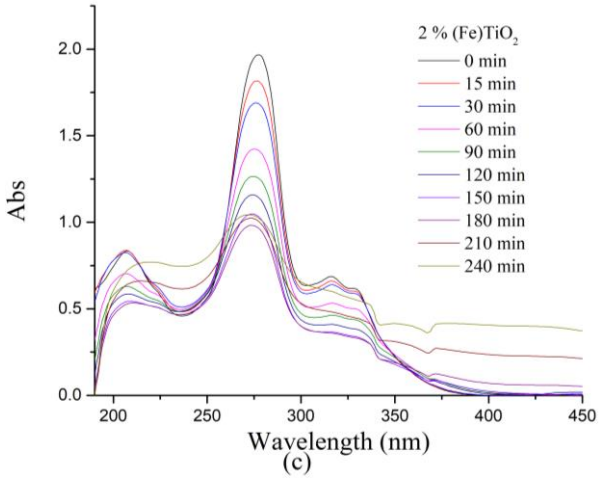


Figure 2. UV-Vis spectra of the ciprofloxacin solution of the initial concentration 4.75×10^{-4} M during 240 min of photodegradation with 30 mg 0.5 % (Fe)TiO_2 (**a**), 1 % (Fe)TiO_2 (**b**) and 2 % (Fe)TiO_2 (**c**).

Ciprofloxacin degradation efficiency was measured as the relative depletion of absorbance of the characteristic peak at 277 nm. Degradation rate constants were calculated from the decrease in absorbance at 277 nm, assuming the pseudo-first-order kinetics (Equation (1)):

$$A=A_0 \cdot e^{-kt} \quad (1)$$

where A_0 is the absorbance at time at zero minute, and k (min^{-1}) is a pseudo-first-order rate constant. The linearization of Equation (1) was applied to obtain the rate constant k from the slope of the graph (Equation (2)).

$$\ln(A/A_0)=-kt \quad (2)$$

The resulting kinetic curves of photodegradation of ciprofloxacin solution with 30 mg photocatalysts are represented in Figure 3.

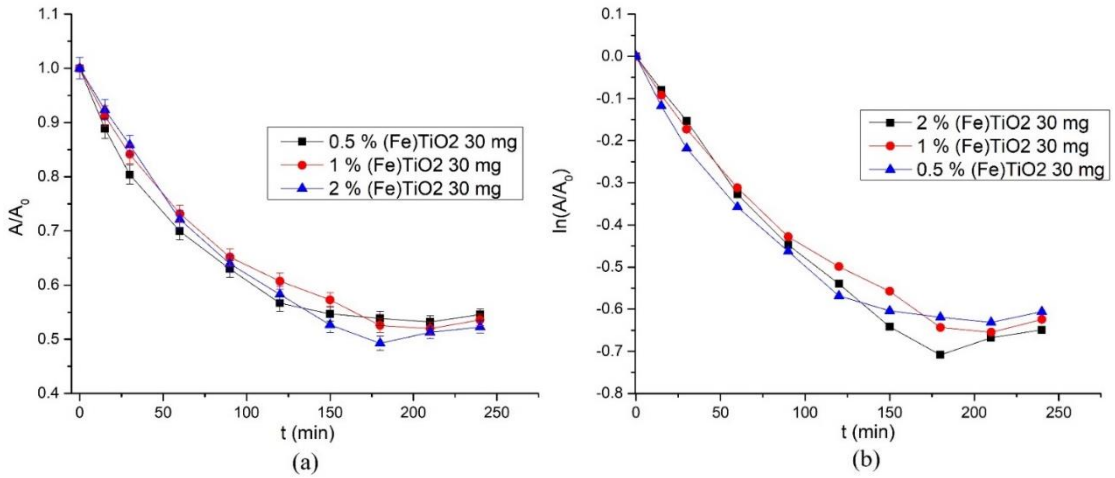


Figure 3. Degradation curves (a) and their linearized pseudo-first-order fits (b) of ciprofloxacin commercial solution for the infusion.

Calculated pseudo-first-order rate constants, coefficient of determination and the percentage of degradation based on decreasing the absorbance values at 277 nm are presented in Table 1. These values were calculated based only on UV-Vis spectra. However, as we can see from Figures 2 and 3, in the first 90 minutes degradation process the absorbance drops, but after 120 minutes values start to grow again. The increase of absorbance at higher wavelengths in the spectra after 120

minutes is probably due to the light scattering on colloidal particles formed during the degradation process, possibly upon oxidation of iron-based deposit. Consequently, tracking by only UV-Vis is probably insufficient to achieve the real degree of ciprofloxacin degradation. Analyzing its final products can be determined with another analytical method, such as LC/MS.

Table 1. Calculated pseudo-first-order rate constants of CIP degradation and percentage of degradation.

Photocatalyst	**k (min^{-1})**	**R^2**	**Degradation of CIP (%)**
0.5 % (Fe)TiO_2	0.0025 ± 0.0004	0.81281	45.44
1 % (Fe)TiO_2	0.0027 ± 0.0003	0.89444	46.45
2 % (Fe)TiO_2	0.0030 ± 0.0004	0.86573	47.76

CONCLUSION

Prepared photocatalysts – Fe-modified TiO_2 at three molar ratios (0.5, 1 and 2 %) were applied for the degradation of the ciprofloxacin commercial solution for the infusion during 240 min. The result from UV-Vis spectra indicate degradation efficiency around 50 %. On the other hand, due the high concentration of photocatalysts results in fast and efficient degradation of ciprofloxacin after one hour, but after 2 hours the absorbance curves are shifted too much and the UV-Vis spectroscopy is not suitable for tracking the degradation.

Acknowledgment

This research was funded by the Ministry of Science, Technological Development and Innovation of the Republic of Serbia (grant number: 451-03-66/2024-03/200017).

REFERENCES

[1] T. Gezahegn, B. Tegegne, F. Zewge, B. S. Chandravanshi, BMC Chem., 13 (2019) 28.
[2] M. Kovačević, S. Živković, M. Ognjanović, M. Momčilović, D. Relić, D. Vasić Anićijević, Materials, (2023) 16.
[3] A. Kutuzova, T. Dontsova, W. Kwapinski, Catalysts, (2021) 11.
[4] H. Eskandarloo, A. Badiei, M. A. Behnajady, G. Mohammadi Ziarani, Photochem Photobiol, 91 (2015) 797.
[5] K. S. Varma, R. J. Tayade, K. J. Shah, P. A. Joshi, A. D. Shukla, V. G. Gandhi, Water-Energy Nexus, 3 (2020) 46.
[6] M. Qutob, M. A. Hussein, K. A. Alamry, M. Rafatullah, RSC Adv., 12 (2022) 18373.
[7] H. N. C. Dharma, J. Jaafar, N. Widiastuti, H. Matsuyama, S. Rajabsadeh, M. H. D. Othman, M. A. Rahman, N. N. M. Jafri, N. S. Suhaimin, A. M. Nasir, N. H. Alias, Membranes (Basel) (2022) 12.
[8] A. G. Akerdi, S. H. Bahrami, J Environ. Chem. Eng., 7 (2019) 103283.

IMPACT OF INITIAL CONCENTRATION OF H_2O_2 ON BPA DEGRADATION EFFICIENCY BY FENTON REAGENT

M. Simić, D. Aćimović, M. Kovačević, K. Stojanović, B. Savić Rosić, D. Vasić Anićijević and T. Brdarić

University of Belgrade, VINČA Institute of Nuclear Sciences-National Institute of the Republic of Serbia, Department of Physical Chemistry, Mike Petrovića Alasa 12-14, 11000, Belgrade, Serbia. (marija.simic@vin.bg.ac.rs)

DOI: https://doi.org/10.46793/Phys.Chem24I.077S

ABSTRACT

Due to its widespread use, bisphenol A (BPA) is commonly found as a contaminant in wastewater, posing significant environmental and health risks. Conventional treatment methods often fail to completely remove it, necessitating the development of more effective technologies. Advanced oxidation processes (AOPs), particularly the Fenton reaction, have garnered considerable attention for the degradation of organic pollutants. The Fenton reagent uses hydrogen peroxide (H_2O_2) and ferrous iron (Fe^{2+}) to generate hydroxyl radicals (•OH), which are highly reactive and capable of breaking down BPA. This study investigates the effect of H_2O_2 concentration on the efficiency and kinetics of BPA degradation in sulfate-rich wastewater using the Fenton process. The results show that increasing H_2O_2 concentration enhances BPA degradation, with a pseudo-first-order kinetic model describing the process. These findings support the optimization of the Fenton process for the efficient removal of BPA from wastewater.

INTRODUCTION

BPA is a synthetic organic compound extensively used in the production of polycarbonate plastics and epoxy resins. It is known to be an endocrine disruptor, meaning it can interfere with hormone systems in organisms, leading to various health problems such as reproductive disorders, developmental issues, and even cancer [1, 2].

The persistence of BPA in the environment is a major concern because of its resistance to natural degradation processes. Numerous methods have been developed to remove BPA from wastewater [3-5]. Among them, AOPs have shown great promise due to their ability to generate highly reactive species that can degrade recalcitrant organic pollutants like BPA. One of the most effective AOPs for the degradation of BPA is the Fenton process. The Fenton reaction (1) involves the use of H_2O_2 and Fe^{2+} as catalysts to produce •OH:

$$Fe^{2+} + H_2O_2 \longrightarrow Fe^{3+} + \bullet OH + OH^- \quad (1)$$

The •OH generated in this process are highly effective at breaking down organic molecules into smaller, less harmful compounds, ultimately leading to mineralization into carbon dioxide and water. H_2O_2, along with treatment time, Fe^{2+} concentration, and pH levels, is a critical component of the Fenton reagens, serving as the source of •OH. It is well known that the concentration of H_2O_2 significantly impacts the efficiency of organic molecule degradation. However, there is not much literature available on the topic of removing BPA using the Fenton process, according to the author's understanding.

In this study, the effect of H_2O_2 concentration on the efficiency and kinetics of BPA degradation in sulfate-rich wastewater was investigated. The presented results may be useful as a model system for the future development of green environmental technologies for the treatment of wastewater contaminated with BPA.

METHODS

All experiments were carried out in a 60 mL batch reactor. A Fenton reagent consisting of Fe^{2+} ions (concentration 0.1 mM) and H_2O_2 (Zorka, Šabac, Serbia) in various concentrations (15 mM, 75 mM, 100 mM, and 150 mM) was used for BPA oxidation using the Fenton process. The experiments were performed by adding the Fenton reagent to a 0.1 M Na_2SO_4 (Sigma-Aldrich, USA) wastewater model solution in which the BPA (Sigma-Aldrich, USA) concentration was 30 mg L^{-1}. The initial pH was set at 4.0. The BPA oxidation process lasted 300 minutes. Aliquots were withdrawn from the reactor at selected intervals, followed by stopping the Fenton process by adding a 5 M NaOH solution, and further preparation for analysis by gas chromatography/mass spectrometry (GC-MS).

A GC-MS system (Agilent Technologies 7890B GC System, Agilent Technologies 5977 MSD, Santa Clara, California, USA) was employed for the quantitative analysis of BPA using a fused silica GC capillary column (Agilent J&W HP-5 ms 30 m × 0.25 mm i.d., film thickness 0.25 μm). Sample preparation, analysis of aliquots, and measurement conditions are described in detail in our previous study [5].

Determination of BPA concentration in model solution was based on calibration curve. Degradation efficiency was calculated according to following equation (2):

$$Degradation\ efficiency(\%) = \frac{C_0 - C}{C_n} \cdot 100 \quad (2)$$

were C_0 is initial concentration of BPA, C is concentration in taken aliquot in time of treatment.

RESULTS AND DISCUSSION

Figure 1 shows the concentration profiles of BPA at different initial H_2O_2 concentrations during treatment time with Fenton reagent. The results indicate that the concentration of BPA decreases with increasing H_2O_2 concentration and treatment time. When the H_2O_2 concentration increased to 150 mM, 11 % degradation of BPA was achieved after 60 minutes. H_2O_2 concentrations less than 100 mM did not induce a significant change in the initial concentration of BPA during the first hour of treatment. BPA degradation of 30 % and 50 % was achieved after 300 minutes when the H_2O_2 concentrations were 100 mM and 150 mM, respectively.

Generally, an increase in H_2O_2 concentration leads to enhanced BPA degradation due to the generation of more OH radicals, which are the primary oxidizing species responsible for breaking down BPA molecules. At lower H_2O_2 concentrations, the production of •OH may be limited, resulting in slower BPA degradation rates. However, as the initial H_2O_2 concentration rises, more OH radicals are generated, facilitating faster BPA degradation kinetics. On the other hand, H_2O_2 can act as a scavenger of •OH, producing a less potent perhydroxyl radical, which results in less BPA degradation.

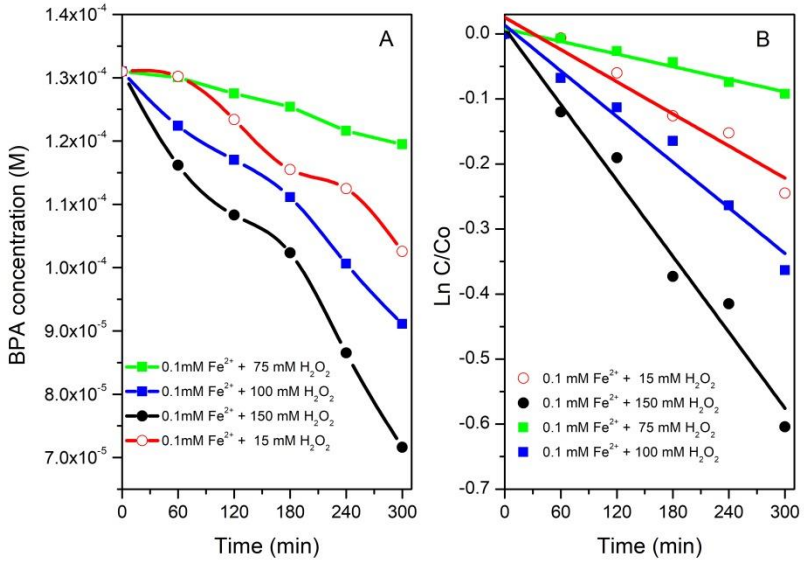


Figure 1. Effect of H_2O_2 concentration on BPA Degradation (A) and Pseudo First-Order Plot (B).

To describe the effect of H_2O_2 concentration on the kinetics of BPA degradation, a pseudo-first-order kinetic model with respect to the concentration of BPA and the initial concentration of H_2O_2 (**Figure 1B**) was applied. The pseudo-first-order rate constants (k) were determined from the slopes of the plots of ln(*C/Co*) *versus* treatment time. The linearity of these plots confirms that BPA degradation by the Fenton process follows pseudo-first-order kinetics. Experimental values for k and the regression coefficient (R) are reported in Table 1. The observed pseudo-first-order kinetics are in good agreement with previous research data on organic pollutant degradation under similar conditions [6].

Table 1. Kinetic parameters of pseudo first-order model.

H_2O_2 concentration (mM)	**k (min $^{-1}$)**	**R**
15	0.0008	0.94
75	0.0006	0.97
100	0.0011	0.97
150	0.0019	0.97

CONCLUSION

This study demonstrates that increasing the concentration of hydrogen peroxide (H_2O_2) significantly enhances the degradation of BPA in sulfate-rich wastewater using the Fenton process. The degradation follows pseudo-first-order kinetics and higher H_2O_2 concentrations result in more efficient BPA breakdown due to the increased generation of hydroxyl radicals. These findings underline the potential of optimizing the Fenton process for effective BPA removal from wastewater, contributing to the development of greener environmental technologies.

Acknowledgment
This work was supported by Ministry of Science, Technological Development, and Innovation of the Republic of Serbia [grant number 451-03-66/2024-03/200017].

REFERENCES

[1] A. Kowalczyk, M. Wrzecińska, E. Czerniawska-Piątkowska, J.P. Araújo, P. Cwynar, Biomed. Pharmacother., 155 (2022) 113730.
[2] I. Paterni, C. Granchi, F. Minutolo, Crit. Rev. Food Sci. Nutr., 57 (2017) 3384.
[3] J. Ding, L. Bu, B. Cui, G. Zhao, Q. Gao, L. Wei, Q. Zhao, D. D. Dionysiou, Environ. Sci. Ecotechnology., 3 (2020) 100036.
[4] B.N. Malinović, J. Markelj, A. Žgajnar Gotvajn, I. Kralj Cigić, H. Prosen, Environ. Chem. Lett., 20 (2022) 3765.
[5] M.D. Simić, B.G. Savić, M.R. Ognjanović, D.M. Stanković, D.J. Relić, D.D. Aćimović, T.P. Brdarić, J. Water Process Eng., 51 (2023) 103416.
[6] H. Gallard, J. De Laat, Wat. Res., 34 (2000) 3107.

PREDICTION OF BISPHENOL A DEGRADATION PATHWAYS DURING ELECTROCHEMICAL OXIDATION

M. Simić, M. Kovačević, K. Stojanović, M. Ječmenica Dučić, D. Vasić Anićijević, T. Brdarić and D. Aćimović

University of Belgrade, VINČA Institute of Nuclear Sciences-National Institute of the Republic of Serbia, Department of Physical Chemistry, Mike Petrovića Alasa 12-14, 11000, Belgrade, Serbia. (marija.simic@vin.bg.ac.rs)

DOI: https://doi.org/10.46793/Phys.Chem24I.081S

ABSTRACT

Electrochemical oxidation emerges as a highly promising technique for removing organic pollutants from water and wastewater, employing electrons as a clean reagent. In this study, we aim to evaluate the oxidative degradation of bisphenol A by identifying its intermediates and projecting the degradation pathway over a five-hour period of electrochemical oxidation on SnO_2-MWCNT electrode. The presence of BPA and its derivatives in wastewater treatment poses a common challenge in environmental chemistry. During electrochemical oxidation, nine BPA intermediates were identified. The process involved silanization to generate trisilyl esters and ethers, aiding in the determination of their structures. Based on these findings, two primary degradation pathways were identified: hydroxylation of the aromatic ring of BPA and direct cleavage of the BPA molecule. Ultimately, both pathways lead to the production of diverse aliphatic acids, along with the release of CO_2 and water.

INTRODUCTION

Bisphenol A (BPA), also known as 4, 4'-isopropylidenediphenol, is a synthetic compound widely utilized in the manufacture of polycarbonate plastics, epoxy and phenolic resins, and various consumer goods [1]. It enters the environment through industrial and household wastewater, posing a significant threat to surface and groundwater quality. Contaminating water sources, BPA presents a risk to public health by potentially entering drinking water supplies. BPA's interference with the endocrine system disrupts hormone function, leading to adverse effects on both aquatic organisms and human fertility [2]. The presence of BPA and its derivatives in wastewater treatment represents a common issue in environmental chemistry. Traditional wastewater treatment techniques face challenges in effectively removing BPA. Therefore, advanced oxidation processes (AOPs), which involve the generation of highly reactive species on-site, offer an alternative solution for BPA removal in wastewater treatment. Electrochemical oxidation stands out as one of the most promising methods for eliminating organic pollutants from water and wastewater. This process utilizes electrons as a "clean" reagent, devoid of chemical involvement and generating no toxic waste after completion of treatment [3].

The primary aim of this study is to assess the oxidative breakdown of BPA by identifying its intermediates and projecting the degradation pathway over a five-hour period of electrochemical oxidation.

METHODS

The electrochemical oxidation was conducted using a two-electrode electrolytic cell. The anode was made of a prepared SnO_2-MWCNT (multi-walled carbon nanotubes) electrode, while a stainless steel (SS) plate, with a surface area matching that of the anode (2 cm^2), served as the cathode. These

electrodes were submerged in a 60 mL of electrolyte solution containing 0.1 M Na_2SO_4 (Sigma-Aldrich, USA) at a pH of approximately 4, and 30 mg L^{-1} BPA (Sigma-Aldrich, USA). Distance between electrodes was 1 cm. Chronopotentiometry experiments were performed, applying current densities of 15.0 mA cm^{-2} during 5 hours. To determine the BPA intermediates at each hour, the electrochemical oxidation was stopped (after the 1st, 2nd, 3rd, 4th, and 5th hour), followed by the extraction of BPA intermediates according to a modified procedure described by Poerschmann et al [4]. During this procedure, liquid-liquid extraction with diethyl ether (Merck, Germany) was conducted, followed by silanization using N, O–Bis(trimethylsilyl)trifluoroacetamide - BSTFA (Sigma-Aldrich, Germany).

BPA, its intermediates, and degradation products were analyzed using gas chromatography/mass spectrometry (GC-MS) with an Agilent Technologies 7890B GC System and Agilent Technologies 5977 MSD (California, USA). The system was equipped with a fused silica GC capillary column (Agilent J&W HP-5 ms, 30 m × 0.25 mm i.d., film thickness 0.25 μm). Helium of grade 5.0 served as the carrier gas at a constant flow rate of 1.0 mL min^{-1}. The gas chromatograph parameters included a splitless injector temperature of 250 °C, an injection volume of 1 μL, a transfer line temperature of 300 °C, and an oven temperature program ranging from 50 °C (2 min hold) with a ramp of 9 °C min^{-1} to 320 °C (5 min hold), then a ramp of 9 °C min^{-1} to 320 °C min^{-1} (1 min hold). Data acquisition was conducted in full scan mode within the m/z range of 33–800 amu for identification purposes. The analysis and processing of GC-MS data were performed using Agilent GC–MS MassHunter software and the NIST 14 mass spectral library.

RESULTS AND DISCUSSION

During the electrochemical oxidation, nine BPA intermediates were identified. The process involved silanization to produce trisilyl esters and ethers, facilitating the determination of their structures. This was achieved through mass-to-charge ratio (m/z) measurements and characteristic ion spectra obtained via GC-MS [5]. Additionally, the instrument software utilized the NIST library to suggest pseudo-molecular formulas, as detailed in Table 1.

Table 1. BPA intermediates formed during electrochemical oxidation of BPA.

Name	m/z [1]	Pseudo-molecular formula
Bisphenol A	228.29 (372.66)	$C_{15}H_{16}O_2$
Product 1	260.10 (549.02)	$C_{15}H_{16}O_4$
Product 2	258.27 (474.21)	$C_{15}H_{14}O_4$
Product 3	244.07 (460.19)	$C_{14}H_{12}O_4$
Product 4	244.07 (388.15)	$C_{14}H_{12}O_4$
Benzoic Acid	122.12 (194.31)	$C_7H_6O_2$
4-isopropenylphenol	134.18 (206.36)	$C_9H_{16}O$
Hydroxyquinone	110.04 (254.12)	$C_6H_6O_2$
4-hydroxyacetophenone	136.15 (208.09)	$C_8H_8O_2$
4-hydroxybenzoic acid	138.12 (282.11)	$C_7H_6O_3$

[1] m/z of the non-derivatized analyte and its trimethilsilyl ether/ester, in Da

BPA intermediates are primarily formed through OH radical attack. Although OH radicals are non-selective, a DFT study reports that OH radical attacks on the BPA molecule occur at specific positions [6]. The attack of OH radicals is favored at the ortho position (relative to the OH group of the aromatic ring). Hydroxylated BPA intermediates are formed as products of this reaction, which are later degraded into single-ring BPA intermediates. This is one of the main degradation pathways

of BPA molecules through electrochemical oxidation, denoted as Degradation Pathway 1 in **Figure 1**.

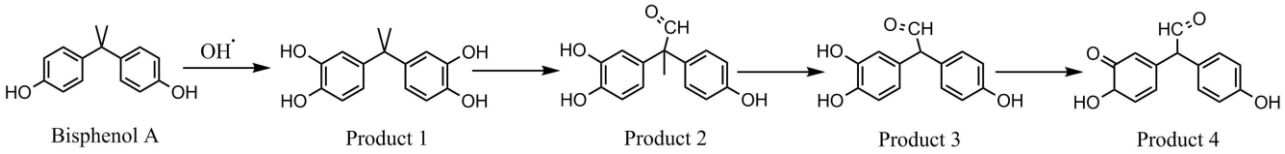


Figure 1. Degradation Pathway 1 **of BPA**.

Simultaneously with this degradation pathway, single-ring BPA products arise through the attack of OH radicals on the carbon atom closest to the aliphatic chain of the BPA molecule. They include: benzoic acid, 4-isopropenylphenol, benzoquinone, hydroxyquinone, 4-hydroxyacetophenone and 4-hydroxybenzoic acid (named as Degradation pathway 2 at **Figure 2**).

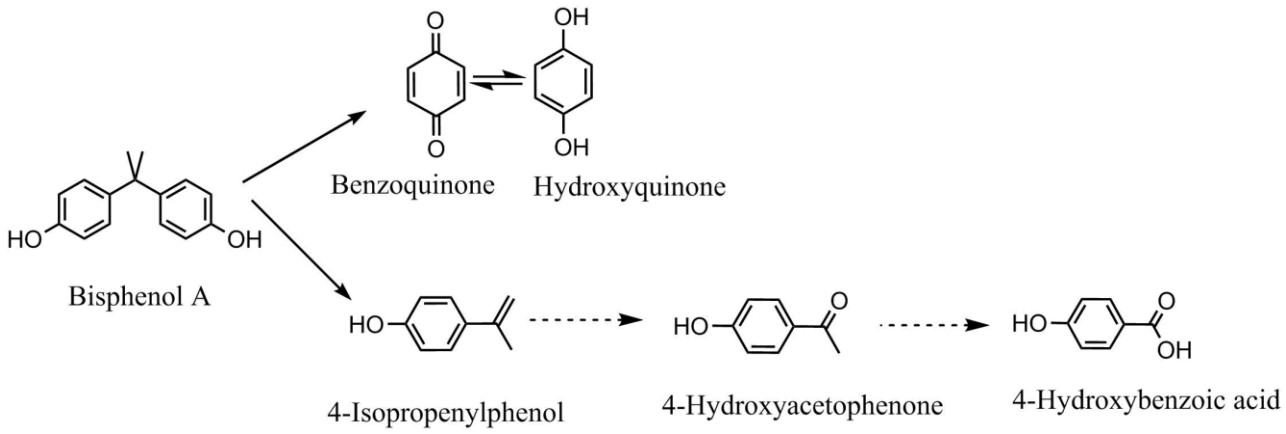


Figure 2. Degradation Pathway 2 of BPA.

Further application of electrochemical oxidation results in the opening of the single-ring BPA intermediate, leading to the formation of aliphatic acids, ultimately resulting in carbon dioxide and water.

Based on these results, two main degradation pathways can be identified. The first involves the hydroxylation of the aromatic ring of BPA, while the second entails the direct cleavage of the BPA molecule. Ultimately, both pathways result in the production of diverse aliphatic acids, accompanied by the release of CO_2 and water. The proposed pathways have also been recognized as primary routes for BPA oxidation through various AOPs employing hydroxyl radicals [5, 6].

CONCLUSION

While liquid chromatography-mass spectrometry is more commonly used than GC-MS for detecting degradation products, numerous intermediates have been successfully identified as electrochemical degradation products. Based on the detected intermediates, two degradation pathways were proposed, which are in accordance with the previous findings.

In future experiments, toxicity estimation of the electrochemical oxidation with SnO_2-MWCNT electrodes on BPA could be conducted, drawing on proposed degradation pathways and detected intermediates.

Acknowledgment
This work was supported by Ministry of Science, Technological Development, and Innovation of the Republic of Serbia [grant number 451-03-66/2024-03/200017].

REFERENCES

[1] B.N. Malinović, J. Markelj, A. Ž. Gotvajn, I. K. Cigić, H. Prosen, Environ. Chem. Lett. 20 (2022) 3765–3787.
[2] A. Kowalczyk, M. Wrzecińska, E. Czerniawska-Piątkowska, J.P. Araújo, P. Cwynar, Biomed. Pharmacother. 155 (2022) 113730.
[3] M.D. Simić, B.G. Savić, M.R. Ognjanović, D.M. Stanković, D.J. Relić, D.D. Aćimović, T.P. Brdarić, J. Water Process Eng. 51 (2023) 103416.
[4] J. Poerschmann, U. Trommler, T. Górecki, Chemosphere. 79 (2010) 975–986.
[5] B. Darsinou, Z. Frontistis, M. Antonopoulou, I. Konstantinou, D. Mantzavinos, Chem. Eng. J. 280 (2015) 623–633.
[6] Q. Han, M. Wang, F. Sun, B. Yu, Z. Dong, P. Li, J. Luo, M. Li, X. Jin, Z. Dai, Environ. Res. 216 (2023).

GREEN g-C_3N_4/CMC/SA HYDROGEL FOR PHOTOCATALYTIC WASTEWATER REMEDIATION

K. Milošević [1], D. Lončarević [1], M. Kalagasidis Krušić [2] M. Hadnađev-Kostić [3] and J. Dostanić [1]

[1] *University of Belgrade, Institute of Chemistry, Technology and Metallurgy, National Institute of Republic of Serbia, Njegoševa 12, 11000 Belgrade, Serbia. (ksenija.milosevic@ihtm.bg.ac.rs)*
[2] *University of Belgrade, Faculty of Technology and Metallurgy, Karnegijeva 4, 11000 Belgrade, Serbia*
[3] *University of Novi Sad, Faculty of Technology, Bulevar Cara Lazara 1, 21000 Novi Sad, Serbia*

DOI: https://doi.org/10.46793/Phys.Chem24I.085M

ABSTRACT

Due to its potential to provide sustainable solutions to pollution and contamination, photocatalysis is a promising area of research in the fields of environmental protection and water remediation. The main objective of this work was to prepare an environmentally friendly, durable, easily-separable, and reusable nanocomposite hydrogel with g-C_3N_4 encapsulated into a carboxymethylcellulose (CMC) and sodium alginate (SA) polymer matrix for wastewater remediation. The physicochemical properties of the prepared hydrogel were characterized by FE-SEM and ATR-FTIR spectroscopy. The g-C_3N_4/CMC/SA hydrogel photocatalytic efficiency was investigated using an anionic Orange G (OG) dye as a model pollutant.

INTRODUCTION

The discharge of excessive amounts of wastewater containing harmful organic pollutants into clean water bodies has become a significant environmental issue. The organic pollutants are usually non-biodegradable, highly toxic, thermally stable, photo-resistant, and intensely colored, making them especially challenging to remove [1]. Traditional wastewater treatment methods are generally categorized into chemical, biological, and physical-mechanical processes [2]. A significant drawback of these approaches is that they are non-destructive, merely transferring contaminants from one phase to another, which can lead to secondary pollution. Heterogeneous photocatalysis offers several advantages over conventional wastewater treatment methods. It is straightforward, harnesses renewable and clean solar energy, allows sufficient time for complete pollutant degradation, does not produce secondary waste, ensures good reproducibility, and is cost-effective [1]. Light-responsive, nano-based semiconductor photocatalysts have garnered notable attention for the degradation of organic pollutants over the past few decades.

Graphitic carbon nitride (g-C_3N_4) has emerged as an attractive organic semiconductor in photocatalysis due to its metal-free composition, cost-effectiveness, photostability, chemical and biological inertness, and natural abundance [3]. The primary limitation hindering the large-scale application and cyclic reusability of g-C_3N_4 is agglomeration of nanoparticles, which complicates their separation from the reaction solution [4]. Encapsulating the g-C3N4 particles in polymer supports facilitates their easy recovery and separation. Natural polymers like carboxymethylcellulose (CMC) and sodium alginate (SA) have gained significant interest as polymer supports due to their sustainability, non-toxicity, low cost, and biodegradability. They also offer good biocompatibility, high adsorption capacity, and excellent recyclability [5]. It is common practice to crosslink SA with divalent and multivalent cations and form hydrogels.

The aim of this work was to develop an environmentally friendly nanocomposite hydrogel based on g-C_3N_4, CMC, and SA using a straightforward synthesis method with eco-friendly cross-linkers,

$CaCl_2$ and citric acid. The photocatalytic activity of resulting hydrogel was tested in degradation of the anionic dye Orange G.

METHODS

Materials

Melamine ($C_3H_6N_6$), OG, and CMC were obtained from Aldrich, USA. calcium chloride ($CaCl_2$), SA, and citric acid (CA) were obtained from Merck, Germany. All chemical reagents used to synthesize g-C_3N_4 and polymer hydrogels were of analytical grade and used without further purification.

Synthesis

Photocatalytically active g-C_3N_4 was synthesized by mixing 2.0 g of urea and 2.0 g of melamine in a ceramic crucible at 550 ºC for 2 h (step ramping rate of 10 ºC min^{-1}). After cooling down to room temperature, g-C_3N_4 was put into an ethanol/distilled water solution (1/5) after which it was ultrasonically dispersed for a few hours. The g-C_3N_4 particles were then dried at 80 ºC for 12 hours. The CMC/SA solution was prepared by dissolving 187.5 mg of CMC and 187.5 mg of SA in 15 mL of distilled water with continuous stirring. Simultaneously, 75 mg of g-C_3N_4 was added to the polymer solution until the mixture was completely homogeneous. Further, the g-C_3N_4/CMC/SA solution was dropped into a 2.5% $CaCl_2$ solution using a plastic syringe under gentle stirring. The g-C_3N_4/CMC/SA hydrogel was then added into a 2.9% CA ethanol solution and kept at 80 ºC for 10 h. The prepared nanocomposite hydrogels were washed with ethanol and distilled water and stored in distilled water in a refrigerator.

Characterization

The morphology of the nanocomposite was characterized by field emission scanning electron microscopy (FE-SEM, Tescan FE-SEM Mira 3 XMU, Tescan a. s., Brno, Czech Republic, operated at 20 keV). The chemical structure of the samples was characterized by Attenuated Total Reflectance Fourier Transform Infrared spectroscopy (ATR-FTIR) in the range of 400–4000 cm^{-1} with 2 cm^{-1} scanning resolution.

Photocatalytic degradation tests

The photocatalytic activity of the obtained hydrogel was tested using a model pollutant – OG dye in an aqueous solution. The photocatalytic reactor consisted of a 250-mL open cylindrical thermostatic Pyrex cell and a 300 W Osram Ultra Vitalux lamp, the spectrum of which simulated sunlight. The lamp was placed 50 cm above the surface of the reaction solution. The concentration of the dye in the solution was monitored before and during the photocatalytic reaction by UV/Vis spectrophotometry (Thermo Electron Nicolet Evolution 500).

RESULTS AND DISCUSSION

Characterization of nanocomposite hydrogel

The surface morphology of the neat polymer hydrogel (CMC/SA), the neat g-C_3N_4 and the nanocomposite hydrogel (g-C_3N_4/CMC/SA), characterized by FE-SEM is shown in Figure 1a-e. FE-SEM micrographs of the CMC/SA show regular sheet-like morphologies with smooth surfaces. The g-C_3N_4 has the structure of porous nanoparticles with irregular shapes. The g-C_3N_4/CMC/SA micrographs display regular sheet-like morphologies, with a rugged-like structure of g-C_3N_4 nanoparticles uniformly dispersed into the polymer matrix. The CMC/SA and g-C_3N_4/CMC/SA micrographs illustrate that all hydrogels possess homogeneous surfaces. The FTIR spectra of neat CMC/SA, neat g-C_3N_4, and g-C_3N_4/CMC/SA are shown in Figure 1f. The peaks corresponding to neat g-C_3N_4 indicate a structure typical of g-C_3N_4. Several intense bands in the region of 1200–1650 cm^{-1} are observed and assigned to the stretching vibrations of aromatic C–N heterocycles. The single absorption band at 806 cm^{-1} is attributed to the characteristic breathing mode of tri-s-triazine

units. The broad band at around 3150 cm^{-1} is indicative of N–H stretching vibration modes. In the spectra of CMC/SA, the broad band at around 3410 cm^{-1}, was attributed to the –OH stretching vibration of the polysaccharides of alginate and carboxymethylcellulose, and the band at around 2930 cm^{-1} originates from the stretching vibration of methylene C–H group. These bands indicate that there is a large number of –OH and $–CH_2$ groups in CMC/SA. The significant absorption band at 1730 cm^{-1} is attributed to the stretching vibration of the C=O group. After encapsulation of g-C_3N_4 in the CMC/SA matrix, absorption bands at around 3160 cm^{-1} and 3400 cm^{-1} are merging and broadening. The intensity of bands in g-C_3N_4/CMC/SA is weaker compared to neat g-C_3N_4 and CMC/SA which verifies their structural integrity after the encapsulation.

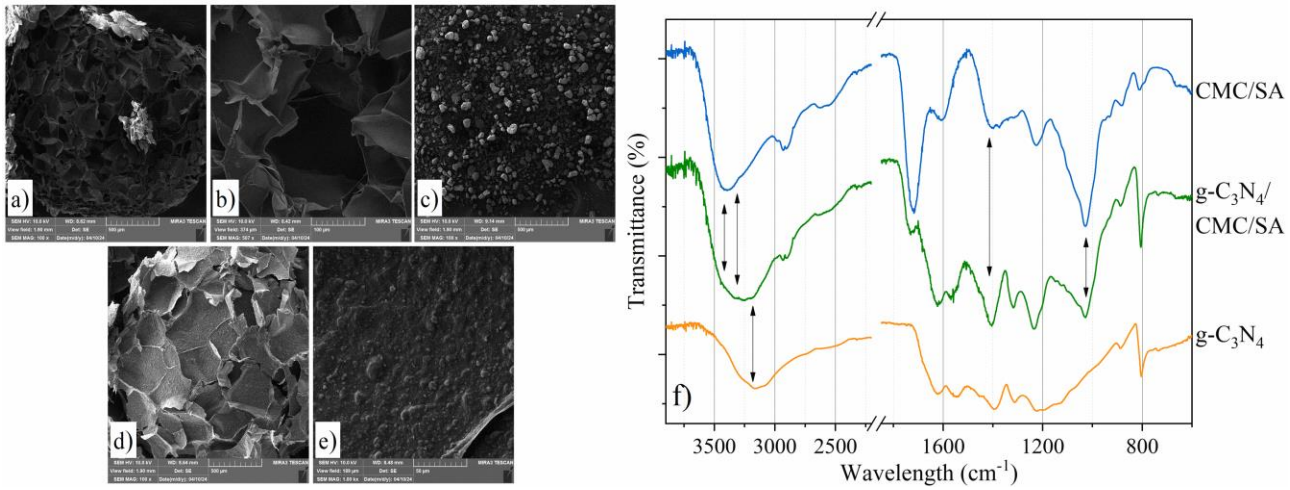


Figure 1. FE-SEM micrographs of (a, b) neat polymer hydrogel, (c) neat g-C_3N_4, and (d, e) nanocomposite hydrogel at different magnifications; (f) FTIR spectra of neat polymer hydrogel, neat g-C_3N_4, and nanocomposite hydrogel.

Photocatalytic activity of nanocomposite hydrogel

The photocatalytic activity of nanocomposite hydrogel was evaluated by following the decomposition of OG dye under solar light irradiation. Prior to irradiation, the photocatalyst was dispersed in an aqueous solution of the OG dye and stirred in the dark for an hour to reach an adsorption equilibrium. The equilibrium was attained when 28% of the OG dye was taken up by neat g-C_3N_4, while 13% was taken up by the g-C_3N_4/CMC/SA hydrogel. A lower adsorption capacity of g-C_3N_4/CMC/SA hydrogel compared to that of neat g-C_3N_4 was probably due to the electrostatic repulsion between negatively charged CMC/SA polymer matrix (rich in –OH and COO^- functional groups) and the anionic OG dye. Figure 2 illustrates the course of the reaction when neat g-C_3N_4 and composite g-C_3N_4/CMC/SA hydrogel were used as photocatalysts. The graph reveals that complete photocatalytic degradation of OG dye using neat g-C_3N_4 occurs within 2 h, while more than 90% of the dye is decomposed after 3 h when g-C_3N_4/CMC/SA hydrogel is used as a catalyst. The encapsulation of g-C_3N_4 into the polymer matrix resulted in somewhat slower OG photodegradation, particularly within the first hour, when the encapsulated catalyst exhibited 50% seen with the neat g-C_3N_4. The final percent decomposition of the dye, reached after 3 h, was only slightly lower with the encapsulated catalyst. This implies that the active centers were not affected by the polymer coating and that their number was not significantly reduced by the encapsulation.

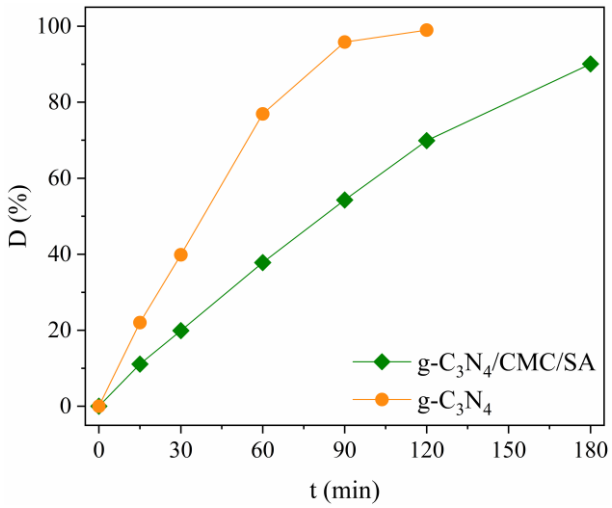


Figure 2. Photocatalytic degradation of OG dye in the presence of neat g-C_3N_4 and g-C_3N_4/CMC/SA hydrogel. Experimental conditions: T=25 °C, pH=3.8, c_0(OG)=10 ppm, m(g-C_3N_4)=75 mg, simulated solar light irradiation.

CONCLUSION

Photocatalytically active g-C_3N_4/CMC/SA hydrogel nanocomposite was synthesized, characterized by SEM and FTIR spectroscopy and tested as a photocatalyst in the degradation of OG dye. The hydrogel composite showed a sheet-like morphology with g-C_3N_4 nanoparticles uniformly dispersed into the polymer matrix. The structural integrity of both g-C_3N_4 and polymers after the g-C_3N_4 encapsulation was verified. The encapsulation of g-C_3N_4 into CMC/SA polymer has slightly, but not significantly affected the final photocatalytic efficiency, which makes g-C_3N_4/CMC/SA a promising material for the photodegradation of organic pollutants from wastewater.

Acknowledgment

This research has been supported by the Ministry of Science, Technological Development and Innovation of the Republic of Serbia (Contract No: 451-03-66/2024-03/200026 and 451-03-65/2024-03/200135).

REFERENCES

[1] A. Rafiq, M. Ikram, S. Ali, F. Niaz, M. Khan, Q. Khan, M. Maqbool, J. Ind. Eng. Chem. 97 (2021) 111–128.
[2] R. Rashid, I. Shafiq, P. Akhter, M.J. Iqbal, M. Hussain. Environ Sci Pollut Res 28 (2021) 9050–9066.
[3] M. Raaja Rajeshwari, S. Kokilavani, S. Sudheer Khan, Chemosphere 291 (2022) 132735.
[4] S. Vigneshwaran, J. Preethi, S. Meenakshi, Int. J. Biol. Macromol. 132 (2019) 289–299.
[5] Y. Cong, X. Chen, Q. Zheng, Y. Zhang, S-W. Lv, Environ. Res. 215 (2022) 114414.

EFFECT OF QUERCETIN ON MICELAR PROPERTIES OF CETYLTRIMETHYLAMMONIUM BROMIDE IN ETHANOL–WATER MIXTURES: A CONTUCTIVITY STUDY

S. Mićić, J. Rupar, A. Janošević Ležaić and N. Pejić

University of Belgrade–Faculty of Pharmacy, Vojvode Stepe 450, 11000 Belgrade, Serbia (natasa.pejic@pharmacy.bg.ac.rs)

DOI: https://doi.org/10.46793/Phys.Chem24I.089M

ABSTRACT

Investigation of the micellization of cationic surfactant, cetyltrimethylammonium bromide (CTAB) in the presence of flavonoid–quercetin (QR) was performed by conductance method. Specific conductivity data of CTAB + QR system in mixed ethanol–water solvent (10, 20 and 30% v/v) were obtained by increasing the CTAB concentration, whereas the QR concentration was kept constant at T = 27 °C. It was found that the critical micelle concentration (CMC) increased with increasing ethanol percentage in water. Moreover, two CMC values (CMC_1 and CMC_2) of CTAB, in the absence and presence of QR, were determined in 10% and 20% ethanolic solutions, whereas in 30% ethanol only one CMC was achieved in the examined CTAB concentration region.

INTRODUCTION

Recent efforts in creating a novel therapeutic formulations and pharmaceutical delivery systems made research of the surfactant and micellar interactions with drugs a topic of high research interest. These, as well as other applications are mainly based on the surfactant capacity to improve the solubility of drugs in both pharmaceutical solvents and body fluids, and to enhance skin penetration of these active compounds. Due to surfactants amphiphilic nature, these compounds can form micelles, and the minimum concentration at which the phenomenon of micellization occurs is the so-called critical micelle concentration (CMC).

In some cases [1], a second CMC can appear at a surfactant concentration larger than the first one, depending on the solution properties, and most frequently related to structural transitions of micelles induced by introduction of some additives, especially alcohols. Although evidence about a second transition in the postmicellar region in both pure and mixed cationic surfactant systems has been reported, detailed studies about the possibility of forming more than one kind of micelle in surfactant solutions is still relatively rare. The main reason for this is that the second break may not be as clearly defined experimentally as the first one under particular experimental conditions (the insensitivity of methods to detect CMC_2), as well as the fact that the concentrations of examined surfactants were normally varied only in a limited range above the CMC_1. Regarding the latter, CMC_2 may occur at concentrations of about 2–10 times that of CMC_1 in dependence on the type of 1:1 ionic surfactant [2]. However, given the popularity of CTAB solutions in numerous applications such as micellar solubilization of drugs as well as its uses in drug carrier systems, it is of interest to investigate the physicochemical properties of these solutions within a broader concentration range, i.e. surfactant concentrations which exceed the CMC_1 as there are numerous limitations in surfactant formulation, solubilization and their interactions with membranes which must be considered in mentioned applications.

Quercetin (QR), potent lipophilic antioxidant, possesses various biological and biochemical effects, such as anti-inflammatory, cardio-protective and anti-cancer activity. Despite that, there are

the problems of its poor water solubility and low bioavailability that can be overcome by incorporating QR into surfactant micellar structure. Thus, study of QR-surfactant interactions is of fundamental importance. Several studies have explored the interactions between QR and different surfactants [3,4]. Among them, CTAB, cationic surfactant widely used as antiseptic, solubilizing agent for pharmaceuticals, etc., was used to simulate cells and proteins in the living systems [5].

This study utilizes conductivity measurements to examine the interaction between CTAB and QR in solutions with different ethanol contents to assess QR impact on association nature of CTAB in CTAB + QR mixed system, i.e. determine the micellar parameters (CMC and the degree of micelle ionization, α) as well as the standard molar Gibbs free energy (ΔG_m^0) at T = 300.2 K. In this work, different ethanol contents as cosolvent were used to determine the most suitable concentration in which the micellar system provides thermodynamically stable and effective results. Namely, to utilize micelles containing QR in different pharmaceutical preparation, such as in preparing topical formulations, selection of ethanol-water mixture as solvent system provides more solubility than aqueous buffers [6].

EXPERIMENTAL

The conductivity measurements of examined surfactant systems (CTAB in absence and presence of QR) were carried out with digital conductivity meter HI8820N (Hanna instruments, Portugal) with the accuracy ±0.5%, and with the matching HI17684W probe that uses the 4-ring method. Specific conductivity values of each set containing about 20 different CTAB concentrations (3.0×10^{-4} mol $L^{-1} \leq c_{CTAB} \leq 6.5\times10^{-3}$ mol L^{-1}) at a fixed QR concentration ($c_{QR} = 5.0\times10^{-5}$ mol L^{-1}) in a ethanolic aqueous solution (10 – 30% v/v) were taken at T = 27°C (this temperature was chosen because of the Krafft temperature of CTAB which is around 25°C [7]). A circulating water bath was used for maintaining those temperatures within uncertainties of ± 0.2 K.

RESULTS AND DISCUSSION

The conductivities of CTAB + QR system in different solvent compositions, containing fixed QR concentration ($c_{QR} = 5.0\times10^{-5}$ mol L^{-1}), were investigated. Characteristic plot between specific conductance (κ) of the examined systems (CTAB in presence and absence of QR) and increasing CTAB concentration (c_{CTAB}) are shown in Fig. 1. Two breaks, as well as one break on the plots (indicated by arrows) were obtained.

For the mixed systems of CTAB+QR in 20% ethanol (Fig. 1a) as well as in 10% ethanol, two clear inflection points were obtained (designated as CMC_1 and CMC_2, respectively). The pre-micellar slopes were always found to be higher than that of the post-micellar one, allowing us to determine the degree of micelle ionization (α). If the slopes of the three linear segments of the plots are denoted as S_1, S_2 and S_3, than the degree of ionization at CMC_1 is $\alpha_1 = S_2/S_1$, and correspondingly the degree of ionization at the CMC_2 is $\alpha_2 = S_3/S_1$. Standard Gibbs free energy change (ΔG_m^0) was calculated from equation: $\Delta G_m^0 = (2 - \alpha)\ RT\ \ln X_{CMC}$, where X_{CMC} is the molar fraction of the surfactant at CMC. Using the same approach, we can estimate the standard Gibbs free energy of micellization at the CMC_2, i.e. at 2nd CMC. The obtained micellar parameters of examined surfactant systems in different percentages of ethanol in water, are all summarized in Table 1.

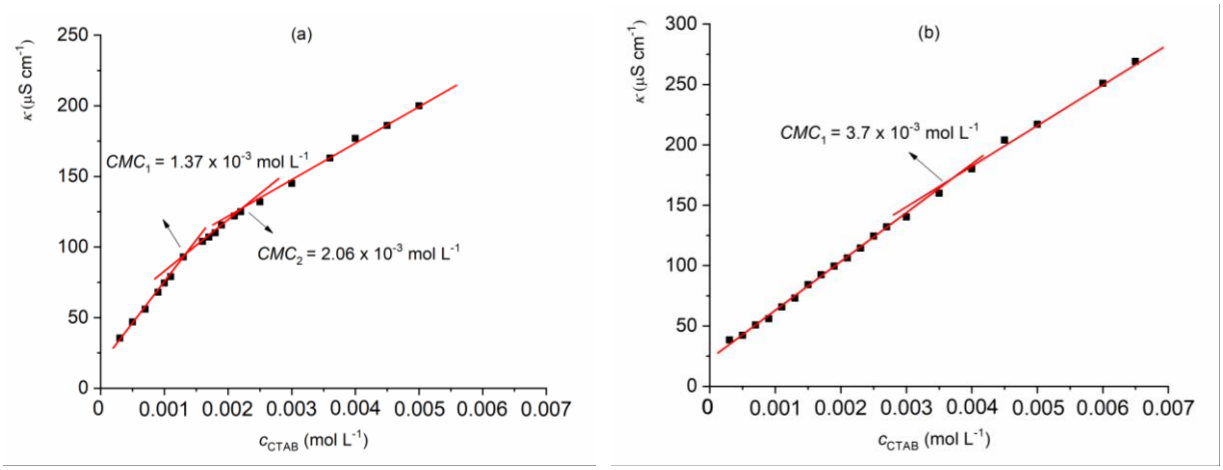


Figure 1. Plots κ–c_{CTAB} for the CTAB + QR in different ethanolic solutions: 20% (a) and 30% (b) at T = 27°C.

Table 1. Micellar parameters of CTAB in absence and presence of QR (5.0×10 mol L^{-1}) in different ethanolic aqueous solutions: critical micelle concentration (CMC_1 and CMC_2), the degree of ionization (α_1 and α_2) and standard Gibbs free energy changes (ΔG_m^0).

Ethanol % (v/v)	Surfactant system	CMC (mmol L^{-1})		α		ΔG_m^0 (kJ mol^{-1})	
		CMC_1	CMC_2	α_1	α_2	ΔG_1^0	ΔG_2^0
10	CTAB	0.90	2.58	0.47	0.36	–42.1	–40.8
	CTAB+QR	1.04	2.30	0.49	0.40	–41.0	–40.3
20	CTAB	2.17	2.82	0.65	0.48	–34.2	–37.5
	CTAB+QR	1.37	2.06	0.64	0.49	–36.0	–38.4
30	CTAB	2.80	/	0.91	/	–27.2	/
	CTAB+QR	3.70	/	0.90	/	–26.4	/

As expected, obtained CMCs are ethanol content dependent [8], and the occurrence of a second break on the κ *vs*. c_{CTAB} plots in the postmicellar region at about 3 and 2 times the CMC, respectively, has also been detected. The ratio of CMC (CMC_2/CMC_1) for CTAB + QR system decreases from 2.2 to 1.5 with increase of ethanol content.

Values of CMCs of CTAB + QR mixtures in ethanolic solutions increased with an increasing percentages of ethanol in water. Thus, the addition of ethanol disfavors the micellization of the CTAB + QR mixed system. The values of standard Gibbs free energy change (ΔG_m^0) also decrease with increasing ethanol composition, reflecting the disfavoring of micelle formation. Besides, at a fixed solvent composition, the higher specific conductivity of CTAB in presence of QR than these obtained in absence of QR could be attributed to an QR–CTAB interactions and formation of ion-pair or CTAB–QR complex.

CONCLUSION

Micellization of CTAB + QR mixed system in different ethanol percentage at T = 27 °C, were investigated by conductometry. Two CMC (CMC_1 and CMC_2), i.e. two clear infection points, for the both CTAB in presence and absence of QR in 10% and 20% ethanol, were detected. These

inflection points can be linked with the formation of CTAB–QR complex and/or the structural micellar changes. On the other hand, for CTAB + QR in the highest ethanol content (30% v/v) which was examined in our study, only one break on the $\kappa - c_{CTAB}$ plot was obtained; in this system the second break is not defined in the examined CTAB concentration region as the first one. Whatever, CTAB micellization was disfavored with increase in ethanol content of the solvent mixture regardless of the QR presence.

Acknowledgement
This work was partially supported by the Ministry for Education, Science and Technological Development of the Republic of Serbia (Grant no. 451-03-65/2024-03/200161).

REFERENCES

[1] G. Basu Ray, I. Chakraborty, S. Ghosh, S. P. Moulik, R. Palepu, Langmuir, 21 (2005) 10958–10967.
[2] A. Gonzàlez-Pèrez J. Czapkiewicz, G. Prieto J.R. Rodrìguez, Colloid Polym Sci (2003) 281: 1191–1195.
[3] J. C. Alva-Ensastegui, M. Palomar-Pardavé, M. Romero-Romo, M. T. Ramirez-Siolva, RCS Adv., 8 (2018) 10980–10986.
[4] V. R. S. Anjali, P. Rajesh, S. Dash, J. Biomol. Struct. Dyn., 2023, 41 (2023) 12521-1253.
[5] W. Liu, R. Guo R., J. Colloid Interface Sci, 302 (2006) 625–632.
[6] V. Abbot, P. Sharma, Chem. Phys, 538, 2020, 110921.
[7] J. Manojlovic, J. J. Ser. Chem. Soc., 85 (1), 2020, 67–78.
[8] N. Nazir, M. S. Ahanger, A. Akbar, J. Disper. Sci. Technol., 30 (2009) 51–55.

THE EFFECT OF THE CARBONIZATION TEMPERATURE ON THE CATALYTIC ACTIVITY OF Co-BASED CARBONIZED HYBRID CLAY NANOCOMPOSITE

J. Parlić[1], S. Marinović[1], M. Ajduković[1], P. Banković[1], J. Krstić[1], B. Nedić-Vasiljević[2] and N. Jović-Jovičić[1]

[1] *University of Belgrade, Institute of Chemistry, Technology and Metallurgy, Njegoševa 12, 11000 Belgrade, Serbia. (jovan.parlic@ihtm.bg.ac.rs)*
[2]*University of Belgrade, Faculty for Physical Chemistry, Studentski trg 12-16, 11000 Belgrade, Serbia*

DOI: https://doi.org/10.46793/Phys.Chem24I.093P

ABSTRACT

The influence of carbonization temperature in the synthesis of Co-supported hybrid inorganic-organic carbon-smectite catalysts was investigated. The catalysts were synthetized by simultaneous intercalation of inorganic Al-Keggin cations and organic hexadecyltrimethylammonium cations, followed by wet impregnation by Co^{2+} ions. The obtained samples were carbonized at 400 °C, 500 °C, and 600 °C in the flow of Ar providing inert atmosphere. The textural properties were obtained based on adsorption-desorption isotherms of nitrogen at -196 °C. The synthesized nanocomposites were tested as heterogeneous catalysts in advanced oxidation process of Acid Orange G degradation in the presence of Oxone® ($2KHSO_5 \cdot KHSO_4 \cdot K_2SO_4$). It was found that catalyst obtained by carbonization at 400 °C has the most developed surface area and showed the highest percent of degradation of Acid Orange G.

INTRODUCTION

The carbon phase derived from carbonized organic matter plays a significant role in the behavior and performance of catalytically active species in heterogeneous catalysts. Delocalized electrons of carbonaceous materials contribute to charge distribution via electron transfer, impacting the oxidation state and catalytic activity of active species. Furthermore, the carbon phase enhances specific surface area and porosity of the material [1]. On the other hand, Al-pillared clays have micro- and/or mesoporosity and thermal and chemical stability, which makes them as suitable support for transition-metals heterogeneous catalysts [2]. Combining the properties of carbonaceous materials and pillared clays the new hybrid nanocomposite was created with promising support potential. Oxone® ($2KHSO_5 \cdot KHSO_4 \cdot K_2SO_4$) has been used in catalytic oxidative degradation of various organic waste water pollutants. For its activation cobalt immobilized on various supports were the most frequently used [1, 2].

In this work, domestic bentonite clay (Gadžin Han, Serbia) was intercalated with hexadecyltrimethylammonium bromide ($HDTMA^+Br^-$) and pillared with Al-Keggin ions. The obtained material was impregnated with cobalt(II)-acetate and submitted to the heat treatment in an inert argon atmosphere at 400 °C, 500 °C, and 600 °C. The obtained catalysts were evaluated in the oxidative degradation of the color Acid orange G (AOG) in relation to the carbonization temperature used for the preparation of the catalyst.

METHODS

Materials

The chemicals used for catalyst synthesis: $Co(CH_3COO)_2 \cdot 4H_2O$ (≥ 98 % purity), NaOH (≥ 98 % purity), and HDTMA-Br (≥ 98 % purity) were supplied by Alfa Aesar, while $Al(NO_3)_3 \cdot 9H_2O$ (≥ 98 % purity) was supplied by Centrohem Belgrade. Oxone® ($2KHSO_5 \cdot KHSO_4 \cdot K_2SO_4$) and Acid Orange G – $C_{16}H_{10}N_2Na_2O_7S_2$ were supplied by Sigma Aldrich. All chemicals were used as received.

Synthesis of catalysts

The 5 g of smectite-rich bentonite clay (particle size below 2 μm) underwent a simultaneous intercalation process with $HDTMA^+$ ions and Al-Keggin ions at 60°C, as described in literature [3]. The quantity of $HDTMA^+Br^-$ used (0.6972 g) corresponded to half of the smectite cation exchange capacity (CEC = 75 mmol per 100 g of dry smectite). The Al-Keggin ions were obtained by using 0.2 M solutions of the $Al(NO_3)_3$ and NaOH in volume ratio of 1:2. The wet impregnation of hybrid Al pillared/HDTMA+/smectite nanocomposite was performed by $Co(CH_3COO)_2$ aqueous solution with the applied Co^{2+} content of 3 mass %. The impregnated material was rinsed, dried at 60 °C and carbonized in an Ar atmosphere for 2h, at temperatures 400 °C, 500 °C, and 600 °C. The samples were denoted as $Co/C_{400}HAl\text{-}S$, $Co/C_{500}HAl\text{-}S$, and $Co/C_{600}HAl\text{-}S$.

Characterization of catalysts

The specific surface area (S_{BET}) of the samples was determined using N_2 adsorption part of isotherms (Sorptomatic 1990, Thermo Finnigen), using the Brunauer-Emmett-Teller (BET) method. Before measurement, the sample was prepared by degassing at 200 °C for 16 h under reduced pressure. The volume of the mesopores was calculated from the desorption isotherm. The volume of the micropores was calculated according to the Dubinin and Raduskevich method [4,5]. All textural parameters are calculated using dedicated software ADP 5.13 Thermo Electron.

Catalytic tests

Catalytic tests were conducted by stirring 10 mg of each catalyst in 200 cm³ of an aqueous AOG solution (γ_0=50.0 mg dm^{-3}) with 0.130 mmol of Oxone®. The tests were conducted in a Pyrex reactor equipped with a mechanical stirrer and thermostated using a Julabo® circulating bath, at 30 °C. For each test, the catalyst was added to the reaction mixture of AOG and Oxone®. The addition of the catalyst to the AOG and Oxone® reaction mixture marked the start of the reaction (0 min). Samples of the AOG solution were collected at predetermined time intervals. Each catalyst was separated from reaction solution by centrifugation at 17000 rpm for 2 min. The degradation was monitored by observing the peak at 478 nm, corresponding to the AOG chromophore, using a Thermo Scientific Evolution 220 UV-Visible Spectrophotometer.

RESULTS AND DISCUSSION

Characterization

The adsorption–desorption isotherms of nitrogen at -196 °C for $Co/C_{400}HAl\text{-}S$, $Co/C_{500}HAl\text{-}S$, and $Co/C_{600}HAl\text{-}S$ are presented in **Figure 1**. The textural properties calculated from these isotherms using appropriate models are presented in **Table 1**. According to **Figure 1**, all isotherms have combined type II and IV with H2b hysteresis according to the IUPAC nomenclature. A well-defined hysteresis is typical of slit-shaped pore systems present in clays, while the hint of a plateau in high p/p_0 values indicates the presence of mesopores (through their successful filling). Based on the results presented in **Table 1**, it is obvious that $Co/C_{400}HAl\text{-}S$ has the highest specific surface area of 117 m^2g^{-1} and the most pronounced microporosity. The samples $Co/C_{500}HAl\text{-}S$ and $Co/C_{600}HAl\text{-}S$ have similar specific surface area and almost the same volume of meso- and micropores.

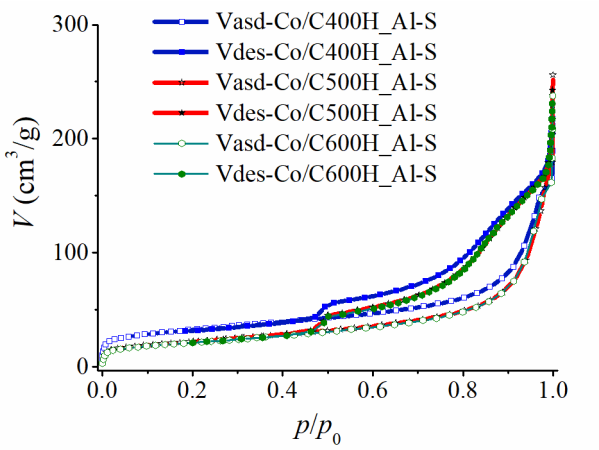


Figure 1. N_2 adsorption-desorption isotherms at -196 °C.

Table 1. Textural parameters of catalysts.

	Co/C$_{400}$HAl-S	**Co/C$_{500}$HAl-S**	**Co/C$_{600}$HAl-S**
S_{BET} [m^2 g^{-1}]	117	79.8	76.9
V_{meso}[cm^3 g^{-1}]	0.250	0.261	0.261
V_{micro}[cm^3 g^{-1}]	0.047	0.030	0.029

Where: S_{BET} – specific surface area; V_{meso}- mesopore volume and V_{micro} - micropore volume.

Catalytic tests

The experimental data of the catalytic decolorization of AOG in the presence of catalysts synthetized at different carbonization temperatures are presented in **Figure 2**. The results show that the catalyst carbonized at the lowest temperature, 400 °C (Co/C$_{400}$HAl-S), is the most effective, achieving a degradation degree of 86% in 4 hours. Catalysts carbonized at 500 °C and 600 °C (Co/C$_{500}$HAl-S and Co/C$_{600}$HAl-S) exhibited almost identical behavior, with degradation degrees of 43% and 46%, respectively.

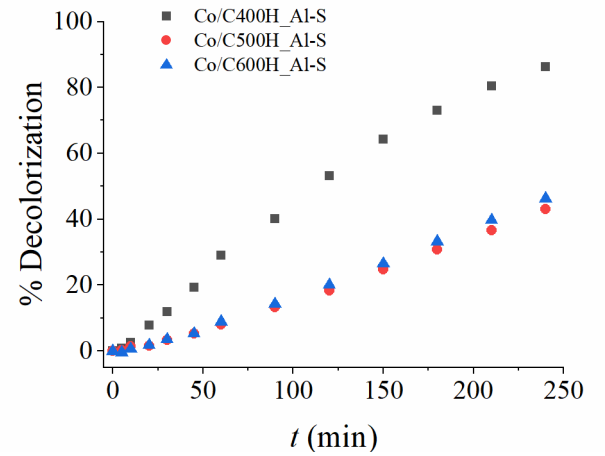


Figure 2. Catalytic decolorization of AOG in the presence of catalysts carbonized at 400 °C, 500 °C, and 600 °C monitored at λ=478 nm (m_{cat}=10.0 mg, V_0= 200 cm^3, C_0= 50.0 mg dm^{-3}; 0.130 mmol of Oxone®).

The catalytic behavior of Co/C_{400}HAl-S could be attributed to the higher surface area of compared to the other two investigated catalysts, allowing for a higher number of available active sites on surface of the catalyst.

CONCLUSION

The catalysts obtained by $Co(CH_3COO)_2$ wet impregnation of bentonite clay composite with incorporated $HDTMA^+$ and Al-Keggin ions were carbonized in inert atmosphere at temperatures 400 °C, 500 °C, and 600 °C. The catalysts textural properties were calculated based on low physisorption of nitrogen at -196 °C. It was found that increasing of temperature led to decay of the specific surface area and microporosity of sample. The effect of the carbonization temperature was tested in the oxidative degradation of Acid Orange G dye in the presence of Oxone®. The results of characterization and catalytic tests showed good correlation between specific surface of catalysts and their catalytic efficiency. In the presence of Co/C_{400}HAl-S the higher degradation degree of AOG was achieved than for other two catalysts. Co/C_{500}HAl-S and Co/C_{600}HAl-S showed very similar textural and catalytic properties as well as catalytic activity.

Acknowledgment

This research was financially supported by the Ministry of Science, Technological Development and Innovation of Republic of Serbia (Contract No: 451-03-66/2024-03/200026).

REFERENCES

[1] G. Stevanović, N. Jović-Jovičić, J. Krstić, A. Milutinović-Nikolić, P. Banković, A. Popović, M. Ajduković, App.Clay Science 230 (2022) 106718.
[2] M. Marković, S. Marinović, T. Mudrinić, M. Ajduković, N. Jović-Jovičić, Z. Mojović, J. Orlić, A. Milutinović-Nikolić, P. Banković, Appl. Clay Science Applied Clay Science 182 (2019) 105276.
[3] R. Zhu,T. Wang, F. Ge, W. Chen, Z. You, J. Coll. and Interf. Sci., 335 (2003) 77-83.
[4] F. Rouquerol, J. Rouquerol, K. Sing, Adsorption by Powders and Porous Solids, Principles, Methodology and Applications, Academic Press, London, 1999.
[5] M. M. Dubinin, Progress in Surface and Membrane Science, Academic Press, New York 1975.

ADVANCED OXIDATIVE DEGRADATION OF ANTHRAQUINONE-DYE IN THE PRESENCE OF CARBONIZED HYBRID CLAY COMPOSITE AS Co SUPPORT: KINETIC AND THERMODINAMIC STUDY

J. Parlić, G. Stevanović, M. Ajduković, B. Dojčinović, B. Pantić, T. Mudrinić and N. Jović-Jovičić

University of Belgrade, Institute of Chemistry, Technology and Metallurgy,National Institute of the Republic of Serbia, Njegoševa 12, 11000 Belgrade, Serbia. (jovan.parlic@ihtm.bg.ac.rs)

DOI: https://doi.org/10.46793/Phys.Chem24I.097P

ABSTRACT

The catalytic degradation of Remazol Brilliant Blue R (RBBR) in the presence of potassium peroxymonosulfate (Oxone®) was investigated, using Co-supported hybrid inorganic-organic carbon-smectite as a catalyst. The catalyst was synthetized by simultaneously intercalation of inorganic Al-Keggin and organic hexadecyltrimethylammonium ($HDTMA^+$) cations, followed by wet impregnation by Co^{2+} ions, and finally submitted to heat treatment in Ar atmosphere at 500 °C. The catalytic tests were performed in temperature range from 25 °C to 45 °C in order to determinate kinetics parameters. The kinetics data showed best fit with the pseudo-zero-order kinetics model. Arrhenius equation was used to calculate the activation energy of the degradation process.

INTRODUCTION

Anthraquinone dyes pose a serious environmental problem as their reinforced structure makes them difficult to degrade naturally. Existing methods of decolorization might be effective but are neither efficient nor practical due to extended time, space, and cost requirements [1]. Pillared inorganic-organic clays (IOCs) are a hybrid material obtained by combining the pillaring of an inorganic Keggin cations and an organic species such as quaternary ammonium cations. These hybrid materials have proven to be effective in adsorbing various pollutants in water because they combine the properties of pillared clay materials and organoclays [2]. Further carbonization of the organic phase in controled conditions contributes to both surface development and facilitated electron transport in the oxidation process. Advanced oxidation of various organic pollutants can be performed using peroxymonosulfates (PMS), which require activation in order to generate sulfate anion radicals, because the self-activation of PMS is slow. Heterogenous catalysts with transition metal ions are good activators of PMS. Among transition metals, cobalt is the most efficient [3].

In this work, domestic smectite clay (Gadžin Han, Serbia) was simultaneously intercalated with hexadecyltrimethylammonium bromide ($HDTMA^+Br^-$) and pillared with aluminum nitrate, impregnated with cobalt(II) acetate and submitted to the heat treatment in an inert argon atmosphere at 500 ºC. The obtained catalyst was evaluated in the oxidative degradation of dye RBBR with respect to degradation time and temperature. The catalytic tests are performed to deducate the kinetic and thermodynamic parameters.

METHODS

Materials

The chemicals used for catalyst synthesis: $Co(CH_3COO)_2{\cdot}4H_2O$ (≥ 98 % purity), NaOH (≥ 98 % purity), and HDTMA-Br (≥ 98 % purity) were supplied by Alfa Aesar, while $Al(NO_3)_3{\cdot}9H_2O$ (≥ 98 % purity) was supplied by Centrohem Belgrade. Oxone® ($2KHSO_5{\cdot}KHSO_4{\cdot}K_2SO_4$) and Remazol Brilliant Blue R – $C_{22}H_{16}N_2Na_2O_{11}S_3$ were supplied by Sigma Aldrich. All chemicals were used as received.

Catalyst syntheses and characterization

The 2.5 g of smectite-rich bentonite clay (fraction below 2 μm, Gadžin Han, Serbia) was submitted to the simultaneous intercalation process by $HDTMA^+$ ions and Al-Keggin ion according to the procedure described in literature [4]. The amount of the applied $HDTMA^+Br^-$ (0.3486 g) was ½ of the smectite cations exchange capacity (CEC= 75 mmol per 100 g of dry smectite). In order to obtain Al-Keggin ions the 125 cm^3 of 0.2 M solution of the $Al(NO_3)_3$ and 250 cm^3 of 0.2 M solution of NaOH were used. The obtained composite was rinsed with deionized water and dried at 60 ºC and submitted to wet impregnation by $Co(CH_3COO)_2$. The mass of Co^{2+} was 3%. The impregnated material was raised, dried at 60 °C, and submitted to the carbonization at 500 °C in an Ar atmosphere for 2 h. The sample was denoted as Co/CH_Al -S. The sample was characterized by low-temperature N_2 physisorption (Sorptomatic 1990, Thermo Finnigen) and obtained values for specific surface area, mesopore volume and micropore volume were: 79.8 $m^2\ g^{-1}$, 0.261 $cm^3\ g^{-1}$ and 0.030 $cm^3\ g^{-1}$, respectively. XRPD analysis (Rigaku SmartLab X-ray diffractometer, using Cu Kα radiation λ = 0.15418 nm) confirmed the presence of characteristic montmorillonite and quartz peaks and value of d_{001}= 1.43 nm for Co/CH_Al -S. The value of d_{001} is determined by the presence of Al-pillars and carbonized organic phase in the interlamellar space of clay.

Catalytic tests

Catalytic tests were performed by stirring 10 mg of Co/CH_Al -S in 200 cm^3 of aqueous RBBR solution (γ_0=50.0 mg dm^{-3}) in the presence of 0.130 mmol Oxone®. The tests were conducted in a Pyrex reactor equipped with a mechanical stirrer and thermostated using a Julabo® circulating bath, at the following temperatures: 25 °C, 30 °C, 35 °C, 40 °C, and 45 °C. The catalyst was added to the reaction mixture of RBBR and Oxone® and that moment was taken as the initial (0 min) moment of the reaction. With the respect to this moment, the RBBR solution was taken at predetermined periods of time. The catalyst was separated by centrifugation at 17000 rpm for 2 min. The peak at 592 nm, which is the position of RBBR chromophore, was used for the degradation monitoring (Thermo Scientific, Evolution 220 UV–Visible Spectrophotometer).

The obtained catalytic data for each investigated temperature were treated with pseudo-zero and pseudo-first-order kinetics models. In Eq. 1 the pseudo-zero-order model is given in the linear form:

$$C_t = C_0 - k_0 t \quad (1)$$

where: C_0 and C_t are initial concentration of dye, and concentration in time t (mg dm^{-3}), k_0 is the pseudo-zero-order rate constant.

The model for pseudo-first-order kinetic model in linear form is given in Eq. 2:

$$\ln C_t = lnC_0 - k_1 t \quad (2)$$

where k_1 is the pseudo-first-order rate constant.

Arrhenius law was used to evaluate the activation energy of adsorption:

$$\ln k = lnA - \frac{E_a}{RT} \quad (3)$$

where: k rate constant, E_a is the Arrhenius activation energy (kJ mol^{-1}), A is the Arrhenius factor, R is the gas constant (8.314 J $mol^{-1}\ K^{-1}$) and T is the temperature (K).

RESULTS AND DISCUSSION

The data of the catalytic decolorization of RBBR at different temperatures in the presence of the Co/CH_Al -S catalyst is given in **Figure 1(a)**. It was found that the pseudo-zero-order kinetic model shown better fitting of experimental data than the pseudo-first-order kinetic model. Therefore, the linear plots for this method are presented in **Figure 1(b)**.

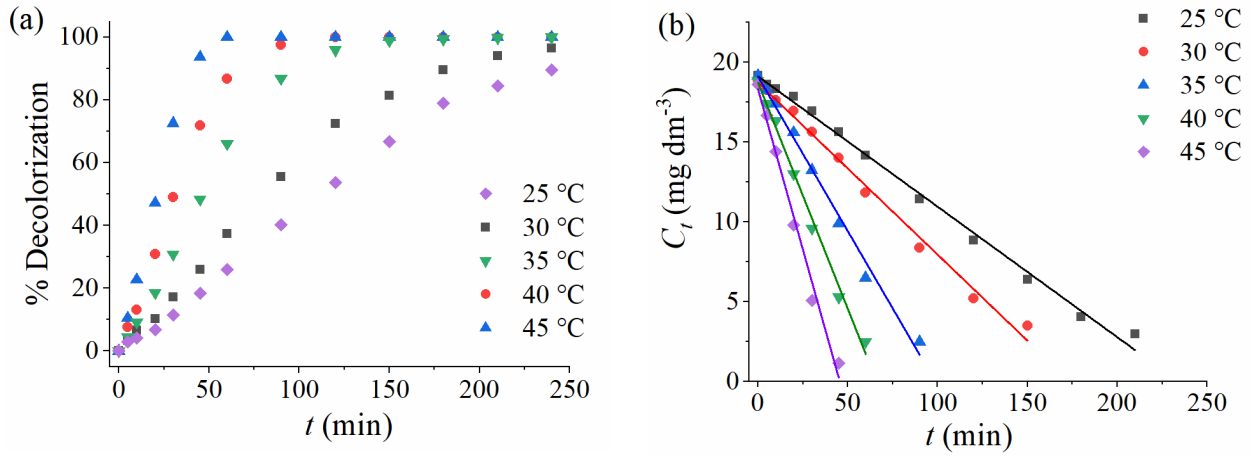


Figure 1. (a) Catalytic decolorization of RBBR in the presence of Co/CH_Al -S catalyst monitored at 592 nm for temperature range from 25 ºC - 45 ºC (m_{cat}=10.0 mg, V_0= 200 cm^3, C_0= 20.0 mg dm^{-3}; 0.130 mmol of Oxone®); **(b)** The linear plots of pseudo-zero-order kinetics model applied at experimental catalytic data of RBBR decolorization.

The results show that raising the temperature led to increase of the RBBR decolorization reaction rate (**Figure 1. (a)**). For the lowest temperature (25 °C) the degradation degree was 90% after 4 h. For the 100% degradation at temperatures in the range of 35 °C to 45 °C, shorter times were needed, i.e., the complete decolorization at temperature 45 °C was achieved in 1 h. The data indicated a good efficiency of the tested catalyst. The calculated kinetic parameters for both models are presented (**Table 1.**).

Table 1. Parameters calculated by fitting experimental data of catalytic degradation of Remazol Brilliant Blue R with pseudo-zero-order and pseudo-first-order kinetic models.

***T* [°C]**	**25**	**30**	**35**	**40**	**45**
Pseudo-zero-order kinetic model					
k_0 [mg dm^{-3} min^{-1}]	0.0817	0.1078	0.1938	0.2836	0.4022
R^2	0.995	0.993	0.992	0.993	0.989
Pseudo-first-order kinetic model					
k_1 [min^{-1}]	0.0131	0.0087	0.0221	0.0332	0.0589
R^2	0.980	0.970	0.959	0.966	0.941

The squares of coefficients of correlations (R^2) for pseudo-zero-order kinetic show better agreement than R^2 for pseudo-first-order kinetic model. Pseudo-zero-order reactions appear in heterogeneous systems when the surface of a solid phase is saturated with a reactant [5]. The obtained k_0 values are used to construct the Arrhenius plot (**Figure 2.**).

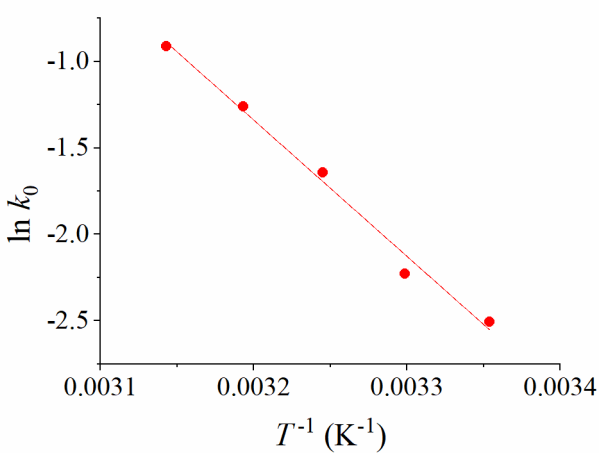


Figure 2. Arrhenius plot of RBBR decolorization in the presence of Co/CH_Al -S.

The Arrhenius plot showed a good linear relationship for lnk_0 versus T^{-1} (R^2 =0.989). The activation energy E_a =65.54 kJ mol^{-1} was obtained from the slope of linear fit (**Figure 2.**).

CONCLUSION

The catalyst obtained by cobalt(II)-acetate wet impregnation of smectite clay composite with incorporated HDTMA$^+$ and Al-Keggin ions was carbonized in inert atmosphere at 500 °C. The catalyst was tested for decolorization of Remazol Brilliant Blue R in the presence of potassium peroxymonosulfate at temperatures in range of 25 °C – 45 °C. The results of kinetics and thermodynamics of dye decolorization were discussed, and the influence of temperature was studied. Total decolorization was achieved within 1.0 h, 1.5 h, and 2.5 h, at 45 ºC, 40 ºC, and 35 ºC, respectively. The kinetic studies showed that the decolorization followed the pseudo-zero-order kinetics. Under the investigated catalytic conditions, the activation energy (E_a) for decolorization of Remazol blue by the peroxomonosulfate was determined to be 65.54 kJ mol^{-1}.

Acknowledgment

This research was financially supported by the Ministry of Science, Technological Development and Innovation of Republic of Serbia (Contract No: 451-03-66/2024-03/200026).

REFERENCES

[1] E. Routoula ,V. S. Patwardhan, Env. Sci. & Tech. 54 (2020) 647-664.
[2] I. S. Rathnayake, Y. Xi, L. R. Frost, A. G.Ayoko , J. Coll. and Interf. Sci., 459 (2015)17-28.
[3] K. A. Lin, Y. Chen, T. Lin, H. Yang, J. Coll. and Interf. Sci., 497 (2017) 325-332.
[4] R. Zhu, T. Wang, F. Ge, W. Chen, Z. You, J. Coll. and Interf. Sci., 335 (2003) 77-83.
[5] L. Arnaut, H. Burrows, Chemical Kinetics: from molecular structure to chemical reactivity, Elsevier, Amsterdam, 2006.

INFLUENCE OF ALCOHOLS AS SACRIFICAL AGENTS IN PHOTOCATALYTIC HYDROGEN PRODUCTION OVER Pt-N/TiO_2

H. Šalipur [1], K. M. Kamal [2], A. Prašnikar [2], M. Huš [2], M. Fronczak [3], J. Dostanić [1] and D. Lončarević [1]

[1] *University of Belgrade, Institute of Chemistry, Technology and Metallurgy, National Institute of Republic of Serbia, Department of Catalysis and Chemical Engineering, Njegoševa 12, 11000 Belgrade, Serbia. (hristina@ihtm.bg.ac.rs)*
[2] *National Institute of Chemistry, Department of Catalysis and Chemical Reaction Engineering, Hajdrihova 19, 1001 Ljubljana, Slovenia*
[3] *Lodz University of Technology, Faculty of Process and Environmental Engineering, Department of Molecular Engineering, Wólczańska 213, PL 93005, Łódź, Poland*

DOI: https://doi.org/10.46793/Phys.Chem24I.101S

ABSTRACT
Pt-N/TiO_2 photocatalysts were synthetized by the alkaline hydrothermal method. Physico-chemical properties of the photocatalysts were obtained by X-ray diffraction (XRD) and scanning electron microscopy (SEM). Activity of the Pt-N/TiO_2 photocatalyst towards hydrogen production was studied in reactions of water splitting and photoreforming of different alcohols. The effect of alcohol structure and the nature of photodecomposition intermediates on hydrogen production rate was discussed. Obtained results highlighted the role of sacrificial agents in photocatalytic hydrogen production.

INTRODUCTION
Photocatalytic water splitting and/or photoreforming is a promising and sustainable technology for hydrogen production. Hydrogen is a clean fuel whose combustion produces water, heat and, most importantly, does not generate harmful emissions. One way of generating hydrogen economically is to utilize the energy from sunlight to generate electron hole pairs in a semiconductor, separate the charge carriers and utilize the electrons to reduce protons from aqueous solutions. For this process to work, the semiconductor should have a bandgap that matches some of the energies from the sun spectrum. TiO_2 has been one of the most extensively studied materials because it has high chemical stability, it is relatively cheap, non-toxic, and ecologically friendly. Another prerequisite is that the generated electron-hole pairs do not recombine before they can be utilized efficiently – electrons for reduction of protons and holes as electron sinks for some easily oxidizable molecules. As TiO_2 suffers from fast recombination rates of the photogenerated electron-hole pairs, it is often modified with noble metals which have a twofold role – to enhance the charge carrier separation and to reduce the overpotential for H_2 production [1, 2]. Noble metals having a high work function (platinum, for example) have been reported to be the most effective in reducing the hydrogen overpotential [2].

Photoreforming is a process that utilizes the redox ability of photocatalysts under solar irradiation to concurrently force reduction of H^+ into hydrogen and oxidation of organic compounds to alkanes, alkenes, aldehydes, ketones and acids [3]. In addition to being less energy-demanding and more favorable thermodynamically than electrolysis, it allows organic waste to be used as a sacrificial reagent while the products of the photooxidation reaction can be value-added compounds. Additional advantage of photoreforming versus electrolysis is the fact that oxygen is

not evolved in the process, which prevents the back-reaction between hydrogen and oxygen to occur[3].

Alcohols such as methanol, ethanol and glycerol have been found to enhance the efficiency of hydrogen production by donating electrons directly to holes in the valence band. During the process, the sacrificial reagents get oxidized and promote hydrogen production to rates of 25−50 mmol g^{-1} h^{-1} [2]. Bahruji et al. [4] conducted a thorough investigation into the Pd/P25 system, exploring its behavior with 20 distinct sacrificial reagents. The order of reactivity towards hydrogen production was found to be: triols > diols > secondary alcohols > primary alcohols > tertiary alcohols. This hierarchy led to the inference that effective sacrificial hole scavengers should possess an α-H atom adjacent to the OH group(s). Similar finding were reported by Waterhouse et al. reporting the order of glycerol > ethylene glycol > methanol > ethanol [5].

In this study, H_2 photocatalysis was evaluated over Pt-N/TiO_2 photocatalyst using different alcohols as sacrificial reagents (ethanol, 1-propanol, ethylene glycol, and glycerol). We discuss these results in view of our previous studies of detected reaction intermediates generated during the process [6, 7].

METHODS

Synthesis of photocatalyst

N/TiO_2 precursors were synthesized by a hydrothermal method. Commercially available TiO_2 (AEROXIDE® TiO_2 P25) (4 g) was mixed with 250 mL of 10 M NaOH solution in a Teflon-lined autoclave at 150 °C for 24 h. The obtained precipitate was redispersed four times in 125 mL of 2 M NH_4NO_3 solution for 24 h, which led to ion-exchange of Na^+ ions by NH_4^+ ions. The redispersion steps were repeated to ensure complete ion-exchange reactions. The precipitates were dried at 110 °C for 24 h. Pt-N/TiO_2 were synthesized by impregnation method. Appropriate amount of chloroplatinic acid solution was added dropwise in 8 g of N/TiO_2 sample, followed by drying at 80 °C for 12 h after which it was reduced under H_2/Ar flow (5 vol% of H_2 in H_2/Ar mixture, 20 mL/min flow rate) at 500 °C for 3 h with a heating rate of 10 °C /min. The nominal amount of Pt deposited on the final catalysts was 0.5 wt%.

Characterization of photocatalyst

The X-ray diffraction (XRD) powder patterns were recorded using the PANalytical X'Pert Pro instrument under the Cu $K\alpha_{1,2}$ radiation. A scanning electron microscope SUPRA35VP (Carl Zeiss) coupled with an energy-dispersive analysis of X-rays (EDAX) detector Inca 400 (Oxford Instruments) was used to analyze the surface morphology of the photocatalyst.

Photocatalytic hydrogen production tests

The photocatalytic activity of the synthetized catalysts was evaluated in the photocatalytic hydrogen production reaction under UV/Vis irradiation. The photocatalytic tests were performed at 25 °C (maintained by a JULABO F25 circulation thermostat) under atmospheric pressure in a photocatalytic reactor (ACE glass) equipped with a standard reaction vessel, quartz immersion well and 100 W mercury-vapor lamp (7825-30 Ace Glass, Inc.). Prior to illumination, the suspension consisting of 125 mg of photocatalyst, 250 mL of 0.2 M alcohol/water solution was placed in a reaction vessel and purged for 60 min with Ar flow to remove oxygen from the suspension. During illumination, the Ar flow rate was adjusted to 15 mL/min to transfer the generated hydrogen from the reaction vessel to the gas sampling valve on the gas chromatograph (GC). Effluent gas composition was analyzed by the Shimadzu GC-8A equipped with TCD detector.

RESULTS AND DISCUSSION

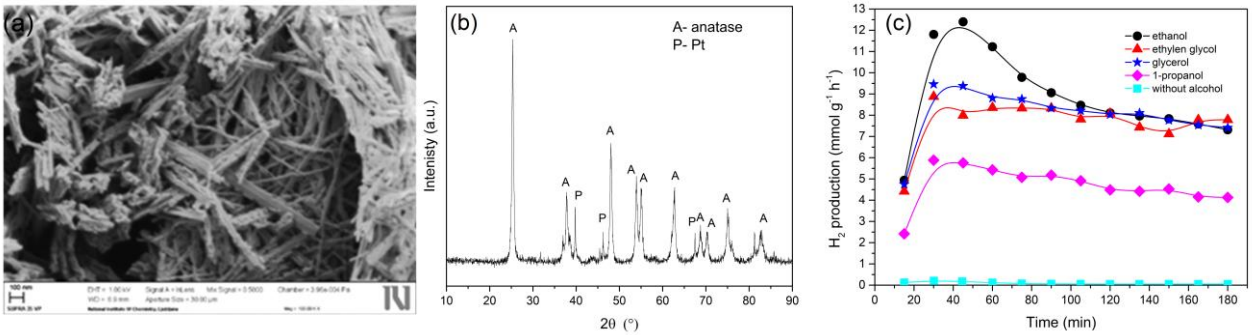


Figure 1. (a) SEM micrograph, (b) XRD pattern, (c) time-dependent hydrogen production rates of Pt-N/TiO_2 photocatalyst.

Figure 1a shows a SEM micrograph of the Pt-N/TiO_2 photocatalyst. Nanofiber morphology with the parts of spike-like nanostructures were observed. Powder XRD patterns of the prepared Pt-N/TiO_2 photocatalyst are shown in **Figure 1b**. The XRD pattern shows the main diffraction peaks corresponding to anatase TiO_2 as well as metallic Pt. The obtained anatase crystalline structure of Pt-N/TiO_2 photocatalyst was found to be critical for achieving H_2 production photoactivity.

As seen in **Figure 1c**, the presence of alcohols has a profound effect on the hydrogen production rate. The H_2 production efficiency using Pt-N/TiO_2 without the use of alcohols was found to be 0.2 mmol g^{-1} h^{-1}. The presence of alcohols significantly enhances hydrogen production rates by over 60 times. The chemical nature of the alcohol also shows to have effect on the hydrogen production rates in the following order: ethanol > glycerol > ethylene glycol > 1- propanol, showing highest rates of 12.5, 9.5; 8.9; 5.9 mmol g^{-1} h^{-1}, respectively. The obtained results revealed that the used sacrificial agents significantly improved the photoefficancy, which indicates that alcohols can suppress electron/hole recombination. In our previous study via temperature-programmed desorption of alcohols, we showed that ethanol photoreforming leads to formation of acetaldehyde and ethylene, 1-propanol forms propionaldehyde and propylene as intermediates [6], while photoreforming of diols and triols was found to result in deeper oxidation to carboxylic acids (ethylene glycol to glycolaldehyde and oxalic acid; glycerol to glycolaldehyde and formic acid) [5]. During photoreforming reactions, different types and/or a higher amount of intermediates are formed. Their ability to adsorb and block the active centers affects the H_2 production rate. In our previous study, we showed that higher amounts of carboxylic acid compared to ketones/aldehydes had suppressing effect on H_2 production rate, confirming that type and amount of intermediates during photoreforming were of critical importance for H_2 production [7].

CONCLUSION

Alcohols used as hole scavengers in water splitting/photoreforming were pivotal for the efficiency of photocatalytic hydrogen production. The presence of alcohols significantly enhanced hydrogen production rates, by more than 60 times suggesting that alcohols have the ability to suppress electron/hole recombination. Most important factors influencing photocatalytic hydrogen production rates were structure of alcohols and type and amount of intermediates formed during the photoreforming process. The highest hydrogen production rate of 12.5 mmol g^{-1} h^{-1} was achieved by using ethanol as a sacrificial agent.

Acknowledgment

This research has been financially supported by the Ministry of Science, Technological Development and Innovation of Republic of Serbia [Contract No: 451-03-66/2024-03/200026].

This research was supported by the Science Fund of the Republic of Serbia, Program PRISMA, Grant No. 5354, Multifunctional visible-light-responsive inorganic-organic hybrids for efficient hydrogen production and disinfection-HYDIS. This research has been supported by Bilateral project between the Republic of Serbia and the Republic of Slovenia "Band structure engineering design for construction of heterojunction semiconductors for enhanced photocatalytic activity. Theoretical and experimental study." [Contract No. 337–00–110/2023–05/05].

REFERENCES

[1] O. Al-Madanat, M. Curti, C. Günnemann, Y. AlSalka, R. Dillert, D.W. Bahnemann, Catal. Today 380 (2021) 3–15.
[2] R. Deas, S. Pearce, K. Goss, Q. Wang, W. Chen, I.N. Waterhouse, Appl. Catal. A: Gen. 602, (2020) 39–41.
[3] C.Y. Toe, C. Tsounis, J. Zhang, H. Masood, D. Gunawan, J. Scott, R. Amal, Energy Environ. Sci., 14 (2021) 1140–1175.
[4] H. Bahruji, M. Bowker, P.R. Davies, F. Pedrono, Appl. Catal. B Environ. 107 (2011) 205–209.
[5] W.T. Chen, A. Chan, D. Sun-Waterhouse, J. Llorca, H. Idriss, G.I.N. Waterhouse, J. Catal. 367 (2018) 27–42.
[6] H. Šalipur, J. Dostanić, D. Lončarević, Physical Chemistry 2022, ISBN 978-86-82475-42-2, 157-160.
[7] H. Šalipur, D. Manojlović, K. Milošević, M. Fronczak, A.G. Silva, D. Lončarević, J. Dostanić, J. Environ. Chem. Eng. 12 (2024) 112862.

D *– Nonlinear Dynamics, Oscillatory Reactions, Chaos*

This section is dedicated to

Professor emeritus

Ljiljana Kolar-Anić

Professor Emeritus Ljiljana Kolar-Anić

Slobodan R. Anić[1,2] and Željko D. Čupić[2]

[1]Faculty of Physical Chemistry, University of Belgrade, Studentski trg 12–16, Belgrade, Serbia
[2]Institute of Chemistry, Technology and Metallurgy, University of Belgrade, Njegoševa 12, Belgrade, Serbia
[*]E-mail of Corresponding author: boban@ffh.bg.ac.rs



Professor emeritus Ljiljana Kolar-Anić
(22.08.1947-17.06.2023)

Describing the life and works of anyone is fraught with the possibility of objectively making a series of omissions and that something is neglected or insufficiently highlighted. This cannot be avoided. Ljilja's biography is very rich, and, on this occasion, it will be given in an appropriate volume.

Ljiljana was a personality who, whenever she did something, she did it absolutely dedicated, deliberate, systematic and successful, but also with heart, selflessly and responsible, not

neglecting her relationship with her relatives, colleagues and friends. Her strong adherence to immutable principles, and determination to stand up to every, even the smallest, injustice was incredible. She could be very harsh, uncompromising, but always constructive.

Ljiljana was born right after the Second World War (1947, Virovitica, Croatia, Yugoslavia), grew up on the ideas of socialism, which she critically accepted, respected and advocated. Thus, in 1967-68, period which is known for the revolt of students all over the world, she participated in the famous June demonstrations, which were raised due to the deviation from the direction of socialism in the development of Yugoslavia. Without a doubt, she deeply believed in and fought for a just society for all, regardless of their ethnic origin, race, religious beliefs. For her, as well as for many like her, "a man is a man", regardless of which social community he belongs to. In her veins flowed the blood of many, Serbs, Croats, Dalmatians, Italians. That is why she felt and declared herself a Yugoslav until the end of her life, despite many who mockingly and condescendingly thought, and many still do today, about Yugoslavs. She had a big handicap because she didn't have the opportunity to meet her paternal grandparents. In the Second World War they, including their immediate and extended family, were executed in the Ustasha camp Jasenovac in the most brutal and cruel way unimaginable to a normal person, as happened to many other Serbs, Jews and Roma. Because of all that, she had a very strong emotional connection with the surviving part of her father's family.

Ljiljana's childhood and youth were filled with many activities. At First Belgrade High School, she was mostly preoccupied with mathematics[1], the drama section and sports. At the same time, she was one of the members of the Sport Club ***Partizan***; her time spent at the club as a member of the national team in athletics was credited towards her pension due to outstanding successes at the Yugoslav level.

She was an excellent housewife: she knew how to cook, bake cakes, sew, embroider. She dressed tastefully and appropriately and did not wear make-up.

Ljiljana was very dedicated to young people as a teacher, colleague, mentor, parent, friend. She wondered and could not understand why young ones do not create families and have children, although it is known that they can do it, that their parents rightly expect it too. What's the matter? Is it conformity, disinterest, indolence, asociality, or is it something else?

EDUCATION

Her original idea was to study technical sciences, but nevertheless, she opted for natural sciences, which occupied her until the end of her life. She came to physical chemistry at the persuasion of her older colleague from the Partizan sports club, who was a student of physical chemistry at the Faculty of Science and Mathematics in Belgrade, but who later never graduated from the same faculty; he remained an eternal senior who needed to pass two exams in order to complete his studies.

In 1966 Ljiljana started to study at the Physical Chemistry Group (now the Faculty of Physical Chemistry) of the Faculty of Science of the University of Belgrade, where she graduated (1970), obtained master's degree (1974), then doctorate (1978), and then got a job and worked continuously until the end of her life. She took the postdoctoral studies (1978-1979), at the Service de Chimie Physique II of Department for Theoretical Physical Chemistry of the Free University of Brussels, headed by Nobel laureate (1977) Ilya Prigogine. Especially at that time, and even later, Prigozhin's department was the world's largest centre that brought together many famous researchers of complex non-equilibrium and non-linear phenomena. (Figure 1) It is widely known that Prigogine's theory of dissipative structure led to pioneering research into self-organized systems. Ljiljana's stay in Brussels during her postdoctoral studies, as well as several stays later, was in the period of the most intensive development of the first

[1] Ljiljana Kolar, Decomposed algebraic functions (1966), Graduation Thesis, First Belgrade High School

personal computers and their applications in computer modelling, especially several well-known chemical oscillators.



Figure 1. Photograph of a scientist from the field of Nonlinear Sciences in Brussels (1987) made during the meeting organized on the 70th birthday of Nobel laureate Ilya Prigogine (first row, five from right to left) under the title *Spatial Inhomogeneities and Transient Behaviour in Chemical Kinetics*. Among them are those with whom Ljiljana will collaborate, get them to be lecturers at the Faculty of Physical Chemistry as well as the Conferences of Physical Chemistry, but also become Honorary Members of the Society of Physical Chemists of Serbia. In the photo you can see, as our Serbian people would say, "leaves of our mountain, forest" young Ljiljana Kolar-Anic (second row, second from left to right) and Slobodan Anić (back row, fourth from left to right).

CEREER – EMPLOYMENT

Ljiljana started (1971) and ended (2012) her official professional career at Physical Chemistry, which transformed over time in terms of organization from the Department of Physical Chemistry of the Faculty of Science and Mathematics to the Faculty of Physical Chemistry of the University of Belgrade (1990). In all the phases of transformations, which were often very stormy, her engagement was significant and successful.

Ljiljana passed through all educative university positions: Assistant (1971-1980), Scientific Associate for the subjects Statistical Thermodynamics and Nonequilibrium Thermodynamics (1980-1984), Docent for the subjects Statistical Thermodynamics and Chemical Reactivity (1984-1991), Associate Professor (1991-1996) and Full professor (1996-2012) for the subjects Statistical Thermodynamics and Nonequilibrium Processes, later Dynamics of Nonlinear Processes (1996-2012). She was elected to position of Emeritus Professor (2017) and also to the position of Full Research Professor (2008) at the Institute of Chemistry, Technology and Metallurgy.

After working at the Faculty of Physical Chemistry, Ljiljana worked for another two years at the University of Belgrade as a Full Research Professor at the Institute of Chemistry, Technology and Metallurgy.

SOME SCIENTIFIC CONTRIBUTIONS

On this occasion, the intention is not to present Liljana's comprehensive and detailed contribution in science, but to mark some of the prominent results which she achieved independently or in collaboration. Those results meant a lot in the further personal and collective scientific development of the researchers in Nonlinear Physical Chemistry and Kinetics.

Heterogeneous processes

She graduated from the field of kinetics of isothermal adsorption on a modified alumina. [1] Also, heterogeneous processes were the subject of a master's study. [2] So, she considers the Weibull function (equations (1) and (2)), as well as the Normal and Gamma functions (but also the connection between mentioned functions) in describing some different heterogeneous processes. [3, 4]

$$F(x) = 1-e^{-[\frac{x-\gamma}{\eta}]^{\beta}} \quad . \tag{1}$$

η is the scalar, β is the shape parameter and γ is the location parameter. This distribution is often used in the form

$$F(x) = 1-e^{-bx^{n}} \quad . \tag{2}$$

Here $F(x)$ can be the reaction yield at time x i.e. t. Parameters b and n have the same meaning as η and β. The Weibull function will be present in later works as well. [5-9] Likewise, and it was found that they must be considered as time functions when the energies of adsorption centres are not equal and have a random distribution. [10] Also, Ljiljana dealt with the stochastic analysis of the chemical and physicochemical processes. [11, 12] Later, that experience proved valuable for the examinations of the activity of plasmonic sensors in multi-analyte environment. [13-16] Ljiljana successfully incorporated the education in statistical mechanics acquired during her master's studies into her doctoral thesis [17] and a series of notable articles. She calculated the partition function of a real gas in a gravitational field. Then, the partition function of the vapor consisting by molecules grouped into clusters of different sizes was also determined. Furthermore, thermodynamic properties and state functions for real gas and steam in a gravitational field were determined. After that, the basic equations for the sedimentation balance of steam in the gravitational field were found. [18-23]. All this was reflected in the real-world application of the phenomenon of nucleation in the atmosphere. For example, Ljiljana was the project manager related to the research and development of means for artificial influence on the weather and the production of some chemical substances that are included in the composition of these means. [24]. In short, the commercial production of an anti-hail mixture was successfully developed and then established, which contained a significantly less essential substance, and had a markedly higher efficiency than all existing mixtures which were previously used in Yugoslavia. (see more Appendix)

Homogeneous oscillatory reactions

Upon return to Belgrade from Bruxelles (1984) Ljiljana was interested in the research on the Bray-Liebhafsky (BL) homogeneous chemical oscillatory reaction [25,26] which have already been performed at Institute of Physical Chemistry (Faculty of Science, University of Belgrade-UB) and parallel at the Security Institute (Federal Secretariat of Internal Affairs of Yugoslavia; the first paper officially announced in 1984 (ref)). In fact, in Belgrade, the first research on the BL system was conducted by Professor Slobodanka Veljković. [27] Her research did not last long especially because of her illness and then her death. Her research did

not last long especially because of her illness and then her death. The investigations will be continued not only in the Security Institute and the Faculty of Physical Chemistry, but also in Institute of Chemistry, Technology and Metallurgy, Institute for General and Physical Chemistry, VINČA Institute of Nuclear Science, the Faculty of Pharmacy etc. All the researchers of the above-mentioned institutions gathered around the Faculty of Physical Chemistry have been identified in the literature as group [28-32] which have produced notable results in the research of oscillatory reactions and their application. [for example, see references 33-39] Without a doubt, Ljiljana was their leader. The Belgrade Group already exists for 40 years. Its research on the BL reaction [25, 26] is still dominant, but the investigation has expanded, both in the phenomenological and theoretical sense, to the Belousov-Zhabotinsky (BZ) [40] and Briggs-Rauscher (BR) [41] reactions, but also the hypothalamic-pituitary-adrenal (HPA) system and to other oscillatory systems. [32-34]

Dynamic of BL reaction

During the experimental investigations of the BL reaction, the knowledge about the existence of regions of regular oscillation (Figure 2 and part of Figure 3) and chaos (Part of figure 3 and Figure 4) was expanded. [33, 34, 42-47]

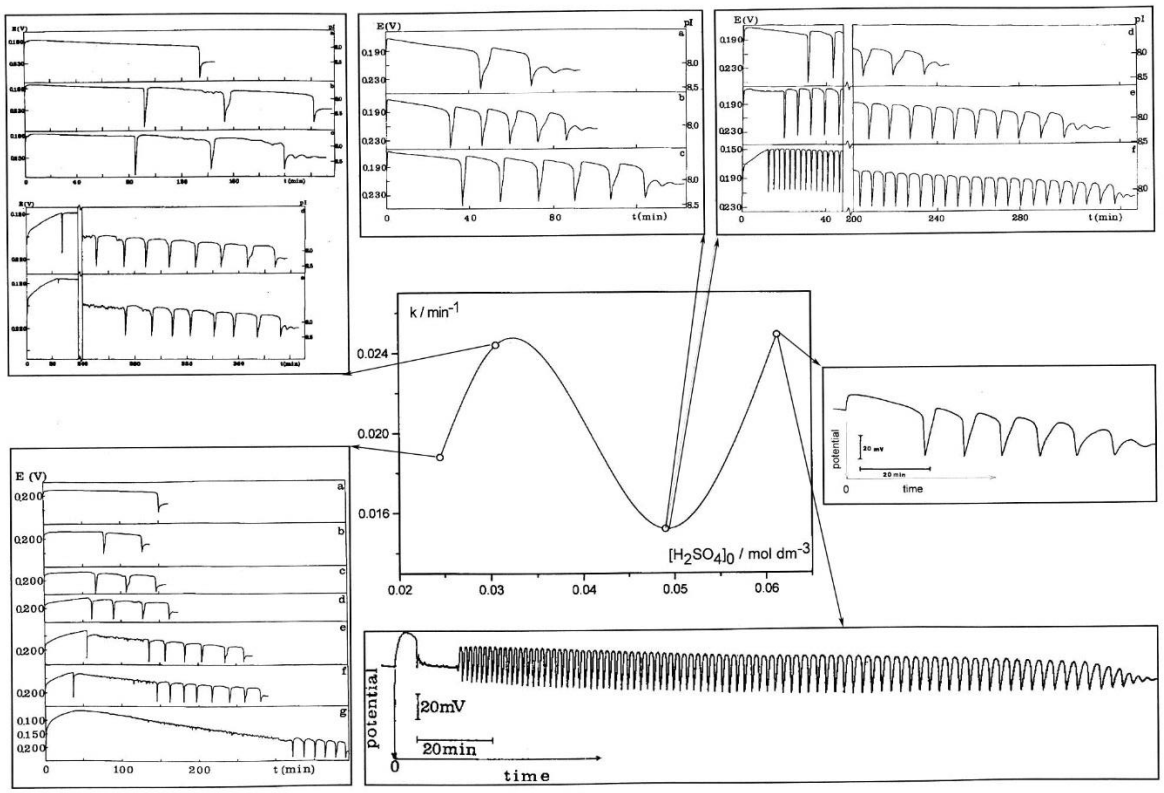


Figure 2. The series of iodide oscillograms, indicated by arrows, with the regular evolutions which have asymmetric relaxing oscillations. In the middle of the picture, it is graph of the dependence of the reaction rate constant ($k=k_D$) of the H_2O_2 decomposition (see below) as a function of acidity. k_D is determining based on the parameters of the given oscillograms (see below). [42]

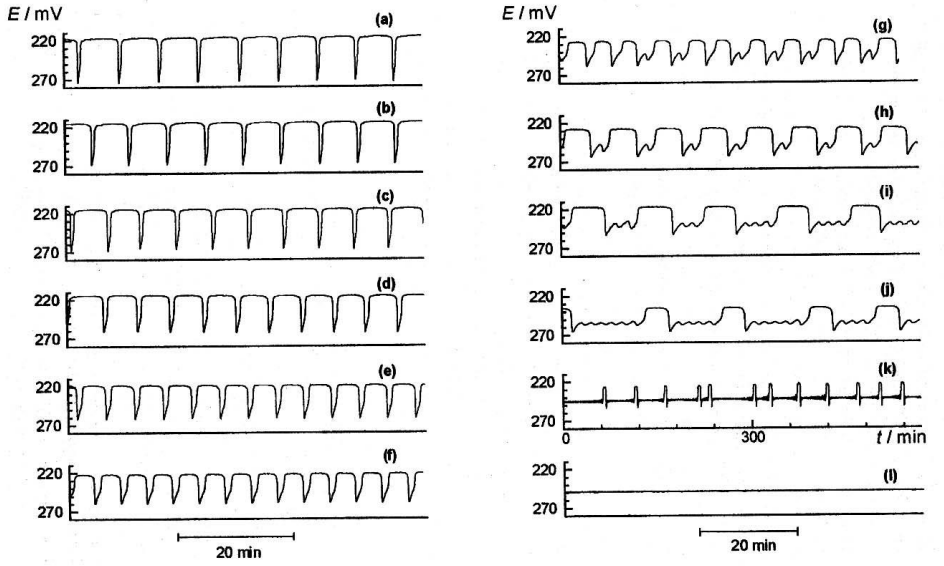


Figure 3. The oscillograms with relax and sinusoidal oscillations of the regular and chaos evolutions of BL systems realized in Continues well Stirred Tank Reactor (CSTR) at temperatures from T=52.8 (a) to T=47.6 ºC (f). The oscillograms recorded by platinum electrode. [43]

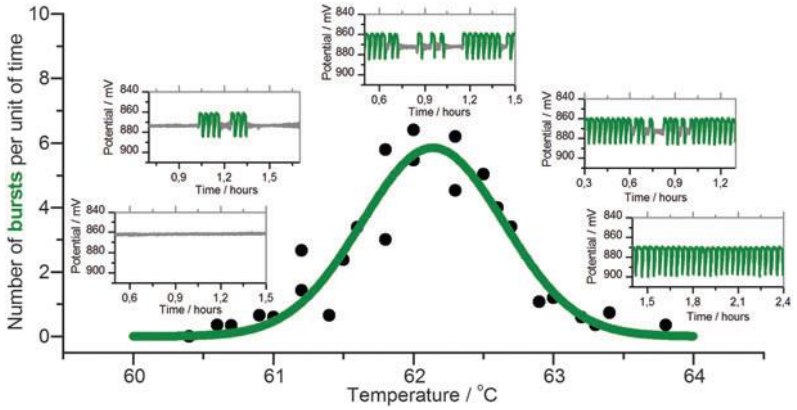


Figure 4. Temperature dependence of number of busters packages which consisted of the relaxation oscillations with large amplitudes realized in CSTR. The oscillograms recorded by platinum electrode. [44]

A few words about deterministic ordered intermittent chaos (IC). The structure of IC is characterized by the stochastic appearing of oscillation packets (busters) that have an irregular duration and number of oscillations but are a deterministic function of the control parameter (temperature, species concentration, specific flow). IC in the BL reaction was first noted by Chopin-Dumas. [48] However, later no one investigated it except the Belgrade Group.

Kinetics of BL reaction

BL reaction [25, 26] realised in mixed water solution of hydrogen peroxide and IO_3^- and H^+ ions as catalysts and it can be represented with overall stochiometric equation

$$2H_2O_2 \xrightarrow{k_D} 2H_2O + O_2 . \qquad (D)$$

This net reaction is results of the successive, or parallel reaction steps

$$2IO_3^- + 2H^+ + 5H_2O_2 \xrightarrow{k_R} I_2 + 6H_2O + 5O_2 \qquad (R)$$

$$I_2 + 5H_2O_2 \xrightarrow{k_O} 2IO_3^- + 2H^+ + 4H_2O\,. \qquad (O)$$

In a closed reactor, based on the empiric parameters of the generated oscillograms and the composition of the BL system (Figure 2), a unique procedure for analysing the kinetics of the reaction (D) was developed. [33, 34, 49-51] It will always be valid if the change in composition, or other control parameters does not affect the qualitative change in the observed kinetics, or in other words, if it does not change the dominant reaction mechanism of reaction (D).

Namely, Figure 5., shows a typical appearance of an oscillogram with one pre-oscillatory period and one oscillatory period with the indicated parameters of the oscillogram.

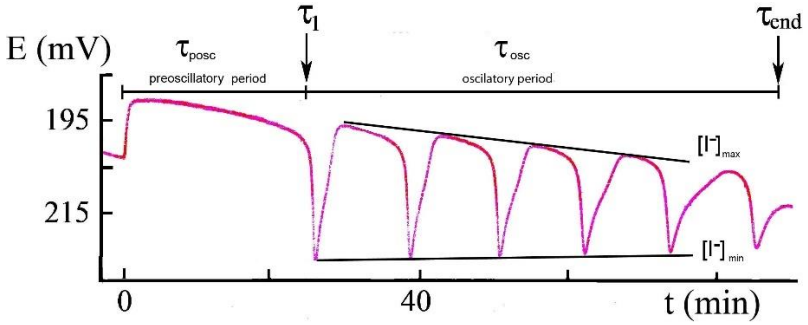


Figure 5. The iodide oscillogram of the regular evolution of the BL reaction generated in an isothermal closed reactor. The slopes of the true maximum (max) and minimum (min) iodide concentrations are constants which the temperature depends can describes with the Arrhenius equation. (see reference 32)

Even earlier, Bray showed [25] that reaction (D) is pseudo-first order with respect to the concentration of hydrogen peroxide. For the oscillatory evolution as it is in Figure 5 defined kinetic equation [49-51]

$$\tau_{end} = -\frac{1}{k_D}\ln\left[H_2O_2\right]_{end} + \frac{1}{k_D}\ln\left[H_2O_2\right]_0 \qquad (3)$$

where $[H_2O_2]_{end}$ and $[H_2O_2]_0$ denote the concentrations at $t = \tau_{end}$ and $t = 0$ minutes respectively. k_D is a pseudo constant which is a function of the reaction mixture composition.

$$k_D = k\left[KIO_3\right]_0^r\left[H_2SO_4\right]_0^q. \qquad (4)$$

k is also pseudo a constant; exponents r and q are pseudo-orders of reaction (D).

Obviously, equation (3) was derived under the assumption that the temporal change in H_2O_2 concentration is monotonous, although it is cascaded in oscillatory processes. Second, the fact is that in $t = \tau_{end}$ the bifurcation of the transition from oscillatory to monotonic evolution occurs. It was assumed that the position of the bifurcation point in the concentration phase space is essentially unchanged regardless of the change in H_2O_2 initial concentration. The set assumptions proved to be acceptable because there is satisfactory approximate agreement between the kinetic results obtained based on equation (3) and the data obtained by the process of determining the current concentration of H_2O_2 by direct titration of aliquots of the reaction solution.[52]

What is the significance of equation (3)? First, thanks to equation (3) there is a very simple way to analyse the kinetics of given BL systems without the need for the laborious and time-consuming determination of instantaneous hydrogen peroxide concentrations. Second, the equation (3) is valid and in all cases when the external species added have concentration which does not change the first order kinetic of decomposition in respect to H_2O_2 concentration. This

also means that the decomposition of hydrogen peroxide in the BR system can be analysed as well as in the BL system. Likewise, the addition of all external species which do not influence a change in the reaction decomposition kinetics (D) will only affect the change in the reaction rate constant k_D (Equation 4). This means that there is a logarithmic proportionality between the constant k_D and the concentration of the given external species a

$$\ln k_D \propto \ln a. \tag{5}$$

The validity of equation (5) can be illustrated by the experimental results obtained by investigating the influence of the cobalt complex on the BL reaction. [53]

Otherwise, equation (3) is valid in the given temperature domain. [54, 55]. Normally, it is also valid in the case of BL equi-concentration systems at different temperatures. Then, the apparent activation energy, not only of reaction (D) but also reactions (R) and (O), can be determined thanks to equation (6) (derived from equation (3)); the analogue of rate constant reactions can be pre-oscillatory period, oscillatory period, oscillogram length, number of oscillations, etc (see Figure 5). [55]

$$\frac{1}{analog} \propto k_D \tag{6}$$

It should be mentioned that, likewise, the same form of equation (3) is valid in the Briggs-Rauscher (BR) [56] and Belousov-Zhabotinsky (BZ) oscillatory reactions. [57]

Modelling the BL and BZ Oscillatory Reaction

Theoretical and computer modelling was always significant part of Ljiljana`s scientific interest. As physical chemist, she followed the general idea that modelling must rely on experimental observation. Hence, she accepted the difficult task to contribute explaining so complex and strange phenomena as chaos and at her forms of emerging behavior generated and observed in non-linear reaction systems far from equilibrium. Oscillatory reactions were appropriate family of systems in physical chemistry, feasible to available techniques in both laboratory and computer experiments. Since there was no experimental technique which would give unambiguous answers to numerous questions about their reaction mechanism, computer modeling was always a necessary component of any research in this field. Theoretical analysis of the reaction mechanism and underlying kinetic models was an intriguing part of research which connects and explains results from laboratory and computer experiments. This was natural environment for Ljiljana`s way of systematic analytical thinking.

Typical examples of oscillatory reactions, which were subject of research in Belgrade Group under the lead of Ljiljana Kolar-Anić, were BL and BZ reactions.

*

The dynamics and kinetics of the BL reaction (D) is a consequence of the given reaction mechanism, which is still an unsolved enigma. There will be more work, although much has already been done.

The articles from 1990 are the beginning of the research in Belgrade on uncovering the mechanism of the BL reaction [58-60] and with the article from 1992 [60] is the beginning of a very fruitful, long-time and continuous collaboration with the Professor G. Schmitz from the Free University of Brussels (ULB). It should be known that Professor Schmitz set up a stoichiometric model of the BL reaction (1977) (Figure 6: the reactions from (R1) to (R6) denoted later as model M(1-6). This model already enables simulation of oscillations with properties which structurally resemble the most significant properties of experimental ones,

although it does not include explicit step of either autocatalysis or autoinhibition. Only the combination of the given steps can generate a reaction of that type. Namely, until then, each model of the mechanism of a homogeneous reaction which was successful in producing oscillatory behavior, included at least one autocatalytic step. Schmitz's model is the first one capable to generate given oscillatory evolutions that is remarkably consistent with the real one. It was further supplemented with reaction (R7) (reactions from (R1) to (R7) form the model M(1-7), and later (R8) (reactions from (R1) to (R8) form model M(1-8). In both cases, the extended models can successfully additionally describe some more complex dynamic structures, observed in closed reactor. [61]. Figure 2 shows the appearance of the simulated changes in the concentrations of BL system species of the given initial composition.

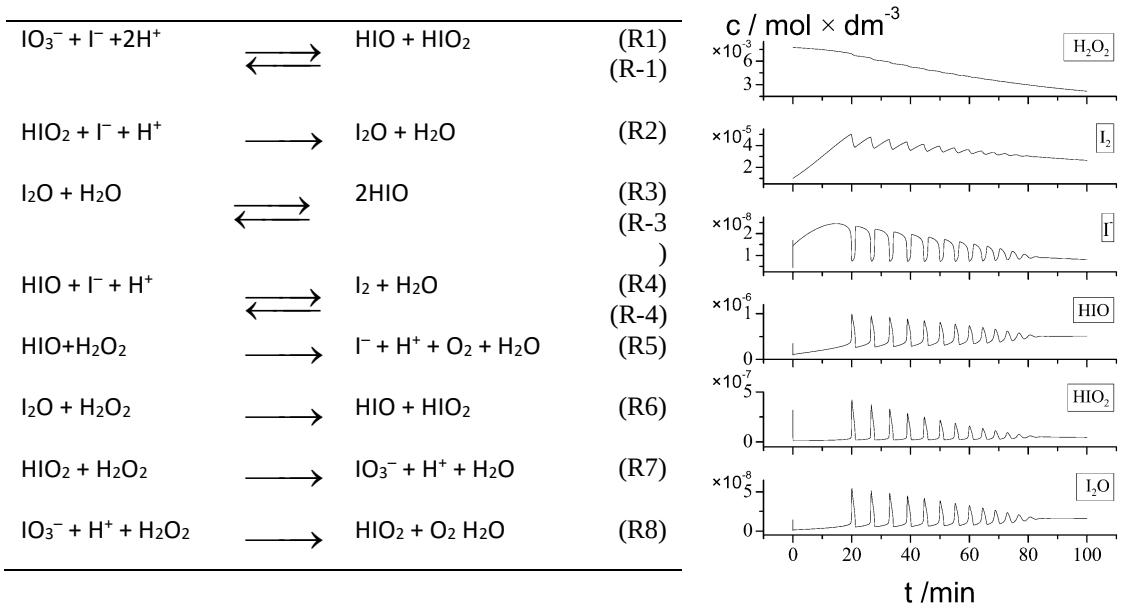


Figure 6. M(1-8) BL system model and numerical simulation of species concentration evolution in it. [34]

Later works were directed toward better understanding of complex forms of dynamical states achieved in experiments using both, closed, and open reactor conditions, including mixed-mode periodic oscillations, chaos and intermittent behaviour of the BL reaction. Much attention was given to identify nature of bifurcations present in both experimental and theoretical model BL systems. It was of tremendous importance for attained results that with Ljiljana`s help and cooperation, several members of Belgrade Group were deeply involved in adoption and further development of so versatile tool as it is the Stoichiometric Network Analysis. This method became one of highlights establishing the Belgrade Group in the sky of few research centres being able to use its advantages for stability analysis. Hence, possibilities were opened for us to investigate systems with more than just few variables.

Although, BL reaction investigation was kind of trademark for Belgrade Group, it was certainly not the only system analysed by engaged researchers, and numerous students passing through the Ljiljana`s school. One of most the significant developments achieved under Ljiljana`s leading role was new variant of the BZ reaction model.

*

The overall reaction of decomposition of malonic acid (MK) in the BZ system is most often described by a stoichiometric equation:

$$2BrO_3^- + 3CH_2(COOH)_2 + 2H^+ \xrightarrow{Ce^{3+}/Ce^{4+}} 2BrCH(COOH)_2 + 3CO_2 + 4H_2O \quad (7)$$

The net (overall) reaction (7) is one possible outcome of long sequence of simpler reaction steps. Model version accepted within Belgrade group [57] achieved tremendous level of agreement between experiments and numerical simulations. Part of numerical results are given in Table besides the reaction mechanism which was used to generate oscillations.

$Br^- + HOBr + H^+ \rightarrow Br_2 + H_2O$
$Br_2 + H_2O \rightarrow Br^- + HOBr + H^+$
$HBrO_2 + Br^- + H^+ \rightarrow Br_2O + H_2O$
$Br_2O + H_2O \rightarrow 2HOBr$
$2HOBr \rightarrow Br_2O + H_2O$
$Br^- + BrO_3^- + 2H^+ \rightarrow HOBr + HBrO_2$
$2HBrO_2 \rightarrow BrO_3^- + HOBr + H^+$
$BrO_3^- + HBrO_2 + H^+ \rightarrow 2BrO_2^\bullet + H_2O$
$2BrO_2^\bullet + H_2O \rightarrow BrO_3^- + HBrO_2 + H^+$
$Ce^{3+} + BrO_2^\bullet + H^+ \rightarrow Ce^{4+} + HBrO_2$
$Ce^{4+} + HBrO_2 \rightarrow Ce^{3+} + BrO_2^\bullet + H^+$
$MK + Br_2 \rightarrow BrMK + Br^- + H^+$
$MK + Ce^{4+} \rightarrow Ce^{3+} + P + H^+$
$BrMK + Ce^{4+} \rightarrow Ce^{3+} + Br^- + P$
$MK + Br_2O \rightarrow BrMK + HOBr$
$Br_2\,(rast) \rightarrow Br_2\,(g)$

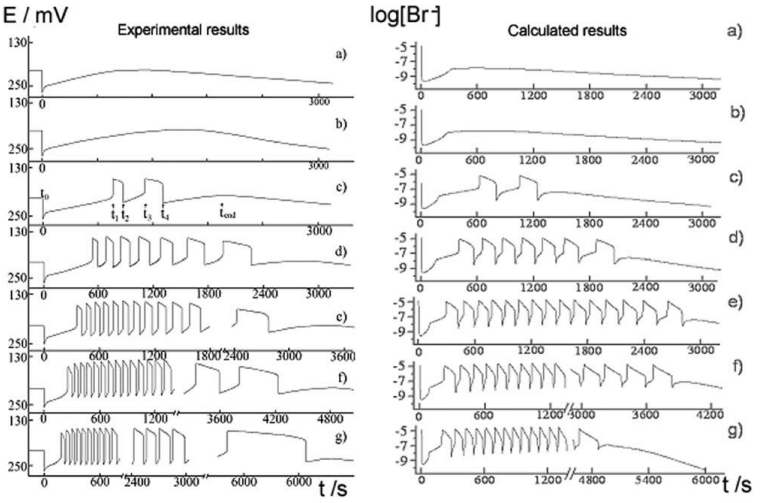


Figure 7. Oscillograms obtained experimentally (left) and by numerical simulation (right) of the BZ reaction at a temperature of 40 °C and an initial concentration of malonic acid (mol dm^{-3}): a) 8.00×10^{-3}; b) 9.00×10^{-3}; c) 1.20×10^{-3}; d) 1.60×10^{-3}; e) 2.20×10^{-3}; f) 3.20×10^{-3}; g) 4.30×10^{-2} .[57d]

Hypothalamo-Pituitary-Adrenal (HPA) system

One of the most important reasons to investigate oscillatory reactions was often its phenomenological analogy with living systems, able to generate spontaneous oscillating behaviour. Therefore, it is not surprising that Ljiljana also used methodology developed in physical chemistry of oscillating reactions, to analyse and to model dynamic phenomena observed in metabolic networks of living organism. [62-76] Most results in this area were done on modelling the *Hypothalamo-Pituitary-Adrenal (HPA) axis.*

Ljiljana guided research in this area as always and developed a specific approach founded on physical chemistry of reaction systems with mass action kinetics. [62] Her approach was particularly convenient for the application of stoichiometric network analysis to estimate numerous unknown parameter values in accordance with instability conditions derived from reaction dynamics equations. [63-68]

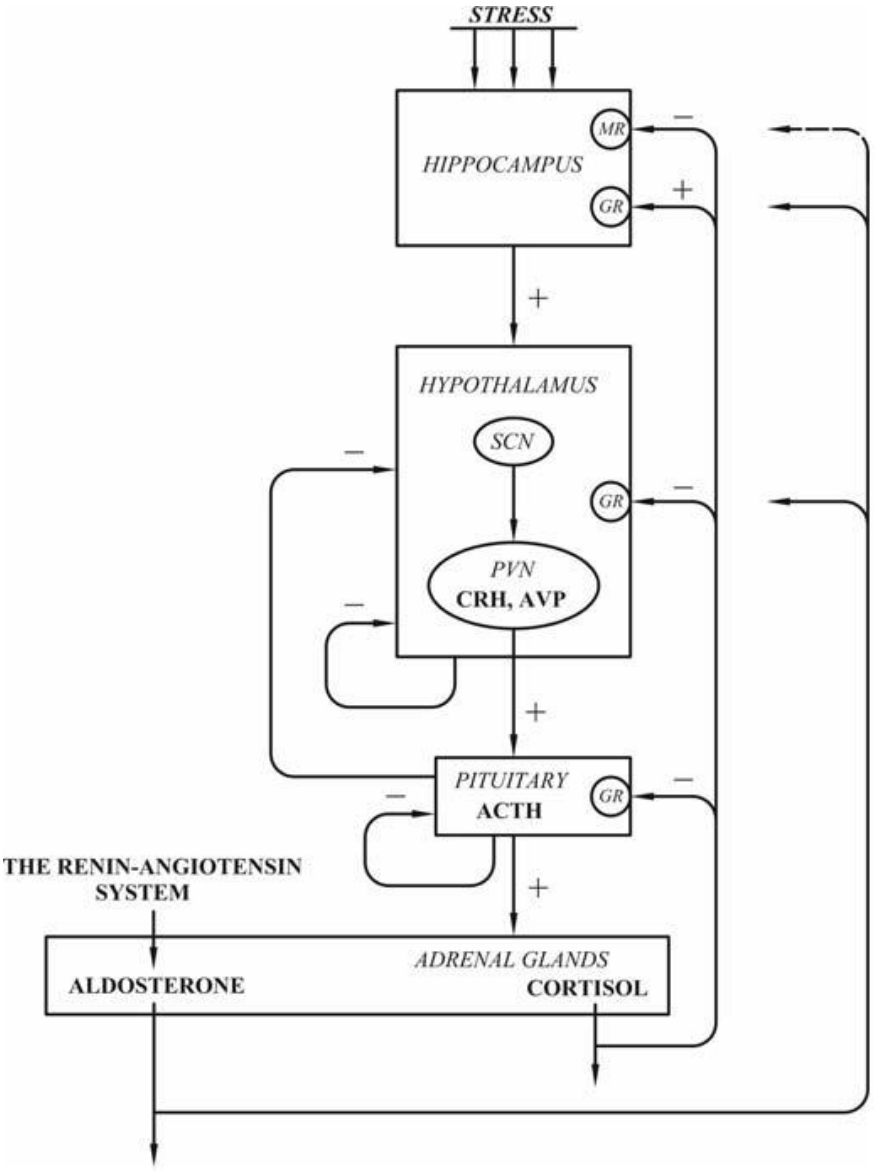


Figure 8. (a) A schematic diagram of the *Hypothalamo-Pituitary-Adrenal (HPA) axis* showing the relationship between key dynamical variables: cholesterol, corticotrophin-releasing hormone (CRH), adrenocorticotropic hormone (ACTH), aldosterone and cortisol. (Reprinted with permission from Ref. [62]

Hence, it was easy to simulate dynamics of the global state of the organism with systems of ordinary differential equations. Although, more detailed description of the HPA system would consider the fact that it includes processes at different (sometimes significantly distant) organs, used approach was in perfect correspondence with usual medical practice relaying on screening the state of the system from instant measurement of hormone concentrations in blood. In the proposed model all signal pathways were incorporated in the reaction network, including both positive and negative feedback. Therefore, it was possible to design a model, simple enough to be analyzed, but rich in nonlinear feedback which makes it applicable to generate complex dynamic phenomena.

Table 1. Model of hypothalamus-pituitary-adrenaline (HPA) system. CRH- cholesterol, corticotrophin-releasing hormone, ALDO- aldosterone, ACTH- adrenocorticotropic hormone, CORT- cortisol.

$$\xrightarrow{k_0} CRH$$

$$\xrightarrow{k_m} ALDO$$

$$CRH \xrightarrow{k_1} ACTH$$

$$ACTH \xrightarrow{k_2} CORT$$

$$ACTH \xrightarrow{k_3} ALDO$$

$$ACTH + 2CORT \xrightarrow{k_4} 3CORT$$

$$ALDO + 2CORT \xrightarrow{k_5} CORT$$

$$ACTH \xrightarrow{k_6} P_1$$

$$CORT \xrightarrow{k_7} P_2$$

This simple model, forced by circadian rhythm through the rate constant of the process responsible for CRH generation was capable to simulate biorhythmic oscillations of cortisol and other HPA axis hormones (see Figure 9).

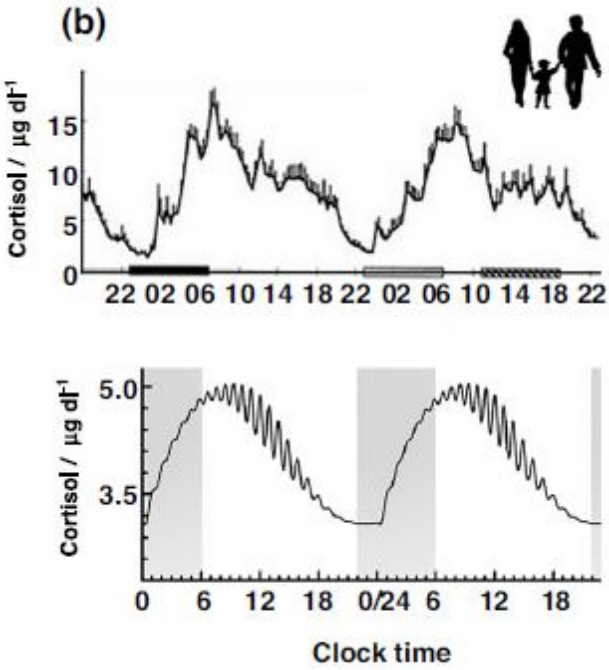


Figure 9. Experimentally determined (top) and numerically simulated (bottom) ultradian and circadian oscillations in cortisol levels in humans [74].

The most important advantage of the proposed modeling approach was adaptability. Thanks to Ljiljana's visionary approach, the proposed model was easily modified to simulate versatile functions of the HPA axis and numerous successful applications extended from this same basic idea.

Moreover, due to inherent ultradian oscillations, the model of the HPA axis has a phase sensitive response on perturbations. This property was crucial for successful simulation of

numerous effects which were previously unexplained, like different reaction on the same stress during the night and during the day. [67, 74]

Because of successful application of the Ljiljana's approach to the HPA axis, Belgrade group extended the same approach to the HPT axis too. [76]

In the end, it should be said. Research related to the HPA and HPT systems is certainly very useful for diagnosing the condition of patients during their treatment, primarily in terms of predicting and determining the optimal protocol for the treatment of patients, that is, defining the optimal amount (dose) of drugs and the time of their consumption.

Application of oscillatory reactions

More of the earlier works of the Belgrade group, as said [78, 79], were in focus attention because its were deal with kinetics and mechanisms of analytical interest. Later there will be significant research in the field of application of oscillatory reactions. [53, 81-97], The new analytical methods are developed. Their kinetic meaning is defined based on stoichiometric models of reactions. And finally, such an approach made it possible to successfully simulate the phenomenological results of the research. And the end, such an approach made it possible to successfully simulate the phenomenological results of the research.

Otherwise, the oscillatory reactions with at least two reaction routes and very low concentrations of intermediate species are extremely sensitive on chemical perturbations. [38, 39] Using them, analyte pulse perturbation techniques were developed for determination of paracetamol, ascorbic acid, morphine (Figure 10), 6-monoacetylmorphyne, piroxicam, and for uric acid in human urine and so on. Other substances were recently used for determination its activities, too. [96, 97]

Moreover, perturbations of oscillatory reactions were used to characterize catalytic activity of various heterogeneous materials. [53, 91-95]

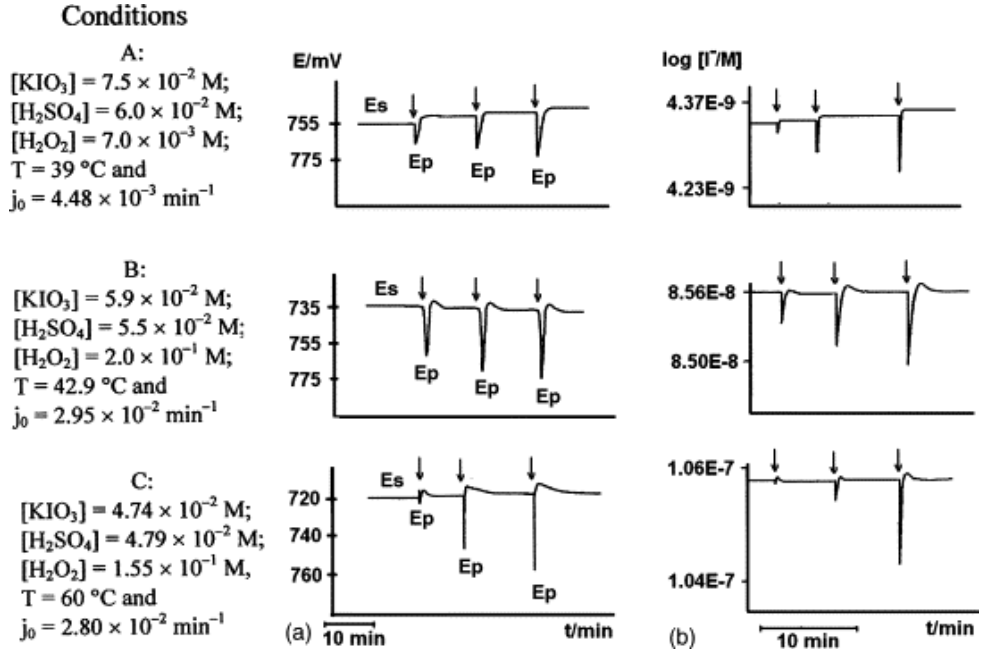


Figure 10. Experimental (a) and simulated (b) responses of BL analytical matrix of different compositions (A-C) realized for given specific flow rates j_0 in CSTR. [85]

Finally, what to say? Ljilja is no more with us, but we know that she was extremely unwaveringly, consistently and responsibly committed to her human and professional goals with all her being and passion, which she always achieved with a smile, with dignity, with love and sincerity that radiated around. She was and will be respected and loved by many. She is one of the jewels of physical chemistry.

Appendix. Part of the text from reference 24

In the official report on the implementation of the Project related to the anti-hail mixture (the so-called reagent), it is said verbatim:

1. This reagent fully meets the technical requirements of the hydrometeorological service of Yugoslavia, because at T= -10 ^{0}C it gives an activity of 7x10^{12}-1x10^{13} nuclei per gram of reagent. This activity exceeds the activity of all reagents used so far in our anti-hail protection.

2. In the entire temperature interval from -4.5^{0}C to -12^{0}C, the reagent significantly exceeds the activities of all reagents used so far.

3. At the crystallization threshold temperature -50^{0}C, the reagent gives a very high activity - about 1x10^{12}, which is more than an order of magnitude higher activity than the reagents used so far.

4. The reagent is a fast-acting reagent, because the largest number of millimetre-sized ice crystals is formed 1-2 minutes after scattering.

REFERENCES

[1] Lj. Kolar, B.Sc. Thesis.: Adsorption characteristics of the modified surfaces of alumina. Faculty of Physical Chemistry-University of Belgrade, Belgrade (Yugoslavia, Serbia), 1970. (*in Serbocroat*)

[2] Lj. Kolar-Anić, M.Sc. Thesis: Mathematical analysis of the kinetics of the complex chemical reactions., Faculty of Physical Chemistry-University of Belgrade, Belgrade, (Yugoslavia, Serbia), 1974. (*in Serbocroat*)

[3] Lj. Kolar-Anić, S. Veljković, S. Kapor, B. Dubljević, Weibull distribution and kinetics of heterogeneous processes, J. Chem. Phys., 1975 (63) 663-668.

[4] Lj. Kolar-Anić, S. Veljković, Statistical foundations of heterogeneous kinetics, J. Chem. Phys., 1975 (63) 669-673.

[5] B. Janković, B. Adnađević, J. Jovanović, D. Minić, Lj. Kolar-Anić, Thermogravimetric analysis of superabsorbing polyacrilic hydrogel, Mater. Sci. Forum, 2005 (494) 193-198.

[6] B. Adnađević, B. Janković, Lj. Kolar-Anić, D. Minić, Normalized Weibull distribution function for modelling the kinetics of non-isothermal dehydration of equilibrium swollen poly(acrylic acid) hydrogel, Chem. Eng. J, 2007 (130) 11-17.

[7] B. Adnađević, B. Janković, Lj. Kolar-Anić, J. Jovanović, Application of the Weibull distribution function for modeling the kinetics of isothermal dehydration of equilibrium swollen poly (acrylic acid) hydrogel, React. Funct. Polym., 2009 (69) 151-158.

[8] Lj. Kolar-Anić, V. Dondur, The average rate constant of the overall process of desorption from the energetically heterogeneous surface, Z.Phys. Chemie, Leipzig, 1989 (270) 737-744.

[9] B. Janković, Lj. Kolar-Anić, I. Smičiklas, S. Dimović, D. Aranđelović, The Non-isothermal Thermogravimetric Tests of Animal Bones Combustion. Part I. Kinetic Analysis, Thermochim. Acta, 2009 (495) 129-138.

[10] B. Janković, B. Adnađević, Lj. Kolar-Anić, I. Smičiklas, The Non-isothermal Thermogravimetric Tests of Animal Bones Combustion. Part II. Statistical Analysis: Application of the Weibull Mixture Model, Thermochim. Acta, 2010 (505) 98–105.
[11] Lj. Kolar-Anić, Stochastic Analysis of the Process of Desorption from the Energetically Heterogenous Surface in: A. Graovac (ed) Studies in the Physical and Theoretical Chemistry. Elsevier, Amsterdam, 1989, pp 379–386.
[12] Lj. Kolar-Anić, N. Cvjetićanin, G. Nicolis, The Stochastic Approach to Monolayer Adsorption. Fluctuations in the Adsorbed Amount, J. Serb. Chem. Soc., 1985 (50) 483–491.
[13] O. M. Jakšić, Ž. D. Čupić, Z. S. Jakšić, D. V. Ranđelović, Lj. Z. Kolar-Anić, Monolayer Gas Adsorption in Plasmonic Sensors: Comparative Analysis of Kinetic Models, Russ. J. Phys. Chem. A, 2013 (87) 2134–2139.
[14] O. M. Jakšić, D. V. Ranđelović, Z. S. Jakšić, Ž. D. Čupić, Lj. Z. Kolar-Anić, Plasmonic Sensors in multi-analyte environment: rate constants and transient analysis, Chem. Eng. Res. Des., 2014 (92) 91–101.
[15] O. M. Jakšić, Z. S. Jakšić, Ž .D. Čupić, D. V. Ranđelović, Lj. Z. Kolar-Anić, Fluctuations in Transient Response of Adsorption-Based Plasmonic Sensors, Sens Actuators B, 2014 (190) 419–428.
[16] O. Jakšić, I. Jokić, Z. Jakšić, Ž. Čupić, Lj. Kolar-Anić, Adsorption-induced fluctuations and noise in plasmonic metamaterial devices, Phys. Scr. T, 2014 (162) 014047.
[17] Ph.D. Physical Chemistry, Faculty of Physical Chemistry, University of Belgrade, Belgrade (Yugoslavia, Serbia), Doctorate Thesis: Equation of State of the Real Gas in the Gravitational Field, 1978.
[18] Lj. Kolar-Anić, B. Milić, Thermodynamic Properties of a Nonideal Gas in Homogeneous Gravitational Field, Physica A, 1979 (98) 325–336.
[19] Lj. Kolar-Anić, R. Balescu, On the Steady-state Solutions of the Kinetics of Homogeneous Nucleation, Chem. Phys., 1980 (46) 281–286.
[20] Lj. Kolar-Anić, Time-independent Solutions of the Kinetics o Homogeneous Nucleation, Chem. Phys. Lett, 1980 (74) 525–530.
[21] Lj. Kolar-Anić, New Solutions for the Kinetic Model of Homogeneous Nucleation, J. Serb. Chem. Soc., 1982 (47) 595–600.
[22] Lj. Kolar-Anić, About the Nucleation Process, J. Serb. Chem. Soc., 1983 (48) 195–206. (*in Serbocroat*)
[23] Lj. Kolar-Anić, New Solutions for the Kinetic Model of Homogeneous Nucleation. II. Approximate Calculations, J. Serb. Chem. Soc. 1983 (48) 501–506.
[24] (a) Agreement and Annexes between the "POLYESTER", Priboj, Serbia, and the Faculty of Science - Institute of Physical Chemistry, University of Belgrade (Document 2440, 14.12.1987); (b) Review of Completed Works with Comments on Achieved Effects, Company "POLYESTER", Priboj (Document 2473/88, 07.12.1988).
[25] W. C. Bray, A Periodic Reaction in Homogeneous Solution and Its Relation to Catalysis, J. Am. Chem. Soc., 1921 (43) 1262-1267.
[26] W. C. Bray, H. A. Liebhafsky, Reaction involving Hydrogen Peroxide, Iodine and Iodate Ion. I. Introduction, J. Am. Chem.Soc., 1931 (53) 38-44.
[27] S. Veljkovic Heterogeneity and Rate Modifications of the Bray-Libehafsky Reaction. Bull Soc. Chim. Beograd, 1981 (46) 711–714.
[28] R. M. Noyes, Mechanisms of chemical oscillators, J. Phys. Chem., 1990 (94) 4404-4412.
[29] L. Triendl, R. M. Noyes, A new Explanation of the Oscillations in the Bray-Liebhafsky Reaction, J. Phys. Chem., 1993 (97) 11354-11362.
[30] G. Schmitz, Historical Overview of Oscillating Reaction. Contribution of Professor Slobodan Anić, Reac. Kinet. Mech. Cat., 2016 (118) 5-13.

[31] S. R. Anić and Ž. D. Čupic, Dynamics and Kinetics of Complex Reaction Systems, Contributions of the Professor emeritus Lj. Kolar-Anić, Reac. Kinet. Mech. Cat., 2018 (123) 1-15.
[32] Lj. Kolar-Anić, Ž. Čupić, S. Anić, Advances made by Belgrade's Group in Research of Oscillatory Reactions, 2016, J. Serb. Soc. Comput. Mech, Special Edition, 2016 (10) 151-167.
[33] Lj. Kolar-Anić, Ž. Čupić, S. Anić, S. Blagojević, A. Ivanović-Šašić, V. Vukojević, Models of Oscillatory Reactions in Encyclopaedia of Physical Organic Chemistry, 6 Volume Set, (Ed. Z. Wang) Wiley, 2017, pp. 1127-1222.
[34] Lj. Kolar-Anić, Ž. Čupić, V. Vukojević, S. Anić, Dynamics of Nonlinear Processes, Publisher Faculty of Physical Chemistry, University of Belgrade, Belgrade, 2011. (*in Serbocroat*)
[35] Ž. Čupić, Lj. Kolar-Anić. Contraction of Complex Models by the Stochiometric Network Analysis, Advanced Science and Technology of Sintering, B. D. Stojanović, V. V. Skorokhod, M. V. Nikolić (Eds), Kluwer Academic/Plenum Publishers, New York, 1999, pp. 75-80.
[36] Lj. Kolar-Anić, S. Anić, Ž. Čupić, Characterization of the Catalysts by Means of an Oscillatory Reaction in: Finely Dispersed Particles: Micro-, Nano-, and Atto-Engineering, A. Spasić and Jyh-Ping Hsu (Eds.), CRC (earlier: Marcel Dekker), Inc., New York 2006, pp. 191-216.
[37] Ž. Čupić, V. Marković, A. Ivanović, Lj. Kolar-Anić, Modelling of the Complex Nonlinear Processes: Determination of the Instability Region by the Stoichiometric Network analysis in: Christopher R. Brennan (Ed.), Mathematical Modelling, Nova Science Publishers Inc., New York, 2013, pp. 111-178.
[38] N. D. Pejić, Review Paper: Analytical Applications of the Pulse Method Bray–Liebhafsky Oscillator Perturbations Reactions realized in Open Reactor, Chemical Industry, 2009 (63) 455–466. (*in Serbian*)
[39] N. D. Pejić, S.R. Anić, Lj. Z. Kolar-Anić, Analytical Applications of Oscillatory Chemical Reactions: Determination of Some Pharmaceutical and Biologically Important Compounds, Chemical Industry, 2009 (63) 455–466. (*in Serbian*)
[40] (a) B. P. A. Belousov, Periodic Reactions and Its Mechanism, Sbornik Referatov po Radiatsionnoi Meditsine, Medigz, Moskow, 1958, 145. (*In Russian*) (b) A. M. Zhabotinski, Periodical Oxidation of Malonic Acid in Liquid Phase, Biofizika, 1964 (9) 306-311. (*In Russian*)
[41] T. S. Briggs, W. C. Rausher, An Oscillating Iodine Clock, J. Chem. Educ. , 1973, (50) 496.
[42] S. Anić, Lj. Kolar-Anić, V. Vukojević, Ž. Čupić, D. Stanisavljev, M. Radenkovic, Bray-Liebhafsky Oscillatory Reaction in S. Anić and D. Marković (Eds.), Professor Dragan Veselinović, Society of Physical Chemists of Serbia and Faculty of Physical Chemistry, Belgrade, 2001, pp. 175-122.
[43] Vladana Vukojević, Ph. D thesis: Bifurcation and perturbation analysis of the Bray-Liebhafsky reaction, University of Belgrade, Belgrade, 2000.
[44] Ž. Čupić, Lj. Kolar-Anić, S. Anić, S. Maćešić, J. Maksimović, M. Pavlović, M. Milenković, I. N. Bubanja, E. Greco, S. D. Furrow, R. Cervellati, Regularity of Intermittent Bursts in Briggs-Rauscher Oscillating System with Phenol, Helv. Chim. Acta, 2014 (97) 321-333.
[45] I. N. Bubanja, S. Maćešić, A. Ivanović-Šašić, Ž. Čupić, S. Anić, Lj. Kolar-Anić, Intermittent chaos in the Bray-Liebhafsky Oscillator. Temperature dependence, Phys. Chem. Chem. Phys., 2016 (18) 9770-9778.

[46] I. N. Bubanja, A. Ivanović-Šašić, Ž. Čupić, S. Anić, Lj. Kolar-Anić, Intermittent Chaos in the Bray-Liebhafsky Oscillator. Dependence of Dynamic States on the Iodate Concentration, Russ. J. Phys. Chem. A, 2017 (91) 2525–2529.

[47] I. N. Bubanja, A. Ivanović-Šašić, Ž. Čupić, S. Anić, Lj. Kolar-Anić, Intermittent Chaos in the CSTR Bray–Liebhafsky Oscillator - Specific Flow Rate Dependence, Front. Chem., 2020 (8) 560274.

[48] Chopin-Dumas, J, Diagramme d'eta de la reaction Bray, Compt. Rend. Hebd. Sciences Acad. Sci. Ser. C, 1978 (287) 553-556.

[49] S. Anić, Lj. Kolar-Anić, Some New Details in the Kinetic Considerations of the Oscillatory Decomposition of Hydrogen Peroxide, Ber. Bunsenges. Phys. Chem., 1986 (90) 539-542.

[50] S. Anić, Lj. Kolar-Anić, Kinetic Aspects of the Bray-Liebhafsky Oscillatory Reaction, J. Chem. Soc. Faraday Trans. I, 1988 (84) 3413-3421.

[51] Slobodan Anić, Directing the development of the oscillatory hydrogen peroxide decomposition, Doctoral thesis, Faculty of Science, Belgrade, 1987 (*in Serbian*).

[52] (a) Ćirić, J, Anić, S, Čupić, Ž, Kolar-Anić, Lj, The Bray-Liebhafsky Oscillatory Reaction. Kinetic Investigation in Reduction and Oxidation Pathways Based on Hydrogen Peroxide Concentration Monitoring, Science of Sintering, 2000, (32) 187-196.) (b) J. Ćirić, Kinetics of cascade decomposition of hydrogen peroxide in acidic iodate solutions, Master's thesis, University of Belgrade, Belgrade, 2000. (*in Serbian*)

[53] S. Anić, J. Maksimović, D. Lončarević, N. Pejć. D. Čupić, Activity of Polymer Supported Cobalt Catalyst in the Bray–Liebhafsky Oscillator, Russ. J. Phys. Chem. A, 2009 (83), 1468–1472.

[54] S. Anić, D. Stanisavljev, G. Krnajski Belovljev, Lj. Kolar-Anić, Examination of the Temperature Variations on the Bray-Liebhafsky Oscillatory Reaction, Ber. Bunsenges. Phys.Chem., 1989 (93) 488-491.

[55] S. Anić, Lj. Kolar-Anić, E. Körös, Metod to Determine Activation Energies for the Two Kinetic States of the Oscillatory Bray-Liebhafsky Reaction, React. Kinet. Catal. Lett., 1997 (61)111-116.

[56]S . Anić, V. Vukojević, M, Radenković, Lj. Kolar-Anić, New Approach to the Study of the Peroxide Kinetics of the Briggs-Rauscher Oscillatory Reaction, J. Serb. Chem. Soc., 1989 (54) 521-526.

[57] (a) S. Blagojević, N. Pejić, S. Anić, Lj. Kolar-Anić, Belousov Zhabitinsky Oscillatory Reaction. Kinetic of Malonic Acid Decomposition, J. Serb. Chem. Soc., 2000, (65) 709-713; (b) Slavica Blagojević, Master's thesis: Activation Energy of Belousov-Zhabotinsky Oscillatory Reactions in Different Steady States of the System, University of Belgrade, Belgrade, 2000; (c) S. M. Blagojević, R. S. Anić, Ž. D. Čupić, N. D. Pejić, Lj. Z. Kolar-Anić, Temparature Influence on the Malonic Acide Decomposition in the Belousov-Zhabotinsky Reaction, R. J. Phys. Chem. A, 2009 (9) 1496-1501; (d) S. M. Blagojević, R. S. Anić, Ž. D. Čupić, N. D. Pejić, Lj. Z. Kolar-Anić, Malonic Acid Concentration as a Control Parameter in the Kinetic Analysis of the Belousov-Zhabotinsky Reaction under Batch Conditions, Phys. Chem. Chem. Phys., 2008 (10) 6658-6664; (e) Slavica Blagojević, Ph.D: Modeling the influence of malonic acid on the evolution of the Belousov-Zhabotinsky oscillatory reaction, Faculty for Physical Chemistry, University of Belgrade, Belgrade, 2009.

[58] Lj. Kolar-Anić, D. Stanisavljev, G. Krnajski Belovljev, Ph. Peeters, S. Anić, The First Maximum of the Iodide Concentration in the Bray-Liebhafsky Reaction, Computers Chem., 1990 (14) 345-347.

[59] Lj. Z. Kolar-Anić, D. M. Mišljenović, D. R. Stanisavljev, S. R. Anić, Applicability of The Schmitz's Model to Dilution- Reinitiated Oscillations in The Bray-Liebhafsky Reaction, J.

Phys. Chem., 1990 (94) 8144-8146.
[60] Lj. Kolar-Anić and G. Schmitz, Mechanism of the Bray–Liebhafsky Reaction: Effect of the Oxidation of Iodous Acid by Hydrogen Peroxide, Farad. Trans. 1992, 88, 2343.
[61] Lj. Kolar-Anić, Đ. Mišljenović, S. Anić, G.Nicolis, Influence of the Reduction of Iodate by Hydrogen Peroxide on the Model of the Bray-Liebhafsky Reaction, React. Kinet. Catal. Lett., 1995 (54) 35-41.
[62] S. Jelić, Ž. Čupić, Lj. Kolar-Anić, Mathematical modeling of the hypothalamic-pituitary-adrenal system activity, Math Biosci., 2005 (197) 173-187.
[63] S. Jelić, Ž. Čupić, Lj. Kolar-Anić, Modeling of the Hypothalamic-Pituitary-Adrenal System Activity Based on the Stoichiometric Analysis, in: New Research on Neurosecretory Systems, E. Romano, S. De Luca (Eds.), Nova Science Publishers Inc, New York, 2008, 225-245.
[64] S. Jelić, Ž. Čupić, Lj. Kolar-Anić, V. Vukojević, Predictive Modeling of the Hypothalamic-Pituitary-Adrenal (HPA) Function. Dynamic Systems Theory Approach by Stoichiometric Network Analysis and Quenching Small Amplitude Oscillations, Int. J. Nonlinear Sci. Numer. Simul., 2009 (10) 1451-1472.
[65] S. Jelić, Ž. Čupić, Lj. Kolar-Anić, V. Vukojević, Predictive Modelling of the Hypothalamic-Pituitary-Adrenal (HPA) function. Dynamic Systems Theory Approach by Stoichiometric Network Analysis and Quenching Small Amplitude Oscillations, Int. J. Nonlin. Sci. Num., 2010 (10) 1451-1472.
[66] V. M. Marković, A. Ivanović, Ž. Čupić, Lj. Kolar-Anić, The Stability of the Extended Model of Hypothalamic-Pituitary-Adrenal (HPA) Axis examined by Stoichiometric Network Analysis (SNA), Russ. J. Phys. Chem. A, 2011 (85) 2327-2335.
[67] V. M. Marković, Ž. Čupić, V. Vukojević, Lj. Kolar-Anić, Predictive Modelling of the Hypothalamic-Pituitary-Adrenal (HPA) Axis Response to Acute and Chronic Stress, Endocr. J., 2011 (58) 889-904.
[68] Ž. Čupić, V. Marković, A. Ivanović, Lj. Kolar-Anić, Modelling of the Complex Nonlinear Processes: Determination of the Instability Region by the Stoichiometric Network Analysis in: Christopher R. Brennan (ed), Mathematical Modelling, Nova Science Publishers Inc., New York, 2011 pp. 111-178.
[69] V. M. Marković, Ž. Čupić, S. Maćešić, A. Stanojević, V. Vukojević, Lj. Kolar-Anić, Modelling Cholesterol Effects on the Dynamics of the Hypothalamic–Pituitary–Adrenal (HPA) axis, Math. Med. Biol., 2016 (33) 1–28.
[70] Ž. Čupić, V. M. Marković, S. Maćešić, A. Stanojević, S. Damjanović, V. Vukojević, Lj. Kolar-Anić, Dynamic Transitions in a Model of the Hypothalamic-pituitary-adrenal (HPA) axis, Chaos: An Interdisciplinary Journal of Nonlinear Science, CHAOS 26 (2016) 033111.
[71] A. Stanojević, V. M. Marković, Ž. Čupić, V. Vukojević, Lj. Kolar-Anić, Modelling of the Hypothalamic-Pituitary-Adrenal Axis Perturbations by Externally Induced Cholesterol Pulses of Finite Duration and with Asymmetrically Distributed Concentration Profile, ISSN 0036-0244, Russ. J. Phys. Chem. A, 2017 (91) 2600-2607.
[72] O. A Abulseoud, M. Choi Ho, Doo-Sup Choi, A. Stanojević, Ž. Čupić, Lj. Kolar-Anić and V. Vukojević, Corticosterone Oscillations during Mania Induction in the Lateral Hypothalamic Kindled Rat — Experimental Observations and Mathematical Modeling. PLoS ONE 2017 (12): e0177551.
[73] Ž. Čupić, A. Stanojević, V. M. Marković, Lj. Kolar-Anić, Lars Terenius, Vladana Vukojević, The HPA axis and Ethanol - a Synthesis of Mathematical Modeling and Experimental Observations, Addict. Biol., 22 (2017) 1486–1500.
[74] A. Stanojević, V. M. Marković, Ž. Čupić, Lj. Kolar-Anić, V. Vukojević, Advances in Mathematical Modelling of the Hypothalamic–Pituitary–Adrenal (HPA) Axis Dnamics and the Neuroendocrine Response to Stress, Curr. Opin. Chem. Eng. 2018 (21) 84–95.

[75] A.S. Stojiljković, Ž. Čupić, S. Maćešić, A. Ivanović -Šašić, Lj. Kolar-Anić, Influence of Arginine Vasopressin on the Ultradian Dynamics of Hypothalamic-Pituitary-Adrenal Axis, Front. Endocrinol., 2022 (13) 01-16.
[76] Lj. Kolar-Anić, Ž. Čupić, S. Maćešić, A. Ivanović-Šašić, J. W. Dietrich, Modelling of the Thyroid Hormone Synthesis as a Part of Nonlinear Reaction Mechanism with Feedback, Comput. Biol. Med.2023 (160) 106980.
[77] E.N. Brown, P.M. Meehan, A.P. Dempster, A Stochastic Differential Equation Model of Diurnal Cortisol Patterns. Am. J. Physiol. Endocrinol. Metab., 2001 (280) E450–E461.
[78] H.A. Mottola, D. Perezbendito, H.B. Mark, Kinetic determinations and some kinetic aspects of analytical chemistry, Anal. Chem, 1990 (62) pp R441-R461.
[79] Stanley R. Crouch, Thomas F. Cullen, Alexander Scheeline, Eva S. Kirkor, Kinetic Determinations and Some Kinetic Aspects of Analytical Chemistry, Anal. Chem., 1998, № 12, p. 53-106
[81] N. Pejić, S. Anić, V. Kuntić, V. Vukojević, Lj. Kolar-Anić, Kinetic Determination of Microquantities of Rutin by Perturbation of the Bray-Liebhafsky Oscillatory Reaction in an Open System, Micro Chem. Acta, 2003 (143) 261-267.
[82] N. Pejić, S. Blagojević, S. Anić, V. Vukojević, Lj. Kolar-Anić, Microquantitative determination of hesperidin by pulse perturbation of the oscillatory reaction system, J. Anal. Bioanal. Chem., 2005 (381) 775-780.
[83] N. Pejić, Lj. Kolar-Anić, S. Anić, D. Stanisavljev, Determination of Paracetamol in Pure and Pharmaceutical Dosage Forms by Pulse Perturbation Technique, J. Pharma. Biomed. Anal., 2006 (41) 610-615.
[84] N. Pejić, S. M. Blagojević, S. Anić, Lj. Kolar-Anić, Dtermination of Ascorbic Acide in Pharamaceutical Dosage Forms an Urine by means of an Oscillatory Reaction System using the Pulse Perturbation Thecnique, Anal. Bioanal. Chem., 2007 (389) 2009-2017.
[85] N. D. Pejić, S. M. Blagojević, S. R. Anić, V. B. Vukojević, M. M. Mijatović, J. S. Ćirić, Z. S. Marković, S. D. Marković, Lj. Z. Kolar-Anić, Kinetic Determination of Morphine by Means of Bray-Liebhafsky Oscillatory Reaction system using Analyte Pulse Perturbation Technique, Anal. Chim. Acta, 2007 (582) 367-374.
[86] N. Pejić, S. Blagojević, J. Vukelić, Lj. Kolar-Anić, S. Anić, Analyte Pulse Perturbation Technique for the Determination 6-monoacetylmorphyne in Seized Street Drug Sample, Bull. Chem. Soc. Jap., 2007 (80) 1942-1948.
[87] N. D. Pejić, J. P. Makismović, S .M. Blagojević, S. R. Anić, Ž. D. Čupić, Lj. Z. Kolar-Anić, Kinetic Analytical Method for Determination of Uric Acid in Human Urine using Analyte Pulse Perturbation Technique, J. Braz. Chem. Soc., 2012 (23) 1450-1459.
[88] N. D. Pejić, N. B. Sarap, J. P. Makismović, S. R. Anić, Lj. Z. Kolar-Anić, Pulse Perturbation Technique for Determination of Piroxicam in Pharmaceuticals using an Oscillatory Reaction System, Central European Journal of Chemistry, 2013 (11) 180-188.
[89] N. Pejić, S. Blagojević, N. Sarap, J. Maksimović, S. Anić, Ž. Čupić, Lj. Kolar-Anić, Perturbations of the Dushman reaction with Piroxicam: experimental and model calculations, Helv. Chim. Acta, 2014 (97) 47-55.
[90] L. Negrojević, A. Lončar, J. Maksimović, S. Anić, Ž. D. Čupić, Lj. Kolar-Anić, N. Pejić, Bray-Liebhafsky Oscillatory Reaction in a Continuous-flow Stirred Tank Reactor as the Matrix System for Determination of Tyrosine, React. Kinet. Mech. Catal., 2022 (134) 1147-1162.
[91] Ž. Čupić, S. Anić, A. Terlecki-Baričević and Lj. Kolar-Anić, Bray-Liebhafsky Reaction. The Influence of Some Polymers Based on Poly (4-vynilpyridine), React. Kin. Catal. Lett., 1995 (54) 43-49.

[92] A. Terlecki-Baričević, Ž. Čupić, S. Anić, Lj. Kolar-Anić, S. Mitrovski and S. Ivanović, Polyvinilpyridine Supported Iron(III)Catalyst in Hydrogen Peroxide Decomposition, J. Serb. Chem. Soc., 1995 (60) 969-979.
[93] N. Pejić, Ž. Čupić, S. Anić, V. Vukojević and Lj. Kolar-Anić, The Oscillatory Bray-Liebhafsky Reaction as a Matrix for Analyzing Enzime and Polymeric Catalysts for Hydrogen Peroxide, Sci. Sinter, 2001 (33) 107-115.
[94] M. Milošević, N. Pejić, Ž. Čupić, S. Anić, and Lj. Kolar-Anić, Examinations of Cross-Linked Polyvinylpyridine in Open Reactor, Material Sciences Forum, Current research in Advanced Materials and Processes, 2005 (494) 369-374.
[95] Lj. Kolar-Anić, S. Anić, Ž. Čupić, Chapter 8: Characterization of the Catalysts by Means of an Oscillatory Reaction, in A. Spasic, J. P. Hsu (Eds): Surfactant Science Series – Finely Dispersed Particles: Micro-, Nano-, and Atto-Engineering, CRC Press - Taylor & Francis Group, Boca Raton London New York, 2006, pp. 191-216. (ISBN: 1-5744-4463-8)
[96] T. V. Maksimović, J. P. Maksimović, P. I. Tančić, N. I. Potkonjak, Z. P. Nedić, Lj. G. Joksović, M. C. Pagnacco, A Possible Connection between Phosphate Tungsten Bronzes Properties and Briggs-Rauscher Oscillatory Reaction Response, Sci. Sinter., 2021 (53) 223-235.
[97] T. Maksimović, P. Tančić, J. Maksimović, D. Mara, M. Ilić, Rik Van Deun, Lj. Joksović, M. Pagnacco, Novel Cerium and Praseodymium doped Phosphate Tungsten Bronzes: Synthesis, Characterization, the Behavior in the Briggs-Rauscher Reaction and Photoluminescence Properties, Opt. Mater, 2023 (143) 114125.

MODELLING OF METABOLIC OSCILLATIONS IN CYANOBACTERIA

I. Schreiber[1,2] and J. Červený[1]

[1]*Department of Adaptive Biotechnologies, Global Change Research Institute, Academy of Science of the Czech Republic, Brno, Czech Republic*
[2]*Department of Chemical Engineering, University of Chemistry and Technology, Prague, Czech Republic*

DOI: https://doi.org/10.46793/Phys.Chem24I.127S

ABSTRACT

We use the theory of reaction networks to construct a compartmental model of metabolic oscillatory dynamics observed in experiments with photosynthesizing diazotrophic cyanobacteria (Cyanothece sp.) in a flow-through photobioreactor. The experimental oscillatory behavior occurs in a population of cells with suppressed activity of their circadian clocks under constant intensity of light. In such restricting conditions the cells are still viable and display oscillations measured by their oxygen release. Such oscillations are assumed to be based solely on metabolism, have period much shorter than the circadian rhythms (about 12-17 h) and therefore have been termed ultradian cycles [1].

The model describes dynamics of component concentrations in two parts of the cell suspension: i) the solution in the reactor including bubbles of CO2 enriched air and ii) the cellular biomass. Components in the solution are nutrients (CO2, N2, O2) and extracellular products (DON), components in the biomass are represented by compartments, which are treated as pseudospecies that interact via power law chemical kinetics. The compartments include pools of the nutrients inside the cells, carbon and nitrogen stores, specific functional compartments as well as a generic functional/structural compartment. The model utilizes empirically determined biomass growth rate expressed in terms of the Monod kinetics. The rate coefficients in the power law expressions were determined by using the method of constrained stoichiometric analysis, which is a combination of stoichiometric network theory and convex linear optimization [2] and has been previously used to determine unknown kinetic parameters in oscillatory enzyme reactions [3].

The model is then used to simulate ultradian oscillations under experimental conditions and provides results closely agreeing with the experimentally observed 14-hour ultradian cycles.

[1] J. Cerveny, M. A. Sinetova, L. Valledor, L .A. Sherman, L. Nedbal, PNAS 110 (2013) 13210–13215.
[2] V. Radojkovic, I. Schreiber, PCCP 20 (2018) 9910-9921.
[3] F. Muzika, R. Jurasek, L. Schreiberova, V. Radojkovic, I. Schreiber, J. Phys. Chem. A 121 (2017) 7518-7523.

MODELING OF THIOL WAVES IN TWO-CHANNEL GEL REACTORS

I. Sütő[1], S. N. Semenov[2], D. Horváth[3] and Á. Tóth[1]

[1] Department of Physical Chemistry and Materials Science, University of Szeged, Rerrich Béla tér 1., H-6720 Szeged, Hungary (atoth@chem.u-szeged.hu)
[2]Department of Molecular Chemistry and Materials Science, Weizmann Institute of Science, Rehovot, Israel
[3]Department of Applied and Environmental Chemistry, University of Szeged, Rerrich Béla tér 1., H-6720 Szeged, Hungary

DOI*:* https://doi.org/10.46793/Phys.Chem24I.129S

ABSTRACT

Chemical systems in biological organisms contain many components (e.g., DNA and enzymes) with thousands of interactions between them. Therefore, finding minimal motifs responsible for emergent behaviors in them (e.g. traveling waves) is very challenging. Using synthetic organic chemistry, we can design systems [1] exhibiting complex behaviors with a minimal number of interacting components, because reaction rates and diffusion coefficients can be controlled by altering the molecular structures of the reactants. Semenov and coworkers [2] have shown that cystamine-based chemical oscillations may evolve in a continuously stirred tank reactor in the presence of maleimide and acrylamide acting as slow and fast inhibitors. The flow of these reactants in a two-channel gel reactor [3] can give rise to wave evolution in the gel. The pattern formation has been characterized by its front speed and the time period between the subsequent waves.

In this work, we have described the reaction with an eight-step, seven-component model, besides considering diffusion in the gel as a transport process. The reactor was approximated by a two-dimensional configuration where the initial and the boundary conditions were set to match the experiments. The CVODE software package was used to solve the generated ordinary differential equations after spatial discretization. With the right choice of parameters we were able to reproduce the chemical waves observed experimentally. The characteristics of the patterns were in qualitative agreement with those of the experimental results. Furthermore, we have studied the spatiotemporal pattern formation at different inhibitor concentrations and diffusion constants. The effect of the flow rate of the reactants and the spatial separation of the fast inhibitors on the emerging patterns has also been investigated. In addition, we have determined the minimum and maximum concentration of the fast inhibitor, between which the existence of diffusion-controlled waves are possible.

Insights into the spatiotemporal behavior originating from synthetic networks may reveal new strategies to synthesize life-inspired systems and materials.

REFERENCES

[1] S. N. Semenov, L. J. Kraft, A. Ainla, M. Zhao, M. Baghbanzadeh, C. E. Campbell, K. Kang, J. M. Fox, G. M. Whitesides, Nature 537 (2016) 656.
[2] A. I. Novichkov, A. I. Hanopolskyi, X. Miao, L. J. W. Shimon, Y. Diskin-Posner, S. N. Semenov, Nat. Commun. 12 (2021) 2994.
[3] B. Dúzs, I. Szalai, Commun. Chem. 3 (2020) 168.

THE OSCILLATING REACTION DISCOVERED BY W. C. BRAY OCCURS IN HOMOGENEOUS SOLUTION

G. Schmitz

Université Libre de Bruxelles, Ecole Polytechnique, CP165/63, Av. F. Roosevelt 50, 1050 Brussels, Belgium

DOI: https://doi.org/10.46793/Phys.Chem24I.131S

SUMMARY

In accordance with the ideas of Bray and Liebhafsky, the oscillating reaction which bears their names occurs in homogeneous solution. Oxygen reactions and the formation of oxygen bubbles produced by the decomposition of H_2O_2 has an effect but does not explain the oscillations. Any model of the Bray-Liebhafsky reaction must take into account the kinetics of the reactions of iodine compounds with each other and with H_2O_2. The proposed model explains all the experimental observations including the effects of oxygen, at least semi-quantitatively. The role of radicals during the Bray-Liebhafsky reaction is discussed and a reaction of radical formation in homogeneous solution is proposed.

INTRODUCTION

The Bray-Liebhafsky (BL) oscillating reaction results from reactions (R) and (O) leading to the catalysis of the decomposition of H_2O_2 by the iodate-iodine couple.

$$2\ IO_3^- + 2\ H^+ + 5\ H_2O_2 \rightarrow I_2 + 5\ O_2 + 6\ H_2O \quad (R)$$

$$I_2 + 5\ H_2O_2 \rightarrow 2\ IO_3^- + 2\ H^+ + 4\ H_2O \quad (O)$$

The BL reaction was discovered in 1921 [1] and its mechanism remained controversial for 103 years. Much of the controversy comes from the effects of oxygen, a product of the reaction. These effects were studied by Sharma and Noyes [2, 3] who concluded that the oscillations should be explained by the formation of oxygen bubbles. The ideas of Sharma and Noyes were taken up later but never made it possible to explain the oscillations discovered by Bray. On the other hand, Liebhafsky, Matsuzaki et al. [4-11] studied not only the oscillations under different experimental conditions but also the kinetics of several reactions that may be part of the mechanism of the BL reaction. Liebhafsky always remained convinced that the oscillations can be explained by reactions in homogeneous solution. This opinion was supported later by Furrow [12, 13] and by Ševčik et al. [14-17]. Based on the results of Liebhafsky and new experiments, a simple model giving oscillations in homogeneous solution was proposed in 1987 [18]. The Belgrade group presented variants of this model [19, 20] and used the SNA (Stoichiometric Network Analysis) method to analyze their properties [21-23]. A new version [24, 25] allowed not only simulations of the experimental oscillations but also explained the complicated kinetics of the iodine oxidation by H_2O_2 discussed below. It is named hereafter model BLH (Bray-Liebhafsky Homogeneous). The effect of oxygen was explained by a global reaction leading to the iodide ions oxidation with a radical mechanism which remained to be elucidated. The role of radicals in the BL reaction is the second subject of controversy.

Stanisavljev et al. [26, 27] showed that radicals can be formed during the BL reaction. They thought that the formation of radicals in homogeneous solutions would requires a too large

activation energy, would therefore be too slow and Stanisavljev et al. [28, 29] proposed another source of radicals, the collapse of germs of oxygen bubbles. However, their model gives oscillations whose shape and size are completely different from those observed experimentally, uses rate constants at 25°C instead of the values estimated at 50°C [25] and involves unlikely reactions: a radical formation (R4 in ref. [29]) with a very large increase in the Gibbs energy, an overall reaction of $I^{\bullet}$ oxidation to iodate (R17) attributed to a mysterious chain, a reaction with an order six not existing in chemical kinetics (R25). Above all, their model does not explain the complicated kinetics of the iodine oxidation by H_2O_2 under conditions where the solution is not saturated with oxygen, where bubbles cannot form, and does not consider numerous previous works devoted to the kinetics of the reactions of iodine compounds with each other and with H_2O_2.

IODINE OXIDATION BY H_2O_2

When H_2O_2 is added to an acidic solution of iodine without iodate, generally no reaction is observed, or only after a non-reproducible induction period. The direct reaction $I_2 + H_2O_2 \rightarrow 2\ HOI$ is not observed because it requires a very large activation energy. However, if the concentration of the iodide ions always present in iodine solutions is sufficiently reduced (for example by precipitation with Ag^+ or Hg^{++} ions) the oxidation begins immediately and is fast. This is also the case if some iodate is added. These experiments prove that there is an oxidation reaction path that does not require a large activation energy. In the BLH model, this path begins with the hydrolysis of iodine (-R4) followed by reactions (-R3) and (R10). The HOIO produced is then oxidized to iodate.

$I_2 + H_2O \rightarrow I^- + H^+ + HOI$ (-R4)

$2\ HOI \rightarrow I_2O + H_2O$ (-R3)

$I_2O + H_2O_2 \rightarrow HOI + HOIO$ (R10)

The intermediate I_2O, analog of the known compounds Cl_2O [30, 31] and Br_2O [32, 33], has not been observed in aqueous solution because its concentration is too small, but it can be prepared in concentrated sulfuric acid and extracted in dichloromethane [34]. It has also been observed in the gas phase [35]. For simplicity, we continue to write I_2O as in our previous articles. However, it is most probably hydrated and a more exact writing of reaction (-R3) would be $2\ HOI \rightarrow H_2O\text{-}I\text{-}O\text{-}I$. This writing shows that reaction (-R3) must be seen as a dimerization rather than as a dehydration. The sum of reactions (-R3) and (R10) gives $HOI + H_2O_2 = HOIO + H_2O$. The Gibbs energies of formation of HOI, H_2O_2 [36] and of HOIO [37] give $K_{-R3}K_{R10} = 3\times10^{17}\ M^{-1}$ and our numerical simulations suggest $K_{-R3} \sim 100$ (order of magnitude). These values show that the activation energy of reactions (-R3) and (R10) can be small so that the oxidation of HOI can be fast. The reaction path (-R4) + (-R3) + (R10) bypasses the high activation barrier of the direct reaction $I_2 + H_2O_2$ used by Stanisavljev et al. [26-29] as an argument against the BLH model.

In the presence of a little iodate added initially to lower the iodide ions concentration, the oxidation of iodine starts immediately with an unusual and very complicated kinetics. Figure 1 shows the values of the experimental rate constant $k_{exp} = (-d[I_2]/dt)/[I_2]$ [24] and their simulations with the BLH model. The rates were measured at small conversions so that the oxygen concentrations were close to the equilibrium value with the atmosphere and had no effect. Stanisavljev et al. did not consider these experimental results in the presence of iodate by arguing that the presence of additional components may mask very important reaction properties [ref.28, p.14023]. On the contrary, these results provide essential information because the O reaction occurs in the presence of iodate during the BL reaction,

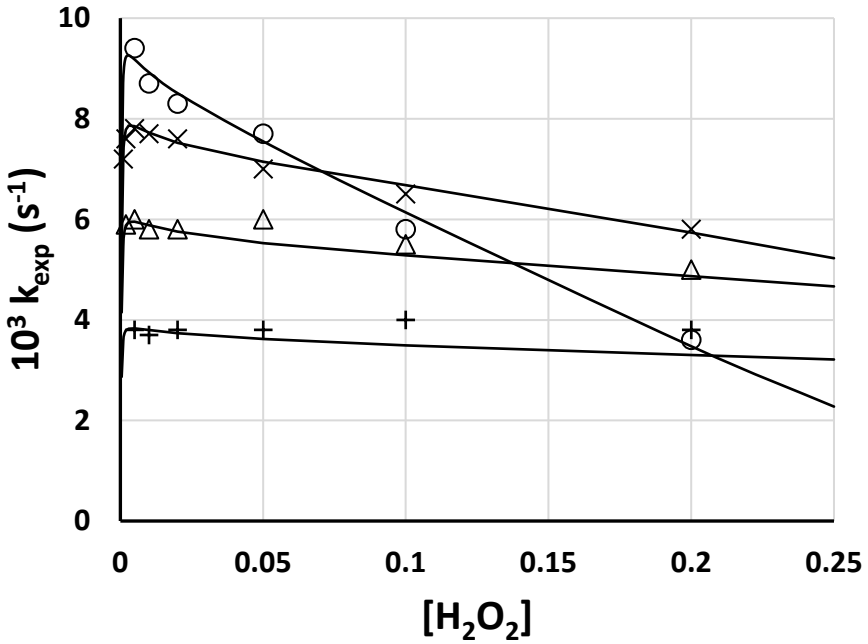


Figure 1. Effect of hydrogen peroxide concentration and acidity on k_{exp} at 25°C. Experimental values if $[NaIO_3]$ = 0.0125 M, $[I_2] = 4\times10^{-4}$ M, $[HClO_4]$ = 0.04 (○), 0.10 (×), 0.20 (Δ), 0.40 (+) M [24] and corresponding values calculated with the BLH model (—).

In the absence of iodate initially, only a very slow decomposition of H_2O_2 is observed. Then, the oxidation of I_2 begins eventually after an induction period. Fig.2.a shows the influence of the interphase area on this period observed by Olexova [38] and Fig.2.b shows the time evolution calculated with the BLH model. The end of the induction period cannot be explained by the formation of oxygen bubbles because oxygen production during the induction is so slow that the solution does not become saturated. Oxygen leaves the solution by diffusion with a rate proportional to the interface. Fig.2.b shows the effect of the transfer coefficient k_{16} in Table I proportional to the interphase area (curves 1 and 2). If it is too large (curve 3), a critical concentration of oxygen is not reached and the rate of iodide ions oxidation is not sufficient to cause the end of the induction period. The observed slow decrease in A(460 nm) over time is due to a loss of iodine in the gas phase. It is indeed the oxygen which causes the end of the induction but as a result of a homogeneous reaction. The oxidation of the iodide ions gives an increase of the HOI concentration so that the oxidation (R10) with a rate increasing with the square of the HOI concentration becomes faster than the rate of reduction with a rate proportional to the HOI concentration.

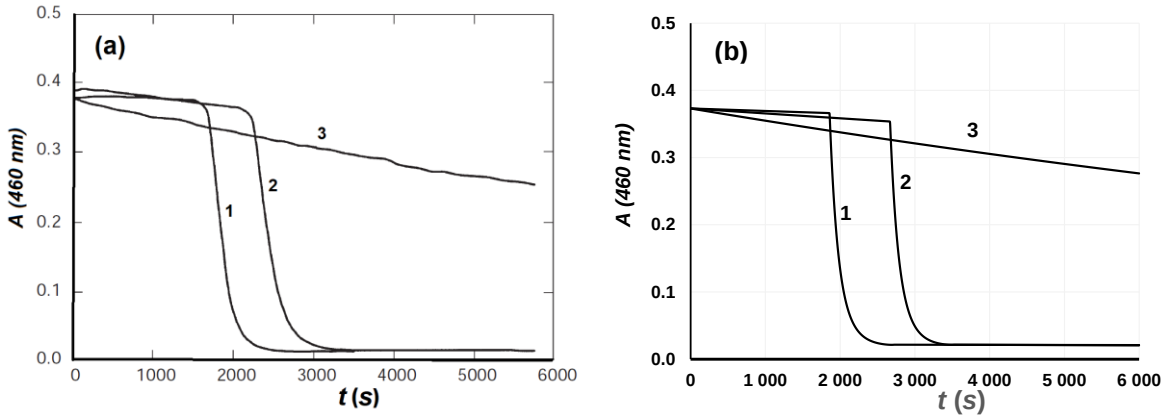


Figure 2. Influence of the interphase area on the induction period of reaction O observed by Olexova [38]. (a) $[HClO_4]$ = 0.07 mol L^{-1}, $[H_2O_2]_0$ = 0.05 mol L^{-1}, $[I_2]_0 = 5\times10^{-4}$ mol L^{-1}, no iodate, 30°C, interphase area 0.19 cm^2 (1), 0.38 cm^2 (2), 1 cm^2 (3). (b) Simulation with the BLH model, k_{12}/k_6 = 0.17 and transfer coefficients k_{16} proportional to the interphase area, 1.7×10^{-4} s^{-1} (1), 3.4×10^{-4} s^{-1} (2), 1×10^{-3} s^{-1} (3).

MECHANISM OF THE IODIDE OXIDATION BY OXYGEN

The reaction $O_2 + 4\ I^- + 4\ H^+ \rightarrow 2\ I_2 + 2\ H_2O$ seems simple but its mechanism remains tentative. The rate of the non-radical path studied by Sigalla [39] is too small to explain the effect of oxygen on the BL reaction and a radical path must be assumed. The reactions producing radicals previously proposed require too large energies and we have proposed a new explanation [40]. The reaction usually written $HOI + H_2O_2 \rightarrow I^- + H^+ + O_2 + H_2O$ is actually the sum of reactions (R5) and (R6) [41, 42]. Consider also reaction (R12) and the sum (R12a) = (R5) + (R12).

$HOOI + H_2O_2 \rightarrow HOO^\bullet + IO^\bullet + H_2O$ (R12)
$HOI + 2\ H_2O_2 \rightarrow HOO^\bullet + IO^\bullet + 2\ H_2O$ (R12a)

$D_fG(HOO^\bullet, aq)$ = 7 kJ/mol [43] and $D_fG(IO^\bullet, g)$ = 98 kJ/mol [44] but $D_fG(IO^\bullet, aq)$ is not known. Compared to similar compounds, a solubility between 10 and 500 M/atm is likely giving $D_fG(IO^\bullet, aq) = 85 \pm 5$ kJ/mol and $D_rG(R12a) = -15 \pm 5$ kJ/mol. Even if the value of $D_fG(IO^\bullet, aq)$ is approximate, we obtain a formation of radicals with a negative Gibbs energy. It is possible in a homogeneous solution with the decomposition of H_2O_2 as the only source of energy. Reaction (R6) is reversible so that the concentration of HOOI and the rate of production of radicals by reaction (R12) increases when the concentration of oxygen increases. Different reactions of these radicals are possible and numerical simulations give similar results provided that they lead globally to the oxidation of the iodide ions by oxygen. This part of the BLH model is not necessary to explain the oscillations but only the effects of oxygen. Among the possibilities, we suggest reactions (R13) to (R15). Reactions (R13) and (R14) are thermodynamically likely. $D_fG(I^\bullet, aq)$ = 78.8 kJ/mol [43] and the estimate of $D_fG(IO^\bullet, aq)$ above gives $D_rG(R13)$ = - 107 kJ/mol and $D_rG(R14)$ = - 53 kJ/mol. Reaction (R14) is also kinetically likely because it is the sum of an electron transfer ($IO^\bullet + I^- \rightarrow IO^- + I^\bullet$) and an acid-base reaction ($IO^- + H^+ = HOI$). The rate constant of the analogous reaction $OH^\bullet + I^- + H^+ \rightarrow I^\bullet + H_2O$ is 10^{10} $M^{-2}s^{-1}$[27] and $k_{15} = 10^{10}$ $M^{-1}s^{-1}$[45].

OSCILLATIONS AT 25°C

To prove that the oscillations he had discovered occur in homogeneous solution, Bray carried out experiments at 25°C under conditions where oxygen is produced so slowly that it leaves the solution by diffusion without forming bubbles. Bray's conclusion being questioned, Stanley Furrow confirmed and supplemented his experiments [46]. The periods are very long and the oscillations difficult to reproduce due to the effect of the oxygen but, Stanley Furrow was able to confirm that oscillations are observed under conditions where bubbles do not form. Figure 3 gives an example of oscillations obtained experimentally and shows that they are very well simulated with the BLH model. The kinetic constants were measured directly or adjusted to the kinetics of the O reaction. Only the constants relating to the effect of oxygen were adjusted to obtain the calculated values. The calculated oxygen concentrations agree with the observations that its rate of production is much larger during reaction O [17] and confirm that the solution never becomes saturated.

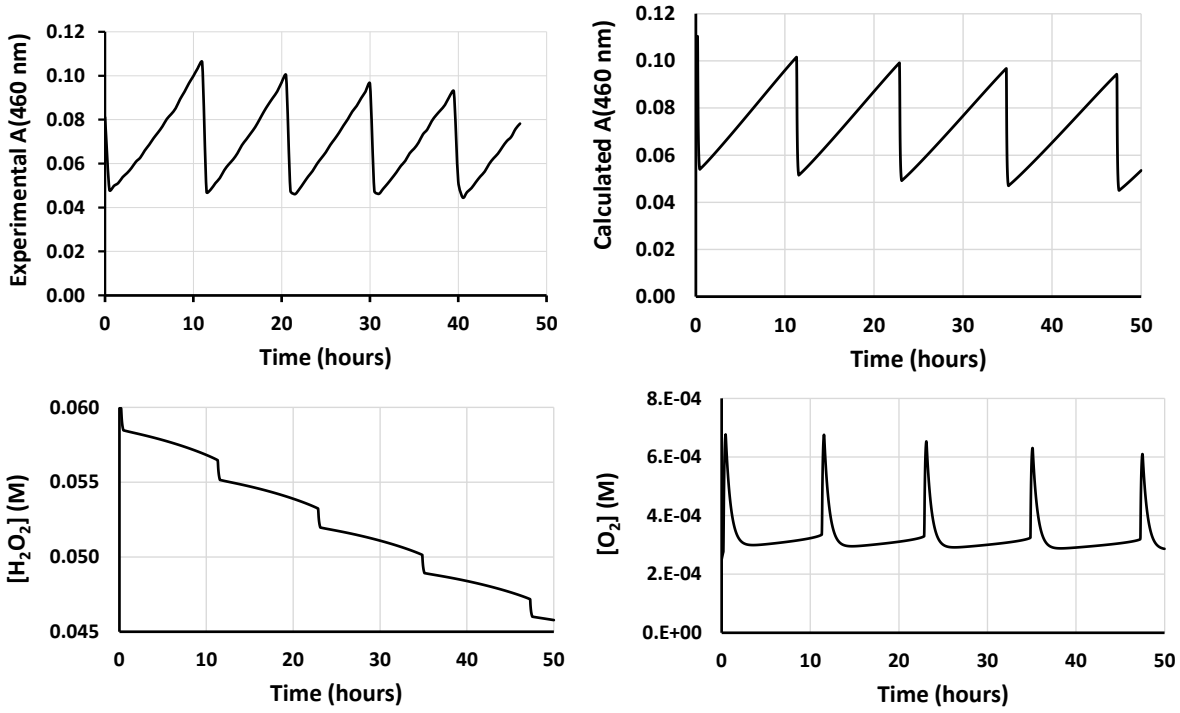


Figure 3. Time evolution of the absorbance at 460 nm observed by S. Furrow [46] and values calculated with the BLH model. $[HClO_4]_0$ = 0.030 M, $[KIO_3]_0$ = 0.048 M, $[H_2O_2]_0$ = 0.060 M, $[I_2]_0$ = 1.2×10^{-4} M, 25°C.

CONCLUSIONS

Bray actually discovered a periodic reaction in homogeneous solution. The BLH model answers an essential question asked by Liebhafsky, how to explain that H_2O_2 usually reduces I(+1) but oxides it when the iodide concentration is very small. It is because H_2O_2 reduces the monomer HOI but oxidizes its dimer I_2O. By adding well-known reactions of iodine compounds with each other and with H_2O_2 we obtain a model giving oscillations. The oxygen produced by the reaction has an effect on the oscillations but does not explain them. It oxidizes iodide ions by a radical mechanism which remains to be confirmed.

Table I. Model BLH-04.28.2024. Rate constants in mol L^{-1} and s.

R1	$IO_3^- + I^- + 2\ H^+ \rightleftharpoons HOI + HOIO$ $r_1 = k_1[IO_3^-]\,[I^-]\,[H^+]^2 - k_{-1}[HOI]\,[HOIO]$	$k_1 = 1500$	$k_{-1} = 210$
R2	$HOIO + I^- + H^+ \rightleftharpoons I_2O + H_2O$ $r_2 = k_2\,[H^+]\,[HOIO]\,[I^-] - k_{-2}\,[I_2O]$	$k_2 = 5\times10^9$	$k_{-2}/k_3 = 1.7\times10^{-7}$
R3	$I_2O + H_2O \rightleftharpoons 2\ HOI$ $r_3 = k_3\,[H^+]\,[I_2O] - k_{-3}\,[H^+]\,[HOI]^2$	$k_3 = 10^6$	$k_{-3} = 1.35\times10^8$
R4	$HOI + I^- + H^+ \rightleftharpoons I_2 + H_2O$ $r_4 = k_4\,[HOI][I^-] - k_{-4}\,[I_2]/[H^+]$	$k_4 = 2.0\times10^9$	$k_{-4} = 1.9\times10^{-3}$
	Down reactions		
R5	$HOI + H_2O_2 \rightleftharpoons HOOI + H_2O$ $r_5 = k_5\,[HOI][H_2O_2] - k_{-5}\,[HOOI]$	$k_5 = 8$	$k_{-5} = 6\times10^{-5}$
R6	$HOOI \rightleftharpoons I^- + H^+ + O_2$ $r_6 = k_6[HOOI] - k_{-6}[I^-][H^+]\,[O_2]$	$k_6/k_{-6} = 100$	$k_{-6} = 1\times10^6$
R7	$HOIO + H_2O_2 \rightarrow HOI + O_2 + H_2O$ $r_7 = k_7\,[HOIO][H_2O_2]/[H^+]$	$k_7 = 0.2$	
R8	$IO_3^- + H^+ + H_2O_2 \rightarrow HOIO + O_2 + H_2O$ $r_8 = (k'_8 + k''_8[H^+])\,[IO_3^-]\,[H_2O_2]$	$k'_8 = 1.3\times10^{-7}$	$k''_8 = 1.5\times10^{-5}$
	Up reactions		
R9	**Net:** $HOIO + H_2O_2 \rightarrow IO_3^- + H^+ + H_2O$ $r_9 = k_9\,[H_2O_2]\,[HOIO]^2/\{[H^+]\,(1+\square_9[H_2O_2])$	$k_9 = 1.7\times10^5$	$a_9 = 10$
R10	$I_2O + H_2O_2 \rightarrow HOI + HOIO$ $r_{10} = (k'_{10} + k''_{10}/[H^+])\,[I_2O]\,[H_2O_2]$	$k'_{10}/k_3 = 9.5\times10^{-2}$	$k''_{10}/k_3 = 9.5\times10^{-3}$
R11	$I^- + H^+ + H_2O_2 \rightarrow\ HOI + H_2O$ $r_{11} = (k'_{11} + k''_{11}[H^+])\,[I^-]\,[H_2O_2]$	$k'_{11} = 0.012$	$k''_{11} = 0.17$
	Effect of oxygen		
R12	$HOOI + H_2O_2 \rightleftharpoons HOO^\bullet + IO^\bullet + H_2O$ $r_{12} = k_{12}\,[HOOI]\,[H_2O_2] - k_{-12}\,[HOO^\bullet][IO^\bullet]$	$k_{12}/k_6 = 0.10$	$k_{-12}/k_{12} = 90$
R13	$HOO^\bullet + I^- + H^+ \rightarrow IO^\bullet + H_2O$ $r_{13} = k_{13}\,[HOO^\bullet][I^-][H^+]$	$k_{13} = 10^8$	
R14	$IO^\bullet + I^-\ (+\ H^+) \rightarrow HOI + I^\bullet$ $r_{14} = k_{14}\,[IO^\bullet][I^-]$	$k_{14} = 10^9$	
R15	$2\ I^\bullet \rightarrow I_2$ $r_{15} = k_{15}\,[I^\bullet]^2$	$k_{15} = 10^{10}$	
R16	$O_2 \rightleftharpoons O_2(g)$ $r_{16} = \max(0;\ k_{16}\,([O_2] - [O_2]_{equ})$	$k_{16} \sim 10^{-4}$ to 10^{-3} (1)	
	Other reactions		
R17	$2\ HOIO \rightarrow IO_3^- + HOI + H^+$ $r_{17} = (k'_{17}/[H^+] + k''_{17}/[H^+]^2)\,[HOIO]^2$	$k'_{17} = 0.045$	$k''_{17} = 0.065$
R18	$I_2 + I^- \rightleftharpoons I_3^-$ $r_{18} = 5\times10^9\,([I_2][I^-] - [I_3^-]/K_{18})$	$K_{18} = 713$	
R19	$IO_3^- + H^+ \rightleftharpoons HIO_3$ $r_{19} = 5\times10^9\,([IO_3^-][H^+] - K_{19}\,[HIO_3])$	$K_{19} = 0.28$	
R20	$HOI + H^+ \rightleftharpoons H_2OI^+$ $r_{20} = 5\times10^9\,(K_{20}\,[HOI]\,[H^+] - [H_2OI^+])$	$K_{20} = 0.3$	
R21	$I_2 \rightleftharpoons I_2(g)$	Usually neglected	

(1) Depends on experimental conditions.

The reactions producing radicals considered previously require too large activation energy and we propose a new formation reaction which finds its energy in the decomposition of H_2O_2 and whose rate increases with the concentration of oxygen. Its concentration in solution depends on its rate of transfer to the gas phase, including the rate of formation of bubbles, but oscillations can be observed under conditions where there is no bubble formation. The proposed mechanism also explains the complicated kinetics of iodine oxidation by H_2O_2 (reaction O). Its kinetics was studied under conditions where the conversions are small and the oxygen concentration close to its equilibrium value with the atmosphere. It also explains the end of the induction period of reaction O without added iodate under conditions where bubble formation is also excluded. Further work should provide more information regarding the radical mechanism of iodide ions oxidation by oxygen.

REFERENCES

[1] W. C. Bray, J. Am. Chem. Soc., 43(6) (1921) 1262-1267.
[2] K. R. Sharma and R. M. Noyes, J. Am. Chem. Soc., 97(1) (1975) 202–204.
[3] K. R. Sharma and R. M. Noyes, J. Am. Chem. Soc., 98(15) (1976) 4345–4361.
[4] H. A. Liebhafsky, J. Am. Chem. Soc., 53 (1931) 896-911.
[5] H. A. Liebhafsky, J. Am. Chem. Soc., 53 (1931) 2074-2090.
[6] H. A. Liebhafsky, J. Am. Chem. Soc., 54 (1932) 3499-508.
[7] I. Matsuzaki, R. Simic and H.A. Liebhafsky, Bull. Chem. Soc. Jpn., 45(11) (1972) 3367-3371.
[8] H. A. Liebhafsky and L.S. Wu, J. Am. Chem. Soc., 96(23) (1974) 7180-7.
[9] H. A. Liebhafsky, W. C. McGavock, R. J. Reyes, G. M. Roe and L.S. Wu, J. Am. Chem. Soc., 100(1) (1978) 87-91.
[10] H. A. Liebhafsky, R. Furuichi, and G. M. Roe, J. Am. Chem. Soc., 103(1) (1981) 51-56.
[11] I. Matsuzaki, T. Nakajima and H. A. Liebhafsky, Chem. Letters, (1974) 1463-1466.
[12] S. D. Furrow in Oscillations and Traveling Waves in Chemical Systems, R. J. Field and M. Burger ed., John Wiley & Sons, New York 1985.
[13] S.D. Furrow, J. Phys. Chem., 91(8) (1987) 2129-2135.
[14] P. Ševčik and L. Adamčiková, J. Phys. Chem. A, 102 (1998) 1288–1291.
[15] P. Ševčik, K. Kissimonová, and L. Adamčiková, J. Phys; Chem. A, 104 (2000) 3958-3963.
[16] K. Kissimonová, I. Valent, L. Adamčiková and P. Ševčik, Chem. Phys. Lett., 341(2001) 345-350.
[17] E. Szabo and P. Ševčík, J. Phys. Chem. A, 117 (2013) 10604−10614.
[18] G. Schmitz, J. Chim. Phys., 84 (1987) 957-965.
[19] Lj. Kolar-Anić, Ž. D. Čupić, S. Anić and G. Schmitz, J. Chem. Soc. Faraday Trans., 93 (1997) 2147
[20] Ž. D. Čupić, A. Ivanović-Šašić, St. Blagojević, Sl. Blagojević, Lj. Kolar-Anić and S. Anić, Kinet. Mech. Cat., 118 (2016) 27-38.
[21] G. Schmitz, Lj. Kolar-Anić, S. Anić and Ž. D. Čupić, J. Phys. Chem.A, 112 (2008)13452-13457.
[22] Lj. Kolar-Anić, Ž. D. Čupić, G. Schmitz and S. Anić, Chem. Eng. Sci., 2010, (65) (2010) 3718-3728.
[23] Ž. D. Čupić, V. Marković, A. Ivanović and Lj. Kolar-Anić, in Mathematical Modelling, C. R. Brennan Ed., Nova Science Publishers Inc., New York, 2011, pp. 111-178.
[24] G. Schmitz, Phys. Chem. Chem. Phys., 12 (2010) 6605-6615.
[25] G. Schmitz, Phys. Chem. Chem. Phys., 13 (2011) 7102-7111.
[26] D. R. Stanisavljev, M.C. Milenković, A. D. Popović-Bijelić and M.D. Mojović, J. Phys. Chem. A, 117 (2013) 3292−3295.

[27] M. C. Milenković and D. R. Stanisavljev, J. Phys. Chem. A, 116 (2012) 5541−5548.
[28] D. R. Stanisavljev, A. Fiona Taylor and I. Nuša Bubanja, Phys. Chem. Chem. Phys., 24 (2022) 14022-14032.
[29] D. R. Stanisavljev, A. Fiona Taylor and I. Nuša Bubanja, Phys. Chem. Chem. Phys., 25(29) (2023) 20109-20120.
[30] M. Reinhard, G. D. Redden and E. A. Voudrias in "Water Chlorination: Environmental Impact and Health Effects", Vol. 6, R. L. Jolley Ed., Lewis Publishers 1990, pp 859-870.
[31] J. D. Sivey, C. E. McCullough and A. L. Roberts, Environ. Sci. Technol., 44 (2010) 3357–3362.
[32] J. D. Sivey, J. S. Arey, P. R. Tentscher and A. L. Roberts, Environ. Sci. Technol., 47(3) (2013) 1330-1338.
[33] M. B. Heeb, J. Criquet, S. G. Zimmermann-Steffens and Urs von Gunten, Water research, 48 (2014) 15-42.
[34] G. Schmitz, Z. Noszticzius, G. Hollo, M. Wittmann and S. D. Furrow, Chem. Phys. Lett., 691 (2018) 44-50.
[35] S. D. Furrow, and G. Schmitz, Chem. Phys. Lett., 730 (2019) 186-190.
[36] D. D. Wagman, W. H. Evans, V. B. Parker, R. H. Schumm, I. Halow, S. M. Bailey, K. L. Churney, and R. L. Nuttall, “The NBS tables of chemical thermodynamic properties,” J. Phys. Chem. Ref. Data 11(Supplement 2), 1982, 1–392.
[37] G. Schmitz, Int. J. Chem. Kinet., 40 (2008) 647-652.
[38] A. Olexová, M. Mrákavová, M. Melicherčik and L. Treindl, Collect. Czech. Chem. Comm, 71(2006) 91−106.
[39] J. Sigalla and C. Herbo, J. Chim. Phys., 54 (1957) 733.
[40] G. Schmitz in Proceedings of the 16th Int. Conf. Fundam. Appl. Aspects Phys. Chem., Belgrade, Sept 26-30, Soc. Phys. Chem. Serbia, (2022) 179-186.
[41] J. M. Ball and J. B. Hnatiw, Can. J. Chem., 79 (2001) 304-311.
[42] G. Schmitz, Russian J. Phys. Chem., 83(9) (2009) 1447-1451.
[43] D. A. Armstrong, R. E. Huie, W. H. Koppenol, S. V. Lymar, G. Merényi, P. Neta, B. Ruscic, D.M. Stanbury, S. Steenken and P. Wardman, IUPAC Technical Report, Pure Appl. Chem., 87 (2015) 1139–1150.
[44] J. B. Burkholder, S. P. Sander, J. Abbatt, J. R. Barker, C. Cappa, J. D. Crounse, T. S. Dibble, R. E. Huie, C. E. Kolb, M. J. Kurylo, V. L. Orkin, C. J. Percival, D. M. Wilmouth and P. H. Wine, “Chemical kinetics and photochemical data for use in atmospheric studies,” Evaluation No. 19, Jet Propulsion Laboratory, Publication 19-5, Pasadena 2020.
[45] A.J. Elliot, Can. J. Chem., 70 (1992) 1658-1651.
[46] S. D. Furrow and G. Schmitz, Reac. Kinet. Mech. Cat., 135 (2022) 1163–1170.

CHITOSAN HYDROGEL BASED MICRONEEDLE TECHNOLOGY FOR PROLONGED RELEASE OF ACTIVES

K. Novakovic [1], E. Hutchinson [2], W.M. Lau [2], T. Abdelghany [3] and K.W. Ng [2]

[1]*School of Engineering, Newcastle University, Newcastle upon Tyne, UK*
(katarina.novakovic@newcastle.ac.uk)
[2]*School of Pharmacy, Newcastle University, Newcastle upon Tyne, UK*
[3]*School of Medicine, University of Aberdeen, Aberdeen, UK*

DOI: https://doi.org/10.46793/Phys.Chem24I.139N

ABSTRACT
Microneedle patches, with needles of sub-millimeter size, are non-invasive and pain free way of drug delivery. The needles penetrate skin, pass stratum corneum, but do not penetrate tissue which contains nerves and blood vessels. In this work, a new and unique chitosan-hydrogel based composite material was formulated to produce microneedle patches and their potency for extended drug delivery was validated using methylene blue as a model drug.

INTRODUCTION
Many chronic diseases require long-term and frequent medication that the patients can find difficult to manage. Transdermal microneedle (MN) patches are convenient as they empower patients to self-medicate in a pain-free way, while avoiding the first-pass effects associated with oral medications, thus increasing bioavailability. This is particularly pertinent for biologics which are almost completely degraded by enzymes in the gastrointestinal tract. However, conventional MN patches have some serious shortcomings including quick drug release, making them short-acting; as well as limited drug load, due to drug loading being constrained to the MN tips only, which inherently are limited in volume. [1,2]

To circumvent the limitations of current MN technology, we have formulated a composite material that provides Ultra-Long and Tunable Release of Actives (ULTRA) and, accordingly, ULTRA MN patches with increased drug loading and extended release of both small drugs and macromolecular biologics. The model drug used in this study was methylene blue (MB), a hydrophilic drug selected to push the limits of extended drug release and demonstrate the capabilities of the ULTRA MN patch.

METHODS
ULTRA MNs were manufactured by micromoulding. The composite was formulated by mixing a 40 % w/w polyvinylpyrrolidone (PVP) solution at a ratio of 1:1 v/v with the chitosan-genipin solution (1.5 % w/v chitosan dissolved in 1 % v/v acetic acid and 1 % w/v genipin dissolved in deionised (DI) water, mixed at a ratio of 9:1 v/v). PVP MN patches (used as control) were made with 40 % w/w PVP and DI water (instead of chitosan-genipin solution) (PVP:DI water = 1:1 v/v). For ULTRA loaded with MB, the drug was dissolved in DI water (20 % w/v) and mixed with the content of each MN array. Approximately 0.8 mL of the formed PVP solution or ULTRA mixture was loaded in each MN array mould [3]. PVP moulds were then kept uncovered to dry at room temperature for 48 h. ULTRA moulds were wrapped in Parafilm to prevent premature drying and incubated at 37°C for 24 h to allow chitosan-genipin gelation. The parafilm was then removed and the ULTRA arrays were allowed to dry at room temperature for 48 h. After drying, the MN arrays were demoulded using thin forceps, and kept in a plastic box at room temperature until further use.

Drug release studies were conducted using Franz diffusion cells (FDCs) where Parafilm was employed as a membrane to support the extended-release study. A receptor chamber (2.5 mL) was filled with PBS and stirred using a magnetic stirrer. The FDCs were placed in a water bath (32±2°C). The PBS in the receptor chambers were collected daily and replaced with fresh PBS. The concentration of MB was measured using a UV-VIS spectrophotometer at 668 nm. MN penetration capabilities were demonstrated using pig skin, responsibly sourced from a Newcastle University farm.

RESULTS AND DISCUSSION

The ULTRA MN patches demonstrated dual properties – the hard MN patch transitioned into a soft state when hydrated. The hard state provided the strength necessary for the ULTRA microneedles to puncture the skin to deliver the drug. The transition into a soft, foam-like material allowed for optimal drug loading and prolonged, controlled drug release (Figure 1).

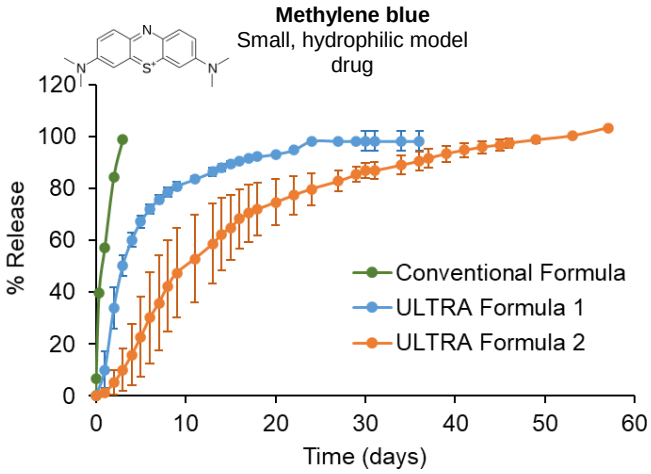


Figure 1. MB release from ULTRA microneedle formulations.

A model drug (MB) release, executed using Parafilm as the membrane in the FDC, demonstrated extended drug release capacity (Figure 1), prolonging drug dosing to over 1 month. Importantly, MN patches were synthesized under mild conditions, at room temperature, without harsh solvents, critical for many drugs especially for labile biologics. In a separate study, biocompatibility of MN formulations has also been confirmed. Due to the construction of the ULTRA MN patch, where the needles and the body of the patch remain connected during use, the ULTRA MN patch has a potential to become a go-to, high-drug-load formulation, replacing the need for daily medication.

CONCLUSION

In this work, a new chitosan-based hydrogel composite material has been constructed and used to produce MN patches loaded with methylene blue. MN patches demonstrated extended drug release and potency for high drug loading, indicating promise to resolve key limitations of existing MN-technology, including extended release whilst allowing for sufficient mechanical properties and incorporation of a variety of drugs.

Acknowledgment

This work was supported by the EPSRC IAA, Northern Accelerator, Newcastle University HEIF funding, and Innovate UK ICURe funding.

REFERENCES

[1] R. F. Donnelly, T. R. R. Singh, M.J. Garland, K. Migalska, R. Majithiya, C. M. McCrudden, P. L. Kole, T. M. T. Mahmood, H. O. McCarthy, A. D. Woolfson, Advanced Functional Materials, 22 (2012) 4879.

[2] J. G. Turner, L. R. White, P. Estrela, H. S. Leese, Macromolecular Bioscience, 21 (2021) 2000307.

[3] E. Smith, W. M. Lau, T. M. Abdelghany, Dj. Vukajlovic, K. Novakovic, K. W. Ng, International Journal of Pharmaceutics, 650 (2024) 123706.

NUMERICAL SIMULATIONS OF SPATIO-TEMPORAL PHENOMENA IN BELOUSOV-ZHABOTINSKY OSCILLATORY REACTION

S. Maćešić [1], A. Ivanović-Šašić [2] and Ž. Čupić [2]

[1]*University of Belgrade, Faculty of Physical Chemistry, Studentski trg 12-16, Belgrade, Serbia. (stevan.macesic@ffh.bg.ac.rs)*
[2] *University of Belgrade, Institute of Chemistry, Technology and Metallurgy, National Institute of the Republic of Serbia*
Njegoševa 12, 11000 Belgrade, Serbia.

DOI: https://doi.org/10.46793/Phys.Chem24I.143M

ABSTRACT
This study investigates the Belousov-Zhabotinsky reaction's spatio-temporal patterns using a realistic numerical model. Our simulations show that when spatially uniform system is unstable conditions, traveling waves emerge from a central point and move inwards when spatial inhomogeneities are introduced. Stable conditions, however, lead to Turing patterns, expanding outwards to form stationary zones of high and low concentrations. These findings emphasize diffusion's key role in shaping the BZ reaction's dynamics, offering insights for understanding nonequilibrium systems and potential applications in reaction engineering.

INTRODUCTION
Nonequilibrium systems captivate researchers with their complex and diverse range of phenomena, encompassing oscillations, pattern formation, and chaotic behaviour. A prime example within this type of systems is the Belousov-Zhabotinsky reaction [1], an oscillatory chemical system that has garnered significant attention from both experimental and theoretical perspectives. Extensive studies have unveiled the remarkable ability of the BZ reaction to manifest various temporal and spatiotemporal phenomena, including oscillations, chaos, traveling waves, and pattern formation. [2] Numerical simulations have emerged as invaluable tools for unravelling the intricate mechanisms governing these captivating phenomena. A deeper understanding of these mechanisms holds immense promise for harnessing the BZ reaction's potential as a smart material. However, previous numerical investigations exploring the BZ reaction under spatially non-uniform conditions have often relied on simplified models like the Oregonator [3]. This paper aims to advance the field by employing a realistic model, previously validated for spatially uniform systems, to simulate the spatiotemporal dynamics of the BZ reaction.

MODEL
The reaction network [4] of the Belousov-Zhabotinsky oscillatory reaction used in this study is described in Table 1. The network consists of 12 reaction steps, four of which are reversible. Additionally, the model includes 16 chemical species: bromide ion (Br^-), hypobromous acid (HOBr), hydrogen ion (H^+), bromine (Br_2), water (H_2O), bromous acid ($HBrO_2$), dibromine monoxide (Br_2O), bromate ($BrO3^-$), bromine dioxide (BrO_2), Ce^{3+}, Ce^{4+}, malonic acid ($CH_2(COOH)_2$), bromomalonic acid ($CHBr(COOH)_2$), P_1, P_2, and gaseous bromine ($Br_2(g)$). Among these, $CH_2(COOH)_2$ and BrO_3^- are the reactants, while $CHBr(COOH)_2$, $Br_2(g)$, P_1, and P_2 are the products of the overall process. The numerical simulations were performed under constant pH conditions, where the concentrations of H+ was considered constant. Concentration of and H_2O was also considered to be constant. To enhance the efficiency of the numerical simulations, the

concentrations of $CH_2(COOH)_2$ and BrO_3^- were also considered to be constant and incorporated into the values of appropriate reaction rate constants, resulting in a model with eight species i.e. variables: Br^-, HOBr, Br_2, $HBrO_2$, Br2O, BrO_2, Ce^{3+}, and Ce^{4+}.

Table 1. A set of reactions representing the model studied. [4]

Reactions	
$Br^- + HOBr + H^+ \longleftrightarrow Br_2 + H_2O$	(R_1),(R_{-1})
$HBrO_2 + Br^- + H^+ \longrightarrow Br_2O + H_2O$	(R_2)
$Br_2O + H_2O \longleftrightarrow 2HOBr$	(R_3), (R_{-3})
$Br^- + BrO_3^- + 2H^+ \longrightarrow HOBr + HBrO_2$	(R_4)
$2HBrO_2 \longrightarrow BrO_3^- + HOBr + H^+$	(R_5)
$BrO_3^- + HBrO_2 + H^+ \longleftrightarrow 2BrO_2^{\cdot} + H_2O$	(R_6), (R_{-6})
$Ce^{3+} + BrO_2^{\cdot} + H^+ \longleftrightarrow Ce^{4+} + HBrO_2$	(R_7), (R_{-7})
$CH_2(COOH)_2 + Br_2 \longrightarrow CHBr(COOH)_2 + Br^- + H^+$	(R_8)
$CH_2(COOH)_2 + Ce^{4+} \longrightarrow Ce^{3+} + P_1 + H^+$	(R_9)
$CHBr(COOH)_2 + Ce^{4+} \longrightarrow Ce^{3+} + Br^- + P_1$	(R_{10})
$Br_2O + CH_2(COOH)_2 \longrightarrow CHBr(COOH)_2 + HOBr$	(R_{11})
$Br_2 \longrightarrow Br_2(g)$	(R_{12})

To describe dynamics of this model the system of eight reaction-diffusion equations was used:

$$\frac{d[Br^-]}{dt} = D_1\nabla^2[Br^-] - k_1[Br^-][HOBr] + k_{-1}[Br_2] - k_2[HBrO_2] - k_4[Br^-] + k_8[Br_2] + k_{10}[Ce^{4+}] \quad (1)$$

$$\frac{d[HOBr]}{dt} = D_2\nabla^2[HOBr] - k_1[Br^-][HOBr] + k_{-1}[Br_2] + 2k_3[Br_2O] - 2k_{-3}[HOBr]^2 + k_4[Br^-] + k_5[HBrO_2]^2 + k_{11}[Br_2O] \quad (2)$$

$$\frac{d[Br_2]}{dt} = D_3\nabla^2[Br_2] + k_1[Br^-][HOBr] - k_{-1}[Br_2] - k_8[Br_2] - k_{12}[Br_2] \quad (3)$$

$$\frac{d[HBrO_2]}{dt} = D_4\nabla^2[HBrO_2] - k_2[Br^-][HBrO_2] + k_4[Br^-] - 2k_5[HBrO_2]^2 - k_6[HBrO_2] + k_6[BrO_2^*]^2 + k_7[BrO_2^*][Ce^{3+}] - k_{-7}[HBrO_2][Ce^{4+}] \quad (4)$$

$$\frac{d[Br_2O]}{dt} = D_5\nabla^2[Br_2O] + k_2[Br^-][HBrO_2] - k_3[Br_2O] + 2k_{-3}[HBrO_2]^2 - k_{11}[Br_2O] \quad (5)$$

$$\frac{d[BrO_2^*]}{dt} = D_6\nabla^2[BrO_2^*] + 2k_6[HBrO_2] - 2k_6[BrO_2^*]^2 - k_7[BrO_2^*][Ce^{3+}] + k_{-7}[HBrO_2][Ce^{4+}] \quad (6)$$

$$\frac{d[Ce^{3+}]}{dt} = D_7\nabla^2[Ce^{3+}] - k_7[BrO_2^*][Ce^{3+}] + k_{-7}[HBrO_2][Ce^{4+}] + k_9[Ce^{4+}] + k_{10}[Ce^{4+}] \quad (7)$$

$$\frac{d[Ce^{4+}]}{dt} = D_8\nabla^2[Ce^{4+}] + k_7[BrO_2^*][Ce^{3+}] - k_{-7}[HBrO_2][Ce^{4+}] - k_9[Ce^{4+}] - k_{10}[Ce^{4+}] \quad (8)$$

METHODS

Reaction-diffusion equations used to describe dynamics of BZ reaction network under spatially nonuniform conditions were used to solve by using numerical methods. For this purpose, FENICS package [5] was used. FENICS package employs finite element method to solve PDEs. An implicit Euler scheme was used to discretise time in the reaction-diffusion equations. To simulate the thin layer of solution in a reaction-diffusion system, a circular computational domain was used while the homogeneous Neumann boundary conditions were applied at the boundaries.

RESULTS AND DISCUSSION

Our numerical analysis of the BZ reaction network, based on the solutions of Eqs. 1-8, revealed two distinct phenomena, the characteristics of which are dictated by the stability of the spatially uniform system. In scenarios where the spatially uniform system exhibits instability, the presence of

diffusion leads to the emergence of traveling waves. These waves originate at the centre of the domain, where a concentration gradient is initially established. As time progresses and concentration gradients permeate the domain, the point of wave emergence gradually shifts away from the centre. Following their formation, the waves propagate at a constant velocity towards the centre of the computational domain. This traveling wave behaviour, as observed in our numerical simulations, is depicted in Figure 1.

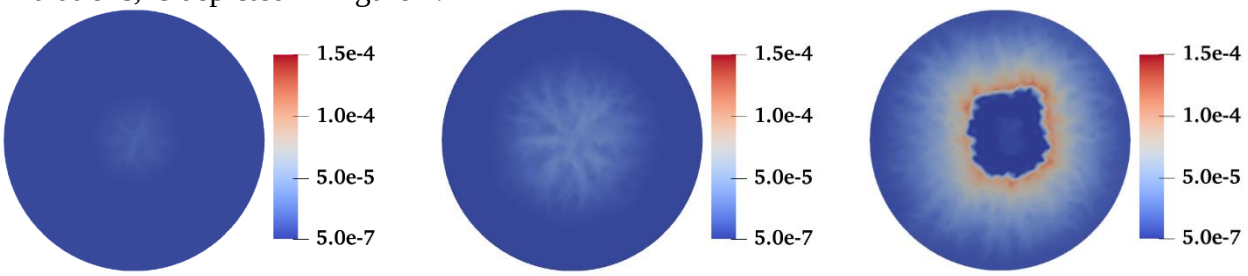


Figure 1. Trowelling waves obtained in the numerical simulations of the model presented in Table 1. Figures a-c represent the change of Br^- concentration in the computational domain over time: Parameters used in simulations: for the values of reaction rate constants are presented in Table 2, Parameters used in simulations: $k_1 = 7.03 \times 10^6\ M^{-2}\ s^{-1}$, $k_{-1} = 1.33 \times 10^{-5}\ s^{-1}$, $k_2 = 4.02 \times 10^5\ M^{-2}\ s^{-1}$, $k_3 = 10.00\ s^{-1}$, $k_{-3} = 1.75 \times 10^4\ M^{-1}\ s^{-1}$, $k_4 = 4.05\ M^{-3}\ s^{-1}$, $k_5 = 3.11\times 10^2\ M^{-1}\ s^{-1}\ M^{-1}\ s^{-1}$, $k_6 = 1.35\ M^{-2}\ s^{-1}$, $k_{-6} = 1.25 \times 10^3\ M^{-1}\ s^{-1}$, $k_7 = 1.01 \times 10^4\ M^{-2}\ s^{-1}$, $k_{-7} = 1.33\ M^{-1}\ s^{-1}$, $k_8 = 9.35 \times 10^{-2}\ M^{-1}\ s^{-1}$, $k_9 = 5.60 \times 10^{-4}\ M^{-1}\ s^{-1}$, $k_{10} = 1.62 \times 10^{-1}\ M^{-1}\ s^{-1}$, $k_{11} = 7.33 \times 10^{-2}\ M^{-1}\ s^{-1}$, $k_{12} = 2.27 \times 10^{-4}\ s^{-1}$;$D_1$-$D_8 = 6.0 \times 10^{-5}\ cm^2\ s^{-1}$. Initial concentrations: $[Br^-] = 5.00 \times 10^{-6}$ M, $[HOBr] = 4.00 \times 10^{-6}$ M, $[Br_2] = 1.50 \times 10^{-3}$ M, $[HBrO_2] = 3.00 \times 10^{-5}$ M, $[Br_2O] = 6.00 \times 10^{-6}$ M, $[BrO_2] = 4.00 \times 10^{-6}$ M, $[Ce^{3+}] = 2.00 \times 10^{-3}$ M, and $[Ce^{4+}] = 5.00 \times 10^{-4}$ M, except the centre of domain where the values of the concentration were set to be 2 times higher.

Conversely, when the spatially uniform system is stable, the introduction of diffusion gives rise to Turing patterns. These patterns emerge from the centre of the domain, where an initial concentration gradient is established, manifesting as stationary regions of high and low $[Br^-]$ concentrations.

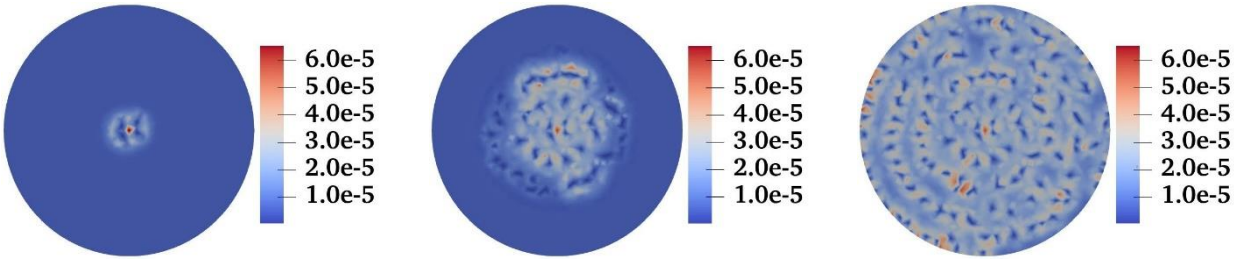


Figure 2. Turing patterns obtained in the numerical simulations of the model presented in Table 1 which represents. Figures a-c represent the change of Br^- concentration in the computational domain over time: Parameters used in simulations: for the values of reaction rate constants are presented in Table 2, Parameters used in simulations: $k_1 = 7.03 \times 10^6\ M^{-2}\ s^{-1}$, $k_{-1} = 1.33 \times 10^{-5}\ s^{-1}$, $k_2 = 4.02 \times 10^4\ M^{-2}\ s^{-1}$, $k_3 = 10.00\ s^{-1}$, $k_{-3} = 1.75 \times 10^4\ M^{-1}\ s^{-1}$, $k_4 = 4.05\ M^{-3}\ s^{-1}$, $k_5 = 3.11\ M^{-1}\ s^{-1}$, $k_6 = 1.35 \times 10^{-1}\ M^{-2}\ s^{-1}$, $k_{-6} = 1.25 \times 10^3\ M^{-1}\ s^{-1}$, $k_7 = 1.01 \times 10^4\ M^{-2}\ s^{-1}$, $k_{-7} = 1.33 \times 10^{-1}\ M^{-1}\ s^{-1}$, $k_8 = 9.35 \times 10^{-2}\ M^{-1}\ s^{-1}$, $k_9 = 5.60 \times 10^{-4}\ M^{-1}\ s^{-1}$, $k_{10} = 1.62 \times 10^{-1}\ M^{-1}\ s^{-1}$, $k_{11} = 7.33 \times 10^{-2}\ M^{-1}\ s^{-1}$, $k_{12} = 2.27 \times 10^{-4}\ s^{-1}$;$D_1$-$D_7 = 6.0 \times 10^{-5}\ cm^2\ s^{-1}$, $D_8 = 3.0 \times 10^{-2}\ cm^2\ s^{-1}$. Initial concentrations: $[Br^-] = 5.00 \times 10^{-6}$ M, $[HOBr] = 4.00 \times 10^{-6}$ M, $[Br_2] = 1.50 \times 10^{-3}$ M, $[HBrO_2] = 3.00 \times 10^{-4}$ M, $[Br_2O] = 6.00 \times 10^{-6}$, $[BrO_2] = 4.00 \times 10^{-6}$ M, $[Ce^{3+}] = 2.00 \times 10^{-3}$ M, and $[Ce^{4+}] = 5.00 \times 10^{-4}$ M, except the centre of domain where the values of the concentration were set to be 2 times higher.

Expanding outward from the centre, these Turing patterns grow until they reach the boundaries of the computational domain, at which point they remain constant in shape. Figure 2 illustrates the Turing patterns observed in our numerical simulations.

CONCLUSION

In conclusion, this study has employed a numerical simulation approach to investigate the spatiotemporal dynamics of the Belousov-Zhabotinsky oscillatory reaction. Our model, grounded in realistic chemical kinetics, successfully captured the emergence of both traveling waves in unstable conditions and Turing patterns in stable conditions. The observed traveling waves originated from a central concentration gradient and propagated towards the centre of the domain. Conversely, Turing patterns arose from a similar gradient, expanding outward to form stationary regions of high and low [Br^-] concentrations. These findings underscore the significant role of diffusion in shaping the spatiotemporal dynamics of the BZ reaction. This study contributes to a deeper understanding of nonequilibrium chemical systems and their potential applications, particularly in areas such as reaction engineering and pattern-forming processes.

Acknowledgment

We are thankful for the financial support from Ministry of Science, Technological Development, and Innovation of the Republic of Serbia (Grant Numbers 172015 and 45001, and Contract numbers 451-03-66/2024-03/200026 and 451-03-66/2024-03/200146. This research was also supported by Science Fund of Republic of Serbia #Grant Number. 7743504, Physicochemical aspects of rhythmicity in neuroendocrine systems: Dynamic and kinetic investigations of underlying reaction networks and their main compounds, NES.

REFERENCES

[1] B. Belousov, Sbornik Referatov Po Radiatsionnoi Meditsine Za (1958) 145–149.
[2] I.R. Epstein, J.A. Pojman in: An Introduction to Nonlinear Chemical Dynamics: Oscillations, Waves, Patterns, and Chaos, Oxford University Press, USA, 1998.
[3] P. Gray, S.K. Scott in: Chemical Oscillations and Instabilities: Non-Linear Chemical Kinetics, Oxford University Press, Oxford, New York, 1994.
[4] S.M. Blagojević, S.R. Anić, Ž.D. Čupić, N.D. Pejić, L.Z. Kolar-Anić, Phys. Chem. Chem. Phys. 10 (2008) 6658–6664.
[5] A. Logg, K.-A. Mardal, G. Wells in: Automated Solution of Differential Equations by the Finite Element Method: The FEniCS Book, Springer Science & Business Media, 2012.

CURVATURE-AMPLIFIED DIFFUSIVE INSTABILITY OF AN AUTOCATALYTIC REACTION-DIFFUSION FRONT – AN EXPERIMENTAL STUDY

L. Negrojević, S.N. Maharana and A. De Wit

Université Libre de Bruxelles, Nonlinear Physical Chemistry Unit (NLPC), CP 231, 1050 Bruxelles, Belgium (luka.negrojevic@ulb.be)

DOI: https://doi.org/10.46793/Phys.Chem24I.147N

ABSTRACT

Differences in the diffusive transport of chemical species can give rise to self-organized patterns like Turing stationary structures or cellular fronts. In this contribution, the diffusive instability patterns arising in radially propagating autocatalytic reaction-diffusion fronts are investigated experimentally. Compared to the traditionally studied cellular fronts in the planar geometry, we find a curvature-induced amplification of the amplitude of the front modulation in a radial geometry. Further experimental, theoretical, and numerical studies are being conducted to better understand these findings.

INTRODUCTION

Patterns are ubiquitous in Nature [1] – appearing in chemical [2], biological [3], and even ecological systems [4]. Understanding the characteristics of these patterns and conditions in which they arise leads to understanding the underlying universal laws that govern their emergence.

One type of chemical systems that can exhibit spatial patterns when coupled with diffusion are autocatalytic reactions, such as a cubic autocatalytic reaction of a scheme $2X+Y \rightarrow 3X$. Namely, when the autocatalyst X diffuses faster than the reactant Y of the autocatalytic reaction, the reaction-diffusion fronts of the autocatalytic reaction propagate through space at a constant speed, as planar fronts with no deformation [5]. However, if the autocatalyst X diffuses at a slower rate than the reactant Y, the front can feature cellular modulations with a characteristic wavelength and amplitude [6, 7].

Various experimental techniques have been developed to enable a selective reduction of the autocatalyst dynamics time scale, favoring the diffusive instability. As an example, for the chlorite-tetrathionate reaction, cellular fronts can be promoted or suppressed by applying an external electric field [8]. Another successful strategy involved immobilizing the autocatalytic species X through reversible reactions with quasi-immobile macromolecules [9], effectively decreasing its diffusive and reaction time scales.

In parallel, previous studies have demonstrated the substantial impact of radial geometries on the dynamics of reaction-diffusion-advection systems due to the inhomogeneity of the radial advective field [10,11,12].

Here we show experimentally that the radial geometry affects reaction-diffusion fronts even in the absence of any flow. We observe an amplification of the diffusive instability's amplitude in a radial system compared to the planar one. This phenomenon is attributed to the changes in the flux of the autocatalyst X and of the reactant Y due to the curvature of the front. Further theoretical and experimental studies to verify this hypothesis are underway.

METHODS

The chlorite-tetrathionate (CT) reaction [13] is used in the experiments. The slightly alkaline (pH=11) mixture of sodium chlorite ($[NaClO_2]_0$ = 20 mM) and potassium tetrathionate ($[K_2S_4O_6]_0$ = 5 mM) acts as the reactant Y of the autocatalytic reaction, while protons act as the autocatalytic species X. Bromophenol blue, an acidity indicator, is used for visualization of the reaction front as it provides a clear contrast between the reacted X and unreacted Y solutions.

A decrease in the mobility of the autocatalytic species, necessary for the emergence of lateral diffusive instabilities, is achieved by adding sodium polyacrylate SPA (MW = 100 kDa, concentration 24 mM), which binds reversibly with X, to the reactive mixture.

All reactions are performed within 2 mm thick chemically inert 2% agarose gels to ensure the absence of convection. In the radial configuration, the reaction is triggered by piercing the center of a circular gel using a needle soaked in an acidic solution. For the rectilinear configuration, initiating the reaction involves cutting a gel into two parts, soaking one part in an acid solution, and reuniting the pieces. The evolution of the instability is then monitored using a camera capturing images of the gels at one-minute intervals.

RESULTS AND DISCUSSION

Upon initiating the chemical reaction, a reaction-diffusion front of the CT autocatalytic reaction emerges. This front propagates at a constant velocity, transforming the slightly alkaline unreacted solution Y into the acidic, reacted one X. These regions can be differentiated by their color thanks to the presence of the acidity indicator, bromophenol blue.

The velocity of the front is significantly decreased with the addition of the complexing agent, sodium polyacrylate. The velocity reported in the absence of SPA was (360 ± 60) mm/min [12,13], while the one observed in these experiments, in the presence of SPA, is significantly lower, with a value of (0.18 ± 0.04) mm/min. After a certain time, as the front propagates, its symmetry is broken and the characteristic cellular patterns begin to emerge, both in the radial and rectilinear settings (Figure 1).

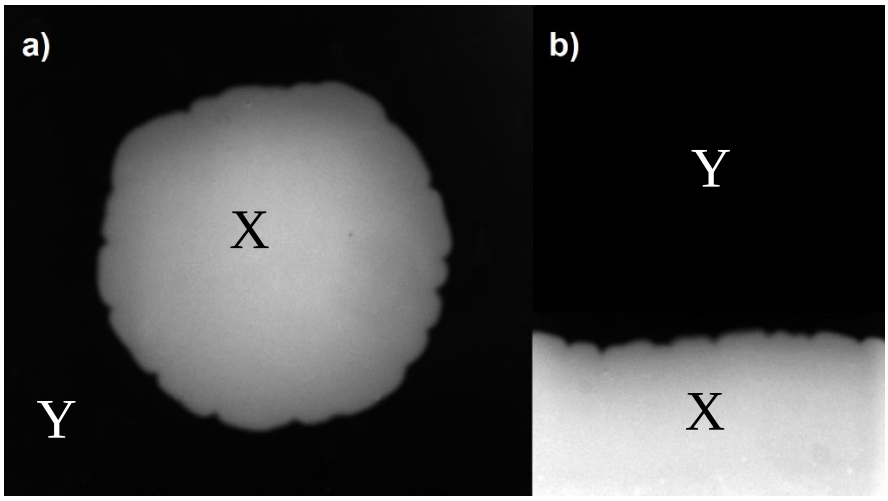


Figure 1. Cellular front of the chlorite-tetrathionate reaction in a (a) radial and (b) rectilinear geometry, 3 hours after initiation. X denotes the region filled with the autocatalyst, while Y presents the unreacted solution.

The analysis of the cellular modulation's amplitude evolution (Figure 2) shows that the amplitude in the radial configuration continues to grow for some time, even after its value in the planar geometry has reached a constant value. Once the amplitude reaches its constant value both in radial and rectilinear configurations, a significant difference is observed. The amplitude value in the radial case is (4.2 ± 0.5) mm and only (1.8 ± 0.3) mm in the planar case. This observation implies that the radial geometry can amplify the amplitude of the cellular modulation more than twice. Given these findings, it seems that the front is more unstable in radial settings, presumably due to the influence of curvature on diffusive transport.

CONCLUSION

In this contribution, we experimentally compared the emergence of the lateral instabilities of chlorite-tetrathionate reaction-diffusion fronts in both radial and rectilinear geometries in a convection-free medium.

We observe that the amplitude of the cellular modulation of the front is larger in radial settings than in the rectilinear ones, indicating that curvature plays a significant role in the dynamics of chemical fronts, even in the absence of advection.

These results underline the importance of geometrical considerations in spatially extended chemical systems. Further studies are being conducted to better understand these findings.

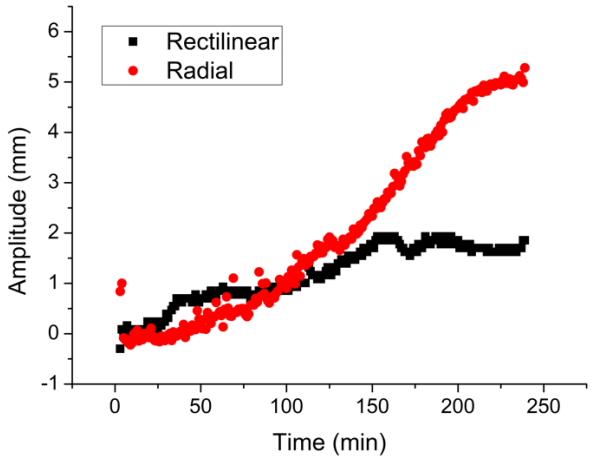


Figure 2. Comparison of experimentally observed temporal evolutions of diffusive instabilities in rectilinear and radial settings. Curvature inherent to radial geometries enhances the amplitude of the cellular modulation of the front.

Acknowledgments

The authors thank A. Comolli and F. Brau for fruitful discussions. LN and AD acknowledge the CoPerMix project funded by the European Union's Horizon 2020 research and innovation programme under the Marie Sklodowska-Curie grant agreement no 956457. SNM and AD thank the Actions de recherche concertées CREDI Programme of ULB for financial support.

REFERENCES

[1] M.C Cross, & P.C. Hohenberg, P.C. Rev. Mod. Phys. 65 (1993) 851–1112.
[2] A. De Wit, Annu. Rev. Fluid Mech. 52 (2020) 531–555.
[3] J. D. Murray, Mathematical Biology. vol. 17 (Springer New York, 1989).
[4] R. Lefever, O. & Lejeune, Bull. Math. Biol. 59 (1997) 263–294.
[5] A. N. Kolmogorov, I. G. Petrovsky, and N. S. Piskunov, Bull. Moscow State Univ. Ser. A: Math. Mech 1(6) (1937) 1-25.
[6] D. Horváth, V. Petrov, S. K. Scott, K. & Showalter, J. Chem. Phys. 98 (1993) 6332–6343.
[7] Á Tóth, I. Lagzi, & D. Horváth, J. Phys. Chem. 100 (1996) 14837–14839.
[8] Z. Virányi, A. Szommer, Á. Tóth, & D. Horváth, Phys. Chem. Chem. Phys. 006 (2004) 3396–3401.

[9] T. Rica, E. Pópity-Tóth, D. Horváth, & Á. Tóth, Phys. D Nonlinear Phenom. 239 (2010) 831–837.
[10] F. Brau, G. Schuszter, G. & A. De Wit, Phys. Rev. Lett. 118 (2017) 134101.
[11] F. Brau, &A. De Wit, J. Chem. Phys. 152 (2020) 054716.
[12] A. Comolli, L. Negrojević, F. Brau & A. De Wit, Phys. Chem. Chem. Phys. 25 (2023) 10604–10619.
[13] Á. Tóth, D. Horváth, & A. Siska, A. J. Chem. Soc. - Faraday Trans. 93 (1997) 73–76.

MODULATION OF OSCILLATORY PATTERNS IN BELOUSOV-ZHABOTINSKY SYSTEM

J. Maksimović [1], A. Hedrih [2], Ž. Čupić[3], M. Choiński[4], S. Maćešić[1] and A. Ivanović-Šašić[3]

[1] *Faculty of Physical Chemistry, University of Belgrade, Belgrade, Serbia*
[2] *Department of Mechanics, Mathematical Institute of Serbian Academy of Sciences and Arts (MI SANU) Knez Mihailova 36, 11 000 Belgrade, Serbia* (*handjelka@mi.sanu.ac.rs)*
[3] *Department of Catalysis and Chemical Engineering, Institute of Chemistry, Technology and Metallurgy, University of Belgrade, Belgrade, Serbia*
[4]*Institute of Information Technology, Warsaw University of Life Sciences - SGGW, Warsaw, Poland*

DOI: https://doi.org/10.46793/Phys.Chem24I.151M

ABSTRACT

The Belousov-Zhabotinsky reaction is a well-known nonlinear chemical oscillator. When this reaction is conducted in a Petri dish, it exhibits both temporal nonlinearity and spatial nonlinearity showing various spatial phenomena such as standard waves, accelerated waves, wave packets, spirals, anti-spirals, Turing structures, segmented spirals, and chaos. The purpose of this study is to investigate the changes in the oscillatory dynamics of the BZ reaction both in a closed reactor and in a Petri dish upon the addition of glycerol at a constant temperature. Glycerol was chosen for its affordability, wide availability, and versatile applications. Adding glycerol shortens the oscillograms both in closed reactor system and in a Petri dish. Obtained results indicate that in the Petri dish observed patterns included dash waves and segmented spirals in both the control and experimental setups; neither Turing structures nor anti-spirals were present in both cases.

INTRODUCTION

Belousov-Zhabotinsky (BZ) reaction is both thermosensitive and photosensitive and highly nonlinear oscillatory reaction [1]. The oscillatory dynamics of the BZ reaction can be influenced by various substances and different experimental designs. Namely, the BZ reaction can be modulated by silver thread [2], heavy water [3], lipid bilayer [4], liposomes [5], electric potential [6] and etc. Among potential substances that can react with the reactants of the BZ reaction, such as malonic and sulfuric acids, glycerol [7,8] (propane-1,2,3-triol) is proposed as a modulator of the oscillatory response. Glycerol is widely used in the cosmetic, chemical, food, and pharmaceutical industries. Due to its physical and chemical properties, it is used as a sweetener, in toothpaste for its bacteriostatic properties, as a thickening agent in liqueurs. Its low freezing point allows its use as an antifreeze. Its ability to bind water makes it valuable in ointments and skin care products. Because it reacts with nitric acid, glycerol has been used in the production of explosives, such as nitroglycerin. Additionally, it reacts with organic acids like citric and malic acids, and fatty acids like oleic and palmitic acids, serving as a key component in the production of triacylglycerol. Recently, it has become a byproduct of biodiesel production. Glycerol can be useful as corrosion protection substance [9].

METHODS

Experiments were performed in two independent series:

1. In a stationary well-stirred (rotational speed 900 rpm), thermostated (jacketed) reactor (temperature 36.8 ^{o}C). The total reaction volume was 26.0 ml. The temporal evolution of the system was monitored potentiometrically using a Pt electrode as a working electrode and a $Hg/HgSO_4$

electrode as a reference. 200 µl of different concentrations of glycerol (1.38 M; 2.76 M; 4.12 M and 5.51 M) were added to the BZ reaction at the minimum of the fifth oscillation.

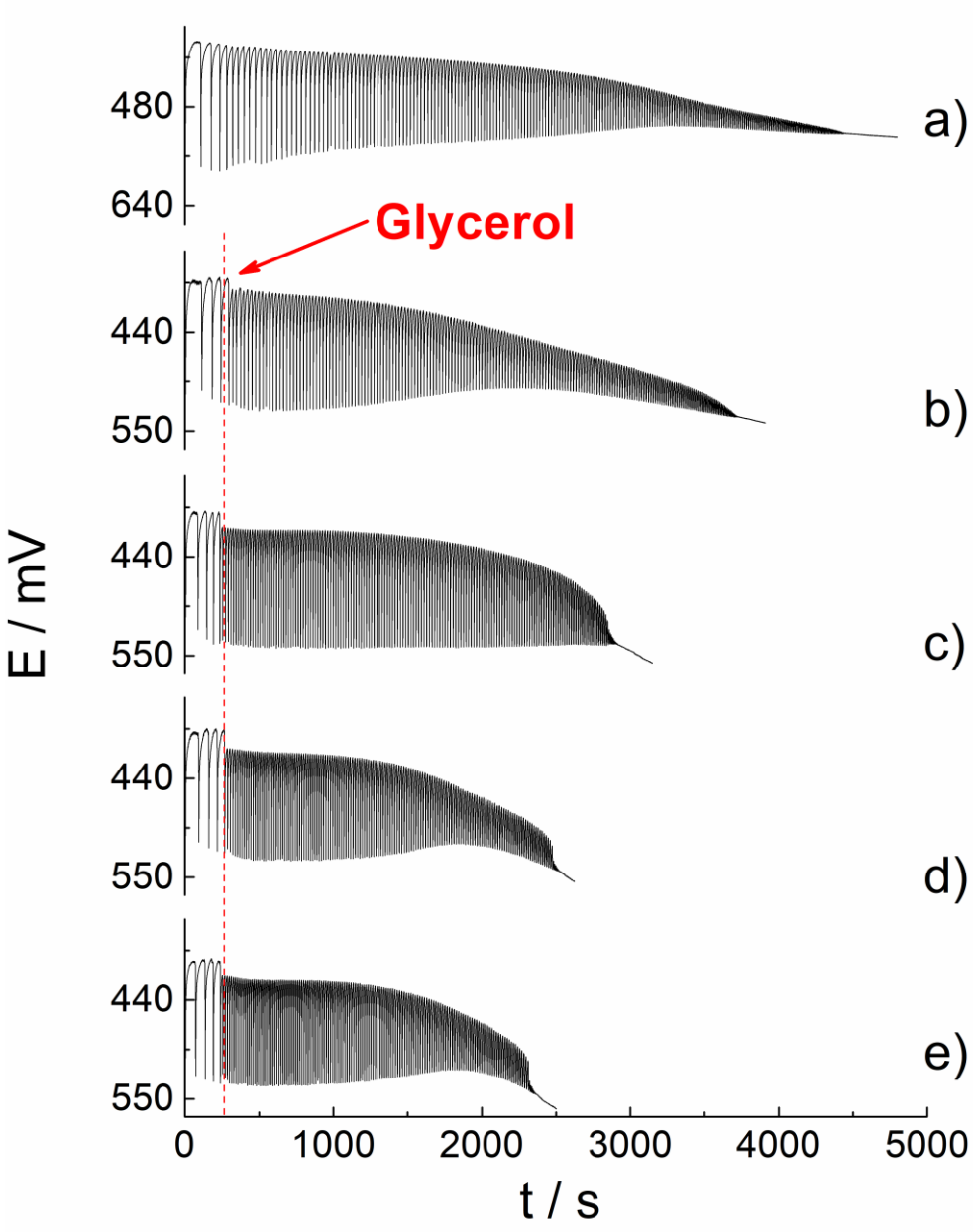


Figure 1. Experimentally obtained oscillograms – electrode potential (E) vs. time (t): without glycerol (a) and in the presence of different glycerol concentration: (b) 0.0105 M; (c) 0.0210 M; (d) 0.0315 M and (e) 0.0420 M. In all experiment glycerol was added at the minimum of the fifth oscillation.

2. In two Petri dishes, without stirring and at a constant temperature (25.0 °C). The total reaction volume in each Petri dish was 4 ml. The temporal evolution in the BZ system was recorded by a camera (Canon EOS 70D). One Petri dish is marked K (control) and the BZ reaction itself is monitored spatially therein, while the other Petri dish is marked E (experiment) and 15 minutes after the initiation of the BZ reaction with the ferroin solution, 30.5 µl of glycerol solution with a concentration of 2.7552 M was added. The concentration of glycerol in the BZ system was 0.0208 M.

In both series of experiments, the initial concentrations of reactants were: $[KBrO_3]_0$ = 0.259 M $[H_2SO_4]_0$ = 0.323 M, [Malonic Acid]$_0$ = 0.166 M, $[KBr]_0$ = 0.0746 M, [Feroin]$_0$ = $9.61 \cdot 10^{-4}$ M.

RESULTS AND DISCUSSION

The influence of glycerol concentration on the dynamical state in (BZ) oscillatory reaction was examined experimentally in closed system that is under batch conditions as well as in Petri dish. Obtained results showed that glycerol modulates amplitude, period, and time of BZ oscillatory reaction and these effects are glycerol quantity dependent. More precisely, as the amount of glycerol is increased in the system, both the period and amplitude decrease as well as the total duration of oscillations. It was concluded that the smallest used amount of glycerol has significant influence on the BZ dynamics, **Figure 1.**

During the evolution of BZ reaction in Petri dish specific types of structures were recorded.

Obtained results in Petri dish show that there are no anti-spirals in both K and E dishes. Dash waves and segmented spirals in both K and E are observed, Figure 2. In K dash waves gradually change into segmented spirals but in the end of reaction the spirals disappear. In E injecting the substance firstly does not affect the global behavior, although local dynamics is immediately lost and the system is turned to its oxidized form. Out of the injection point and its vicinity, waves are changing into spirals, but later this change is damped and reversed, and dash waves remain. As the reaction proceeds, substance diffuses to surrounding area and there are no patterns. Glycerol reacts both with malonic and sulfuric acid from the BZ reaction, forming esters. The specific types of esters form and their respective ratios under the given initial conditions can be determined through further analysis of the final reaction products.

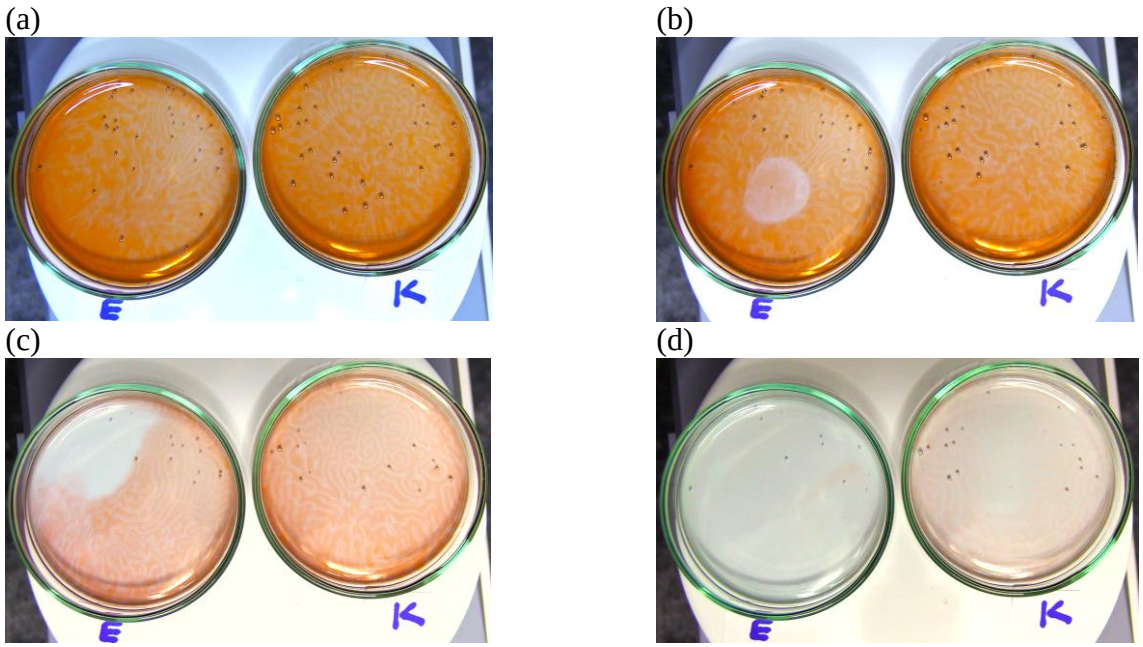


Figure 2. Time evolution of Belousov-Zhabotinsky oscillatory reaction perturbed with glycerol in Petri dish at (a) 4 min, (b) 17 min, (c) 60 min and (d) 100 min after reaction started. Glycerol concentration is 0.0208 M; **K - control** - BZ reaction mixture without the addition of glycerol, **E – experiment** - BZ reaction mixture to which glycerol was added 15 minutes after initiation of the reaction.

.

CONCLUSION

The oscillatory dynamics of the BZ reaction upon the addition of glycerol in both a closed reactor and a Petri dish were studied. The reaction was performed at a constant temperature. The obtained

results showed that glycerol modulates the amplitude, period, and duration of the BZ oscillatory reaction, and these effects are dependent on the quantity of glycerol. During the evolution of the BZ reaction in the Petri dish, dash waves and segmented spirals were observed in both the control and experimental dishes. Glycerol reacts with both malonic and sulfuric acids from the BZ reaction, forming esters.

The specific types of esters formed and their respective ratios could be influenced by temperature and glycerol concentration. Further analysis of the final reaction products of the modulated BZ reaction can reveal the types of esters as well as their specific ratios. Our future investigation will aim to study whether the type of esters, as the final product of the BZ reaction modulated by glycerol, can be controlled by temperature and/or glycerol concentration. It would be of great importance to investigate the potential applications of the esters formed in this way.

Acknowledgement

We are grateful to the financial support from Ministry of Science, Technological Development, and Innovation of Republic of Serbia trough University of Belgrade - Institute of Chemistry, Technology and Metallurgy – National Institute of the Republic of Serbia, (Contract numbers 451-03-66/2024-03/200026 and 451-03-66/2024-03/200146) and trough Mathematical Institute of Serbian Academy of Sciences and Arts. This research was also supported by Science Fund of Republic of Serbia #Grant Number. 7743504, NES.

REFERENCES

[1] V. Valérie in: Emergent properties of the compartmentalised Belousov-Zhabotinsky reaction, Chimie Nouvelle N°, 2018.
[2] A. S. Y. Wong, W. T. S. Huck, Beilstein J. Org. Chem., 13 (2017) 1486.
[3] O. Klink, W. Hanke, E. Gerbershagen, M. V. Fernandes de Lima in: Tech book: Wave Propagation in Materials for Modern Applications, Ch 12, 2010.
[4] M. S. Chern, N. Watanabe, K. Suga, Y. Okamoto, H. Umakoshi, Langmuir, 37 (2021) 6811.
[5] Y. Okamoto, K. Suga, N. Watanabe, H. Umakoshi, J. Phys. Chem. B., 124 (2020) 44 9862.
[6] M. Kuze, M. Horisaka, N. J. Suematsu, T. Amemiya, O. Steinbock, S. Nakata, Phys. Chem. A, 123(23) (2019) 4853.
[7] N. S. Audish, L. A. Jamil, S. A. Naman in: Conference: 4th International Scientific Conference of Salahaddin University Erbil April, 2011.
[8] A. Hedrih,_J. Maksimović, A. Ivanović-Šašić, Ž. Čupić in: Conference: ICTAM 2024, Daegu, Korea, August 25-30, 2024.
[9] L. Diaz-Ballote, L. Maldonado-Lopez, L. San-Pedro, E. H. Nuñez, J. Genesca, J. Serb. Chem. Soc., 87(7-8) (2022) 845.

MICROWAVE FIELD EFFECTS ON THE DYNAMICS OF BRAY-LIEBHAFSKY OSCILLATORY REACTION

K. Perić, I. N. Bubanja and D. Stanisavljev

University of Belgrade, Faculty of Physical Chemistry,
Studentski trg 12-16, 11000 Belgrade, Serbia. (itana.bubanja@ffh.bg.ac.rs)

DOI: https://doi.org/10.46793/Phys.Chem24I.155P

ABSTRACT

Even after 100 years of study, the mechanism of one of the simplest chemical oscillators (Bray-Liebhafsky (BL) reaction) still remains under great scientific debate. A better insight in to the reaction mechanism could be accomplished by non-chemical perturbations of the reaction dynamics. With this regard, in the present investigation, we examined effect of microwave (MW) field on the oscillatory evolution of BL reaction. We have found that a MW field of 188W emitted power, under isothermal conditions at 59 ^{o}C, disturbs the coherence of processes involved leading to irregular oscillations with significantly smaller amplitudes. Obtained results indicate that applied MW field inhibits quenching of oscillations and keeps the whole process in the state characterized with higher oxygen production (e.g. oxidation branch).

INTRODUCTION

The Bray-Liebhafsky [1,2] oscillatory reaction represents catalytic decomposition of hydrogen peroxide in to water and oxygen, in acidic medium and in the presence of iodate ions:

$$2H_2O_2 \xrightarrow{IO_3^-,\ H^+} 2H_2O + O_2 \quad (1)$$

It owes its oscillatory character to periodic alternation of two reaction pathways in which hydrogen peroxide may act either as reducing (Reduction branch, eq. 2) or oxidizing (Oxidation branch, eq. 3) agent.

$$2IO_3^- + 2H^+ + 5H_2O_2 \rightarrow I_2 + 6H_2O + 5O_2 \quad (2)$$

$$I_2 + 5H_2O_2 \rightarrow 2IO_3^- + 2H^+ + 4H_2O \quad (3)$$

Even though the core of BL reaction mechanism is accepted, its detailed mechanism still remains under great scientific debate, mostly because even modern techniques aren't completely suitable to follow and detect all reactive intermediates which are being formed and consumed in complex reaction pathways (2) and (3). Moreover, the key problem in understanding detailed BL reaction mechanism is closely related with iodine oxidation reaction or oxidation branch (3) which regardless of being kinetically unfavorable, due to a large thermodynamic barrier, periodically dominates overall BL reaction. Previous thermodynamic discussion [3] indicated that mentioned energetic barrier may be surmounted only in the presence of highly reactive radical species. This opened up many questions about possible energy redistribution mechanisms which could cause sudden formation of reactive radical species. Experimental investigations performed solely on BL oxidation branch showed that long induction period (caused by large energetic barrier) may be significantly reduced if oxygen removal from reaction mixture is restricted [4]. Previously published experimental investigations [5, 6] also confirm this. Namely, it is observed that when oxidation branch is performed without mixing short induction times are noticed. However if

reaction is performed under mild mixing conditions, induction periods are extremely prolonged and with noticeable stochasticity. [5] On the other hand, it is also noticed that stochasticity of induction periods is seriously reduced when inert glass particles, are added to the system. [6] Both effects strongly suggest participation of nucleation in the reaction mechanism, since formation of nucleuses is related with local fluctuations of dissolved oxygen concentrations and the stochasticity of the whole process. Therefore, without mixing (or with mixing in the presence of inert glass particles which may act as nucleation centers) induction periods are short and without stochasticity since at those conditions the nucleation is greatly facilitated. Moreover, adiabatic collapse of unstable oxygen nucleuses is accompanied by local energy release which may act as a coupling mechanism between heterogeneous processes and initiation of energetically demanding iodine oxidation reaction [6]. Effects of mixing were also observed, in milder form, in overall BL reaction [7]. Based on investigations of oxidation branch alone and previous investigations of D_2O [8] effects, microwave (MW) heating effects [9] on BL oscillatory evolution, periodic excitation of hydrogen peroxide [10], a new model of oscillatory BL reaction is proposed [11].

In the work presented here we have investigated the influence of MW irradiation on BL reaction dynamics. In comparison to previously published results [9], here an experimental setup was simplified in order to enable more unambiguous results, safer and more user-friendly procedure for following reaction dynamics by measuring gas flow instead of potentiometric method.

The microwave heating may have specific influence on the BL reaction mechanism since it changes dynamics of hydrogen bonds. The heat generated in a solution irradiated with microwaves is due to forced rotation of highly dipolar water molecules, causing hydrogen bonds to be broken and reformed constantly. In a similar way, ions present in the solution undergo forced translation, also breaking and reforming hydrogen bonds as they translate. The importance hydrogen bonds have in explaining oscillatory mechanisms has been explored through NMR spectroscopy, which showed large changes of H-NMR spectra during the oxidation branch domination, suggesting possible deformation of hydrogen bonds in local high energy regions. [8]

METHODS

BL reaction dynamics was followed by gas flow measurements during the course of reaction. This particular method was chosen in order to avoid any ambiguities which may arise from using potentiometric measurements along with a microwave field, considering the fact that a small part of the electrode must stay unshielded, and could result in a net field on the tip of the electrode, possibly interfering with the reaction pathways. For this purpose, a reaction vessel was constructed (Figure 1), consisting of three channels, one for the fiber optic temperature sensor, one connected to the gas flow meter and one for the insertion of H_2O_2.

Reaction vessel initially contained solution of KIO_3 and H_2SO_4 and when temperature reached constant value H_2O_2 was added. The initial concentrations of the components at the start of the reaction were: $[KIO_3]_0 = 3.4 \times 10^{-1}$ M, $[H_2SO_4]_0 = 5 \times 10^{-2}$ M, $[H_2O_2]_0 = 3.3 \times 10^{-1}$ M. The solutions were prepared with deionized water (18 MΩ cm). Temperature during MW heating was kept constant at 59 ^oC within 1 ^oC, by a PolyScience thermostat connected to the reaction vessel. Once the gas evolution starts, it is first guided through a gas-washing bottle with drierite to eliminate humidity and iodine vapors which could damage the flow meter. Another empty gas-washing bottle is placed after the detector, to provide more stable conditions and to compensate for changes in the airflow inside the laboratory. The flow meter used is Winsen gas flow meter connected to a homemade voltmeter (PC-MultiLab EH4 16-bit ADC) adjusted so that gas flow information can be continuously recorded. The reaction vessel along with the water recirculation jacket connected to the thermostat is placed into the CEM MW reactor with modifiable emitted power (Discover). First, a reference oscillogram was obtained, following the reaction in the absence

of a MW field. This was also done with the vessel inside the reactor, setting the power to 0 W, with the purpose of having the same mixing conditions, by using magnetic stirrer built in MW reactor in both experiments. The same mixture was used to determine the thermostat temperature needed to obtain 59 ºC once the reactor is working at 188W. The second oscillogram was recorded during the irradiation of the solution with microwaves at a power of 188W.

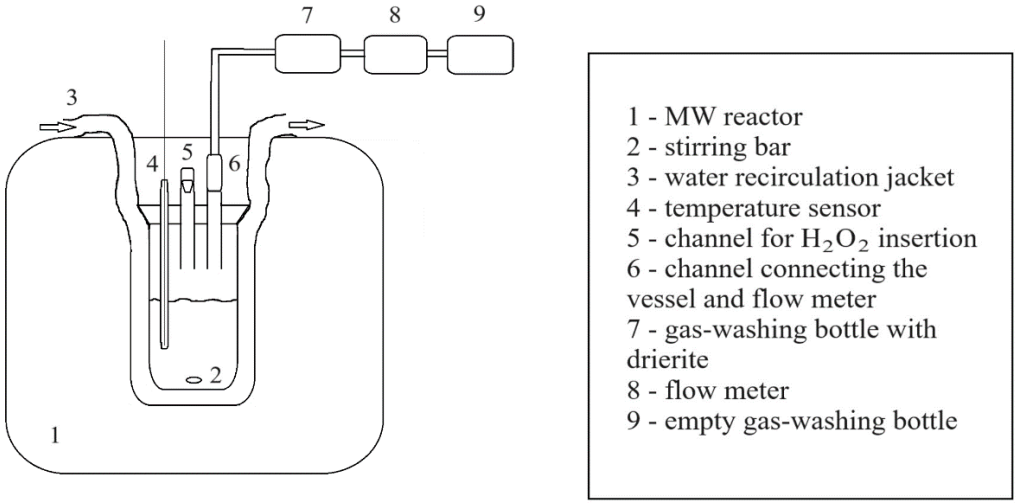


Figure 1. Schematic view of experimental setup.

RESULTS AND DISCUSSION

As can be seen in Figure 2, in comparison to reference oscillogram (Figure 2. (a)) once the reaction mixture is irradiated with 188W MW emitted power (Figure 2. (b)) irregular oscillations with significantly smaller amplitudes take place which is in good agreement with previously published studies of MW effects on BL oscillator followed by potentiometric method [9].

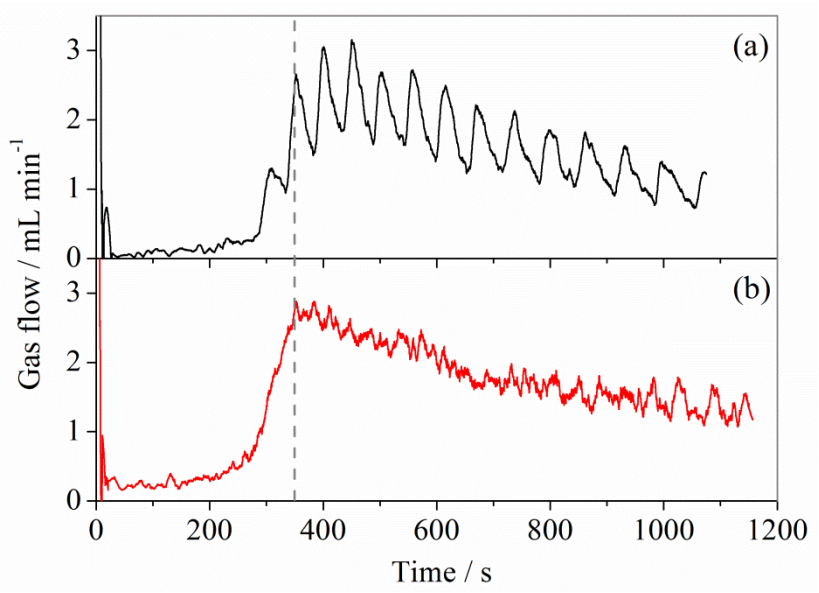


Figure 2. Smoothed signal of the gas flow over the course of BL reaction obtained (a) without and (b) with MW irradiation.

In accordance with our proposed BL model, fate of unstable oxygen nucleuses is a twofold, they can either collapse or facilitate oxidation branch or they may grow through coalescence and diffusion into a larger bubbles thus leaving the solution and preventing the process of nucleation. Results indicate that application of MW irradiation showed no visible influence on the length of induction period. On the other hand, it seems that in experiment performed under MW irradiation system favours the state in which oxidation branch is the dominant process since high gas flow values are maintained with not fully and clearly developed oscillations e.g. irregular oscillations with very small amplitudes. Observed effects could be potentially explained in a way that MW disrupts the coherent evolving of oscillations trough changing dynamics of water hydrogen-bond-network. Decoherence of oscillations means that processes in different parts of the reaction volume are not in tune and are evolving with incoherent phases.

CONCLUSION

The influence of microwaves on the dynamics of BL oscillatory reaction was examined and followed by improved experimental design involving continuous measurements of gas flow instead of usually used potentiometric method. Obtained results suggest that applied MW field of 188 W disrupts the ordered evolution of reduction and oxidation processes (1) and (2) leading to incoherent oscillations by changing dynamics of water hydrogen-bond-network, and keeping the whole process in the state characterized with higher oxygen production. This confirms previous findings in which MW effects on BL reaction were followed with potentiometric method under different experimental conditions. We hope that the investigation of nonchemical perturbations of the BL reaction dynamics may provide more profound understanding of its peculiar mechanism.

Acknowledgment

This work was supported by the Ministry of Science, Technological Development and Innovation of the Republic of Serbia (grant no 451-03-65/2024-03/200146).

REFERENCES

[1] W. C. Bray, J. Am. Chem. Soc., 43 (1921) 1262.
[2] W. C. Bray, H. A. Liebhafsky, J. Am. Chem. Soc., 53 (1931) 38.
[3] K. Stevanović, I. N. Bubanja, D. Stanisavljev, Chem. Phys. Lett., 684 (2017) 257.
[4] A. Olexová, M. Mrákavová, M. Melicherčík, Ľ. Treindl, Collect. Czechoslov. Chem. Commun., 71 (2006) 91.
[5] D. Stanisavljev, K. Stevanović, I. N. Bubanja, Chem. Phys. Lett., 706 (2018) 120.
[6] K. Stevanović, I. N. Bubanja, D. Stanisavljev, J. Phys. Chem. C, 123 (2019) 16671.
[7] I. N. Bubanja, D. Stanisavljev, Inorg. Chem. Commun., 141 (2022) 109528.
[8] D. Stanisavljev, N. Begović, Z. Žujović, D. Vučelić, G. Bačić, J. Phys. Chem. C, 102 (1998) 6887.
[9] D. Stanisavljev, A. Djordjević, V. Likar-Smiljanić, Chem. Phys. Lett., 423 (2006) 59.
[10] D. Stanisavljev, A. F. Taylor, I. N. Bubanja, Phys. Chem. Chem. Phys., 25 (2023) 20109.
[11] D. Stanisavljev, J. Phys. Chem. A, 114 (2010) 725.

NONLINEAR PULSE PAIRS WITH OSCILLATORY TAILS IN A QUINTIC REACTION-DIFFUSION MODEL WITH CROSS DIFFUSION AND CROSS ADVECTION

E. P. Zemskov

FRC CSC RAS, Russian Academy of Sciences,
Vavilova 40, 119333 Moscow, Russia
(dr.zemskov@gmail.com)

DOI: https://doi.org/10.46793/Phys.Chem24I.159Z

ABSTRACT
We describe analytically nonlinear traveling waves with oscillatory tails in a tristable piecewise-linear reaction-diffusion system, which approximates a quintic FitzHugh-Nagumo model, with linear cross-diffusion and cross-advection terms of opposite signs. Bound states of the waves, namely pairs of coupled traveling pulses, are studied. The wave profiles are found and the speed of propagation is calculated. The pattern of the pulse pairs is similar to the bright-dark-bright soliton complexes.

INTRODUCTION

Nonlinear waves in many excitable media demonstrate complex dynamics when they interact. So far, the interaction of pulse waves leads to the pattern formation of stable localized structures or bound states. In a similar reaction-diffusion system with a quintic kinetic term related to the description of catalytic or electrochemical oscillations [1] also occur different spatiotemporal patterns. Multiplicity of patterns and waves has been observed in a variety of reaction-diffusion systems with cross diffusion [2]. In the FitzHugh-Nagumo (FHN) model with cross diffusion [3], [4], wavy traveling fronts [5], solitary pulses and their infinite sequences (periodic wave trains) [6] have been described, as well as hybrid pulse-front waves [7] and traveling bound states or finite pulse sequences (so-called multipulsons) [8]. Such traveling bound states, namely the pulse pairs, are the aim of the present research of an extension of the FHN model to a quintic nonlinearity [9] and with cross-advection terms [10]. As in previous study [9], we use the McKean's piecewise-linear approximation [11], [12] with two Heaviside step functions for the quintic nonlinearity of the activator reaction term in the model. Such a construction allow us to find a variety of waves with complex profiles that are specific to the quintic FHN model with cross terms, the traveling bright-dark-bright pulses, in analogy with solitons of similar shapes in the nonlinear Schrödinger-Ginzburg-Landau [13] and the quintic Swift-Hohenberg [14] equations.

METHODS

The quintic FHN model with linear cross diffusion exhibits different traveling waves: standard (kink-type) and non-monotonic fronts, pulses of simple and complex shapes, and infinite sequences of pulses - periodic wave trains [9]. Moreover, here are expected different bound states of these traveling waves - finite sequences of pulses that have been observed [8] in the bistable FHN model with cross diffusion. Here we describe such a bound state, namely a pair of coupled traveling pulses, in the piecewise-linear version of the quintic FHN model. This construction consists of seven parts, those analytical expressions have been obtained earlier in [5].

The prototypical FitzHugh-Nagumo model with a quintic nonlinear term is [9]

$$\frac{\partial u}{\partial t} = u(1-u^2)(u-a)(u-b) - v + D\frac{\partial^2 u}{\partial x^2} + h\frac{\partial^2 v}{\partial x^2},$$

$$\frac{\partial v}{\partial t} = \varepsilon(u-\gamma v) + D\frac{\partial^2 v}{\partial x^2} - h\frac{\partial^2 u}{\partial x^2},$$

where the constants *a* and *b* are the excitation thresholds, *D* and *h* are the self- and cross-diffusion coefficients and ε is the ratio of the time scales. The corresponding piecewise-linear McKean-type model (for the tristable case) with cross-advection terms is described by the equations

$$\frac{\partial u}{\partial t} = f(u,v) + D\frac{\partial^2 u}{\partial x^2} + h\frac{\partial^2 v}{\partial x^2} + j\frac{\partial v}{\partial x},$$

$$\frac{\partial v}{\partial t} = \varepsilon(u-v) + D\frac{\partial^2 v}{\partial x^2} - h\frac{\partial^2 u}{\partial x^2} - j\frac{\partial u}{\partial x},$$

where *j* is the cross-advection constant and the reaction function (kinetic term) reads

$$f(u,v) = \begin{cases} -u-v-1, & u \le b, \\ -u-v, & b < u \le a, \\ -u-v+1, & u > a, \end{cases}$$

i.e., the activator kinetic term contains two Heaviside step functions *H(u - a)* and *H(u - b)*. In this research we restrict ourselves to the symmetric case with $a = -b = 1/4$ and $\varepsilon = 1$. Analytical solutions for the traveling waves have the form $u = u(\xi)$ and $v = v(\xi)$, where $\xi = x - ct$ is the traveling frame coordinate and *c* is the wave speed.

RESULTS AND DISCUSSION

We find a solution for the traveling wave with a zigzag-shaped profile, which is specific to the quintic (tristable) model. This solution contains normal and inverted peaks in the core of the wave. Two normal peaks are located in the upper part of the piecewise-linear system, while the inverted peak is in the lower part, providing the interior zone with the growing and decaying pieces of the wave

$$u(\xi) = \begin{cases} u_1^+(\xi), \\ u_2^+(\xi) + u_2^-(\xi) + 1/2, \\ u_3^+(\xi) + u_3^-(\xi), \\ u_4^+(\xi) + u_4^-(\xi) - 1/2, \\ u_5^+(\xi) + u_5^-(\xi), \\ u_6^+(\xi) + u_6^-(\xi) + 1/2, \\ u_7^-(\xi), \end{cases} \quad v(\xi) = \begin{cases} v_1^+(\xi), \\ v_2^+(\xi) + v_2^-(\xi) + 1/2, \\ v_3^+(\xi) + v_3^-(\xi), \\ v_4^+(\xi) + v_4^-(\xi) - 1/2, \\ v_5^+(\xi) + v_5^-(\xi), \\ v_6^+(\xi) + v_6^-(\xi) + 1/2, \\ v_7^-(\xi), \end{cases}$$

where

$$u_n^{\pm}(\xi) = e^{k_{\pm}\xi}\left[A_{n1,2}\cos(l_{\mp}\xi) + A_{n3,4}\sin(l_{\mp}\xi)\right],$$

$$v_n^{\pm}(\xi) = e^{k_{\pm}\xi}\left[B_{n1,2}\cos(l_{\mp}\xi) + B_{n3,4}\sin(l_{\mp}\xi)\right],$$

$$n = 1,2,\dots,7,$$

and the solution parameters and the integration constants are the same as in [5]. The results of the analytical calculations for these traveling waves (pulse pairs) are illustrated in **Figure 1** in pure cross-diffusion and cross-advection case, i.e., when the self-diffusion terms vanish.

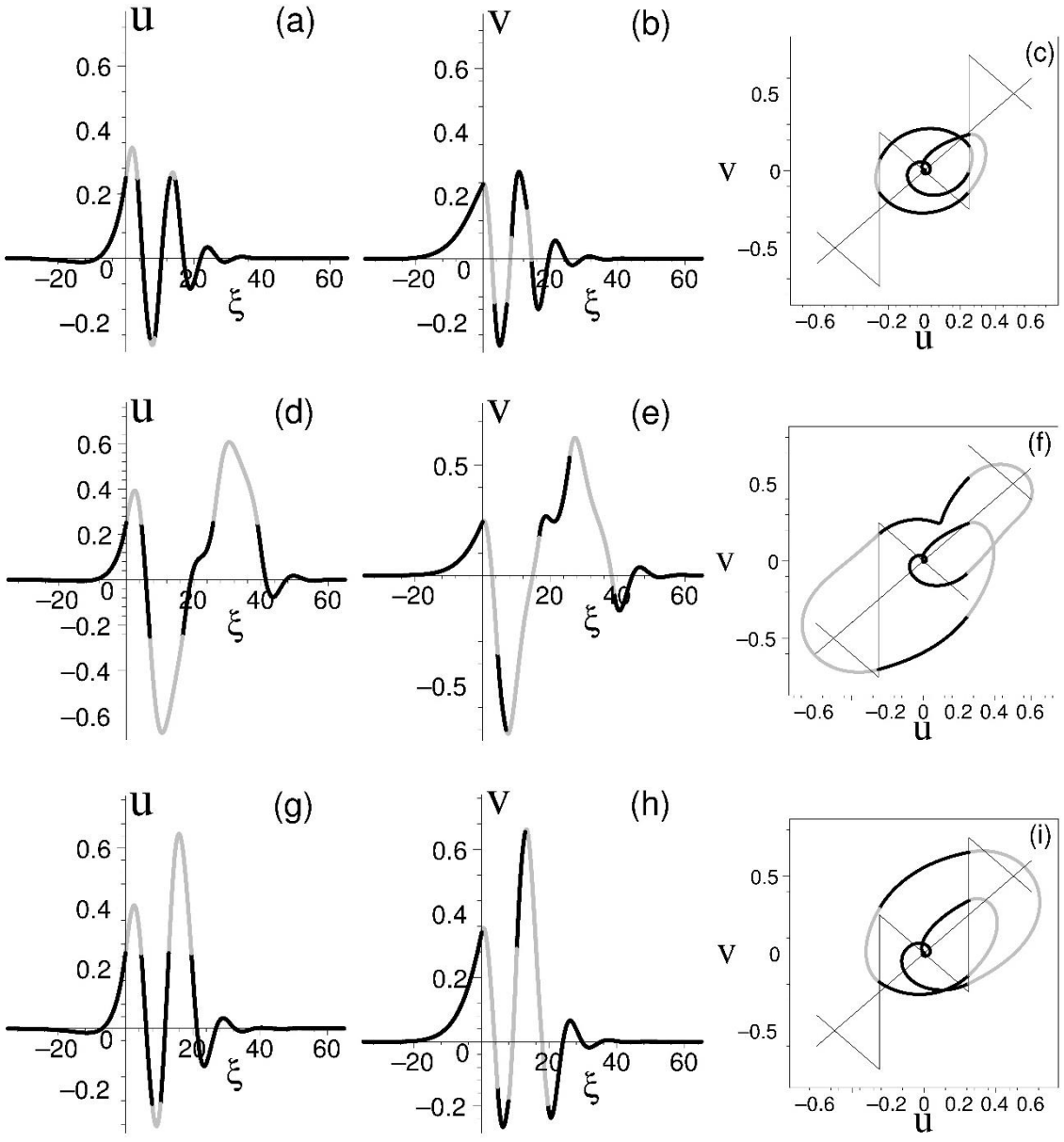


Figure 1. Examples of pulse pairs (bound states) in the quintic FitzHugh-Nagumo model with pure cross diffusion and cross advection. The waves propagate from left to right in panels (a,b,d,e,g,h). The speeds of propagation are: (a,b,c) $c \approx 7.212$, (d,e,f) $c \approx 6.046$, (g,h,i) $c \approx 6.474$. The nullclines of the model are shown as thin lines in panels (c,f,i). The values of the model parameters are fixed at $a = -b = 1/4, \varepsilon = 1, D = 0, h = 10, j = 0.1$.

There exist several waves with different profiles and values of the propagation speed, three examples are shown in **Figure 1**. Such a multiwave regime of propagation is the characteristic feature of the FHN model with cross diffusion [6], [7], [8], [9], [10]. The behavior of the solutions for the system with pure cross diffusion (with $j = 0$) is similar. The common characteristic feature of all solutions is the specific oscillatory character of the wave profiles, which forms a spiral in the (*u*,*v*)-plane (**Figure 1 c,f,i**).

CONCLUSION

We have studied the extension of the FitzHugh-Nagumo model with cross diffusion and cross advection and described the form of analytical solutions for traveling pulse pairs representing localized bound states. The inclusion of cross-diffusion terms in the model equations leads to a new feature: specific behavior of wave propagation, namely solitonic-type interaction upon their collision [15], [16], [17]. The investigation of the wave interactions in this FitzHugh-Nagumo model may be direction for the future research.

REFERENCES

[1] M. Sheintuch, O. Nekhamkina, J. Chem. Phys., 109 (1998) 10612.
[2] V. K. Vanag, I. R. Epstein, Phys. Chem. Chem. Phys., 11 (2009) 897.
[3] V. N. Biktashev, M. A. Tsyganov, Proc. Royal Soc. A, 461 (2005) 3711.
[4] F. Berezovskaya in: Mathematical Sciences with Multidisciplinary Applications, Vol.157, B. Toni (Ed.), Springer, Cham, 2016.
[5] E. P. Zemskov, K. Kassner, M. J. B. Hauser, Phys. Rev. E, 77 (2008) 036219.
[6] E. P. Zemskov, M. A. Tsyganov, W. Horsthemke, Phys. Rev. E, 95 (2017) 012203.
[7] E. P. Zemskov, M. A. Tsyganov, W. Horsthemke, Phys. Rev. E, 97 (2018) 062206.
[8] E. P. Zemskov, M. A. Tsyganov, W. Horsthemke, Phys. Rev. E, 101 (2020) 032208.
[9] E. P. Zemskov, M. A. Tsyganov, K. Kassner, W. Horsthemke, Chaos, 31 (2021) 033141.
[10] E. P. Zemskov, M. A. Tsyganov, G. R. Ivanitsky, W. Horsthemke, Phys. Rev. E, 105 (2022) 014207.
[11] H. P. McKean, Adv. Math., 4 (1970) 209.
[12] J. Rinzel, J. B. Keller, Biophys. J., 13 (1973) 1313.
[13] B. A. Malomed, Phys. Rev. A, 44 (1991) 6954.
[14] H. Sakaguchi, H. R. Brand, Physica D, 97 (1996) 274.
[15] M. A. Tsyganov, J. Brindley, A. V. Holden, V. N. Biktashev, Phys. Rev. Lett., 91 (2003) 218102.
[16] M. A. Tsyganov, V. N. Biktashev, J. Brindley, A. V. Holden, G. R. Ivanitsky, Phys. - Uspekhi, 50 (2007) 263.
[17] V. N. Biktashev, M. A. Tsyganov, Phys. Rev. Lett., 107 (2011) 134101.

AN ALTERNATIVE WAY OF PRESENTING THE TEMPERATURE DEPENDENCE IN THE BRIGGS-RAUSCHER OSCILLATORY REACTION

J. Maksimović [1], K. Stevanović [2], M. Simović-Pavlović [3] J. Senćanski [4] and M. Pagnacco [5]

[1] *University of Belgrade, Faculty for Physical Chemistry, Studentski trg 12-14, 11158 Belgrade, Serbia.*
[2] *University of Belgrade, Institute of Nuclear Sciences Vinča, Department for Bioinformatics and Computational Chemistry, Mike Petrovića Alasa 12-14, 11351 Vinča, Belgrade, Serbia. (kristina.stevanovic@vin.bg.ac.rs)*
[3] *University of Belgrade, Faculty of Mechanical Engineering, Kraljice Marije 12-16, 11120 Belgrade, Serbia.*
[4] *University of Belgrade, Institute for General and Physical Chemistry, Studentski trg 12/V, 11158, Belgrade, Serbia.*
[5] *University of Belgrade, Institute of Chemistry, Technology and Metallurgy, Center of Catalysis and Chemical Engineering, Njegoševa 12, 11000 Belgrade, Serbia.*

DOI: https://doi.org/10.46793/Phys.Chem24I.163M

ABSTRACT
The Briggs-Rauscher (BR) reaction represents one of the most conspicuous oscillatory systems. Despite numerous studies that have been conducted, the mechanism and kinetics of this process remain mysterious. Investigating the impact of temperature is one way to gain valuable insight into the behavior of the BR reaction. Here, the BR reaction in a closed reactor, under selected conditions, was followed at three different temperatures potentiometrically. An alternative method of illustrating the potential change at various temperatures by finding the first derivative of the measured potential with time was proposed. This way of presentation revealed new, interesting insights into the dynamics of the reaction.

INTRODUCTION

One of the most outstanding oscillating chemical systems is the Briggs-Rauscher (BR) reaction, where metal (usually manganese(II)) ions catalyze the acidic oxidation of malonic acid by hydrogen peroxide and iodate [1]:

$$CH_2(COOH)_2 + IO_3^- + 2H_2O_2 + H^+ \xrightarrow{Mn^{2+}} CHI(COOH)_2 + 2O_2 + 3H_2O \quad (1)$$

Because of the striking color change, the oscillating BR reaction is frequently employed in the chemical demonstration when starch serves as an indicator [2]. The BR reaction's oscillatory phenomena have been thoroughly studied from a number of perspectives, including the impact of different additions and substitutions, evaluating sensitivity to different external parameters, examining certain subsystems, etc [3-6]. It is well known that the BR reaction is sensitive to a wide range of stimuli [3,6,7]. Understanding how temperature affects the reaction's path can provide light on the mechanism and, most importantly, its kinetics. It is possible to identify the temperature range in which the oscillatory regime exists and to establish the specificities of the reaction oscillations as the temperature varies by conducting BR reaction over a broad temperature range.

The purpose of this work is to get novel insights that might not be obvious at first appear by presenting the impact of temperature on the BR system in an alternative manner than usual. This could yield insightful findings that can help clarify the mechanism of this reaction, which is still

entirely enigmatic despite years of study. The mechanism of temperature impacts on various chemical self-oscillating systems, including some that are more complex, can also be studied using the obtained results.

METHODS

The BR oscillatory reaction was carried out in a stationary, isothermal, constantly stirred reactor, with a reaction volume of 25 ml. Each experiment was conducted in a glass vessel (METHROM EA 876-20, Switzerland) wrapped in a water recirculation jacket connected to a thermostat (Julabo ED, Germany). Using a magnetic stirrer (Ingenieurbüro, M. Zipperrer GmbH, Cat-ECM5, Staufen, Denmark) the reaction mixture was stirred at 900 rpm. The potentiometric method was used to monitor the reaction. A double-junction Ag/AgCl reference electrode was linked to the working Pt electrode. An electrochemical device (PC-Multilab EH4 16-bit ADC) connected to a personal computer recorded the potential-time evolution of the BR reaction. The chemicals employed were of pro-analysis grade purity ($HClO_4$, KIO_3, H_2O_2, and $MnSO_4$ from Fluka, and $CH_2(COOH)_2$ from Acrōs Organics). For the solutions, deionized water, produced by the Millipore system (Milli-Q, Bedford, USA), with a specific resistance of 18 $M\Omega cm^{-1}$, was used. The reaction vessel was filled with the reactants in the following order: 7 ml of $CH_2(COOH)_2$, 5 ml of $MnSO_4$, 5 ml of $HClO_4$, 5 ml of KIO_3, and 3 ml of H_2O_2 once the temperature and the potential of the working electrode reached the appropriate value. The addition of hydrogen peroxide was considered to represent the beginning of the BR reaction. The initial reactant concentrations in the system were: $[CH_2(COOH)_2]_0$ = 0.0789 $moldm^{-3}$, $[MnSO_4]_0$ = 0.00752 $moldm^{-3}$, $[HClO_4]_0$ = 0.03 $moldm^{-3}$, $[KIO_3]_0$ = 0.0752 $moldm^{-3}$, and $[H_2O_2]_0$ = 1.176 $moldm^{-3}$. The working temperatures were 25.6, 33.5, and 37.0 °C, and controlled within 0.1 °C. The first derivative of the potential by the reaction time was obtained in the program OriginPro 8.

RESULTS AND DISCUSSION

Figure 1 shows the oscillograms obtained at three distinct working temperatures, using the Pt electrode. It is evident that the BR oscillatory period significantly decreases with rising temperatures, which is, due to the faster kinetics, the expected behavior.

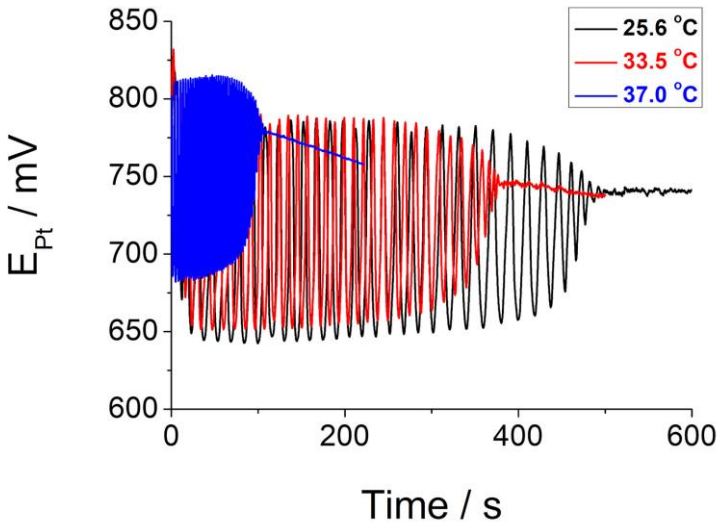


Figure 1. The BR oscillograms obtained with Pt electrode for three different working temperatures.

The presentation in the Figure 1 is a common way of displaying oscillatory dynamics. Here, nevertheless, we have attempted to interpret the temperature effect using an alternative approach. The phase diagrams seen in Figure 2 were created by calculating the first derivative of the potential by time of the reaction (for each of the three working temperatures).

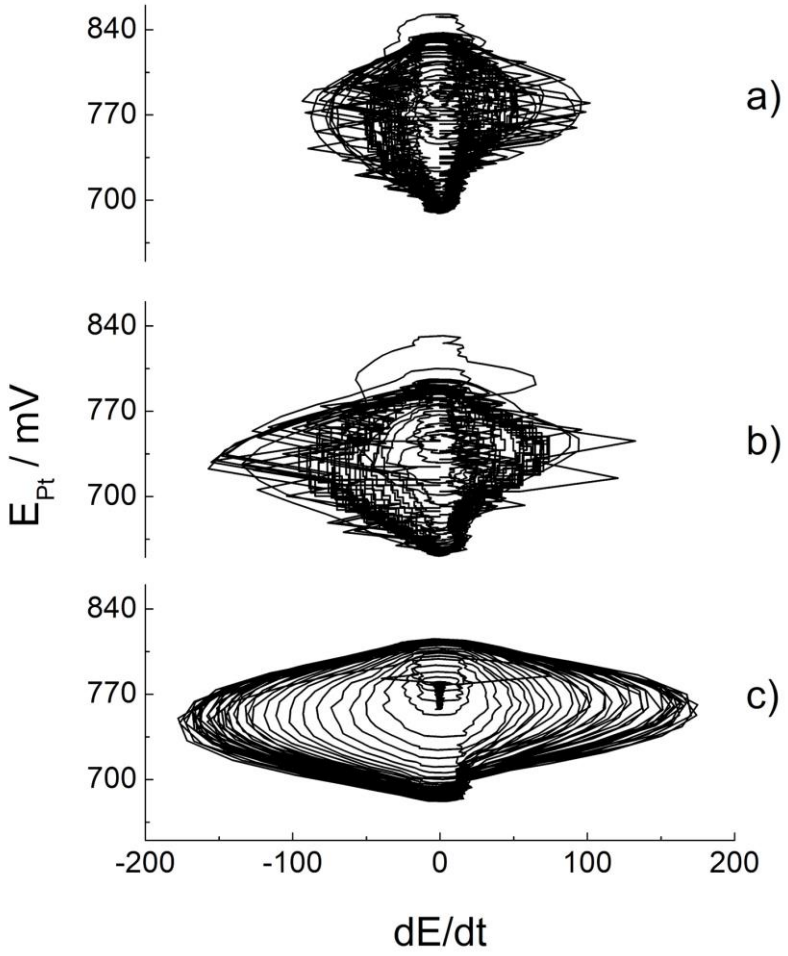


Figure 2. Phase diagrams obtained by finding the first derivative of the potential by time at: a) 25.6 °C, b) 33.5 °C, and c) 37.0 °C.

Figure 1 makes it clearly apparent that the amplitude of the oscillation is the smallest at the highest temperature. The presentation from Figure 2 illustrates this as well, showing how the y axis' boundaries distinctly shrink with temperature. Because of their higher dynamics, the phase diagrams at higher temperatures also exhibit a shift along the x axis, representing dE/dt. What is an interesting feature is the diagram's increasing symmetry with temperature. Although it is clearly asymmetric at the first two temperatures, at the third one can already see some symmetry. Furthermore, compared to curves obtained at lower temperatures, the potential change curve at higher temperatures is shown to be smoother.

The result leads to the conclusion that some aspects of the diagram correspond with the associated oscillograms. More intriguingly, certain behaviors that are not immediately apparent from the oscillogram are also readily observable. To fully understand the physical significance of the results obtained separate studies of the points of entry and exit into the oscillatory region of the phase space are necessary.

CONCLUSION

In this work, a different method of illustrating the dependence of the potentiometrically determined potential was used to investigate the impact of temperature on the BR reaction dynamics. Certain behaviors were demonstrated by this kind of representation that would not have been readily apparent in conventional oscillograms. The results obtained have the potential to aid in the clarification of the BR reaction mechanism through additional investigation.

Acknowledgment

This work was supported by the Ministry of Education, Science and Technological Development of the Republic of Serbia (grants no 451-03-66/2024-03/200017, 451-03-66/2024-03/200026 and 451-03-66/2024-03/200051). M.P. and M.S.P. acknowledge the support of the EU: the EIC Pathfinder Challenges 2022 call through the Research Grant 101115149 (project ARTEMIS), as well as the support of the Office of Naval Research Global through the Research Grant N62902-22-1-2024.

REFERENCES

[1] T. S. Briggs, W. Rauscher, J. Chem. Educ., 50 (1973) 496.
[2] S. D. Furow, J. Chem. Educ., 89 (2012) 1421.
[3] R. Cervellati, K. Höner, S. D. Furrow, C. Neddens, S. Costa, Helv. Chim. Acta, 84 (2001) 3533.
[4] S. D. Furrow, J. Phys. Chem., 99 (1995) 11131.
[5] S. D. Furrow, R. Cervellati, G. Amadori, J. Phys. Chem. A., 106 (2002) 5841.
[6] M. Pagnacco, J. Maksimović, T. Mudrinić, P. Banković, B. Nedić-Vasiljević, A. Milutinović-Nikolić, ChemistrySelect, *5* (2020) 8137.
[7] N. Okazaki, I. Hanazaki, J. Chem. Phys., 109 (1998) 637.

INVESTIGATION OF THE EFFECT OF EVERNIC ACID ON TWO IODATE-BASED OSCILLATORY REACTIONS: BRAY-LIEBHAFSKY AND BRIGGS-RAUSCHER

J. Maksimović[1], Ž. Čupić[2], A. Ivanović-Šašić[2], S. Maćešić[1] and N. Manojlović[3]

[1]*Faculty of Physical Chemistry, University of Belgrade, Studentski trg 12-16, 11000 Belgrade, Serbia (jelena.maksimovic@ffh.bg.ac.rs)*
[2] *Department of Catalysis and Chemical Engineering, Institute of Chemistry, Technology and Metallurgy, University of Belgrade, Njegoševa 12, 11000 Belgrade, Serbia.*
[3]*Faculty of Medical Sciences, University of Kragujevac, Svetozara Markovića 69, 34000 Kragujevac, Serbia*

DOI: https://doi.org/10.46793/Phys.Chem24I.167M

ABSTRACT
For the first time the influence of evernic acid was investigated in two iodate based oscillatory reactions: Bray Liebhafsky and Briggs-Raucher with the aim of possible application in determining the unknown concentration of this acid in complex compound. Obtained results show that evernic acid added in similar concentration has different influence on these two oscillatory systems.

INTRODUCTION
Oscillatory reactions, such as Bray-Liebhafsky (BL) [1] and Briggs-Rauscher (BR) [2], are extremely sensitive to the presence of external analytes. Adding the analyte can affect the amplitude, number of oscillations, period between oscillations, length of the oscillogram, and can even completely extinguish the oscillatory evolution. However, it has been shown that some analytes react in both oscillatory reactions (BL [3] and BR [4]), while some can only react in one reaction and not in the other [5]. In this paper, we wanted to examine which of the two iodate-based oscillatory reactions Bray–Liebhafsky and Briggs–Rauscher is more sensitive to the addition of evernic acid.

Evernic acid, with the structure shown in **Figure 1.**, is a secondary metabolite produced by certain lichen species [6]. This compound belongs to the depsides, compounds composed of two monocyclic aromatic units linked by an ester group. It is used in after-shave lotions, cosmetic products, fragrances and perfumes. Evernic acid has been found to inhibit growth of various microorganisms in laboratory tests. Additionally, it has the potential to be used as a drug target for antimicrobial agents against infectious diseases.

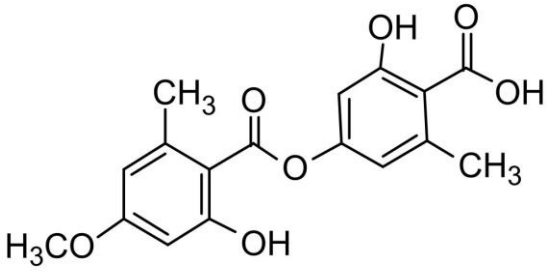


Figure 1. The chemical structures of evernic acid

EXPERIMENTAL
Evernic acid was isolated from the lichen *Evernia prunastri* collected on Suva mountain in June 2020. Air-dried powdered thalli of the lichen was extracted by maceration with acetone at room temperature for 24 h. The extract was filtered and then concentrated under reduced pressure, and evernic acid was separated on a chromatographic column (silica gel 60, Merck, Darmstadt,

Germany) using different solvent systems (acetone, acetone:methanol and methanol). Evernic acid was identified based on the spectroscopic methods [7]

Experimental tests of evernic acid were performed in a closed well-stirred (900 rpm) reactor in two oscillatory reactions (BL and BR reactions). The temporal evolution of the system was monitored potentiometrically using a Pt electrode as a working electrode and an Ag/AgCl electrode as a reference electrode.

BL experimental conditions were: T = 62.0 ºC, $[KIO_3]_o = 7.35 \times 10^{-2}$ mol dm^{-3}, $[H_2SO_4]_0 = 6.13 \times 10^{-2}$ mol dm^{-3}, $[H_2O_2]_o = 5.10 \times 10^{-3}$ mol dm^{-3}. Different concentrations of evernic acid were added to the BL reaction mixture 10 minutes after the addition of hydrogen peroxide, i.e. in the pre-oscillatory period.

BR experimental conditions were: T = 36.7 ºC, [Malonic acid] = 7.89×10^{-2} mol dm^{-3}, $[MnSO_4] = 7.52 \times 10^{-3}$ mol dm^{-3}, $[HClO_4] = 3.0 \times 10^{-2}$ mol dm^{-3}, $[KIO_3] = 7.52 \times 10^{-2}$ mol dm^{-3}, $[H_2O_2] = 1.176$ mol dm^{-3}. Different concentrations of evernic acid were added to the BR reaction mixture 3 minutes before the addition of hydrogen peroxide, i.e. before initiating the BR reaction.

All chemicals used were pro analysis grade, and their solutions were prepared in deionized water (18 MΩ cm), except for evernic acid solution, which was prepared in ethanol.

RESULTS AND DISCUSSION

Response of the systems to the addition of different concentations of evernic acid is presented in **Figures** 2 and 3. **Figure 2(A)** presents Bray-Liebhafsky oscillograms without the addition of analyte a) and with the addition of various concentrations of evernic acid during the pre-oscillatory period: $2.44 \cdot 10^{-6}$ mol dm^{-3} (b), $4.87 \cdot 10^{-6}$ mol dm^{-3} (c), $7.29 \cdot 10^{-6}$ mol dm^{-3} (d), $9.71 \cdot 10^{-6}$ mol dm^{-3} (e), $1.21 \cdot 10^{-5}$ mol dm^{-3} (f) and $1.45 \cdot 10^{-5}$ mol dm^{-3} (g). From **Figure 2(A).** we can see that when evernic acid is added to the BL system in the pre-oscillatory period, there is a change in the amplitude of the oscillation, and an extension of the pre-oscillatory period, and therefore an extension of the length of the oscillogram. The time from the addition of evernic acid to the appearance of the first visible oscillation is marked as τ_{inh} (**Figure 2(A). (b)**) and represents the inhibition time. The added concentration of evernic acid is in good positive correlation with inhibition time, **Figure 2(B). Figure 2(B).** shows that in evernic acid concentration range from 0-$1.45 \cdot 10^{-5}$ mol dm^{-3}, the concentration dependence of inhibition time shows linearity with regression equation: $\tau_{inh} = 1.65 \cdot 10^{-6} \times C_{Evernic\ Acid} + 5.91$ (concentration presented in mol dm^{-3} and τ_{inh} denoted in minutes), which can be used to measure the unknown concentration of evernic acid.

Figure 3. shows BR oscillograms without the addition of analyte (a) and with the addition of different concentrations of evernic acid added 3 minutes before the initiation of the BR reaction: $2.63 \cdot 10^{-6}$ mol dm^{-3} (b), $5.26 \cdot 10^{-6}$ mol dm^{-3} (c), $7.87 \cdot 10^{-6}$ mol dm^{-3} (d), $1.05 \cdot 10^{-5}$mol dm^{-3} (e), $1.31 \cdot 10^{-5}$ mol dm^{-3} (f) and $1.56 \cdot 10^{-5}$ mol dm^{-3} (g). From **Figure 3.** we can see that evernic acid has a weak effect on the BR reaction, which is reflected only in the change of the oscillation amplitudes. Also, from **Figure 3**, we can notice that evernic acid does not affect the characteristic periods of the BR reaction, such as the oscillatory period, the length of the oscillogram, etc.

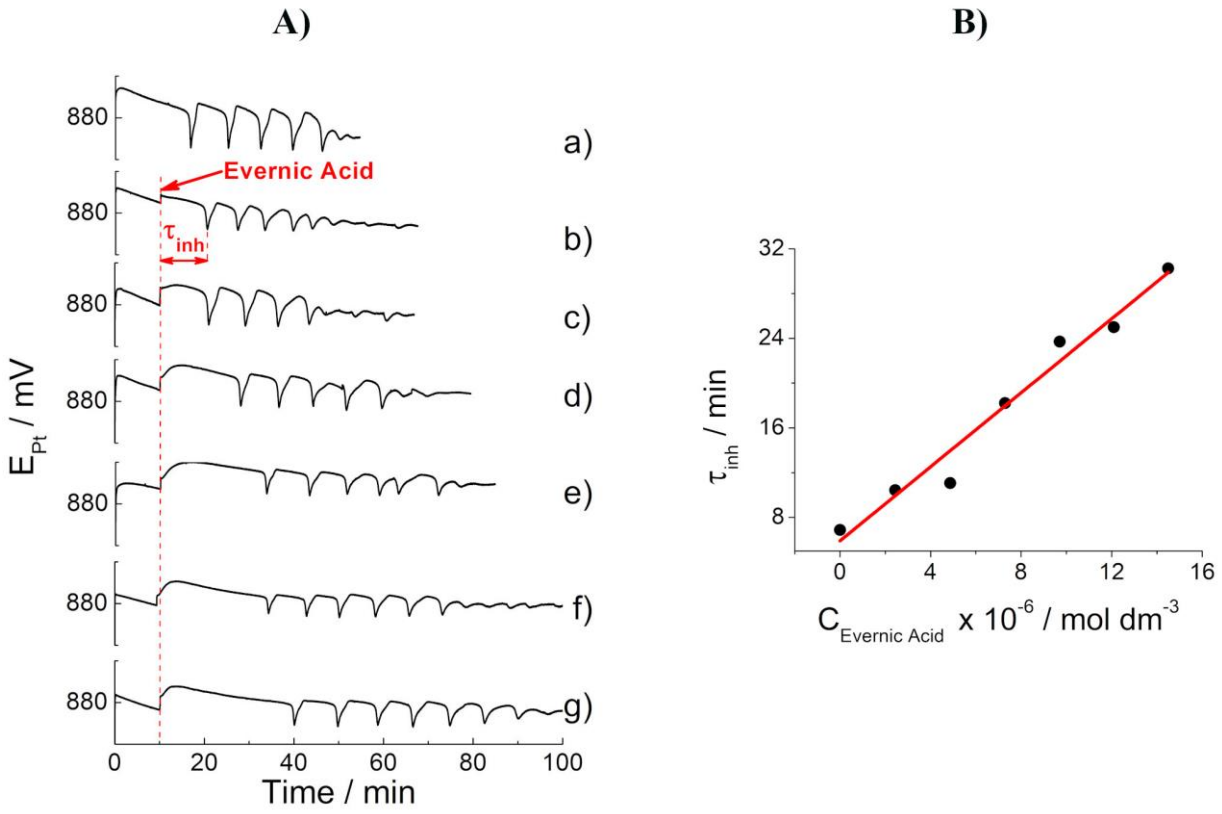


Figure 2. **(A)** Bray-Liebhafsky oscillograms without the addition of analyte a) and with the addition of various concentrations of evernic acid during the pre-oscillatory period: $2.44 \cdot 10^{-6}$ mol dm^{-3} (b), $4.87 \cdot 10^{-6}$ mol dm^{-3} (c), $7.29 \cdot 10^{-6}$ mol dm^{-3} (d), $9.71 \cdot 10^{-6}$ mol dm^{-3} (e), $1.21 \cdot 10^{-5}$ mol dm^{-3} (f) and $1.45 \cdot 10^{-5}$ mol dm^{-3} (g). **(B)** Dependence of the inhibition time (τ_{inh}) on evernic acid concentration.

CONCLUSION

Effect of evernic acid isolated from the lichen *Evernia prunastri* on two iodate-based oscillatory reactions, Bray–Liebhafsky (BL) and Briggs–Rauscher (BR), was monitored by the potentiometric method. It was obtained that the addition of similar concentrations of evernic acid has different influence on two oscillatory systems. The evernic acid addition did not make a characteristic response of the BR system, such as the changes in length of the oscillogram, oscillatory period, etc. Unlike the BR system, the addition of evernic acid in BL prolonged the length of the pre-oscillatory period and the dependence of the inhibition time on the added concentration of evernic acid is linear. This is the first time that the effect of some depside on two iodate-based oscillatory reactions, Bray-Liebhafsky and Briggs-Rauscher, has been investigated.

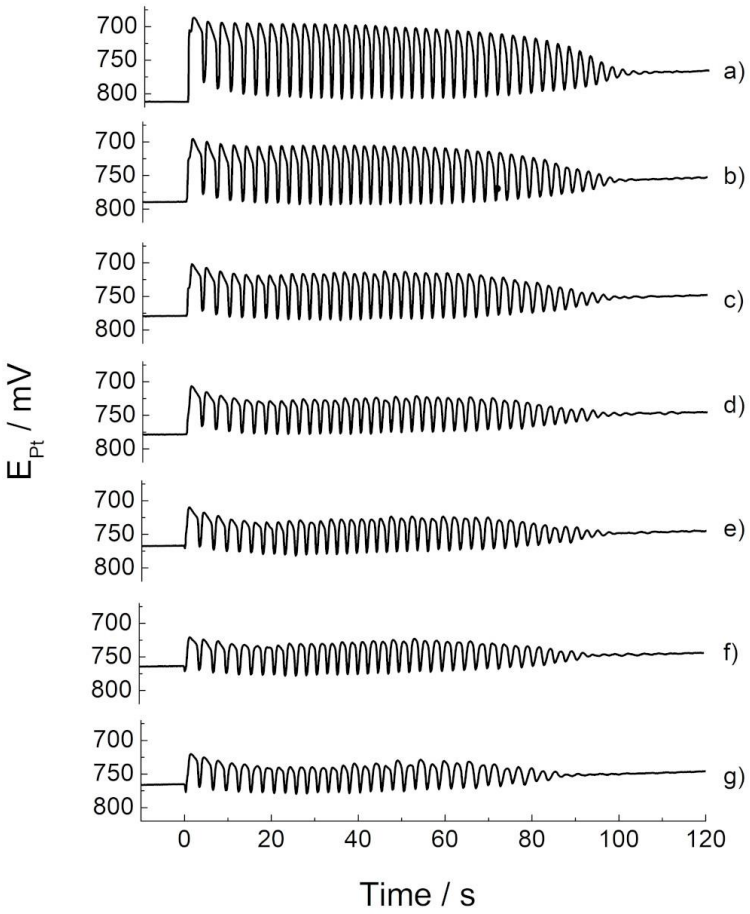


Figure 3. Briggs-Rauscher oscillograms without the addition of analyte a) and with the addition of various concentrations of evernic acid added 3 minutes before the addition of hydrogen peroxide: $2.63 \cdot 10^{-6}$ mol dm^{-3} (b), $5.26 \cdot 10^{-6}$ mol dm^{-3} (c), $7.87 \cdot 10^{-6}$ mol dm^{-3} (d), $1.05 \cdot 10^{-5}$mol dm^{-3} (e), $1.31 \cdot 10^{-5}$ mol dm^{-3} (f) and $1.56 \cdot 10^{-5}$ mol dm^{-3} (g).

Acknowledgment

We are grateful to the financial support from Ministry of Science, Technological Development, and Innovation of Republic of Serbia trough University of Belgrade - Faculty of Physical Chemistry and Institute of Chemistry, Technology and Metallurgy – National Institute of the Republic of Serbia, (Contract numbers 451-03-66/2024-03/200146, 451–03–66/2024–03/200026 and 451-03-65/2024-03/200111). This research was also supported by Science Fund of Republic of Serbia #Grant Number. 7743504, NES.

REFERENCES

[1] W. C. Bray, J. Am. Chem. Soc., 43 (1921) 362.
[2] T. S. Briggs, W. C. Rauscher, J. Chem. Educ., 50 (1973) 496.
[3] J. P. Maksimović, J. Tošović, M. C. Pagnacco, BCSJ, 93(5) (2020) 676.
[4] R. Cervellati, K. Höner, S. Furrow, C. Neddens, S. Costa, Helv. Chim. Acta, 84 (2001) 3533.
[5] I. N. Bubanja, M. C. Pagnacco, J. P. Maksimović, K. Stevanović, D. Stanisavljev, Reac. Kinet. Mech. Cat., 123(1) (2018) 47.
[6] M. Kosanić, N. Manojlović, S. Janković, T. Stanojković, B. Ranković, Food Chem. Toxicol., 53 (2013) 112.
[7] S. Huneck, I. Yoshimura in: Identification of lichen substances. Springer, Berlin, Heidelberg, 1996.

E *– Electrochemistry*

DEVELOPMENT OF COST-EFFECTIVE ELECTROCATALYST FOR ELECTROCHEMICAL GLUCOSE SENSORS BASED ON ALUMINUM PILLARED CLAY—SUPPORTED COBALT OXIDE

T. Mudrinić, B.Pantić and P. Banković

University of Belgrade, Institute of Chemistry, Technology and Metallurgy, Njegoševa 12, 11000 Belgrade, Republic of Serbia (tihana.mudrinic@ihtm.bg.ac.rs)

DOI: https://doi.org/10.46793/Phys.Chem24I.173M

ABSTRACT

There is no doubt that electrochemical glucose sensors have revolutionized the management of diabetes and improved the quality of life of diabetic patients. However, these sensors typically rely on enzymatic-based catalysts, which are thermally and pH unstable or noble metals, which are expensive. Nanostructured non-precious transition metal-based catalysts (NNPTM) are considered promising alternatives. However, NNPTMs also have weaknesses that limit their practical application, such as the agglomeration of nanoparticles and the fact that they can operate only in highly alkaline conditions.

Our research aims to address these issues by developing electrocatalyst based on cost-effective, non-toxic material—aluminum pillared clay with incorporated cobalt as the active phase (CoAP). The main goal of our research is to produce an efficient and cost-effective electrocatalyst to make electrochemical glucose sensors accessible to a widespread population, especially to the poorest one.

The good stability of CoAP over a prolonged period of measurements and after being left under environmental conditions revealed that aluminum pillared clay (AP) can effectively prevent cobalt particle agglomeration. Additionally, CoAP exhibits good sensitivity, accuracy, and selectivity towards typical blood constituents. Like other cobalt-based catalysts, CoAP requires a strongly alkaline medium to oxidize glucose, which prevents its use for measuring glucose level directly in physiological fluids. However, CoAP can measure a wide range of glucose concentrations. This means that CoAP could measure glucose concentration typically found in the blood of healthy individuals and diabetic patients, even if the blood is diluted with an alkaline solution to ensure its work.

In this talk, I will briefly overview our several years of research on developing CoAP for the electrooxidation of glucose. I will discuss how various parameters affect the electrocatalytic and electroanalytical performance of CoAP, including different cobalt loadings, methods of cobalt incorporation into the AP, and the impact of adding other non-precious transition metals as dopants. Additionally, I will discuss the future direction for the development of CoAP to enhance its application in physiological fluids.

Acknowledgment

This research has been financially supported by the Ministry of Science, Technological Development and Innovation of Republic of Serbia (Contract No: 451-03-66/2024-03/200026).

ELECTROCHEMICAL BEHAVIOR OF ALUMINA-Cu BASED ELECTRODE IN THE ALKALINE SOLUTION

T. Novaković and Z. Mojović

University of Belgrade, Institute of Chemistry, Technology and Metallurgy, Njegoševa 12, 11000 Belgrade, Serbia. (zorica.mojovic@ihtm.bg.ac.rs)

DOI: https://doi.org/10.46793/Phys.Chem24I.175N

ABSTRACT

The surface of two types of alumina, anhydrous (A) and trihydrate (T) alumina, was modified by copper through an ion-exchange procedure. The obtained samples were used as modifiers of carbon paste electrodes, and the electrochemical behavior of the obtained samples was investigated in an alkaline solution in the potential range -1.5 V to +1.5 V vs. Ag/AgCl. The copper-containing samples showed expected peaks corresponding to Cu/Cu(I) and Cu(I)/Cu(II) oxidation, although higher currents were obtained for anhydrous alumina. The additional peak at high anodic potential was recorded and ascribed to the formation of metal oxy/hydroxide. The influence of the cathodic limit of the potential scan on the current of this peak was investigated. The response of copper containing alumina electrode in the presence of glutamic acid was tested.

INTRODUCTION

Chemically modified electrodes are investigated in order to increase electrode performance, such as sensitivity, selectivity, and activity, over time. In the last decade, alumina-based electrodes have been investigated. It has been observed that the electrochemical characteristics of glassy carbon electrode polished with alumina are influenced by the shape and structure of the alumina particles [1, 2]. In HER and OER studies, graphene-alumina composite electrodes demonstrated efficiency comparable to platinum standards [3].The alumina type plays a crucial role in the electrochemical performance of an alumina-modified carbon paste electrode [4]. The behavior of these electrodes at various pHs depended on the type and number of alumina surface groups. Although alumina is an insulating material, as a modifier of glassy carbon or carbon paste electrodes, it exhibits certain electroactivity. This feature of alumina could be exploited for the development of new sensors.

Alumina supported metal oxides have recently been investigated [5, 6] as electrocatalysts. The role of alumina in these electrocatalysts is to serve as a support for metal-oxide, which is electroactive component, providing chemical and hydrothermal stability.

The aim of this work was to investigate the behavior of alumina and alumina-Cu composite electrodes in alkaline media. Alumina is prone to the corrosion in highly alkaline solutions [7]. The type of alumina plays important role due to its surface chemistry. The presence of surface functional groups affected the response of alumina-based electrodes, but also influenced the amount of copper ions attached to its surface. The response of the electrodes in the presence of glutamic acid in alkaline solution is also investigated.

METHODS

Industrial Al_2O_3 (designated as anhydrous alumina, A) and $Al_2O_3{\cdot}3H_2O$ (designated as trihydrate alumina, T) were acquired from alumina refinery (Alumina Ltd., Zvornik, B&H). Copper modified alumina samples were prepared by ion exchange procedure with a solution of 0.1 M $CuSO_4{*}5H_2O$. The alumina and solution in the ratio 1:20 were stirred for 1 hour at room temperature. The sample was filtered and rinsed with distilled water. Cu-alumina samples were dried at 110 ^oC overnight and

designated as A-Cu and T-Cu. Carbon pastes modified with alumina samples were prepared by hand mixing 0.1 g carbon black (CB) (Vulcan-XC 72R), 0.4 g of alumina sample with 1.2 g of paraffin oil.

The electrochemical properties were tested by cyclic voltammetry (CV) and linear sweep voltammetry (LSV) in 0.1 M NaOH. The response of the electrode in the presence of glutamic acid was tested by linear sweep voltammetry.

RESULTS AND DISCUSSION

The response of alumina with and without copper was tested by cyclic voltammetry in 0.1 M NaOH over a broad range of potentials (**Figure 1a**). The anodic behavior of Al_2O_3 films was mainly investigated as a step in the corrosion behavior of aluminum. The anodic dissolution of aluminum is expected to proceed through electrochemical formation of oxide/hydroxide film and its chemical dissolution through subsequent formation of soluble $[Al(OH)_4]^-$ [8]. The alumina film formed in the electrochemical step can be composed of various species of oxides or oxy/hydroxides, Al_2O_3, $Al(OH)_3$ and/or AlOOH.

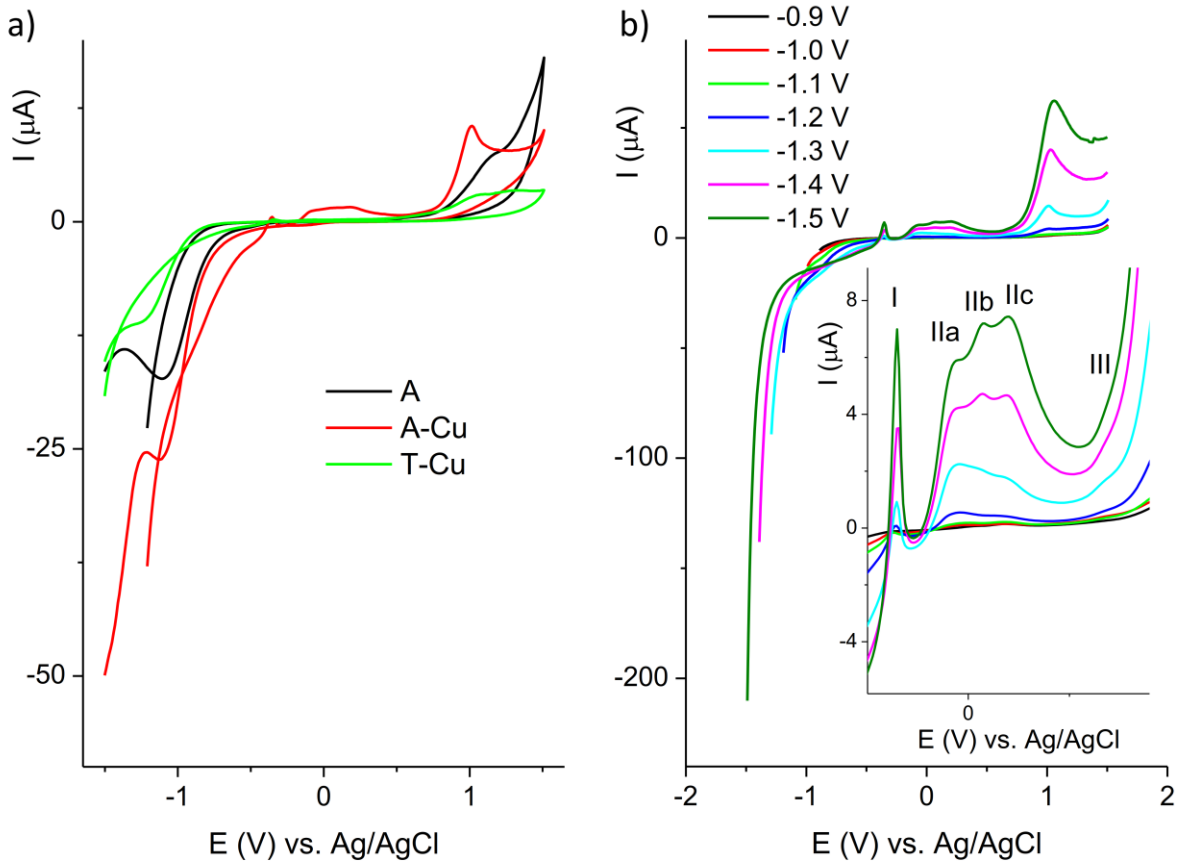


Figure 1. a) Cyclic voltammograms of alumina and alumina-Cu samples recorded in 0.1 M NaOH at scan rate of 100 mV s^{-1}; b) The influence of cathodic potential on linear sweep voltammogram profile of alumina-Cu sample.

The anodic wave around 1 V was recorded for anhydrous alumina. The same wave is noticed at the cyclic voltammogram of trihydrate alumina, although the recorded current was significantly lower (not shown). The presence of copper on the surface of both alumina samples resulted in

higher currents in the CV of copper containing samples. The cathodic peak at around -1 V is also present for all investigated samples, and an increase in current is noticed for samples with copper.

In the potential range between -0.5 V and 0.5 V characteristic peaks of oxidation and reduction of copper species can be seen. The currents are significantly higher for the A-Cu sample than for the T-Cu sample as a result of higher concentration of copper in the A-Cu sample.

In order to gain insight in possible origin of anodic peak the influence of cathodic limit on the shape of cyclic voltammogram is studied (**Figure 1b**). The current of the anodic peak at around 1 V increased with the shift of cathodic potential limit toward more negative values. Furthermore, this shift was followed by a change in the profile of copper species (inset figure in **Figure 1b**). Two regions can be noticed in the cyclic voltammogram of alumina-copper samples. Region I corresponds to Cu(0) to Cu(I) oxidation, while region II corresponds to Cu(I) to Cu(II) oxidation. This region usually contains two peaks, IIa and IIc, corresponding to the formation of CuO and $Cu(OH)_2$. When the cathodic limit was placed at -1.4 V vs. Ag/AgCl, the middle peak IIb appeared. This peak most likely indicates the formation of complex Cu(II) specie ($Cu(OH)_4^{2-}$, $HCuO_2^-$ or CuO_2^{2-}) [9]. Further oxidation of copper, Cu(II)/Cu(III), is reported to occur at potentials higher than 0.5 V. It is expected that species formed at high anodic potential include CuOOH and/or $Cu(OH)_4^-$.

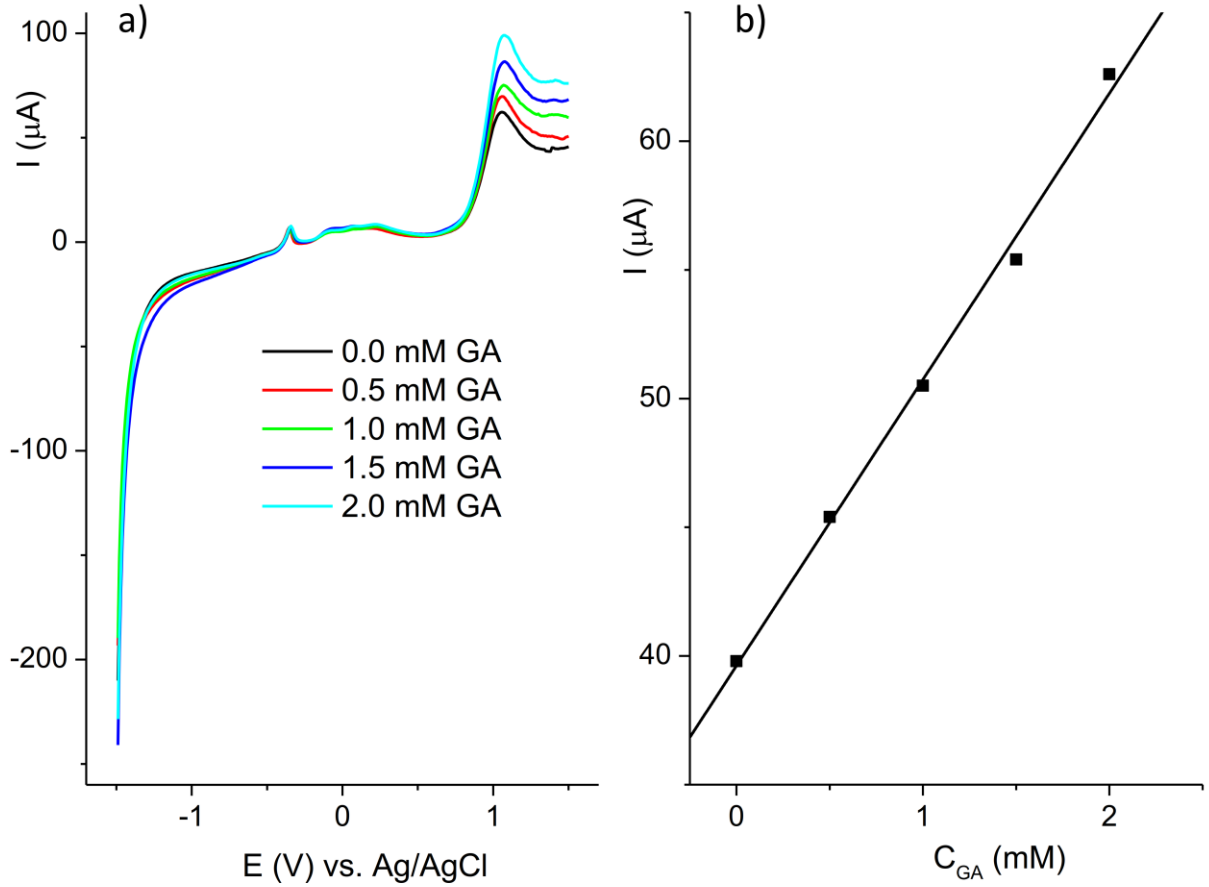


Figure 2. a) Linear sweep voltammograms recorded on the A-Cu electrode in 0.1 M NaOH without and with glutamic acid at scan rate of 100 mVs^{-1}; b) calibration curve.

LSV of A-Cu electrode in 0.1 M NaOH containing various concentration of glutamic acid showed an increase of currents with an increase of concentration of glutamic acid (**Figure 2a**) due

to oxidation of glutamic acid. The cathodic limit was set to the -1.5 V in order to obtain the highest response. The electrode composed of alumina without copper also showed an increase in peak current with addition of glutamic acid (not shown) although the increase was less pronounced. The peak obtained at 1 V was used for plotting calibration curve (**Figure 2b**). The peak current vs. concentration plot for A-Cu was linear with slope of 11.1 μA/mM. The electrooxidation of glutamic acid on nickel-based electrode was investigated and suggested mechanism includes reaction between NiOOH and glutamic acid to produce $Ni(OH)_2$ and 2-oxo glutaric acid [10]. Similar mechanism can be considered for the electrode investigated in this study since formation of AlOOH and CuOOH is expected at the potential of glutamic acid oxidation.

CONCLUSION

The electrochemical behavior of alumina samples modified with copper in alkaline media was investigated in the potential range of -1.5 V to +1.5 V vs. Ag/AgCl. Two types of alumina were used, anhydrous and trihydrate. Anhydrous alumina with and without copper showed a higher current response than trihydrate samples. A cyclic voltammogram of copper containing alumina showed typical peaks of copper oxidation. At the potential around 1 V additional peak corresponding to formation of MOOH specie was recorded. The peak current of MOOH formation increased with the cathodic shift of potential scan range. The peak current of MOOH increased with the increase of the concentration of glutamic acid showing good liner relationship.

Acknowledgment

This work was supported by the Ministry of Science, Technological Development and Innovation of the Republic of Serbia (grant no. 451-03-66/2024-03/200026).

REFERENCES

[1] A.P. Lima, W.T.P. dos Santos, E. Nossol, E.M. Richter, R.A.A. Munoz, Electrochim. Acta, 358 (2020) 136925.
[2] A.P. Lima, P.L.M.R. Almeida, R.M.F. Sousa, E.M. Richter, E. Nossol, R.A.A. Munoz, J. Electroanal. Chem., 851 (2019) 113385
[3] X.X. Ma, X.Q. He, J. Power Sources, 353 (2017) 28.
[4] T. Novaković, T. Barudžija, M. Čomor, P. Banković, Z. Mojović, J. Electroanal.Chem., 862 (2020) 114010.
[5] S. Khan, S. S. Shah, N. K. Janjua, A. B. Yurtcan, M. T. Nazir, K. M. Katubi, N. S. Alsaiari, Chemosphere, 315 (2023) 137659.
[6] S. Khan, S.S. Shah, A. Ahmad, A.B. Yurtcan, E. Jabeen, R.A. Alshgari, N.K. Janjua, J. Electroanal. Chem., 917 (2022) 116422.
[7] I. Boukerche, S. Djerad, L. Benmansour, L. Tifouti, K. Saleh, Corros. Sci., 78 (2014) 343.
[8] S-I. Pyun, S-Mo. Moon, J. Solid State Electrochem., 4 (2000) 267.
[9] J. Ambrose, R. G. Barradas, D. W. Shoesmith, J. Electroanal. Chem. Interf. Electrochem., 47 (1973) 47.
[10] Y. Xu, T. Zhu, Y. Niu, B-C Ye, Microchemical Journal. 175 (2022) 107229.

FLEXIBLE COMPOSITE ELECTRODE OF POLY(VINYL ALCOHOL) AND CARBON BLACK

A. Radosavljević[1], J. Spasojević[1], I. Vukoje[1], M. Milošević[1] and Z. Mojović[2]

[1] *Vinča Institute of Nuclear Sciences, National Institute of the Republic of Serbia, University of Belgrade, Mike Petrovića Alasa 12-14, 11351 Vinča, Belgrade, Serbia*
[2]*University of Belgrade, Institute of Chemistry, Technology and Metallurgy, Njegoševa 12, 11000 Belgrade, Serbia. (zorica.mojovic@ihtm.bg.ac.rs)*

DOI: https://doi.org/10.46793/Phys.Chem24I.179R

ABSTRACT

Screen-printed electrodes are easily fabricated and exhibit high-performance results when employed as electrochemical sensors. The major drawback of these electrodes is that the conducting layer is not an integral part of the electrode. Composite polymer/carbon electrodes are investigated with the aim to overcome this problem. Flexible composite electrodes were prepared from poly(vinyl alcohol) (PVA) and carbon black (CB). The investigation of the electrode by cyclic voltammetry and electrochemical impedance spectroscopy showed significant influence of PVA-CB ratio on their electrochemical activity.

INTRODUCTION

Composite electrodes made of polymer and conductive carbon material have raised research interest in recent years. These electrodes are developed to overcome the drawbacks of widely used screen-printed electrodes (SPE). SPE are easily fabricated, with performances above their traditional counterparts. The printing ink can be easily modified or used as an immobilization matrix for biomolecules. The major problem with screen-printed electrodes is that the conducting layer is coated on the substrate, not being their integral part. Additionally, standard procedure for SPE production includes the curing of ink by heat treatment what severely affects the activities of the biomolecules that are often part of sensors.

Composite polymer/carbon electrodes offer several advantages: good electrical and mechanical properties, flexibility, and low-cost. These electrodes are eco-friendly if the biodegradable polymer is used. Several polymers and carbon materials have been tested for the production of these electrodes. Various polymers, poly (butylene adipate-co-terephthalate) (PBAT) [1], poly(methyl methacrylate) (PMMA) [2] and thermoplastic starch [3] were tested due to their good mechanical and thermal properties. Graphite is most commonly used as a conductive carbon. The properties of the electrode can be further tuned by a modifier which can be easily introduced during the preparation procedure [4].

In this paper, we investigated flexible composite electrodes prepared from poly(vinyl alcohol) (PVA) and carbon black (CB). PVA is a non-toxic and biodegradable polymer and therefore is a good choice for the development of eco-friendly composites. It is also biocompatible enabling possible application of investigated electrodes as wearable electrodes. Carbon black is used as a conductive carbon due to its good conductivity and high specific surface area. The paper aimed to establish the influence of the PVA-CB ratio on the electrical conductivity of the investigated electrodes, as well as their usefulness for sensing applications.

METHODS

Poly(vinyl alcohol) (PVA), with an average molecular weight of 72 kDa and 99% minimal degree of hydrolysis was supplied from Merck (Germany), while the carbon black Vulcan XC-72 (CB) was purchased from Cabot Corporation. PVA aqueous solution (5% w/v) was prepared under continuous stirring at 70 °C for 1 h and cooled to room temperature. The appropriate amount of CB was added to the PVA solution to obtain dispersions of PVA-CB with mass ratios of (1:0.05), (1:0.1), (1:0.2) and (1:0.5). After solvent evaporation, in Petri dishes at room temperature, the flexible composite electrodes were obtained. The composite PVA-CB with mass ratio (1:0.5) was not flexible and therefore it was excluded from further investigation.

Electrochemical experiments were performed in a three-electrode glass cell. The working electrode was a composite PVA-CB electrode, the reference electrode was Ag/AgCl in 3 M KCl, while a platinum rod served as the counter electrode. The electrodes are designated according to the ratio of CB in the electrode composition as PVA-CB_0.05, PVA-CB_0.1 and PVA-CB_0.2. The electrodes were cut so that a surface of 1 cm^2 was used for measurement. The electrochemical measurements were performed using the Autolab electrochemical workstation (Autolab PGSTAT302N, Metrohm-Autolab BV, Netherlands). The electrodes were characterized by cyclic voltammetry and electrochemical impedance spectroscopy (EIS) in 5 mM $[Fe(CN)_6]^{3-/4-}$ in 0.2 M KCl. The sensing properties of the electrodes were tested in 0.1 M phosphate buffer solution pH 7 with 1 mM 4-nitrophenol (4-NP) as an analyte.

RESULTS AND DISCUSSION

The electrochemical characterization was performed in 5 mM $[Fe(CN)_6]^{3-/4-}$ in 0.2 M KCl by cyclic voltammetry (**Figure 1a.**) Both faradic and capacitive currents increase with the increase of the content of the carbon black in the composite. The characteristic pair of peaks originating from oxido-reduction of $[Fe(CN)_6]^{3-/4-}$ redox probe is clearly resolved only for PVA-CB_0.2 electrode, while only a slight wave appears for PVA-CB_0.1 electrode. The cyclic voltammogram of PVA-CB_0.05 electrode expressed only a slight increase of anodic current. The peak-to-peak separation was 141 mV and 272 mV for PVA-CB_0.2 and PVA-CB_0.1, respectively. Peak-to-peak separation provides qualitative estimation of the rate of electron transfer that originates in the redox process at the electrode surface. The reported values of peak-to-peak separation clearly indicated that increased amount of carbon black in the electrode composition led to the higher electron transfer rate.

Electrochemical impedance spectroscopy (EIS) was performed in the same solution. The recorded Nyquist plots are presented in **Figure 1b**. The impedance reduced with the increase of the carbon content in the samples. The capacitive behavior at high frequencies (almost vertical line at the beginning of the Nyquist plot) is the consequence of additional cable and crocodile clip used for the measurement. The dominating feature of all spectra was diffusion at low frequencies. This is probably the consequence of electrode wetting during the recording. The spectra of samples PVA-CB_0.05 and PVA-CB_0.1 revealed significant dissipation of data. This behavior can be ascribed to the time instability of investigated electrodes [5]. The Nyquist plot of PVA-CB_0.2 sample is presented in the inserted figure at **Figure 1b**. The Nyquist plot of PVA-CB_0.2 is well defined and could be fitted with the Randles circuit (χ^2 = 0.002). The resistance to charge transfer was 20 Ω, double-layer capacitance 54 μF and admittance of Warburg element was 3.03 $mSs^{1/2}$.

The PVA-CB composite electrodes were tested for sensing applications by linear sweep voltammetry (LSV) with 4-nitrophenol as the model analyte. LSV of composite electrodes in 0.1 M phosphate buffer pH 7, with and without 1 mM 4-NP are presented in **Figure 1c.** The samples with the highest ratio of carbon black showed a peak originating from reduction of $–NO_2$ to –NHOH [6],

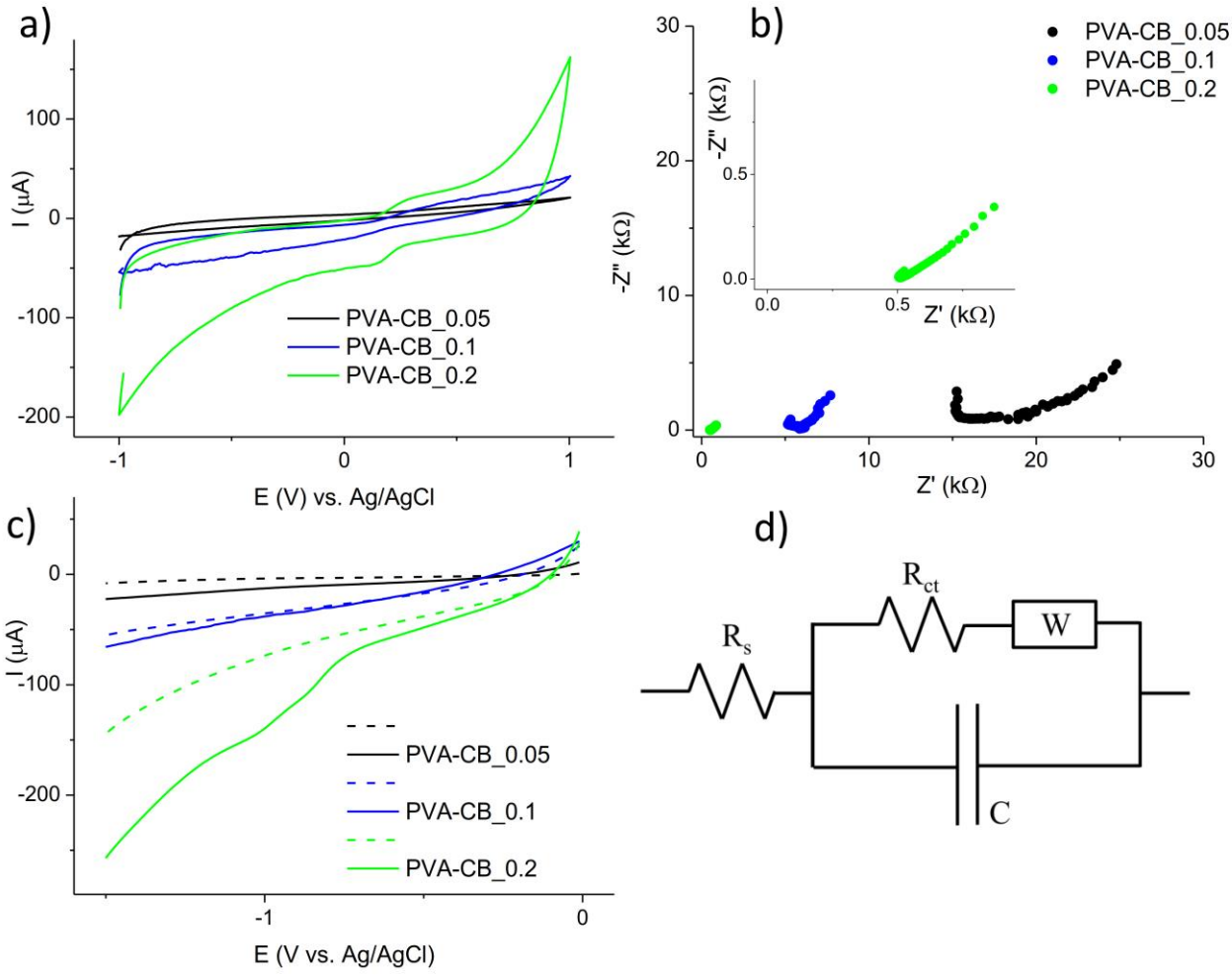


Figure 1. a) Cyclic voltammograms of plastic chip PVA-CB electrodes KCl recorded at scan rate of 10 mVs^{-1} 5 mM $[Fe(CN)_6]^{3-/4-}$ in 0.2 M KCl; b) Nyquist plots recorded at OCP in 5 mM $[Fe(CN)_6]^{3-/4-}$ in 0.2 M KCl; the inserted figure represents enlarged Nyquist plot of PVA-CB_0.2 sample; c) Linear sweep voltammograms of plastic chip PVA-CB electrodes in phosphate buffer pH 7 without (dashed lines) and with 1 mM 4-NP (solid lines) recorded at scan rate of 50 mVs^{-1}; d) the equivalent electric circuit used to fit EIS data.

although the peak was not well resolved. In a previous investigation, it was shown that PVA might have negative effect on oxido-reduction of nitrophenol [7]. As previously noted, the influence of PVA depended on the ratio of PVA to other components of electrode. Nevertheless, the recorded current for PVA-CB_0.2 was sufficiently high to warrant further investigation of these electrodes. Carbon black provided conductivity to the electrode, while PVA enables preparation of flexible, eco-friendly electrode.

CONCLUSION

Flexible composite electrodes based on poly(vinyl alcohol) (PVA) and carbon black (CB) were prepared with varying PVA-CB ratios. The amount of carbon black influenced the flexibility and electrochemical activity of the electrode. With increasing carbon black content, the electrode became less flexible and more electroactive. The PVA-CB electrodes were tested for sensing 4-

nitrophenol. A high current response was obtained for the PVA-CB electrode with the highest investigated amount of carbon black, although the peak was not well resolved. Nevertheless, the flexible electrodes prepared in this manner can be easily modified and show great potential.

Acknowledgment
This work was supported by the Ministry of Science, Technological Development and Innovation of the Republic of Serbia (grant no 451-03-66/2024-03/200026 and 451-03-66/2024-03/200017).

REFERENCES

[1] C. C. Maciel, L. F. de Lima, A. L. Ferreira, W. R. de Araujo, M. Ferreira, Sens. Actuators. Rep., 4 (2022) 100091.
[2] M. Perween, D. B. Parmar, G. R. Bhadua, D. N. Srivastava, Analyst, 139 (2014) 5919.
[3] A. de S. M. de Freitas, C. C. Maciel, A. P. Lemes, M. Ferreira, ESC Advances 1 (2022) 036504.
[4] C. C. Maciel, A. de S. M. de Freitas, J. P. Medrades, M. Ferreira, J. Electrochem. Soc., 169 (2022) 027505.
[5] G. S. Popkirov, R. N. Schindler, Electochim. Acta, 38 (1993) 861.
[6] M. Pontié, G. Thouand, F. De Nardi, I. Tapsoba, S. Lherbette, Electroanalysis 23 (2011) 1579.
[7] S. Marinović, T. Mudrinić, N. Jović-Jovičić, M. Ajduković, A. Milutinović–Nikolić, P. Banković, Z. Mojović, J. Electroanal. Chem., 848 (2019) 113280.

ELECTROCHEMICAL PERFORMANCE OF IRON-DOPED COBALT OXIDE CATALYST SUPPORTED ON ALUMINUM-PILLARED CLAY TOWARD GLUCOSE OXIDATION

B. Pantić [1], S. Marinović[1], G. Stevanović[1], R. Petrović[2], J. Krstić[1] and T. Mudrinić[1]

[1] University of Belgrade, Institute of Chemistry, Technology and Metallurgy, Njegoševa 12, 11000 Belgrade, Republic of Serbia. (biljana.milovanovic@ihtm.bg.ac.rs)
[2]University of Belgrade, Faculty of Technology and Metallurgy, Karnegijeva 4, 11000 Belgrade, Republic of Serbia

DOI: https://doi.org/10.46793/Phys.Chem24I.183P

ABSTRACT
This study aimed to investigate the effect of iron doping on the electrochemical performance of a cobalt oxide catalyst supported on aluminum-pillared clay (Co/AP) in the glucose oxidation reaction. For this purpose, Co/AP and Fe-doped Co/AP were synthesized. The results of the kinetic study, physicochemical, and electrochemical characterizations were correlated. The results indicated that the introduction of Fe as a dopant could be a promising strategy to enhance the efficiency of Co/AP for glucose oxidation reaction.

INTRODUCTION
In our previous work [1], it was demonstrated that the cobalt oxide catalyst supported on aluminum-pillared clay (Co/AP) exhibited high sensitivity and accuracy in alkaline glucose-containing solutions at concentrations found in the blood of healthy persons and those suffering from diabetes [1,2]. The goal of this study is to further improve the performance of Co/AP, especially in terms of sensitivity, as well as extend the response range toward lower and higher glucose concentrations. Most studies have shown that bimetallic catalysts based on cobalt oxide exhibit enhanced electrochemical performance toward glucose detection in comparison to monometallic cobalt-based catalysts. Among the various transition metals, iron has attracted considerable attention as a second metal for the fabrication of bimetallic catalysts based on cobalt oxide. This is because iron can enhance electron transfer processes and has excellent catalytic activity toward glucose. Additionally, iron is inexpensive and Earth-abundant [3].

Inspired by these findings, we prepared the Co/AP and Fe-doped Co/AP catalysts and studied their electrochemical performance in the glucose oxidation reaction. The electroanalytical (sensitivity) and kinetic parameters (charge transfer coefficient (α), the catalytic rate constant (k_{cat}), and the diffusion coefficient (D)) of the electrooxidation of glucose over investigated catalysts were examined in detail.

MATERIALS AND METHODS
The cobalt oxide and iron-doped cobalt oxide catalysts supported on aluminum-pillared clay were synthesized by the incipient wetness impregnation method [4]. The impregnation was performed using the metal nitrate aqueous solutions precursors ($Co(NO_3)_2$, $Fe(NO_3)_3$). The total supported cobalt and cobalt/iron content was 4 wt. %, while the cobalt:iron molar ratio was 9:1. The obtained catalytic materials (Co/AP and CoFe/AP) were characterized by ICP-OES, XRPD, low-temperature N_2 physisorption, and HR-TEM.

The electrochemical characterization of the catalysts was performed using cyclic voltammetry and chronoamperometry. The catalysts were tested in the form of the carbon paste electrode. For simplicity, the electrodes retained the designation of the catalysts throughout the text. The

procedure for the preparation of the electrodes as well as the determination of kinetic parameters were fully described in our previous paper [1]. The estimated errors of measured parameters in this study do not exceed 5%. All values have rounded to an appropriate number of digits to reflect this precision.

RESULTS AND DISCUSSION

The physicochemical characterization of the Co/AP and CoFe/AP

The results of the ICP-OES analysis and textural properties of the Co/AP and CoFe/AP catalysts are given (**Table 1.)**.

Table 1. Selected chemical, and textural properties of catalysts.

Catalyst	**Measured Co, [wt. %]**	**Measured Fe, [wt. %]**	**S_{BET}, [m^2 g^{-1}]**	**V_{mes}, [cm^3 g^{-1}]**	**V_{mic-DR}, [cm^3 g^{-1}]**
Co/AP	3.3	2.3	108	0.087	0.045
CoFe/AP	3.3	2.6	111	0.060	0.046

The measured contents of Co and Fe metals in the catalysts are close to the theoretical metal values, indicating the successful incorporation of electroactive species into AP. It can be seen that AP clay naturally contains iron. As expected, Co/AP doped with iron led to an increase in iron content in the CoFe/AP catalyst following nominal concentration. The results of XRPD analysis (**Figure 1.** (a)) identified montmorillonite and quartz in both catalysts, with no phases corresponding to the introduced metal oxide observed. The specific surface area (S_{BET}), mesopore volume (V_{mes}), and micropore volume (V_{mic-DR}) were similar for both examined catalysts (**Table 1.**). HR-TEM images do not show the presence of second-phase aggregates, which suggests that the active species of the catalysts are well dispersed on the AP (**Figs. 1.** (b) and (c)).

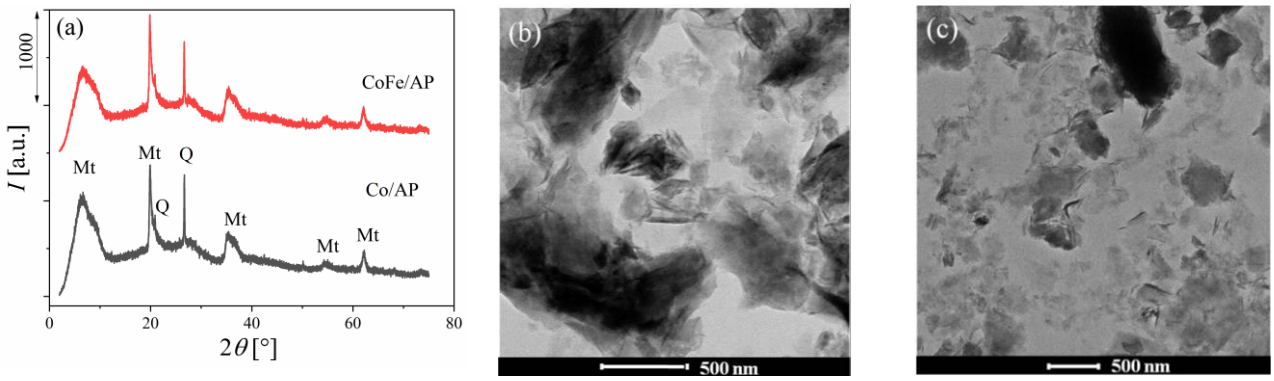


Figure 1. XRPD patterns of: (a) CoAP and CoFe/AP and HR-TEM images of: (b) Co/AP and (c) CoFe/AP catalysts.

Electrochemical characterization of the Co/AP and CoFe/AP

Figure 2. shows the stable cyclovoltammograms (CV) of the Co/AP and CoFe/AP recorded in a 1 M NaOH electrolyte. The CV of Co/AP displayed peaks corresponding to the redox reactions of cobalt species supported on aluminum-pillared clay [1,2]. The addition of iron resulted in a change in the intensities of the peaks and a significant anodic shift of the V/IV pair of peaks, indicating a strong interaction between Fe and Co [5].

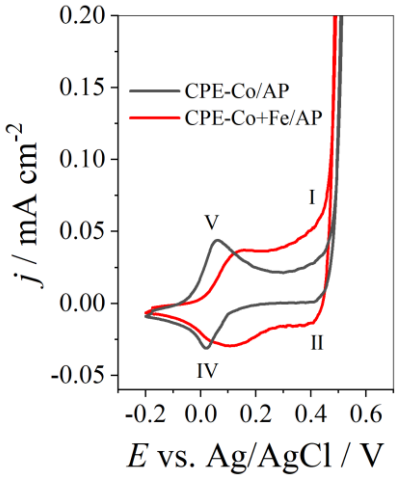


Figure 2. The stable CV of Co/AP and CoFe/AP in a 1 M NaOH electrolyte.

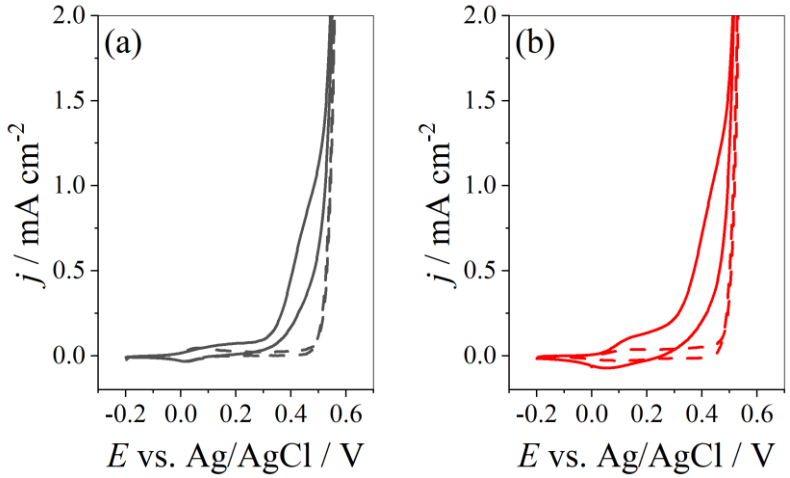


Figure 3. CV of: (a) Co/AP and (b) CoFe/AP in the absence (dashed line) and presence (solid line) of 5 mM glucose in a 1 M NaOH electrolyte.

In the presence of 5 mM glucose, the intensities of peak V and peak I increased for both investigated electrodes (**Figs. 3.** (a) and (b)). The intensity of the peak I increased significantly more. This means that the oxidation of glucose is primarily mediated by CoO_2 [6]. The CoO_2 species chemically oxidizes glucose to gluconolactone, while CoO_2 is reduced to CoOOH (chemical step). The obtained CoOOH is then electrochemically regenerated to CoO_2 (electrochemical step), leading to an increase in the intensity of peak I [6]. The higher current response was obtained for the CoFe/AP, suggesting that the presence of Fe may also improve the electroanalytical performance (sensitivity) of Co/AP.

The chronoamperometric curves of Co/AP and CoFe/AP were recorded at the glucose oxidation peak (peak I) in the glucose concentration range from 0.025 mM to 28 mM.

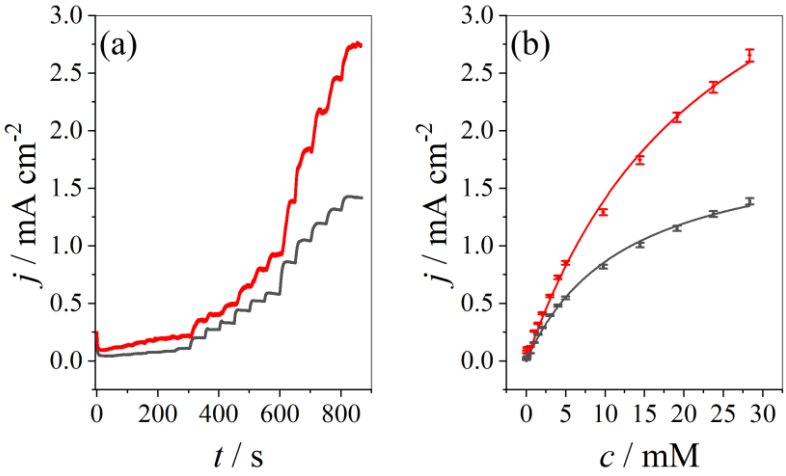


Figure. 4. (a) Chronoamperometric response of glucose in a 1 M NaOH electrolyte at the glucose oxidation peak and (b) corresponding data and fitting curves of Co/AP (black line) and CoFe/AP (red line).

The step-like growth of the current density increased with the increase of the glucose concentrations and a higher current density was obtained for CoFe/AP (**Figure 4.** (a)). The calibration plots (*j*-*c*) showed non-linearity in the whole glucose concentration range (**Figure 4.**

(b)). These results were fitted using the Langmuir equation [6]. The glucose concentration interval was divided into two ranges: from 0.025 to 5 mM and from 5 to 28 mM. In the low glucose concentration ranges, the sensitivities were 112 μA mM^{-1} cm^{-2} and 162 μA mM^{-1} cm^{-2} while in the high glucose concentration ranges, the sensitivities were 30 μA mM^{-1} cm^{-2} and 72 μA mM^{-1} cm^{-2} for the Co/AP and CoFe/AP, respectively.

The kinetic parameters of the glucose oxidation reaction for the Co/AP and CoFe/AP electrodes were calculated and presented (**Table 2.**).

Table 2. Kinetic parameters of the glucose oxidation reaction for investigated electrodes.

Electrode	α	k_{cat}, **[cm^3 mol^{-1} s^{-1}]**	D **[cm^2 s^{-1}]**
Co/AP	0.33	$2.6 \cdot 10^7$	$1.9 \cdot 10^{-5}$
CoFe/AP	0.41	$6.8 \cdot 10^7$	$2.4 \cdot 10^{-5}$

It was found that all investigated kinetic parameters (α, k_{cat}, and D) were higher for CoFe/AP than for Co/AP, which indicates an improvement in the electron transfer ability (electrochemical step) and efficiency in the catalytic reaction (chemical step).

CONCLUSION

In this work, the Co/AP and CoFe/AP catalysts were synthesized using the impregnation method, and their electrochemical performance in the glucose electrooxidation reaction was examined. CoFe/AP exhibited a higher current response and improved sensitivity compared to Co/AP. The results of the kinetics study showed that the presence of Fe not only enhances the electron transfer ability at the CoFe/AP electrolyte/electrode interfaces but also improves the efficiency of catalytic reaction, resulting in an overall improvement in the performance of CoFe/AP. The HR-TEM and XRPD of CoFe/AP showed no formation of a separate iron phase. The introduction of Fe in addition to Co causes a negligible change in the textural properties of the catalyst. On the other hand, the cyclic voltammograms revealed that the presence of Fe caused an anodic shift of the peaks corresponding to the Co species, indicating a strong interaction between Fe and Co. These findings suggest that the enhancement of CoFe/AP performance could be attributed to changes in intrinsic properties, i.e. a synergetic effect between iron and cobalt, rather than external ones.

Acknowledgment

This research has been financially supported by the Ministry of Science, Technological Development and Innovation of Republic of Serbia (Contract No. 451-03-66/2024-03/200026).

REFERENCES

[1] B. Milovanović, S. Marinović, Z. Vuković, A. Milutinović-Nikolić, R. Petrović, P. Banković, T. Mudrinić, J. of E. Chem. 915 (2022) 116332.
[2] T. Mudrinić, S. Marinović, A. Milutinović-Nikolić, N. Jović-Jovičić, M. Ajduković, Z. Mojović, P. Banković, Sens. and Actuat. B: Chem. 299 (2019) 126976.
[3] M. Janyasupab, C.-W. Liu, N. Chanlek, S. Chio-Srichan, C. Promptmas, W. Surareungchai, Sens. and Actuat. B: Chem. 286 (2019) 550–563.
[4] F. Pinna, Cat. Tod. 41 (1998) 129–137.
[5] L. Reith, J. N. Hausmann, S. Mebs, I. Mondal, H. Dau, M. Driess, P.W. Menezes, A. E. M. 13 (2023) 2203886.
[6] Y. Ding, Y. Wang, L. Su, M. Bellagamba, H. Zhang, Y. Lei, Bios. and Bioele. 26 (2010) 542–548.

A NOVEL DUAL-DOPED CARBON ELECTROCATALYST FOR ENHANCED OXYGEN REDUCTION REACTION

S. Brković, P. Laušević, I. Perović, M. Seović, M. Pijović Radovanović, J. Georgijević and N. Zdolšek

University of Belgrade, Vinča Institute of Nuclear Sciences, National Institute of the Republic of Serbia, Mike Petrovića Alasa 12-14, 11351 Vinča, Serbia.
(snezana.miulovic@vin.bg.ac.rs)

DOI: https://doi.org/10.46793/Phys.Chem24I.187B

ABSTRACT
This study addresses the crucial role of oxygen reduction reaction (ORR) in enhancing the performance of fuel cells and metal-air batteries, vital to the advancement of green energy technologies. The primary challenge with ORR lies in its inherently slow kinetics, which necessitates the development of efficient and stable electrocatalysts. Our research introduces a novel, low-cost bifunctional carbon-based electrocatalyst, dual-doped with selenium (Se) and vanadium (V), synthesized through a straightforward direct carbonization mixtures of 1-butyl-3-methylimidazolium bis(trifluoromethylsulfonyl)imide with Se and V. This method proves effective in reducing overpotential and enhancing ORR kinetics, demonstrating significant promise for improving the efficacy of renewable energy technologies.

INTRODUCTION
The global push towards renewable and green energy solutions is driven by the need to address both energy shortages and environmental concerns stemming from fossil fuel usage. Oxygen reduction reaction (ORR) stands out as a pivotal process, particularly in fuel cell and metal-air battery technologies, which hold significant promise for energy conversion and storage [1]. However, ORR poses challenges due to its sluggish kinetics, necessitating intensive research efforts aimed at developing electrocatalysts that are both highly efficient and stable. These catalysts play a critical role in reducing overpotential and accelerating ORR kinetics, thereby enhancing the overall performance of fuel cells and metal-air batteries.

Our study focus on synthesizing a low-cost bifunctional carbon electrocatalyst for ORR (oxygen reduction reaction) by dual-doping carbon material with selenium (Se) and vanadium (V). The synthesis method involves a simple approach of direct carbonization using 1-Butyl-3-methylimidazolium bis (trifluoromethylsulfonyl) imide [2].

METHODS
Material was prepared by mixing 10g ionic liquid (IL) 1-Butyl-3-methylimidazolium bis (trifluoromethylsulfonyl) imide (Sigma Aldrich) with 0.2g Se (metal powder) and 0.4 VCl_2 (Sigma Aldrich). The mole ratio of Se to V is 1:1. The prepared mixture was carbonized in a tube furnace (Protherm Electrical Tube Furnace) under N_2 atmosphere, with the heating rate of 5°C min^{-1} until reaching 800°C, and then in a stream of CO_2 for 120 minutes at 800°C. Material prepared by carbonization was denoted as IL-SeV. The same procedure was repeated for carbonization of pure ionic liquid and a sample noted IL.

The preparation of the working electrodes involved dispersing of the synthesized materials (5 mg) in 980 µL of deionized water and 20 µL of 5% Nafion (Sigma Aldrich). These mixtures underwent sonication for 30 minutes at room temperature to achieve a homogeneous catalytic ink.

Subsequently, 10 µL of the catalytic ink was applied onto the glassy carbon electrode (GCE) and allowed to dry at room temperature.

All electrochemical measurements were conducted employing the Gamry Interface 1000E Potentiostat/Galvanostat/ZRA within a three-electrode electrochemical cell at room temperature. The modified GCE served as the working electrode, platinum was utilized as the counter electrode, and a saturated calomel electrode (SCE) functioned as the reference electrode. Throughout the article, all potentials are reported relative to the reversible hydrogen electrode (RHE). The current densities (*j*) presented were calculated using the geometric area of the electrodes (0.19625 cm²).

Prior to the oxygen reduction measurement, a 0.1 M KOH (Sigma Aldrich) electrolyte was saturated with high-purity N_2 or O_2 gas for 30 minutes. Cyclic voltammetry (CV) tests were conducted within the range of -0.8 to 0.2 V (vs. SCE) at a sweep rate of 20 mV s^{-1}. Linear sweep voltammetry (LSV) using a rotating disc electrode (RDE) was performed from -0.8 to 0.2 V (vs. SCE) with a sweep rate of 5 mV s^{-1}, varying rotating speeds (ω) from 200 to 2000 rpm. The currents recorded with RDE in O_2-saturated electrolyte were adjusted for background currents by subtracting those recorded in N_2-saturated electrolyte.

RESULTS AND DISCUSSION

The ORR performance of the IL-SeV and IL samples are evaluated by cyclic voltammetry (CV) measurements in O_2/N_2-saturated 0.1 M KOH. As shown in **Figure 1**, in comparison to those in N_2-saturated electrolyte, an obviously enhanced cathodic peak is seen in O_2-saturated one, implying efficient ORR activity. Control cyclic voltammograms recorded in N_2-saturated electrolyte showed no redox peaks. The cathodic peaks at 0.822 V (vs. RHE) and 0.797 V (vs. RHE) was observed for IL-SeV and IL, respectively. The more positive value of the peak potential of IL-SeV suggests its higher electrocatalytic activity for ORR. Additionally, it is important to note that our electrocatalyst demonstrated a more positive ORR potential than other carbon materials doped with cobalt, manganese, and various other metals, typically ranging between 0.7 V and 0.8 V [3,4].

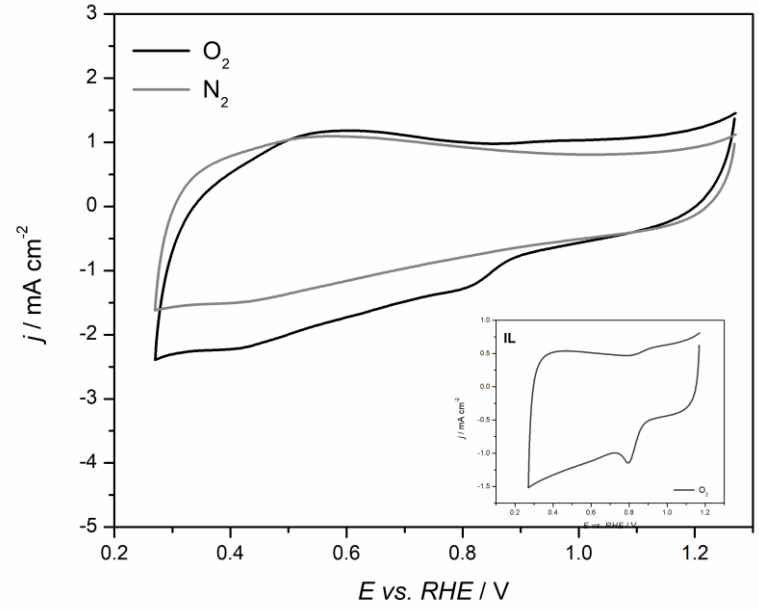


Figure 1. CVs in N_2- or O_2-saturated 0.1 M KOH electrolyte for IL-SeV and CVs for IL in O_2-saturated 0.1 M KOH electrolyte (inset).

LSV RDE measurements were used for detailed investigation and evaluation of kinetic parameters of ORR (**Figure 2, left**). LSV RDE data were analyzed using Koutecky-Levich (K-L) equation [5]. Number of electrons (n) transferred during ORR was determined from the slope of Koutecky-Levich plots (j^{-1} *vs.* $\omega^{-1/2}$), while kinetic current density (j_k) values were determined from the intercept of Koutecky-Levich plots. ORR number of electrons values were found to be 3 in the whole investigated potential range (**Figure 2, right**) suggests co-existence of both two- and four-electron ORR pathway at IL-SeV material, while for IL material it is four-electron ORR pathway.

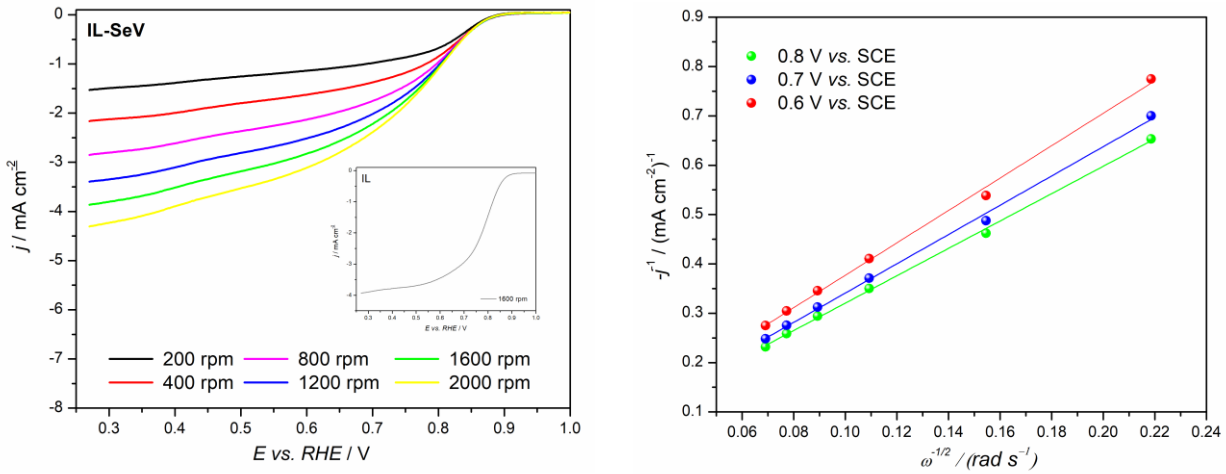


Figure 2. LSV RDE curves for IL-SeV with inset LSV RDE curve on 1600 rpm for IL (left) and corresponding Koutecky-Levich plots for IL-SeV (right).

The polarization curve (LSV) showing a plateau that becomes more inclined with increasing rotation rate suggests that the system's kinetics are not fully diffusion-controlled. The limiting currents densities (j_d) of 3.83 mA cm^{-2} (for IL-SeV) and 3.89 mA cm^{-2} (for IL), determined from the LSV RDE at 1600 rpm, indicates the maximum current density achievable under the given experimental conditions. The values of j_k for the potential of 0.8 V was determined to be 23.3 mA cm^{-2} for IL-SeV and 11.9 mA cm^{-2} for IL (**Table 1**). We can say that Selenium (Se) and Vanadium (V) doping have significant effects on the kinetics of oxygen reduction reactions (ORR).

Table 1. Kinetic current density (j_k) at different potentials.

No.	***E vs.* SCE / mV**	**j_k / mA cm^{-2}** for IL-SeV	**j_k / mA cm^{-2}** for IL
1.	800	23.3	11.9
2.	700	22.7	10.1
3.	600	20.5	11.3

The onset potential (E_{onset}) serves as a crucial metric for assessing the electrocatalytic performance of new electrode materials. However, it's important to note that there isn't a universally accepted method for determining E_{onset} [6]. Typically, it's identified as the potential where the measured current noticeably diverges from the background signal [6]. According to the most recent definition, E_{onset}, as an indicator of oxygen reduction reaction (ORR) activity, is defined as the electrode potential at a current density of approximately -3 µA cm^{-2} [7]. In this study, the onset potential of the studied electrocatalyst, determined through linear sweep voltammetry (LSV) at

1600 rpm, was found to be 0.899 V (*vs*. RHE) and 0.897 V (*vs*. RHE) for IL-SeV and IL, respectively.

CONCLUSION

The paper showcases a straightforward and cost-effective synthesis technique for integrating selenium (Se) and vanadium (V) into carbon materials simultaneously. This method involves directly carbonizing ionic liquid 1-butyl-3-methylimidazolium bis(trifluoromethylsulfonyl)imide, mixed with Se and V, without any additional chemical or electrochemical treatments. The resulting IL-SeV carbon material demonstrate remarkable activity in the oxygen reduction reaction (ORR), characterized by a 3-electron mechanism and a notably high onset potential of 0.899 V. Additionally, the kinetic current densities (j_k) at a potential of 0.8 V were calculated to be 23.3 mA cm^{-2} for IL-SeV, significantly higher in comparison with the material obtained by carbonization of pure ionic liquid (11.9 mA cm^{-2} for IL). This approach holds promise for producing efficient ORR catalysts without the need for complex synthesis processes.

Acknowledgment

This work was supported by the Ministry of Education, Science and Technological Development of the Republic of Serbia (grant no 451-03-66/2024-03/200017)

REFERENCES

[1] X. Tian, X. Feng Lu, B. Yu Xia, X. Wen Lou, Joule, 4 (2020) 45.
[2] G. Prasad, K. Muralidhar Reddy, R. Padamasuvarna, T. Madhu Mohan, T. Vijaya Krishna, V. Ramesh Kumar, J. Mol. Liq., 251 (2018) 335.
[3] L. Bai, Z. Duan, X. Wen, R. Si, J. Guan, Appl Catal B Environ, 257 (2019) 117930.
[4] Y. Su, Y. Zhu, H. Jiang, J. Shen, X. Yang, W. Zou, J. Chen, C. Li, Nanoscale, 6 (2014) 15080.
[5] J. Wu, Z. Yang, X. Li, Q. Sun, C. Jin, P. Strasser, R. Yang, J Mater Chem A, 1 (2013) 9889.
[6] A.J.R. Botz, M. Nebel, R.A. Rincón, E. Ventosa, W. Schuhmann, Electrochim Acta, 179 (201) 38.
[7] Y. Hu, X. Zhao, Y. Huang, Q. Li, N.J. Bjerrum, C. Liu, W. Xing, J Power Sources, 225 (2013) 129.

SUSTAINABLE METAL RECOVERY: CPU RECYCLING FOR ENHANCED HYDROGEN EVOLUTION REACTION

S. Mitrović, S. Brković, M. Seović, N. Zdolšek, P. Laušević, M. Pijović Radovanović and I. Perović

University of Belgrade, Vinča Institute of Nuclear Sciences, National Institute of the Republic of Serbia, Mike Petrovića Alasa 12-14, 11351 Vinča, Serbia.
(snezana.miulovic@vin.bg.ac.rs)

DOI: https://doi.org/10.46793/Phys.Chem24I.191M

ABSTRACT
This paper explores the feasibility and efficacy of employing whole CPU (Central Processing Unit) recycling as a sustainable source of metals for catalyst coatings in the Hydrogen Evolution Reaction (HER). With the escalating global issue of electronic waste (e-waste), repurposing discarded CPUs offers a promising avenue for metal recovery and utilization. Through systematic experimentation, CPU preparation technique was evaluated for formation of electrode catalytic layer and the kinetics of HER in alkaline media. The resulting electrodeposited cathode was assessed for electrocatalytic efficiency. Our findings highlight the potential of utilizing e-waste-derived metals, particularly gold and copper, as effective catalyst coatings for HER, thus contributing to sustainable metal recovery and utilization strategies.

INTRODUCTION
In recent modern times, driven by the remarkably swift evolution of technology and increased consumer demands, the electronics industry stands as one of the most rapidly expanding sectors. The accelerated production of novel and advanced electronic components has, however, artificially reduced their lifespan. Consequently, the global accumulation of electronic waste, or e-waste, has witnessed a substantial upswing.

Based on a data collected, the global volume of electronic and electrical waste in 2019 reached a staggering 53.6 million metric tons [1]. This marked an increase of approximately 17.16% compared to 2014's figure of around 44.4 million metric tons, and the estimation for 2025 of around 65.3 million metric tons [1].

Electronic components represent extremely complex systems with around of 70 elements from periodic table. Precious metals such as silver, gold and copper dominate the mix, but other metals such as aluminium, nickel and titanium, also make their presence. Given that the metals on Earth are limited, and conventional mining and extraction processes are harmful to the environment, recycling of these metals from electronic waste presents a promising direction of research [2].

Our work showcases a potential application of recycled metals, specifically precious metals sourced from electronic waste, in the field of hydrogen production. Considering the extensively documented catalytic effectiveness of noble metals in the hydrogen evolution reaction and other reactions of interest in energy converting applications, this investigation is gaining substantial momentum.

METHODS
The main topic of this research is the investigation of potential use of recycled and leached metals extracted from waste CPU-s as a catalyst for hydrogen evolution reaction. The preparation method for metal extraction can have the biggest influence on electrodeposition and hydrogen evolution efficiency.

Computer CPU-s were obtained from disassembled desktop computers, carefully extracted and cleaned from dirt and thermal paste.

For this research, sample preparation was simple. The whole cleaned CPU was immersed in leaching solution containing 0.6 g sodium-chloride, 9.5 ml 1.4 M hydrochloric acid and 0.5 ml 30 % hydrogen peroxide, with combined volume off 30 ml. Leaching time was 96 h and the solution was held at 70 °C through the first 6 h, and for the remaining time the leaching solution was at room temperature [3]. For the later electrodeposition, the same solution was used (leaching solution plus the leached metals from CPU).

For all electrochemical testing, a 6 M KOH solution was used.

Electrodepostion was conducted in a standard two-electrode glass cell, with high-purity (99.99 %) metallic nickel electrode as working electrode. Counter electrode in this system was a high-surface-area platinum mesh. The electrodeposition process was carried out using Gamry 1000E Potentiostat at current density of 10 $mAcm^{-2}$ for two hours with constant stirring at 300 rpm.

Electrochemical evaluations were performed in a three-electrode glass cell. The working electrode was the metallic nickel electrode with electrodeposited catalyst. The counter electrode remained a high-surface-area platinum mesh, and a reference electrode was an SCE (saturated calomel electrode). Before all tests, electrolyte was purged with hydrogen for 15 minutes. Electrochemical characterization for determination of hydrogen evolution reaction (HER) kinetic parameters for electrodeposited catalyst consisted of recording and analyzing the polarization curves and Electrochemical Impedance Spectroscopy spectra (EIS). Polarization curves were recorded by changing the electrode potential in the range from -1.6 V to -0.6 V, at a rate of 1 mVs^{-1}. For impedance analysis, spectra were recorded in the frequency range from 0.01 Hz to 100 kHz using an alternating signal with an amplitude of 10 mV superimposed on a constant overvoltage value in a range from -50 mV to -200 mV. Before each measurement, the working electrode was conditioned for 20 min at a constant current of 100 mA, while the temperature of the solution was held at 298 K.

RESULTS AND DISCUSSION

In this study, the sample was prepared as mentioned and the deposition bath was used to obtain catalyst deposit for hydrogen production. The whole CPU was immerged in a leaching bath for 96 hours. The color of solution before and after leaching was drastically changed. From completely clear to some mixture of dark green and brown color (**Figure 1**). After leaching, CPU was removed and the solution was directly used as electrodeposition bath.



Figure 1. W-CPU-1.4 M immediately after immersion (left) and after leaching for 96 h (right).

The kinetics parameters and general mechanism of hydrogen evolution reaction (HER) on cathode electrodeposited from leaching solution were analyzed via Tafel analysis and Electrochemical Impedance Spectroscopy (EIS). Polarization curves and EIS spectra were acquired in 6 M KOH and compared to bare nickel. These polarization curves and EIS spectra are presented in **Figure 2**.

a) b)

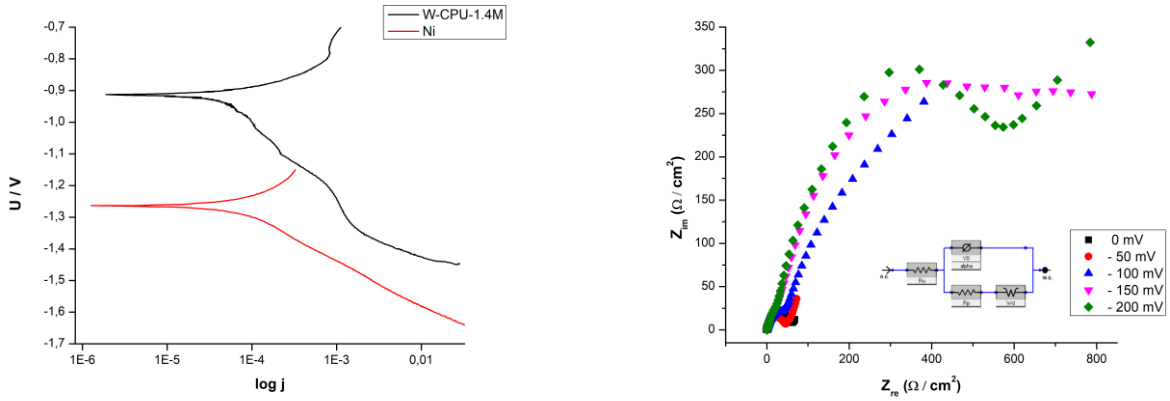


Figure 2. Polarization curve for HER in 6 M KOH with nickel electrode and electrode coated with catalyst (a); impedance diagram (Nyquist plot) of coated electrode recorded at potential range between 0 mV and 200 mV with inset of circuit used for modeling (b).

A Tafel analysis was performed on obtained polarization curves for both electrodes: bare metallic Ni electrode and Ni electrode coated with electrodeposited catalyst. Observing these polarization curves it can be noted that electrode with coated catalyst gravitates toward less negative potential values in comparison with the pristine Ni electrode. The curve's slope, known as the Tafel slope, provides insight into the reactions activation energy, implying a reaction rate. Tafel slope values are detailed in **Table 1**.

Table 1. Tafel slope values for coated electrode and bate Ni electrode in 6 M KOH.

Sample	Tafel Slope (mV/dec)
W-CPU-1.4M	111.5
Ni	120.0

Based on the Tafel slope values, three mechanisms can be categorized: activation-controlled, diffusion-controlled and mixed-controlled reactions. The electrodeposited catalyst in this study exhibits values spanning between 90 and 120 mV/dec, correlating with mixed-controlled reaction mechanism. The same mechanism can be also observed for bare nickel electrode.

The EIS spectra were recorded at ambient temperature over the range of overpotentials between 0 mV and 200 mV. Nyquist plots manifest as a distorted semicircle with a short diffusion tale at higher overpotential values.

Table 2. EIS parameters for electrodeposited catalyst coat.

T (K)	-η (mV)	R_e (Ω cm^2)	R_{ct} (Ω cm^2)	α	C_{dl} (μF cm^{-1})	σ	τ
298.15	0	0.526	58.650	0.746	795.917	40	0.047
	50	0.523	42.119	0.718	559.854	28	0.024
	100	0.535	32.707	0.756	362.116	18	0.012
	150	0.465	45.506	0.658	348.883	17	0.010
	200	0.481	42.987	0.687	323.464	13	0.009

Acquired EIS spectra were modelled using a hybrid Randles circuit (**Figure 2b**), incorporating a constant phase element (CPE), diffusion coefficient, electrolyte resistance and charge transfer resistance. These parameters enabled the calculation of the electrode surface roughness factor (σ) and the single time constant (τ) (**Table 2**). The roughness factor was approximately 20, which correlates with electrode active surface, and double layer capacitance showcased favourable metrics [4].

CONCLUSION

This study has explored a simple yet effective method for recycling electronic waste and extracting valuable metals. By immersing the entire CPU in a leaching solution, metals were extracted, and by the process of electrodeposition a catalyst coating was obtained. Subsequent detailed electrochemical analysis revealed that the metal composition deposited on the electrode surface exhibits considerable promise as a catalyst for the hydrogen evolution reaction in alkaline media. This innovative fusion of recycling and direct application as a catalyst not only presents an exciting avenue for resource recovery but also holds significant potential for fostering a circular economy. Such an approach not only mitigates electronic waste accumulation but also contributes to sustainable practices, thereby yielding substantial ecological benefits. By harnessing the dual benefits of recycling and catalysis, this research underscores the potential for creating a more environmentally conscious and resource-efficient future.

Acknowledgment

This work was supported by the Ministry of Education, Science and Technological Development of the Republic of Serbia (grant no 451-03-66/2024-03/ 200017)

REFERENCES

[1] V. Forti, C.P. Baldé, R. Kuehr, G. Bel, The Global E-waste Monitor 2020: Quantities, Flows, and the circular economy potential, Bonn/Geneva/Rotterdam, 2020.
[2] B. H. Robinson, Sci. Total Environ., 408 (2009) 183.
[3] S. Mitrović, S. Brković, S. Živković, N. Zdolšek, M. Seovič, J. Georgijević, I. Perović, Materials, 16 (2023) 20.
[4] A. Lasia, Mod. Asp. Electrochem., 32 (2002).

FROM PEEL TO POWER: ACTIVATED CARBON FOR SUPERCAPACITORS FROM LEMON PEEL WASTE

M. Seović, S. Brković, N. Zdolsek, P. Laušević, S. Mitrović, J. Georgijević and I. Perović

University of Belgrade, Vinča Institute of Nuclear Sciences, National Institute of the Republic of Serbia, Mike Petrovića Alasa 12-14, 11351 Vinča, Serbia (snezana.miulovic@vin.bg.ac.rs)

DOI: https://doi.org/10.46793/Phys.Chem24I.195S

ABSTRACT

This study explores the production of activated carbon (AC) from lemon peel, an agricultural waste, using phosphoric acid activation, presenting a sustainable alternative to conventional AC derived from fossil fuels. The processed lemon peel AC exhibited promising electrochemical properties suitable for supercapacitors, including high specific capacitance of 138.9 F/g at a scan rate of 20 mV/s and excellent stability in an alkaline environment. These findings demonstrate the potential of bio-waste as a cost-effective and environmentally friendly precursor for AC production. This approach not only supports waste minimization but also contributes to sustainable resource utilization in the field of energy storage.

INTRODUCTION

Efforts to convert agricultural waste into activated carbon (AC) have indeed gained traction in recent decades. Firstly, it reduces the environmental burden by repurposing waste that would otherwise require disposal. Secondly, it presents an economically viable alternative to traditional AC fabrication methods, potentially driving down production costs. This dual advantage not only addresses waste management concerns but also contributes to sustainable resource utilization and cost-effective manufacturing processes [1]. The growing use of activated carbons (AC) in commercial supercapacitors is largely attributed to their beneficial characteristics. These include exceptional electrochemical stability, a high surface area, and various other advantageous electrochemical properties. Activated carbons are favored for their ability to efficiently store electrical charge, primarily due to their porous structure which allows increased surface contact with electrolytes [2]. This feature, combined with the material's inherent chemical resilience and conductivity, makes them ideal for use in energy storage applications where durability and efficiency are paramount [3]. However, the scalability of AC production faces challenges due to rising raw material costs and limited precursor availability. Fossil fuels, the traditional source for such materials, are not renewable and hence cannot sustain the growing demand. Bio-waste emerges as a promising alternative precursor for AC production, primarily due to its widespread availability and low-cost accessibility. This shift towards bio-waste as a precursor, holds significant potential to meet the rising demand for AC in various applications, including supercapacitors, while fostering sustainability and resource efficiency [4].

In this work, lemon peel *(lat. Citrus x limon)* chemically activated with phosphoric acid (H_3PO_4) acid is used as a precursor for production of activated carbon. The elemental composition of the resulting activated carbon was examined using X-ray fluorescence (XRF), and its electrocatalytic properties were investigated through cyclic voltammetry (CV).

METHODS

Preparation of lemon peel derived activated carbon (LP-AC) was done as follows. The fresh lemon peel was initially dried at 100°C for 24 hours. During a standard synthesis procedure, 60 grams of the dried peel were combined with 15 grams of phosphoric acid (H_3PO_4), analytical grade from Alfa Aesar, in 100 milliliters of distilled water. This mixture was stirred at room temperature for 24 hours, followed by drying at 100°C. Subsequently, carbonization was conducted in a Protherm Electrical Tube Furnace (PTF 16/38/250) under a nitrogen gas flow. The temperature was gradually increased to 800°C, with the heating rate of 5°C min^{-1}, and maintained at this peak for one hour before allowing it to cool to room temperature. After carbonization, the samples were washed with distilled water and then acetone, filtered, and dried once more at 100°C for another 24 hours.

The electrochemical properties of the catalyst were evaluated using cyclic voltammetry (CV) studies conducted at room temperature (25°C) on a Gamry INTERFACE 1000E potentiostat. For these tests, a glassy carbon (GC) electrode with an area of 1 cm^2 served as the working electrode. The GC was polished with alumina powder until a mirror finish was achieved. To prepare the working electrode, a slurry of LP-AC was created by ultrasonically dispersing 20 mg of LP-AC in 50 µL of ethanol and 5 wt% Nafion solution for 30 minutes. Subsequently, 10 mg of this catalyst ink was applied to coat the GC electrode, which was then dried at 60°C for 30 minutes. The electrochemical properties of LP-AC electrodes were tested in 6 M KOH using CV by three electrode system. A Pt mesh and a saturated calomel electrode (SCE) were utilized as the counter and reference electrodes, respectively, in a conventional three-electrode electrochemical cell.
The elemental composition of the obtained sample was analyzed at room temperature using a Thermo Scientific Niton XL3t XRF analyzer.

RESULTS AND DISCUSSION

The elemental composition of the obtained LP-AC material was analyzed using the X-ray fluorescence (XRF) method, and the results are presented in Table 1. The analysis revealed a high phosphorus content in the sample, followed by chromium, vanadium, and zinc. The combined presence of these elements can synergistically enhance the electrochemical properties of the activated carbon. The transition metals (Cr, V, Zn) and the non-metal (P) can improve both electrical conductivity and capacitance through doping effects, redox activity, and the creation of additional active sites.

Table 1. Amounts of most abundant elements determined by XRF analysis in LP-AC sample.

Element	P	Cr	V	Zn	Ti	W	Cu	Se
%	82.348	10.432	2.994	1.478	0.976	0.660	0.659	0.119

The specific capacitance value is a key metric in optimizing the chemical activation of biowaste from lemon peel into activated carbon electrodes for electric double-layer capacitors (EDLCs). To explore the specific capacitance behavior of the lemon peel activated carbon (LP-AC), cyclic voltammetry (CV) studies were carried out. The results are presented in **Figure 1**. The quasi-rectangular shape of the cyclic voltammogram, obtained in a 6 M KOH electrolyte, underscores the significant role of charge storage in the electrochemical double layer of the carbon materials. Furthermore, the cyclic voltammogram indicates that the electrode maintains stability in an alkaline environment within the tested potential range.

(a) (b)

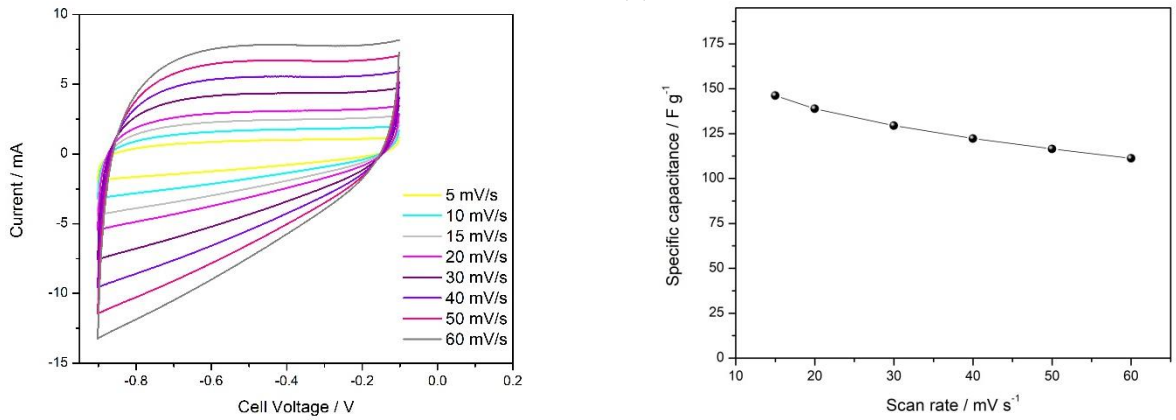


Figure 1. CV curves of LP-AC in 6M KOH at different scan rates (a); Specific capacitance with respect to scan rate (b).

Specific capacitance was calculated from CV curves recorded at different scan rates according to **Equation 1** [5].

$$C = \frac{\int i \cdot dV}{2 \cdot m \cdot v \cdot \Delta V} \quad (1)$$

where $\int i \cdot dV$, m, v, and ΔV is the area under the curve (current density), the weight of materials, scanning rate, and the working potential range of cyclic voltammetry.

The specific capacitance values calculated for different scan rates are displayed in **Figure 1b**. As anticipated, the capacitance value decreases with increasing scan rate due to the limited diffusion of ions into the inner pores of the carbon electrode at higher rates. Specifically, a capacitance value of 138.9 F/g is recorded at a scan rate of 20 mV/s. In comparison to existing literature, the specific capacitance value of 138.9 F/g achieved in this study is competitive and promising [6]. Values for AC derived from other bio-wastes typically range from about 100 F/g to 150 F/g, depending on the activation method and the raw material used. Therefore, the capacitance value obtained from lemon peel not only reinforces the viability of using fruit peel waste but also positions it as an effective material for high-performance energy storage applications. This makes the lemon peel-derived AC a compelling option for advancing supercapacitor technologies with a focus on cost-effectiveness and environmental sustainability.

CONCLUSION

This study has successfully demonstrated the feasibility of utilizing lemon peel as a precursor for the production of activated carbon (AC), highlighting a sustainable approach to both waste management and materials science. By chemically activating the lemon peel with phosphoric acid, we were able to transform this bio-waste into activated carbon with properties conducive to use in supercapacitors, including high specific capacitance and excellent electrochemical stability.

The specific capacitance of the lemon peel-derived activated carbon reached as high as 138.9 F/g at a scan rate of 20 mV/s, underscoring its potential in energy storage applications. Furthermore, the cyclic voltammetry studies revealed that the AC exhibited a stable electrochemical behavior in an alkaline medium, which is critical for real-world applications.

Acknowledgment
This work was supported by the Ministry of Education, Science and Technological Development of the Republic of Serbia (grant no 452-03-9/2020-14/200014-0902105).

REFERENCES

[1] M. Rafatullah, O. Sulaiman, R. Hashim, A. Ahmad, J. Hazard. Mater., 177 (2010) 70.
[2] P. Chaudhary, S. Bansal, B. B. Sharma, S. Saini, A. Joshi, J. Energy Storage, 78 (2024) 109996.
[3] L. Luo, Y. Lan, Q. Zhang, J. Deng, L. Luo, Q. Zeng, H. Gao, W. Zhao, J. Energy Storage, 55 (2022) 105839.
[4] A. Garg, S. Basu, N. P. Shetti, M. Bhattu, A. N. Alodhayb, S. Pandiaraj, Environ. Res., 250 (2024) 118503.
[5] M.Vujković, L. Matović, J. Krstić, M. Stojmenović, A. Đukić, B. Babić, S. Mentus, Electrochim. Acta 245 (2017) 796.
[6] K. Surya, M.S. Michael, Biomass and Bioenergy, 152 (2021) 106175.

SQUARE WAVE VOLTAMMETRIC METHOD FOR ERLOTINIB DETERMINATION AT DNA MODIFIED GLASSY CARBON ELECTRODE

M. Aleksić [1], M. Jovanović [2], M. Čarapić [3] and K. Nikolic [4]

[1] *University of Belgrade − Faculty of Pharmacy, Department of Physical Chemistry and Instrumental Methods, Vojvode Stepe 450, P.O.Box 146, 11221 Belgrade, Serbia. (mara.aleksic@pharmacy.bg.ac.rs)*
[2] *University of Belgrade - "VINČA" Institute of Nuclear Sciences - National Institute of the Republic of Serbia, Department of Molecular Biology and Endocrinology, Mike Petrovića Alasa 12-14, 11351 Vinča, Belgrade, Serbia.*
[3] *Medicines and Medical Devices Agency of Serbia, Vojvode Stepe 458, 11000 Belgrade, Serbia*
[4] *University of Belgrade − Faculty of Pharmacy, Department of Pharmaceutical Chemistry, Vojvode Stepe 450, P.O.Box 146, 11221 Belgrade, Serbia.*

DOI: https://doi.org/10.46793/Phys.Chem24I.199A

ABSTRACT

Erlotinib (ERL) is tyrosine kinase inhibitor which interacts with DNA double helix. It is electroactive compound capable of being irreversibly oxidized at glassy carbon electrode (GCE) in the pH range from 2 to 9. The intensity of the square wave voltammetric oxidation peak of ERL decreased with the increase of pH, while its peak potential is shifted towards less positive values. The best condition to follow the interaction between ERL and DNA is at pH 4.6 where both compounds are stable and SWV peaks are well pronounced. The aim of this work was to utilize the interaction of ERL with DNA in order to determine the minimum amount of ERL that is capable to react with DNA. For that purpose GCE modified with adsorbed layer of DNA on its surface was used. On the basis of the achieved linear dependence of peak current intensity on ERL concentration in the solution ranged 3.0×10^{-7} M – 2.0×10^{-6} M, the lowest detectable content of ERL able to interact with DNA was obtained as LOD=1.45×10^{-7} M.

INTRODUCTION

Kinases represent a large group of enzymes that catalyze the transfer of a phosphate group from adenosine triphosphate (ATP) to a specific substrate, i.e. protein phosphorylation, thereby indirectly promote the proliferation, survival and migration of cells, and are associated with carcinogenesis and metastases of various types of cancer [1]. Targeted action on kinases has led to the development of kinase inhibitors, compounds with the role to suppress tumorigenesis, thus achieving a significant advance in cancer treatment [1]. Erlotinib is a tyrosine kinase inhibitor that belongs to the class of reversible EGFR/HER1 (human epidermal growth factor receptor type I) kinase inhibitors type I which binds to the active form of enzyme. It is considered that the additional mechanisms of action for some anticancer drugs targeting inhibition of protein kinase is their ability to interact with DNA double helix in order to achieve modification of cancer cells DNA [2]. Our previous study [3] has shown that ERL can interact with the DNA double helix. Following the interaction the between surface-immobilized DNA and ERL in the solution an intercalation binding mode of ERL to DNA, and/or possible groove binding, was suggested. The binding constant of ERL to the ct-DNA was calculated, and the obtained value of $K = 8.25\times10^{4}$ M^{-1} indicates moderate interaction strength. These findings were verified by molecular docking and molecular dynamics analysis [3].

The aim of this work was to use the DNA modified GCE to investigate the concentration profile of ERL and to determine the lowest detectable content able to interact with DNA. To achieve this goal very sensitive pulse voltammetric method is needed. There are several reasons for choosing SWV over DPV in this study: higher speed as a consequence of high effective scan rate, increased signal-to-noise ratio and repetitiveness, and the lower consumption of electroactive species.

METHODS

The μAutolab analyzer supported by GPES 4.9 software (EcoChemie, Utrecht, The Nederlands) was used to perform square wave voltammetric measurements. Three-electrode system that consisted of glassy carbon working electrode (GCE d = 3 mm, CH Instruments, Inc., Austin, TX, USA), Ag/AgCl reference (3.00 M KCl) and Pt auxiliary electrode was applied. Before each measurement, the GCE was pretreated by polishing with an aqueous slurry of Al_2O_3 powder (particle size 0.05 μm), and afterwards sonicated in deionized water and absolute ethanol for 2 minutes in each. The pH measurements were performed using PHM 220 pH meter with combined electrode Radiometer GK2401B.

Both erlotinib-hydrochloride and deoxyribonucleic acid sodium salt from calf thymus (Calf thymus DNA (ct-DNA) Product Number D 1501) were obtained from Sigma Aldrich. Different buffer solutions, all with ionic strength of 0.1 M, were used in this study: citrate (pH 2.20 and 3.06), acetate (pH 3.58, 4.64, 5.05 and 5.64), phosphate (pH 5.89, 6.94 and 8.05) and ammonia (pH 8.51 and 8.90). The chemicals used for their preparation were all of analytical grade purity (p.a.). The stock solution of 1×10^{-3} M ERL was prepared in methanol, and the stock solution of DNA, 73.95 μg/mL in 0.1 M acetate buffer pH 4.6, and both were stored at 4 °C. Final solutions of different ERL concentration were prepared *ex tempore* by diluting the stock solution in different buffers.

The DNA modified GC electrode (GCE/DNA) was prepared by covering the surface of glassy carbon electrode successively with three drops of ct-DNA stock solution (5 μL, 73.95 μg mL^{-1}) and allowing it to dry in nitrogen atmosphere [4].

The measurements were performed by using SW voltammetry under the following conditions: frequency 25 Hz, step potential 0.001 V, effective scan rate of 0.025 V s^{-1} and pulse amplitude of 0.005 V. For better graphical representation the voltammograms were baseline-corrected with moving average application with step windows of 0.005 V and smoothed using a Savitzky-Golay smoothing algorithm (level 4), while the values for peak current were always determined from the original voltammograms. All the analysis was performed using the GPES 4.9 software.

RESULTS AND DISCUSSION

Solutions of 2×10^{-4} M ERL in different buffers pH ranged between 2.0 and 9.0 were used for obtaining information about oxidation behavior by recording SW voltammograms at bare GCE. While the potential was scanned in positive direction starting from 0.0V up to 1.6V, one anodic peak was detected across the whole examined pH region, with peak potential shifting to less positive potential, from +1.2 V in acid medium to +0.7 V in alkaline medium (**Figure 1A.**). According to the intensity and the shape, any oxidation peak obtained at pH ≤ 5 may be used for ERL determination. SWV is also used for reversibility predictions since during the experiment the current is sampled in positive and negative-going pulses at the same time. By analyzing the forward and backward components of the ERL oxidation SW peak current, (**Figure 1B.**) both peak components, as well as the total peak current, were oriented in the same direction indicating the irreversible nature of the process. This is in accordance with previously obtained CV results [3].

It is known that DNA is electroactive specie showing two SWV oxidation peaks (dG and dA). Considering the stability of the DNA double helix, measurements may be performed within physiological limits 4.5 < pH < 8.0.

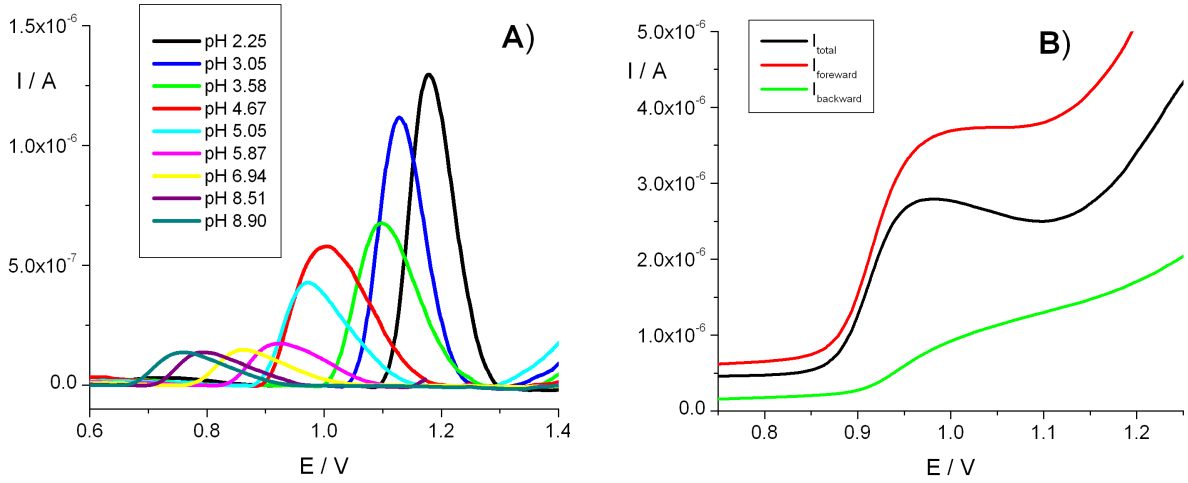


Figure 1. SW voltammograms of 2 × 10^{-4} M ERL **A)** in different buffers at bare GCE; **B)** in acetate buffer pH 4.6; I_{total} - total current, $I_{forward}$ - forward current, $I_{backward}$ - backward current.

The most intense DNA oxidation signals are obtained at pH 4.6: peak dG due to the oxidation of deoxyguanosine at 1.1V and dA as oxidation peak of deoxyadenosine at potential of 1.3V [4]. Since both ERL and DNA show well-defined signals at pH 4.6 it was chosen for further work. When the drug-DNA interaction occurs, the ERL and dG oxidation peaks (which occur at close potentials) may overlap and are not useful for analysis. Therefore, only the change in the dA peak can be used as a measure of the amount of drug bound to DNA. The 30-minutes long interaction between the ERL present in the solution and DNA immobilized on the surface of the modified electrode was followed by a decrease in the intensity of the dA peak. The decrease of the signal is proportional to the increased concentration of ERL in the solution. As long as the decrease in the signal shows a linear dependence, it can be considered that the drug has completely bound to the DNA, when the decrease in the signal starts to level off, it can be assumed that the DNA layer on the electrode is saturated with the drug. The area of linear dependence can be used to determine the lowest detectable content of ERL able to interact with DNA.

The linear decrease in dA peak current intensity was detected when ERL was present in the solution in the concentration ranged from 3.0×10^{-7} M to 2.0×10^{-6} M (**Figure 2**).

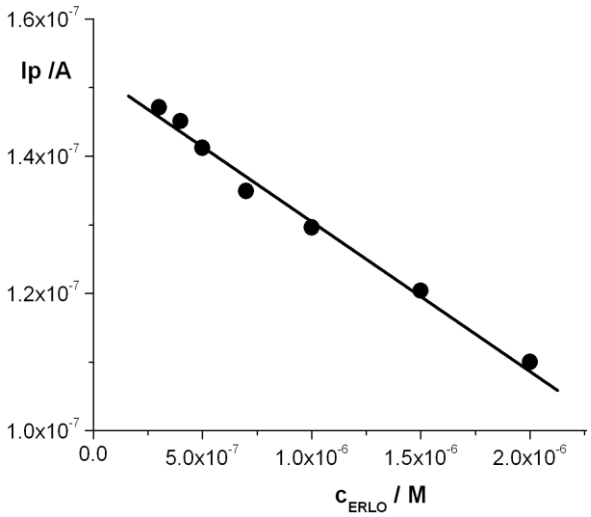


Figure 2. Dependence of SWV dA peak current on the concentration of ERL incubation solutions. Concentration range: 3 × 10^{-7} M − 2 × 10^{-6} M; y = –0.0217 × + 1.52 × 10^{-7}; R = –0.9951.

The limit of detection (LOD = 1.45×10^{-7} M) and limit of quantification (LOQ = 4.84×10^{-7} M) for ERL quantification with DNA modified GCE following the SWV measurement procedure were calculated using the equations LOD = $3S_a/b$ and LOQ = $10S_a/b$ where S_a represents the standard deviation of the intercept, and b is the slope of the calibration curve. All basic statistic data of the regression line for ERL quantification at DNA/GCE by SWV are given in **Table 1**.

Table 1. Electroanalytical parameters of quantitative ERL assay with GCE/DNA.

Parameters	**SWV method**
Ep, V	1.316 ± 0.002
Sensitivity, A/M (Slope)	0.022 ± 0.001
Linear range, M	$3\times10^{-7} – 2\times10^{-6}$
Limit of detection LOD, M	1.45×10^{-7}
Limit of quantification LOQ, M	4.84×10^{-7}
Linear regression equation*	$Ip = 1.52\times10^{-7} – 0.022c_{ERL}$
Correlation coefficient, R	– 0.9951

*Ip corresponds to the oxidative currents (peak heights) for dA peak; c_{ERL} is a concentration of ERL solution in which GCE/DNA was incubated for 30 minutes.

CONCLUSION

The main goal of this investigation was to determine the lowest detectable content of ERL able to interact with DNA. By using GCE modified with adsorbed layer of DNA on its surface, the change in deoxyadenosine oxidation signal (dA) with increasing concentration of ERL in incubation solution was followed. According to obtained linear dependence the lowest detectable content of ERL able to interact with DNA was determined. Both LOD and LOQ values confirmed the sensitivity of the proposed method.

Acknowledgment

This research was supported by the Ministry of Science, Technological Development and Innovation, Republic of Serbia through Grant Agreement with University of Belgrade-Faculty of Pharmacy No: 451-03-65/2024-03/ 200161

REFERENCES

[1] K.S. Bhullar, N.O. Lagarón, E.M. McGowan, I. Parmar, A. Jha, B.P. Hubbard, H.P.V. Rupasinghe, Mol. Cancer., 17 (2018) 1.

[2] Z. Zhang, L. Bu, J. Luo, J. Guo, Biochim. Et. Biophys. Acta (BBA) - Rev. Cancer 1877 (2022) 188738.

[3] M. Jovanović, K. Nikolic, M. Čarapić, M. M. Aleksić, J. Pharm. Biomed. Anal 234 (2023) 115560.

[4] J. Rupar, V. Dobričić, J. Brborić, O. Čudina, M. M. Aleksić, Bioelectrochemistry,149 (2023) 108323.

ELECTROCHEMICAL BEHAVIOR AND INTERACTION OF THE NEWLY SYNTHESIZED POTENTIAL ALDOSE REDUCTASE INHIBITOR WITH HUMAN SERUM ALBUMIN IN THE PRESENCE OF POLYSORBATE 80

M. Aleksić [1] J. Rupar [1], N. Vučković [1], L. Kováčiková [3,4], A. Boháč[4,5] and V. Dobričić [2]

[1] *University of Belgrade − Faculty of Pharmacy, Department of Physical Chemistry and Instrumental Methods, Vojvode Stepe 450, P.O.Box 146, 11221 Belgrade, Serbia (mara.aleksic@pharmacy.bg.ac.rs)*
[2] *University of Belgrade − Faculty of Pharmacy, Department of Pharmaceutical Chemistry, Vojvode Stepe 450, P.O.Box 146, 11221 Belgrade, Serbia*
[3] *Institute of Experimental Pharmacology and Toxicology, CEM, SAS, Dúbravská cesta 9,841 04 Bratislava, Slovakia*
[4] *Department of Organic Chemistry, Faculty of Natural Sciences, Comenius University in Bratislava, Ilkovičova 6, 842 15 Bratislava, Slovakia*
[5] *Biomagi, Ltd., Mamateyova 26, 851 04 Bratislava, Slovakia*

DOI: https://doi.org/10.46793/Phys.Chem24I.203A

ABSTRACT

Albumin is the most abundant protein in blood plasma and has a great ability to bind numerous molecules. Since inhibition of the enzyme aldose reductase can be used in the treatment of diabetes, it is important to investigate the interaction between albumin and aldose reductase inhibitors (ARI). The aim of this work is to investigate the electrochemical behavior of the newly synthesized potential ARI and to examine the possibility of studying the interaction of ARI with human serum albumin (HSA) by voltammetry.

The reduction of ARI is an irreversible, diffusion-controlled process. The application of the albumin-modified electrode showed no significant result in the investigation of the interaction of ARI and HSA. The study of the interaction in solution was difficult due to the poor solubility of ARI (poor reproducibility of signal). Due to the presence of polysorbate 80 in solution, satisfactory reproducibility was achieved and it was possible to detect the interaction of ARI and HSA.

INTRODUCTION

Albumin is a globular protein and the most abundant protein in blood plasma. At a pH value of 7.4, which corresponds to the pH value of venous blood, albumin is present in the form of anions. The parameters that characterize the formation of complexes with albumin in human serum are important for the characterization of the drug for commercial use and for the determination of its pharmacokinetics. Although human serum albumin (HSA) has a greater affinity for compounds with acidic properties, it can also bind compounds with basic properties and neutral compounds.

Electrochemical methods are used to determine the binding constant, stoichiometry and the percentage of free/bound drug. These methods are characterized by versatility, high sensitivity and simplicity. They are inexpensive and provide rapid results [1].

The compound that is the subject of this work, 2-(2-(2-hydroxyethyl)-3-oxo-2H-[1,2,4]triaazino[5,6-b]indol-5(3H)-yl)acetic acid is a newly synthesized potential aldose reductase inhibitor (ARI) (Figure 1). The enzyme aldose reductase is of crucial importance for the metabolism of glucose and other sugars, as it catalyzes the reduction of aldehydes to alcohols. Blocking this enzyme can be used for therapeutic purposes, particularly in the treatment of diabetes, as it can

prevent undesirable metabolic disorders associated with chronically high blood glucose levels, such as neuropathy, retinopathy and nephropathy.
The newly synthesized compound shows good solubility in dimethyl sulfoxide (DMSO), as opposed to aqueous solutions.

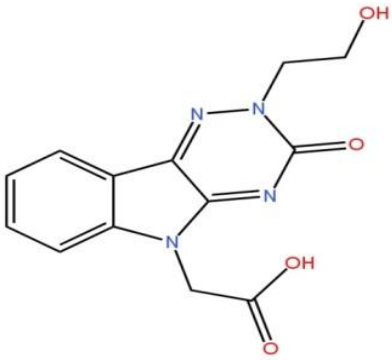


Figure 1. ARI structure.

Since there is evidence in the literature that polysorbate 80 can be used to help dissolve poorly soluble compounds in water, to either improve the dispersion or prevent precipitation of compounds, polysorbate 80 is used in this work with the aim of improving the solubility of ARI in an aqueous environment [2]. In addition, polysorbates can also affect the structure of proteins in solution and prevent aggregation [3] so it is expected that the reproducible results can be obtained by using polysorbate 80 when studying the interaction of ARI and HSA.

The aim of this work is to investigate the electrochemical behavior of the newly synthesized compound ARI and the possibility of using voltammetric methods to monitor and study the formation of ARI complexes with human serum albumin.

EXPERIMENTAL

The voltammetric measurements were performed with μAutolab analyzer (EcoChemie, Utrecht, Nederlands). A three-electrode system with a GCE working electrode, an Ag/AgCl reference electrode and a Pt-auxiliary electrode was used. Before each experiment the GCE was manually polished with an aqueous slurry of Al_2O_3 powder (particle size 0.05 μm) on a smooth polishing pad, sonicated in deionized water and then in absolute ethanol. Phosphate buffer saline (PBS), pH 7.4 was used as the supporting electrolyte. All chemicals used to prepare this buffer were of high purity. The experiments were carried out with deaerated PBS buffer.

A stock solution of HSA (Sigma-Aldrich) in PBS, at a concentration of 1×10^{-4} mol L^{-1} was used. A stock solution of 2-(2-(2-hydroxyethyl)-3-oxo-2*H*-[1,2,4]triaazino[5,6-b]indol-5(3*H*)-yl)acetic acid (ARI) in DMSO at a concentration of 6.94×10^{-3} mol L^{-1} was used. Each stock solution was diluted with PBS.

To improve the solubility of the ARI compound and to achieve reproducibility of the measurement results, a stock solution of the nonionic surfactant polysorbate 80 (1×10^{-2} mol L^{-1}) in PBS was used.

The electrochemical behavior of ARI on GCE was investigated by cyclic voltammetry (CV) in the negative potential range from 0.0 V to −1.6 V with a potential rate change of 5 - 100 mVs^{-1}. In the same potential range, pulse techniques were applied under the following conditions: for differential pulse voltammetry (DPV), potential change increment: 0.005 V, amplitude: 0.005 V, pulse modulation time: 0.05 s, duration of potential pulse period: 1 s was used. Square wave voltammetry (SWV) was performed with a frequency of 25 Hz, a potential change of 0.001 V and a pulse amplitude of 0.05 V.

The interaction between ARI and HSA was tested in two ways: with HSA immobilized on the surface of the GCE (with a modified electrode) and by testing the interaction in solution. The modified GCE electrode was formed by applying a drop of HSA solution (volume 3 μL, 1×10^{-4} mol L^{-1}). After application of the droplet, the electrode was dried with nitrogen for 15 minutes, then washed with deionized water, transferred to an electrochemical cell with PBS buffer and finally DPV was recorded under specific conditions. In the study of the interaction of HSA with ARI, the human serum albumin-modified electrode was incubated for 10 minutes at an analyte concentration of 5×10^{-5} mol L^{-1}, after which the electrode was washed with deionized water, immersed in an

electrochemical cell and voltammograms were recorded. To test the interaction in the solution, an ARI solution with a concentration of 1×10^{-4} M, and HSA solution with a concentration of 5.0×10^{-6} mol L^{-1} to 5×10^{-5} mol L^{-1} were used.

With the aim of improving the solubility of the ARI compound and achieving reproducibility of the measurement results, polysorbate 80 was used at a concentration of 2×10^{-5} mol L^{-1}.

RESULTS AND DISCUSSION

The electrochemical reduction of the compound ARI at a concentration of 8×10^{-5} mol L^{-1} in PBS buffer pH 7.4 was investigated using CV, DPV and SWV. When analyzing the CVs, a main cathodic peak (Ic) at a potential of about −0.9 V and a smaller anodic peak at a potential of about −0.5 V were observed. Analyzing the position and presence of oxidation and reduction peaks in three consecutive recording cycles, it can be concluded that ARI undergoes independent oxidation and reduction processes, and both processes are irreversible, confirming by the absence of corresponding peaks in the return part of the cycle.

At a pH of 7.4, the influence of the rate of potential change on the potential and current of peak Ic was investigated. The shift of the peak potential to more negative values with increasing scan rate confirms that the reduction process occurs as an irreversible process. The current intensity of the ARI reduction peak increases linearly with the square root of the rate of potential change:

$I_{p,Ic}$ (A) = 4.31×10^{-6}(A/(V s^{-1})$^{1/2}$) $v^{1/2}$ – 8.77×10^{-8} (A); r = 0.9835

These results indicate that the reduction process is diffusion controlled. The analysis of the linear dependence log $I_{p,Ic}$ = f (log v), where the obtained slope value of 0.46 is close to the theoretical value of 0.5 for a diffusion-controlled process, confirms that the reduction process is diffusion-controlled. Although diffusion of the electroactive material dominates, adsorption also makes a small contribution, as shown by the value of the intercept in the equation I_{pIc} = f($v^{1/2}$). Since the value of the current of the reduction peak decreases from the first to the third cycle, this phenomenon can also be attributed to adsorption.

In addition to using CV, the reversibility/irreversibility of the process can also be determined by analyzing the data obtained with SWV. The SWV of an 8×10^{-5} mol L^{-1} ARI solution at a pH of 7.4 confirmed the irreversible nature of the ARI reduction, as the two current components, forward and backward had the same directon.

Since ARI is an electrochemically active compound and HSA is not electrochemically active, it was hypothesized that the application of an albumin-modified electrode could be used to study the interaction between ARI and HSA. No electrochemical signal was observed after 10 minutes of incubation of ARI with HSA. This indicates that the ARI is not able to pass through the layer of adsorbed albumin and approach the electrode surface under these conditions.

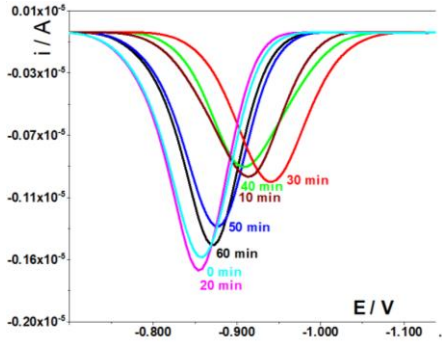


Figure 2. DPVs of ARI (8×10^{-5} mol L^{-1}) in PBS during 60 min.

To study the interaction of ARI with HSA, the interaction in solution was investigated. DPVs of ARI (8×10^{-5} mol L^{-1}) during 60 minutes (Figure 2) showed that the signal of the reduction peak varied, *i.e.*, no-reproducibility was achieved for either the peak current intensity or the peak potential. Since the stock solution of the ARI compound was prepared in DMSO and the recordings were made in PBS buffer, it was assumed that the reason for the non-reproducible signal was the limited solubility of the ARI compound in the aqueous medium.

After addition of HSA (1×10^{-7} mol L^{-1}) voltammograms were also recorded for 60 minutes. It was unequivocally observed that the presence of HSA in the solution resulted in a

much more pronounced change in peak height compared to the voltammograms of the ARI solution. In this case, however, it cannot be determined to what extent the change in peak current intensity and peak potential is due to the interaction and to what extent the influence of the non-reproducibility of the method.

After the addition of polysorbate 80, the peak describing the reduction of ARI was shifted to more negative potentials, and reproducibility of the signal was achieved within 60 min, probably as a result of solubilization of the compound (Figure 3).

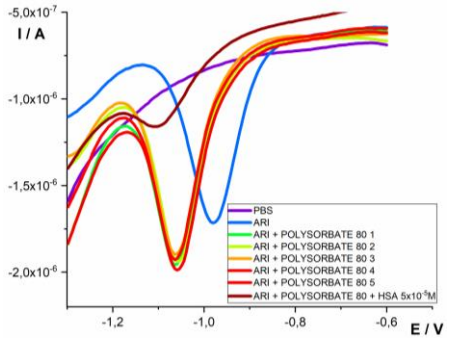


Figure 3. DPVs of ARI in PBS, ARI during 60 min with Polysorbate 80 and ARI with Polysorbate and HSA.

After a stable ARI signal was obtained, the interaction between ARI and HSA was investigated. The measurements were performed at an ARI concentration of 1×10^{-4} mol L^{-1} in the presence of polysorbate 80 (2×10^{-5} mol L^{-1}). The HSA concentrations ranged from 5×10^{-6} to 5×10^{-5} mol L^{-1}. During the interaction with 5×10^{-5} mol L^{-1} HSA, a decrease in the intensity of the peak reduction current by about 80% was observed (Figure 3), while the peak potential was shifted by about 40 mV towards more negative potentials, clearly indicating an interaction between ARI and HSA (Figure 3). When investigating the interaction between ARI and HSA, satisfactory reproducibility of the results was obtained in the presence of polysorbate 80.

CONCLUSION

Voltammetric tests of the compound ARI in PBS buffer (pH 7.4) showed that the reduction process is irreversible and diffusion controlled. The application of the albumin-modified electrode to test the interaction of ARI and HSA showed no significant result under the experimental conditions used in this work. The study of the interaction in solution was also difficult, as most likely due to the poor solubility of the ARI compound, no satisfactory reproducibility of the results could be achieved. However, it was possible to detect an interaction with HSA. The application of polysorbate 80 at a concentration of 2×10^{-5} mol L^{-1} enabled the solubilization of ARI and the achievement of satisfactory reproducibility of current and reduction peak potential. In the solution in the presence of polysorbate 80, it was possible to detect the interaction between ARI and different concentrations of HSA, where at a concentration of 5×10^{-5} mol L^{-1} HSA, a decrease in the intensity of the reduction peak current by about 80% was observed, while the peak potential was shifted by about 40 mV towards more negative potentials.

Acknowledgment

This research was supported by the Ministry of Science, Technological Development and Innovation, Republic of Serbia through Grant Agreement with University of Belgrade-Faculty of Pharmacy No: 451-03-65/2024-03/200161

REFERENCES

[1] D. Ravelli, P. Isernia, A. Acquarulo, A. Profumo, D. Merli, Journal of the American Chemical Society 91 (2019) 10110–10115.
[2] R. W. Tejwani, H. Joshi, S. A. Varia, A. Serajuddin. Journal of Pharmaceutical Sciences, 89 (2000), 946-950.
[3] B. A. Kerwin. Journal of Pharmaceutical Sciences, 97 (2008).

APPLICATION OF MICROBIAL FUEL CELLS FOR THE ELECTROCHEMICAL DECOLORIZATION OF ACID YELLOW 99 DYE

K. Joksimović[1], A. Žerađanin[1], I. Kodranov[2], D. Manojlović[2], S. Spasić[1], D. Randjelović[1] and V. Beškoski[2]

[1]University of Belgrade, Institute of Chemistry, Technology and Metallurgy, National Institute of the Republic of Serbia Njegoševa 12, 11000 Belgrade, Serbia. (kristina.joksimovic@ihtm.bg.ac.rs)
[2]University of Belgrade, Faculty of Chemistry, Studentski trg 12-16, 11000 Belgrade, Serbia, Njegoševa 12, 11000 Belgrade, Serbia.

DOI: https://doi.org/10.46793/Phys.Chem24I.207J

ABSTRACT

Due to the constant growth of the human population on Earth and growingly ambitious social and economic goals, the sustainability of natural resources is of increasing concern. Among other things, urbanization in developing countries creates pressure on water resources, where increased demand affects their availability and promotes the reuse of wastewater. Microbial fuel cells (MFCs) are one of the ways to reuse wastewater and have shown great potential as a single solution to three key problems facing the world today: energy security, global warming, and wastewater management. MFCs represent a multidisciplinary platform for research that includes knowledge of biochemistry and engineering sciences. A microbial fuel cell uses microorganisms to oxidize organic materials to produce electricity. This process releases electrons that are transferred to the anode and then travel to the cathode, where they combine with a reducing agent (most often oxygen) to produce water. This study aims to evaluate the performance of MFCs with carbon fibre electrodes, specifically focusing on the application of carbon fibers in the electrochemical degradation of Acid Yellow 99 dye (AY99).

INTRODUCTION

The rapid growth of the human population and ambitious socio-economic goals raise significant concerns about the sustainability of natural resources. Urbanization in developing countries exerts substantial pressure on water resources, increasing demand and necessitating wastewater reuse. Microbial fuel cells (MFCs) have emerged as a promising technology for wastewater treatment, addressing energy security, global warming, and wastewater management [1,2].

MFCs combine biology and electrochemistry to convert organic materials into electricity through microorganism metabolism. A typical two-chamber MFC includes an anode and cathode chamber separated by a proton exchange membrane (PEM), facilitating the study of each component independently. Single-chamber MFCs, which expose the cathode directly to air, are simpler and more cost-effective [3]. MFCs operate by anaerobic oxidation of organic substances at the anode, releasing protons, electrons, and CO_2. Electrons travel through the anode to the cathode, generating electric current, and combine with oxygen or other acceptors to form water or other products [4].

The performance of MFCs depends on the electrode materials, especially the anode, which supports extracellular electron transfer (EET). Ideal electrode materials have high conductivity, corrosion resistance, mechanical strength, biocompatibility, non-toxicity, large surface area, environmental friendliness, and low cost. Carbon-based materials, particularly carbon fibers, excel as MFC electrodes due to their conductivity, surface area, inertness, and biocompatibility. Enhancements such as electrochemical oxidation, acid activation, and heat treatment can further

improve their performance by reducing internal resistance, improving hydrophilicity, and creating functional group-rich surfaces for biofilm adhesion [4]. The primary indicator of pollution from the different industries is the presence of various dyes on the water surface. Due to the detrimental impacts on the environment and human health, removing or decomposing organic compounds before wastewater discharge is imperative. Additionally, many dyes must be treated before being released into the environment [5].

METHODS

Sediments used to construct MFCs were collected from the Danube at the confluence with the Sava River (location: 44°49'22.0" N 20°26'32.7" E). All samples were collected and brought to the laboratory, where they were combined into a composite sediment and stored in a refrigerator at 4°C. The complete characterization of chemical and microbiological parameters of the sediment were described in our previous study [6].

A simple single-chamber MFCs were designed and constructed, with a volume of approximately 360 cm^3. The MFCs consisted of a plastic container, two electrodes, and sediment. To ensure an inert environment for the microbes, the electrodes were fabricated from carbon fiber conforming to the IC 316 standard. Both the anode and cathode have identical designs and materials. The cell consists of a rectangular carbon fiber component (11 cm x 7.3 cm) (DowAksa, Turkey), sourced from Serbia, a thin frame holding the carbon fiber plexiglass, and a narrow elongated rectangular component made from inox foil (Good Fellow, England). The inox foil components are insulated from the sediment using heat-shrink tubing. To determine the current and power densities, voltage measurements were taken across a series of resistors externally connected to the MFC system, following the procedure described in detail elsewhere [7].

An aqueous solution of Acid Yellow 99 (98%, Orco, USA) was employed for the electrochemical degradation of azo dyes, utilizing a microbial fuel cell (MFC) as the electricity source. The working solution of Acid Yellow 99 was prepared at a concentration of 25 mg/L in a total volume of 100 mL with supporting electrolyte 0.1 M Na_2SO_4 solution was used as the supporting electrolyte (Jović et al., 2013). Hydrogen peroxide (30% w/w, Zorka) was added to the undivided electrochemical cell at concentrations of 0.5 and 1 mM to generate hydroxyl radicals via the electro-Fenton reaction. To determine the contribution of MFC-generated electricity to the overall decolorization of Acid Yellow 99, a control experiment was conducted using identical ratios of Acid Yellow 99 and hydrogen peroxide, but without the inclusion of the MFC in the circuit. A two-electrode system, consisting of a Pt electrode (3 cm^2) and a working electrode containing iron (15% Fe, 12.56 cm^2), was employed for the degradation process. The working electrode used in the study is a microporous graphite electrode with 15% Fe and the procedure for its preparation has been previously described [8]. The potential difference between the electrodes during degradation was monitored using a pH meter (MA 5705, Iskra, Yugoslavia). All measurements were performed in triplicate.

The efficiency of dye decolorization was monitored by recording the absorbance spectrum in the range of 200–800 nm (UV 1280 SHIMADZU spectrometer). Aliquots (2 mL) of the solutions were taken during electrochemical treatment after 0 h, 2 h, 4 h, 6 h and 24 h of treatment. The percentage of dye degradation was determined using the following equation:

$$Dye\ decolorization\ (\%) = (A_0 - A)/A \cdot 100,$$

where A_0 is measured absorbance of initial dye solution (0 h) at the maximum absorption wavelength (λ_{max} = 392 nm) while A denotes absorbance of solution after the electrochemical treatment at the maximum absorption wavelength.

RESULTS AND DISCUSSION

For the electrochemical decolorization of Acid Yellow 99 (AY99) dye, a direct connection was established between the microbial fuel cell (MFC) system, the working electrode, and the platinum (Pt) electrode, which were immersed in the dye solution. Prior to the dye treatment, the electrochemical performance of the MFC with carbon fiber electrodes was evaluated. The voltage generated by the cell was monitored across a series of resistors ranging from 1 kΩ to 10 MΩ over a period of 9 days. Using Ohm's law, the current and power output of the cell were calculated based on the voltage measurements across the resistors. The results presented in Fig. 1 show that the maximum voltage recorded on the fourth day was 371 mV, while the peak values for current density and power density were observed on the fifth day, at 21.03 mA/m² and 3.63 W/m², respectively.

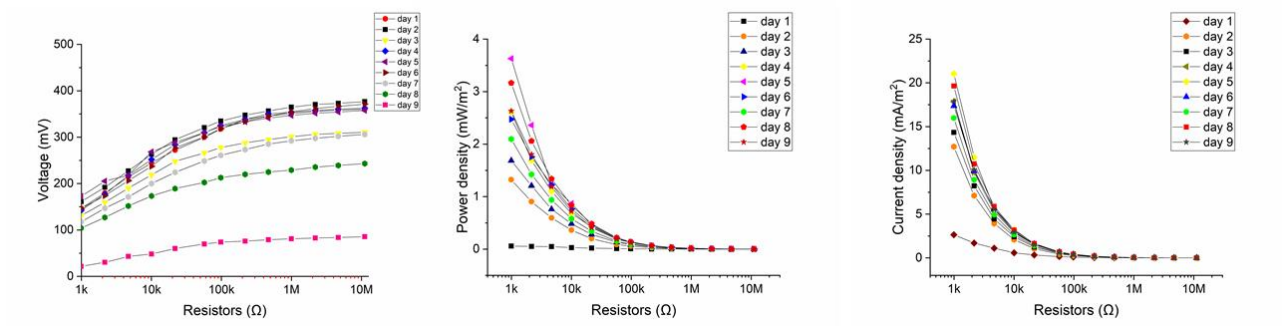


Figure 1. Results of electrical characterization of the MFC system used in the AY99 electrochemical treatment per days: A) Voltage; B) Power density; C) Current density.

A concentration of 25 mg/L was used to test the decolorization efficiency due to the small amount of voltage generated by the MFC system. All experiments were performed under the same conditions (25°C) within experimental error. However, since the process involves heterogeneous catalysis, the inhomogeneous distribution of iron and magnetite particles on the active surface of the electrode may cause occasional changes in the electrode's catalytic activity. Analytical methods were used to confirm the dye decolorization. The first of them involved recording the UV/VIS absorption of AY99 paint in the range from 200 to 800 nm. The wavelength at which the change was monitored corresponds to a maximum of 392 nm. A dye concentration of 25 mg/L proved to be an ideal model system for variations with peroxide in our electrochemical degradations. With 0.5 mM H_2O_2, decolorization of 75.5% was achieved after 24 hours. Concentration of 1 mM H_2O_2, decolorization reached slightly better values of 76%, with improved efficiency compared to the control. The results are presented in the Table 1.

Table 1. Decolorization after 2, 4, 6 and 24h in the presence of 0.5 and 1.0 mM H_2O_2.

Percentage of decolorization, %					**Measured voltage during decolorization, mV**
Time	**25 mg L^{-1} dye with 0.5% H_2O_2**	**Control**	**25 mg L^{-1} dye with 1.0% H_2O_2**	**Control**	
2 h	6.2	0.5	6.5	0.3	± 330
4 h	19.0	0.7	27.1	11.9	± 360
6 h	/	/	35.0	10.7	± 348
24 h	75.5	6.1	76.4	0.2	± 327

Prior research into dye decolorization has indicated that the use of low concentrations of H_2O_2 can enhance the efficiency of dye removal. Consequently, it was chosen to employ these low concentrations. This decision is based on the observation that higher concentrations of H_2O_2 lead to an increased consumption of hydroxyl radicals (·OH), thereby reducing their availability to react with the dye [8, 9]. A small amount of current is extremely effective for this type of decolorization, with intensity even less than in some other studies testing Acid Yellow.

CONCLUSION

The results demonstrated that the microbial fuel cell, utilizing carbon fibre, serves as a commendable energy source, delivering sufficient current density and power output. Notably, employing low concentrations of peroxide at 0.5% and 1.0% as a catalyst for the electro-Fenton process resulted in a 76% dye decolorization after 24 hours of treatment, showcasing remarkable efficiency given the modest amount of electricity generated.

Acknowledgment

This work was supported by the Ministry of Education, Science and Technological Development of the Republic of Serbia (grant no 451-03-66/2024-03/200026 and 451-03-66/2024-03/200168).

REFERENCES

[1] N. Bazina, T.G. Ahmed, M. Almdaaf, S. Jibia, M., Sarker, J. Biotehnol., 374 (2023) 17-30.
[2] V. Meylani, E. Suarahman, A. Fudholi, W. Hassan Almalki, N. Ilyas, R.Z. Sayyed, J. Environ. Chem. Eng. 11 (2023) 109503.
[3] S. S. Khan, M. Amjad, H. Shareef, S. Larkin, Energ. Explor. Exploit. 41 (2024) 373-398.
[4] W. C. Bray, J. Am. Chem. Soc., 43 (1921) 1362.
[5] N. I. Iberahim, N. A. Lutpi, L. Ho, Y. Wong, S. Ong, F. A. Dahalan. Environ. Quality Manage. 1-10 (2024).
[6] K. Joksimovic, A. Žerađanin, D. Randjelovic, J. Avdalović, S. Miletić, G. Gojgić-Cvijović, V. P. Beškoski. J. Power Sources 476 (2020) 228739.
[7] K. Joksimovic, I. Kodranov, D. Randjelovic, L. S. Beškoski, J. Radulovic, M. Lješević, D. Manojlović, V. P. Beškoski. Bioelectrochemistry. 145 (2022) 108088.
[8] J. Li, Z. Chen, Chem. Eng. J., 489 (2024) 151323.
[9] E. GilPavas, I. Dobrosz-Gomez, M.A. Gomez-Garcia, J. Environ. Chem. Eng. 142 (2016) (11).

F *– Biophysical Chemistry,*
EPR investigations of Bio-systems

FLUORESCENCE CORRELATION SPECTROSCOPY (FCS) – 50 YEARS AND BEYOND

S. Oasa [1], A. J. Krmpot [2], S. N. Nikolić [2], A. Tiiman [1], and V. Vukojević [1]

[1]*Karolinska Institutet, Department of Clinical Neurosciences, Center for Molecular Medicine, Visionsgatan 18, 17176 Stockholm, Sweden (Vladana.Vukojevic@ki.se)*
[2]*University of Belgrade, Institute of Physics Belgrade, Pregrevica 118, 11080 Belgrade, Serbia*

DOI: https://doi.org/10.46793/Phys.Chem24I.213O

ABSTRACT
This lecture will present the theoretical background and historical milestones of fluorescence correlation spectroscopy (FCS), reflecting on key scientific contributions and the transformative impact of this technique on modern biomedical research.

INTRODUCTION

FCS is a powerful and versatile time-resolved quantitative analytical technique that enables us to nondestructively characterize the concentration, mobility and interactions of molecules in solutions and in live cells with the ultimate, single-molecule sensitivity. Its history, spanning over five decades, testifies to the power of integrating sophisticated theoretical ideas with state-of-the-art technology.

The origins of FCS can be traced back to the early 1970s when researchers Douglas Magde, Elliot Elson and Watt W. Webb at Cornell University, USA and Rudolf Rigler at Karolinska Institutet, Sweden demonstrated that mathematical analysis of time-resolved fluctuations in fluorescence intensity originating from molecular diffusion through a small volume (several fl (10^{-15} liters)) could be used to extract information about molecular concentrations, translational and rotational diffusion, and interactions [1-4]. This approach marked a significant departure from traditional fluorescence spectroscopy techniques, which averaged fluorescence signal over long time and large populations of molecules, missing thereby the possibility to probe dynamic molecular processes at the single-molecule scale.

Following these remarkable breakthroughs, FCS faced challenges throughout the 1980s, primarily due to technical limitations (*e.g.*, low laser stability and detector sensitivity). However, the early 1990s saw the resolution of these problems and integration of FCS with confocal microscopy [5], which dramatically improved FCS sensitivity as it enabled the observation of fluorescence intensity fluctuations within even smaller volumes (10^{-16}-10^{-15} liters) thereby making possible measurements in live cells. This further underscored FCS's potential as a non-invasive tool for characterizing molecular mechanisms underlying complex biological phenomena.

I will present two detailed examples from our work that demonstrate the application of FCS in biomedical research. The first example focuses on basic research, where we have advanced the instrumentation [6] and used it to characterize in live salivary glands *ex vivo* how transcription factors interact with chromatin to locate their target DNA sequences [7,8]. The second example highlights the potential of FCS in translational research, particularly as a prospective tool for blood-based diagnosis of amyloid diseases, such as Alzheimer's disease [9]. Finally, I will discuss our recent advancements in extending FCS to imaging, which enables quantitative, scanning-free

confocal fluorescence microscopy through massively parallel FCS (mpFCS). Additionally, we have integrated mpFCS with fluorescence lifetime imaging microscopy (mpFCS/FLIM), significantly enhancing FCS's versatility. This integration allows us to use fluorophores as sensors that respond to local changes in the intracellular environment, providing deeper insights into molecular mechanisms underlying cellular functions.

REFERENCES

[1] D. Magde, E. L. Elson, W. W. Webb, Phys. Rev. Lett., 29 (1972) 705.
[2] E. Elson, D. Magde D, Biopolymers, 13 (1974) 1.
[3] D. Magde, E. L. Elson, W. W. Webb, Biopolymers, 13 (1974) 29.
[4] M. Ehrenberg, R. Rigler, Chem. Phys. 4(3) (1974) 390.
[5] R. Rigler, Ü. Mets, J. Widengren, P. Kask, Eur. Biophys. J., 22 (1993) 169.
[6] V. Vukojević, M. Heidkamp, Y. Ming, B. Johansson, L. Terenius, R. Rigler, Proc. Natl. Acad. Sci. USA, 105 (2008) 18176.
[7] V. Vukojević, D. K. Papadopoulos, L. Terenius, W. Gehring, R. Rigler, Proc. Natl. Acad. Sci. USA, 107 (2010) 4087.
[8] D. K. Papadopoulos, V. Vukojević, J. Adachi, L. Terenius, R. Rigler, W. Gehring, Proc. Natl. Acad. Sci. USA, 107 (2010) 4093.
[9] A. Tiiman, V. Jelić, J. Jarvet, P. Järemo, N. Bogdanović, R. Rigler, L. Terenius, A. Gräslund, V. Vukojević V. J. Alzheimer's Dis., 68 (2019) 571.
[10] A. J. Krmpot, S. N. Nikolić, S. Oasa, D. K. Papadopoulos, M. Vitali, M. Oura, S. Mikuni, P. Thyberg, S. Tisa, M. Kinjo, L. Nilsson, L. Terenius, R. Rigler, V. Vukojević, Anal. Chem., 91 (2019) 11129.
[11] S. Oasa, A. J. Krmpot, S. N. Nikolić, A. H. A. Clayton, I. F. Tsigelny, J. P. Changeux, L. Terenius, R. Rigler, V. Vukojević, Anal. Chem. 93 (2021) 12011.
[12] S. N. Nikolić, S. Oasa, A. J. Krmpot, L. Terenius, M. R. Belić, R. Rigler, V. Vukojević, Anal. Chem. 95 (2023) 15171.

NON-IMPRINTED POLYMERS AS SYNTHETIC ANTIBODIES FOR PROTEIN RECOGNITION: A PERSPECTIVE FROM MOLECULAR DYNAMICS SIMULATION

X. Xu, M-H. Xie, S-J. Luo and X. Jia

Nanjing University of Science and Technology, School of Chemistry and Chemical Engineering, Xiaolingwei 200, 210094 Nanjing, China. (xuxiao@njust.edu.cn)

DOI: https://doi.org/10.46793/Phys.Chem24I.215X

ABSTRACT

The "lock-and-key" model, which underscores the importance of chemical-structural complementarity, serves as the fundamental mechanism for elucidating the specificity between small ligands and larger adsorbent molecules. In our study, focusing on copolymer chains composed solely of N-isopropylacrylamide (NIPAm) and hydrophobic N-tert-butylacrylamide (TBAm) monomers, and employing extensive atomistic molecular dynamics simulations, we unveil a surprising phenomenon. Despite the absence of hydrophobic matching and strong structural complementarity, the flexible copolymer chain demonstrates notable binding affinity for the biomarker protein epithelial cell adhesion molecule. This unexpected binding behavior, not predicted by the "lock-and-key" model, is attributed to preferential interactions established by the copolymer with the protein's hydrophilic exterior. Interestingly, an increase in the fraction of incorporated TBAm monomers results in enhanced interactions with asparagine and glutamine amino acids, facilitated by emerging hydrogen bonding with both NIPAm and TBAm monomers. Our results suggest the emergence of highly specific and high-affinity binding sites on the protein through tailored engineering of copolymer composition, thus fostering the potential applications of copolymers as protein affinity reagents.

INTRODUCTION

Molecularly imprinted polymers (MIPs) [1] serve as a form of synthetic antibodies featuring specialized "imprinted cavities," which are created by synthesizing polymeric matrices in the presence of template molecules. To date, a range of nano-sized MIPs has been developed successfully, specifically tailored to target tumor-related antigens for applications in cancer imaging and therapy. Another cost-effective alternative lies in synthetic copolymer nanoparticles (NPs), which can mimic numerous functionalities of natural antibodies [2]. Indeed, emerging evidence suggests that the utilization of synthetic linear copolymers or copolymer NPs, incorporating a strategic combination of hydrophobic and charged group functionalities, can function as selective binding agents akin to MIPs, eliminating the requirement for a template molecule [3,4].

The non-imprinted copolymer NPs do not carry the imprinted cavities. Thus, the arising molecular recognition capacity can not be rationalized by MIPs. Moreover, the non-imprinted copolymer NPs of low branching functionality do not have a well-folded structure like natural antibodies. The randomness of their monomer sequence after the free radical polymerization also impairs the creation of chemical complementarity with the antigen molecule. Thus, there is still a lack of the understanding at the molecular level about how the non-imprinted copolymer NP may attain its proven high binding affinity essentially in view of the randomness both in its sequence and structure.

Here, our attention is directed towards the most basic setup of the copolymer model, consisting of a linear block copolymer chain containing hydrophilic N-isopropylacrylamide (NIPAm) and

hydrophobic N-tert-butylacrylamide (TBAm) monomers. With extensive Molecular Dynamics (MD) simulations, we introduce a fresh perspective on the binding mechanism between the protein and dynamically flexible polymers, along with exploring the potential molecular basis for the arising binding selectivity. Such insights are crucial for leveraging polymers as synthetic antibodies.

METHODS

The entire study is focused on the biomarker protein EpCAM. As the potential binding counterpart of EpCAM, we've opted for a relatively short copolymer chain with a degree of polymerization ranging from 45 to 48. This copolymer amalgamates hydrophobic TBAm monomers with NIPAm groups. Our simulations solely focus on periodic copolymers, designated as $(N_xT_y)_n$, where *n* signifies the count of identical fragments, and each fragment comprises *x* NIPAm and *y* TBAm monomers. We explore copolymers $(N_4T)_9$, $(N_2T)_{16}$, $(NT)_{24}$, and $(N_2T_2)_{12}$, exhibiting varied fractions of TBAm monomers (ρ_T) ranging from 20% to 50%, while maintaining a roughly consistent degree of polymerization. To augment sampling, besides extending the duration of individual simulation runs, we strategically position the copolymer in proximity to one of four discrete regions of the protein: left wing (L), right wing (R), front side (F), and back side (B), that is, the copolymer is severally released from different positions of the protein.

RESULTS AND DISCUSSION

In this study, we explore the binding dynamics between the biomarker protein EpCAM and copolymer ligands that vary in the composition and sequence of their functional monomers. Utilizing detailed all-atom molecular dynamics (MD) simulations, we discover that copolymers interact with the protein differently from small-molecule ligands. This unique interaction is largely influenced by the copolymers' considerable size, which directs their binding primarily to the protein's hydrophilic exterior. The exemplified binding complex between the EpCAM and the copolymer $(N_2T_2)_{12}$ is exhibited in the **Fig. 1**. As a result, the traditional method of hydrophobic matching, commonly used in ligand design to enhance specificity, does not adequately predict the structure of polymer-protein conjugates. Instead, the interaction depends on the protein's specific side-chain properties, allowing copolymer ligands to form preferential interactions with certain types of hydrophilic amino acids (AAs) (**Figure 1**). This interaction leads to an enrichment of these AAs at the binding interface, potentially resulting in significant binding affinity and specificity towards the target protein.

We have determined that amino acids (AAs) with amide side chains are preferentially targeted by copolymers composed of TBAm and NIPAm monomers, which significantly enhances hydrogen bonding between the protein and the copolymer. While aromatic and nucleophilic AAs also have the capacity to serve as hydrogen donors or acceptors, they were not prominently observed in the simulation due to the higher polarity of amide AAs, making them more accessible to copolymers. Additionally, the incorporation of amide groups within all constituent monomers of the copolymer promotes enthalpic stability through amide-amide interactions with AAs that also feature amide side chains. Charged AAs can contribute to hydrogen bonding, and the hydrogen bonds formed are strong due to their nonzero charge. For copolymers (N4T)9 and (N2T)16, a significant contribution of hydrogen bonds from these charged AAs was observed. However, a predominance of hydrogen bonding interactions with amide AAs was noted for copolymers (N2T2)12 and (NT)24. It appears that the presence of hydrophobic TBAm monomers may inhibit interactions with charged AAs, often due to repulsions exerted on the hydrophobic TBAm monomers in the high-polarity environments created by these charged AAs.

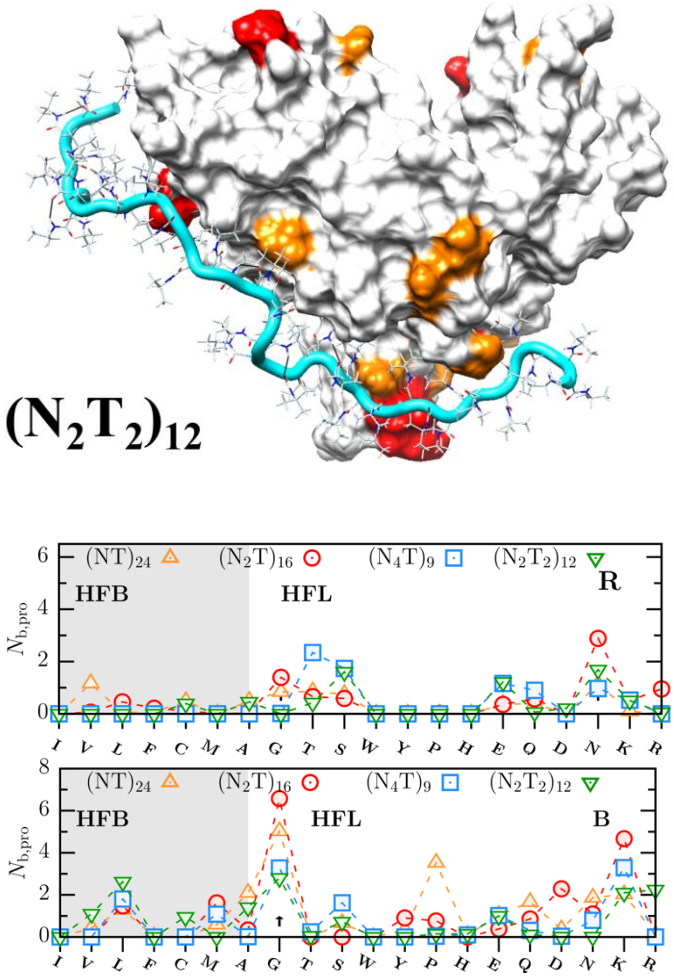


Figure 1. In the left hand side, The simulated binding complex for the copolymer $(N_2T_2)_{12}$ that bound at the protein left wing. The orange and red color depict the Gln and Asn residues, respectively. The back bond of the copolymer is highlighted in cyan. In the right hand side, the number of protein residues $N_{b,pro}$ for all 20 types of AA (x-axis) on the protein in contact with the copolymer for four copolymers $(N_4T)_9$, $(N_2T)_{16}$, $(NT)_{24}$ and $(N_2T_2)_{12}$, respectively. The two panels correspond to the copolymer bound with the right wing (top), and back side (lower) of the protein.

CONCLUSION

This analysis helps to understand the diverse adsorption behaviors of different copolymers, especially in identifying specific AAs as binding hotspots and their associated high ligand binding affinity, based on the tunable monomer composition of the copolymer. This could represent a significant advancement for the emerging applications of copolymers as antibodies, driving a rational design strategy for these copolymers and predicting their binding sites on proteins.

Acknowledgment

The authors acknowledge the National Science Foundation of China (21903045) and Qing Lan Project of Jiangsu Province for financial support. Authors thank Dr S. Angioletti-Uberti for the fruitful discussions.

REFERENCES

[1] J. J. BelBruno. Chem. Rev., 119 (2018) 94.
[2] H. Koide, K. Yoshimatsu, Y. Hoshino, S. H. Lee, A. Okajima, S. Ariizumi, Y. Narita, Y. Yonamine, A. C. Weisman, Y. Nishimura, N. Oku, Y. Miura, K. J. Shea. Nat. Chem., 9 (2017) 715.
[3] X. Xu, M. Xie, S. Luo, X. Jia. J. Phys. Chem. Lett., 15 (2024) 773.
[4] M. Xie, X. Jia, X. Xu, Phys. Chem. Phys. Chem., 26 (2024) 4052.

CHARACTERISATION OF MICROBIAL COMMUNITIES IN PETROLEUM-CONTAMINATED SOIL

J. Milić[1], B. Pantelić[2], G. Dević[1], J. Avdalović[1] and M. Ilić[1]

[1] University of Belgrade, Institute of Chemistry, Technology and Metallurgy, Njegoševa 12, 11000 Belgrade, Serbia. (gordana.devic@ihtm.bg.ac.rs)
[2]University of Belgrade, Institute of Molecular Genetics and Genetic Engineering, Vojvode Stepe 444a,11042 Brlgrade, Serbia

DOI: https://doi.org/10.46793/Phys.Chem24I.219M

ABSTRACT

The widespread use of petroleum and its derivatives has led to substantial environmental contamination through extraction, processing, transport, and utilization of this fuel. Despite exposure to toxic stress, some microorganisms can tolerate these conditions, and those capable of rapid pollutant decomposition are more likely to survive. This is a report on the members of the microbial community in soil polluted with petroleum and its derivatives, outlining the physicochemical and biological characteristics of these unique habitats. Most of the examined bacteria showed sensitivity only to higher concentrations of heavy metals, indicating their resistance and adaptation to high concentrations of these metals. The clustering analysis aligned with the phylogenetic diversity of strains, with strains exhibiting the highest bioremediation capabilities, such as *Planomicrobium* sp. RNP01 and *Planococcus* sp. RNP07 and *Rhodococcus* sp. RNP05 clustered tightly.

INTRODUCTION

Microorganisms that thrive in extreme conditions have significant scientific and biotechnological interest due to their unique biochemical and physiological characteristics. Because of that, they have important industrial and environmental applications, such as the soil remediation of areas contaminated by pesticides, herbicides, and other organic pollutants, wastewater treatment, petroleum bioremediation, and heavy metal detoxification [1].

The widespread use of petroleum and its derivatives has led to substantial environmental contamination through extraction, processing, transport, and use of this fuel. Many petroleum compounds are mutagenic, carcinogenic, and teratogenic, and some of them are the most widespread contaminants on the planet [2]. Despite exposure to toxic stress, some microorganisms can tolerate these conditions, and those capable of more rapid pollutant decomposition are more likely to survive. To date, many microorganisms have been shown to convert these pollutants into less toxic substances or even completely biodegrade them.

Bioremediation is a sustainability technology due to its capacity to naturally degrade environmental pollutants through the action of microorganisms. This eco-friendly approach reduces the reliance on chemical treatments and physical removal methods, which can be costly and harmful to the environment. By using the power of biological processes, bioremediation helps restore polluted ecosystems to their natural state, promoting biodiversity and environmental health. Its implementation supports sustainable development goals by ensuring cleaner soil, water, and air, ultimately contributing to a healthier planet for future generations. The success of microbial bioremediation technologies depends on a thorough understanding of the microbial community and its response to toxic stress [3].

This study represents a report on the members of a microbial community in soil polluted with petroleum and its derivatives from the Petroleum Oil Refinery Pančevo in Serbia and outlines the physicochemical and biological characteristics of these unique habitats.

METHODS

Soil Sample

Eight bacterial strains have been isolated from heavily contaminated petroleum contaminated soil originating from Petroleum Refinery Pančevo, Serbia. The concentration of total petroleum hydrocarbons in the soil sample was 29.99% mg/g dry soil, ash content 68.2% [4].

Genotype identification

Bacterial isolates were previously identified by molecular analysis of 16S rDNA. Taxonomic analysis was conducted using the BLAST program and sequences were deposited in the NCBI GenBank, a public database of genomic and gene sequences (Table 1.) [4].

Table 1. Genotype identification of bacterial strains.

	Gen Bank accession number:	**Number of nucleotides**	**Sequencing coverage [%]**
***Planomicrobium sp.* RNP01**	JN683359	1330	100
***Micrococcus sp.* RNP02**	JN683360	1215	100
***Staphylococcus sp.* RNP03**	JN683361	1327	99
***Micrococcus sp.* RNP04**	JN683362	1285	100
***Rhodococcus sp.* RNP05**	JQ065876	1389	100
***Staphylococcus sp.* RNP06**	JN683363	1321	100
***Planococcus sp.* RNP07**	JN683364	1205	99
***Micrococcus sp* RNP08**	JN683365	1176	100

Phenotypic Characterization

The cellular morphology and Gram stain were visualized by optical microscopy. The API 20NE (combining 8 conventional tests and 12 assimilation tests), API CORYNE (enzymatic activity profiling), and API 50CHB (carbon assimilation profiling) Test Systems (API System S.A., La-Balme Les Grottes, France) were used for biochemical characterization according to the manufacturer's instructions [5]. The subsequent biochemical assays provided insights into the enzymatic activities and metabolic pathways of the tested bacteria, allowing them to survive and proliferate in a hydrocarbon-rich environment.

Antibiotic and Heavy Metal Resistance

The diffusion method was used to analyze the sensitivity of the isolated strains to both heavy metals and antibiotics. The sensitivity was analyzed for the following antibiotics and heavy metals, respectively: erythromycin, ampicillin, penicillin, tetracycline, streptomycin, neomycin, fusidic acid, methicillin; and Ni, Cu, Fe, Cr, Zn, Pb, Cd. All antibiotics were tested using antibiogram tablets of defined concentrations manufactured by Torlak, except for streptomycin, which was tested as a solution (30 μL of a solution with a concentration of 1 mg/mL). Mueller-Hinton agar was used as the medium.

Biodegradation Screening Assay

Bacterial isolates were screened for their ability to biodegrade various hydrocarbons (toluene - TOL, phenanthrene - PHE, pyrene - PYR, dibenzothiophene - DBT) using the modified 2,6-dichlorophenol- -indophenol (2,6-DCPIP) assay [6].

Hierarchical Cluster Analysis

Global parameters, antibiotic resistance, heavy metal resistance, enzymatic activity and carbohydrate metabolism were used for hierarchical cluster analysis of 8 selected strains. All of the metrics were reduced to values ranging from 0 to 100%. The analysis was performed using Wards's method with squared Euclidean distance in SPSS software.

RESULTS AND DISCUSSION

Most of the examined bacteria showed sensitivity only at higher concentrations of heavy metals, indicating their resistance and adaptation to high concentrations of these metals. *Rhodococcus* sp. RNP05 showed the highest resistance and was significantly more sensitive to Cu. Significant resistance was also shown by strain *Micrococcus* sp. RNP08, which was highly resistant to Zn, Pb, and Cd and showed moderate sensitivity to other analyzed metals. All bacteria showed a negative reaction to arginine dehydrolase, indicating that all strains were aerobic. The production of extracellular enzymes, such as protease, alkaline phosphatase, and β-glucosidase, is present in most strains. Of the other diagnostic enzyme markers, not a single isolate can produce β-glucuronidase, indicating its non-pathogenicity, given that these are enzyme markers for bacteria and human pathogens. (**Figure 1.**).

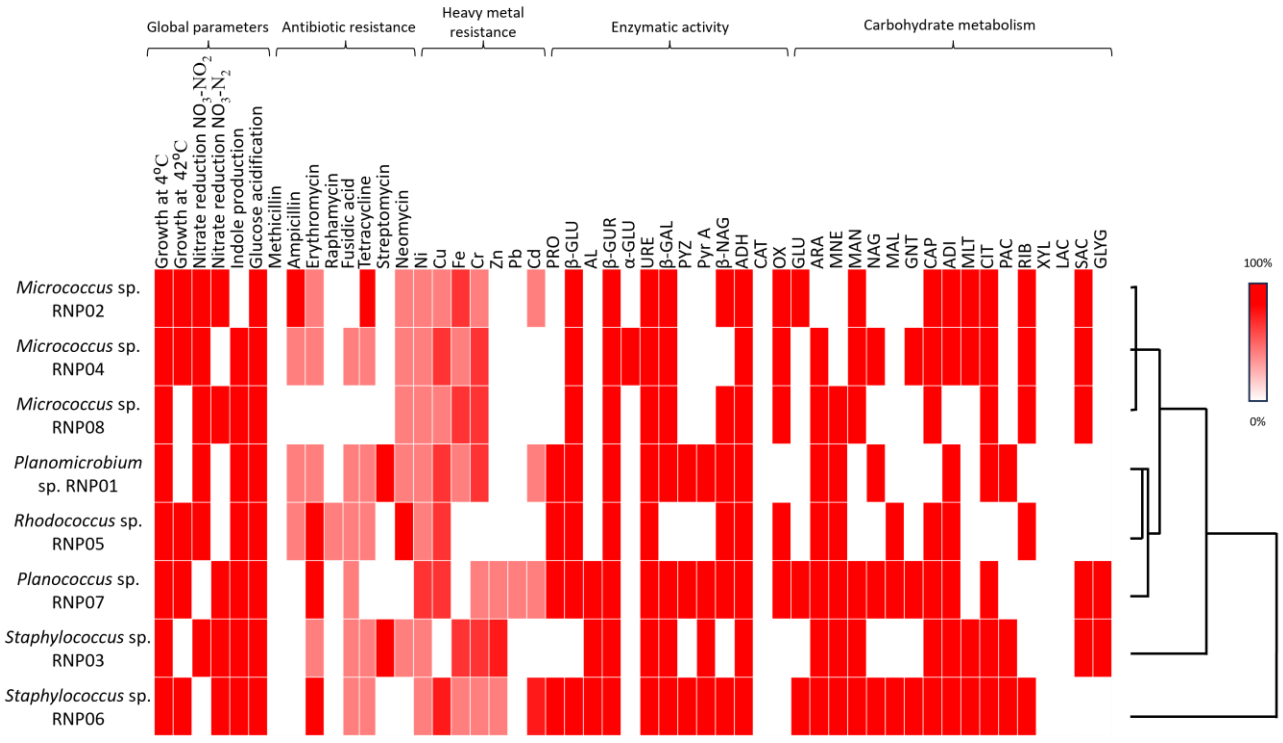


Figure 1. Dendrogram of hierarchical cluster analysis of the resistance to antibiotic and heavy metals and enzyme activity for selected petroleum compounds.

The clustering analysis was aligned with the phylogenetic diversity of strains. Interestingly, the strains with the highest bioremediation capabilities *Planomicrobium* sp. RNP01, *Planococcus* sp.

RNP07 and *Rhodococcus* sp. RNP05 clustered tightly together. All three strains displayed phenanthrene, pyrene and DBT degrading activity while *Rhodococcus* sp. RNP05 could degrade benzene, toluene and xylene as well [3].

CONCLUSION

The study highlights the resilience and adaptability of microorganisms in petroleum-contaminated soils, specifically those from the Petroleum Oil Refinery Pančevo in Serbia. The findings demonstrate that many of the examined bacteria can tolerate high concentrations of heavy metals, showcasing their resistance and adaptation mechanisms. The clustering analysis, which aligns with the phylogenetic diversity of the strains, reveals that the strains with the highest bioremediation capabilities, namely *Planomicrobium* sp. RNP01, *Planococcus* sp. RNP07, and *Rhodococcus* sp. RNP05, form a closely related group. This underscores their potential utility in bioremediation efforts to mitigate petroleum-derived environmental contamination. The unique physicochemical and biological characteristics of these habitats further emphasize the importance of understanding microbial communities in developing effective bioremediation strategies. The results presented here may provide a road map for identifying potential bioremediation strains based on standard biochemical and physiological characteristics. Our findings contribute to the growing body of knowledge on microbial adaptation to pollutants and highlight the potential use of these bacteria in environmental cleanup strategies.

Acknowledgment

This work was supported by the Ministry of Education, Science and Technological Development of the Republic of Serbia (grant no 451-03-66/2024-03/200026 and 451-03-66/2024-03/200042).

REFERENCES

[1] O.T. Olaniyan, C.O. Adetunji, Biochemical Role of Beneficial Microorganisms: An Overview on Recent Development in Environmental and Agro Science, in: C.O. Adetunji, D.G. Panpatte, Y.K. Jhala (Eds.), Microbial Rejuvenation of Polluted Environment, Microorganisms for Sustainability, vol 27, Springer, Singapore, 2021. https://doi.org/10.1007/978-981-15-7459-7_2.

[2] S. Kuppusamy, N.R. Maddela, M. Megharaj, K. Venkateswarlu, Impact of Total Petroleum Hydrocarbons on Human Health, in: Total Petroleum Hydrocarbons, Springer, Cham, 2020. https://doi.org/10.1007/978-3-030-24035-6_6.

[3] J. Milić, J. Avdalović, T. Šolević-Knudsen, G. Gojgić-Cvijović, T. Jednak, M.M. Vrvić, Chem. Ind. Chem. Eng. Q., 22 (2016) 293-299. https://doi.org/10.2298/CICEQ150606043M

[4] J. Milić, J. Avdalović, T.Š. Knudsen, Microbial bioremediation of the oil polluted environment and the sustainable development goals of pillar Planet of the Agenda 2030, Environ. Dev. Sustain., (2024). https://doi.org/10.1007/s10668-024-04848-3

[5] API Technical Manual, Procedure Manual, Toronto Medical Laboratories/Mount Sinai Hospital Microbiology Department, Microbiology Department Policy & Procedure Manual, Toronto.

[6] K. Kubota, D. Koma, Y. Matsumiya, S.Y. Chung, M. Kubo, Biodegradation, 19 (2008) 749-757.

PERFORMANCE OF RANDOM FORESTS, EXTREME GRADIENT BOOSTING AND SUPPORT VECTOR MACHINES EMPLOYED IN LIPIDOMICS

D. Pirić and R. Masnikosa

University of Belgrade, Vinča Institute of Nuclear Sciences - National Institute of the Republic of Serbia, Department of Physical Chemistry, Mike Petrovića Alasa 12-14, 11000 Belgrade, Republic of Serbia. (david.piric@vin.bg.ac.rs)

DOI: https://doi.org/10.46793/Phys.Chem24I.223P

ABSTRACT

Herein we present the performance of three supervised machine learning (ML) algorithms: random forests (RF), extreme gradient boosting (XGB) and support vector machines (SVM) in classification of human serum samples into pancreatic cancer or control group, using a lipidomic dataset retrieved from the research article „Lipidomic profiling of human serum enables detection of pancreatic cancer“ by Wolrab et al. [1]. Our main objective was to assess and compare, for the three ML techniques, the performance metrics, that is accuracy, precision, sensitivity, F1 score and ROC-AUC, with those computed by decision trees (DT), which is the basis of RF and XGB algorithms, and commonly used partial least squares – discriminant analysis (PLS-DA) and orthogonal projections to latent structures – discriminant analysis (OPLS-DA). We suggest that RF, XGB and SVM represent excellent binary classifiers, making these three promising candidates for future use in the discovery of potential lipid biomarkers.

INTRODUCTION

In the last decade lipidomics has emerged as a dynamic scientific field that provides a deep insight into complex lipidomic landscape of biological systems. A vast area of interest is study of lipidomic alterations in plasma or serum of diseased individuals, due to the availability of this biological fluid. The primary goal of such studies is to discover a lipid signature of a disease that can eventually be developed into a potential diagnostic or prognostic biomarker. A typical lipidomic experiment produces a big dataset, which consists of big hundreds of lipids measured in hundreds of samples. Powerful machine learning algorithms are required to extract the biological meaning out of such data. To assess a biomarker potential of measured lipid species, lipidomics dataset is often subjected to PLS-DA or OPLS-DA. One such example is a lipidomic study of pancreatic cancer (PC), where concentrations of 190 lipids in serum samples obtained from 546 PC patients and 262 healthy control persons were measured, as published by Wolrab et al. [1]. The aim of the original study was to test the potential of differentially expressed lipids to discriminate PC patients from healthy people, by using OPLS-DA, which is basically a linear transformation that converts the data to fit into a lower dimensional space. However, when the relationship between input variables (lipid concentrations) and the response (binary variable, PC vs. healthy) is non-linear, as is often the case in biology, then linear models perform sub-optimally. Herein, we examined the potential of non-linear ML models: random forests (RF), extreme gradient boosting (XGB) and support vector machines (SVM) to perform binary classification between PC and healthy group. We evaluated metrics for our RF, XGB and SVM models, as well as DT, because it is the basis of tree-based algorithms (RF and XGB) and compared them to PLS-DA and OPLS-DA model, which was originally used in [1].

METHODS

Data set with molar concentrations [nmol/mL] of lipid species in human was retrieved from ref [1]. The dataset format, n x p = 808 x 190 was divided into two single-gender datasets. The lipidomic dataset for males contains 275 PC cases and 128 controls, while that for females 271 PC cases and 134 controls. Both datasets were divided into a training and testing set (80/20), by random choice. All the models were built using solely the training set and verified on the testing set, through the performance metrics (Table 1). Supervised ML algorithms: PLS-DA, DT, RF, XGB and SVM were used to compute binary classifiers (models). PLS-DA model was built from the unit-variance scaled data. In RF, XGB and SVM, set.seed was set to 1. In RF, mtry and ntree were adjusted to minimize the class-separated (PC vs. control) errors. In SVM, both linear and radial basis function (RBF) kernels were tried and the type C-classification was chosen, while cost was set to 10. An automatic search for the best combination of hyperparameter values was performed by iterating over a range of possible values; then, each combination was tested against a performance metric in order to find the best one. We used R software environment (https://www.r-project.org, v 4.3.3), using its packages: ropls (v 1.34.0) for PLS-DA, party (v 1.3.14) for DT, randomForest (v 4.7.1.1) for RF, xgboost (v 1.7.7.1) for XGB and e1071 (v 1.7.14) for SVM.

RESULTS AND DISCUSSION

Space-wise, only single-gender plots are displayed, those for females. The lipidomic landscape in the form of heatmap, alongside with the Volcano plot showing the most significantly altered lipid species are in Figure 1.

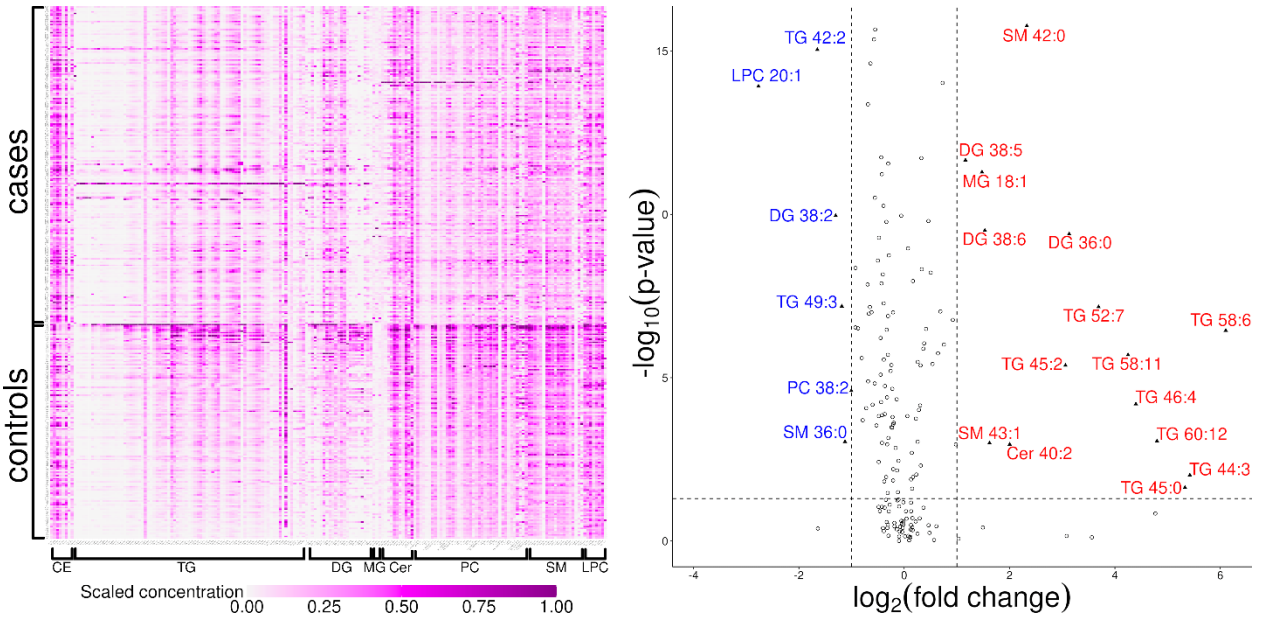


Figure 1. Heatmap (left) showing min-max scaled concentrations of serum lipid species in PC cases and controls, from the lowest to the highest average scaled concentration; Volcano plot (right), p-values from between-groups means comparisons, fold change (FC) is the ratio of mean lipid concentrations in PC cases and controls, triangles represent significantly altered lipid levels (p-value < 0.05 and $\log_2|FC| > 1$).

To be able to present the multidimensional lipidomic data set (n x p = 405 x 190) in 3D space, we computed novel variables (Dim 1-3) using RF model (Figure 2, left). For our tree-based ML models (RF, XGB) we extracted the feature importance – those lipid species that contributed the most to the binary classification of the serum samples; the feature importance was expressed as mean decrease in Gini and SHAP values for RF and XGB, respectively (Figure 2, center and right). Regarding the two SVM models, that is linear and RBF kernel, their scores are presented in Figure 3 (left and center). We have also computed the feature importance for the linear kernel based SVM through model based coefficients (Figure 3, right).

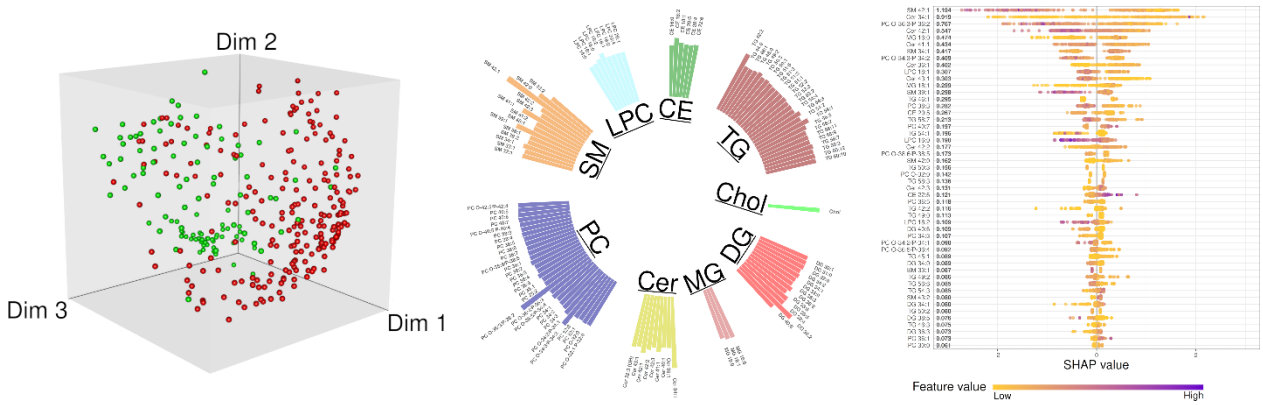


Figure 2. RF scatter plot (left), PC cases are in red, controls in green; mean decrease in Gini (center) from the RF (> 0.3 are shown); SHAP values (right) from XGB model (the first 50 lipid species with the high values); set.seed = 1, mtry = 37, ntree = 300 (RF); set.seed = 1, max.depth = 5, eta = 0.5 and nrounds = 100 (XGB).

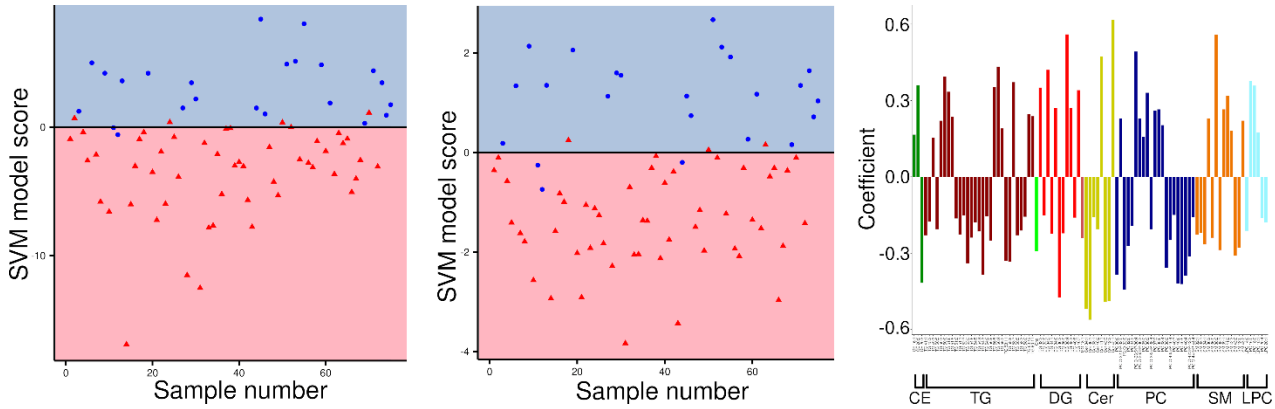


Figure 3. SVM model score for the testing set with linear kernel (left) and RBF kernel (center), PC cases are red triangles, controls are blue circles; the coefficients from SVM with linear kernel (right) with absolute values greater than 0.15; the SVM parameters were set.seed = 1, cost = 10 and gamma = 0.003448.

The scores were further used to calculate the performance of models in terms of accuracy, precision, sensitivity, F1 score and area-under-the-receiver-operating-characteristic-curve (AUC_ROC), which are presented in Table 1. The majority of the evaluated ML models performed better for the female subjects than for males, except for the XGB.

Table 1. Performance comparison of seven binary classifiers.

Model	Gender	Accuracy	Precision	Sensitivity	F1_score	AUC_ROC
PLS-DA	male	0.849	0.918	0.865	0.891	0.837
	female	0.933	0.927	0.981	0.953	0.903
	mean	0.891	0.923	0.923	0.922	0.870
OPLS-DA	male	0.904	0.941	0.923	0.932	0.890
	female	0.907	0.895	0.981	0.936	0.860
	mean	0.906	0.918	**0.952**	**0.934**	0.875
DT	male	0.753	0.886	0.750	0.813	0.756
	female	0.920	0.979	0.904	0.940	0.930
	mean	0.837	0.933	0.827	0.877	0.843
RF	male	0.877	0.906	0.923	0.914	0.842
	female	0.920	0.926	0.962	0.943	0.894
	mean	0.899	0.916	**0.943**	0.929	0.868
XGB	male	0.945	0.980	0.942	0.961	0.947
	female	0.920	0.942	0.942	0.942	0.906
	mean	**0.933**	**0.961**	**0.942**	**0.952**	**0.927**
SVM with linear kernel	male	0.849	0.936	0.846	0.889	0.852
	female	0.920	0.960	0.923	0.941	0.918
	mean	0.885	**0.948**	0.885	0.915	0.885
SVM with RBF kernel	male	0.904	0.959	0.904	0.931	0.904
	female	0.920	0.942	0.942	0.942	0.906
	mean	**0.912**	**0.950**	0.923	**0.937**	**0.905**

CONCLUSION

AS the binary classifiers for the PC serum lipidomic dataset, tree-based or non-linear models such as RF, XGB and SVM generally performed better than a widely used in lipidomics OPLS-DA. XGB and SVM with RBF kernel exhibited the best performance. Though we listed the significant lipid species contributing the most to the models, we still need additional analyses (enrichment and pathway analysis), combined with a knowledge-based data mining, to fully understand the picture of altered lipid metabolism in PC.

Acknowledgment

This research is funded by the Ministry of Science, Technological Development and Innovation, Republic of Serbia, Grants: No. 451-03-66/2024-03/200017.

REFERENCES

[1] D. Wolrab et al., Lipidomic profiling of human serum enables detection of pancreatic cancer, Nature communications, 13 (2022), 124.

RANDOMIZATION VERSUS POPULATION MODELS EMPLOYED IN LIPIDOMIC DATA ANALYSIS

D. Pirić, V. Vasić and R. Masnikosa

University of Belgrade, Vinča Institute of Nuclear Sciences - National Institute of the Republic of Serbia, Department of Physical Chemistry, Mike Petrovića Alasa 12-14, 11000 Belgrade, Republic of Serbia. (david.piric@vin.bg.ac.rs)
[2]International educational system Ruđer Bošković, Belgrade, Republic of Serbia

DOI: https://doi.org/10.46793/Phys.Chem24I.227P

ABSTRACT
Herein we present the analysis and comparing fundamental chemometric methods: fold change (FC) analysis and univariate statistics for identifying differentially expressed lipids in human serum samples into pancreatic cancer or control group, using a lipidomic datasets retrieved from the research article „Lipidomic profiling of human serum enables detection of pancreatic cancer“ by Wolrab et al. [1]. Our main objective was to assess and compare basic chemometric methods, as well as the potential using a smaller number of samples in lipidomic studies. We have concluded that it is possible to use a smaller number of samples for basic chemometric analysis, but the exact number depends on the level of accuracy required.

INTRODUCTION
Lipidomics is a mass spectrometry (MS)-based analytical method for the measurement of concentrations of hundreds of lipid species in biological materials. The primary goal of a lipidomics study is to measure as many lipid species as possible in order to confirm the initial hypothesis, that there is a distinct lipid content between case and control group. The secondary goal is to identify the set of differentially expressed lipids (DEL) in the two groups. DEL are identified using statistical methods: fold change (FC) analysis and univariate statistics. Though the FC definition is simple, it is the ratio of average concentrations of a lipid in case group vs. that in control group, it can be calculated either using the mean values or the medians. Moreover, FC can be computed either from molar concentrations or the normalized concentrations of lipids, e.g. data converted to mol% of total lipid amount in a sample. Regarding univariate statistical analysis of lipidomics data (UniStat), life scientists, in most cases, prefer classical parametric tests (Students or Welch t-test) or non-parametric tests (albeit less frequently), which are both based on the population model. That is because they are more familiar with the population model and the adequate software, with graphical user interfaces, is readily available. Unfortunately, parametric tests come with certain assumptions: random sampling, normal distribution (ND) of data, and homogeneity of variance (homoskedasticity) between groups, which are rarely fulfilled by real-world data. The lipid data is usually skewed and the variance is usually much greater in cases than in controls. Non-parametric tests have their own drawbacks, such as converting data into ranks, which results in a loss of information even before statistical testing. Permutation tests are based on randomization model and offer a solution for these problems, because neither data structure nor the number of samples affect them. The premise behind the randomization model is that a sample of experimental units (measured lipid levels) is randomly divided into two groups exposed to two different conditions (disease vs. healthy). The null hypothesis is that the two conditions have no differential effect on the groups with respect to the means. Importantly, there is no reference to a population and, hence, no requirement that it should conform to a mathematically definable frequency distribution. Instead,

for each experiment, the unique sampling distribution of the mean is compiled exactly by permutation [2]. The first goal of our study of this computational study was to compare the FC values determined by using different metrics. The major goal of the study was to compare the population with the randomization model, when both are applied on the lipidomics datasets retrieved from ref [1]. We also wanted to assess how the accuracy of FC and p-values depend on the number of samples in the groups.

METHODS

Datasets consisting of molar concentrations [nmol/mL] of lipid species, measured in human sera of pancreatic cancer (PC) patients and healthy controls, in three phases (P1, P2, P3) by different MS methods were retrieved from ref [1]. They were: MALDI-MS, Shotgun MS, UHPSFC-MS and RP-UHPLC-MS. The datasets (n x p) were as following: 64 x 42 (P1, MALDI-MS), 364 x 270 (P1, Shotgun MS), 364 x 168 (P1, UHPSFC-MS), 536 x 183 (P2, HR Shotgun MS), 536 x 232 (P2, LR Shotgun MS), 538 x 376 (P2, RP-UHPLC-MS), 538 x 202 (P2, UHPSFC-MS), 808 x 202 (P3, UHPSFC-MS); each was divided into two single-gender datasets; this way, 16 datasets were created. Besides the molar concentrations, we also used normalized lipid concentrations, computed as mol% of the total lipid amount, separately for each sample. P-value < 0.05 was considered significant. All calculations were performed in R software environment and its packages (https://www.r-project.org, v 4.3.3).

RESULTS AND DISCUSSION

FC were calculated from mean and median values, using molar concentrations and mol% across all 16 datasets. Then, Spearman correlations were determined between the pairs: FC(means of nmol/L) vs. FC(medians of nmol/mL), also FC(means of mol%) vs. FC(medians of mol%), FC(means of nmol/mL) vs. FC(means of mol%.), and, finally, FC(medians of nmol/mL) vs. FC(medians of mol%.) This was done for each of 16 datasets independently. Then, the mean value and standard deviation (SD) of correlation coefficients was calculated for each of the four combinations (Table 1).

Table 1. Mean values of Spearman's correlation coefficients for FC.

FC1	FC2	mean	SD
FC mean – nmol/mL	FC median – nmol/mL	0.843	0.081
FC mean – data in mol%	FC median – data in mol%	0.875	0.080
FC mean – nmol/mL	FC mean – data in mol%	0.981	0.015
FC median – nmol/mL	FC median – data in mol%	0.917	0.069

First, the mean- and median-based FC values, determined from molar levels, are concordant, i.e. they share a high correlation coefficient. Similarly, the mean- and median-based FC values, determined from data normalized to mol%, share a great correlation coefficient. Finally, FC values calculated from means are almost identical, regardless whether we used original or normalized molar lipid concentrations. In other words, the normalization is not necessary.

After that, we tried to calculate FC, by using a smaller number of samples per group, but only means of molar concentrations of lipids. The number of samples in the two groups started from 10 in each (randomly chosen samples), then, the group size was gradually increased, by the random re-sampling of 15 samples/group, then 20 samples/group, then 25 samples/group, until all the samples were grouped. The method is referred to as "sampling" and was repeated ten times. Ratios of FC(any group size) and FC(maximum group size) were calculated; and if they were over 1, their

reciprocal values were taken to evaluate the "extent of accuracy" of those FC values that were calculated from the reduced data (as compared with the FC obtained from the whole dataset). The average "extent of accuracy" for 10 “samplings” as a function of the number of samples/group is shown in a boxplot (Figure 1A). The possibility of approximation even with a smaller number of samples, depending on the required accuracy, can be seen.

To test the ND we employed Shapiro-Wilk (SW) test, separately for all 16 datasets, which all exhibited a high percentage of deviation from normality. For example, 95.8% of lipid species measured in females were not ND (SD = 6.5%). In order to normalize data to fit into ND, many suggest logarithmic transformation, so we log10-transformed the lipid data. However, log10-data still deviated from the ND, albeit at a lesser extent. If we use the earlier example, 68.4% of lipid species measured in females still were not ND (SD = 15.3%). Even when the data were converted to mol%, the situation was similar, with a higher standard deviation.

The homoskedasticity of data was assessed through the Levene’s test p-values. Many heteroskedastic variables were noticed in all 16 datasets, with the prevalence of 0.262 (SD = 0.123) and 0.363 (SD = 0.168) in the nmol/mL and mol% datasets, respectively. Then, the homoskedasticity in nmol/mL- data was compared to that in mol%-data, for each of the 16 datasets; 16 misclassification tables were constructed, and the accuracy for each was determined; the mean accuracy was 0.363 (SD = 0.168). Interestingly, there are homoskedastic lipid variables when expressed as nmol/mL, which were not homoskedastic when normalized to mol%, and vice versa.

The “sampling” method was performed for the assessment of homoskedasticity, where the average p-values were calculated for 10 “sampling” iterations, and a representative boxplot showing these p-values against the number of samples is in Figure 1B. The average p-value decreases with an increase in the number of samples, indicating a higher prevalence of homoskedasticity in smaller number of samples per group.

Given that a great number of lipid species suffer of non-normal distribution and heteroskedasticity, a logical choice would be non-parametric Mann-Whitney U test also known as Wilcoxon signed-rank (WSR) test. For comparison, the parametric Welch’s t-test, which is a Student’s t-test adjusted for heteroskedasticity, was conducted. Misclassification tables were constructed for all 16 datasets to compare the significance of p-values from these tests, and the average accuracy was 0.873 (SD = 0.054). The “sampling” was also performed for the Welch and WSR, very much the same as done previously and the representative dependence of p-values vs. number of samples/group is presented in Figure 1C. A general decrease in p-values with an increase in the number of samples/group can be seen in a hyperbolic manner. It is, therefore, possible to approximate p-values with a smaller number of samples, depending on the required accuracy.

Comparing the Welch and WSR test using nmol/mL-data and normalized-to-mol%-data for all 16 datasets to generate misclassification tables, WSR and Welch’s average accuracy were 0.668 (SD = 0.157) and 0.662 (SD = 0.131), respectively. In other words, statistics done by the two tests gave different results.

It is highly recommendable to correct for the multiple comparisons after the p-values are obtained, the most commonly used being Bonferroni correction and Benjamini-Hochberg (BH) false discovery rate, with the threshold of 0.05. For 64x42 MALDI dataset, the similar results were obtained by both types of corrections, whereas, in case of other datasets, Bonferroni was more stringent, stripping off many lipid species from the list of significantly altered (which is why it is not popular in the lipidomic community). Interestingly, the graph p(Bonferroni) = f(p, BH) resembles the receiver operating characteristic curve of good machine learning models (Figure 1D). Misclassification tables were created to compare Bonferroni and BH corrections with a threshold of 0.05, and accuracy was calculated for all 16 datasets, averaging at 0.806 (SD = 0.086).

Importantly, we compared the permutation test (Monte Carlo approximation with 100,000 iterations) with each of WSR and Welch's test. Misclassification tables were generated, and the average accuracy for all tables but MALDI (Table 2) was calculated. A solid agreement with population-based statistics was observed, with Welch's t-test showing a greater alignment with the permutation test than the WSR.

Table 2. The average accuracy of misclassification tables for the permutation test (Monte Carlo approximation with 100,000 iterations) compared to population-based stats; the "sig-ns" type referres to 2x2 misclassification tables, where p-values are either significant or non-significant (a threshold 0.05); if the type is "*", a 5x5 misclassification table is being referred to, where p-values have 4 levels of significance (0.05, 0.01, 0.001, 0.0001).

Test	Type	mean	sd
Wilcoxon signed-rank test	*	0.780	0.066
Wilcoxon signed-rank test	sig-ns	0.945	0.028
Welch's t-test	*	0.877	0.060
Welch's t-test	sig-ns	0.972	0.021

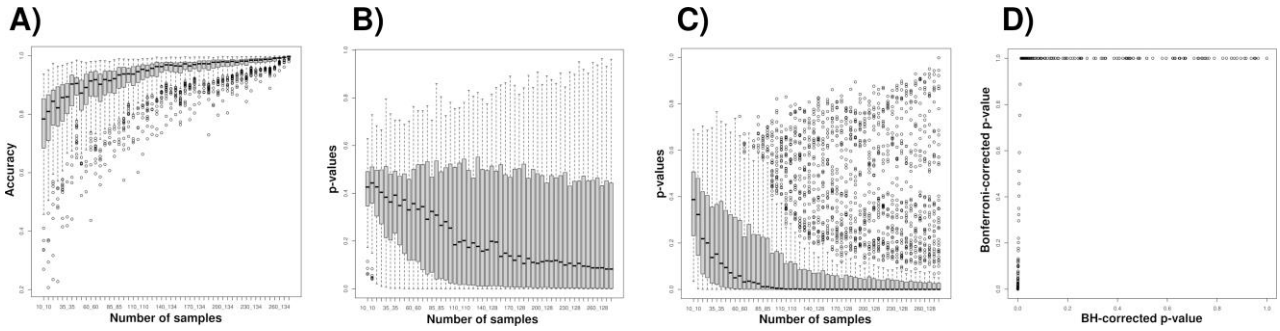


Figure 1. A) accuracy of FC(mean) vs. # of samples (P3, females); B) Levene's p-values vs. # of samples (P3, males); C) WSR p-values vs. # of samples (P3, males); D) Bonferroni-corrected p-values vs. BH-adjusted p-values (P1, Shotgun-MS, females).

CONCLUSION

In general, statistical analysis of normalized-to-mol%-lipidomic data give different results compared to the analysis of original molar concentrations. Expectedly, there was a high concordance between the results of permutation tests and population-based UniStat when applied to lipidomic data. We found that, even with a smaller number of samples, it is possible to obtain a high extent of accuracy of FC and p-values. This is important given that human samples are difficult to obtain in great numbers due to many factors (ethical issues, rare diseases, etc).

Acknowledgment

This research is funded by the Ministry of Science, Technological Development and Innovation, Republic of Serbia, Grants: No. 451-03-66/2024-03/200017.

REFERENCES

[1] D. Wolrab et al, Nature communications, 13 (2022), 124.

[2] Ludbrook, John and Hugh Dudley, The American statistician 52 (2) (1998) 127–32.

LIPOSOMAL FORMULATIONS OF ORIGANUM DICTAMNUS EXTRACTS FOR IMPROVED THERAPEUTIC EFFICACY – AN EPR STUDY

Đ. Nakarada, M. Radulović and M. Mojović

University of Belgrade, Faculty of Physical Chemistry,
Studentski trg 12-16, 11000 Belgrade, Serbia. (milos@ffh.bg.ac.rs)

DOI: https://doi.org/10.46793/Phys.Chem24I.231N

ABSTRACT

Origanum dictamnus, also known as Dittany of Crete, is an aromatic herb from the *Lamiaceae family*, valued for its medicinal properties. This study investigates the antioxidant potential of *Origanum dictamnus* extracts prepared using different solvents (water, ethanol, 50% ethanol, and methanol) and their subsequent encapsulation into soy lecithin liposomes. The extracts were evaluated for their antiradical scavenging activities against DPPH and •OH radicals using electron paramagnetic resonance (EPR) spectroscopy. Methanol and 50% ethanol extracts demonstrated the highest antioxidant potential and were encapsulated into liposomes to enhance their stability and therapeutic efficacy. The liposomal formulations maintained the extracts' antiradical activity, confirming their potential for treating conditions associated with oxidative stress.

INTRODUCTION

Origanum dictamnus, known as Dittany of Crete, is a highly aromatic perennial herb from the *Lamiaceae* family. It is native to the island of Crete, where it grows wild on the mountainsides. Classified as vulnerable on the IUCN Red List of Threatened Plant Species, it is still available through cultivation sources. *Origanum dictamnus* has been used since ancient times as an ornamental plant in temples, as a food flavoring, and as a medicinal panacea. It was believed to have magical properties, which secured its place in mythology. Historically, it was highly prized and well-documented by prominent figures such as Hippocrates, Aristotle, and Theophrastus. In modern medicine, Dittany of Crete is valued as an herbal remedy known for a plethora of biological activities, including anti-inflammatory, antiseptic, and antimicrobial effects. The main constituents of its essential oil are carvacrol (68.96%), *β*-phellandrene (18.34%), and *p*-cymene (4.68%). Dittany of Crete is used in herbal teas and tinctures to aid digestion, relieve respiratory issues, and soothe stomach ailments. Its essential oils are utilized in treating minor wounds and burns due to their antiseptic and anti-inflammatory properties. Additionally, the plant's antimicrobial properties have been confirmed in scientific studies, highlighting its effectiveness against certain bacteria and fungi. It is also used in aromatherapy to promote relaxation and alleviate stress. Given these historical and modern uses, innovative methods are being explored to further enhance the efficacy of *Origanum dictamnus* extracts. Incorporating these extracts into liposomes offers several significant advantages that enhance the therapeutic efficacy and stability of these bioactive compounds. Liposomes are microscopic vesicles composed of lipid bilayers that can encapsulate both hydrophilic and hydrophobic substances, providing a protective environment that shields the delicate essential oils from degradation. This encapsulation improves the bioavailability and controlled release of the active constituents of *Origanum Dictamnus* extracts, maximizing their anti-inflammatory, antiseptic, and antimicrobial effects. Furthermore, liposomes facilitate targeted delivery, ensuring that the extracts reach specific tissues or cells more efficiently, reducing the required dosage and minimizing potential side effects.

Compared to UV-Vis spectrometry or electrochemical measurements, which are routinely used for studying antioxidative activities of different compounds towards free radicals, electron paramagnetic resonance (EPR) spectroscopy provides much higher sensitivity and reproducibility. Liposomal encapsulation is crucial for EPR studies because it enables the incorporation of water-insoluble antioxidant molecules into lipid structures, allowing them to be studied in a water medium without generating interfering carbon-based radicals. This method ensures accurate and reliable detection of biologically relevant free radicals such as $^{\bullet}OH$, $^{\bullet}O_2^-$, and $NO^{\bullet}$.

Herein, we prepared extracts of *Origanum dictamnus* in water, ethanol (EtOH), 50% ethanol, and methanol (MeOH) to determine which extract has the highest antiradical scavenging potential towards DPPH and $^{\bullet}OH$ radicals. The extract with the highest activity was then incorporated into biocompatible soy lecithin liposomes to confirm that its scavenging potential against these species remained unchanged in this formulation, demonstrating the therapeutic potential of liposomes containing *Origanum dictamnus* extracts.

EXPERIMENTAL

Extracts of *Origanum dictamnus* have been prepared by adding 1 g of dry herb to 10 ml of selected solvents: water, 50% EtOH, MeOH. This mixture was stirred for 3 hours at 40 °C. Dry residue was removed by vacuum filtration, and the supernatant was transferred into the microcentrifuge tube and centrifuged 10 min at 10 000 rpm. The extracts were further filtered through the 0.22 μm HPLC filter and stored at -80 °C. Multilamellar liposomes were prepared from the obtained extracts and hydrogenized soy lecithin by the modified thin-film method [1] and ultrasound probing. This involved dissolving 48 mg of lecithin in the mixture of chloroform and methanol (4:1 v/v) in a rotary flask, followed by the addition of 1 ml of the *Origanum dictamnus* extract. Solvent was slowly evaporated at room temperature using rotary vacuum evaporator. The remaining thin film was hydrated with 20 ml of 18 MΩ water followed by 3 min of vigorous vortexing and 3 min of ultrasounding using ultrasound ice bath. The suspension was further sonicated for 30 minutes using an ultrasound probe with a maximum power of 900W, set to 10% power, in a regimen where it ran for 30 seconds and stayed idle for the next 30 seconds. Control liposomes were prepared following the same procedure, without the addition of *Origanum dictamnus* extracts. The size and zeta potential of the obtained liposomes were determined using dynamic light scattering (DLS) technique.

EPR spin-trapping technique was employed in order to trap short-lived free radical species generated directly in the liposome suspension, and to quantify the amount of their interaction with liposomes. In order to study the interaction of hydroxyl radical with *Origanum dictamnus* extracts, the intensity of hydroxyl spin-adduct EPR signal was measured. 1 μl of the extract was mixed together with 25 μl of deionized water, 2 μl of 5 mM H_2O_2 and 1 μl of 100 mM 5-(diethoxyphosphoryl)-5-methyl-1-pyrroline-N-oxide (DEPMPO). After the addition of 1 μl of 5 mM $FeSO_4$, the mixture was transferred into 1 mm diameter teflon tube, and EPR spectra were recorded [2].

The interaction of DPPH free radicals with *Origanum dictamnus* extracts was studied by measuring the intensity of the DPPH EPR signal. 1 μl of the extract was mixed with 28 μl of deionized water and 1μl of mM DPPH, prior to transferring the mixture into 1 mm diameter teflon tube and recording the EPR spectra.

All EPR spectra were recorded 2 min upon generation/introduction of free radical species into the system, under the following parameters: center field 3500 G, microwave power 10 mW, microwave frequency 9.85 GHz, modulation frequency 100 kHz, modulation amplitude 1 G. The same procedure was followed in order to determine the scavenging activity of liposomes containing *Origanum dictamnus* extracts, with the modification that a liposome suspension was used instead of

the extract solution. Control experiments have been made following the same procedures, using water instead of liposome suspension.

RESULTS AND DISCUSSION

The decrease of the intensities of DEPMPO/OH adduct and DPPH EPR signals were measured for 2 min after their generation in the system containing *Origanum dictamnus* extracts (Figure 1). The reduction of the EPR signal was calculated using the formula:

$$\Delta h = \frac{h_i - h_2}{h_i} \times 100\ (\%)$$

where h_i and h_2 refer to the intensities of the control free radical signal and the signal obtained after 2 min upon addition of *Origanum Dictamnus* extracts. The calculated percentage of the DEPMPO/OH EPR signal reduction by selected extracts were 50.22% (water), 88.01% (50% EtOH), 89.13% (EtOH) and 91.38% (MeOH). The same extracts were able to reduce DPPH EPR signal for 26.99% (water), 98.13% (50% EtOH), 36.82% (EtOH) and 50.36% (MeOH). These results indicate that all extracts exert significant antioxidant potential towards selected free radical species, with MeOH and 50% EtOH extracts being the most potent scavengers of ˙OH and DPPH radicals, respectively. These two extracts were selected to be incorporated into hydrogenized soy lecithin liposomes. Upon formation, their size was determined using DLS. The results indicate that all liposomes were of similar size, ranging from 58.77 to 78.82 nm. Their zeta potential was in range of -35.4 to -36.1 mV. These results indicate that all liposomes were uniform in size, and have long-term stability. To remove any potential excess of active compounds which were not incorporated/integrated into liposomes, they were dialysed in water overnight. Following this, the antiradical activity of the liposomes against the selected radical species was determined using the previously described procedure. The obtained results indicate that liposomes containing MeOH extracts of *Origanum dictamnus* have removed 18.39% of ˙OH and 19.80% of DPPH radicals from system, while liposomes containing 50% EtOH extract have removed 11.52% and 41.34% of those radical, respectively. To confirm that results arise solely from *Origanum dictamnus* extracts, and not from lecithin, control experiments were performed using 100 % soy lecithin liposomes, showing no signal reduction (data not shown).

The results presented in this paper strongly indicate that *Origanum dictamnus* extracts possess significant antioxidant potential, with MeOH and 50% EtOH extracts being the most potent. Their activity remained substantial even after incorporation into soy lecithin liposomes, confirming that encapsulation maximizes their anti-inflammatory, antiseptic, and antimicrobial effects. This enhancement highlights their pharmaceutical potential, especially in treating conditions related to elevated radical production and oxidative stress.

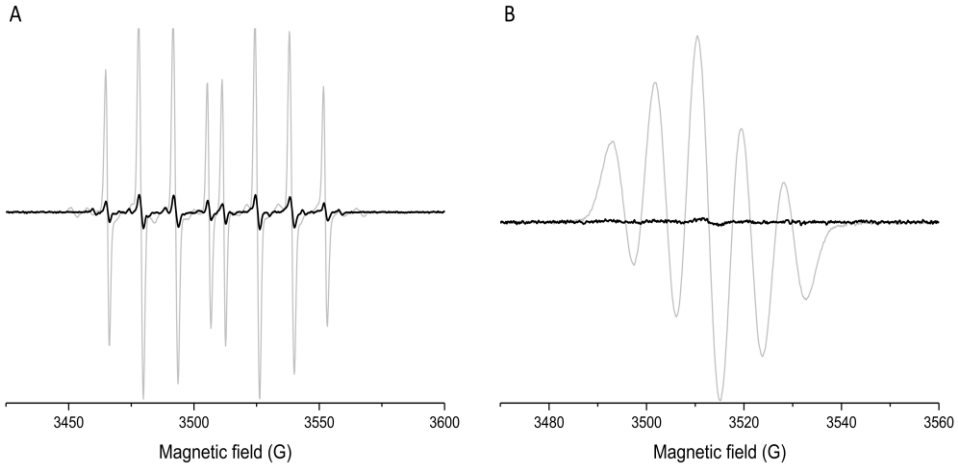


Figure 1. EPR spectra of DEPMPO/OH adduct (A) and DPPH radical (B) recorded in the control sample (gray) and 2 min (black) after their generation in the suspension of liposomes containing *Origanum dictamnus* extracts in MeOH (A) and 50% EtOH (B).

CONCLUSION

The findings of this study demonstrate that *Origanum dictamnus* extracts possess significant antioxidant properties, particularly those prepared with methanol and 50% ethanol. The encapsulation of these extracts into soy lecithin liposomes not only preserved their antiradical activity but also enhanced their stability and bioavailability. This liposomal formulation offers a promising approach to maximizing the therapeutic potential of *Origanum dictamnus*, especially in addressing conditions related to oxidative stress and elevated free radical production.

Acknowledgement

This work was partially supported by the Ministry of Science, Technological Development and Innovation of the Republic of Serbia (Grant no. 451-03-65/2024-03/200146 and 451-03-66/2024-03/200146).

REFERENCES

[1] V. Weissig, Liposomes: Methods and Protocols, Vol. 1: Pharmaceutical Nanocarriers, Humana Press, Mumbai, 2010.
[2] M. Mojović, M. Vuletić, G. Bačić, Ann. N. Y. Acad. Sci., 1048 (2006) 471 – 475.
[3] V.Roubaud, S. Sankarapandi, P. Kuppusamy, P. Tordo, J. Zweier, Free Radic. Res. Commun., 19 (1993) 79 – 87.

IN VIVO EPR IMAGING: A NEW WINDOW INTO HONEY BEE HEALTH

Đ. Nakarada [1], U. Glavinić [2], M. Ristanić [2], M. Popović [1], J. Stevanović [2], Z. Stanimirović [2] and M. Mojović [1]

[1]*University of Belgrade, Faculty of Physical Chemistry, Studentski trg 12-16, 11000 Belgrade, Serbia. (milos@ffh.bg.ac.rs)*
[2]*University of Belgrade, Faculty of Veterinary Medicine, Bulevar oslobođenja 18, 11000 Belgrade, Serbia*

DOI: https://doi.org/10.46793/Phys.Chem24I.235N

ABSTRACT
Honey bees are crucial to ecosystems and human health as pollinators and producers of health-promoting products. However, honey bee colony mortality is rising globally due to parasites, pesticides, habitat loss, poor nutrition, and climate change, affecting the environment, economy, and human welfare. This paper presents the first 2D *in vivo* EPR imaging experiment on a honey bee, showing the redox status of their intestines. By monitoring spatio-temporal changes in the EPR signal of redox-active spin-probes, we can gain vital information on bee pathologies and the effectiveness of treatments. Using various spin-probes can further reveal pH levels and oxygen concentrations in bee tissues, allowing non-invasive assessments of bee physiology. This approach offers promising ways to safeguard pollinators, understand their biology, and promote their well-being and ecological balance.

INTRODUCTION

Honey bees (*Apis mellifera*) stand as remarkable creatures, holding immense significance for humankind and nature. However, the mortality of honey bee colonies is increasing caused by parasites and pathogens, pesticides, loss of habitat due to urbanization, poor nutrition, and climate change. The application of EPR spectroscopy has steadily advanced in biophysical chemistry, with *in vivo* EPR imaging (EPRI) emerging as a hallmark technique for studying small animals, including bees. The redox status, which signifies the balance between oxidants and antioxidants, serves as a pivotal marker of an organism's general health. Determining the *in vivo* redox status of animals is essential for maintaining their health, detecting and addressing potential issues early on, and advancing our understanding of the intricate biological processes occurring within living organisms.

To date, honey bees have already been subject to EPR studies, although these investigations were conducted *ex vivo* [1], [2]. To the best of our knowledge, this paper represents the pioneering *in vivo* EPR honey bees' examination, making way for a more comprehensive view of and insight into the redox processes occurring within bees' digestive systems.

EXPERIMENTAL

The experimental bee brood was sourced from a healthy *Apis mellifera* colony in the experimental apiary at the Faculty of Veterinary Medicine, University of Belgrade. The colony was confirmed as Nosema-free through PCR analysis and no indications of other infections (bacterial, viral, protozoan, or fungal) was indicated over the preceding two years. Seven days after hatching, the bees were subjected to an EPR imaging evaluation. All EPR spectra were acquired using a X/L dual band Bruker ELEXSYS-II E540 spectrometer (Rheinstetten, Germany) equipped with an imaging gradient unit. For the 2D EPR imaging experiment, honey bees were fed with a 400 mM solution of

redox-sensitive membrane-permeable aminoxyl spin-probe 3-carbamoyl PROXYL (3CP) dissolved in Acacia honey. This spin-probe is non-toxic and is commonly employed in *in vivo* studies of small animals. Five minutes after the intake of the spin-probe, the head and the honey bee forelegs were gently rinsed with distilled water to eliminate any unwanted stable radical-induced contamination. Two-dimensional EPR images were reconstructed from the raw data using the Xepr back-projection algorithm.

RESULTS AND DISCUSSION

The endogenous-produced redox-active species readily interact with the nitroxide, affecting its EPR signal and the appearance of the 2D EPR image, revealing the spatio-temporal profile of bees' intestine tissue redox status. 2D EPR images, as illustrated in Fig. 1a and Fig. 1b, reveal that the 3CP spin-probe is predominantly situated within the abdomen of the honey bee. For a more profound insight, a frontal 2D image could be juxtaposed with an anatomical representation of honey bee intestines (Fig. 1c). A more detailed examination of the frontal 2D image (Fig. 1a) discloses that the spin-probe is evident across all three primary body segments, suggesting its likely traversal through the digestive system, possibly within the perivisceral sinus. The signal observed in the head region likely corresponds to the presence within the hypopharyngeal and cephalic salivary glands, while the signal from the thoracic region likely corresponds to the presence within the thoracic salivary glands. The most pronounced signal from the spin-probe is localized in the abdominal region, which aligns with the anatomical position of the crop (compare Fig. 1a and Fig. 1c [3]). The abdominal region displaying a reduced spin-probe signal likely corresponds to a section of the ventriculus. Given the extended duration of around 20 minutes required for EPRI, it is plausible that the honey containing the spin-probe was actively undergoing digestion within the bee. After EPRI measurements, bees were placed in isolation with a small cohort of untreated bees, and the group's well-being was monitored for the subsequent two weeks, during which no bee mortalities were observed.

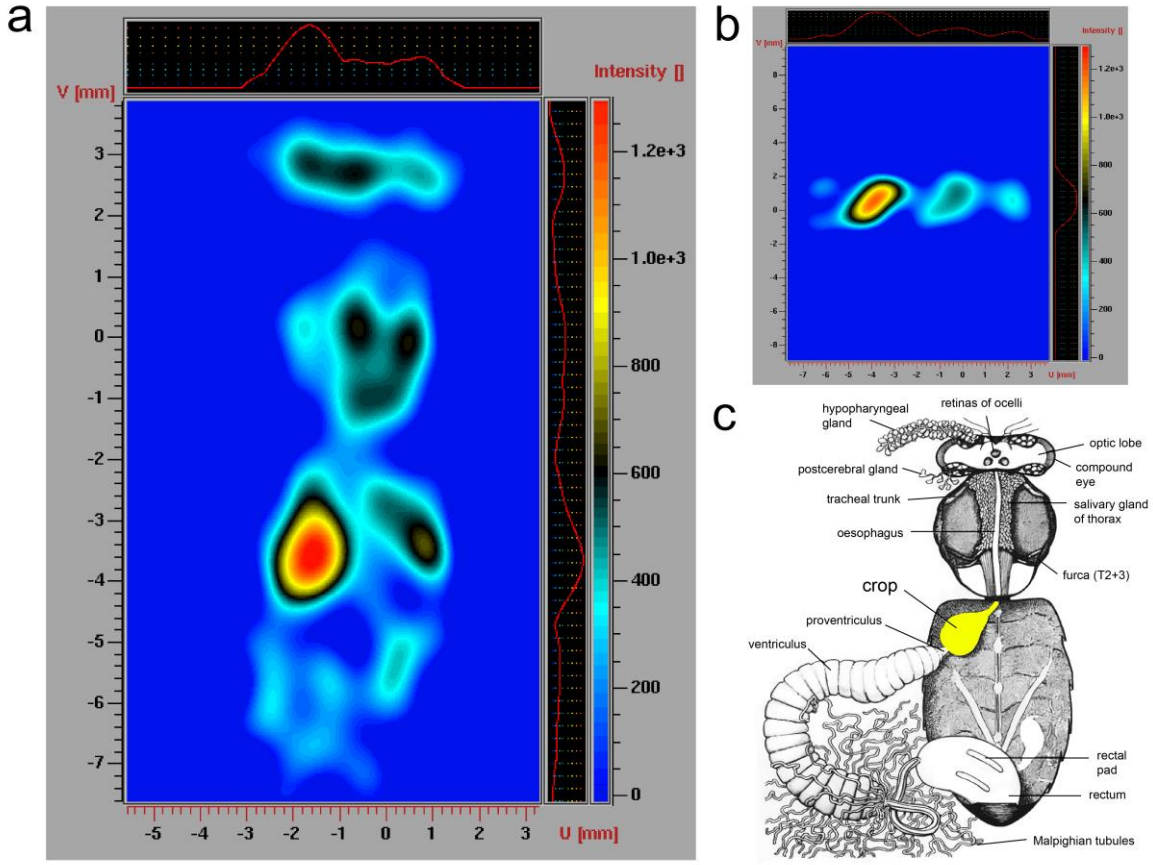


Figure 1. 2D *in vivo* EPR imaging of the honey bee: (a) The honey bee's body captured in two-dimensional images obtained both in the frontal XZ, and (b) sagittal XY planes. Signal intensity was color-coded in arbitrary EPRI units, as indicated by the color bar: high EPRI signal intensities are represented by color range from dark green, to yellow and red, while low to no EPRI signal intensities are represented by light green to blue. EPRI signal intensities below zero have been excluded; (c) Anatomical representation of the internal organs of a honey bee in the frontal plane. The position of the crop is marked yellow, adapted from [3].

It is important to emphasize that, following the measurements, all bees remained unharmed. Complementary imaging studies could also involve the use of a variety of spin-probes. These probes have the ability to independently reveal information about the redox status in different cell areas. Additionally, pH-sensitive spin-probes can be employed to non-invasively evaluate pH levels in various bee tissues and organs. Furthermore, certain spin-probes only become EPR active when they interact with intracellular enzymes, providing us with valuable information essential for a comprehensive understanding of bee physiology and biochemistry on an intracellular level. Additionally, EPR oximetry probes, could similarly be engaged for spatio-temporal measurements of oxygen concentration *in vivo*. In addition to 2D, the application of 3D EPR imaging should also be considered, being able to reveal volume-related images of the spin-probe signal for even better follow-up of redox-related processes in bees during normal, pathological, and rehabilitation processes.

CONCLUSION

This paper represents the pioneering experiment, paving the way for a comprehensive examination of the *in vivo* redox processes taking place within the intestines of the bees. Future studies could give us valuable information related to the redox process in various bees' pathologies. Furthermore, employing diverse spin-probes could elucidate redox status, pH levels, and oxygen concentration in bee tissues, fostering a non-invasive assessment of bee physiology. This approach offers promising avenues for safeguarding pollinators and understanding their biology, fostering their well-being and ecological harmony.

Acknowledgement

This work was partially supported by the Ministry of Science, Technological Development and Innovation of the Republic of Serbia (Grant no. 451-03-65/2024-03/200146 and 451-03-66/2024-03/200146) and the Science Fund of the Republic of Serbia, project Waste2Protect Bees No. 5455.

REFERENCES

[1] N. Charlier, M. Desoil, Y. Gossuin, P. Gillis & B. Gallez, Cell Biochemistry and Biophysics, 78 (2020) 123.
[2] L. J. El-Jaick, D. Acosta-Avalos, D. Mota de Souza Esquivel, E. Wajnberg, & M. Paixao Linhares, European Biophysics Journal, 29 (2001) 579.
[3] H. A. Dade: Anatomy and Dissection of the Honeybee. Bee Research Association, London, UK. (1985).

ELECTROCHEMICAL AND EPR CHARACTERIZATION OF STEM CELLS FOR APPLICATIONS IN REGENERATIVE MEDICINE

Đ. Nakarada[1], T. Tomašević[1], A. Dragićević[1], D. Mitić, A. Savić[1] and M. Mojović[1]

[1]University of Belgrade, Faculty of Physical Chemistry, Studentski trg 12-16, 11000 Belgrade, Serbia. (milos@ffh.bg.ac.rs)
[2] University of Belgrade, Faculty of Dental Medicine, Implant-Research Center, Rankeova 4, 11000 Belgrade, Serbia

DOI: https://doi.org/10.46793/Phys.Chem24I.239N

ABSTRACT
Stem cell research has emerged as a promising course for regenerative medicine. A critical aspect of stem cell applications is the accurate assessment of cell viability and redox status. Traditional methods for evaluating cell viability, such as morphological assessment, cell counting, viability staining, metabolic activity assays, apoptosis detection, and functional assays, are often time-consuming, labor-intensive, and costly. In this study, we explore the use of electrochemical techniques, specifically cyclic voltammetry and electrochemical impedance spectroscopy, to provide a rapid and efficient assessment of dental pulp stem cells (DPSC) viability. Additionally, we employ electron paramagnetic resonance (EPR) spectroscopy to evaluate the redox activity of DPSCs. Our findings suggest that these methods offer an efficient alternative to conventional techniques, potentially enhancing the efficiency of stem cell research and its applications in regenerative medicine.

INTRODUCTION
In the human body, each cell performs a specific function essential for maintaining physiological processes. However, there exists a unique subset of cells, known as stem cells, that are unspecialized and lack a defined role. Despite their lack of specialization, stem cells possess the remarkable potential to differentiate into specialized cells, such as muscle cells, blood cells, and neurons. Furthermore, they have the ability to divide and self-renew over extended periods of time. Stem cell therapy, often referred to as regenerative medicine, aims to harness this potential to generate new cells for therapeutic purposes. This innovative field offers promising solutions for a variety of medical conditions, especially those involving tissue repair and wound healing, where traditional treatments often fall short. A key focus in this area is the investigation of stem cells and stem cell-conditioned media, which contain a diverse array of bioactive molecules, including growth factors, cytokines, and extracellular vesicles [1,2]. These molecules are critical in modulating cellular behavior, enhancing tissue repair, and stimulating regeneration. Stem cells are continuously produced throughout an individual's lifetime and can be sourced from various adult tissues such as bone marrow, brain, liver, and skin. In our research, we utilized adult stem cells isolated from dental pulp. Dental stem cells, a type of adult stem cell found in dental tissues, are multipotent, meaning they can differentiate into a limited range of cell types related to their tissue of origin. To date, three types of dental stem cells have been identified: dental pulp stem cells (DPSC), stem cells from human exfoliated deciduous teeth (SHED), and immature dental pulp stem cells (IDPC) [3]. For our work, we specifically used DPSCs due to their demonstrated ability to enhance wound healing by increasing collagen synthesis and promoting the proliferation and migration of human dermal fibroblasts.

EXPERIMENTAL

The pulp tissues were obtained from the impacted third molars of five healthy patients (aged between 18 and 25 years). After extraction, the teeth were rapidly transported to the laboratory, cut at the enamel-dentin border, and the pulp tissue was carefully removed from the tooth chamber and canals. The tissue was then minced into pieces, washed three times with phosphate-buffered saline (PBS), and seeded into cell culture flasks in complete growth medium. Growth medium is Dulbecco's modified Eagle's medium supplemented with fetal bovine serum (FBS) and a penicillin-streptomycin solution. It contains a high concentration of amino acids, vitamins, glucose, and other components. Cells were cultivated under standard conditions in a humidified atmosphere with 5% CO_2 at 37 ˚C. The complete growth medium in the cultures was changed three times per week, and cells were passaged when reaching a sub-confluence of 80 % [4]. The electrochemical methods used to determine the viability of DPSCs were cyclic voltammetry (CV) and electrochemical impedance spectroscopy (EIS). For electrochemical measurements, a carbon screen-printed with an Ag/AgCl reference electrode was used. The measurements were performed for viable and intentionally killed cells by the process of triple -80°C freezing/60°C heating. Samples were placed as a drop on the electrode to completely cover the surfaces of all three electrodes. The potential stability window used for CV measurements was from -1 V to 1 V, while EIS measurements were performed at a voltage of 0.2 V in the frequency range from 50000 Hz to 5 Hz. The EPR technique was used to detect the redox activity of cells against stable free radical TEMPONE. In brief, 1uL of TEMPONE (final concentration 25 µM) was added to 29 µL of medium containing cells (10^6 cells per mL), and kinetics of its EPR signal reduction was recorded for 20 min under the following parameters: center field 3500 G, microwave power 10 mW, microwave frequency 9.85 GHz, modulation frequency 100 kHz, modulation amplitude 1 G.

RESULTS AND DISCUSSION

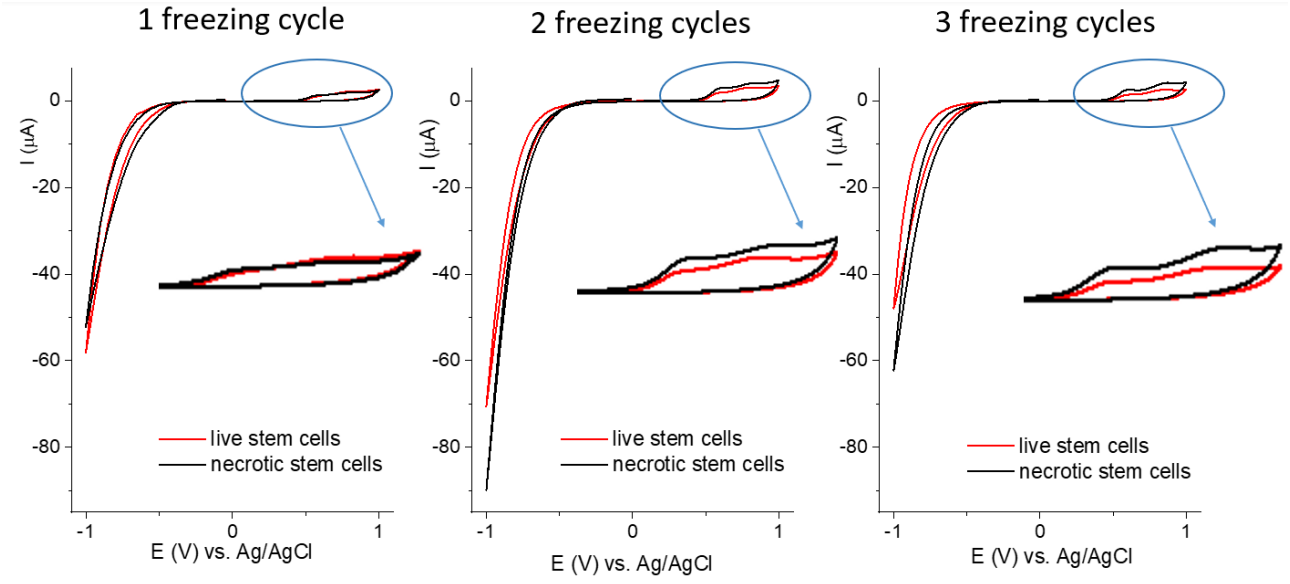


Figure 1. Cyclic voltammograms obtained for different cycles of freezing DPSC.

The first electrochemical method used to determine cell viability was CV. Figure 1 shows that necrotic cells give higher currents than living cells. The reason for this is that when cells are killed, there are various structures in the electrolyte, such as parts of the membrane, different ions, proteins, and a medium consisting of a large number of different analytes. Since the total current

response comes from all these structures, giving a very complex response, CV could be used only in cases where the composition of the sample is well established. Therefore, CV could not be used to confirm cell viability. On the other hand, EIS was more successful.

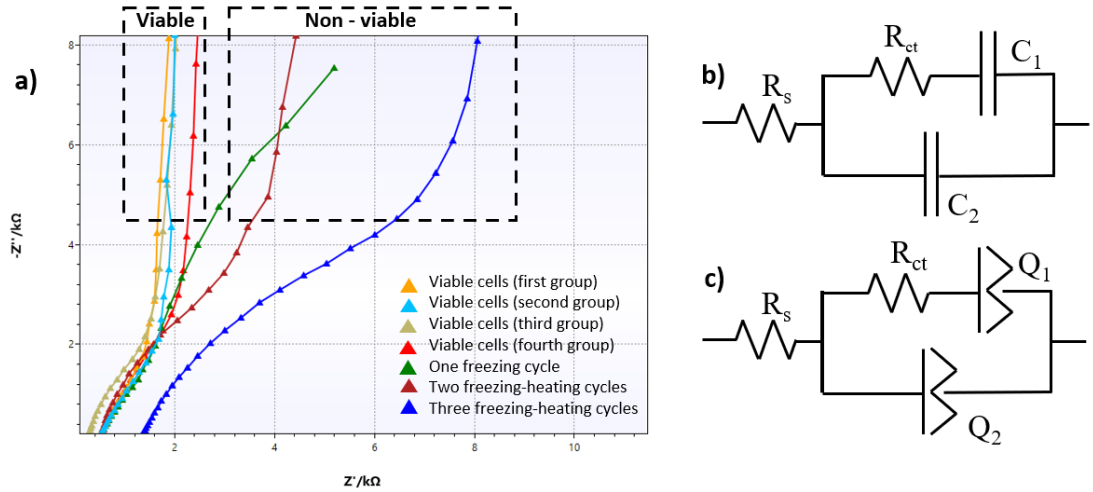


Figure 2. Nyquist plots for viable and non-viable cells in medium (a); Equivalent circuit used for fitting data obtained for live stem cells (b); Equivalent circuit used for fitting data obtained for necrotic stem cells (c).

Nyquist plots for viable cells (Figure 2a) show characteristic capacitive behavior at lower frequencies, which can be attributed to the capacitive behavior of the cell membrane (because the cell has a cell membrane that is itself a capacitor). On the other hand, treated cells showed deviations from this behavior. The degree of deviation is in correlation with the number of freezing-heating cycles, i.e., the number of non-viable cells. A smaller number of viable cells results in a greater deviation from capacitive behavior. The obtained values of characteristic circuit elements with Nyquist plots were used for modeling electric circuits for living and non-living cells (Figure 2 b, c). An electrical circuit for living cells contains electrolyte resistance (Rs), charge transfer resistance (Rct), double-layer capacitance (C_2), and equilibrium capacitance (C_1). Equilibrium capacitance was used instead of the Warburg element for diffusion. This behavior is characteristic of double layer capacitors. In the electric circuit for non-living cells, there are all the same elements as for living ones, only capacitance elements are replaced with constant phase elements to model imperfections in the behavior of the double layer. In this case, inhomogeneous behavior on the electrode surface is caused by the disrupted cell membrane. EPR results (Figure 3) show that cells differently scavenge radicals based on their viability. As the indicator of the amount of the EPR signal reduction, the intensity of the mean peak intensity was measured. Based on the graph, it can be seen that dead cells have a slower EPR signal reduction rate than viable cells, showing that the DPSC in the medium has good redox characteristics. In addition to being used to regenerate wounds, they can also be used to remove radicals that are the result of inflammation.

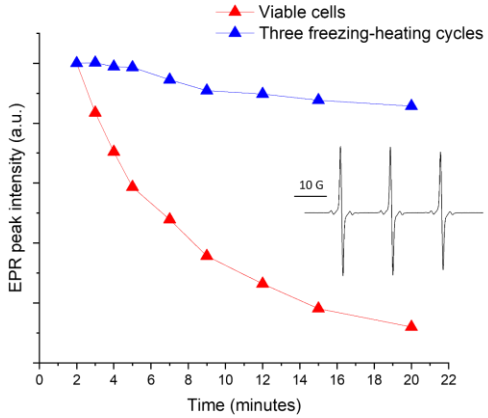


Figure 3. Kinetics of the EPR signal reduction for DPSC. The insert shows the EPR signal shape for the spin-probe TEMPONE.

CONCLUSION

The results of this work indicate that the survival of stem cells in the medium without mixing with any external substances can be determined in a fast and reliable way using electrochemical methods. Of the two electrochemical methods used (CV and EIS), EIS proved to be better. EPR measurements showed that DPSCs possess significant antioxidant properties, due to which they can be further applied in the removal of free radicals and the prevention of various inflammations.

Acknowledgement

This research has been financially supported by the Ministry of Science, Technological Development and Innovation of Republic of Serbia (Contract No. 451-03-65/2024-03/200146, 451-03-66/2024-03/200146 and 451-03-66/2024-03/200026).

REFERENCES

[1] P. Jayaraman, P. Nathan, P. Vasanthan, S. Musa, V. Govindasamy, Cell Biol. Int. 37 (2013) 1122–1128.

[2] A. Yang. L. Shuyan, T. Xiaojie, Z. Shiou, N. Fangfei, Z. Yonghuan, G. Luosha, Z. Chunlei, W. Baicheng, W. Wei, L. Dong, W. Junhao, Cell Proliferation vol. 54 Preprint at https://doi.org/10.1111/cpr.12993 (2021).

[3] V. Todorovic, D. Markovic, N. Milosevic-Jovcic, M. Petakov, B. Balint, M. Colic, A. Milenkovic, I. Colak, V. Jokanovic, N. Nikolic, Stomatoloski Glasnik Srbije, 55 (2008) 170–179.

[4] Vukovic, M. Lazarevic, D. Mitic, M. Jaksic Karisik, B. Ilic, M. Andric, B. Jevtic, J. Roganovic, J. Milasin, Arch. Oral. Biol. 144 (2022) 105564.

PROGESTERONE TREATMENT INCREASES PROGESTERONE RECEPTOR EXPRESSION IN MALE RATS WITH CEREBRAL HYPOPERFUSION

I. Guševac Stojanović [1], J. Martinović [1], Z. Stojanović [2], K. Bobić [1], J. Miletić Vukajlović [3], N. Đorđević [1] and D. Drakulić [1]

[1] *Department of Molecular Biology and Endocrinology, VINČA Institute of Nuclear Sciences-National Institute of the Republic of Serbia, University of Belgrade, Belgrade, Serbia. (igusevac@vin.bg.ac.rs)*
[2] *Institute of Technical Sciences of SASA, University of Belgrade, Knez Mihailova Street 35/4, 11000 Belgrade, Republic of Serbia.*
[3] *Department of Physical Chemistry, VINČA Institute of Nuclear Sciences-National Institute of the Republic of Serbia, University of Belgrade, Belgrade, Serbia.*

DOI: https://doi.org/10.46793/Phys.Chem24I.243GS

ABSTRACT

Chronic cerebral hypoperfusion (CH), a reduced cerebral blood flow, is a significant factor in the development and progression of various neurodegenerative diseases for which adequate treatments are often lacking. To investigate the neuroprotective effects of the steroid hormone progesterone (P4) in a state of CH, we divided male Wistar rats into three groups: control group - rats treated with vehicle (flaxseed oil) and groups consisting of rats subjected to permanent bilateral common carotid artery occlusion (2VO) and treated with either flaxseed oil or P4 for seven days. We isolated the prefrontal cortex (PFC) to investigate the effects of P4 on the protein expression of progesterone receptors A and B (PRA and PRB). Obtained results suggest that CH induced a decrease in protein expression of PRA and PRB and that treatment with P4 restored them to control values. This study sheds light on the potential neuroprotective P4 mechanism in the repeated regiment of administration against CH.

INTRODUCTION

Neurodegenerative diseases result from progressive neuronal death in various regions of the nervous system, which can lead to the occurrence of neurological and psychological disorders and symptoms. The most common cerebrovascular diseases include ischemia, dementia, vascular dementia, Alzheimer's disease, Parkinson's disease, Huntington's disease, and others [1]. They typically occur in the elderly population and are associated with decreased blood flow through the brain, cerebral hypoperfusion (CH), which results in insufficient oxygen and nutrient supply to brain tissue.

Although numerous studies have focused on developing therapeutic strategies, there is no adequate treatment for these impairments.

Literature data indicate that sex hormones are necessary for the survival of neurons and exert their effects across various regions of the central nervous system (CNS) during normal development and ageing. Disruptions in hormone levels have been observed in specific CNS regions among individuals with neurodegenerative diseases.

Progesterone (P4), a female sex hormone and potent natural progestogen, in the brain originates from brain cells, spinal cord cells, and peripheral nervous system cells that synthesize it directly from cholesterol. It is also derived from peripheral tissues and released into the blood, reaching the brain. Due to its lipophilic nature, P4 easily permeates cell membranes, exerting its effects

irrespective of gender via specific receptors found in brain regions such as the prefrontal cortex (PFC).

Progesterone interacts with three types of receptors (progesterone receptor, PR) and exerts genomic and non-genomic actions. The non-genomic mechanism involves the activation of receptors on the cell membrane, cytosolic PR, and/or intracellular cascades via secondary messengers.

Genomic action occurs via two nuclear PRs (PRA and PRB), which rapidly translocate from the cytosol to the nucleus. Unbound receptors form complexes with chaperone molecules, such as heat shock proteins (HSP). Upon P4 binding, they dissociate from chaperones, dimerize, and translocate to the nucleus to bind to specific DNA binding sites in gene promoter regions, initiating transcription [2].

Progesterone exhibits protective effects in many animal experimental models mimicking brain dysfunction observed in older individuals and those with age-related neurodegenerative diseases. In stroke studies, this hormone has been shown to be an effective neuroprotectant, significantly reducing brain infarction. Post-ischemic administration of P4 has also been linked to protective effects and improvements in somatosensory and neurological tests.

The present study aimed to assess the possible therapeutic efficacy of P4 in the rat CH model (induced by the permanent bilateral common carotid artery occlusion model (two-vessel occlusion, 2VO)) by determination of PRA and PRB protein expressions in the cytosolic and nuclear fractions from prefrontal cortex (PFC) of adult male Wistar rats.

METHODS

All research procedures were approved by the Ethical Committee for the Use of Laboratory Animals of VINČA Institute of Nuclear Sciences - National Institute of the Republic of Serbia, Belgrade (authorization numbers 02/11 and 323-07-04253/2016-05) and conducted on adult male Wistar rats.

The animals were divided into three groups (n=4 animals per group): rats that were subjected to sham operation and treated with vehicle (commercial flaxseed oil, 1 mg/kg/day, Sham + V, control animals); rats subjected to permanent common carotid artery occlusion and either vehicle treatment (commercial flaxseed oil, 1 ml/kg/day, 2VO + V) or P4 dissolved in commercial flaxseed oil (1.7 mg/kg/day, 2VO + P4). For that purpose, the rats were anesthetized with chloral hydrate and underwent a ventral midline incision in the neck area. Both common carotid arteries were carefully exposed and separated from the carotid sheaths, cervical sympathetic, and vagus nerve. In the 2VO groups, both common carotid arteries were permanently double-ligated using 5-0 silk sutures, whereas control rats underwent the same surgical procedure without actual artery occlusion. Treatments were administered subcutaneously and lasted for 7 days across all experimental groups. After the treatment period, the animals were euthanized by decapitation using a guillotine. The PFC was then isolated on ice, rapidly frozen in liquid nitrogen, and stored at -70°C until further analysis [3].

To obtain the necessary cellular fractions, a series of differential centrifugations were performed according to the previously described protocol [4].

Western blot analysis was performed to assess protein expressions of the molecules of interest with the PR primary antibody (Santa Cruz Biotechnology Inc., CA, USA sc-810 1:1000) and appropriate secondary antibody (Anti-mouse IgG-HRP Santa Cruz Biotechnology Inc., CA, USA sc-2318 1:5000) Protocol for this method is described in the study by Stanojlovic et al., 2020 [4]. The relative protein abundance of investigated proteins in Sham + V group was normalized to β-actin and arbitrarily defined as 100%, whereas levels in 2VO + V and 2VO + P4 groups were also normalized to β-actin and calculated with respect to this value.

Statistical analysis was performed by one-way analysis of variance (one-way ANOVA) followed by Tukey's posthoc test using GraphPad Prism 8.02 Software. The significance level was set at $p < 0.05$, with values expressed as a percentage of the mean of the values in Sham + V group ± SEM (standard error of the mean).

RESULTS AND DISCUSSION

As shown in **Figure 1**, in 2VO animals treated with flaxseed oil, a decrease in the expression of both PR isoforms (PRA and PRB) was observed in both subcellular fractions ($^{***}p < 0.001$) compared to Sham + V group. In 2VO + P4 group, the expression of both PR isoforms in cytosolic and nuclear fractions was increased compared to the 2VO + V group ($^{\#\#\#}p < 0.01$) and returned to the levels observed in sham-operated animals treated with flaxseed oil.

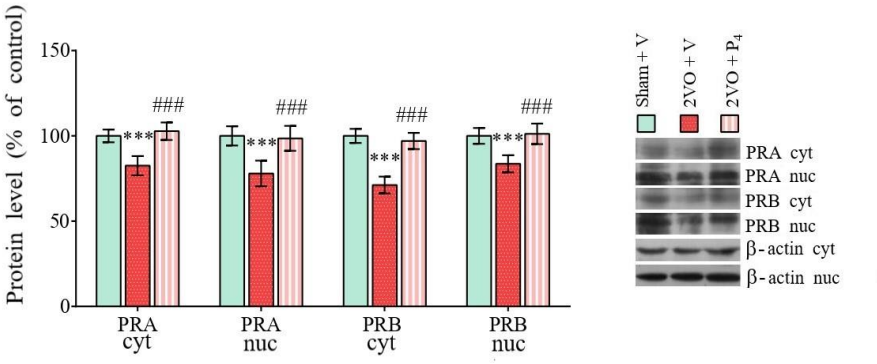


Figure 1. Progesterone modulates progesterone receptor (PRA and PRB) protein levels in cytosolic (cyt) and nuclear (nuc) fractions obtained from the prefrontal cortex of rats subjected to permanent common carotid occlusion (2VO). Data are presented as mean ± SEM, whereas the values of the sham-operated group treated with vehicle (Sham + V) were set as 100%. Statistical analysis was performed using one-way ANOVA followed by Tukey's post hoc test ($^{***}p < 0.001$ Sham + V vs. 2VO + V, and $^{\#\#\#}p < ++0.001$ 2VO + V vs. 2VO + P4).

Other studies have shown that following various brain injuries, the level of P4 increases in human serum [5], in both serum and brain tissue of mice [6], as well as in the brain of rats [7]. Shortly after the injury, endogenous P4 protects the brain through steroidogenesis and activation of PR, which act as transcription factors regulating the expression of target genes [8]. This was demonstrated in a study by Liu and colleagues (2012), who also observed that this increase provides protection for up to 48 hours [6]. For long-term neuroprotection, both exogenous P4 treatment and the presence of adequate levels of PR are necessary [6]. The results of this study are consistent with those of the mentioned studies and demonstrate that exogenously administered P4 restores the disrupted expression of PRA and PRB in both subcellular fractions to control levels.

Given that numerous gene promoters contain regulatory sequences for PRA and PRB, it is likely that various signaling pathways are further activated following CH and the administration of this potent hormone.

CONCLUSION

Understanding the intricate changes linked to the onset and advancement of CH, alongside exploring the potential protective effects of substances/compounds in animal models, is paramount. This research enhances comprehension of the mechanisms driving CH development and

progression, as well as the mechanisms by which seven-day P4 treatment operates in male rat post-CH.

Acknowledgment
This research was funded by the Ministry of Science, Technological Development and Innovation of the Republic of Serbia, grant 451-03-66/2024-03/200017.

REFERENCES

[1] C. G. Chung, H. Lee, S. B. Lee, Cell. Mol. Life Sci., 75 (2018) 3159–3180.
[2] R. D. Brinton, R. F. Thompson, M. R. Foy, M. Baudry, J. Wang, C. E. Finch, T. E. Morgan, C. J. Pike, W. J. Mack, F. Z. Stanczyk, J. Nilsen, Front. Neuroendocrinol., 29 (2008) 313–339.
[3] M. Stanojlović, I. Guševac, I. Grković, J. Zlatković, N. Mitrović, M. Zarić, A. Horvat, D. Drakulić, Neuroscience., 311 (2015) 308–321.
[4] M. Stanojlović, I. Guševac Stojanović, M. Zarić, J. Martinović, N. Mitrović, I. Grković, D. Drakulić, Cell Mol Neurobiol., 40 (2020) 829–843.
[5] G. P. Wagner, Y. Tong, D. Emera, R. Romero, J. Perinat. Med., 40 (2012) 345–51.
[6] H. Liu, J. Zhang, Y. Yang, L. Zhang, X. Zeng, Curr. Neurovasc. Res., 9 (2012) 152–158.
[7] D. Meffre, F. Labombarda, B. Delespierre, A. Chastre, A. F. De Nicola, D. G. Stein, M. Schumacher, R. Guennoun, Neuroscience, 231 (2013) 111–124.
[8] S. Mani, Endocrinology, 149 (2008) 2750–2756.

G *– Organic Physical Chemistry*

SYNTHESIS OF VANILLIN-THIOSEMICARBAZONE IN ETHANOLIC SOLUTION OF CITRIC ACID UNDER MILDER CONDITIONS

S. S. Konstantinović, J. Savić and D. Z. Troter

University of Niš, Faculty of Technology, Bulevar oslobodjenja 124, 16000 Leskovac, Serbia. (sandra@tf.ni.ac.rs)

DOI: https://doi.org/10.46793/Phys.Chem24I.249K

ABSTRACT

Synthesis of vanillin-thiosemicarbazone was performed by "greener" one-pot batch technological procedure in ethanolic solution of citric acid under extremely mild operating conditions (20 °C and 10 min). The obtained compound was identified by elemental microanalysis, as well as FTIR and UV/Vis spectroscopic methods. Since ethanolic solution of citric acid behaved both as catalyst and solvent, the reaction was performed without any additional acidic catalyst. Compared to the conventional H_2SO_4-catalyzed synthesis in ethanol, the reaction time was shorter and the yield of obtained compound was higher.

INTRODUCTION

The synthesis of azomethines via conventional method is traditionally carried out in the presence of catalysts and organic solvents. Although effective, this method is a time-consuming process that requires heating, as well as using volatile, toxic and corrosive chemicals (mineral acids and methanol). The consequences of this process are both environmental and techno-economical problems; due to the danger reflected towards operators and the environment, it is crucial to undertake special precautions and remove toxic and dangerous chemicals after their use, making the technological process of azomethines' production more expensive [1].

The use of various fruit juices and extracts in organic synthesis is expanding due to their appropriate acidity, safety, biodegradability, availability, low price and the favorable action of the enzymes present in them. The moderate acidity of natural juices and extracts enables the catalysis of the synthesis of organic compounds already at room temperature, where they play a double role: as solvents and biocatalysts.

For instance, an efficient and economical method for the synthesis of azomethine with antimicrobial and antioxidant activity using tamarind extract and lemon juice was performed by condensation of benzaldehyde and aniline or urea, benzylidene-aniline and benzylidene-urea, obtaining the products in higher yields [1].

When equimolar amounts of benzaldehyde and aniline were stirred in lemon juice, grape juice or water extract of unripe mango at 25 °C, the reactions were successfully completed after only 2 min-4 min. Since these juices and extracts contain organic acids (malic, tartaric, citric and oxalic), an optimal pH value was reached for the successful protonation of heteroatoms and obtaining azomethine [2]. Desai and Shinde (2015) combined ethanolic solution of nicotinic acid hydrazide and selected aldehydes at room temperature in lemon juice [3]. Jadhao and Patil (2016) first synthesized a precursor from acetophenone and semicarbazide hydrochloride, which was later added to alcoholic solutions of selected aldehydes acidified with lemon juice at 25 °C for 90 min [4].

The goal of this research was the production of azomethine derivatives of vanillin via unconventional, „greener" and ecologically acceptable „one-pot" technological process. The synthesis was carried out under extremely mild operating conditions in a batch reactor with a

magnetic stirrer, excluding the need for reflux condenser and substances that are corrosive, toxic and unsafe for both operators and the environment.

METHODS

The following chemicals were used: vanillin (p.a., Centrohem, Serbia), thiosemicarbazide (≥98%, Acros Organics), citric acid·H_2O (≥99,5%, Zorka Šabac, Serbia), absolute ethanol (Zorka Šabac, Serbia), DMSO (≥99,9%, VWR International, France), DMF (p.a., Fischer Scientific, UK) and KBr (≥99,9%, Sigma-Aldrich).

The reaction was performed in a 100 cm^3 glass reactor equipped with a magnetic stirrer, for 10 min, at 20 °C. Vanillin-thiosemicarbazone was synthesized by mixing equimolar amount of vanillin and thiosemicarbazide in ethanolic solution of citric acid (**Figure 1**). The yellow product was filtered, washed with ethanol and dried *in vacuo* over $CaCl_2$.

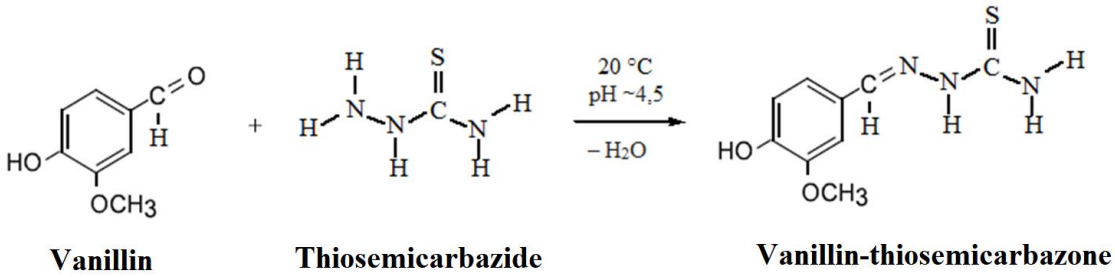


Figure 1. Synthesis of vanillin-thiosemicarbazone

Microanalysis for carbon, hydrogen and nitrogen was carried out with a Carlo Erba 1106 microanalyser. The Fourier transformed infrared (FTIR) spectra were recorded using a Michaelson Bomen MB-series spectrophotometer, using the KBr pellet (1 mg/100 mg) technique. The electronic spectra (UV/VIS) were recorded on a Perkin-Elmer Lambda 15 UV/VIS spectrophotometer using 10^{-3} mol/dm^3 solutions of DMSO.

Color: yellow; m.p: 205±0.2 °C; UV (DMSO): λ(nm)/$\varepsilon\times10^3$(dm^3/mol·cm): 298/2.3207, 353/2.6005; FTIR (1/cm): 3521, 3469, 3345, 3300, 3199,3072, 2986, 1692, 1650, 1606, 1587, 1518, 1462, 1437, 1381, 1272, 1204, 814; Combustion analysis for $C_9H_{11}N_3S$ (%) Calcd.: C 47.99, H 4.92, N 18.65, S 14.23; (%) Found: C 47.89, H 4.98, N 18.10, N 14.25. Solubility: Methanol, Ethanol, DMF, DMSO.

RESULTS AND DISCUSSION

The electronic spectrum of vanillin-thiosemicarbazone in DMF exhibits two absorption bands, assigned to $\pi\rightarrow\pi^*$ (λ_{max} = 298 nm) and $n\rightarrow\pi^*$ (λ_{max} = 353 nm) transitions. An ν(C=O) stretching vibration from carbonyl group in thiosemicarbazone part of molecule can be observed at 1692 cm^{-1} in FTIR spectrum of vanillin-thiosemicarbazone (**Figure 2**). The band at 1587 cm^{-1} belongs to ν(C=N) stretching vibration, which confirms successful carbonyl-amine condensation reaction between vanillin and thiosemicarbazide. The characteristic double peak for aldehyde at 2850 and 2750 cm^{-1} could not be observed, which suggests reaction between CHO group from vanillin and NH_2 group from thiosemicarbazide occurred [5,6].

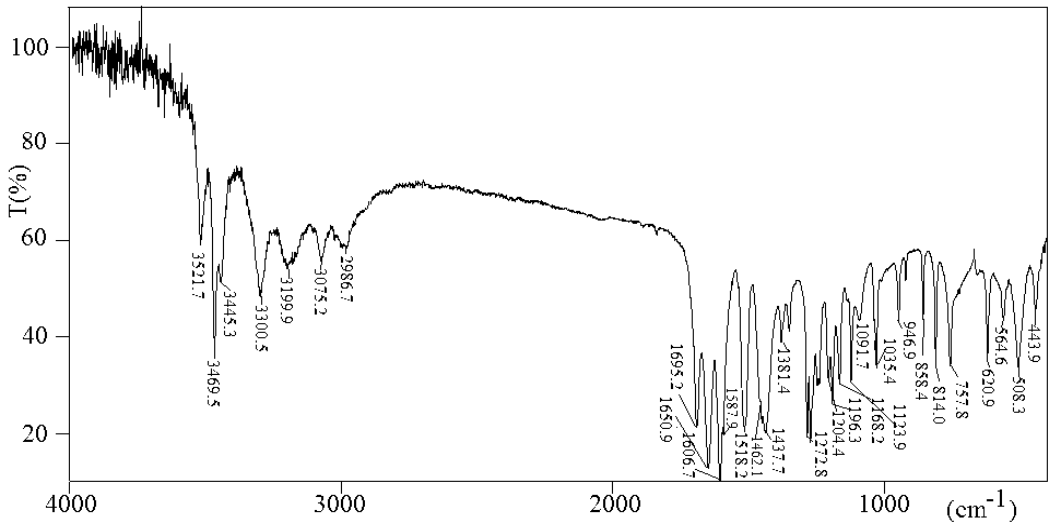


Figure 2. FTIR spectrum of vanillin-thiosemicarbazone.

The conventional synthesis of vanillin-thiosemicarbazone in ethanol requires the presence of H_2SO_4, necessary to catalyze the nucleophilic attack of the amine component on the carbonyl group at pH range of 4–4.5 and ensure faster water elimination. However, citric acid can serve as more convenient H_2SO_4 replacement; the ethanolic solution of citric acid behaves both as a medium and a catalyst [7,8].

In ethanolic solution of citric acid (**Table 1**), the reaction occurred at lower temperature (20 °C), and compared to the conventional synthesis, the reaction times was shorter (Δ=35 min), and the yield of obtained compound was higher (Δ=20.54 min) [7,8].

Table 1. Comparison of vanillin-thiosemicarbazone synthesis in ethanol and ethanolic solution of citric acid.

Solvent	Yield (%)	Reaction time (min)	Catalyst	Temp. (°C)
Ethanolic solution of citric acid	77.54	10	No	20
Ethanol	57	45	H_2SO_4	50

The advantages of the production of vanillin-thiosemicarbazone in the suggested "greener" hydrophilic system (ethanolic solution of citric acid) compared to the conventional method are: easy preparation of solvents using cheap, natural, safe, available, and biodegradable components; safer process for operators; adequate acidity and the dual role of the ethanol solution of citric acid in the process (catalyst and reaction medium); shorter time and significantly lower temperature for performing the process; simpler apparatus (batch reactor with magnetic stirrer without condenser); avoided necessity for acid catalysts (harmful, corrosive, and toxic mineral acids); easy separation of products; and the possibility of recycling and reuse of solvents. The above-mentioned reasons justify the use of ethanol acidified with citric acid in the production of vanillin derivatives in an ecological and techno-economic sense, with a special reference to the ensured process safety for technological equipment and process contractors.

CONCLUSION

The synthesis of vanillin-thiosemicarbazone was carried out by a carbonyl-amine condensation reaction between vanillin and thiosemicarbazide in an ethanolic solution of citric acid.

The proposed unconventional batch technological procedure for obtaining the azomethine derivative of vanillin is "greener" and environmentally friendly; it takes place under extremely mild operating conditions (20 °C and 10 min) in a batch reactor with a magnetic stirrer without the use of a catalyst, as well as corrosive substances that are toxic and unsafe.

Acknowledgment

This work was supported by the Republic of Serbia - Ministry of Science, Technological Development and Innovation (Programs for financing scientific research: 451-03-65/2024-03/200133 and 451-03-66/2024-03/200133 assigned to the University of Niš, Faculty of Technology, Leskovac).

REFERENCES

[1] A. Wahab, S. S. Haider, I. Mahmood, T. Mahmood, S. K. Sherwani, S. Kanwal, FUUAST J. Biol. 4 (2014) 27.
[2] G. Yadav, J.V. Mani, Int. J. Sci. Res. 4 (2015) 121.
[3] V. Desai, R. Shinde, Int. J. Pharm. 5 (2015) 930.
[4] P. S. Jadhao, A. B. Patil, Int. J. Pharm. Sci. Res 7 (2016) 4125.
[5] S. S. Konstantinović, B.V. Konstantinović, J. M. Jovanović, CI&CEQ 15 (2009) 279.
[6] S. S. Konstantinović, A. Kapor, B. C. Radovanović, A. Deak, CI&CEQ 14 (2008) 27.
[7] M. B. Jovanović, S. S. Konstantinović, S. B. Ilić, V. B., Veljković, Adv. Technol. 2 (2013) 38.
[8] J. Savić, Synthesis and characterization of azomethine derivatives of vanillin, Master thesis, Univesity of Niš, Faculty of Technology, Leskovac, 2023.

CHEMICAL THERMODYNAMICS OF THEOPHYLLINE

A.V. Knyazev [1], V.N. Emel'yanenko [2], D.H. Zautsau [3], V.V. Turovtsev [4], N.N. Smirnova [1] and S.S. Knyazeva [1]

[1] *Lobachevsky University, Gagarin Prospekt 23/2,603022, Nizhni Novgorod, Russian Federation (knyazevav@gmail.com)*
[2] *Department of Physical Chemistry, University of Rostock, 18059 Rostock, Germany*
[3] *Institute of Technical Thermodynamics University of Rostock and FVTR Research Center of combustion Engines and Thermodynamics, 18059 Rostock, Germany*
[4] *Department of Physics, Mathematics and Medical Informatics, Tver State Medical University, Sovetskaya 4, 170100, Tver, Russian Federation*

DOI: https://doi.org/10.46793/Phys.Chem24I.253K

ABSTRACT
The standard molar enthalpy of formation of theophylline was measured by using high-precision combustion calorimetry. The temperature dependence of heat capacity for theophylline has been measured for the first time over the temperature range from 5.6 to 356 K using precision adiabatic vacuum calorimetry. Using the transpiration method, the temperature dependence of the vapor pressure of substance was measured. Based on the obtained data, the values of enthalpy of sublimation and enthalpy of formation of this compound at 298.15 K was found. Using the G4 method, the enthalpy of formation of theophylline in the gas phase was calculated.

INTRODUCTION
Theophylline (1,3-dimethyl-7H-purine-2,6-dione, CAS 58-55-9) is purine derivative playing an important role in the chemistry of natural compounds [1]. Along with caffeine, this substance is the alkaloid present in cocoa beans and many other products. It's widely used in medical and pharmacological fields [2]. Theophylline is known as a remedy to treat asthma and other chronic lung disease (emphysema and chronic bronchitis) [3]. The therapeutic index of theophylline is narrow implying that administering outside of a small dosage interval would lead to side effects. Theophylline, a methylxanthine, has been described to enhance insulin secretion by adding to the glucose stimulation buffer [4]. Theophylline binds with RNA aptamers leading to a stable structure while the binding site is unstable and disordered in the absence of theophylline. Theophylline being purine derivative by their structure can be used to predict and assess the reliability of various properties of other purine derivatives, such as adenine, xanthine, guanine, diaminopurine etc. In this work being a continuation of consecutive research devoted to the study of the thermodynamic properties of biologically active and important compounds, we carried out experimental measurements of the thermodynamic characteristics of theophylline and assessed the reliability of the obtained results.

METHODS
Commercial sample of compound was additionally purified by fractional vacuum sublimation. A confirmation of the absence of changes in acid structure along with the final degree of their purity has been carried out using a GC equipped with an HP-1 capillary column and equals to 99.9 mol %. A mass fraction of water in the purified sample was determined using coulometric titration with Schott Instruments Model TitriLine KF Trace Karl Fisher Titrator with Hydronal Coulomat AG reagent.

An isoperibolic calorimeter with a static bomb and a stirred water bath has been used to measure standard molar enthalpies of combustion of compounds. The energy equivalent of the calorimeter was determined by burning samples of benzoic acid. The energy equivalent of the calorimeter was 14886.0 ± 1.1 $J \cdot K^{-1}$. The energy of ignition was accounted under calibration conditions. The solid samples were pressed in pellets and burned in presence of oxygen with addition of 1.00 g of water to the bomb with addition of polyethylene as auxiliary compound. Correction for nitric acid formation was based on titration with 0.1 $mol \cdot dm^{-3}$ NaOH (aq). To increase the completeness of combustion, polyethylene was added as an auxiliary substance. Atomic weights were taken from the IUPAC Technical Report as the average values of the stated intervals. Overall, six calorimetric experiments were conducted.

To measure the heat capacity of the tested substance in the range from 5.6 to 356 K a BKT-3.0 automatic precision adiabatic vacuum calorimeter with discrete heating was used. The calorimeter was tested by measuring the heat capacity of high-purity copper and reference samples of synthetic corundum and K-2 benzoic acid. The analysis of the results showed that standard uncertainty of the heat capacity of the substance at liquid helium temperatures was within ±2%, then it decreased to ±0.5% as the temperature was rising to 40 K, and was equal to ±0.2% at T > 40 K.

Temperature dependence of absolute vapour pressures of compounds were measured using the method of transpiration. A controlled flow of N_2 was passed through a U-shaped saturator. The saturator filled with a certain amount of a sample mixed with small glass beads. The substance was transported with the carrier gas flow and collected in a trap cooled to room temperature. The amount of the condensed samples of theophylline was determined by weighing with microbalances of 0.0001 g resolution. Vapor pressures (p_{sat}) at each temperature (T_i) were calculated using the amount of the product, assuming the validity of Dalton`s Law applied to the N_2 stream saturated with the substance *i*. The vapor pressure p_i at each temperature T_i was calculated from the amount of the product collected within a definite time:

$$p_{sat} = m_i \cdot R \cdot T_a / V \cdot M_i \qquad V = (n_{N2} + n_i) \cdot R \cdot T_a / P_a \tag{1}$$

where R is the molar gas constant (R = 8.31446 $J \cdot K^{-1} \cdot mol^{-1}$), V is the volume of the gas phase consisting of the n_{N2} moles of the carrier gas and n_i mole of gaseous compound under study at the atmospheric pressure P_a and the ambient temperature T_a. The N_2 gas flowrate was measured with the HP soap film flow meter (model 0101-0113). The amount of the carrier gas n_{N2} was determined from the flow rate and the time measurement. The amount of the compound under study n_i in the carrier gas was estimated applying the ideal gas law at each temperature.

Quantum chemical calculations were performed with the Gaussian 09 series software. Energy of the molecule involved in this study was calculated using the G4 method. The Gaussian-4 (G4) composite model combines high-level correlation/moderate basis set calculations with lower level correlation/larger basis set calculations to approximate the results of a more expensive calculation. The G4 model contains new features, including extrapolation to the HF limit, use of CCSD(T). Mean absolute deviation of enthalpies of formation for G3/05 dataset calculated by the procedure "from atomization reaction" was reported to be 3.4 $kJ \cdot mol^{-1}$. The enthalpies of formation in gaseous state of most stable conformers of compounds were computed with the “from atomization reaction” procedure.

RESULTS AND DISCUSSION

The standard specific energy of combustion of crystalline theophylline have been used to derive the standard molar enthalpy of combustion and the standard molar enthalpy of formation in the crystalline state (table 1). Values of energy of combustion and enthalpy of formation are referenced to reaction:

$$C_7H_8O_2N_4\ (cr) + 8\ O_2\ (g) = 7\ CO_2\ (g) + 4\ H_2O\ (l) + 2N_2\ (g) \tag{2}$$

Table 1. Results of thermodynamic studies of theophylline, $C_7H_8O_2N_4$, T = 298.15 K, p = 0.1 MPa.

$-\Delta_c H°_m$ (cr) (kJ·mol^{-1}) [a]	3540.7 ± 2.1
$-\Delta_f H°_m$(cr) (kJ·mol^{-1}) [b]	359.7 ± 2.2 350.55±1.29 [5]
$S°$(cr) (J·K^{-1}·mol^{-1})	226.4 ± 0.5
$-\Delta_f S°_m$(cr) (J·K^{-1}·mol^{-1})	924 ± 7
$-\Delta_f G°_m$ (cr) (kJ·mol^{-1})	84 ± 3
$\Delta_{cr}{}^g H°_m$ (kJ·mol^{-1})	124.9 ± 1.0 131.7±4.7 [5]
$-\Delta_f H°_m$ (g) $_{exp}$ (kJ·mol^{-1}) [c]	234.8 ± 2.4 218.9±4.9 [5]
$-\Delta_f H°_m$ (g) $_{calc}$ (kJ·mol^{-1}) [c]	235.4 ± 3.4

Temperature dependent absolute vapor pressures p_{sat} were fitted with the following Eq. (3):

$$R \cdot \ln {}^{p_{sat}}\!/_{p^o} = a + \frac{b}{T} + \Delta_{cr}^{g} C_{p,m}^{\circ} \cdot \ln \frac{T}{T_0} \quad (3)$$

where a and b are adjustable parameters and $\Delta_{cr}^{g} C_{p,m}^{\circ}$ (-32.0 ± 23 J·K^{-1}·mol^{-1}) is the difference of the molar heat capacities of the gaseous and the crystal phases respectively. T_0 appearing in Eq. (3) is an arbitrarily chosen reference temperature (which has been chosen to be T = 298.15 K). p^o is the reference pressure (chosen to 1 Pa). The complete set of enthalpy characteristics of theophylline measured in this work is provided in Table 1. The calculated at G4 level of theory total energy at 0 K (E_0), total enthalpy at 298.15 K (H_{298}) of theophylline is given in the Table 2. The value of the enthalpy of formation in the gas phase theophylline obtained in this work is in good agreement with the calculated value (table 1).

Table 2. The calculated at G4 level of theory total energy at 0 K (E_0), total enthalpy at 298.15 K (H_{298}) of theophylline.

Compound	E_0	H_{298}
	Hartree	
theophylline	-640.772402	-640.760050

The heat capacity measurements were carried out between 5.6 and 356 K. The heat capacity of the sample varied from 30% to 50% of the total heat capacity of calorimetric ampoule + substance over the range between 5.6 and 356 K. The experimental points of heat capacity were fitted by means of the least-squares method and polynomial equations.

Partitioning into 4 intervals of the temperature dependence of the heat capacity contributes to the best smoothing of the experimental curve. The experimental values of the molar heat capacity of theophylline over the range from 5.6 to 356 K is presented in Figure 1. The heat capacity of this substance gradually increases with rising temperature and does not show any peculiarities.

To calculate the standard thermodynamic functions of theophylline, heat capacity values of it were extrapolated from the starting temperature of the measurement (approximately 6 K) to 0K by Debye's function of heat capacity ($\theta_D(C_7H_8O_2N_4)$ = 62.3 K are specially selected parameters).

From the absolute value of the entropy of the theophylline, carbon in the form of graphite, gaseous hydrogen, nitrogen and oxygen the standard entropy of formation of theophylline at T=298.15 K was calculated. The Gibbs function of formation of the theophylline was evaluated

from the enthalpy of formation and entropy of formation values (Table 1). The values conform to the following process:

$$7\cdot C\,(gr) + 4\cdot H_2\,(g) + 2\cdot N_2\,(g) + O_2\,(g) \rightarrow C_7H_8O_2N_4\,(cr) \quad (4)$$

The standard molar thermodynamic functions in the crystalline state collected in Table 1 can be used for optimization of methods of synthesis, as well as for validation of theoretical and empirical methods for prediction of thermodynamic properties.

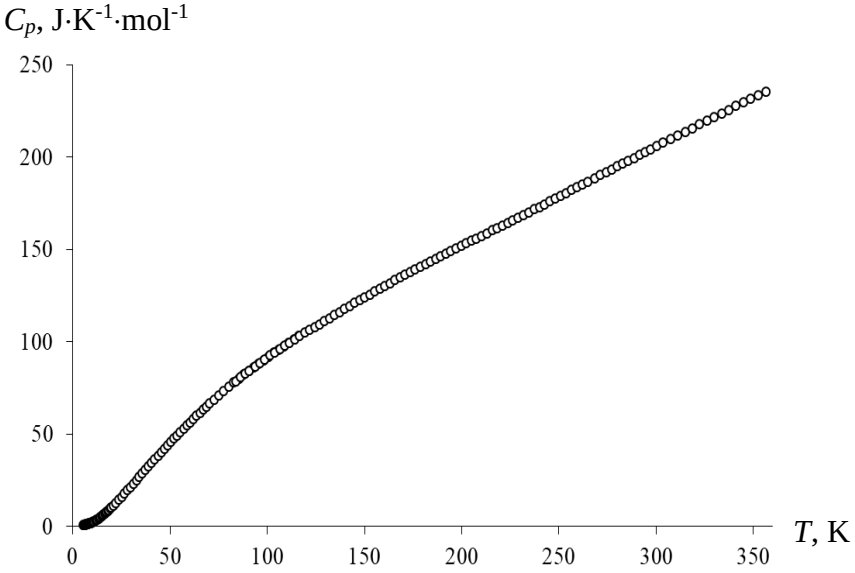


Figure 1. Temperature dependence of heat capacity of theophylline.

CONCLUSION

In this work, the measurements of the thermodynamic characteristics of the theophylline have been performed. For the first time, the temperature dependence of heat capacity was studied and the enthalpy of sublimation was determined.

Acknowledgment

The authors express special gratitude to Prof. S.P. Verevkin for providing the possibility of experimental studies in his laboratory and for help in discussion of the results obtained. The computations in part were performed on computational facilities of the Thermodynamics Research Center at the National Institute of Standards and Technology.

The work was supported financially by the Ministry of Science and Higher Education of the Russian Federation (the basic part of the state task, project no. FSWR-2023-0025).

REFERENCES

[1] W. M. Malisoff (1943). Dictionary of Bio-Chemistry and Related Subjects. Philosophical Library. pp. 311, 530, 573.
[2] J. Timson. Theobromine and theophylline. Mutat Res., 32(2) (1975) 169-178.
[3] Drug bank. Theophylline. http://www.drugbank.ca/drugs/DB00277.
[4] A.J. Weinhaus, P. Poronnik, D.I. Cook, B.E. Tuch, Insulin secretagogues, but not glucose, stimulate an increase in [Ca_2^+]i in the fetal rat β-cell. Diabetes, 44 (1995) 118–124.
[5] J. Baudelio Campos, E. Orozco-Guareno. Standard enthalpies of formation of theophylline, theophylline-7-acetic acid, 7-(β-hydroxyethyl) theophylline and 7-(2,3-dihydroxypropyl) theophylline. Thermochim. Acta. 709 (2022) 179158.

AN EXTENDED STUDY OF THE APPLICATION OF THE BARRIERS TO ROTATION AROUND THE C=C BOND OF 2-ALKYLIDENE-4-OXOTHIAZOLIDINES TO QUANTIFY THEIR PUSH–PULL EFFECT UNDER SOLVENT CONDITIONS

A. Rašović [1] and V. A. Blagojević [2]

[1]*Center for Chemistry ICTM, University of Belgrade, Studentski trg 16, P. O. Box 473, 11000 Belgrade, Serbia (arasovic@chem.bg.ac.rs)*
[2]*TBP Software, Solunska 11, 11000 Belgrade, Serbia*

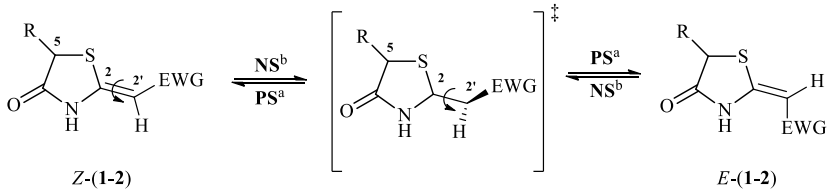
DOI: https://doi.org/10.46793/Phys.Chem24I.257R

ABSTRACT

As we reported previously, the barriers to rotation ($\Delta G^{\ddagger}$) around the C(2)C(2') double of the selected thiazolidine derivatives **1-2** showed to be an efficient parameter to quantify their *push–pull* effect both under the same and different solvent conditions (at least three solvents studied: chloroform, dimethyl sulfoxide, and water). This work reports an extended study regarding solvent conditions. Additionally, this research has involved model compound **3**, which does not possess a *push–pull* effect. The archived excellent linear correlations between the barriers to rotation ($\Delta G^{\ddagger}$) around the C(2)C(2') double bond of ground state (GS) structures of **1-2** and their bond lengths confirmed our previous findings.

INTRODUCTION

The *push–pull* alkenes are a group of different classes of organic compounds. Their main feature is a *push–pull* effect, i.e., electron transfer from electron-donating to electron-withdrawing (EWG) groups. As a result, as illustrated in Scheme 1 on the example of 2-alkylidene-4-oxothiazolidines, the π-bond order of the central double bond is reduced (decreasing the rotational barrier/$\Delta G^{\ddagger}$). Thus, due to the reduced restriction for rotation around the partial C=C double bond, the configurational isomerization occurred, whose direction is dictated by the solvent polarity [1,2].



Z-(**1-2**) *E*-(**1-2**)

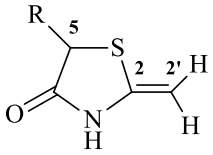
[a] The polar solvents (PS) shifts equilibrium to the *Z* isomer due to the breaking the intramolecular hydrogen bond (IHB) in the *E*-counterpart.
[b] In the nonpolar solvents (NS) the IHB is favored.

(*Z*)-**1a**: EWG = COPh; R = CH_2COOEt
(*Z*)-**1b**: EWG = CONHPh; R = CH_2COOEt
(*Z*)-**1c**: EWG = $CONH(CH_2)Ph$; R = H
(*Z*)-**1d**: EWG = COOEt; R = CH_2COOEt
(2*E*, 5*Z*)-**1e**: EWG = COOEt; R = -CHCOOEt
(*Z*)-**2a**: EWG = CSPh; R = CH_3
(*E*)-**2b**: EWG = $CSNH_2$; R = CH_2COOEt
(*Z*)-**2c**: EWG = $CSNH(CH_2)Ph$; R = H

Scheme 1. The configurational isomerization of 2-alkylidene-4-oxothiazolidines **1-2**.

Concerning our research interest, the *push–pull* effect is of significant importance because it determines the properties, dynamic behaviour, and chemical reactivity of 2-alkylidene-4-oxothiazolidines. To the latter, a broader series of thiazolidines **1**, which were synthesized in our laboratory, has attracted our attention owing to their use as substrates for several selective

transformations leading to various heterocyclic systems, such as 3,3aλ^4,4-trithia-1-azapentalenes, 1,3-thiazines, and other thiazolidine derivatives [3,4]. Since the π-bond order of the double bond in **1-2** is reduced, we previously efficiently employed the calculated $\Delta G^{\neq}$ to quantify their *push–pull* effect in a vacuum at 298 K as well as the calculated and experimental ones for the quantification of the *push–pull* effect of selected thiazolidines (*Z*)-**1a**, (2*E*, 5*Z*)-**1e**, and (*E*)-**2b** under solvent conditions (at least two studied solvents: chloroform and DMSO) [3]. More recently, we reported the high efficiency of calculated barriers to rotations to quantify the *push–pull* effect of selected thiazolidines **1-2** under the same and different solvent conditions (at least three studied solvents: chloroform, weakly polar solvent; DMSO, strongly polar solvent; water, extremely polar solvent) [5,6]. This work explores the efficiency of calculated barriers to rotations to quantify the *push–pull* effect of selected thiazolidines **1-2** under extended solvent conditions (two more solvents studied: toluene and methanol; the chloroform served as the standard solvent). The obtained results are in great consent with previously published ones. In addition, this research is expanded for model compound **3**, which does not manifest the *push–pull* effect because it does not possess an electron-withdrawing group (Figure 1).



3

Figure 1. The structure of the model compound **3**.

COMPUTATIONAL DETAILS

Geometry optimization and frequency analysis of *Z* and *E* isomers of studied compounds was conducted at the M06-2X/6-311G** level, using the Gaussian 09 program package. Transition state structures (TS) were determined using the Synchronous Transit-Guided Quasi-Newton method at the M06-2X/6-311G** level. To account for solvent effects, the structures of the three derivatives, **1-2**, were re-optimized along with their TS, using the continuum solvation COSMO model (conductor-like screening model). All transition state structures were characterized by an imaginary frequency, the vibrational mode of which corresponded to the rotation around the C(2)–C(2') bond [3]. As outlined in Figure 2, the $\Delta G^{\neq}$ is plotted against the $d_{C=C}$/Å for rotation around the C(2)=C(2') double bond in 4-oxothiazolidines **1-2** at 298 K for the different solvent conditions (at least three solvents studied).

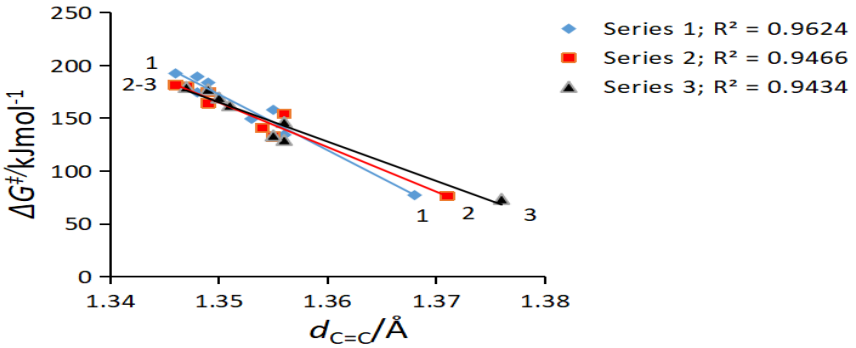


Figure 2. Correlation between the barriers to rotation ($\Delta G^{\neq}$) and the bond lengths ($d_{C=C}$) of ground state (GS) structures **1-2** calculated for *Z* to *E* or *E* to *Z* isomerization under (A) nonpolar solvent conditions (*Series 1*, toluene, $Z \rightarrow E$; *Series 2*, chloroform, $Z \rightarrow E$), and (B) polar solvent conditions (*Series 3*, methanol, $E \rightarrow Z$).

RESULTS AND DISCUSSION

In Table 1 are listed the C(2)C(2') bond lengths (Å) in ground states (GS) and barrier to rotation ($\Delta G^{\ddagger}$, kJ mol^{-1}) around the C=C double bond of studied thiazolidine derivatives **1-3** calculated for toluene, chloroform, and methanol. Regarding the $\Delta G^{\ddagger}$ determined for the **1-2**, they span from 73.6 kJ mol^{-1} determined for **2a** in methanol, which manifests the largest *push–pull* effect, to 192.5 kJ mol^{-1} determined for **1c** in toluene, which has the lowest one. To the efficiency of the $\Delta G^{\ddagger}$ to quantify their *push–pull* effect under the same solvent conditions, they decrease with the increase of their *push–pull* effect as follows: **2a** > **2b** > **2c** > **1a** > **1d** > **1e** > **1b** > **1c**. Generally, solvents decrease $\Delta G^{\ddagger}$ values because the more polar TS (due to the complete charge separation) is more solvated than the less polar GS. The $\Delta G^{\ddagger}$ values decrease with the increase of the solvent polarity, as follows: the more polar solvent it is, the $\Delta G^{\ddagger}$ values are lower. Thus, regarding different solvent conditions, the $\Delta G^{\ddagger}$ values slightly decrease with an increase in the solvent polarity from chloroform to methanol, and under these solvent conditions, their efficiency for quantification of the *push–pull* effect is not affected by the solvent (both solvent relationships were considered $\Delta G^{\ddagger}$ (less polar solvent)/$\Delta G^{\ddagger}$ (more polar solvent), and vice versa). On the other hand, concerning the efficiency of comparison $\Delta G^{\ddagger}$ (less polar solvent)/$\Delta G^{\ddagger}$ (more polar solvent), the $\Delta G^{\ddagger}$ calculated in toluene showed to be less useful for this purpose compared to those calculated for chloroform and methanol. Additionally, in the solvent relationships $\Delta G^{\ddagger}$ (more polar solvent)/$\Delta G^{\ddagger}$ (less polar solvent), the $\Delta G^{\ddagger}$ showed good efficiency in quantifying the *push–pull* effect of the **1-2** for all solvents studied. In this sense, the above-decreasing order of the *push–pull* effect for the **1-2** with the increase of the $\Delta G^{\ddagger}$ has also been established under different solvent conditions, significantly supporting our previously reported findings and conclusions [5,6]. Furthermore, as we expected, the calculated $\Delta G^{\ddagger}$ values for model compound **3**, which does not possess a *push–pull* effect, are the highest, and there is no observed rule of the impact of solvent polarity on them.

Table 1. The C(2)C(2') bond lengths (Å) in GS and barrier to rotation($\Delta G^{\ddagger}$, kJ mol^{-1}) around the C=C double bond of studied thiazolidine derivatives **1-3** calculated for toluene, chloroform, and methanol.

Ent	**Comp**	**Toluene**		**Chloroform**		**Methanol**	
		$\Delta G^{\ddagger}$	$d_{C=C}$ (GS)	$\Delta G^{\ddagger}$	$d_{C=C}$ (GS)	$\Delta G^{\ddagger}$	$d_{C=C}$ (GS)
		$Z \rightarrow E$	*Z isomer*	$Z \rightarrow E$	*Z isomer*	$E \rightarrow Z$	*E isomer*
1	**1a**	158.0	1.355	154.4	1.356	146.4	1.356
2	**1b**	189.5	1.348	180.2	1.347	177.4	1.349
3	**1c**	192.5	1.346	181.6	1.346	179.6	1.347
4	**1d**	174.5	1.348	164.2	1.349	162.3	1.351
5	**1e**	183.8	1.349	174.9	1.349	169.6	1.350
6	**2a**	77.2	1.368	76.3	1.371	73.6	1.376
7	**2b**	134.4	1.356	132.7	1.355	129.5	1.356
8	**2c**	149.5	1.353	141.0	1.354	133.7	1.355
9	**3**	227.2	1.330	230.3	1.330	225.3	1.330

Concerning those above results (Table 1), as the next step, we correlated the barriers to rotation with the C=C bond lengths of the ground state structures of the **1-2** calculated for toluene (nonpolar solvent), chloroform (weakly polar solvent), and methanol (strongly polar solvent), respectively (Figure 2). The excellent linear correlations obtained for both isomerization directions proved that magnitudes of rotational barriers reflect changes in the strength of the *push–pull* effect in the

studied compounds. That confirmed the above-decreasing order of the *push–pull* effect strength of the **1-2** previously established by us (when the *push–pull* effect increases, the $\Delta G^{\ddagger}$ values decrease) [3,5-6]. Another conclusion is that the bond lengths of the C=C double bond of the **1-2** slightly increase with the increase of the solvent polarity from toluene to methanol (Table 1), which could be explained by the better stabilization of polarizable GS of these compounds, through solute-solvent interactions, under polar solvent conditions than under nonpolar ones. The rate of the change of the $\Delta G^{\ddagger}$ with the changes of the $d_{C=C}$ is approximately the same for weak polar (chloroform) to polar (methanol) solvent conditions. That confirmed our previously reported findings of the slight effect of solvents both on the barriers to rotation around the C=C double bond and their bond lengths when considering polar solvent conditions from weakly polar (chloroform) to extremely polar one (water) [5-6]. Furthermore, the rate of the change of the $\Delta G^{\ddagger}$ with the changes of the $d_{C=C}$ for toluene (nonpolar solvent condition) is bigger when compared with those determined for both weakly polar and polar ones, which is in agreement with the above conclusion that the $\Delta G^{\ddagger}$ calculated for toluene showed lower efficiency when are used to quantify the *push–pull* effect of the **1-2** under different solvent conditions. As we expected, for model compound **3**, which does not possess the *push–pull* effect, the $d_{C=C}$ of 1330 calculated for all solvent conditions is the lowest and not affected by the solvent.

CONCLUSION

This work reported an extended study of the use of the barriers to rotation around the C=C double bond of selected thiazolidines **1-2** under solvent conditions. The obtained excellent linear correlations between the $\Delta G^{\ddagger}$ and the C=C bond lengths of the ground state structures of the **1-2** calculated for toluene, chloroform, and methanol for both isomerization directions proved that magnitudes of rotational barriers reflect changes in the strength of the *push–pull* effect in the studied compounds. Concerning different solvent conditions, in the case of the $\Delta G^{\ddagger}$ calculated for toluene, they have achieved lower efficiency when used to quantify the *push–pull* effect of the **1-2** compared to calculated those for chloroform and methanol.

Acknowledgment

This work was supported by the Ministry of Education, Science and Technological Development of the Republic of Serbia (grant no 451-03-66/2024-03/200026).

REFERENCES

[1] J. Sandström, Top. Stereochem., 14 (1983) 83-181.
[2] E. Kleinpeter, *J. Serb. Chem. Soc.*, 71 (2006) 1-17.
[3] A. Rašović, V. Blagojević, M. Baranac-Stojanović, E. Kleinpeter, R. Marković, D. M. Minić, *New J. Chem.*, 40 (2016) 6364-6373, and references therein.
[4] A. Rašović in: Comprehensive Heterocyclic Chemistry, Vol. 4, D. StC Black, J. Cossy, C. V. Stevens, Eds-in-Chief, R. A. Aitken, Vol. Ed, Elsevier Ltd., Oxford, 2022.
[5] A. Rašović and V. A. Blagojević, The barriers to rotation around the C=C bond by the means to quantify the *push–pull* effect of the broader series of selected 2-alkylidene-4-oxothiazolidines under different solvent conditions: *Proceedings of the 15th International Conference on Fundamental and Applied Aspects of Pysical Chemistry, September 20-24, Belgrade, Physical Chemistry,* (2021) 359-362.
[6] A. Rašović, M. Stojanović and V. A. Blagojević, The correlation between the C=C bond lengths and its barriers to rotation: en route to quantify the *push–pull* effect of 2-alkylidene-4-oxothiazolidines under solvent conditions: *Proceedings of the 16th International Conference on Fundamental and Applied Aspects of Pysical Chemistry, September 26-30, Belgrade, Physical Chemistry*, (2022) 311-314.

THE C(2)C(2') SINGLE BOND LENGTHS OF THE TRANSITION STATES IN THE CONFIGURATIONAL ISOMERIZATION OF 2-ALKYLIDENE-4-OXOTHIAZOLIDINES BY THE MEANES TO QUANTIFY THEIR PUSH–PULL EFFECT UNDER SOLVENT CONDITIONS

A. Rašović [1] and V. A. Blagojević [2]

[1]*Center for Chemistry ICTM, University of Belgrade, Studentski trg 16, P. O. Box 473, 11000 Belgrade, Serbia (arasovic@chem.bg.ac.rs)*
[2]*TBP Software, Solunska 11, 11000 Belgrade, Serbia*

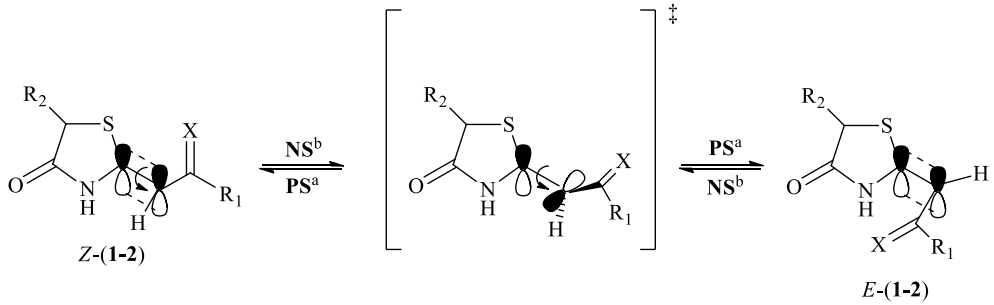
DOI: https://doi.org/10.46793/Phys.Chem24I.261R

ABSTRACT

We reported previously that the barriers to rotation ($\Delta G^{\ddagger}$) around the C(2)C(2') double of the selected thiazolidine derivatives **1-2** proved to be an efficient parameter to quantify the *push–pull* effect of these compounds both under the same and different solvent conditions. As a continuation of the research of potential parameters that could be applied for this purpose, this work explored calculated C(2)C(2') single bonds of their transition states (TS). Regarding this, they showed to be of great interest.

INTRODUCTION

As the result of the electron transfer from donors (Don; NH_{ring}/S_{ring}) to acceptor (Acc; R_1CX) groups, the so-called *push–pull* effect [1,2], C(2)C(2') double bond in 2-alkylidene-4-oxothiazolidines is reduced. Consequently, as exemplified by selected thiazolidines **1-2**, starting from an isomer, the configuration isomerization occurred through rotation around the CC σ bond until it reached the free energy of activation ($\Delta G^{\ddagger}$) at the point of formation of the transition state (TS). In this stage two *p* orbitals used to construct the π bond are perpendicular, and the π bond broken. Further rotation in the same direction results in the production of another isomer (Figure 1).



[a] The polar solvents (PS) shifts equilibrium to the *Z* isomer due to the breaking the intramolecular hydrogen bond (IHB) in the *E*-counterpart.
[b] In the nonpolar solvents (NS) the IHB is favored.

(*Z*)-**1a**: R_1 = Ph; R_2 = CH_2COOEt; X = O
(*Z*)-**1b**: R_1 = NHPh; R_2 = CH_2COOEt; X = O
(*Z*)-**1c**: R_1 = $NH(CH)_2Ph$; R_2 = H; X = O
(*Z*)-**1d**: R_1 = OEt; R_2 = CH_2COOEt; X = O
(2E, 5Z)-**1e**: R_1 = OEt; R_2 = -CHCOOEt; X = O
(*Z*)-**2a**: R_1 = Ph; R_2 = CH_3; X = S
(*E*)-**2b**: R_1 = NH_2; R_2 = CH_2COOEt; X = S
(*Z*)-**2c**: R_1 = $NH(CH)_2Ph$; R_2 = H; X = S

Figure. 1. The configurational isomerization of thiazolidines **1-2**.

We previously showed that calculated barriers to rotation ($\Delta G^{\ddagger}$) proved to be an efficient parameter, using quantifying the *push–pull* effect of selected thiazolidines **1-2**, both under the same and different solvent conditions, i.e., for all solvent relationships [3-5]. Additionally, excellent linear correlations have been achieved between their barriers to rotation and the C(2)=C(2') double bond lengths of their ground state (GS) structures [4,5]. Moreover, the enthalpy–entropy effect has been recently recognized as the main factor that enables the use of the $\Delta G^{\ddagger}$ to quantify their *push–pull* effect under solvent conditions [6]. As a continuation, this work reports the application of the calculated C(2)C(2') single bond lengths of the **1-2** transition states (TS) to quantify their *push–pull* effect. Regarding this, herein has been established that for all solvent conditions (at least the five solvents studied) the C(2)C(2') TS single bond lengths of these compounds increase in line with the increase of their *push–pull* effect.

COMPUTATIONAL DETAILS

Geometry optimization and frequency analysis of *Z* and *E* isomers of studied compounds was conducted at the M06-2X/6-311G** level, using the Gaussian 09 program package. Transition state structures (TS) were determined using the Synchronous Transit-Guided Quasi-Newton method at the M06-2X/6-311G** level. To account for solvent effects, the structures of the three derivatives, **1-2**, were re-optimized along with their TS, using the continuum solvation COSMO model (conductor-like screening model). All transition state structures were characterized by an imaginary frequency, the vibrational mode of which corresponded to the rotation around the C(2)–C(2') bond [7]. In Table 1 are listed the C(2)C(2') single bond lengths (Å) in transition states (TS) of studied thiazolidine derivatives **1-2** calculated for solvent conditions, showing that the C(2)C(2') TS single bond lengths of these compounds increase in line with the increase of their *push–pull* effect (at least five solvents studied).

Table 1. The C(2)C(2') single bond lengths (Å) in transition states (TS) of studied thiazolidine derivatives **1-2** calculated for toluene, chloroform, methanol, dimethyl sulfoxide, and water.

Ent	**Comp**	**Toluene** $d_{C=C}$ (TS)	**$CHCl_3$** $d_{C=C}$ (TS)	**MeOH** $d_{C=C}$ (TS)	**DMSO** $d_{C=C}$ (TS)	**H_2O** $d_{C=C}$ (TS)
1	**1a**	1.43564	1.43990	1.44305	1.44386	1.44342
2	**1b**	1.43013	1.43363	1.43695	1.43681	1.43727
3	**1c**	1.42938	1.43299	1.43622	1.43654	1.43655
4	**1d**	1.43086	1.43445	1.43787	1.43846	1.43828
5	**1e**	1.43024	1.43416	1.43761	1.43741	1.43792
6	**2a**	1.50242	1.50254	1.50257	1.50253	1.50258
7	**2b**	1.44598	1.44705	1.44910	1.44947	1.44934
8	**2c**	1.44369	1.44507	1.44744	1.44917	1.44741

RESULTS AND DISCUSSION

Concerning all solvent conditions studied, in the ground state of both *Z* and *E* isomers, the 4-oxothiazolidine ring and the exocyclic carbon atom of the double bond with its C=X substituent are in the same plane. During the configurational isomerization, the free energy of the **1-2** increases, and reaching the transition state becomes equal to $\Delta G^{\ddagger}$ when the C(2)=C(2') double bond has broken. In transition state structures, the thiazolidine ring as the donor part and the acceptor moiety are nearly perpendicular to each other. The C(2)C(2') bond is elongated, becoming a single bond in TS, while the C(2)–S_{ring}, C(2)–N_{ring}, and C(2')–C bonds are shortened (Figures 1 and 2).

By analysis of data shown in Table 1, it can be concluded that the C(2)C(2') single bond length in TS increases with the increase in the *push–pull* effect of the derivative **1-2**, i.e., with an increase in their electron-accepting ability as follows: CSPh > $CSNH_2$ > $CSNHCH_2CH_2Ph$ > COPh > CO_2Et > $CONHPh$ > $CONH(CH_2)_2Ph$. The obtained trend is in agreement with our understanding of the electronic properties of substituents and also concurs with our previously reported trend, which was established based on our previously published data and conclusions [3-5,7].

However, despite the similarity, consideration of the strength of the *push–pull* effect in the light of the strength of π-electronic interaction between electron-donating (N_{ring}, S_{ring}) and electron-withdrawing (R_1CX) groups, which occurs *via* the C(2)=C(2') double bond in **1-2** ground states does not work in the case of their transition states since that type interaction does not exist. In principle, for the sake of a better understanding of both mechanisms, since the donors are the same (N_{ring}, S_{ring}), the key promoter of the *push–pull* effect strength is the electron-accepting ability of electron-withdrawing groups. In this sense, the main factor determining this could be the resonance stabilization of the C(2')CX fragment in the electron-withdrawing groups of the TS. Thus, with the increase in its stability the tendency of the sharing σ electrons between C(2)and C(2') carbon atoms becomes lower, and C(2)C(2') single bond longer. Therefore, the role of the increase of the electron-withdrawing capability R_1CX groups with increased resonance stabilization of the C(2')CX fragment is valuable, and the larger it is, the *push–pull* effect of the **1-2** is greater, and both a C(2)C(2') double bond in the ground state as well as C(2)C(2') single bond in the transition state become longer.

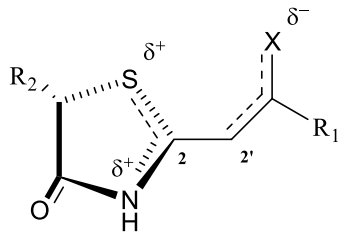


Figure 2. The structure of the **1-2** thiazolidines transition states (TS).

Since for all solvents studied, the calculated C(2)C(2') single bond lengths in TS of the **1-2** increase with the increase of the strength of electron-withdrawing ability of R_1CX, they could be excellent parameter using the quantifying *push–pull* effect of this and similar systems under the same solvent conditions. To this, there is the issue of their efficiency in the estimation of the *push–pull* effect of the **1-2** under different solvent conditions. Thus, as these data show, the calculated bond lengths span from 1.42938 Å, determined for **1c** in toluene, showing the lowest *push–pull* effect, to 1.50258 Å, determined for **2a** in water, showing the largest one. In this way, if the C(2)C(2') single bond length values are compared for all solvent relationships, their decreasing order of values is in good agreement with a decreased electron-withdrawing ability of the acceptor groups. In comparison between $d_{C=C}$ (TS) of the **1-2**, we considered both relationships, less polar solvent/more polar solvent, and vice versa. Concerning this, when comparing $d_{C=C}$ (TS) values to quantify the *push–pull* effect of

the **1-2** for less polar solvent/more polar solvent and more polar solvent/less polar solvent relationships, they achieved lower efficiency for the first. In the solvent relationships of more polar solvent/less polar solvent, the $d_{C=C}$ (TS) showed excellent efficiency in quantifying the *push–pull* effect of the **1-2** under different solvent conditions. These findings greatly corroborate our previously reported ones [3-5]. Therefore, in terms of its application to quantify the *push–pull* effect of this system compounds and similar ones, this parameter should be of significant importance.

Furthermore, when considering the effect of solvent polarity on the TS C(2)C(2') single bond lengths of the **1**-**2**, they slightly decrease with increasing polarity from toluene to methanol, which can be attributed to better stability of TS in polar solvents due to stronger intermolecular interactions. Further increased polarity from methanol to water slightly affects these bond lengths, which can be explained by reaching the limiting values in the contribution of the solvent in the stability of TS and approximately the same strength of the TS/solvent interactions.

CONCLUSION

This work has studied the application of the C(2)C(2') single bond lengths of TS in the configurational isomerization of the thiazolidines **1-2** for quantification of their *push–pull* effect. Concerning this, they showed to be an efficient parameter used for this purpose, both under the same and different solvent conditions. Thus, we established the role: the longer they are, it is the greater the *push–pull* effect of the **1**-**2**. In our opinion, this is the first efficient application of this parameter for this purpose.

Acknowledgment

This work was supported by the Ministry of Education, Science and Technological Development of the Republic of Serbia (grant no 451-03-66/2024-03/200026).

REFERENCES

[1] J. Sandström, Top. Stereochem., 14 (1983) 83-181.

[2] E. Kleinpeter, *J. Serb. Chem. Soc.*, 71 (2006)1-17.

[3] A. Rašović and V. A. Blagojević, The barriers to rotation around the C=C bond by the means to quantify the *push–pull* effect of the broader series of selected 2-alkylidene-4-oxothiazolidines under different solvent conditions: *Proceedings of the 15th International Conference on Fundamental and Applied Aspects of Pysical Chemistry, September 20-24, Belgrade, Physical Chemistry*, (2021) 359-362.

[4] A. Rašović, M. Stojanović and V. A. Blagojević, The correlation between the C=C bond lengths and its barriers to rotation: en route to quantify the *push–pull* effect of 2-alkylidene-4-oxothiazolidines under solvent conditions: *Proceedings of the 16th International Conference on Fundamental and Applied Aspects of Pysical Chemistry, September 26-30, Belgrade, Physical Chemistry*, (2022) 311-314.

[5] A. Rašović and V. A. Blagojević, An extended study of the application of the barriers to rotation around the C=C bond of 2-alkylidene-4-oxothiazolidines to quantify their *push–pull* effect under solvent conditions: *Proceedings of the 17th International Conference on Fundamental and Applied Aspects of Pysical Chemistry, September 23-27, Belgrade, Physical Chemistry*, 2024.

[6] A. Rašović, The enthalpy–entropy compensation mechanism observed in the configurational isomerization of selected 2-alkylidene-4-oxothiazolidines under the same and different solvent conditions: *Proceedings of the 15th International Conference on Fundamental and Applied Aspects of Pysical Chemistry, September 20-24, Belgrade, Physical Chemistry*, 2021, 363-366.

[7] A. Rašović, V. Blagojević, M. Baranac-Stojanović, E. Kleinpeter, R. Marković, D. M. Minić, *New J. Chem.***,** 40 **(**2016**)** 6364-6373.

THE CORRELATION BETWEEN THE C(2)C(2') SINGLE BOND LENGTHS OF THE TRANSITION STATES AND BARRIERS TO ROTATION AROUND THE C(2)C(2') DOUBLE BOND OF GROUND STATES IN THE CONFIGURATIONAL ISOMERIZATION OF 2-ALKYLIDENE-4-OXOTHIAZOLIDINES

A. Rašović [1] and V. A. Blagojević [2]

[1]*Center for Chemistry ICTM, University of Belgrade, Studentski trg 16, P. O. Box 473, 11000 Belgrade, Serbia (arasovic@chem.bg.ac.rs)*
[2]*TBP Software, Solunska 11, 11000 Belgrade, Serbia*

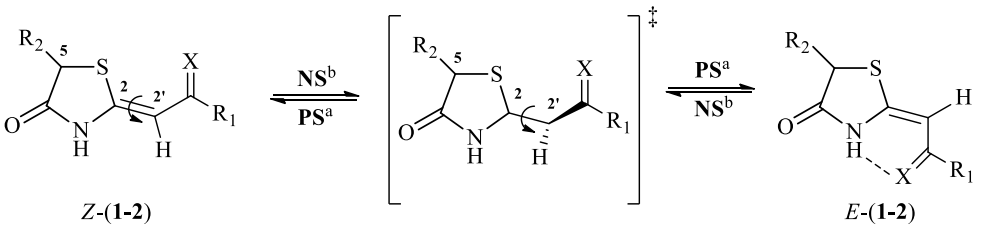
DOI: https://doi.org/10.46793/Phys.Chem24I.264R

ABSTRACT

Our previous works reported that the barriers to rotation ($\Delta G^{\neq}$) around the C(2)C(2') double the ground states (GS) as well as C(2)C(2') single bond lengths of transition states (TS) in the configurational isomerization of thiazolidines **1-2** are efficient parameters using quantifying their *push–pull* effect both under the same and different solvent conditions. Since they follow similar trends, this work reports achieved good linear correlations between these parameters.

INTRODUCTION

The configurational isomerization of thiazolidines **1-2** is happening due to their C(2)C(2') double bond being significantly reduced by the *push–pull* effect [1,2], i.e., by the π-electronic interaction between their electron-donating (N_{ring}, S_{ring}) and electron-withdrawing (R_1CX) groups. The equilibrium of this transformation is determined by the solvent polarity. In this sense, under polar solvent conditions, the Z/E equilibrium is shifted to the left because the intramolecular hydrogen bond in the *E*-isomer has broken with the action of polar solvent molecules. On the other hand, this one is stable under nonpolar solvent conditions, and the equilibrium shifted to the right (Scheme 1).



Z-(**1-2**) *E*-(**1-2**)

[a] The polar solvents (PS) shifts equilibrium to the *Z* isomer due to the breaking the intramolecular hydrogen bond (IHB) in the *E*-counterpart.
[b] In the nonpolar solvents (NS) the IHB is favored.

(*Z*)-**1a**: R_1 = Ph; R_2 = CH_2COOEt; X = O
(*Z*)-**1b**: R_1 = NHPh; R_2 = CH_2COOEt; X = O
(*Z*)-**1c**: R_1 = $NH(CH)_2Ph$; R_2 = H; X = O
(*Z*)-**1d**: R_1 = OEt; R_2 = CH_2COOEt; X = O
(2*E*, 5*Z*)-**1e**: R_1 = OEt; R_2 = -CHCOOEt; X = O
(*Z*)-**2a**: R_1 = Ph; R_2 = CH_3; X = S
(*E*)-**2b**: R_1 = NH_2; R_2 = CH_2COOEt; X = S
(*Z*)-**2c**: R_1 = $NH(CH)_2Ph$; R_2 = H; X = S

Scheme 1. The configurational isomerization of 2-alkylidene-4-oxothiazolidines **1-2**.

Given the significance of the *push–pull* effect on the chemical behaviour of these compounds, we dedicated its quantification great attention to explaining their structural characteristics, reactivity, and mechanical aspects of their transformations into other systems. We used for this purpose (i) experimental and calculated C(2')-*H* proton chemical shift values, [3,4] (ii) experimental and calculated ^{13}C NMR chemical shift difference $\Delta\delta_{C=C}$ between the two carbon atoms of the central partial C(2)=C(2') double bond, [3,4] (iii) the calculated bond lengths of the C(2)=C(2') double bond, [3,6,7] (iv) the quotient of the occupation numbers of the π* antibonding and π bonding orbitals (π*/π) of the C(2)=C(2') double bond, available from theoretical calculations combined with the Natural Bond Orbital (NBO) analysis, [4] and (v) barriers to rotation ($\Delta G^{\ddagger}$) around the C(2)=C(2') double bond [3,5-7]. Thus, the latter two showed to be very sensitive when used for this purpose. We also reported that the calculated C(2)C(2') single bond lengths of TS showed to be good parameter when used for this under the same and different solvent conditions [8]. In this sense, we established the role: the longer they are, that is greater the *push–pull* effect of the **1-2**. As a continuation, this work reports a correlation between the calculated C(2)C(2') single bond lengths of transition states (TS) [8] and barriers to rotation around the C(2)=C(2') double bond in the configurational isomerization of the **1-2**. Thus, good linear correlations have been achieved for nonpolar and polar solvent conditions.

COMPUTATIONAL DETAILS

Geometry optimization and frequency analysis of *Z* and *E* isomers of studied compounds was conducted at the M06-2X/6-311G** level, using the Gaussian 09 program package. Transition state structures (TS) were determined using the Synchronous Transit-Guided Quasi-Newton method at the M06-2X/6-311G** level. To account for solvent effects, the structures of the three derivatives, **1-2**, were re-optimized along with their TS, using the continuum solvation COSMO model (conductor-like screening model). All transition state structures were characterized by an imaginary frequency, the vibrational mode of which corresponded to the rotation around the C(2)–C(2') bond [3]. As outlined in Figure 1, the barriers to rotation ($\Delta G^{\ddagger}$) around the C(2)C(2') double bond of ground states (GS) are plotted against the C(2)C(2') single bond lengths of transition states (TS) at 298 K in the configurational isomerization of the **1-2** at 298 K for the different solvent conditions.

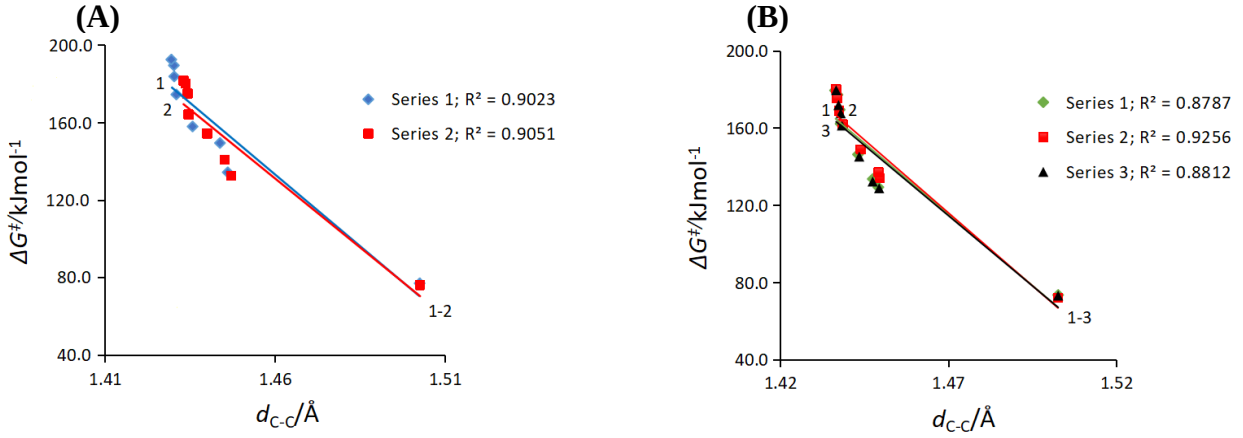


Figure 1. Correlation between the barriers to rotation ($\Delta G^{\ddagger}$) around the C(2)C(2') double bond of GS structures and C(2)C(2') single bond lengths of TS in the configurational isomerization of the **1-2** calculated for *Z* to *E* or *E* to *Z* isomerization under (A) nonpolar solvent conditions (*Series 1*, toluene, $Z \rightarrow E$; *Series 2*, chloroform, $Z \rightarrow E$), and (B) polar solvent conditions (*Series 1*, methanol, $E \rightarrow Z$; *Series 2*, DMSO; $E \rightarrow Z$; *Series 3*, water, $E \rightarrow Z$).

RESULTS AND DISCUSSION

As exemplified by selected thiazolidines **1-2**, starting from an isomer, the configuration isomerization occurs through rotation around the C(2)C(2') σ bond until it reaches the free energy of activation ($\Delta G^{\ddagger}$) when the formation of the transition state (TS) is accomplished, and the π bond broken, so the two *p* orbitals used to construct this bond are perpendicular (Scheme 1). Thus, the C(2)C(2') double bond is elongated, becoming a single bond in TS.

We have previously reported that the C(2)C(2') single bond lengths in TS of the **1-2** increase with an increase in their *push–pull* effect. Thus, their lengths vary from 1.42938 Å, determined for **1c** in toluene, showing the lowest *push–pull* effect, to 1.50258 Å, determined for **2a** in water, showing the largest one [8]. The main factor responsible for this has been recognized as the resonance stabilization of the C(2')CX fragment in the electron-withdrawing groups of the TS. Therefore, with the increase in its stability, the tendency of the sharing σ electrons between C(2) and C(2') carbon atoms becomes lower, and C(2)C(2') single bond longer.

From data listed in Table 1, a conclusion can be reached that barriers rotation around the C(2)=C(2') double bond of the **1-2** span from 72.1 kJ mol^{-1} determined for **2a** in DMSO**,** which manifests the largest *push–pull* effect to 192.5 kJ mol^{-1} determined for **1c** in toluene, which has the lowest one. For solvents studied, the $\Delta G^{\ddagger}$ values decrease with increased *push–pull* effect the **1-2**. Another notion would be that their $\Delta G^{\ddagger}$ slightly decreases with an increase in the solvent polarity from chloroform to water, and under these solvent conditions, the solvent does not impact their efficiency for the quantification of the *push–pull* effect of these compounds (both solvent relationships were considered $\Delta G^{\ddagger}$ (less polar solvent)/$\Delta G^{\ddagger}$ (more polar solvent), and vice versa). On the other hand, the efficiency of comparison $\Delta G^{\ddagger}$ (toluene)/$\Delta G^{\ddagger}$ (another solvent) decreases with the increase of polarity of the other solvent, which made $\Delta G^{\ddagger}$ calculated in toluene less useful to quantify the *push–pull* effect of the **1-2** under different solvent conditions. All the above fully corroborate our previous reports [5-7]. Furthermore, for all solvents studied, in the solvent relationships $\Delta G^{\ddagger}$ (more polar solvent)/$\Delta G^{\ddagger}$ (less polar solvent), the $\Delta G^{\ddagger}$ showed good efficiency in quantifying the *push–pull* effect of the **1-2**. Additionally, when used for this purpose, the C(2)C(2') single bonds of TS in configurational isomerization of the **1-2** follow a similar trend (if they are longer, that is greater the *push–pull* effect of the **1-2**) [8]. Regarding this, we were intrigued to do correlations between them and the $\Delta G^{\ddagger}$.

Table 1. The barriers to rotation ($\Delta G^{\ddagger}$, kJ mol^{-1}) around the C(2)C(2') double bond of studied thiazolidine derivatives **1-2** calculated for toluene, chloroform, methanol dimethylsulfoxide and water.

Ent	**Comp**	**Toluene** $\Delta G^{\ddagger}$	**Chloroform** $\Delta G^{\ddagger}$	**Methanol** $\Delta G^{\ddagger}$	**DMSO** $\Delta G^{\ddagger}$	**Water** $\Delta G^{\ddagger}$
		$Z \rightarrow E$	$Z \rightarrow E$	$E \rightarrow Z$	$E \rightarrow Z$	$E \rightarrow Z$
1	(*Z*)-**1a**	158.0	154.4	146.4	149.1	145.3
2	(*Z*)-**1b**	189.5	180.2	177.4	175.4	172.0
3	(*Z*)-**1c**	192.5	181.6	179.6	180.3	179.7
4	(*Z*)-**1d**	174.5	164.2	162.3	162.1	161.4
5	(2*E*, 5*Z*)-**1e**	183.8	174.9	169.6	169.1	167.7
6	(*Z*)-**2a**	77.2	76.3	73.6	72.1	73.3
7	(*E*)-**2b**	134.4	132.7	129.5	134.1	128.9
8	(*Z*)-**2c**	149.5	141.0	133.7	137.2	132.4

Therefore, the correlations between the barriers to rotation around the C(2)C(2') double bond of the ground state structures of the **1-2** and C(2)C(2') single bonds of their TS have been achieved in good linear ones. Thus, based on these findings (when the *push–pull* effect increases the $\Delta G^{\ddagger}$ values decrease, and contrary, the calculated C(2)C(2') single bond lengths of TS increase), we confirmed the order of electron-accepting ability R_1CX in **1-2** for all solvent conditions, previously established by us, in the following: CSPh > $CSNH_2$ > $CSNHCH_2CH_2Ph$ > COPh > CO_2Et > CONHPh > $CONH(CH_2)_2Ph$ [5-8]. Since the change of the $\Delta G^{\ddagger}$ with the $d_{C\text{-}C}$ of the TS C(2)C(2') single bonds of the **1-2** is approximately the same for all solvents studied, for a better overview, they are shown in separate diagrams, for nonpolar and polar solvent conditions (Figure 1).

CONCLUSION

This work reports good linear correlations between the barriers to rotation around the C(2)C(2') double bond of the ground state structures of the **1-2** and C(2)C(2') single bonds of their TS. Those confirmed our previous report concerning the possibility of the application of the TS C(2)C(2') single bonds to quantify the *push–pull* effect of these compounds independently of solvent conditions. In our opinion, those are the first efficiently conducted correlations used for this purpose.

Acknowledgment

This work was supported by the Ministry of Education, Science and Technological Development of the Republic of Serbia (grant no 451-03-66/2024-03/200026).

REFERENCES

[1] J. Sandström, Top. Stereochem., 14 (1983) 83-181.
[2] E. Kleinpeter, J. Serb. Chem. Soc., 71 (2006) 1-17.
[3] A. Rašović, V. Blagojević, M. Baranac-Stojanović, E. Kleinpeter, R. Marković, D. M. Minić, New J. Chem., 40 (2016) 6364-6373.
[4] M. Baranac-Stojanović, U. Klaumünzer, R. Marković and E. Kleinpeter, Tetrahedron, 66 (2010) 8958-8967.
[5] A. Rašović and V. A. Blagojević, The barriers to rotation around the C=C bond by the means to quantify the *push–pull* effect of the broader series of selected 2-alkylidene-4-oxothiazolidines under different solvent conditions: *Proceedings of the 15th International Conference on Fundamental and Applied Aspects of Pysical Chemistry, September 20-24, Belgrade, Physical Chemistry*, (2021) 359-362.
[6] A. Rašović, M. Stojanović and V. A. Blagojević, The correlation between the C=C bond lengths and its barriers to rotation: en route to quantify the *push–pull* effect of 2-alkylidene-4-oxothiazolidines under solvent conditions: *Proceedings of the 16th International Conference on Fundamental and Applied Aspects of Pysical Chemistry, September 26-30, Belgrade, Physical Chemistry*, (2022) 311-314.
[7] A. Rašović and V. A. Blagojević, An extended study of the application of the barriers to rotation around the C=C bond of 2-alkylidene-4-oxothiazolidines to quantify their *push–pull* effect under solvent conditions: *Proceedings of the International Conference on Fundamental and Applied Aspects of Pysical Chemistry, September 23-27, Belgrade, Physical Chemistry*, 2024.
[8] A. Rašović and V. A. Blagojević, The C(2)C(2') single bond lengths of the transition states in the configurational isomerization of 2-alkylidene-4-oxothiazolidines by the means to quantify their *push–pull* effect under solvent conditions: *Proceedings of the 17th International Conference on Fundamental and Applied Aspects of Pysical Chemistry, September 23-27, Belgrade, Physical Chemistry*, 2024.

DETECTION OF OXA COMPLEX CONTAINING MANGANESE BY LDI MASS SPECTROMETRY

F. Veljković[1], B. Božić[2], M. Stoiljković[1], I. Stajčić[1], B. Janković[1], M. Janković[1] and S. Veličković[1]

[1]VINČA Institute of Nuclear Sciences - National institute of the Republic of Serbia, University of Belgrade, P.O.Box 522, 11001 Belgrade, Republic of Serbia. (filipveljkovic@vin.bg.ac.rs)
[2]University of Belgrade, Faculty of biology, Studentski trg 16, 11158 Belgrade, Republic of Serbia.

DOI: https://doi.org/10.46793/Phys.Chem24I.269V

ABSTRACT
Complexes containing transition metal ions, especially with oxaprozin, have significant potential for cancer treatment. In this study, laser desorption/ionization (LDI) with a commercial matrix-assisted LDI time-of-flight mass spectrometer was used to investigate the possibility of detecting an oxaprozin complex with Mn, [$(C_{18}H_{14}NO_3)_2Mn$]. The results showed that the LDI mass spectrum of [$(C_{18}H_{14}NO_3)_2Mn$] (obtained at a laser intensity of 2900 to 3400 a.u., an accelerating voltage of 18000 V, a grid voltage of 80 % and extraction delay times of 100 to 300 ns) contains three groups of peaks corresponding to the molecular ion at *m/z* 639.79, 640.77, 641.49, the sodium adduct at *m/z* 661.76, 662.76, 663.77 and the potassium adduct at *m/z* 677.71, 678.69. Under these conditions, the experimental isotopology exactly matched the theoretical values of the oxaprozine complex with Mn. LDI-MS thus proves to be promising for the characterization of new organometallic compounds.

INTRODUCTION

Oxaprozin, a non-steroidal anti-inflammatory drug (NSAID) known as 3-(4,5-diphenyl-1,3-oxazol-2-yl)propanoic acid, has analgesic and antipyretic properties [1-3]. Continuous NSAID therapy has been shown to have potential for cancer chemoprevention and as an adjunct therapy for cancer patients [4-5]. Transition metal ions, which are key components in many enzymatic reactive centers, have attracted interest due to their ability to form complexes with NSAIDs that are more potent and have fewer side effects than the parent drugs [6-11]. For example, a metal- containing complex with ketoprofen has shown remarkable antiproliferative effects on a human breast cancer cell line rich in progesterone receptors [12].

Matrix-assisted laser desorption/ionization time-of-flight mass spectrometry (MALDI-TOF) is widely used for the analysis of high-molecular weight and unstable compounds, including bioorganic and organometallic species [13]. An alternative to MALDI, laser desorption/ionization (LDI) without matrix, which can be used to effectively detect and characterize metal compounds, including coordination and organometallic complexes as well as inorganic species. Proper selection of LDI mass spectrometer parameters minimizes ion fragmentation, enabling the detection of accurate molecular weights of unstable organometallic compounds, which is crucial for their characterization [14]. The main advantage of LDI is that it mainly generates singly charged ions, which facilitates the analysis of complex mixtures [15]. The aim of this study was to detect the oxaprozin-Mn complex by varying the instrumental parameters of the LDI mass spectrometer. Considering the limited data on how these parameters affect the LDI mass spectra of organometallic complexes, the results of this study are significant.

METHODS

A 0.35 mg sample of the synthesized Mn complex with oxaprozin was dissolved in 25 µL of dimethyl sulfoxide (DMSO). The analyte and solvent were mechanically mixed and transferred to a stainless-steel plate. Half a microliter of this suspension was dried and then introduced into the ionization chamber of the MALDI mass spectrometer. The MALDI target plate with the sample was inserted into a Voyager-DE PRO mass spectrometer from Sciex (USA), equipped with a TOF analyzer operating in positive reflection mode with pulsed extraction. The sample was ionized with an ultraviolet nitrogen laser (wavelength 337 nm, pulse width 3 ns, and repetition rates of 20.00 Hz) and a time-of-flight (TOF) analyzer. One hundred and fifty shots were summed for the measurements. The laser intensity was controlled using a slider on the Manual Laser Control page, with a range of 0–4600 a.u. (arbitrary units). The accelerating voltage was 18 kV, with 80% grid voltage and an extraction delay time of 100 ns.

RESULTS AND DISCUSSION

In this study, the influence of the instrumental parameters of the LDI TOF mass spectrometer for the detection of previously synthesized NSAIDs Mn complexes with oxaprozin was investigated. During the experiment the laser intensity was varied from 2900 a.u. to 3400 a.u., the accelerating voltage from 15000 to 25000 V, the grid voltage from 60 to 90%, and the extraction delay time from 100 to 300 ns.

A part of the LDI mass spectrum in the positive mode of the complex of Mn with oxaprozin is shown in Figure 1. The experimental values relevant to this study and their corresponding theoretical values are listed in Table 1.

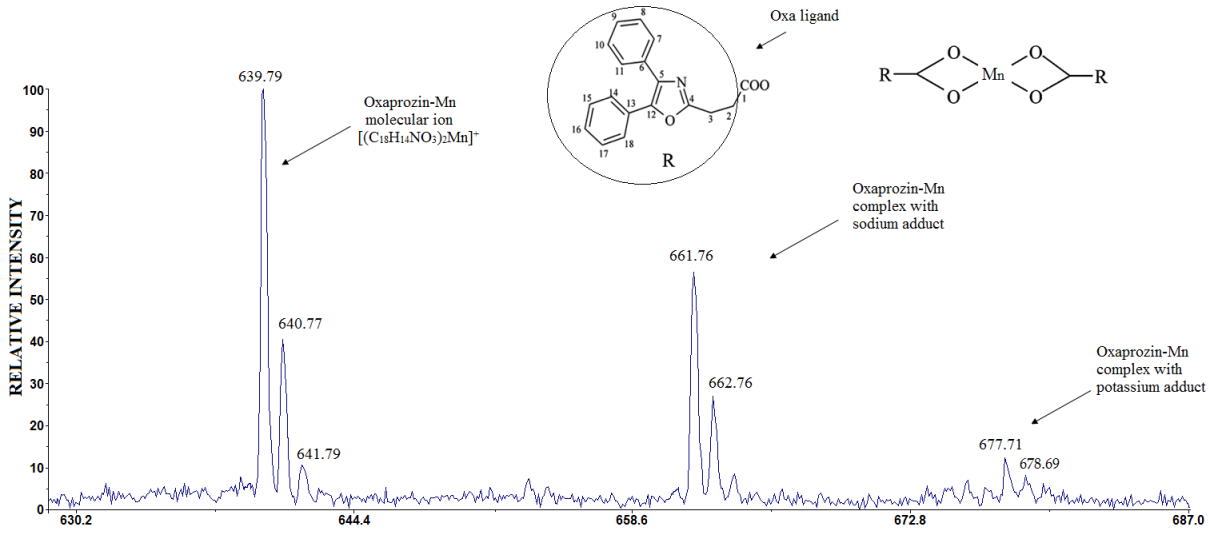


Figure 1. Experimentally obtained mass spectrum of Mn complex with Oxaprozin, structure of oxa ligand and proposed structure of the Mn-oxacomplex.

As can be seen from **Figure 1**., a selected part of the positive mode LDI mass spectrum of the complex of Mn with oxaprozin contains three signal groups corresponding to its molecular ion at *m/z* values 639.79, 640.77, 641.79 and two adducts: sodium adduct at *m/z* values 661.76, 662.76, 663.77 and potassium adduct at *m/z* values 677.71, 678.69. The molecular ion is the most intense, while the adduct with potassium is the least intense. The experimentally obtained isotopology for

the molecular ion and the two adducts of the oxaprozin metal complex with Mn are in good agreement with the theoretical calculations.

Table 1. Experimentally determined *m/z* values of the Mn complex with Oxaprozin and corresponding theoretical values.

Chemical Formula	Experimental *m/z*	Theoretical *m/z*
	639.79	639.13
$[(C_{18}H_{14}NO_3)_2Mn]^+$	640.77	640.14
	641.79	641.14
	661.76	662.12
$[(C_{18}H_{14}NO_3)_2Mn+Na]^+$	662.76	663.12
	663.77	664.13
	677.71	678.10
$[(C_{18}H_{14}NO_3)_2Mn+K]^+$	678.69	679.10

It was found that the relative intensity of the adduct ions increased with the increase in laser intensity from 2900 to 3400 a.u. The optimum value of the accelerating voltage was 18000 V, the grid voltage 80%, while the variation of the extraction delay time showed no significant effects, like the three previous variables.

CONCLUSION

In this work, the possibility of using LDI-TOF MS to detect Mn organometallic complexes with commercially available NSAID was investigated. The positive mode of the LDI mass spectra measured in the laser intensity range of 2900–3400 a.u. ensures that the experimental isotopology is in good agreement with the theoretical values. LDI-MS can be a useful method for the future study of various organometallic complexes containing other metals such as Co(II), Ni(II), Zn(II), etc.

Acknowledgment

This work was financially supported by the Ministry of Education, Science and Technological Development of the Republic of Serbia, contract numbers: 451-03-66/2024-03/200017 and 451-03-66/2024-03/200178.

REFERENCES

[1] M. A. al-Faks, M. C. Pugh, Orthop. Rev., 21 (1992) 558–563.
[2] J. J. Talley, D. L. Brown, J. S. Carter, M. J. Graneto, C. M. Koboldt., J. L. Masferrer, W. E. Perkins, R. S. Rogers, A. F. Shaffer, Y. Y. Zhang, B. S. Zweifel, K. Seibert, J. Med. Chem., 43 (2000) 775–777.
[3] B. D. Bozic, J. R. Rogan, D. D. Poleti, N. P. Trisovic, G. S. Uscumlic, Chem Pharm Bull.,60 (2012) 865–869.
[4] J. A. Baron, Prog Exp Tumor Res., 37 (2003) 1–24.
[5] R. Ettarh, A. Cullen, A. Calamai, Pharmaceuticals (Ott.), 3 (2010) 2007–2021.
[6] Y. Iizuka, E. Sakurai, Y. Tanaka, Riken Review, 35 (2001) 3–4.
[7] S. J. Lippard, J. M. Berg, “Principles of Bioinorganic Chemistry”, University Science Books, Mill Valley, 1994.
[8] R.K. Szilagyi, P. A. Bryngelson, M. J. Maroney, B. Hedman, K. O. Hodgson, E. I. Solomon, J

Am Chem Soc.,126 (2004) 3018–3019.
[9] M. H. Stipanuk, “Biochemical, Physiological & Molecular Aspects of Human Nutrition,” 2nd ed., W. B. Saunders Company, New York, 2006.
[10] M. Kobayashi, S. Shimizu, Eur J Biochem., 261 (1999) 1–9.
[11] P. Lay, T. Hambley, WO Patent 109843, 2007.
[12] D. K. Saha, S. Padhye, S. Padhye, Met Based Drugs, 8 (2001) 73–77.
[13] J. H. Banoub, R. P. Newton, E. Esmans, D. F. Ewing, G. Mackenzie, Chem. Rev., 105 (2005) 1869.
[14] M. Wyatt, J. Mass Spec., 46 (2011) 712.
[15] W. Henderson, J. S. McIndoe, Mass Spectrometry of Inorganic, Coordination and Organometallic Compounds, 2005.

H *– Material Science*

COMPARISON OF MODIFIED CELLULOSE AND LIGNOCELLULOSIC BIOMASS FOR ADSORPTIVE RECOVERY OF LITHIUM FROM WATER: BATCH AND COLUMN STUDIES

A. Yüksel [1,2] and Y. K. Recepoğlu [1]

[1]*Department of Chemical Engineering, Izmir Institute of Technology*
Urla, 35430 İzmir, Türkiye. (asliyuksel@iyte.edu.tr)
[2]*Geothermal Energy Research and Application Center, Izmir Institute of Technology*
Urla, 35430 İzmir, Türkiye.

DOI: https://doi.org/10.46793/Phys.Chem24I.275Y

ABSTRACT

Investigating efficient bio-based adsorbents is crucial for lithium (Li) recovery due to the increased demand from electric vehicles and energy storage, making Li a pivotal metal in the 21st century. This study entails the comparison of batch and column mode assessments to determine the efficacy of lithium-capable biosorbents, namely phosphorylated cellulose (FC) and phosphorylated hazelnut shell waste (FHS). Several influencing factors were investigated, such as biosorbent dosage, initial concentration, contact time, and pH. The Langmuir model determined the maximum sorption capacity to be 9.60 mg/g for FC and 7.71 mg/g for FHS at 25°C. Notably, the kinetics of the biosorbents were as rapid as 3 min in achieving Li sorption. Moreover, in a packed bed column, the use of FC and FHS resulted in a threefold increase in sorption capacity under dynamic flow, particularly at lower flow rates. 5% H_2SO_4 solution proved sufficient to desorb around 100% of Li from the saturated biosorbents.

INTRODUCTION

As new renewable energy technologies like electric energy storage and new electric vehicles develop, the need for Li salts is likely to soar [1]. Since the 1990s, Li as an electrode material in rechargeable batteries has been a significant commercial potential [2]. Li is generally derived from Li rocks and liquid Li resources; however, due to over-mining, the grade of Li ores has decreased. As a result, Li recovery from aqueous sources such as seawater, geothermal water, and salt-lake brines has become a critical component of Li salt manufacturing [3]. Solar evaporation is the most extensively used commercial method for extracting Li from brines [4]. Several potential strategies, including adsorption [5], solvent extraction [6], and membrane-related technologies [7], for Li recovery from brines have been reported to replace solar evaporation since it needs a long time to concentrate considerable amounts of Li. Adsorption is the most promising approach for extracting Li from aqueous resources since it is more environmentally friendly and effective in an industrial operation [8].

Although there are many studies reported in the literature regarding metal ions extraction based on different functionalized composite materials [9], aluminum hydroxides (AlOH) [10], aluminum oxides (AlO_x) [11], manganese oxides (MnO_x) [12], and titanium oxides (TiO_x) [13] have been known to be the most selective Li adsorbents until now. They are classified as inorganic crystalline solids either being studied for direct Li extraction from brines or employed as cathode materials in Li-ion batteries. Furthermore, researchers have been looking at using strong acid cation-exchange resins as organic sorbents to recover Li from seawater and other Li-containing fluids selectively. Lewatit K2629, TP 207 and TP 208 [14], and Lewatit TP 260 [15] are some of the organic sorbents exhibiting low selectivity of Li because they only become effective for selective Li extraction when

impregnated with inorganic, Li-selective sorbents. Ion-imprinted polymers are another technology developed as organic sorbents to separate Li selectively from aqueous medium [16]. Li recovery using low-cost and sustainable sources containing a considerable portion of cellulose is an unexplored field with scant literature. Sustainability and green chemistry have been important for the development of the next generation of materials over the last decade, with the use of bio-based polymer matrices potentially allowing for lower environmental impacts through the use of renewable carbon and more easily biodegradable or reusable materials [17].

In this study, cellulose and a natural cellulose resource, hazelnut shell waste, were modified and utilized for Li recovery from water through batch and column modes of operations. The performance of the materials was compared with several parameters, such as biosorbent dosage, initial concentration, contact time, and pH in batch mode. Furthermore, the column mode effectiveness of the materials was compared with different flow rates and bed heights.

METHODS

Preparation of the biosorbents

Microcrystalline cellulose and/or hazelnut shell waste (10 g) undergo a treatment and activation process before chemical modification in which a 10 M NaOH solution (100 mL) is introduced, and the resulting mixture is stirred at room temperature (25°C) for 2 h. Subsequently, to neutralize the solution and precipitate cellulose and/or hazelnut shell, 10 M HCl (100 mL) is added. The mixture is thoroughly washed with excess water and then subjected to filtration to eliminate alkaline residues. The remaining material is dried at 70°C for 6 h and further processed by grinding it in a mortar and pestle.

The modification process begins with the introduction of a phosphorylating chemical solution composed of phosphoric acid (0.15 mol), diammonium hydrogen phosphate (0.2 mol), and urea (1 mol) dissolved in water (150 mL) into NaOH-treated cellulose and/or hazelnut shell water (10 g). After thorough mixing, the resultant mixture is left to stand at room temperature (25°C) for 1 h, followed by the evaporation of water content, and the residue is completely dried at 105°C for 18 h. The mixture is then subjected to a reaction at 150°C for 2 h. The ensuing reaction product undergoes washing with excess water, drying at 70°C for 6 h, and grinding in a mortar and pestle to yield phosphorylated functional cellulose and/or hazelnut shell [18].

Batch mode Li sorption studies

A set of experiments assessed the Li sorption capacities of phosphorylated functional cellulose and/or hazelnut shell waste in a model Li solution.

The effect of biosorbent dosage were investigated by introducing different quantities ranging from 0.1 to 0.5 g of FC and/or FHS into plastic bottles containing 25 mL of LiCl solution (Li^+: 10 mg L^{-1}). These solutions were shaken at ambient temperature (25°C) for 24 h at a speed of 180 rpm.

To investigate the impact of the initial concentration of Li ions on the adsorption process, sealed plastic bottles, each containing LiCl solution (25 mL) at various concentrations (ranging from 10 to 100 mg L^{-1}), along with a consistent mass of either FC (0.3 g) or FHS (0.35 g), was subjected to agitation at 25°C for 24 h at a speed of 180 rpm.

In kinetic experiments, biosorbents were exposed to a 100 mg L^{-1} of Li at 10 g L^{-1} dose at 25°C. To examine the influence of contact time on lithium recovery, periodic sampling was done within a time interval of 0 to 60 minutes.

The effect of pH on the sorption process was studied in a closed plastic bottle containing 25 mL of LiCl solution (Li^+: 10 mg L^{-1}) along with a consistent mass of FC (0.3 g) or FHS (0.35 g). The mixture underwent agitation at various pH values (ranging from 2 to 6) for a duration of 24 h at 180 rpm.

Following each experiment, the biosorbents were isolated from the solution through filtration. The filtrate was appropriately diluted, and the concentrations of Li in the filtrate were analyzed using an ICP-OES instrument (Agilent Technologies, 5110).

The adsorption capacity of the biosorbents and removal percentage of Li were calculated by the following equations, respectively:

$Q_e=[(C_0 – C_e)V]/m$ (1)

$R= [(C_0 – C_e)/C_0]x100$ (2)

where Q_e is the unit adsorption capacity (mg g^{-1}), R is the recovery percentage of Li, C_0, and C_e are the initial Li concentration (mg L^{-1}) and Li concentration at equilibrium (mg L^{-1}), respectively. V is the volume of Li solution (L), and m is the adsorbent (g) weight.

Column mode Li sorption studies

Chromatographic separation of Li from aqueous solution was conducted using a 0.7 cm diameter and 12 cm high glass column filled with FC or FHS. Their column performances were compared with different flow rates (0.25- and 1.0-mL min^{-1}) and bed heights (1.0 and 1.5 cm) for Li sorption by introducing a feed solution with an initial Li concentration of 10 mg L^{-1} through a column flowing from top to bottom. In sorption experiments, 3 mL of samples were collected over time using a peristaltic pump (SHENCHEN model) and a fraction collector (BÜCHI C-660). Li desorption experiments were carried out with a 5% H_2SO_4 solution at a flow rate of 0.12 mL min^{-1}, collecting 2 mL fractions. The Li concentration in the samples was determined using a flame photometer (JENWAY PFP7) instrument.

RESULTS AND DISCUSSION

The effect of biosorbent dosage

Figure 1 shows the effect of biosorbent dosage on Li removal from water for FC and FHS, comparatively. The most effective FC dosage, determined to be 12.0 g L^{-1}, resulted in approximately 94% Li removal. At this dosage, sorption equilibrium for Li was achieved, and no significant increase in removal was observed beyond this point. Consequently, 12.0 g L^{-1} was selected as the optimal biosorbent dosage for FC for the subsequent experiments.

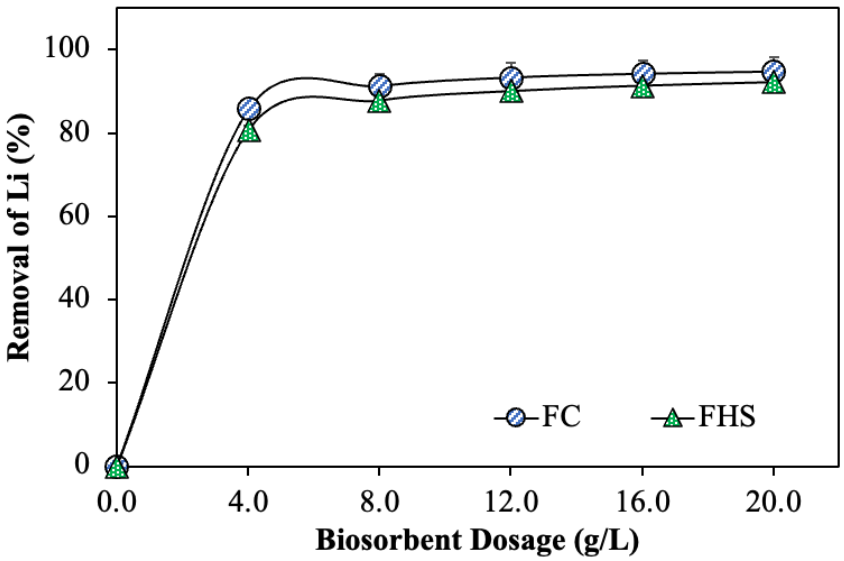


Figure 1. The effect of biosorbent dosage on Li removal efficiency using FC and FHS (C_0=10 mg L^{-1} Li; T=25°C, pH=6, shaking rate=180 rpm).

Similarly, an optimal Li sorption rate of 92% was attained within a 12 to 16 g L^{-1} FHS dosage range. Consequently, selecting a 14 g L^{-1} biosorbent dosage for FHS is deemed economically justified for Li recovery from aqueous solutions, as it offers a high sorption efficiency with no substantial additional benefit observed at higher dosages.

The effect of initial concentration

The initial Li concentration is pivotal in establishing a substantial driving gradient force to surmount the mass transfer resistance between aqueous and solid phases. The effect of initial Li concentration on Li uptake onto FC and FHS is shown in **Figure 2**. A noticeable trend emerges where an increase in the initial concentration of Li corresponds to a proportional rise in Li sorption on the biosorbents. This increased sorption capacity with rising initial concentration is attributed to an elevated likelihood of collisions between the adsorbent and the adsorbate, suggesting a positive correlation between these factors in the Li adsorption process. In the case of FC, the data reveals an elevation in the Li sorption capacity of FC from 0.75 to 6.13 mg g^{-1} as the Li concentration increases from 10 to 100 mg L^{-1} at 25°C, while the sorption capacity varied between 0.67 and 5.48 mg g^{-1} for FHS.

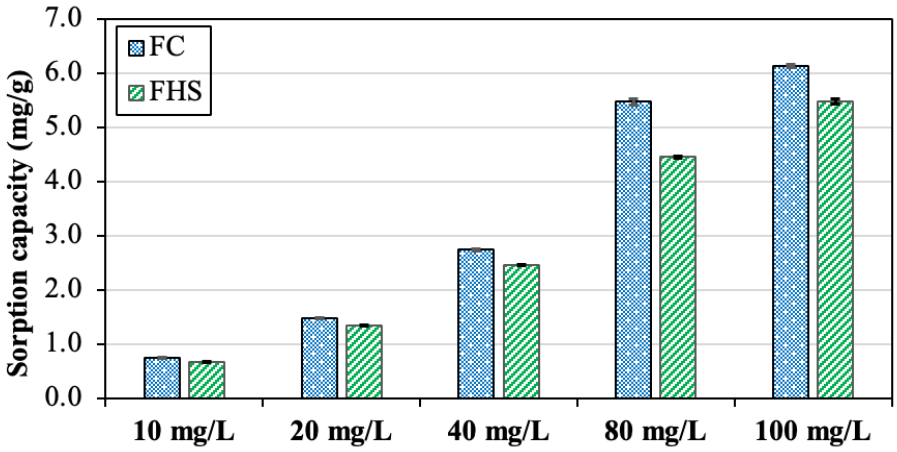


Figure 2. The effect of initial concentration on Li sorption capacity of FC and FHS (Biosorbent dose: 12 g L^{-1} FC and 14 g L^{-1} FHS; pH=6, T=25°C, shaking rate=180 rpm).

Selecting the proper correlation for equilibrium curves is vital for optimizing adsorption system design. The chosen correlation should accurately reflect the relationship between adsorbate and adsorbent to ensure reliable predictions and enhance overall system effectiveness. Well-known Langmuir and Freundlich isotherm models were used to describe the sorption behavior and process of phosphorylated functional biosorbents at 25°C. **Table 1** presents the parameters of the examined sorption isotherms, which were determined using MATLAB through the nonlinear regression technique. Despite the challenge in differentiation, the experimental data exhibited better agreement with the Langmuir isotherm, as evidenced by a relatively higher R^2 value of 0.997 and a lower SSE value of 0.038 for FC. On the other hand, R^2 and SSE analyses indicated that the Freundlich model better described the sorption equilibrium experimental data for FHS than the Langmuir model. Based on the Langmuir model assumption, the monolayer maximum adsorption capacities (Q_{max}) of FC and FHS were determined to be 9.60 and 7.71 mg g^{-1}, respectively. The K_F value, representing a constant associated with temperature and indicative of adsorption capacity in Freundlich isotherm, was found to be 0.7728 for FC and 0.7129 for FHS. Overall, both biosorbents exhibited a similar adsorption behavior for Li sorption from water.

Table 1. Investigation of Li sorption behavior of FC and FHS using Langmuir and Freundlich isotherm models and associated model parameters at 25°C.

Model	Equation	Paramaters	
		FC	FHS
Langmuir	$Q_e=[(Q_{max}K_LC_e)/(1+K_LC_e)]$	Q_{max}=9.60 mg g^{-1} K_L=0.0529 L mg^{-1} R^2=0.997 SSE=0.0038	Q_{max}=7.71 mg g^{-1} K_L=0.0579 L mg^{-1} R^2=0.991 SSE=0.0247
Freundlich	$Q_e=K_FC_e^{1/n}$	K_F=0.7728 n=1.6753 R^2=0.990 SSE=0.056	K_F=0.7129 n=1.7834 R^2=0.999 SSE=0.0204

*Q_{max}: the maximum sorption capacity (mg g^{-1}), K_L is the Langmuir constant (L mg^{-1}); K_F, and n are the Freundlich isotherm constants related sorption capacity and intensity.

The effect of contact time

The effect of contact time on Li sorption efficiency is illustrated in **Figure 3**. The graph indicates an initial rapid increase in sorption rate, followed by a more gradual process, ultimately reaching optimum efficiency within approximately 3 minutes. Subsequently, no significant changes were observed from 3 to 60 minutes. This suggests a remarkably fast sorption process, particularly when the influx of Li ions from the medium surpasses the available sorption sites. The findings imply a high affinity of phosphorylated functional biosorbents (FC and FHS) for Li ions in aqueous solutions. Their unexpectedly high Li ion sorption rate adds to its notable characteristics.

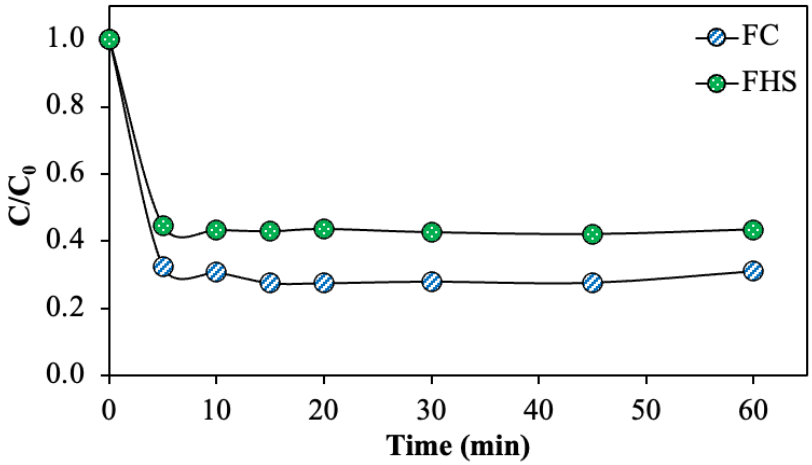


Figure 3. The effect of contact time on Li removal efficiency using FC and FHS (Biosorbent dose: 10 g L^{-1} FC and FHS; C_0=100 mg L^{-1}, T=25°C, mixing rate=180 rpm).

The effect of pH

The data depicted in **Figure 4** shows the sorption efficiency of phosphorylated functional biosorbents across a pH range of 2 to 6. As anticipated, comparatively lower sorption was observed at pH 2 for both FC and FHS. However, with the initial pH increasing up to 6, the efficiency of Li sorption reached higher than 90% under specified conditions. This is because the biosorbents, containing functional groups derived from phosphoric acid with pKa values of 2.16, 7.21, and 12.32, reveal that at pH 2, the functional groups tend to remain in the molecular form, resulting in

comparatively low Li sorption. However, with an increase in solution pH from 2 to 6, the ionization of the functional groups of the biosorbents occurs, leading to enhanced Li sorption, particularly as the next pKa value is 7.21. Given the minor effect of pH on Li sorption within the investigated pH range, sorption studies were conducted in the pH range of 5-6, corresponding to the original pH of the LiCl solution.

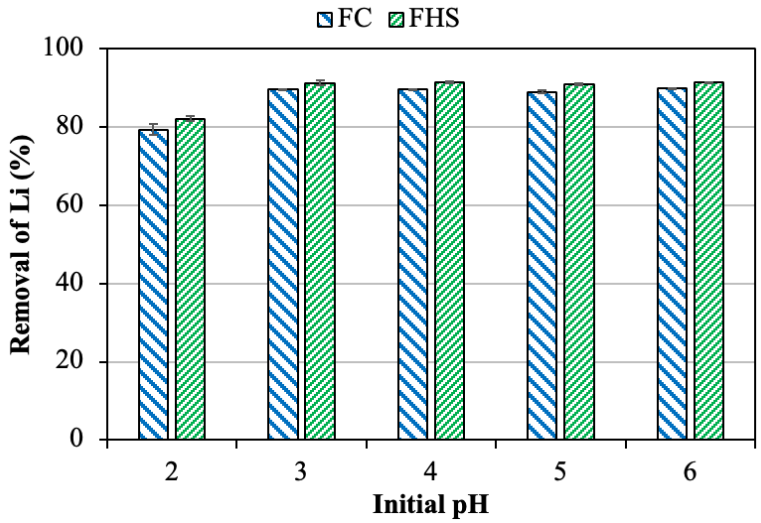


Figure 4. The effect of pH on Li removal efficiency using FC and FHS (Biosorbent dose: 12 g L^{-1} FC and 14 g L^{-1} FHS; C_0=10 mg L^{-1}, T=25°C, shaking rate=180 rpm).

Comparison of column performances of functional cellulose and hazelnut shell waste

To compare the column performances of FC and FHS under different conditions, the breakthrough curves were presented in **Figures 5(a)** and **5(b)** with a flow rate of 1.0 mL min^{-1} and a bed height of 1.0 cm and a flow rate of 0.25 mL min^{-1} and a bed height of 1.5 cm, respectively. Comparing the breakthrough curves in both cases showed a similar column performance profile, and according to the findings in **Table 2**, breakthrough and total capacities were comparable for FC and FHS. For example, the breakthrough capacity of FC with a flow rate of 1.0 mL min^{-1} and a bed height of 1.0 cm was 3.43 mg Li/mL sorbent, while it was 3.15 mg Li/mL sorbent for FHS. Their total capacity was 4.13 and 3.91 mg Li/mL sorbent, respectively. Meanwhile, the different capacities per gram of the same sorbent volume are due to the different densities of the materials. The density of FC was 0.187 g mL^{-1}, while the density of FHS was 0.232 g mL^{-1}. Although FC at a higher flow rate (1.0 mL min^{-1}) and lower bed height (1.0 cm) perform relatively better with bed volumes of 411 and 918 both at the breakthrough point and total capacity, respectively, these values for FHS were found to be 338 and 805, respectively. The degree of column utilization of both materials under the selected operating conditions was calculated as approximately 80%, which indicates that the utilization of the materials in the column is quite suitable. When the flow rate is 0.25 mL min^{-1} and the bed height is 1.5 cm, i.e. at a lower flow rate and higher bed height, the breakthrough curves of both materials almost overlap, and the column study findings showed similar performance in the column. **Figures 6(a)** and **6(b)** show FC and FHS elution profiles for different sorption conditions. The Li could be concentrated as high as 725 mg L^{-1} at the maximum, depending on the studied conditions, such as 0.25 mL min^{-1} flow rate and 1.5 cm bed height for FHS and it was around 650 mg L^{-1} for FC, but due to relatively higher sorption capacity FC had second highest concentrated point close to the maximum. Because the biosorbents are easily regenerated with the 5% H_2SO_4, almost 100% elution efficiencies were obtained. Moreover, the degree of column utilization was 80% on average for each condition.

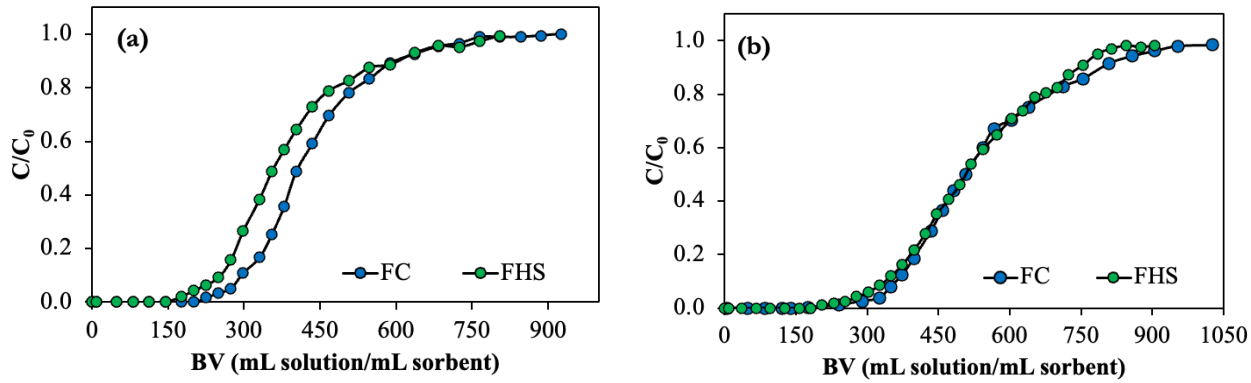


Figure 5. Comparison of the breakthrough curves of FC and FHS under different conditions **(a)** C_0=10 mg L^{-1}, T=25ºC, ϑ=1.0 mL min^{-1}, bed height=1.0 cm, **(b)** C_0=10 mg L^{-1}, T=25ºC, ϑ=0.25 mL min^{-1}, bed height=1.5 cm.

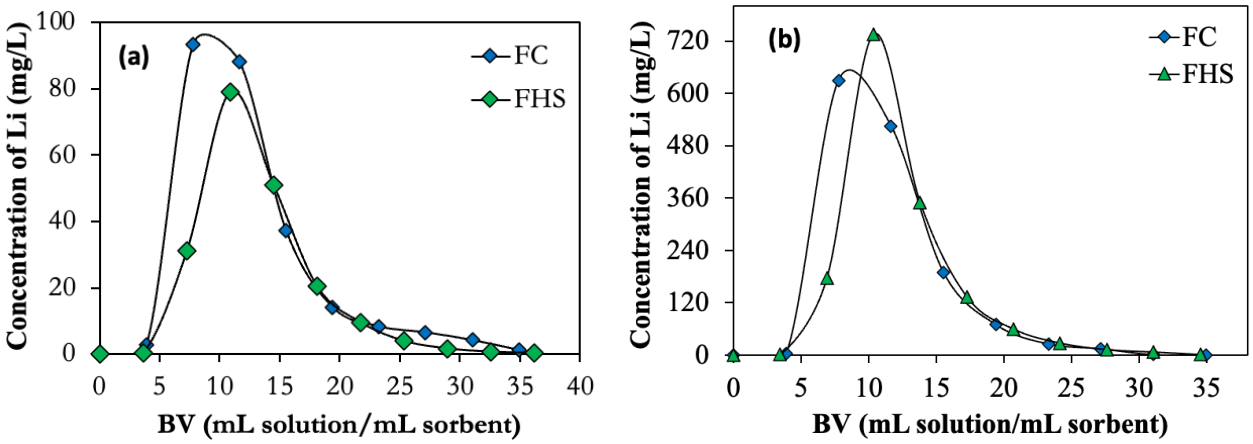


Figure 6. Comparison of the elution curves of FC and FHS for different sorption conditions **(a)** C_0=10 mg L^{-1}, T=25ºC, ϑ=1.0 mL min^{-1}, bed height=1.0 cm, **(b)** C_0=10 mg L^{-1}, T=25ºC, ϑ=0.25 mL min^{-1}, bed height=1.5 cm.

Table 2. Comparison of column performances of FC and FHS under different conditions.

	ϑ=1.0 mL min^{-1}, bed height=1.0 cm		**ϑ=0.25 mL min^{-1}, bed height=1.5 cm**	
Sorbent	**FC**	**FHS**	**FC**	**FHS**
Breakthrough capacity, mg Li/mL sorbent	3.43	3.15	4.83	4.20
Breakthrough capacity, mg Li/g-sorbent	18.33	13.56	25.82	18.10
BV at breakthrough point, mL solution/mL sorbent	411	338	477	477
Total capacity, mg Li/mL sorbent	4.13	3.91	6.28	5.17
Total capacity, mg Li/g-sorbent	22.08	16.84	33.56	22.29
BV at saturation point, mL solution/mL sorbent	918	805	1050	941
Degree of column utilization, %	83.02	80.52	76.92	81.20
Elution efficiency, %	99.9	99.9	99.9	99.9

CONCLUSION

The present study showed that FC and FHS are promising novel biosorbents for use in the recovery of Li from water. Sorption of Li was found to increase with the increase in the biosorbent amount and initial concentration. Equilibrium data were fitted to non-linear Langmuir and Freundlich models. The Langmuir isotherm model best described the equilibrium data for FC, while the Freundlich isotherm was relatively more suitable for FHS. The kinetics of the sorption process was found to complete in 3 minutes. No considerable effect is observed for the solution pH except pH 2, given that they can work in a wide range of pH. According to the results of the column-mode study, novel types of cellulose-based sorbents exhibited promising performance in the recovery of Li from water. It was considered that the breakthrough and total ion exchange capacities of the modified functional biosorbents were remarkable when they were compared with the Li-capable adsorbents that had been reported before.

Acknowledgment

This work was supported by The Scientific and Technological Research Council of Turkey (TUBITAK grant no 219M219). The authors express sincere appreciation to Assoc. Prof. Dr. Özgür Arar of Ege University, Chemistry Department, for his generous assistance. Additionally, gratitude is extended to the "Center for Materials Research" for conducting characterization analyses and the "Environmental Research and Development Center" for performing ICP-OES analyses at the Integrated Research Center of Izmir Institute of Technology.

REFERENCES

[1] W. T. Stringfellow and P. F. Dobson, Energies (Basel), 14 (2021) 6805.
[2] B. Swain, Sep. Purif. Technol., 2017, 172 (2017) 388–403.
[3] Y. Zhang, J. Liu, Y. Yang, S. Lin, P. Li, Sep. Purif. Technol., 267 (2021) 118613.
[4] V. Flexer, C. F. Baspineiro, C. I. Galli, Sci. Total Environ., 639 (2018) 1188–1204.
[5] J. Liu, Y. Zhang, Y. Miao, Y. Yang, P. Li, Ind. Eng. Chem. Res. 60 (2021) 16457–16468.
[6] T. Wesselborg, S. Virolainen, T. Sainio, Hydrometallurgy, 202 (2021) 105593.
[7] H. Peng and Q. Zhao, Adv. Funct. Mater., 31 (2021) 2009430.
[8] K. Yoshizuka, S. Nishihama, M. Takano, S. Asano, Solvent Extr. Ion Exch., 39 (2021) 604–621.
[9] M. R. Awual, M. M. Hasan, J. Iqbal, M. A. Islam, A. Islam, S. Khandaker, A. M. Asiri, M. M. Rahman, J. Environ. Chem. Eng., 8, (2020) 103591.
[10] Y. Lee, J. Cha, D. Jung, Chem. Asian J., 16 (2021) 974–980.
[11] T. Kitamura and H. Wada, Nippon Kaisui Gakkai-Shi, 32 (1978) 78–81.
[12] F. Qian, B. Zhao, M. Guo, Z. Wu, W. Zhou, Z. Liu, Sep. Purif. Technol., 256 (2021) 117583.
[13] K. Zhao, B. Tong, X. Yu, Y. Guo, Y. Xie, T. Deng, Chem. Eng. J., 430 (2022) 131423.
[14] F. Arroyo, J. Morillo, J. Usero, D. Rosado, H. El Bakouri, Desalination, 468 (2019) 114073.
[15] A. Çiçek, O. Yilmaz, Ö. Arar, J. Serb. Chem. Soc., 83 (2018) 1059–1069.
[16] X. Luo, B. Guo, J. Luo, F. Deng, S. Zhang, S. Luo, J. Crittenden, ACS Sustain. Chem. Eng., 3, (2015) 460–467.
[17] H. Günan Yücel, Z. Aksu, T. Usta, S. E. Karatay, G. Dönmez, Prep. Biochem. Biotechnol., 51 (2021) 892–900.
[18] K. Yabusaki, Google Patents September 28, 2010, Patent No: US 7,803,937 B2, (2010).

SELF-ASSEMBLY OF BENT-CORE MOLECULES AS A ROUTE TOWARDS FUNCTIONAL SOFT MATERIALS

N. Trišović

University of Belgrade, Faculty of Technology and Metallurgy, Karnegijeva 4, 11120 Belgrade, Serbia (ntrisovic@tmf.bg.ac.rs)

DOI: https://doi.org/10.46793/Phys.Chem24I.283T

ABSTRACT

Bent-core liquid crystals (BCLCs) represent a promising field of research in both materials chemistry and supramolecular chemistry. Emergence of new polar mesophases, induction of supramolecular chirality using achiral molecules and their significant ferroelectric and antiferroelectric properties have attracted considerable interest in these compounds [1]. Some of important aspects that determine the application of BCLCs include their transition temperatures, the mesophase range and the ability to control their morphology. Although a progress has been made in lowering the transition temperatures of these compounds, new BCLCs that meet the commercial temperature range are still needed. An additional factor limiting their application is related to bulk phase alignment, as the conventional procedures used for LCs are not applicable to these systems.

The ability to reversibly tune the material properties using an external stimulus is an important concept in materials science. Light is particularly interesting in this regard. It can be delivered remotely and momentarily, leading to dynamic supramolecular architectures that exist as long as the stimulus is applied. An attractive way to render BCLCs responsive to light involves incorporating a photoisomerisable chromophore such as the *trans*-azobenzene building blocks into their molecular structure. Exposure to UV light causes azobenzene to isomerize to the more polar *cis*-isomer, which induces metastable supramolecular arrangements that disintegrate in the dark within a few hours [2].

We present our contribution to the fundamental understanding of the structure–property relationship of the azo-containing BCLCs. Incorporating this photoisomerizable chromophore into BCLC design has provided access to new multifunctional materials where the polar response can be modulated by light. Azobenzenes with a strong push–pull configuration show very fast *cis-trans* isomerization kinetics even at room temperature [3]. Imparting control over structural features has led to novel photoswitchable materials with fast and efficient responses.

Acknowledgment

This work was supported by the Ministry of Science, Innovation and Technological Development of the Republic of Serbia (grant no 451-03-65/2024-03/200135).

REFERENCES

[1] J. Etxebarria, M. B. Ros, J. Mater. Chem. 18 (2008) 2919.
[2] S. Das, P. Ranjan, P. S. Maiti, G. Singh, G. Leitus, R. Klajn, Adv. Mater. 25 (2013) 422.
[3] J. García-Amorós, D. Velasco, Beilstein J. Org. Chem. 8 (2012) 1003.

TETRAKIS(4-METHOXYBENZENE)TIN(IV) IMMOBILISED INTO MCM-41 AND SBA-15 MESOPOROUS NANOSTRUCTURES

T. J. Becker [1,2], T. Krajnović [3], V. Gordić [3], S. Mijatović [3], D. Maksimović-Ivanić [3], E. Hey-Hawkins [2] and G. N. Kaluđerović [1]

[1] *Department of Engineering and Natural Sciences, University of Applied Sciences Merseburg, Eberhard-Leibnitz-Str. 2, 06217 Merseburg, Germany (til_julian.becker@stud.hs-merseburg.de)*
[2] *Faculty of Chemistry and Mineralogy, Institute of Bioanalytical Chemistry, Leipzig University, Deutscher Platz 5, 04103 Leipzig, Germany*
[3] *Institute for Biological Research "Siniša Stanković", National Institute of the Republic of Serbia, University of Belgrade, Bulevar despota Stefana 142, 11108 Belgrade, Serbia*

DOI: https://doi.org/10.46793/Phys.Chem24I.285B

ABSTRACT

Tetraaryltin(IV) compounds are suitable compounds to replace platinum-based chemotherapeutics since they provide promising *in vitro* results. To further decrease toxicity and side effects, passive drug targeting *via* nanostructures can be utilised, since tumour tissues provide the ability to accumulate bigger particles than healthy ones. In this study, tetrakis(4-methoxybenzene)tin(IV) (**1**) is immobilised in two mesoporous silica nanostructures (MCM-41|**1** and SBA-15|**1**), which are synthesised and characterised herein. Employing MTT and CV assays, the antitumour activity of the organotin(IV) compound against human (A375) and murine (B16) melanoma cells, as well as human (HCT116) and murine (CT26) colon cancer cells is observed for its free form and when loaded into MCM-41 and SBA-15. MCM-41|**1** showed even higher activity than **1** alone against all investigated tumour cells (MC_{50} obtained by CV, MTT: 2.0 – 4.3 µg/mL).

INTRODUCTION

With cancer still being one of the leading causes of death worldwide, advancements in cancer treatments persist. While cisplatin and other platinum-based drugs stand out as chemotherapeutic agents with broad efficacy against malignant tissues, they lead to several side effects which are caused by their systemic interaction, ranging from nephrotoxicity to neurotoxicity [1]. To address these limitations and enhance the therapeutic outcome, novel metal-based compounds are developed and investigated, among them organotin(IV) compounds [2].

Demonstrating high anticancer activity against malignant tissues, organotin(IV) compounds are promising candidates for cancer treatment [3]. To enhance their activity, they can be incorporated into mesoporous silica nanostructures (MSN). With cancerous tissues exhibiting enhanced permeability and retention time towards bigger structures, biological inactive MSN can be utilised as drug delivery systems to address those tissues *via* passive drug targeting, allowing the compound to interact with the malignant tissue on a local way to reduce chemotherapy-associated side effects [4].

Herein, an organotin(IV) compound, namely tetrakis(4-methoxybenzene)tin(IV) (**1**), already known in the literature [5], is immobilised in two different MSN materials (MCM-41 and SBA-15) and tested *in vitro* in its free and immobilised form, to examine the anticancer potential.

METHODS

Reactions were performed under nitrogen atmosphere using standard Schlenk technique, unless otherwise stated. Tetrahydrofuran (THF) was degassed, distilled over potassium and stored under activated 4 Å molecular sieves. 4-Methoxybromobenzene (Sigma Aldrich), tin(IV) chloride ((Sigma Aldrich), magnesium shavings (TCI), L-menthol, 1,10-phenanthrolin, tetraethylorthosilicate (TEOS, Sigma Aldrich), P123 polymer and cetrimonium bromide (CTAB) were used as purchased. NMR spectra were recorded on a Bruker AVANCE DRX 400 spectrometer and measured in $CDCl_3$ (stored over activated 4 Å molecular sieves). ^{1}H (400.131 MHz), ^{13}C (100.63 MHz), ^{119}Sn (149.2 MHz) and 2D NMR spectra are referenced to deuterated solvent residual shifts (^{1}H and ^{13}C NMR) or to external standard (^{119}Sn NMR, $SnPh_4$). The chemical shifts δ are reported in parts per million (ppm). Elemental analysis was carried out with a Heraeus VARIO EL oven. A VEGA3 was used for scanning electron microscopy (SEM) images, as well to determine the immobilisation yield via energy-dispersive X-ray spectroscopy (EDX). Nitrogen isotherms were measured on an Autosorb iQ/ASiQwin.

1 was synthesised according to the literature [5]. Yield: 0.438 g (34%). ^{1}H NMR (400 MHz, $CDCl_3$): δ [ppm] = 7.51–7.47 (m, 8H, *o-H*), 6.97–6.92 (m, 8H, *m-H*), 3.81 (s, 12H, O*CH*$_3$). $^{13}C\{^{1}H\}$ NMR (101 MHz, $CDCl_3$): δ [ppm] = 160.4 (*p-C*, $^{4}J(^{13}C\text{-}^{119}Sn)$ = 11.7 Hz), 138.3 (*o*-C, $^{2}J(^{13}C\text{-}^{119}Sn)$ = 42.9 Hz), 128.8 (*ipso-C*, $^{1}J(^{13}C\text{-}^{119}Sn)$ = 541 Hz), 114.5 (*m-C*, $^{3}J(^{13}C\text{-}^{119}Sn)$ = 55.3 Hz), 55.0 (O*C*H$_3$). ^{119}Sn NMR (149 MHz, $CDCl_3$): δ [ppm] = –116.0. Elemental analysis: Found: C, 61.14; H, 5.14. Calc. for $C_{28}H_{28}O_4Sn$: C, 61.46; H, 5.16.

SBA-15 and MCM-41 were prepared according to known procedures, with slight modification for the latter [6,7]. To synthesise MCM-41 particles, CTAB (3.5 g) is dissolved in distilled water (1680 mL) in a 2 L three headed round bottom flask, stirring over night at room temperature to reach a clear, foamless solution. After reaching reaction conditions (80 °C), NaOH (2 M, 12.25 mL) is added to the mixture, followed by slow addition of TEOS (17.5 mL) over 15 min while stirring vigorously. After addition, the mixture is stirred for 2 h. The mixture is filtered while still hot and the remaining precipitate washed with distilled water and EtOH, respectively. The resulting white solid is dried in an oven for 16 h (90 °C) and later the surfactant is removed *via* calcination (550 °C, heating rate 1 °C min^{-1}) for 5 h to give mesoporous silica MCM-41. Yield: 3.8 g; BET surface: 1036 m^2 g^{-1}.

For the synthesis of SBA-15, in a 2 L three headed round bottom flask, P123 (24 g) is dissolved in a mixture of distilled water (180 mL) and HCl (2 M, 700 mL). The mixture is heated to 35 °C. When no longer chunky, TEOS (51 g) is added dropwise and the mixture is stirred vigorously for 20 h, then for 24 h at 80 °C. Particles are filtered and washed with distilled water and dried in an oven for 16 h (90 °C). Afterwards, particles are calcined (500 °C, heating rate 1 °C min^{-1}) for 24 h. Yield: 16.6 g; BET surface: 678 m^2 g^{-1}.

For the immobilisation of the organotin(IV) compound into MCM-41 and SBA-15, respectively, a literature procedure was followed [8]. Freshly ground compound **1** (0.2 mol) is added as a solution in dry toluene (30 mL) to activated MCM-41 or SBA-15 (0.2 g, vacuum, 150 °C, 16 h) and stirred for 48 h (80 °C). After filtration *via* a P4 frit, the solid material is washed with toluene (2×10 mL) and n-pentane (3×10 mL) and the loaded MSN dried at room temperature.

MCM-41|**1**: 109 mg of **1**, 200 mg of MCM-41; yield: 268 mg.

SBA-15|**1**: 109 mg of **1**, 200 mg of SBA-15; yield: 212 mg.

Tumour cell lines were cultivated in HEPES-buffered (4-(2-hydroxyethyl)-1-piperazineethanesulfonic acid) RPMI-1640 medium supplemented with 10% heat-inactivated fetal bovine serum (Capricorn Scientific GmbH, Hessen, Germany) and antibiotics (100 U/mL penicillin and 100 µg mL^{-1} streptomycin) (Biological Industries, Cromwell, USA). Cells were grown at 37 °C in a humidified atmosphere with 5% CO_2. Prior to cell passaging and seeding, cells were washed

with phosphate-buffered saline (Sigma-Aldrich, St. Louis, USA) and detached by using 0.05% trypsin/0.02% EDTA (Capricorn Scientific GmbH, Hessen, Germany). All tumour cells were exposed to a wide range of concentrations of tested compounds for 72 h, followed by cell viability assessment using MTT (3-(4,5-dimethylthiazol-2-yl)-2,5-diphenyltetrazolium bromide, AppliChem, St. Louis, MO, USA) and CV (crystal violet, Sigma-Aldrich, St. Louis, USA) assays, as previously reported [2,3]. Tetrakis(4-methoxybenzene)tin(IV) (**1**) stock solution was prepared in DMSO at a concentration of 20 mM and stored at -20 ºC. Stock solutions (2 mg mL^{-1}) of immobilised forms as well as all working concentrations were freshly made in a culture medium before every usage.

RESULTS AND DISCUSSION

Complex **1** is already described in the literature [5]. It could be confirmed with time-resolved ^{1}H NMR spectroscopy that the compound is stable in water containing DMSO for 7 days. Mesoporous silica nanostructures were synthesised according to the literature and characterised with SEM (**Figure 1.A** and **B**) and BET isotherms (**Figure 1.C**).

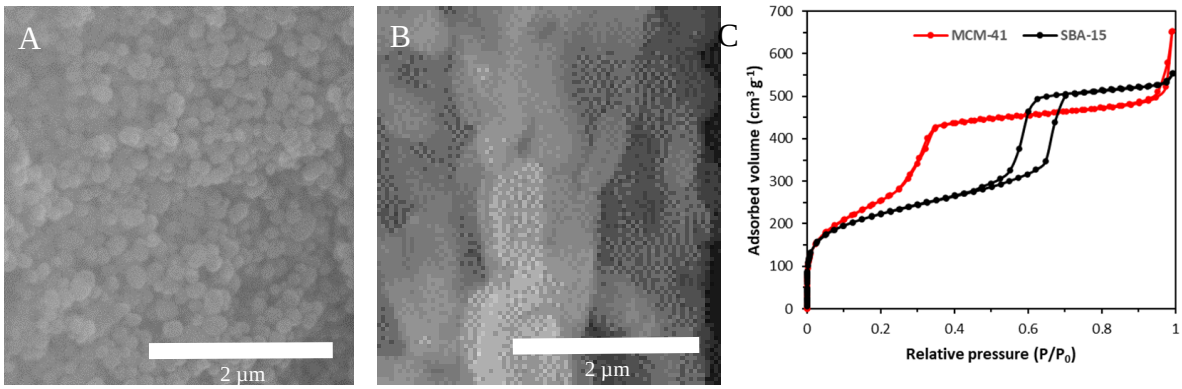


Figure 1. SEM of (**A**) spherical MCM-41 particles (100-200 nm) and (**B**) rod shaped SBA-15 particles (600-800 nm), showing typical particles sizes. (**C**) N_2 adsorption-desorption isotherms for MCM-41 (red) and SBA-15 (black).

Nitrogen adsorption-desorption isotherms of both MSNs can be assigned to type IV isotherms, which is characterised by capillary pore condensation [9]. Noticeable is that isotherms for SBA-15 provide hysteresis, but not for MCM-41. For MCM-41 nanostructures with pore sizes smaller than 4 nm an absence of hysteresis has been reported before [10]. In this case, the nanostructures provide an average pore radius of 1.6 nm, explaining the absence of hysteresis.

Loading of **1** into nanostructures was further confirmed by EDX measurements. The compound was successfully loaded into the nanostructures with encapsulation efficiencies of 79.7% (SBA-15) and 93.1% (MCM-41), giving concentrations of 0.41 and 0.38 *wt*%, respectively.

The prepared MSNs as well as free complex **1** have been investigated *in vitro* using MTT and CV assays. The anticancer activities of **1** alone and when immobilised into MCM-41 and SBA-15 nanoparticles, were determined on a panel of four tumour cell lines: human (A375) and murine (B16) melanoma cells, as well as human (HCT116) and murine (CT26) colon cancer cells (**Table 1**). Compound **1** showed moderate activity against selected tumour cells. However, the discrepancy between MTT and CV results suggests that cell respiration was affected. SBA-15|**1** was found to exhibit low or no activity, while MCM-41 MSNs enhanced the activity of **1**. Contrary to **1** alone, the MC_{50} values for MCM-41|**1** obtained from MTT and CV assays were in agreement, suggesting that the mechanism of action may be modulated by using MSNs.

Table 1. Inhibitory concentrations: IC_{50} (μM) for **1**; MC_{50} (μg mL^{-1}) for MCM-41|**1** and SBA-15|**1** on melanoma and colon cancer cell lines calculated from MTT and CV assays. The values represent SV ± SD of three independently performed experiments.

Compound	Viability assay	Cell line			
		A375	**B16**	**HCT116**	**CT26**
1	MTT	10.7 ± 3.4	27.4 ± 7.14	11.7 ± 0.78	3.9 ± 1.06
	CV	22.5 ± 2.76	41.6 ± 3.04	28.5 ± 4.53	12.5 ± 0.00
MCM-41|**1**	MTT	2.0 ± 0.21	3.5 ± 0.92	2.3 ± 0.28	2.2 ± 0.14
	CV	2.7 ± 0.07	4.3 ± 0.85	3.7 ± 0.28	3.2 ± 0.71
SBA-15|**1**	MTT	> 100	> 100	40.2 ± 3.11	> 100
	CV	> 100	> 100	69.5 ± 4.45	> 100

CONCLUSION

Tetrakis(4-methoxybenzene)tin(IV) (**1**) was immobilised in SBA-15 and MCM-41 MSNs. Materials are characterised with SEM, BET and EDX, confirming loading with 0.75 (SBA-15|**1**) or 0.69 mmol (MCM-41|**1**) of **1** per g SiO_2. MCM-41 enhanced the activity of **1** and modulated its mechanism of action against melanoma A375 and B16 as well as colon cancer HCT116 and CT26 cells.

Acknowledgment

This work was supported by the Landesgraduiertenstipendium, German Academic Exchange Service DAAD PPP (Project number: 57704188) and Ministry of Science, Technological Development and Innovation of the Republic of Serbia (grant No 451-03-66/2024-03/20007).

REFERENCES

[1] F. Tixier, F. Ranchon, A. Iltis, N. Vantard, V. Schwiertz, E. Bachy, F. Bouafia-Sauvy, C. Sarkozy, J. F. Tournamille, E. Gyan, G. Salles, C. Rioufol, Hematol. Oncol. 35 (2017) 584–590.
[2] N. Đ. Pantelić, B. Božić, B. B. Zmejkovski, N. R. Banjac, B. Dojčinović, L. A. Wessjohann, G. N. Kaluđerović, Molecules 26 (2021) 3199.
[3] M. Z. Bulatović, D. Maksimović-Ivanić, C. Bensing, S. Gómez-Ruiz, D. Steinborn, H. Schmidt, M. Mojić, A. Korać, I. Golić, D. Pérez-Quintanilla, M. Momčilović, S. Mijatović, G. N. Kaluđerović, Angew. Chem. Int. Ed. 53 (2014) 5982–5987.
[4] A. Watermann, J. Brieger, Nanomaterials 7 (2017) 189.
[5] Y. Liu, C. Wang, L. Huang, D. Xue, Synlett 31 (2020) 1613–1618.
[6] Z. Tao, Y. Xie, J. Goodisman, T. Asefa, Langmuir 26 (2010) 8914–8924.
[7] M. Mladenović, I. Morgan, N. Ilić, M. Saoud, M. V. Pergal, G. N. Kaluđerović, N. Ž. Knežević, Pharmaceutics 13 (2021) 460.
[8] I. Predarska, M. Saoud, D. Drača, I. Morgan, T. Komazec, T. Eichhorn, E. Mihajlović, D. Dunđerović, S. Mijatović, D. Maksimović-Ivanić, E. Hey-Hawkins, G. N. Kaluđerović, Nanomaterials 12 (2022) 3767.
[9] M. Thommes, K. Kaneko, A. V. Neimark, J. P. Olivier, F. Rodriguez-Reinoso, J. Rouquerol, K. S. W. Sing, Pure Appl. Chem. 87 (2015) 1051–1069.
[10] R. Schmidt, M. Stöcker, E. Hansen, D. Akporiaye, O. H. Ellestad, Microporous Mat. 3 (1995) 443–448.

EXPLORING SURFACE EFFECTS IN HOLLOW IRON OXIDE NANOPARTICLES

S. Slimani[1,4], M. Vasilakaki[2], K.N. Trohidou[2], N. Yaacoub[3], and D. Peddis[1,4]

[1]*Department of Chemistry and Industrial Chemistry & Genova, INSTM RU, nM2-Lab, University of Genova, 16146 Genova, Italy.*
[2]*Institute of Nanoscience and Nanotechnology, NCSR "Demokritos", 15310 Agia Paraskevi, Attiki, Greece.*
[3]*Institut Des Molécules Et Matériaux du Mans (IMMM) CNRS UMR-6283, Le Mans Université, Avenue Messiaen, 72085, Le Mans, France.*
[4]*Institute of Structure of Matter, National Research Council, nM2-Lab, Via Salaria km 29.300, Monterotondo Scalo 00015, Roma, Italy.*

DOI: https://doi.org/10.46793/Phys.Chem24I.289S

ABSTRACT
The large surface-to-volume ratio (R=S/V) in the nanoparticles is proving to be a key factor for the novel physical, chemical, and magnetic properties compared to those of the corresponding bulk material. The possibility to synthesize spherical hollow magnetic nanoparticles allows R to be further enhanced with a consequent increase of the disorder and magnetic frustration, thus opening new perspectives to explore the surface magnetism at the nanoscale. In this context, here we present a comparative study of the morpho-structural and magnetic properties of full and hollow maghemite (γ-Fe_2O_3) nanoparticles (NPs), characterized by a big surface to volume ratio, of corresponding sizes 5.0(5) nm and 7.4(7) nm. These systems have been thoroughly characterized by means of DC magnetization measurement and in field ^{57}Fe Mössbauer spectrometry. The in-field hyperfine structure analysis suggested the presence of non-collinear structure for hollow NPs originated from the increased surface role due to the hollow morphology. Interestingly, an exchange bias effect was noted in the hollow structure, which is demonstrated by the recorded shifted M(H) hysteresis loop curve after field cooling. Monte Carlo (MC) simulations on ferrimagnetic hollow nanoparticles unambiguously corroborate the critical role of the surface. MC simulation results show that the spins in the external thicker surface and at the interface are strongly exchange coupled. This strong exchange coupling enhances the antiferromagnetic character of the hollow particle leading to the decrease of its M_s. At the interface, this strong spin exchange coupling results in an exchange bias field and in the enhancement of the coercive field, in agreement with the experimental results.

INTRODUCTION

Magnetic nanoarchitectures have spurred a growing interest due to their unique physical properties, including hollow nanoparticles (HNPs). These systems are characterized by their large surface-to-volume ratios, low density, and double surfaces. Such attributes make them suitable for a variety of applications, including energy storage (e.g., lithium-ion batteries), targeted drug delivery, diagnostics, gas sensing, and catalysis[1].

On the other hand, iron-oxide nanoparticles have been the materials of choice due to their substantial magnetic moments, biocompatibility, and established synthesis methods. These methods provide consistent results, with narrow size distributions and precise control over shape and size. The magnetic properties of ferrite nanoparticles have been extensively studied in solid spherical forms over the past two decades. However, the surface effect and the magnetic property in hollow nanoparticles is still relatively underdeveloped. The hollow structure amplifies surface-driven

effects due to the presence of inner and outer surfaces and increased anisotropy compared to their full counterparts of similar size. Furthermore, the interaction between components within the internal structure of the hollow shell adds to the system's complexity, offering new challenges and opportunities for research in this field.

In this context, in our study we investigate deeply the effect of surface in hollow structure on the static and dynamic magnetic behavior of a 7.4 (7) nm ensemble of Fe_3O_4 hollow nanoparticles. Our experimental observations, complemented by Monte Carlo simulations (MC) [2], reveal that spins in the external thicker surface and at the interface are strongly exchange coupled. This coupling leads to a decrease in the saturation magnetization (enhances the antiferromagnetic character), as well as the presence of an exchange bias phenomenon.

METHODS

The synthesis of HNPs was carried out using Template-free method, the Kirkendall effect, (i.e. the different diffusion velocity of the ions at the interface between two materials)[3]. In brief, oleylamine (0.003 mol) was dissolved in octadecene (10 mL) at room temperature and under vigorous magnetic stirring. The solution was then degassed under an argon atmosphere at 120 °C for 30 minutes. Following this, the temperature of the reaction mixture increased to 220 °C. At this point, $Fe(CO)_5$ was introduced into the mixture, which was maintained at the same temperature for 20 minutes. The obtained hollow nanoparticles were morpho-structurally characterized with Transmission electron microscopy (TEM) and X-ray diffractogram respectively. Field and temperature dependence of magnetization measurements up to 5 T were carried out using Quantum Design physical property measurement system (PPMS) equipped with VSM option. For the magnetization versus temperature measurements, the Zero Field Cooled (ZFC), Field Cooled (FC) protocols were used. To perform ZFC measurements the sample was first cooled from room temperature down to 5 K in zero field; then the magnetization (MZFC) was recorded warming up from 5 to 300 K, under a static applied magnetic field, while the MFC was recorded during the subsequent cooling from 300 down to 5 K.

The magnetic structure of our samples was investigated by using ^{57}Fe Mössbauer spectrometry. Mössbauer spectra were obtained using a $^{57}Co/Rh$ γ-ray source mounted on an electromagnetic transducer with a triangular velocity form. Mössbauer spectra were recorded at 11 K under external magnetic field of 8 T oriented parallel to the γ-beam. The samples consist of a thin layer containing about 5mg Fe/cm^2 of the powdered compound located in a sample holder. The hyperfine structure was modeled by means of a least-square fitting procedure involving Zeeman sextets composed of Lorentzian or Gaussian lines using program ‘MOSFIT’.

RESULTS AND DISCUSSION

The effect of the large surface area of HNPs originated from inner and outer surface contributions strongly influences the magnetic structure. Indeed, hollow nanoparticles do exhibit a large spin disorder. The spin noncollinearity was clearly established from the shape of the in-field Mössbauer spectrum. It consists of two rather well split sextets but with broadened lines as well as large intensities for the intermediate lines (2 and 5). The fitting of the experimental spectrum was reproduced by means of two components, each one involving a distribution correlating the effective fields with the angles for each component, giving rise thus to 2 distributions of hyperfine fields. The distribution of hyperfine field corresponding to the octahedral site is found larger than that of the tetrahedral site, as well as that of the spin canting angle θ. Contrary to the collinear ferrimagnetic structures expected in spinel iron oxides, the evidence of a distribution of canting angles, consistently with a noncollinear magnetic structure indicates that the hollow morphology of the present nanoparticles enhances the surface contribution and consequently the magnetically

disordered structure. The results of Monte Carlo simulation highlighted the role of the additional surface and confirmed the picture described by magnetic measurements (**Figure 1**) that shows the increase in the coercive field (Hc= 0.04(1) T) and a decrease in the saturation magnetization (~30 Am^2Kg^{-1}), compared to full particles. In addition, the field dependence of magnetization at low temperature and field cooled 2 T shows an evident horizontal shift, indicating the presence of interface exchange coupling (IEC) in hollow sample. The M vs. H curves of the HNPs sample were examined for the presence of IEC effects. The presence of IEC would be evidence for the presence of disordered spin glass states at the surface of the particle, which could have useful applications in data storage in which IEC effects are widely exploited. This was done at a variety of applied fields, and at different temperatures. Analysis of the obtained results reveals that the application of larger fields (>0.5 T) does not increase the effect, suggesting that source of IEC that it may not just due to the surface area. While a comparison study with full particles with approximately the same size displays no IEC at all, despite the high surface to volume ratio in this case. The effect of temperature on H_{IEC} under a constant 2 T applied field was also studied. The results are as would be expected, with the effect dropping rapidly with increased temperature, due to thermal energy disrupting the coupling. This is also in agreement with MC that shows the strong anisotropy of the hollow nanoparticles combined with the strong interface coupling induces a strong exchange bias effect and enhanced coercive field.

On the other hand, a decrease in the saturation magnetization (M_S) of HNPs was also reported. The origin of the decrease in theM_S, increase in $H_C$and the interface exchange coupling can be explained by the fact that the spins in the external thicker surface and at the interface are strongly exchange coupled, which enhances the antiferromagnetic character of the hollow particle. All these features could be correlated and attributed to the large surface-to-volume ratio R, which is strongly enhanced in the case of hollow nanoparticles morphology.

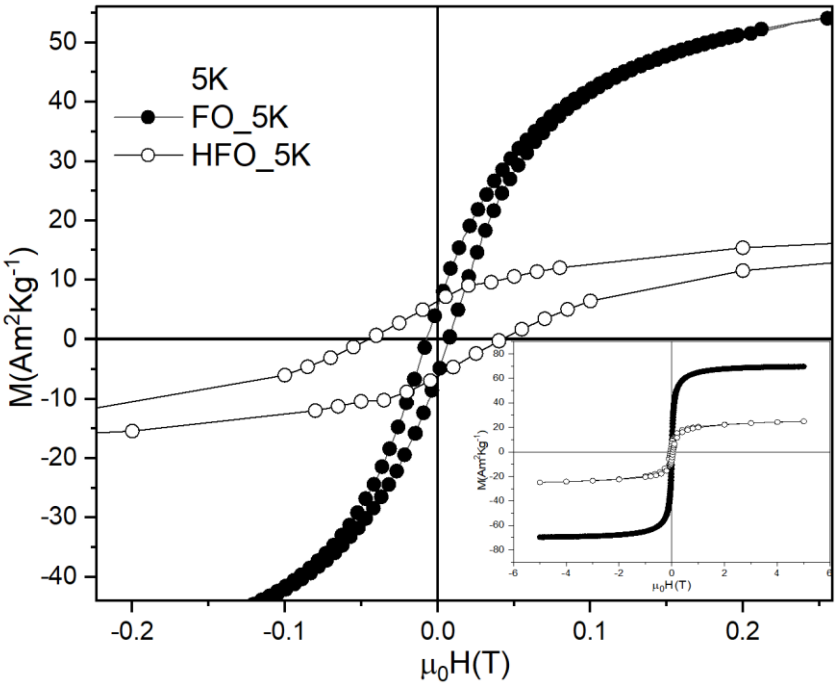


Figure 1. M vs H curves measured at 5 K for full and hollow spinel iron oxide nanoparticles.

CONCLUSION

To the best of our knowledge, we are the first to report a comparative study on both full and hollow nanoparticles, with a particular attention to the correlation between magnetic structure and magnetic properties in a system of hollow nanoparticles. These results were deduced from different experimental characterization techniques including Mössbauer spectrometry, which have shown that it is a relevant technique in identifying the magnetic structure, in addition to the results obtained from other techniques as PPMS magnetometer. The results focused on the effect of enhanced surface on the magnetic structure: large spin canting angle obtained from Mössbauer results, reduction of magnetization, significant coercivity, and exchange bias field in HNPs compared to full NPs. All this can be attributed to the presence of spin disorder in such kind of nanoparticles.

REFERENCES

[1] F. Sayed et al., J. Phys. Chem. C.,122 (2018) 7516–7524.
[2] A. Lappas et al., Phys. Review X., 9 (2019) 41044.
[3] M.-Y. Liao et al., J. Mater. Chem., 22 (2011) 7974.

SYNTHESIS OF ZEOLITIC IMIDAZOLATE FRAMEWORK-8 (ZIF-8) IN TIME-PROGRAMMED MANNER AND SOLID HYDROGELS

N. Német [1,2], G. Holló [1,3,4], S. Farkas [1], G. Schuszter [5], N. Valletti [6], F. Rossi [6] and I. Lagzi [1,3]

[1] *Department of Physics, Institute of Physics, Budapest University of Technology and Economics, Műegyetem rkp. 3., Budapest H-1111, Hungary (nnorbert141@gmail.com)*
[2] *Department of Organic Chemistry and Technology, Budapest University of Technology and Economics, Műegyetem rkp. 3., Budapest H-1111, Hungary.*
[3] *HU-REN–BME Condensed Matter Physics Research Group, Budapest University of Technology and Economics, Műegyetem rkp. 3., Budapest H-1111, Hungary.*
[4] *Department of Fundamental Microbiology, University of Lausanne, Biophore Building, Lausanne 1015, Switzerland.*
[5] *Department of Physical Chemistry and Materials Science, University of Szeged, Rerrich Béla tér 1., Szeged H-6720, Hungary.*
[6] *Department of Physical Sciences, Earth and Environment, University of Siena, piazzetta Enzo Tiezzi 1., Siena 53100, Italy.*

DOI: https://doi.org/10.46793/Phys.Chem24I.293N

ABSTRACT

One of the most widely used techniques for generating crystalline materials is wet synthesis. In this procedure, the reagents are mixed, and crystals form due to the nucleation and growth processes. In crystal growth and engineering, the most crucial is the temporal control of the processes over time to obtain samples with a desired average size and dispersity. Here, we review recent alternative methods for the synthesis of the zeolitic imidazolate framework-8 (ZIF-8). We present the chemically coded time-programmed method driven by a clock reaction. Additionally, we highlight the advantage of the application of a gel reactor utilizing diffusion and ionic migration driven by a direct electric field.

INTRODUCTION

Metal-organic frameworks (MOFs) are crystalline materials of metal ions coordinated to organic ligands to form one-, two-, or three-dimensional structures. ZIF-8 is a well-known member of the zeolitic imidazolate frameworks (ZIFs), a subclass of MOFs. ZIF-8 is highly regarded for its exceptional structural stability, high porosity, and customizable chemical properties, making it a potential candidate for various applications. [1] [2] It comprises zinc ions (Zn^{2+}) coordinated with 2-methylimidazole (2-met) ligands, creating a three-dimensional framework with a zeolite-like topology. The structure of ZIF-8 features large pores and a high surface area, typically around 1500–2000 m^2/g, which enable the adsorption and storage of various gases and molecules.

Various methods are available for generating MOFs, each with its own advantages and limitations. The most common methods are solvothermal and hydrothermal techniques. [3] These methods involve dissolving metal salts and organic linkers in a solvent and crystallization under controlled temperature and pressure conditions. They are popular due to their simplicity and ability to produce MOF crystals, even on an industrial scale.

In recent years, alternative synthesis approaches have emerged. [3] For example, microwave-assisted synthesis uses microwave radiation to rapidly heat the reaction mixture, reducing synthesis time and often improving crystallinity. A mechanochemical synthesis is a solvent-free approach that uses mechanical force to induce chemical reactions, offering a greener and more sustainable route

to MOF production. Electrochemical synthesis utilizes an electric current to drive the formation of MOFs, generating metal cations in the system. Sonochemical synthesis employs ultrasonic waves to accelerate reactions, facilitating the rapid formation of MOF crystals.

The choice of synthesis method can significantly influence the physical and chemical properties of MOFs. Therefore, understanding the principles and techniques of MOF synthesis is essential in material design and engineering. This study briefly summarizes the results achieved in synthesizing ZIF-8 crystals in a time-programmed autonomous way using the sulfite–formaldehyde clock reaction and utilizing the reaction and mass transport (diffusion and ionic migration) of the reagents in a solid hydrogel.

METHODS

Time-programmed experiments were conducted in a batch system using a glass cuvette. This was achieved by combining four solutions to obtain specific concentrations of reagents in the reactor: (i) sodium sulfite/sodium bisulfite buffer ($[SO_3^{2-}]_0$ = 5–60 mM, $[HSO_3^-]_0$ = 1200 mM); (ii) 2-met solution (100 mM); (iii) zinc sulfate solution (2 mM), and (iv) formaldehyde solution (1200 mM). During the process, the reactor was continuously stirred using a magnetic stirrer, and the process was monitored by recording pH and the turbidity (using a UV-Vis spectrophotometer at λ = 600 nm) change at room temperature (22 ± 0.5 °C). [4]

The hydrogel reactor for the diffusion synthesis was prepared using the following protocol. Agarose powder and zinc ions were dissolved in a mixture of distilled water and *N*,*N*-dimethylformamide (DMF). The mixture was continuously stirred using a magnetic stirrer at an elevated temperature until the agarose was completely dissolved. Then, the solution was gently poured into test tubes. The gelation process occurred in a refrigerator at ~ 5 °C. After gelation (~ 24 hours), the gel column was allowed to rest for 1 hour at room temperature. Next, a solution of 2-met, dissolved in a mixture of distilled water and DMF, was gently poured on top of the solid hydrogel column. All experiments were conducted at room temperature (22 ± 0.5°C) for one week. After one week, all test tubes were photographed, and the formed ZIF-8 crystals were extracted from the gel matrix and investigated using scanning electron microscopy (SEM) measurements. [5]

In experiments utilizing ionic migration of the charged chemical species, applying a direct electric field, agarose powder and 2-met were dissolved in a mixture of distilled water and DMF with a 1:1 ratio containing 1 mM of potassium nitrate as an inert conductive salt in the experiments. The gel preparation was the same as described in diffusion experiments. The hot gel solution was placed in a U-shaped glass tube. After the gelation, the solutions containing zinc acetate and 2-met (dissolved in a mixture of water and DMF) were placed on top of the gel surfaces. Platinum wires were used as electrodes, and positive and negative electrodes were placed in the solutions of the zinc ions and 2-met, respectively. The galvanostatic condition was applied in the experiments. All experiments were conducted at room temperature (22 ± 0.5°C) for four days. We also carried out control experiments in the absence of an electric field. [6]

RESULTS AND DISCUSSION

The autocatalytic reaction began in an acidic environment, where ZIF-8 formation did not occur. However, when the pH became alkaline, the formation of ZIF-8 crystals started, as shown by the increasing turbidity of the samples (**Figure 1 a** and **b**). As the pH continued to increase, the turbidity changed further. Once the pH reached a steady level, the turbidity stopped increasing (depending on the sulfite concentration), indicating that the formaldehyde-sulfite clock reaction initiated the formation of ZIF-8. The induction time varied from 7 to 22 seconds depending on the initial concentration of the reagents. A higher sulfite concentration resulted in a shorter initiation period and a quicker appearance of ZIF-8 particles. Since the synthesis of ZIF-8 is pH-dependent,

the start of ZIF-8 particle formation can be controlled autonomously. To examine the shape and crystalline structure of the synthesized ZIF-8 crystals, we used scanning electron microscopy (SEM) and observed the formation of dodecahedral ZIF-8 crystals (**Figure 1 c**).

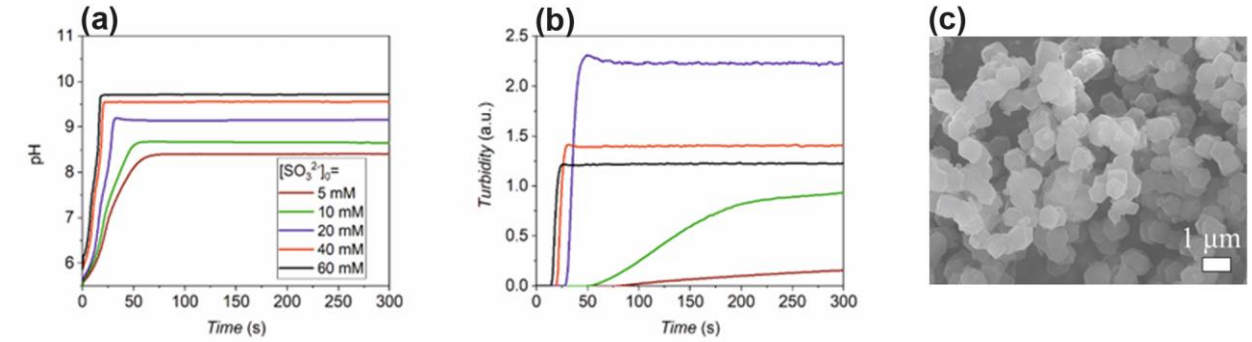


Figure 1. The time-programmed synthesis of ZIF-8 crystals using the formaldehyde−sulfite reaction, (a) pH and (b) turbidity change in the presence of zinc ions (2 mM) and 2-met (100 mM) using various initial sulfite concentrations (5, 10, 20 40, and 60 mM). (c) SEM micrographs of a sample of the synthesized ZIF-8 crystals using the formaldehyde−sulfite clock reaction using 20 mM of sulfite. The figures are reproduced from Ref [4].

In a typical experiment utilizing diffusion of the reagents, the metal ions were homogeneously distributed in the agarose gel in test tubes. After the solution of 2-met was poured on top of the gel column, the reaction started, and a white precipitation zone formed near the liquid-gel interface. The formation of the ZIF-8 crystals continued and evolved to the generation of periodic precipitation of ZIF-8 (**Figure 2a**). The SEM measurements revealed the formation of crystals with a size greater than 1 µm, and at the end of the gel column, the size of ZIF-8 particles reached 10 µm, greater than the size of the crystals generated in wet synthesis methods.

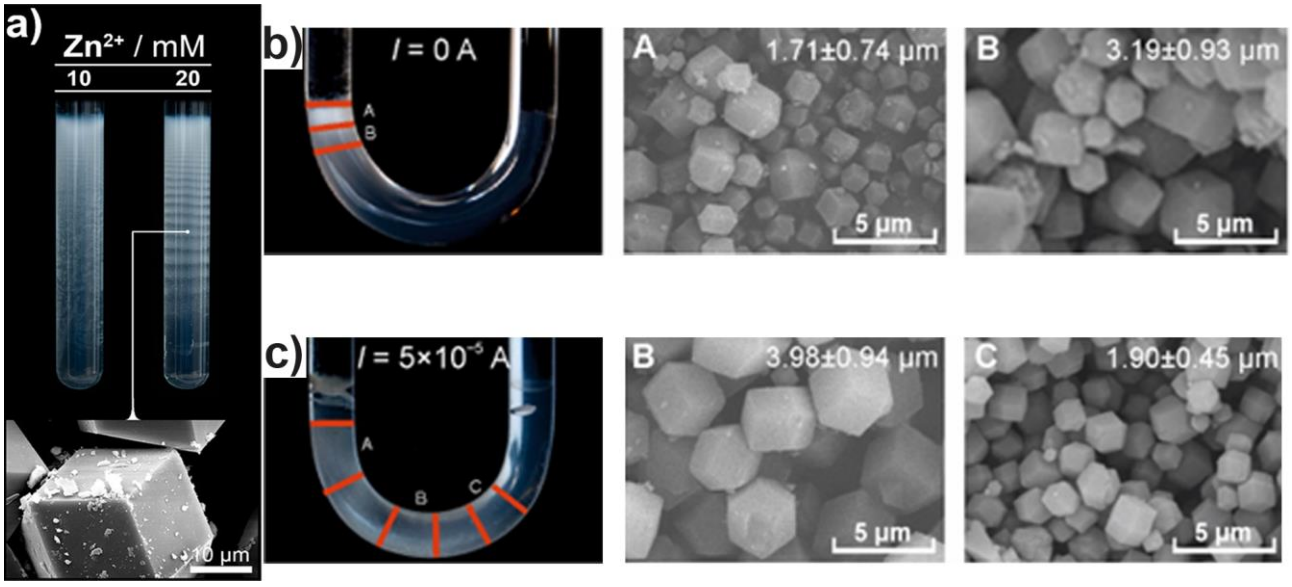


Figure 2. Pattern formation in ZIF-8 system. (a) The pattern of ZIF-8 particles in a 1% m/v agarose gel, and the SEM micrographs of the produced crystal extracted from the solid gel. Patterns of ZIF-8 and SEM micrographs of the crystals in a 1% m/v agarose gel in the absence (b) and presence (c) of an electric field. The figures are reproduced from Refs [5] and [6].

To show the magnificent power of the mass-transport-driven synthesis methods, we carried out experiments facilitating the mass transport of the charged species using a direct electric field. The precipitation process always starts near the interface between the liquid and the gel on the anodic side. In the absence of an electric field (I = 0), the ZIF-8 continuously forms from the liquid-gel interface on the anodic side. Meanwhile, the size and distribution of ZIF-8 particles increased along the diffusion path (Figure 2b), which is consistent with observations in other reaction-diffusion systems. Two things happened when we increased the electric current ($I = 5\times10^{-5}$ A). First, the length of the precipitation zone increased, likely due to enhanced ionic migration of zinc ions toward the cathode. Second, a precipitation-free zone appeared near the anode side (Figure 2c). The electric field influenced the shape of the formed particles. When applying an electric field, the size of the particles decreased, and the dispersity of the samples became lower. This unexpected behavior contrasts with trends observed in reaction-diffusion systems. In a pure reaction-diffusion scenario, higher supersaturation near the liquid-gel interface results in smaller particles with higher particle concentrations. However, farther from the liquid-gel interface, lower supersaturation creates larger particles with lower particle concentrations. In an electric field, enhanced mass transport of the zinc ions can create higher supersaturation in segments farther from the liquid-gel interface, generating small particles. Under moderate electric currents, we found an optimal value ($I = 5\times10^{-5}$ A), resulting in ZIF-8 particles with an average size of ~ 4 μm. This size is twice as large as observed in cases involving only diffusion.

CONCLUSION

Using a formaldehyde-sulfite clock reaction, we demonstrated an autonomous time-programmed method for synthesizing ZIF-8. The novelty of our approach is that the delay in the onset of the ZIF-8 formation can be controlled by adjusting the initial concentration of one reagent in the chemical clock. The autonomously synthesized ZIF-8 exhibited excellent morphology and crystallinity. Mass transport of chemical species is widely used to control and engineer particles and chemical structures. Diffusion and electric field affect the flux of chemical species in the system, influencing nucleation and crystal growth. Therefore, control of mass transport of the chemical species can be used to tune the morphology, average size, and size distribution of the ZIF-8 crystals.

Acknowledgment

This work was supported by the National Research, Development and Innovation Office of Hungary (K146071), the HUN-REN Hungarian Research Network, the Ministry of Culture and Innovation, and the National Research, Development and Innovation Office under Grant Nr. TKP2021-EGA-02 and ÚNKP-22-3-II-BME-13 New National Excellence program of the Ministry for Culture and Innovation.

REFERENCES

[1] S. R. Venna, J. B. Jasinski, M. A. Carreon, J. Am. Chem. Soc., 132(51) (2010) 18030–18033.
[2] Z. Lai, Curr. Opin. Chem. Eng., 20 (2018) 78–85.
[3] Y.-R. Lee, M.-S. Jang, H.-Y. Cho, H.-J. Kwon, S. Kim, W.-S. Ahn, Chem. Eng. J., 271 (2015) 276–280.
[4] N. Német, G. Holló, G. Schuszter, D. Horváth, Á. Tóth, F. Rossi, I. Lagzi, Chem. Commun., 58 (38) (2022) 5777–5780.
[5] S. Farkas, M. S. Fónyi, G. Holló, N. Német, N. Valletti, Á. Kukovecz, G. Schuszter, F. Rossi, I. Lagzi, J. Phys. Chem. C, 126(22) (2022) 9580–9586.
[6] N. Német, G. Holló, N. Valletti, S. Farkas, B. Dúzs, Á. Kukovecz, G. Schuszter, I. Szalai, F. Rossi, I. Lagzi, Mater. Adv., 5 (2024) 1199–1204.

ADVANCED MATERIALS AGAINST INSECTS AND TICKS

S.A. Zverev [1], S.V. Andreev [1,2], D.V. Savraeva [3], A.A. Selivanova [2], A.S. Zvereva[1] and K.A. Sakharov [4]

[1]*Disinfectology Institute of F.F. Erisman FSCH of Rospotrebnadzor, 18 Nauchnyi drive, Moscow, 117246 Russia. (zverev.s.chem01@gmail.com)*
[2]*MIREA – Russian Technological University (M.V. Lomonosov Institute of Fine Chemical Technologies), 86 Vernadsky Avenue, Moscow, 119571 Russia.*
[3]*The Hebrew University of Jerusalem, Edmond J. Safra Campus, Givat Ram, Jerusalem, 9190401 Israel.*
[4]*School of Materials Science and Engineering, Nanyang Technological University (NTU): 50 Nanyang Avenue, Singapore, 639798 Republic of Singapore.*

DOI: https://doi.org/10.46793/Phys.Chem24I.297Z

ABSTRACT
The use of materials that protect people from attacks by blood-sucking mosquitoes and ticks can significantly reduce the transmission of vector-borne infections. The results of this study demonstrate that inorganic oxides can be employed as repellent carrier substances to develop controlled-release materials. However, there was no direct correlation between the adsorption activity Qe (mg/g) and the concentration of *N*,*N*-diethyl-3-methylbenzamide (DEET) in the fabric(mg/m^2). The most effective materials were produced using Al_2O_3 and ZrO_2 oxides (more than 80 mg/m^2 of DEET), as they contained the highest repellent concentration and therefore will have the greatest biological effect with the lowest economic costs. The materials have a high potential against blood-sucking insects and can be used in various conditions due to their controlled and prolonged effect.

INTRODUCTION

The development of chemistry and related sciences is gradually leading to the application of approaches from another field of knowledge - materials science. New materials are in use in every industry and are an integral part of human life [1].

According to the World Health Organization (WHO), vector-borne diseases account for more than 17% of all infectious diseases and cause more than 700,000 deaths each year [2]. In the majority of cases, arthropods act as vectors for pathogens that cause infectious and parasitic diseases. The most common arthropods involved are bloodsuckers, such as mosquitoes and ticks. [3]. The most epidemiologically significant species of ixodid ticks, in recent times, is the taiga tick (*Ixodes* persulcatus) [4]. The range of this tick has been expanding recently, and it is anticipated that this species may appear in the Balkans, Alaska, and some Canadian provinces in the coming years [5,6]. Thus, it is necessary not only to improve existing means of defense against ixodid tick attacks, but also to introduce new tactics to make protection more personalized [7]. One of the most crucial objectives in this area is the safeguarding of the population, which for a limited period may be present in areas with an elevated probability of attacks by ticks, mosquitoes, and other insects. It would appear that the creation of materials with acaricidal and repellent properties would be an appropriate solution to the problem of simultaneous protection against both tick attacks and mosquito bites.

The biological differences between mosquitoes and ticks make it difficult to create a universal defense against them. Materials with a controlled yield of the active ingredient that is deposited on

the support appear to be the most promising [8]. To develop materials with controlled release of the active ingredient, it is necessary to select a carrier and to determine the method of exposure of the material necessary to release the active ingredient. To create such a material, it is essential to understand the biological properties of the active ingredient, to study the physicochemical basis of the interaction between the active ingredient and the carrier, and to determine the optimal effect on the material to achieve the desired efficacy.

METHODS

Static sorption of DEET

DEET (Sigma Aldrich, (US)) isothermal sorption process was carried out by mixing 100 mg of zirconia, alumina (synthesised) or silicas (Elsico, (Russia)) with repellent solutions ($C_{solutions}$ = 100-1000 mg/L) in 40 ml of acetonitrile (Honeywell, (US)) for 120 min at 24±1 °C. To determine changes in the concentration of repellent solutions, samples were collected after 5, 15, 30, 60, 120, and 360 min and filtered through 0.45 μm PTFE filter. The optical density of DEET in the analyzed samples was recorded on a spectrophotometer (Varian Cary 50 UV-Vis, (US)) in the spectral range of 190-210 nm. Concentrations of DEET in the samples were calculated using the absolute calibration method.

The DEET repellent solutions that were used to plot the calibration curves were prepared by dilution the stock solution. Stock solution was prepared by accurately measuring the necessary amount of the compound to an approximation of the fourth decimal number, and diluting it in acetonitrile.

Manufacturing and characterization of repellent-based impregnated textiles

The inorganic oxides (zirconia, alumina, silica) incorporated into the repellent were mixed with a polyester binding agent (Etris, (Russia)). We then transferred the reaction mixture to a fabric impregnation bowl and immersed the 5x5 cm aramid fabric (Tchaikovsky Textile, Russia) (the fabric density was 180 g/m^2) in the impregnation solution for 3 minutes. The fabrics were then dried at 170°C for 3 minutes and placed in heat-sealed polyester bags to prevent loss of repellency from the fabric surface. The amount of repellent in the solution (g/l) was determined by high performance liquid chromatography (HPLC) (Thermo Scientific UltiMate 3000, (US)) and then converted to its observed amount in the textile (mg/m^2).

RESULTS AND DISCUSSION

It seems that there is a promising direction to be explored in the field of protective textiles against insect and mite attacks: the use of repellents [9]. They appear to be highly effective and less toxic than insecticides, which makes them an attractive option.

However, the main difficulty with repellents is their poor solubility in water. In addition, to create materials with controlled release of the active ingredient, an approach is needed to act externally on the material.

In order to fix the repellent on the fabric (or any other carrier matrix), we conducted a study on the sorption capacity of inorganic oxides towards repellent (DEET) [10]. The results showed that zirconia, alumina and silica-phenyl have adsorption activity (Qe) towards DEET (67, 119 and 239 mg/g, respectively), which allows their use in the development of textiles with repellent properties (Fig. 1).

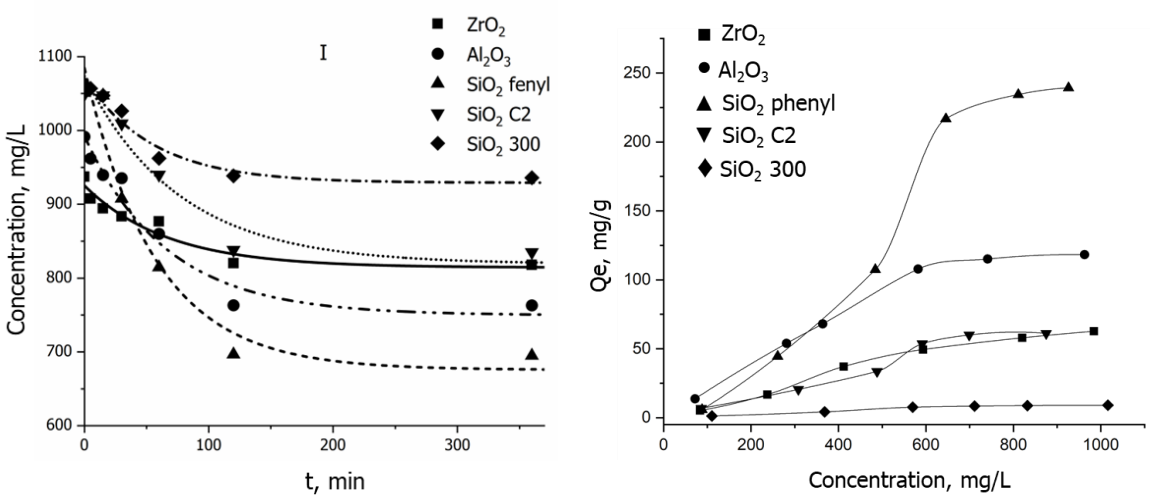


Figure 1. Study the adsorption capacity of inorganic oxides for DEET.

Following the sorption step of the repellents on porous oxides, they were mixed with a polyacrylate binder solution for subsequent fixation to the fabric. The binder was then thermally fixed and the repellent was extracted in ethyl acetate to determine the concentration of DEET in the fabric. The results of the chromatographic determination showed that the alumina and zirconia fabrics contained more than 80 mg/m^2 of DEET. While the silica-phenyl demonstrated a high adsorption capacity, the fabric treated with this sorbent exhibited a lower DEET content than the other samples. This could be attributed to the reduced desorption of the repellent from the oxide into the polymer binder. The stability of the obtained materials for 5 days was also studied and it was shown that such materials are stable in relation to environmental factors (Fig. 2).

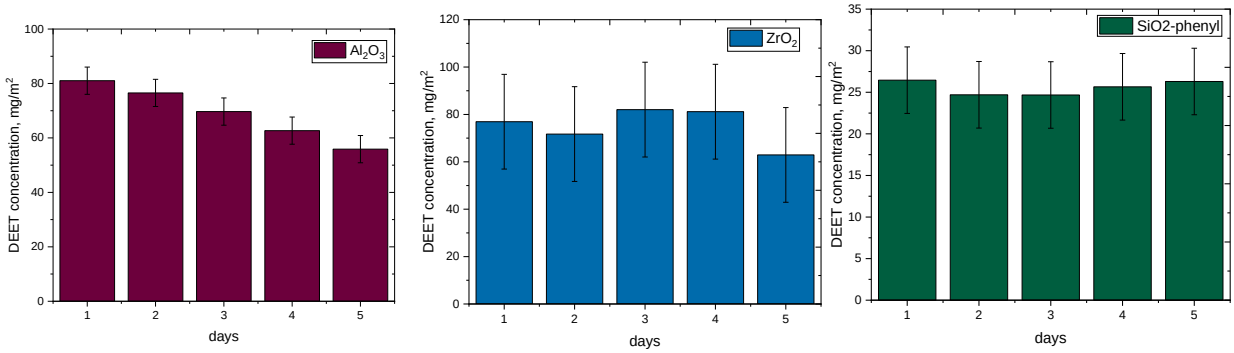


Figure 2. Stability studies of textile materials with repellent additives.

CONCLUSION

The results of this study demonstrate that inorganic oxides can be employed as repellent carrier substances to develop controlled-release materials. However, there was no direct correlation between the adsorption activity Qe (mg/g) and the concentration of DEET in the fabric (mg/m^2). The most effective materials were produced using Al_2O_3 and ZrO_2 oxides, as they contained the highest repellent concentration and therefore will have the greatest biological effect with the lowest economic costs.

The controlled-release materials developed in this study have the potential to be an effective solution for controlling dangerous ticks and mosquitoes. The materials have a high potential against blood-sucking insects and can be used in various conditions due to their controlled and prolonged effect.

Acknowledgment
The work was carried out at the expense of the industry research program of Rospotrebnadzor for 2024-2025 (No. 1023032900395-5-1.6.23) and supported by Singapore MAR grant 04INS000458C150OOE01.

REFERENCES

[1] W. D. Callister, D. G. Rethwisch, John Wiley & Sons, 2020. P. 975
[2] Vector-borne diseases [Electronic resource]. 2020. URL: https://www.who.int/news-room/fact-sheets/detail/vector-borne-diseases (accessed: 21.08.2023).
[3] C.M. Barker, W. K. Reisen, Medical and Veterinary Entomology. Elsevier, 2019. P. 33–49.
[4] S.V. Bugmyrin et al., Ticks Tick. Borne. Dis., 13(6) (2022) 102045.
[5] T. Shah et al., Front. Microbiol. 14 (2023).
[6] S. S. Wang et al., One Heal. 2023(16) (2023) 100508.
[7] S. A. Zverev et al., Exp. Appl. Acarol., 89(2) (2023) 275–286.
[8] A. Ashitha, J. Mathew, Cham: Springer International Publishing, (2020) 141–153.
[9] S. V. Andreev et al. Acarina, 32(1) (2024) 59-68.
[10] S. A. Zverev et al., Colloid and Polymer Science, (2024) 1-10.

IN VITRO RELEASE STUDY OF DICLOFENAC SODIUM FROM TEMPERATURE-RESPONSIVE POLY(OLIGO(ALKYLENE GLYCOL)) METHACRYLATE HYDROGEL MATRICES

Z. R. Miladinović, M. Krstić, D. Miličević and E. Suljovrujić

University of Belgrade - Vinča Institute of Nuclear Sciences, National Institute of the Republic of Serbia, Mike Petrovića Alasa 12-14, 11000 Belgrade, Serbia. (zoranar@vin.bg.ac.rs)

DOI: https://doi.org/10.46793/Phys.Chem24I.301M

ABSTRACT

This study investigates a novel poly(oligo(alkylene glycol)) methacrylate hydrogel, synthesized via radiation-induced copolymerization of oligo(propylene glycol) methacrylate (OPGMA) and oligo(ethylene glycol) methacrylate (OEGMA) at equal mole fractions. The copolymerization aimed to explore its effect on hydrogel swelling properties compared to their homopolymeric counterparts, POPGMA and POEGMA, with distinct volume phase transition temperatures (VPTT) of around 13 and 70 °C, respectively. The resulting copolymeric hydrogel displayed a VPTT within the range of heightened physiological temperatures, indicating successful property tuning through copolymerization. Furthermore, we conducted tests on these three hydrogels as carriers for diclofenac sodium delivery *in vitro*. The evaluation of controlled drug delivery indicated encouraging prospects for the resulting copolymeric hydrogel in medical applications.

INTRODUCTION

Hydrogels are excellent matrices for drug delivery due to their porous structure and ability to retain a large amount of water, which resembles human tissue and facilitates the encapsulation and controlled release of drugs [1]. Their tunable properties allow for customization of release kinetics, ensuring precise delivery of therapeutic agents. Additionally, hydrogels offer versatility in formulation, enabling administration via various routes such as oral, transdermal, rectal, or buccal, making them suitable for a wide range of medical applications [2].

The burst effect, often observed during *in vitro* drug delivery from hydrogels, refers to the initial rapid release of a significant portion of the encapsulated drug within a short period. This phenomenon occurs due to the drug molecules located near the surface or within the loosely bound regions of the hydrogel matrix being released rapidly upon exposure to the surrounding medium. Despite the burst effect being a common occurrence, it can be minimized or controlled through various strategies such as optimizing the polymer composition, adjusting crosslinking density, incorporating drug release modifiers, or employing multi-layered hydrogel systems [3]. By mitigating the burst effect, hydrogels can achieve more sustained and controlled drug release profiles, enhancing their effectiveness for therapeutic applications.

In this study, we present the effect of copolymerization of methacrylate-based monomers on the swelling behavior of hydrogel. Our key objective is to highlight how this copolymerization process facilitates the optimization of the burst effect, primarily essential for enhancing therapeutic efficacy in drug delivery applications.

METHODS

The synthesis process commenced with dissolving OEGMA and/or OPGMA monomers, alongside ethylene glycol dimethacrylate (EGDMA) as a crosslinking reagent, all sourced from Sigma-Aldrich, in an ethanol/water (1/1, v/v) solution. The solution was then degassed under nitrogen to

remove any dissolved gases, ensuring a pristine reaction environment. Next, the degassed solution was carefully poured between two parallel plates. Subsequently, the solution underwent gamma radiation exposure from a cobalt-60 source at a specific dose rate of 0.5 kGy/h until reaching a total absorbed dose of 25 kGy.

Following radiation exposure, the hydrogel precursors were incubated in an oven at 40 °C for 24 hours to allow for post-polymerization crosslinking and stabilization [4]. Afterward, the hydrogels were carefully extracted from the plates and cut into discs, which were then dried to a constant weight.

After a predetermined period, Soxhlet extraction was employed to remove unreacted components. The process was conducted at 40 °C in an ethanol/water solution for 48 hours, followed by drying for an additional 72 hours at the same temperature in a vacuum oven to achieve constant weight.

The synthesis yielded a P(OEGMA/OPGMA) copolymeric hydrogel with a monomer feed ratio of OEGMA to OPGMA set at 50:50, alongside two homopolymeric hydrogels, POEGMA and POPGMA.

To evaluate the thermosensitivity of the obtained hydrogels, a swelling analysis was conducted. Xerogels were immersed in a pH 7.4 buffer solution, and the equilibrium swelling degree was determined at intervals of 2.5 °C within a temperature range of 5 to 80 °C using the equation: $Q_e = (W_e - W_0)/W_0$, where W_e represents the weight of the swollen hydrogel at equilibrium, and W_0 is the weight of the xerogel. All reported results represent the mean value of measurements conducted in triplicate.

The controlled release analysis of diclofenac sodium (DS) (obtained from Galenika, Beograd) from the xerogel matrices was performed under *in vitro* conditions using a permeation technique. The technique involved fully formed hydrogels immersed in a 2 mg ml^{-1} DS-solution at 5 °C for two days until reaching equilibrium swelling of the hydrogel matrices. Subsequently, the DS-absorbed hydrogels were dried to a constant mass at room temperature in the absence of light. Following a period of three weeks, controlled drug delivery experiments were conducted using DS-absorbed xerogels. Xerogels containing the absorbed drug were immersed in 30 ml of pH 7.4 buffer solution and subjected to constant stirring on a magnetic stirrer equipped with heating and a digital thermostat. The system was maintained at 37 °C, mimicking the human physiological environment.

The drug release kinetics were tracked over seven days using a Shimadzu 1800 UV-vis spectrophotometer, with absorbance measurements of solution aliquots taken at 276 nm [5]. Each release experiment was performed in triplicate, and the data were analyzed using Origin Microcal 8.0 software.

RESULTS AND DISCUSSION

The initial step in characterizing obtained hydrogels involved evaluating their swelling behavior. Considering the potential application of these hydrogels as carriers for controlled release, tests were conducted at a physiological pH 7.4. Furthermore, volume phase transition (VPT) values were determined. Results revealed a distinct contrast in the swelling dynamics between hydrogels containing solely oligo(ethylene glycol) monomer units and those containing only oligo(propylene glycol) units (**Figure 1**).

Notably, POEGMA hydrogel exhibited significantly higher degrees of swelling and displayed weak temperature dependence up to approximately 40 °C, as evidenced by a gradual decrease in the equilibrium degree of swelling with the increase in temperature. Consequently, the temperatures of volume phase transitions were markedly higher than physiological temperatures, making them less suitable for biomedical applications.

On the contrary, hydrogels composed solely of OPGMA monomers displayed lower degrees of swelling and a sharper temperature transition. Incorporating OEGMA into such hydrogel yielded the copolymeric P(OEGMA$_{50}$/OPGMA$_{50}$) hydrogel, which not only shifted the phase transition to higher temperatures but also increased the equilibrium degree of swelling. Specifically, the volume phase transition temperatures (VPTTs) for this series of hydrogels were determined as 13.4, 41.9, and 70.3 °C for POPGMA homopolymeric hydrogel, P(OEGMA$_{50}$/OPGMA$_{50}$) copolymeric hydrogel, and POEGMA homopolymeric hydrogel, respectively.

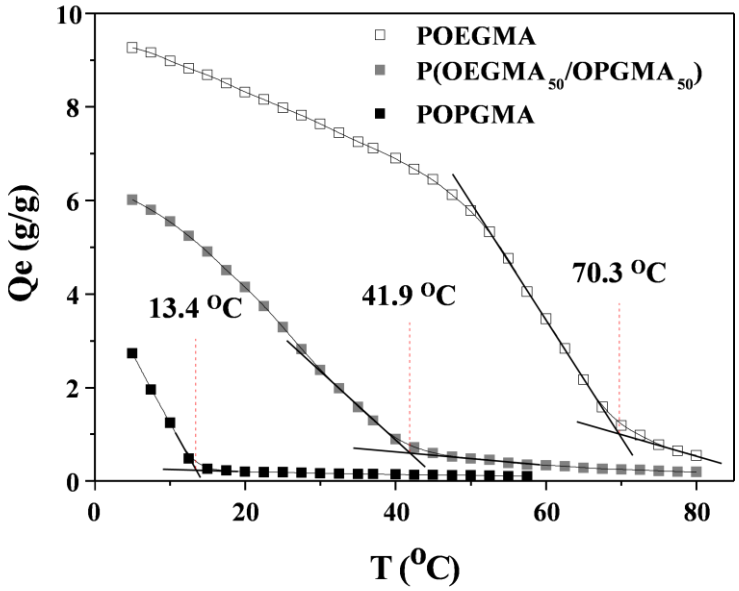


Figure 1. Effect of temperature change on the equilibrium degree of swelling of POPGMA, P(OEGMA$_{50}$/OPGMA$_{50}$), and POEGMA hydrogels in pH 7.4 buffer solution.

Subsequent investigation focused on the release profiles of diclofenac sodium from hydrogel matrices, including DS-loaded P(OEGMA$_{50}$/OPGMA$_{50}$) copolymeric hydrogel, as well as POEGMA and POPGMA homopolymers, in pH 7.4 buffer solution at 37 °C (**Figure 2**). While POEGMA exhibited distinct behavior with a pronounced burst effect, the POPGMA homopolymeric hydrogel exhibited sustained release kinetics without an initial burst effect, suggesting a controlled drug release mechanism. Copolymerization of OEGMA with the hydrophobic OPGMA monomer successfully modulated burst release characteristics, although the release kinetics of the copolymeric P(OEGMA$_{50}$/OPGMA$_{50}$) hydrogel were notably influenced by the proportion of OEGMA monomer present.

Furthermore, the diffusion exponent values of 0.44, 0.48, and 0.50 for POPGMA homopolymeric hydrogel, P(OEGMA$_{50}$/OPGMA$_{50}$) copolymeric hydrogel, and POEGMA homopolymeric hydrogel, respectively, obtained from release profiles of DS-drug, indicated that the drug release process can be described by Fick's transport mechanism and is diffusion-controlled. The increase in ethylene glycol (EG) units in the hydrogel correlated with heightened swelling and diffusion coefficients, suggesting enhanced mobility of sodium diclofenac within the hydrogel.

These findings underscore the potential of these hydrogels for controlled-release applications, particularly in biomedical contexts where tailored release kinetics are crucial for therapeutic efficacy.

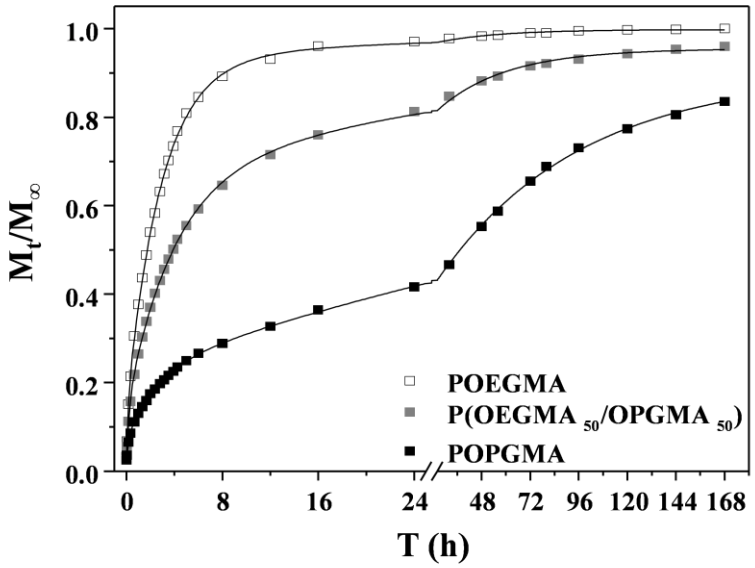


Figure 2. Release profiles of diclofenac sodium from POEGMA, P($OEGMA_{50}$/$OPGMA_{50}$), and POPGMA hydrogels.

CONCLUSION

In summary, this study has yielded significant insights into the copolymerization process involving the OEGMA monomer and the comparatively hydrophobic OPGMA monomer. This synthesis has led to the incorporation of a non-polar region within the hydrogel matrix, consequently reducing its water uptake and swelling capacity. As a result, the diffusion rate of drug molecules through the P($OEGMA_{50}$/$OPGMA_{50}$) hydrogel is slowed, leading to a more controlled release.

These results indicate successful copolymerization and demonstrate that the resulting copolymeric P($OEGMA_{50}$/$OPGMA_{50}$) hydrogel exhibits a VPTT at the upper limit of physiological temperatures. This characteristic makes it a promising candidate for further applications as a matrix for controlled drug release in cancer treatment modalities such as magnetic or photothermal therapy.

Acknowledgment

The research was funded by the Ministry of Science, Technological Development and Innovation of the Republic of Serbia (No. 451-03-66/2024-03/ 200017).

REFERENCES

[1] Q. Feng, J. Xu, K. Zhang, H. Yao, N. Zheng, L. Zheng, J. Wang, K. Wei, X. Xiao, L. Qin, L. Bian., ACS Cent. Sci., 5(3) (2019) 440.
[2] A. Ahsan, W. - X. Tian, M. A. Farooq, D. H. Khan, Int. J. Polym. Mater., 70(8) (2021) 574.
[3] M. Nichifor, Polymers, 15(5) (2023) 1065.
[4] Z. R. Miladinovic, M. Micic, A. Mrakovic, E. Suljovrujic, J. Polym. Res. 25 (2018) 1.
[5] J. M. M. Vidart, T. L. D. Silva, P. C. P. Rosa, M. G. A. Vieira, M. G. C. D. Silva, J. Appl. Polym. Sci., 135(12) (2018) 45919.

DETERMINATION OF THE VOLUME PHASE TRANSITION TEMPERATURE OF SMART HYDROGELS WITH ETHYLENE GLYCOL AND PROPYLENE GLYCOL PENDANT CHAINS

Z. R. Miladinović [1], M. Krstić [1], G. Stamboliev [2], and E. Suljovrujić [1]

[1] *University of Belgrade - Vinča Institute of Nuclear Sciences, National Institute of the Republic of Serbia, Mike Petrovića Alasa 12-14, 11000 Belgrade, Serbia. (zoranar@vin.bg.ac.rs)*
[2] *Global Supply Line, Adelaide, Australia.*

DOI: https://doi.org/10.46793/Phys.Chem24I.305M

ABSTRACT

This study investigates the thermal properties of methacrylate hydrogels modified with short ethylene glycol (EG) and propylene glycol (PG) pendant chains, synthesized via radiation-induced crosslinking and polymerization. The hydrogels were characterized through swelling behavior and differential scanning calorimetry (DSC) measurements to determine volume phase transition temperatures (VPTT). While polymeric systems with EG chains exhibit high biocompatibility with a VPTT exceeding physiological levels, systems with PG chains display thermosensitivity below 13 °C due to their hydrophobic nature. To obtain hydrogels with VPTT around physiological temperatures, hydrogels with both EG and PG pendant chains, which have a predetermined ratio of EG and PG units within the methacrylate hydrogel backbone, were synthesized. Our findings highlight the influence of EG and PG compositions on the temperature-responsive behavior of hydrogels, crucial for biomedical applications.

INTRODUCTION

Temperature-responsive hydrogels have emerged as a pivotal class of smart polymeric materials. These hydrogels possess an exceptional ability to dynamically adjust their physical and chemical properties in response to variations in temperature. Moreover, their ability to undergo reversible phase transitions upon exposure to temperature changes renders them indispensable for numerous biomedical applications, including precise modulation of drug release kinetics, promotion of enhanced tissue regeneration, and customization of therapeutic interventions [1].

Despite their promising utility, the design and optimization of temperature-responsive hydrogels remain ongoing challenges, particularly in the context of elucidating their underlying mechanisms and tailoring their properties to specific applications. In this context, our study endeavors to explore deeper into the thermal properties and temperature-response mechanisms of a specific subset of temperature-responsive hydrogels: methacrylate hydrogels functionalized with ethylene glycol (EG) and propylene glycol (PG) pendant chains.

Through a comprehensive study of the thermal behavior and temperature responsiveness of these hydrogels, our research aims to not only expand fundamental understanding but also uncover practical insights that can drive advancements in biomedical engineering. By elucidating the intricate relationship between molecular structure, thermal properties, and functionality, we seek to contribute to the development of advanced therapeutic systems that harness the unique capabilities of temperature-responsive hydrogels.

METHODS

Monomers, including ethylene glycol$_6$ methacrylate (EG_6MA), ethylene glycol$_6$ propylene glycol$_3$ methacrylate (EG_6PG_3MA), ethylene glycol$_3$ propylene glycol$_6$ methacrylate (EG_3PG_6MA) and,

propylene glycol$_5$ methacrylate (PG_5MA), were dissolved in a water/ethanol mixture (1:1, v/v) at room temperature. To optimize crosslinking efficiency, small amounts of ethylene glycol dimethacrylate (EGDMA), as a crosslinking agent, were added to each reaction mixture [2]. The reaction mixtures were degassed by saturating with argon gas for 20 minutes and then sealed between two glass plates. Radiation-induced synthesis was performed using a ^{60}Co gamma source under ambient conditions at a dose rate of 0.5 kGy/h until reaching an absorbed dose of 25 kGy. Following irradiation, hydrogel specimens were cut into discs and dried in a vacuum oven at 40 °C to constant weight.

Swelling measurements were conducted in a buffer solution at pH 7.4, which is particularly relevant for biomedical applications, across a temperature range from 5 to 90 °C. The swelling ratios of the hydrogels were measured gravimetrically [3]. The equilibrium degree of swelling (Q_e) was calculated as $Q_e = (W_e - W_0)/W_0$, where W_e is the weight of the swollen hydrogel at equilibrium, and W_0 is the weight of the xerogel [4]. The mean value of three measurements obtained from distinct specimens of the same hydrogel was taken.

The volume phase transition temperature (VPTT) values of the synthesized temperature-responsive hydrogels were determined using equilibrium swelling data obtained across a wide temperature range. The VPTT was identified as the point at which a significant change in the slope of the equilibrium swelling ratio curve occurred, indicating pivotal changes in swelling volume beyond this critical temperature. Subsequently, differential scanning calorimetry (DSC) was employed to confirm the VPTT of the hydrogels. DSC measurements were conducted using TA Instruments' Q2000 Differential Scanning Calorimeter, with a heating rate of 1 °C min^{-1} ranging from 4 to 90 °C. Before the DSC heating scan, xerogels were immersed in a pH 7.4 buffer solution and allowed to equilibrate at 4 °C. The temperature corresponding to the onset point of the DSC endothermic peak was defined as the VPTT, following the previously established methodology [5].

RESULTS AND DISCUSSION

The significant changes in the balance between hydrophilicity and hydrophobicity, along with the transition of polymer pendant chains from a spread coil state to a collapsed globule upon heating, are apparent through the expulsion of water from their network.

The volume phase transition temperature (VPTT) was observed to be below 50 °C for hydrogels containing propylene glycol (PG), as anticipated. Specifically, for PPG_5MA, the VPTT was below room temperature (13.4 °C), for PEG_3PG_6MA it was approximately 32 °C, and for PEG_6PG_3MA it was about 47 °C. Conversely, the PEG_6MA hydrogel exhibited VPTT behavior at much higher temperatures (>70 °C), which is irrelevant for biomedical applications **(Figure 1a)**. Additionally, the inclusion of ethylene glycol (EG) units in the hydrogel composition not only shifted the VPTT to higher temperatures but also increased the degree of swelling due to the greater hydrophilicity of EG compared to PG units.

In addition to the swelling method, differential scanning calorimetry (DSC) was employed to determine the VPTT as well. DSC heating scans of the hydrogels, equilibrated in pH 7.4 buffer solution, are depicted in **Figure 1b**. The temperature corresponding to the onset point of the endothermic peak is considered the VPTT. The obtained values are 13.7, 33.1, 48.3, and 72.1 °C for PPG_5MA, PEG_3PG_6MA, PEG_6PG_3MA, and PEG_6MA hydrogels, respectively. This observation underscores the consistency between the DSC results and those derived from the swelling method.

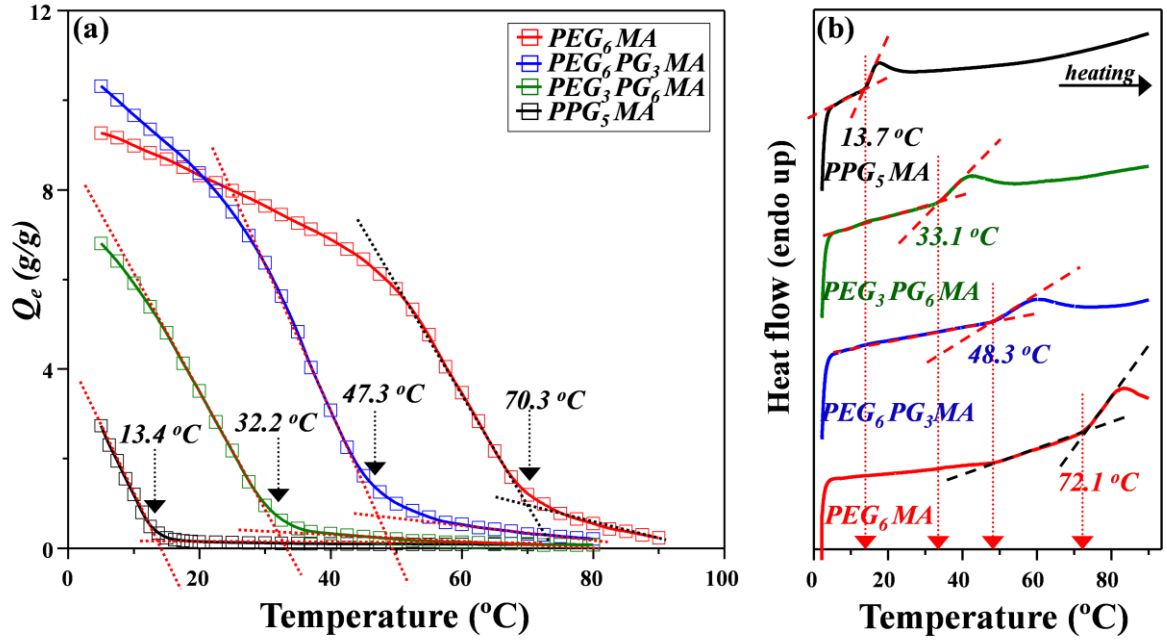


Figure 1. (a) Equilibrium swelling degree (Q_e) of PPG_5MA, PEG_3PG_6MA, PEG_6PG_3MA, and PEG_6MA hydrogels in pH 7.4 buffer solution as a function of temperature; **(b)** DSC heating scans obtained for PPG_5MA, PEG_3PG_6MA, PEG_6PG_3MA, and PEG_6MA hydrogels.

However, since the VPTT of the PEG_6PG_3MA hydrogel is slightly higher than physiological temperatures under physiological pH conditions, this hydrogel shows promise as a potential drug carrier in hyperthermia therapy (such as magnetic or photothermal hyperthermia), which involves heating organs or tissues to temperatures up to 50 °C for cancer treatment.

CONCLUSION

This study utilized gamma radiation to synthesize four temperature-responsive hydrogels: PEG_6MA, PEG_6PG_3MA, PEG_3PG_6MA, and PPG_5MA. Our primary focus centered on the PEG_6PG_3MA hydrogel, distinguished by its EGPG pendant chains. Unlike hydrogels based solely on PG or EG units in their pendant chains, which exhibited VPTTs significantly below or above physiological temperatures, the VPTT of PEG_6PG_3MA was observed to be approximately 47 °C. Given that this VPTT falls slightly above physiological temperatures, this hydrogel holds promise as an "on-demand" carrier for hyperthermia therapy.

Our findings suggest that by incorporating pendant chains with EGPG units, it is feasible to tune the VPTT of poly(alkylene glycol) methacrylate (PAGMA) hydrogels closer to body temperatures. To enable the broader application of PEGPGMA hydrogels across various biomedical contexts, further investigation into the influence of the number and ratio of EG and PG units in EGPG pendant chains on properties such as VPTT and biocompatibility is required.

Acknowledgment

The research was funded by the Ministry of Science, Technological Development and Innovation of the Republic of Serbia (No. 451-03-66/2024-03/ 200017).

REFERENCES

[1] K. Zhang, K. Xue, X. J. Loh, Gels, 7 (2021) 77.

[2] M. Krstic, Z. R. Miladinovic, T. Barudzija, A. Mladenovic, E. Suljovrujic, React. Funct. Polym., 170 (2022) 105140.
[3] E. Suljovrujic, M. Micic, Nucl. Instrum. Meth. B, 342 (2015) 206.
[4] C. L. Bell, N. A. Peppas, J. Control. Release, 37 (1995) 277.
[5] J. T. Zhang, R. Bhat, K. D. Jandt, Acta Biomater., 5 (2009) 488.

MAGNETIC $Fe_3O_4/SiO_2/ZrO_2$ NANOCOMPOSITE AS PHOTOCATALYST

T. Vulić [1], M. Carević [1], Z. Mojović [2] and M. Čomor [1]

[1] *University of Belgrade, Vinča Institute of Nuclear Sciences, National Institute of RS, Mike Petrovića Alasa 12-14, 11351 Belgrade, Serbia. (tanja030@vin.bg.ac.rs)*
[2] *University of Belgrade, Institute of Chemistry, Technology and Metallurgy, Njegoševa 12, 11000 Belgrade, Serbia.*

DOI: https://doi.org/10.46793/Phys.Chem24I.309V

ABSTRACT

Nanocomposite powder $Fe_3O_4/SiO_2/ZrO_2$ was synthesized in several steps. Firstly, magnetite nanoparticles with a protective layer of SiO_2 were synthesized. Silica layer protects magnetite core and prevents the transfer of electrons from the conduction band of ZrO_2 to magnetite during illumination. Secondly, a layer of ZrO_2 was added to the surface of nanoparticles by the solvothermal method. The resulting powder was purified with the help of a strong magnet that ensures complete separation of the magnetic material from the solution. Thus synthesized magnetic material was characterized using X-ray diffraction technique, UV/Vis reflectance spectroscopy and flat band potentials were calculated using Mott-Schottky plots. Photocatalytic efficacy was obtained in the decomposition reaction of 2,4,6-trichlorophenol in aqueous solutions with Simulated Solar light as an irradiation source. The results showed that nanocomposite is an effective adsorber and photocatalyst for selected pollutant.

INTRODUCTION

Magnetic separation provides an easy way for removal and recycling of magnetized materials [1]. Various types of photocatalytic reactions can be catalyzed using magnetic mesoporous nanocomposites with photocatalyst on the surface of nanoparticles [1, 2]. Bare magnetic iron-based nanoparticles possess a problem of instability over repeated use due to the strong tendency to aggregation. Additionally, they can become chemically unstable when exposed to certain environments (especially acidic). To overcome these problems magnetic nanoparticles are usually coated with thin layer of isolating material like SiO_2, as homogenously as possible, in core shell geometry. Literature showed that this type of magnetic cores is mostly used [3]. SiO_2 is ideal substrate for immobilization of photocatalysts thick film coating and formation of oxide based heterostructure [1]. In the scope of this study, detailed characterization of core shell photocatalytically active nanocomposite made of Fe_3O_4/SiO_2 core and ZrO_2 shell, was performed. ZrO_2 was chosen because it already showed exquisite photocatalytic efficacy after doping with Si^{4+} ions [4], which are also present in the form of silica film, even comparable with the most popular commercial photocatalyst Degussa P25, when 2,4,6-trichlorophenol (TCP) was degraded.

METHODS

Nanocomposite powder $Fe_3O_4/SiO_2/ZrO_2$ was synthesized in several steps. Magnetite nanoparticles were synthesized through process of alkali hydrolysis of mixture of Fe^{2+} and Fe^{3+} ions (Sigma-Aldrich). Obtained powder was washed with water and separated with magnet. Dry magnetite (0.5 g) was suspended in 2.5 mL of 0.1 M HNO_3, then in dispersion was added 5.5 mL of tetraethoxysilane (Alfa Aeser, 98%) dissolved in 2-propanole (1:4.5). After 30 min of sonication 1 mL of Zirconium (IV) propoxide (ZIP, Sigma-Aldrich, 70 wt% solution in 1-propanol) was added

and mixture was autoclaved in Teflon vessel for 24 h at 200 °C. Autoclave was left to cool naturally and powder was washed, separated with strong magnet, and subsequently dried.

The resulting powder was characterized using x-ray diffraction technique (PHILIPS 1050, Eindhoven, The Netherlands) and UV/Vis reflectance spectroscopy (DRS, Shimadzu UV-2600 S. Corp. Tokyo, Japan) equipped with an integrated sphere (ISR-2600 plus for UV-2600). Default Kubelka–Munk transformation was used for the automatic calculation of absorption spectra from reflectance. Photocatalysis was performed as previously reported [4], concentration of TCP was followed by high performance liquid chromatography with diode array detection (HPLC, UltiMate 3000 with Hypersil GOLD Column). Aliquots were extracted from TCP/ photocatalyst suspensions in regular time intervals and filtered before injection of 10 μL sample for concentration measurements.

Electrochemical experiments were performed using Autolab electrochemical workstation (Autolab PGSTAT302N, Metrohm-Autolab BV, Netherlands) and three-electrode cell composed of Ag/AgCl in 3 M KCl as reference electrode, platinum rod as counter electrode and glassy carbon electrode (GCE) coated with the investigated sample as the working electrode. The coating of GCE was performed in the following manner: 10 mg of sample was homogeneously dispersed in 0.95 ml of ethanol and 0.05 ml of 5wt. % Nafion using an ultrasonic bath. 10 μl of suspension was placed on the surface of the GCE (0.071 cm^2). A uniformly distributed sample was obtained at the surface of GCE after solvent evaporation. Mott–Schottky measurements were performed at the frequency of 1000 Hz, with the voltage applied at successive steps of 50 mV from 1 V to -1 V. The measurements were performed in 0.1 M Na_2SO_4 (pH = 5.6).

RESULTS AND DISCUSSION

In the **Figure 1a.** XRD patterns of synthesized nanoparticles are presented. Magnetite crystalline phase was fully developed with peaks assignable to JPDCS: 19-0629 card. Silica layer didn't induce any new peaks in XRD, although the hallo at about 22 deg. can be assigned to amorphous silica. Addition of ZrO_2 disrupted crystallinity of the composite. It is obvious that zirconia layer is amorphous and thick enough to make magnetite untraceable by XRD technique. Also, doping of zirconia with Si^{4+} ions from silica layer on magnetite core, could be the reason for formation of amorphous zirconia. As was stated in literature [4], doping of zirconia with low concentration of Si^{4+} ions induced suppression of particle growth (to max few nm), and decrease of crystallinity resulting in large peak broadening. UV/Vis absorption and reflection spectra of composite $Fe_3O_4/SiO_2/ZrO_2$ are presented in **Figure 1b**. Composite is compared with pure ZrO_2 doped with Si^{4+} ions for the reasons already given. Large differences between zirconia and $Fe_3O_4/SiO_2/ZrO_2$ are visible. Estimated band gap of composite is approximately 1 eV smaller than for zirconia, the while the pure zirconia is white, the nanocomposite is pale orange, as a result of mixture of magnetite and zirconia colors.

Kinetic curves of 2,4,6-trichlorophenol photodegradation (initial concentration of TCP was 100 ppm) in the suspension of the ZrO_2 or $Fe_3O_4/SiO_2/ZrO_2$ as a photocatalyst (0.5 mg/ml), are presented in **Figure 1c**. Magnetic $Fe_3O_4/SiO_2/ZrO_2$ composite was recycled from the solution (using magnet) and used in two consecutive photodegradation cycles. Pure ZrO_2 and $Fe_3O_4/SiO_2/ZrO_2$ composite in first cycle showed similar efficacy, 50% of TCP was removed from the solution after 120 min and 100 min of illumination, respectively. After 150 min of illumination in the second cycle, 50% of the TCP was photodegraded on the reused photocatalysts. Althought photodegradation process was sligtly slower than in the first cycle, probably due photocatalys's surface poisoning with intermediates and products from the previous process, results indicated on stability of synthesized composite and further confirmed presence of ZrO_2 on the composite's

surface. Additional proof was gained by electrochemical measurements, namely determination of the flat band potentials by Mott-Schottky measurements.

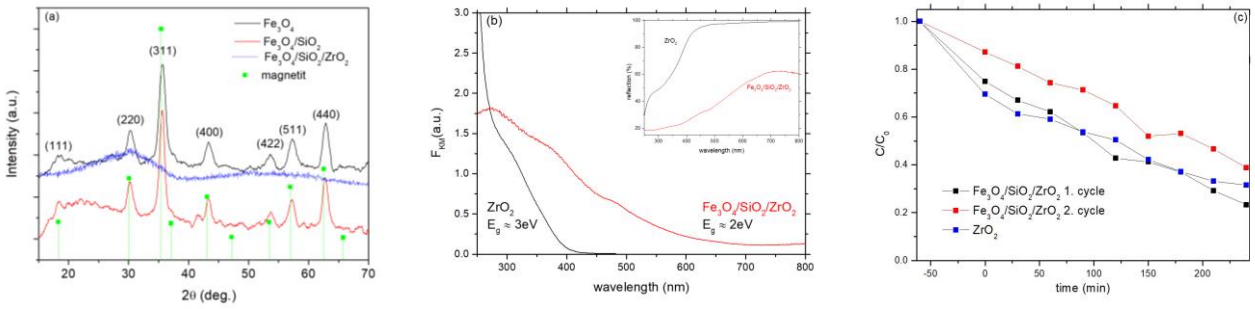


Figure 1. (a) XRD patterns of pure magnetite particles and composites, and JPDCS: 19-0629 for magnetite; (b) UV/Vis reflection (inset) and absorption spectra of pure ZrO_2 and composite nanoparticles (band gaps were calculated from Taucs plots); (c) kinetic curves for degradation of TCP using pure ZrO_2 and magnetic composite - two cycles were presented as evidence of magnetic separation.

Results of the Mott-Schottky measurements are presented in **Figure 2**. The dC/dE plot gave a straight line with an intercept with a potential axis at E_{fb}. The positive slope of the plots indicated that all investigated samples were n-type semiconductors, formation of the $Fe_3O_4/SiO_2/ZrO_2$ composite didn't change the nature of the nanoparticle core.

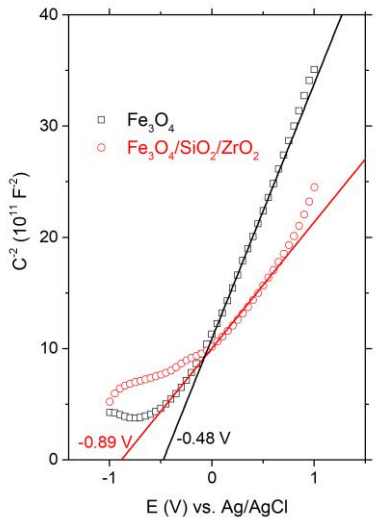


Figure 2: Mott-Schottky plots of Fe_3O_4 and $Fe_3O_4/SiO_2/ZrO_2$ measured at 1000 Hz in 0.1 M Na_2SO_4 solution (pH = 5.6).

Mott-Schottky relationship is given as eq. (1) [5]:

$$\frac{1}{C^2} = \frac{2}{\varepsilon\varepsilon_0 eN}\left(E - E_{fb} - \frac{kT}{e}\right) \quad (1)$$

where C is the interfacial capacitance, ε is the relative electric permittivity of sample, ε_0 is the electric permittivity of vacuum, e is the elementary charge, N is the charge carrier density, E is the applied potential, E_{fb} is the flat band potential, k is the Boltzmann constant and T is the absolute temperature. The obtained values of flat band potentials are given in respect to RHE and SHE and are listed in Table 1. The literature data of flat band potential for Fe_3O_4 varies in the range -0.20 V to -0.50 V vs. Ag/AgCl [6, 7]. The value of Fe_3O_4 flat band potential significantly depends on its magnetic properties. Introducing structural chirality in Fe_3O_4 shifts flat band potential toward more positive potentials, while the flat band potential of normal Fe_3O_4 tends to be in the region from -0.4 to -0.5 V vs. Ag/AgCl. The value of flat band potential of $Fe_3O_4/SiO_2/ZrO_2$ is shifted toward more negative potential. At the same time the slope of Mott-Schottky plot decreased twice. Since plot is inversely proportional to the charge carrier density (N) it can be concluded that in composite sample their number was doubled in comparison to pure Fe_3O_4[7]. The value of flat band potential for composite $Fe_3O_4/SiO_2/ZrO_2$ sample is close to value that can be obtained for pure ZrO_2,– 0.95 V vs. Ag/AgCl [8]. Although the values of flat band potentials reported for ZrO_2 varied significantly (from -0.69 V vs. Ag/AgCl/ 3 M KCl [9] to -1.25 V

Table 1. Flat band potentials of investigated samples determined from Mott-Schottky plots.

Sample	E_{fb} (V) vs. Ag/AgCl	E_{fb} (V) vs. RHE	E_{fb} (V) vs. SHE	Slope
Fe_3O_4	-0.48	0.06	-0.27	2.29×10^{12}
$Fe_3O_4/SiO_2/ZrO_2$	-0.89	-0.35	-0.68	1.13×10^{12}

vs. Ag/AgCl [10]) it can be estimated that zirconia covered homogenously the surface of magnetic Fe_3O_4/SiO_2 core. Bearing in mind that conduction band of n-type semiconductors is located at 0.1 – 0.2 V to more negative potential than E_{fb}, approximately -1 V (Ag/AgCl) for E_{CB} of the composite can be obtained, which is in a good agreement with literature data for ZrO_2 (about -1.2 V Ag/AgCl).

CONCLUSION

As results showed, magnetic nanocomposite powder $Fe_3O_4/SiO_2/ZrO_2$ was successfully synthesized and used as photocatalyst in degradation of trichlorophenol. Nanocomposite sustained magnetic properties of the core made of magnetite and can be retrieved from reaction solution using magnet. XRD showed presence of nearly amorphous material at the surface of the composite, but UV/Vis reflection and Mott-Schottky analysis gave indirect proof that nanocomposite have zirconia photocatalyst, most probably doped with Si^{4+} ions, is present on the nanocomposite surface, and it is able to efficiently degrade trichlorophenol.

Acknowledgment

This work was supported by the Ministry of Science, Technological Development and Inovation of the Republic of Serbia (grant no 451-03-66/2024-03/200017 and 451-03-66/2024-03/200026).

REFERENCES

[1] M. D. Nguyen, H.-V. Tran, S. Xu, T. R. Lee, Appl. Sci., 11 (2021) 11301.
[2] R. Wang, X. Wang, X. Xi, R. Hu, G. Jiang, Adv. Mater. Sci. Eng., (2012) 109379.
[3] J. R. Rajabathar, R. Thankappan, A. Sutha, H. Al-Lohedan, A. M. Karami, S. A. Kumar, G. Devendrapandi, S. R. Marjorie, R. Balu, Opt. Mat., 148 (2024) 114820.
[4] M. V. Carević, N. D. Abazović, T. B. Novaković, V. B. Pavlović, M. I. Čomor, Appl. Catal. B: Environ., 195 (2016) 112-120.
[5]Bard AJ, Faulkner LR., Electrochemical methods: Fundamentals and Applications.2nd ed. New York, Wiley; 2001.
[6] W. Zhang, C. Jiang, H. Guan, Y. Wang, Y. Hu, W. Wang, W. Tian, L. Hao, Mater. Adv., 5 (2024) 1340–1347.
[7] R. Hariri, S. Dehghanpour, J. Phys. Chem. Solids, 155 (2021) 110126.
[8] T.D. Vulić, M.V. Carević, N.D. Abazović, T.B. Novaković, Z.D. Mojović, M.I. Čomor, Photochem 2 (2022) 905-917.
[9] M. Ismael, Y. Wu, M. Wark, New J. Chem., 43 (2019) 4455-4462.
[10] L. Yu, X. Zhang, G. Li, Y. Cao, Y. Shao, D. Li, Appl. Catal.B: 187 (2016) 301-309.

SYNTHESIS AND CHARACTERIZATION OF DYSPROSIUM-DOPED FLUORAPATITE BY A COPRECIPITATION METHOD

V. Stanić [1], V. Stojiljković [1], I. Jelić[1], D. Jovanović[2], T. Gerić[3], Lj. Gavrilović[1] and S. Tanasković[4]

[1]*Vinča Institute of Nuclear Sciences - National Institute of the Republic of Serbia, University of Belgrade, 11000 Belgrade, Serbia(*voyo@vin,bg.ac.rs*)*
[2]*Faculty of Veterinary Medicine, University of Belgrade, Belgrade, Serbia;*
[3]*Institute of Meat Hygiene and Technology, Belgrade, Serbia*
[4]*Faculty of Pharmacy, University of Belgrade, 11000 Belgrade, Serbia*

DOI: https://doi.org/10.46793/Phys.Chem24I.313S

ABSTRACT
The synthesis of Dy^{3+}-doped fluorapatite was done by a wet precipitation method. XRD analysis showed that the obtained powder crystallized as fluorapatite phase and it did not contain any discernible crystalline impurity. The FTIR analysis showed the presence of characteristic chemical groups of fluorapatite.

INTRODUCTION

Biomaterials based on fluorapatite have been very promising because of their crystallographic similarities to the hydroxyapatite structure. Synthetic fluorapatite, $Ca_{10}(PO_4)_6F_2$ is a promising biomaterial due to its biocompatibility, bioactivity, and biodegradability [1]. Compared to pure hydroxyapatite, fluorapatite has a higher physicochemical stability, such as increased resistance to dissolution by acid and ion reactivity [2]. In vitro studies have showed that the cytotoxic effect of fluorapatite materials have no effect or are negligible [3]. Calcium cations can be partially or completely substituted by other metal species, without breaking the crystallographic symmetry [4]. Metal-doped apatites have shown great osteogenetic potential and may be suitable for obtaining coatings on metal implants, drug delivery systems, and antimicrobial properties, and biomarkers for nanomedical applications. Apatite materials doped with trivalent lanthanide ions have potential applications in medical diagnostics and cancer treatment [5]. Dysprosium represents an appropriate element for doping the materials designed for luminescence imaging applications in medicine. Dy-165 has been demonstrated to be more efficient in treating injured joints than traditional treatment and surgery [6]

Several studies describe the synthesis and potential application of Dy^{3+}-doped apatite biomaterial [7, 8].

In vitro studies have shown that dysprosium doped apatite materials have no significant cytotoxic activity [9, 10].

The present study aims to synthesize fluorapatite nanocrystals doped with Dy^{3+} ions by precipitation. The influence of Dy^{3+} ions on the structural properties of prepared nanopowder was investigated.

METHODS

The chemical reagents used in this study: Dysprosium nitrate ($Dy(NO_3)_3 \cdot H_2O$, ChemPur), calcium nitrate ($Ca(NO_3)_2 \cdot 4H_2O$), disodium hydrogen phosphate (Na_2HPO_4), ammonium hydrogen fluoride ($(NH_4)HF_2$) and ammonium hydroxide (NH_4OH) from Merck, were analytical grade. In addition, deionized water was utilized throughout the experiment.

Dy^{3+}-doped fluorapatite (DyFAP) nanoparticles was synthesized at room temperature in an ambient atmosphere by a wet precipitation method. Appropriate amounts of $Ca(NO_3)_2 \cdot 4H_2O$ and $Dy(NO_3)_3 \cdot H_2O$ were dissolved in water keeping (Ca + Dy) concentration equal to 0.5 M. Dy/(Ca + Dy) molar ratio was selected as 1 mol % , while ((Ca + Dy)/ P molar ratio was 1.67. Subsequently, the solution of 0.3 M of Na_2HPO_4 and 0.05 M of $(NH_4)HF_2$ was added dropwise into the prepared solution under constant stirring. The pH of the reaction medium is adjusted to 10 by additions of an ammonia solution. The precipitate was aged with stirring at room temperature for 2h. The resulting precipitate was washed with ethanol and deionized water. After washing, the precipitate was dried at 105 °C for 24 h.

The structure of the prepared sample was identified using powder X-ray diffraction (XRD) analysis (RIGAKU Ultima IV) in the 2θ range of 20° to 60°, with a step size of 0.02°.

The functional groups present in the prepared sample was identified by FTIR using a Nicolet iS5 FTIR Spectrometer (Thermo Fisher Scientific, Waltham, MA, USA), using the ATR technique. The spectrum was recorded in the range of 400 to 4000 cm^{-1}.

RESULTS AND DISCUSSION

The XRD pattern of the synthesized DyFAP sample is shown in Fig. 1. The obtained powder crystallized as fluorapatite phase $Ca_5(PO_4)_3F$ (PDF card no. 00-015-0876) in the hexagonal space group. no. 176 ($P6_{3/m}$), diffraction peaks were broad, indicating that the obtained product has low crystallinity and that the crystallites were nanosized. There are no other characteristic peaks of impurities, such as CaO and other calcium phosphates.

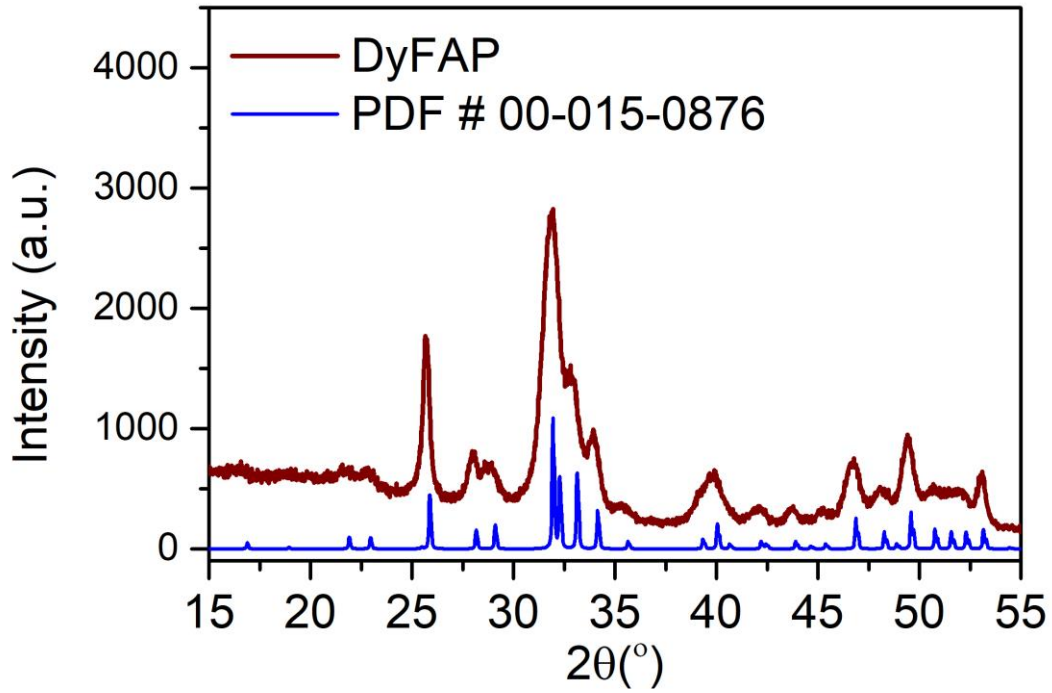


Figure 1. XRD pattern of the DyFAP sample.

Figure 2., shows the FTIR transmittance spectra of the DyFAP sample. The strongest bands at around 1090 cm^{-1} and 1020 cm^{-1} can be attributed to the stretching ν3 mode of PO_4^{3-} while the band at 964 cm^{-1} arises from the stretching ν1 mode of PO_4^{3-}. The two bands present at around 605-560 cm^{-1} is attributed to the bending ν4 mode of PO_4^{3-}, whereas a small band at around 470

cm^{-1} is ascribed to the bending ν2 mode of PO_4^{3-} [11]. The band at 875 cm^{-1} was ascribed to the presence of HPO_4^{2-} ions [12].

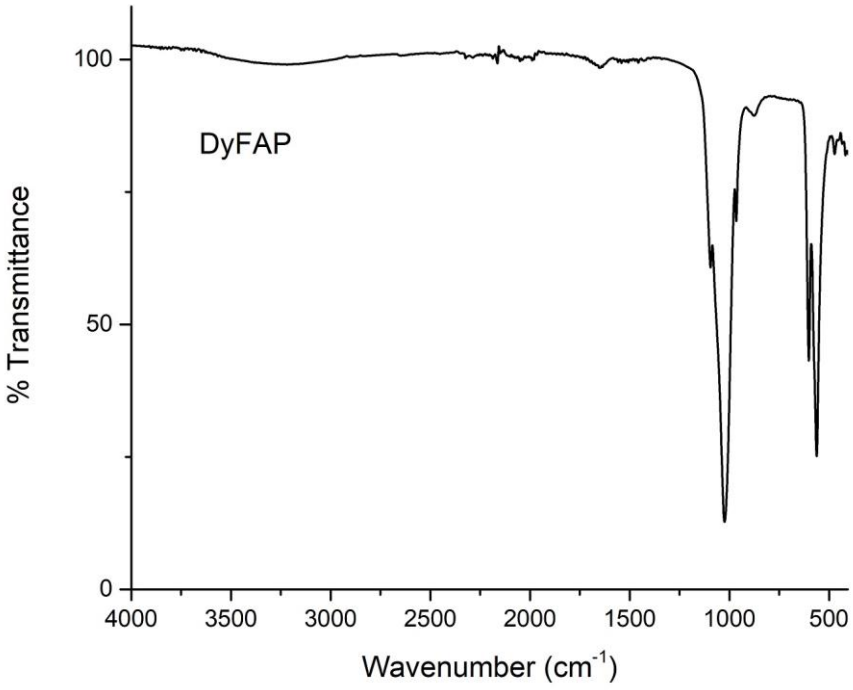


Figure 2. FTIR spectra of the DyFAP sample.

CONCLUSION

In this work, the Dy-doped fluorapatite powder with 1 mol% Dy^{3+} ions, was obtained by the chemical coprecipitation method in a very short synthesis time. XRD analysis revealed the formation of fluorapatite phase. The FTIR spectra showed the characteristic bands of the chemical groups present in the fluorapatite.

Acknowledgment

This work was supported by the Ministry of Science, Technological Development and Innovation of the Republic of Serbia (Research Grants: No.451-03-47/2023-01/200017 and No. 451-03-47/2023-01/ 200161).

REFERENCES

[1] S. Overgaard, K. Søballe, M. Lind, C. Bunger. J. Bone Joint Surg. [Br] 79-B (1997) 654-659.
[2] H. Eslami, M. Solati-Hashjin, M. Tahriri. Mater. Sci. Eng. C 29 (2009) 1387–1398.
[3] L. Borkowski, A. Przekora, A. Belcarz, K. Palka, G. Jozefaciuk, T. Lübek, M. Jojczuk, A. Nogalski, G. Ginalska. Mater. Sci. Eng. C 116 (2020) 1112.
[4] T.S.B. Narasaraju, D.E. Phebe. J. Mater. Sci. 31 (1996) 1–21.
[5] S. Mondal, V. T. Nguyen, S. Park, J. Choi, T. M. T. Vo, J. H. Shin, Y.-H. Kang, J. Oh. Ceram. Int. 46 (2020) 29249–292.
[6] I. A. Neacsu, A. E. Stoica, B. S. Vasile, E. Andronescu. Nanomaterials 9 (2019) 239.

[7] A. K. S. Lafarga, F. P. P. Moisés, A. Gurinov, G. G. Ortiz, G. G. C. Arízaga. Mater. Sci. Eng. C 48 (2015) 541-547.
[8] A.Tesch, C.Wenisch, K.-H.Herrmann, J.R. Reichenbach, P. Warncke, D. Fischer, F.A. Müller. Mater. Sci. Eng. C 81 (2017) 422–431.
[9] Y. Zhang, L. Mei, H. Liu, D. Yang, L. Liao, Z. Huang. Dyes and Pigments 139 (2017) 180e186.
[10] F. İsen, O. Kaygili, N. Bulut, T. Ates, F. Osmanlıoğlu, S. Keser, B. Tatar, İ. Özcan, B. Ates, F. Ercan, I. Ercan, R. O. Kareem. J. Aust. Ceram. Soc. 59 (2023) 849–864.
[11] R.H. Banerjee, R. Alexander, N. Chaudhary, S. Sanyal, P. Sengupta. J. Nucl. Mater. 599 (2024) 155199.
[12] R. Elosrouti, B. Sallek, H. Chaai, K. Digua, H. Oudadesse. Sci. Res. 3 (2015) 1-6.

"GREEN" SYNTHESIS AND REDUCTION ABILITY OF MESOPOROUS SILICA/(BI)METAL NANOPARTICLES TOWARD *E. coli* and *S. aureus*

D. Mašojević[1], V. Vodnik[1], M. Kokunešoski[1], S. Davidović[2], I. Vukoje[1], J. Spasojević[1] and U. Stamenović[1*]

[1] *Vinča Institute of Nuclear Sciences – National Institute of the Republic of Serbia, University of Belgrade, 11001 Belgrade, Serbia (una@vin.bg.ac.rs)*
[2]*Faculty of Technology and Metallurgy, University of Belgrade, 11000 Belgrade, Serbia*

DOI: https://doi.org/10.46793/Phys.Chem24I.317M

ABSTRACT
Antibacterial agents as a combination of silver, gold, and their bimetal nanoparticles (AgNPs, AuNPs, and Ag/AuNPs) with mesoporous silica SBA-15 are presented. In the simple "green" synthetic procedure with L-histidine as a bridge between these two components, three different nanocomposites - SBA-15/Ag, SBA-15/Au, and SBA-15/Ag-Au, were synthesized. Throughout SBA-15 with unchanged, granular morphology, spherical AgNPs, and AuNPs, with 8.5 and 16 nm in diameter, respectively, and peanut-like (7 x 15 nm) Ag/AuNPs were uniformly dispersed. After their characterization, antimicrobial evaluation toward *E. coli* and *S. aureus* was established. After 2h of interaction, 1 ppm of SBA-15/Ag showed a complete reduction of microbial growth, while the other two nanocomposites have insignificant values.

INTRODUCTION
Changes of microbial features and their adaptation to known antimicrobials require a constant search for new, accessible, and cost-effective materials, that could easily stand in the way of their further reproduction. In the continuation of our work considering new materials with promising antimicrobial activity, metal nanoparticles, silver (AgNPs), and gold (AuNPs) and their bimetal (Ag/AuNPs) were incorporated into mesoporous silica (SBA-15). SBA-15, as a highly biocompatible material with unique properties (good biodegradability, tunable pore size, and high surface area, high amount of silanol groups on the surface, etc.) [1-4] is an ideal support for the abovementioned NPs attachment. In this manner, there is a possibility of creating material for controlled antibiotics' delivery and release, sensing applications, etc. [5,6]. These functionalized structures, SBA-15/Ag, SBA-15/Au, and SBA-15/Ag-Au, with high surface area and small amounts of NPs incorporated, were tested against representative microbes, *E. coli* and *S. aureus*, as antibacterial agents. It was found that their interaction with bacterial cell wall disables their functions, leading to microbial death.

EXPERIMENTAL
Materials. All reactants (sodium hydroxide (NaOH), silver nitrate **(**$AgNO_3$), chloroauric acid ($HAuCl_4$), and histidine) were supplied by Sigma and used without further purification. SBA-15 was synthesized at 80 °C, as in our previous work [3,4].
Nanocomposites' synthesis. For all three nanocomposites, SBA-15 (0.05 g) [3,4], together with histidine (10^{-3} M) was dissolved in NaOH (0.1 M, 20 ml), and put on reflux (70-80°C). After 3h of vigorous stirring, water solutions of $AgNO_3$ or $HAuCl_4$ (10^{-3} M), were added dropwise. Color changes of reaction mixtures to yellow in the case of SBA-15/Ag and dark red of SBA-15/Au solution after 24 h, indicated nanocomposites' formation. In the as-prepared SBA-15/Ag, $HAuCl_4$

(10^{-3} M) together with histidine (10^{-3} M) as a reducing agent, was added to produce a third SBA-15/Ag-Au nanocomposite. The violet color of the reaction solution indicated its formation.

Characterization. UV/Vis spectra were recorded by a Termoscientific Evolution 600 spectrophotometer. Transmission and field-emission scanning electron microscopies (TEM and FeSEM) were performed in a JEOL-JEM-2100 at 200 kV and Zeiss ULTRA plus instruments, respectively. The quantitative antibacterial activity of the as-prepared samples (determination of colony forming units - CFU) at the concentration of 1 ppm during 2 h of incubation time, was tested against *E. coli* and *S. aureus*, using the standard test method ASTM E 2149-01, as described in our previous work [7].

RESULTS AND DISCUSSION

In the process of these nanocomposites' formation, histidine has an important dual role – functionalization of SBA-15 surfaces and reduction of metal ions. There is a great affinity between histidine and silica surface, i.e. surface silanol groups serving as binding sites for histidine molecules adsorption, while its developed mesoporous structure enables their ease of diffusion, and adsorption into the pores as well [4,8]. At the same time, as a reducing agent, it will convert Ag^{+} and Au^{3+} to Ag^{0}, and Au^{0}, respectively [9,10], enabling their adsorption onto SBA-15 surface and pores. Furthermore, as-prepared NPs are stabilized by SBA-15, whose structure with a large specific (S_{BET} = 710 m^2g^{-1}) and mesoporous surface (S_{meso} = 481 m^2g^{-1}), and developed microporosity [4] enables them a larger contact area with the environment, and among all, pathogens.

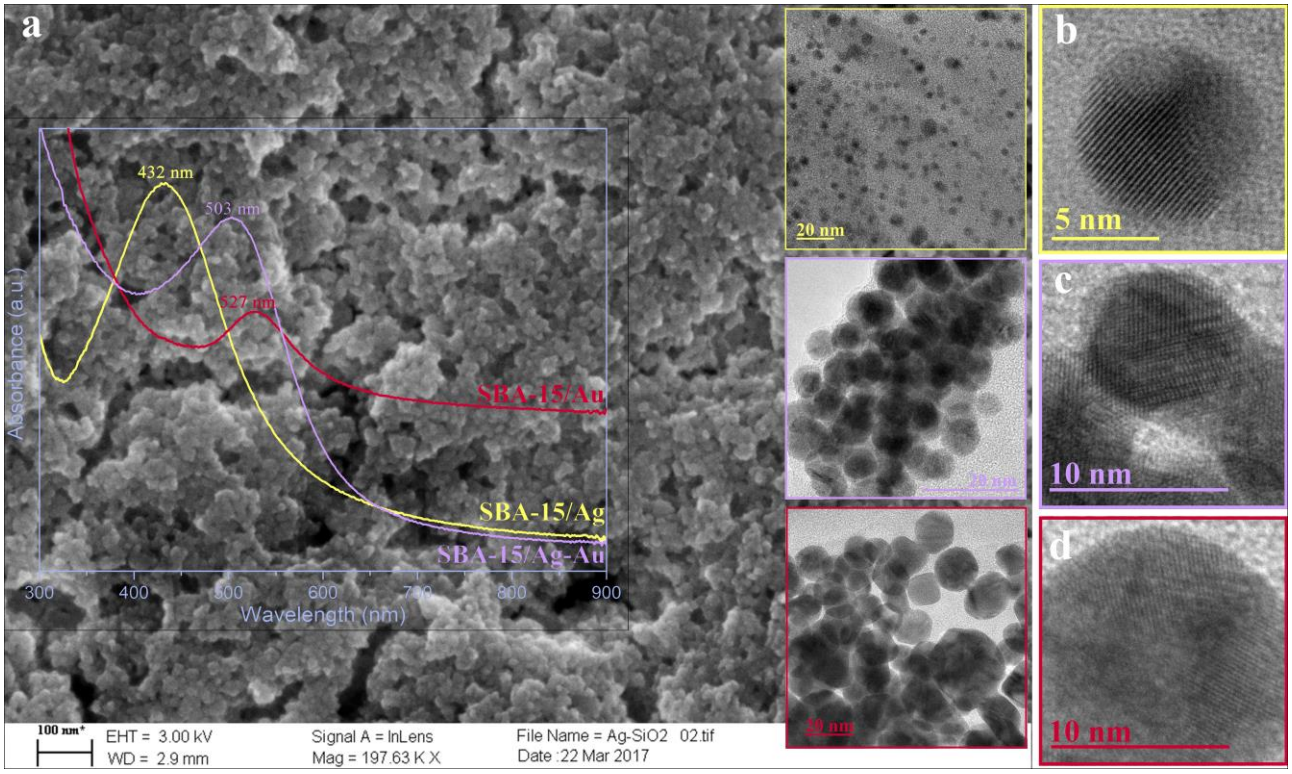


Figure 1. FeSEM image of SBA-15/Ag nanocomposite (a) with UV-Vis spectra of all three nanocomposites (Inset, left) and corresponding TEM images (Inset right); HRTEM images of SBA-15/Ag (b), SBA-15/Ag-Au (c), and SBA-15/Au (d).

Besides the change in the colors of reaction mixtures, the formation of these nanocomposites was recognized through their UV/Vis spectra (**Figure 1a, Inset - left**). Surface plasmon resonance (SPR) bands of AgNPs, AuNPs, and Ag-AuNPs formed throughout SBA-15 are located more/less shifted compared to the positions of "pure" NPs [8], as the result of surroundings of SBA-15, while the absorption band of SBA-15/Ag-Au is superimposed from the SPR bands of AgNPs and AuNPs. The morphology of SBA-15 in these nanocomposites has remained the same as before the reaction (as in Ref. 4) with histidine and metal ions – it is granular (**Figure 1a**). TEM images indicate that spherical nanoparticles are formed in SBA-15/Ag and SBA-15/Au, with mean diameter of 8.5 and 16 nm, respectively, while bimetal has peanuts-like structure with an average length of 15 nm and width of 7 nm (**Figure 1a, Inset - right**). HRTEM images (**Figure 1b, c, and d**) point out NPs' crystallographic planes – (111) and (022), from face-centered cubic (fcc) crystallographic structure.

The results of the quantitative antibacterial efficiency of SBA-15/Ag, SBA-15/Au, and SBA-15/Ag-Au nanocomposites determined over 2 h exposure time with indicator strains of pathogenic bacteria *E. coli* and *S. aureus* are presented in **Table 1**. 2 h of interaction with these microbes, was enough for 1 ppm of SBA-15/Ag to achieve complete antimicrobial action with 99.99% microbial reduction, while the same amount of SBA-15/Au showed somewhat lower activity. After 2 h exposure, its reduction ability was 79.52 and 21.16% toward *E. coli* and *S. aureus*, respectively. The antimicrobial role of SBA-15/Ag-Au toward both pathogens was negligible. Spherical shape and small size (8 nm), as well as reactive (111) planes on AgNPs surface, make them very powerful tools in the combat with microbes, but the role of SBA-15 with all the abovementioned characteristics, must not be neglected either. Thus, SBA-15 is a great platform that provides a large surface area for NPs' contact with microbes – physically surrounding them, and closing their access to nutrients. Besides, released Ag^+ ions interact with bacterial cell wall functional groups, resulting in enzyme deactivation, respiration disruption, and final microbial death [11]. The lower antimicrobial ability of SBA-15/Au is probably due to slightly larger particles (16 nm for AuNPs compared to 8 nm for AgNPs), with a reduced ability to penetrate and interact with microbes, as well as the formation of reactive oxygen species (ROS) [7]. Similarly, nanocomposite with bimetal NPs that are larger than AgNPs and AuNPs and with non-spherical shape showed the smallest and negligible microbial reduction ability.

Table 1. Antibacterial activity of 1 ppm SBA-15/Ag, SBA-15/Au, and SBA-15/Ag-Au after 2 h incubation time with *E. coli* and *S. aureus.*

Sample	*E. coli*		*S. aureus*	
	CFU 2 h after their contact with sample	Microbial reduction (*R*, %)	CFU 2 h after their contact with sample	Microbial reduction (*R*, %)
Control	4.20×10^6	/	1.32×10^7	/
SBA-15/Ag	<10	99.99	2.70×10^3	99.98
SBA-15/Au	8.60×10^5	79.52	1.04×10^7	21.16
SBA-15/Ag-Au	3.08×10^6	26.67	1.14×10^7	13.90

CONCLUSION

Among the presented nanocomposites, SBA-15/Ag showed the most interesting and significant antibacterial activity toward *E. coli* and *S. aureus*, after 2 h exposure. With only 1 ppm of the nanocomposite in the interaction with these strains, the result of 99.99% microbial reduction is compelling, indicating its high antibacterial efficacy at low concentrations. These features are desirable for its application as a disinfectant, that will not be toxic to the environment. However, the other two nanocomposites (SBA-15/Au and SBA-15/Ag-Au), require higher concentration and/or contact time with microbes to achieve their better antimicrobial efficacy.

Acknowledgment
The research was funded by the Ministry of Education, Science and Technological Development of the Republic of Serbia, *via* direct financing of Vinča Institute of Nuclear Sciences – National Institute of Republic of Serbia (contract no. 451-03-66/2024-03/200017).

REFERENCES

[1] A. Bernardos, E. Piacenza, F. Sancenón, M. Hamidi, A. Maleki, R.J. Turner, R. Martínez-Máñez, Small, 15 (2019) 1900669.
[2] D. Zhao, J. Feng, Q. Huo, N. Melosh, G. H. Fredrickson, B. F. Chmelka, G. D. Stucky, Science, 279 (1998) 548.
[3] M. Kokunešoski, J. Gulicovski, B. Matović, B. Babić, J. Optoelectron. Adv. M., 11 (2009) 1659.
[4]. M. Kokunešoski, J. Gulicovski, B. Matović, M. Logar, S.K. Milonjić, B. Babić, Mater. Chem. Phys., 124 (2010) 1248.
[5] G.A. Marcelo, M.P. Duarte, E. Oliveira, SN Applied Sciences, 2 (2020) 1354.
[6] D. Yang, N. Ni, L. Cao, X. Song, Y. Alhamoud, G. Yu, J. Zhao, H. Zhou, Micromachines-Basel, 10 (2019) 268.
[7] D. Mašojević, U. Stamenović, M. Otoničar, S. Davidović, S. Škapin, T. Barudžija, V. Vodnik, Mat. Lett., 338 (2023) 134051.
[8] M. Oszust, K. Gdula, P. Borowski, A. Dąbrowski, M. Barczak, Adsorpt. Sci. Technol., 33 (2015) 6.
[9] C.N. Iswarya, S.C.G. Kiruba Daniel, M. Sivakumar, Mat. Sci. Eng. C-Bio. S, 75 (2017) 393.
[10] A. Ghosh, C.R. Patra, P. Mukherjee, M. Sastry, R. Kumar, Micropor. Mesopor. Mat., 58 (2003) 201.
[11] S. Sohrabnezhad, A. Jafarzadeh, M. Rassa, Iran. J. Chem. Chem. Eng., 39 (2020) 3.

INVESTIGATION OF THE RELEASE OF NOVEL ACRIDINE DERIVATIVE SUPPORTED ONTO Y ZEOLITE

K. Teletina [1], N. Fišić [1], M. Ranković [1], J. Rupar [2], M. Milojević-Rakić [1] and A. Jevremović [1*]

[1] *University of Belgrade - Faculty of Physical Chemistry, 11000 Belgrade, Serbia. (anka@ffh.bg.ac.rs)*
[2] *University of Belgrade-Faculty of Pharmacy, 11221 Belgrade, Serbia.*

DOI: https://doi.org/10.46793/Phys.Chem24I.321T

ABSTRACT
This study investigated 2-(acridin-9-ylamino)-3-(1*H*-indol-3-yl)propanoic acid, acridine derivative as a potential anticancer drug supported on FAU type zeolite Y. Y zeolite before and after the drug impregnation was characterized with the scanning electron microscopy and thermogravimetry, while HPLC/FL and spectrofluorimetry were employed for drug quantification. The morphology of the zeolite did not change during the drug impregnation process, and the resulting drug loading was 17.9 mg/g. The release of 1.2 μM acridine derivative concentration necessary for targeted cancer cytotoxicity and favorable kinetics was established for zeolite-supported acridine.

INTRODUCTION
Conventional drug delivery systems (tablets and intravenous injections) deliver the entire dose of the drug at once, resulting in a high, often toxic, drug concentration that can cause side effects. Traditional drug delivery is unpredictable and ineffective; a large amount of drug is usually required to reach an effective, therapeutic concentration of the drug at the target site [1]. Studies employing zeolite-based drug delivery systems as alternatives to conventional methods indicate improved cellular absorption and reduced side effects while maintaining the desired pharmacological outcomes [2-3].

Acridine derivatives, nitrogen-containing heterocyclic compounds with modified core structures, exhibit various biological activities such as anticancer, anti-inflammatory, and antimicrobial properties by binding to nucleic acids and interacting with proteins. [4] investigates the therapeutic potential of chloroacridines by focusing on the electrochemical behavior of 9-chloroacridine to detect DNA intercalation. Ranković et al. [5] explored the use of zeolite Y as a carrier for acridines, evaluating their effects on cell viability against human colorectal carcinoma and fibroblast cell lines (MTT test), demonstrating stable zeolite structure post-drug impregnation with drug loadings ranging from 18-21 mg/g. Consequently, these promising acridines are being further explored as potential anticancer compounds. This study aimed to provide a novel acridine derivative supported by a Y zeolite and investigate its release. Drug-loaded zeolite was characterized by microscopic and thermogravimetric analysis, and a drug release was investigated using fluorescence measurements.

METHODS
Y zeolite (Zeolyst International CBU780, Si/Al=40, surface area of 780 m^2/g) was used as received. Acridine derivative, 2-(acridin-9-ylamino)-3-(1*H*-indol-3-yl)propanoic acid (abbreviation MMA, M = 395 g/mol) presented in Figure 1, was prepared according to the procedure given in [6].

The drug-supporting procedure involved suspending 100 mg of zeolite into 10 mL of MMA (1 mM) solution, which was then thermostated at a laboratory shaker at 23 °C/110 rpm for 24 h. After drug loading, the sample was centrifuged, dried at 60 °C, and denoted as Y/MMA. The amount of drug remaining in the solution after impregnation was measured using the Waters 2475 HPLC

system equipped with a 2475 Multi λ Fluorescence Detector, with an excitation wavelength of 386 nm and an emission wavelength of 440 nm. The 80/20 vol./vol. acetonitrile/water eluent with a 1 mL/min flow rate and PartiSil C18 column were employed. Morphology was analyzed using a Phenom ProX microscope and an energy-dispersive X-ray (EDX) spectrometer (Thermo Scientific) using the acceleration voltage of 15 kV. At the same time, surface mapping required 128 passes with 10 ms dwell time per point. The thermal behavior of the Y/MMA sample was analyzed by thermogravimetric analysis (TGA) on an SDT 2960 thermoanalytical device (TA instrument). The heating program operated from room temperature up to 800 °C in the air at a flow rate of 70 mL min^{-1}, with a heating rate of 10 °C min^{-1}. The release kinetics of MMA from the Y/MMA sample in phosphate buffer (0.1 M, pH=7.4) was followed by an Agilent Cary 18 Eclipse spectrofluorimeter. After suspending 10 mg of Y/MMA in a volume of 20 mL phosphate buffer for 1, 2, 20, and 48 h, the suspensions were centrifuged, and fluorescence emission spectra were recorded.

RESULTS AND DISCUSSION

The thermogravimetric analysis determined the amount of MMA bound to Y zeolite (Figure 2). By comparing the mass loss values of the original Y zeolite with those of Y/MMA, it was observed that both profiles exhibit similar trends. For the original zeolite, the continuous mass loss is due to the desorption of water from the zeolite's pores, whereas in Y/MMA, the bound drug also contributes to the mass loss. From the difference in mass losses, it was calculated that the MMA loading on Y zeolite is 25 mg/g. This result aligns with the MMA detected in the supernatant after the impregnation process (17.9 mg/g).

During the adsorption of MMA on Y zeolite, the granular morphology of the starting zeolite did not change (SEM micrographs). EDX analysis shows a uniform distribution of MMA on the zeolite surface, as can be seen in the nitrogen distribution map.

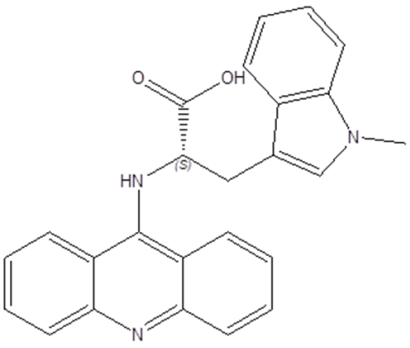


Figure 1. The structure of MMA.

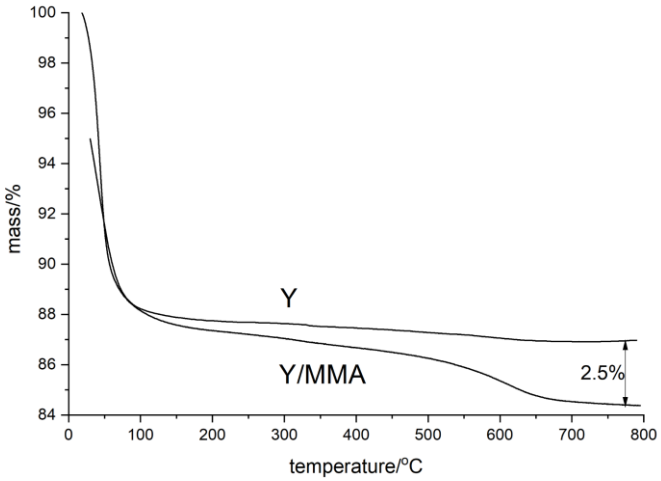


Figure 2. TGA curves of starting zeolite and Y/MMA sample.

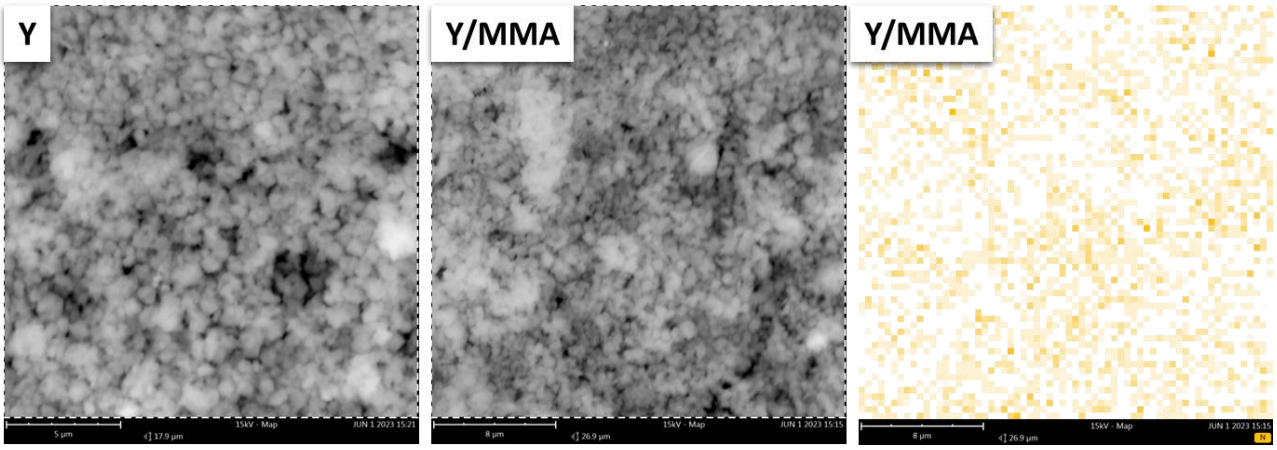


Figure 3. SEM micrographs of pristine Y zeolite, Y supported MMA sample and nitrogen elemental map.

To determine the concentration of the drug released from the zeolite carrier, the emission spectra of MMA in a phosphate buffer were taken in selected time intervals up to 48 h. The ratio of the Y/MMA and the phosphate buffer volume (10 mg/20 mL) followed the concentrations of the suspensions analyzed in the release of acridine-based drugs. The results (Figure 4) show that the concentration of released MMA increases over time following a first-order kinetic. Similar results were seen with 9-amino and 9-chloroacridine derivatives [5]. Given that the obtained concentration of MMA in the suspension, released after 48 h, reaches the level of μM concentration, cytotoxic activity or released drug may be expected. Dobričić et al. previously showed that MMA and other 9-acridinyl amino acid derivatives show a marked efficiency in the treatment of cancer cells where the concentrations affecting the reduction of cell viability were of the order of μM [6].

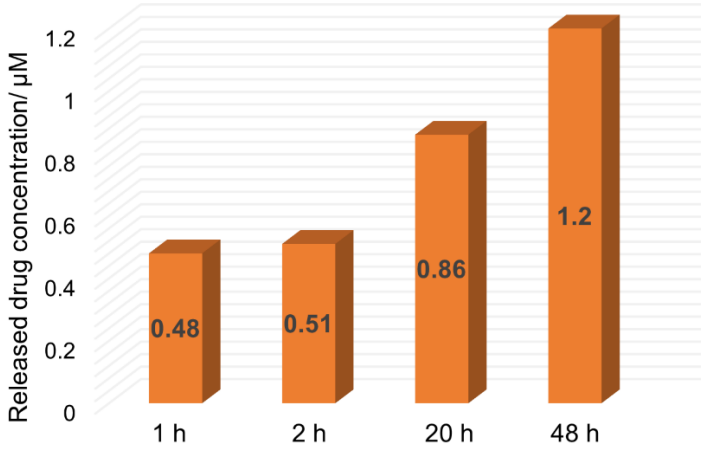


Figure 4. The overall drug release quantity from Y/MMA over time in the buffer.

CONCLUSION

This study presented a novel drug delivery system utilizing 2-(acridin-9-ylamino)-3-(1*H*-indol-3-yl)propanoic acid, an acridine derivative with anticancer properties supported within the Y zeolite carrier. Efficient drug loading was confirmed by chromatographic and thermogravimetric analysis to the extent of 18 mg/g. SEM analysis revealed that the tested acridine was evenly distributed across the zeolite support, and release kinetics indicated a consistent and extended release over 48

h. The drug-loaded zeolite effectively delivered drug concentrations in the μM range in buffer solutions, enabling further testing in the cytotoxicity study.

Acknowledgment
This research was funded by the Ministry of Science, Technological Development and Innovation of the Republic of Serbia, grant numbers 451-03-65/2024-03/200161, 451-03-65/2024-03/200146, and grant 04-4-1133-2018/2023 for collaboration between JINR, Dubna and University of Belgrade.

REFERENCES

[1] Degradable Polymer Microspheres for Controlled Drug Delivery, Vol. 157, U. Edlund, A.C. Albertsson, Vol. 157. Springer, Berlin, Heidelberg, 2002.
[2] J. Hao, M. I. Stavljenić, E. Z. Batu, M. Mravak-Stipetic, K. Pavelić, F. Ozer, Mol. 26 (2021) 6196.
[3] Z. A. Abadeh, G. Saviano, P. Ballirano, M. G. Santonicola, Pure Appl. Chem. 92 (2020) 461–471.
[4] J. Rupar, M. Aleksić, V. Dobričić, J. Brborić, O. Čudina, Bioelectrochem. 135 (2020) 107579.
[5] M. Ranković, A. Jevremović, A. Janošević Ležaić, A. Arsenijević, J. Rupar, V. Dobričić, B. Nedić Vasiljević, N. Gavrilov, D. Bajuk-Bogdanović, M. Milojević-Rakić, J. Funct. Biomater. 14 (2023) 173.
[6] J. Rupar, V. Dobričić, J. Grahovac, S. Radulović, Ž. Skok, J. Ilaš, M. Aleksić, J. Brborić, O. Čudina, RSC Med. Chem, 11 (2020) 378-386.

SYNTHESIS AND PHYSICOCHEMICAL CHARACTERIZATION OF TiO_2/POLY(N-ISOPROPYLACRYLAMIDE) NANOCOMPOSITE HYDROGELS

M. Milošević, I. Vukoje, J. Spasojević , N. Nikolić and A. Radosavljević

Vinča Institute of Nuclear Sciences, National Institute of the Republic of Serbia, University of Belgrade, Mike Petrovića Alasa 12-14, 11351 Vinča, Belgrade, Serbia (milicam@vin.bg.ac.rs)

DOI: https://doi.org/10.46793/Phys.Chem24I.325M

ABSTRACT

In this study, nanocomposite hydrogels were prepared by embedding the different concentrations of TiO_2 nanoparticles (NPs) in a poly(N-isopropylacrylamide) (PNiPAAm) crosslinked matrix. UV-Vis and FTIR spectroscopy have been employed to determine the presence of TiO_2 NPs in the polymer network and examine their molecular interactions, respectively. The TiO_2/PNiPAAm nanocomposite hydrogels showed a slightly higher swelling capacity and a faster swelling/deswelling processes compared to PNiPAAm hydrogel. Additionally, the volume phase transition temperature of nanocomposites is shifted towards somewhat higher values.

INTRODUCTION

It is well known that hydrogels are three-dimensional polymeric networks with a strong affinity to absorb and retain significant amounts of fluids without compromising their structure [1]. Their unique physicochemical properties impel ongoing research and innovation in different fields of material sciences. Understanding and managing these features enables the customization and application of hydrogels for specific purposes, thereby improving their efficiency and functionality in respective domains. Poly(N-isopropylacrylamide) (PNiPAAm) has been extensively investigated primarily for its thermosensitivity, leading to versatile application, especially in the field of biomedicine [2]. One of the advancements in material science is the integration of NPs with hydrogels. This results in the creation of nanocomposite hydrogels that possess enhanced properties when compared to their individual components. It is widely recognized that TiO_2 NPs exhibit photocatalytic activity under UV-Vis light exposure, which can be preserved even when TiO_2 NPs are immobilized within the hydrogel matrix [3]. This introduces new functionalities and potential applications of TiO_2 NPs-based hydrogels, particularly in the fields of environmental remediation and biomedical engineering. These materials are especially useful for degrading contaminants from water sources, such as industrial wastewater or polluted groundwater. Also, they possess antibacterial activity and biocompatibility, which are useful for applications relating to wound dressings and biomedical implants. When it comes to other NPs, TiO_2 NPs stand out for their reduced risk of toxicity, thus minimizing any concerns regarding possible negative impacts on human health or the environment.

In this research, we describe the synthesis and physicochemical properties of TiO_2/PNiPAAm nanocomposite hydrogels. The aim was to examine the possibility of incorporating TiO_2 NPs into a thermosensitive polymer network to obtain stable nanocomposite hydrogels. Such fundamental results are a necessary basis for continued research and the possibility of adjusting material properties to certain applications.

METHODS

Synthesis of TiO_2 NPs and TiO_2/PNiPAAm nanocomposite hydrogels. Colloidal TiO_2 was implied and a brief overview of its synthesis is given [4]: (1) dropwise addition of cooled $TiCl_4$ to cooled water and dialysis against water until pH of the solution reached 3.5; thus the formation and slow growth of amorphous TiO_2 NPs ($d \approx 4.5$ nm) is achieved and (2) thermal treatment in reflux (60 °C, 16 h), which carry on the amorphous-to-crystalline transformation of anatase and hence enhances the potential photocatalytic efficiency of generated NPs ($d \approx 6$ nm) [5]. The concentration of the obtained colloidal TiO_2 was set to 0.12 M.

A synthesis of 10 wt.% PNiPAAm hydrogel (labeled as S0) was performed using 4% of N-methylenebisacrylamide (MBA) as crosslinker, in the presence of potassium persulphate (KPS) as an initiator and tetramethylethylenediamine (TEMED), which accelerates the polymerization [6]. In order to obtain TiO_2/PNiPAAm nanocomposite hydrogels, the polymer matrix was crosslinked in the presence of TiO_2 NPs. The final concentration of TiO_2 in nanocomposite hydrogels was 0.04 M (labeled as S1) and 0.08 M (labeled as S2).

Methods of characterization. After the crosslinking process, the obtained hydrogels were cut into discs, dried to the constant weight, and then extracted in distilled water for 7 days, to remove the uncrosslinked polymer. Extracted hydrogels were dried again in order to determine the gel fraction. The optical properties of TiO_2/PNiPAAm nanocomposite hydrogels were investigated by Thermo Fisher Scientific Evolution 600 UV-Vis spectrophotometer. FTIR spectroscopy was applied to determine the molecular structure of the hydrogel matrix and its interaction with TiO_2 NPs. FTIR analysis was performed using a Thermo Electron Corporation Nicolet 380 Spectrophotometer, with the addition of the Attenuated Total Reflection (ATR) mode. Volume phase transition temperature (VPTT) and dynamic swelling/deswelling measurements were performed in deionized water, using a gravimetric method.

RESULTS AND DISCUSSION

To evaluate the efficiency of the selected crosslinking method, the gel fraction was calculated by the following equation: $Gel\ (\%) = (m_{ae}/m_{be}) \times 100$, where m_{ae} and m_{be} are the weights of dry samples after and before extraction, respectively [1]. The gel fraction of PNiPAAm hydrogel (sample S0) was found to be 96.8%.

The presence of TiO_2 NPs inside the polymer matrix was confirmed by UV-Vis spectroscopy. **Figure 1a** represents the absorption spectra of TiO_2 NPs, S0, S1 and, S2. Characteristic UV-Vis spectrum of TiO_2 NPs, which show strong absorption in the UV region of the spectrum ($\lambda < 400$ nm), is obtained [4]. However, a strong absorption in the UV part of the spectrum was achieved in the S1 and S2 samples, which proves the presence of TiO_2 NPs within the polymer matrix. In addition, observing the S1 and S2 samples, it can be found that the obtained absorption curves show a slight blueshift compared to pure TiO_2, likely due to the presence of PNiPAAm. **Figure 1b** shows the FTIR spectra of TiO_2 NPs, S0, S1, and S2 samples. From FTIR spectrum of TiO_2 NPs, deformative vibration of Ti-OH stretching mode is observed at 1623 cm^{-1}, but the same band also may be attributed to water adsorbed on TiO_2 surface [7]. The characteristic bands of PNiPAAm hydrogel are distributed in three regions: 1680-1500 cm^{-1}, 1420-1350 cm^{-1} and 1300-1100 cm^{-1}, with the broad band around 2800-3400 cm^{-1} belonging to O-H bonds [1]. Observing the spectrum, the main contribution of PNiPAAm to TiO_2/PNiPAAm nanocomposite is reflected in peak assignments for 2971 cm^{-1} (CH_3 asymmetric stretching) and 1533 cm^{-1} (secondary amide C=O stretching) [8]. An obvious increase in intensity of band at 1623 cm^{-1} in TiO_2/PNiPAAm spectra, compared to TiO_2 and PNiPAAm, may be the proof that TiO_2 NPs were successfully incorporated into the PNiPAAm polymer matrix.

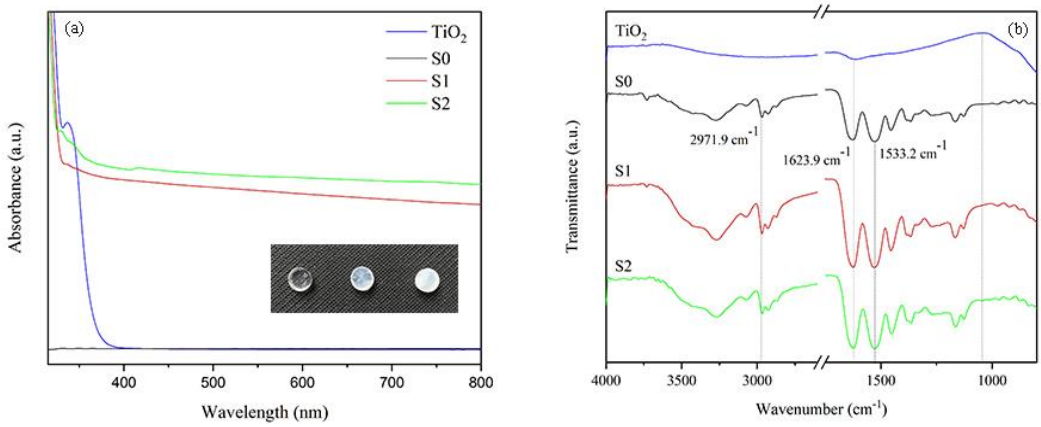


Figure 1. UV-Vis absorption spectra (a) and FTIR spectra (b) of TiO_2 NPs, PNiPAAm (S0) and TiO_2/ PNiPAAm nanocomposite hydrogels (S1 and S2). Inset: Photograph of S0 (transparent hydrogel), S1 (less milky white) and S2 (more intense milky white) nanocomposite hydrogels.

Determining the physicochemical properties of TiO_2/PNiPAAm nanocomposite hydrogels is crucial, especially considering their application sustainability. Therefore, their swelling and deswelling behavior, as well as their volume phase transition temperature were analyzed (**Figure 2**). The equilibrium swelling degree (SD_{eq}) of hydrogels is an essential parameter that has a significant impact on other factors and it can be determined using the following equation: $SD_{eq} = (m_t-m_0)/m_0$, where m_t is a weight of swollen hydrogel at the moment t, and m_0 is the initial weight of the xerogel [1]. It is evident that the presence of TiO_2 NPs in the polymer matrix leads to slightly greater swelling capacity and diffusion coefficients (D), compared to S0, which is a consequence of network expansion (**Figure 2a, Table 1**). On the other hand, the incorporation of different TiO_2 concentrations into polymer network has no significant effect on swelling properties. Moreover, all investigated systems show non-Fickian diffusion ($0.5 < n < 1$) which occurs when the rates of diffusion and polymer chain relaxation are comparable [1].

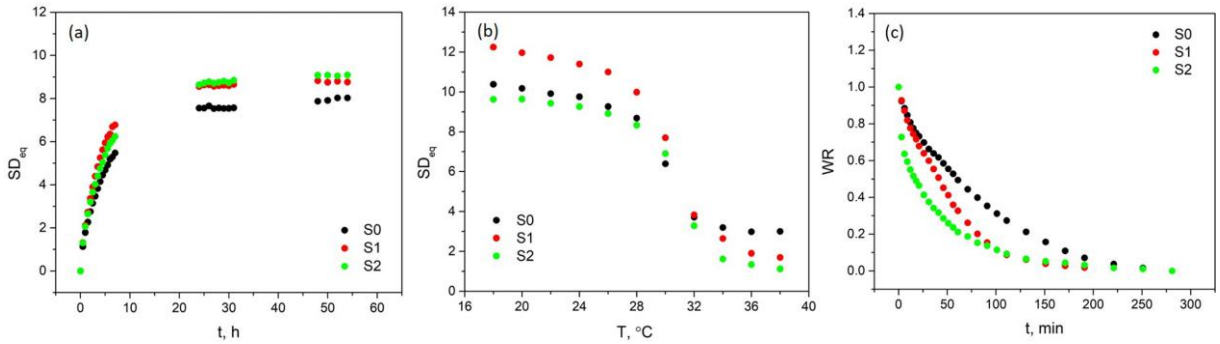


Figure 2. Swelling curves (a), temperature dependence of SD_{eq} (b), and deswelling curves (c) of PNiPAAm (S0) and TiO_2/PNiPAAm nanocomposite hydrogels (S1 and S2).

For the deswelling kinetics studies, the hydrogels that had reached equilibrium swelling were placed in water at a temperature of 48 °C. The rate of deswelling, K, is assumed to follow first-order kinetics and can be determined by analyzing the first-order rate using a semi-logarithmic plot, as previously described [1]. According to the deswelling kinetic curves shown in **Figure 2b**, it is evident that the K value is considerably higher in both samples S1 and S2 when compared to the S0.

The thermosensitivity of PNiPAAm-based hydrogels were investigated through the values of SD_{eq} across the temperature range of 17 °C to 37 °C (**Figure 2b)**. The obtained VPTT values (**Table 1**) indicate that the incorporation of TiO_2 NPs into the polymer matrix shifts the phase transition to somewhat higher temperatures. This behavior is more prominent for higher concentration of TiO_2 NPs and probably can be attributed to the interaction between the polymer chains and NPs as well as to higher swelling capacity. The deswelling kinetics was investigated at temperature above VPTT (at 48 °C). Assuming that the deswelling rate follows first-order kinetics, the deswelling rate constant (*K*) can be determined by a semi-logarithmic plot, as previously described [1]. The deswelling kinetic curves are shown in **Figure 2c**, while from **Table 1.** It is evident that the *K* values are higher in both S1 and S2 nanocomposites, compared to S0.

Table 1. Physicochemical parameters of investigated hydrogels: equilibrium swelling degree (SD_{eq}), diffusion exponent (*n*), kinetic rate constant (*k*), diffusion coefficient (*D*), deswelling rate constant (*K*), and volume phase transition temperature (*VPTT*).

Sample	SD_{eq}	n	k x10^3, min^{-1}	D x 10^6, cm^2min^{-1}	K x 10^3, min^{-1}	VPTT, °C
S0	8.02	0.63	1.6	2.91	16.3	30.1
S1	8.76	0.66	1.5	3.83	18.5	30.5
S2	9.09	0.65	1.7	3.62	56.6	31.1

CONCLUSION

In this study, nanocomposites based on TiO_2 NPs and PNiPAAm hydrogel were successfully synthesized. The presence of TiO_2 NPs inside the polymer matrix was confirmed by UV-Vis absorption spectra as well as by FTIR analysis. The TiO_2/PNiPAAm nanocomposite hydrogel, compared to PNiPAAm, indicates not only higher swelling capacity and swelling/deswelling rate constants, but also the VPTT is shifted to the higher values. The diffusion transport mechanism study shows the non-Fickian transport, indicating that the effects of diffusion and relaxation of polymer chains are comparable.

Acknowledgment

This work was supported by the Ministry of Science, Technological Development and Innovations of the Republic of Serbia (contract number: 451-03-66/2024-03/200017).

REFERENCES

[1] J. Spasojević, A. Radosavljević, J. Krstić, D. Jovanović, V. Spasojević, M. Kalagasidis-Krušić, Z. Kačarević-Popović, Eur. Polym. J., 69 (2015) 168-185.
[2] T. Caykara, S. Kiper, G. Demire, S. Demirci, C. Cakanyildirim, Polym. Int., 56 (2007) 275-282.
[3] N. Papadopoulou-Fermeli, N. Lagopati, N. Pipa, N. Sakellis, N. Boukos, V. G. Gorgoulis, M. Gazouli, E. A. Pavlatou, Pharm., 15 (2023) 135.
[4] M. Milošević, M. Radoičić, S. Ohara, H. Abe, J. Spasojević, L. Mančić, Z. Šaponjić, Cellulose, 30 (2023) 4749-4771.
[5] T. Rajh, J. Nedeljković, L.X. Chen, D.M. Tiede, M.C. Thurnauer, J Adv Oxid Technol, 3 (1998) 292–298.
[6] N. Milašinović, N. Milosavljević, J. Filipović, Z. Knežević-Jugović, M. Kalagasidis Krušić, React. Funct. Polym., 70 (2010) 807-814.
[7] L. S. Chougala, M. S. Yatnatti, R. K. Linganagoudar, R. R. Kamble, J. S. Kadadevarmath, J. Nano-Electron. Phys., 9 (2017) 04005.
[8] L. Zhang, S. Zhang, B. He, Z. Wu, Z. Zhang, Z. Naturforsch, 63b (2008) 973-976.

IMPLEMENTING MONTE CARLO METHOD TO GENERATE 3D MODEL OF PEGYLATED CARBON NANOTUBES

I. Bracanović [1], A. Krstić [2], M. Mirković [1], A. Kalijadis [1] and M. Zlatović [3]

[1]*University of Belgrade, Institute of Nuclear Sciences "Vinča" - National Institute of the Republic of Serbia-Department of Materials, 11000 Belgrade, Serbia*
[2]*University of Belgrade, Institute of Nuclear Sciences "Vinča" - National Institute of the Republic of Serbia - Department of Physical Chemistry, 11000 Belgrade, Serbia (aleksandar.krstic@vinca.rs)*
[3]*University of Belgrade, Faculty of Chemistry, Studentski trg 12-16, 11000 Belgrade, Serbia.*

DOI: https://doi.org/10.46793/Phys.Chem24I.329B

ABSTRACT

In this paper, we describe using computational calculations in order to better understand carbon nanomaterials as drug carriers. The unique physicochemical properties of materials at the nanoscale have opened a plethora of opportunities for applications in the pharmaceutical and medical fields. To analyze drug loading, a 3D model is necessary, and a Monte Carlo simulation can be used to generate it. Monte Carlo simulations can predict the structure of polymer connected to the CNT, analyze the factors affecting it from a microscopic perspective and provide a basis for the structural design of carbon material. To extrapolate interactions that lead to its structure and analyze potential spots for drug carrier-drug interactions, this way generated model was analyzed in DS Visualizer. Results yielded a 3D model that can be used in further work for docking simulations of binding the drug molecules onto the carrier.

INTRODUCTION

Carbon nanotubes (CNTs) are a type of carbon-based nanomaterial that form hollow tubes. They can be either single-walled (SWCNTs) or multi-walled (MWCNTs). CNTs have remarkable physical and chemical properties, making them widely used in various industrial and medical applications. For instance, they have been employed as carriers for targeted drug delivery in cancer treatment. However, prolonged exposure to CNTs can be harmful to human and animal health. MWCNTs have been found in organs such as the liver, kidney, lung, and brain after exposure in mice. The adverse effects of CNTs include cytotoxicity, genotoxicity, and carcinogenicity [1].

The toxicity of carbon nanotubes (CNTs) is influenced by their surface chemical properties so surface modification is the key for lowering the toxicity. Carboxy-modified CNTs exhibit greater biocompatibility compared to pure multi-walled CNTs (MWCNTs). Additionally, CNTs coated with polyethylene glycol (PEG) are more biocompatible than non-PEGylated ones. Furthermore, PEGylated CNTs have better drug uptake than CNTs without polymer [2].

To generate an accurate representation of PEGylated CNTs, Monte Carlo molecular modeling can be used. This modeling approach involves applying Monte Carlo methods to molecular problems, which relies on equilibrium statistical mechanics, generating the states based on the Boltzmann distribution [3].

In this paper, we used computational calculations based on Monte Carlo molecular modeling to generate a 3D model of PEGylated CNTs, study the interaction that polyethylene glycol makes with the CNT and analyze spots on the material where drug may be attached.

METHODS

For generating the structures to be used in Monte Carlo method, we used ACD/ChemSketch (Freeware) to sketch part of a molecular structure of PEGylated CNT [4]. The structure was then optimized in Avogadro software [5]. The optimized structure was saved as a mol2 file, and then Abalone software was used to run the Monte Carlo method to generate a 3D model of the material [6]. For analysis of Monte Carlo-generated structures, we used BIOVIA DS Visualizer [7].

RESULTS AND DISCUSSION

Figure 1. shows the structure of PEGylated CNTs that are drawn in ACD/ChemSketch, considering the process and reaction needed to synthesize this material according to Kumar et al. and surface functional groups of oxidized carbon material [8, 9].

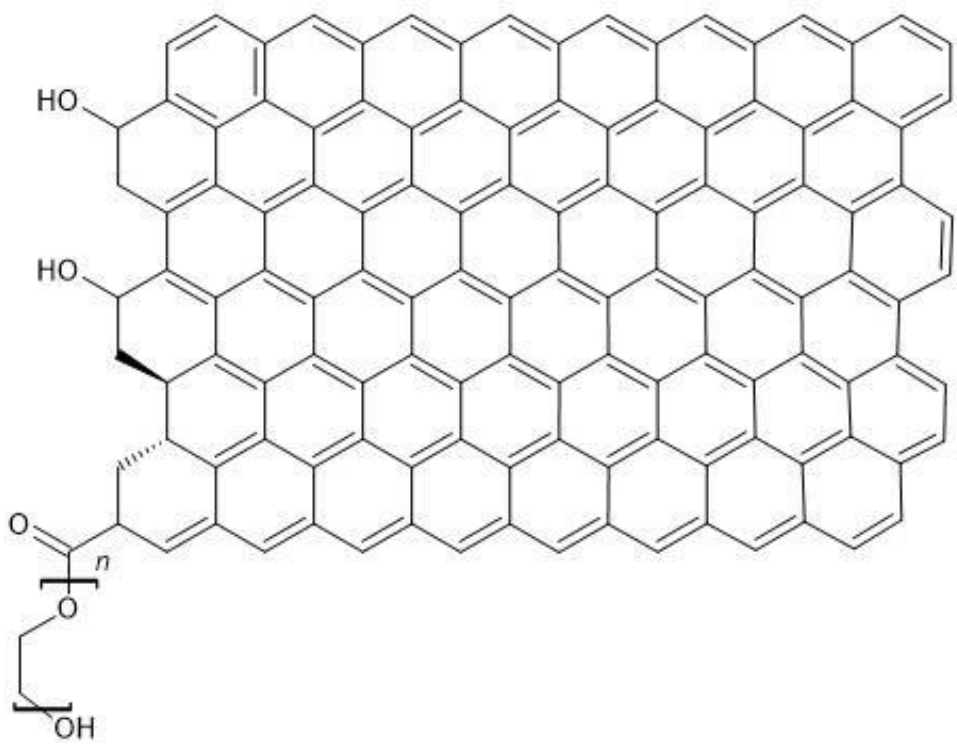


Figure 1. Structure of PEGylated CNT.

Monte Carlo molecular modeling calculations were applied to PEGylated CNTs. First, we had to freeze the CNTs' sp^2 structure to accurately represent its unbending. Then, we started calculations on this structure, using 600000 iterations at a temperature of 298,15 K, which produced a 3D model shown in Figure 2. It can be seen how polyethylene glycol covered the surface of the CNTs, creating a first layer and a second layer above that.

The interactions that led to this were π-σ interactions (purple lines in Figure 2.), that hydrogen in polyethylene glycol made with π electrons of CNTs, and the carbon-hydrogen bond (green lines in Figure 2.) that polyethylene glycol made with itself during bending process around the CNTs and itself. These interactions bind polyethylene glycol to the surface of CNTs. The nature of this polymer and the interaction that it's making with the surface of the material are the reasons for the better biocompatibility of the material and its good potential as a drug carrier.

Also, in Figure 2, spots A and B represent places where the drug can be loaded onto the carbon material. Spot A is between CNTs and polyethylene glycol, and spot B is in the polyethylene glycol part of the structure. The interaction that the drug structure will make with the material in these spots will be the key to its potential loading. These bonds, holding the structure together, are weak and can easily be broken and remade as an intermolecular interaction with the drug molecule when the drug is introduced into the PEGylated CNT.

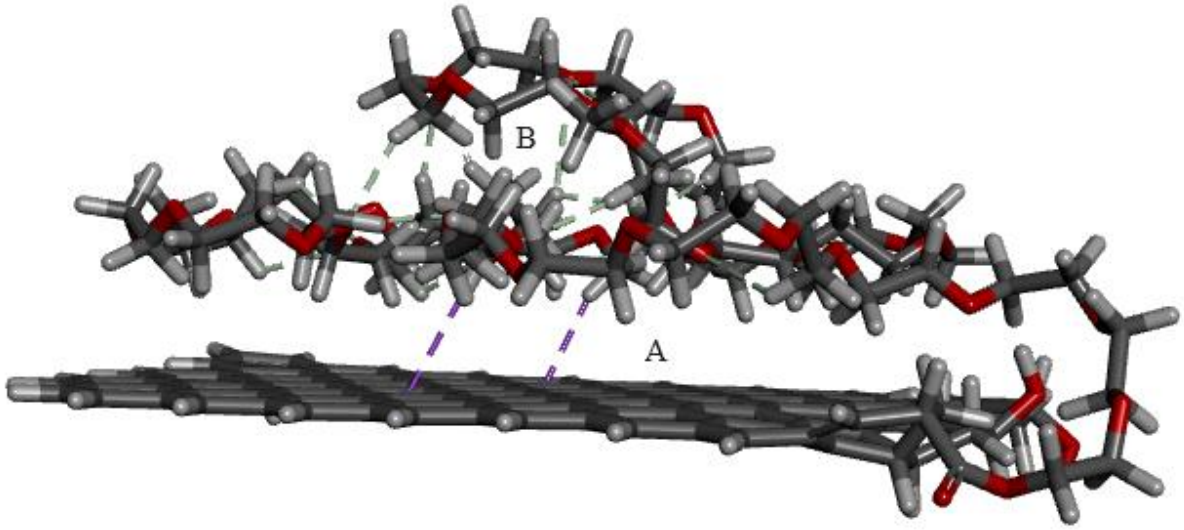


Figure 2. 3D structure of PEGylated CNT generated through the Monte Carlo method.

CONCLUSION

The models showed that π-σ interactions and carbon-hydrogen bonds are the reason why polyethylene glycol sticks to the CNT's surface and makes CNTs more biocompatible. They cover the sharp surface of CNTs, which can no longer interact with the cell membrane. Even though these interactions are weak, their abundance makes them significant, and this structure holds together, creating the sites for potential drug loading.

This model also shows two different possible drug-loading spots (spots A and B), that can be used for molecular docking, giving us a possibility to compare and analyze drug interactions with the drug carrier and calculating the likelihood of their adsorption.

Acknowledgment

This work was supported by the Ministry of Education, Science and Technological Development of the Republic of Serbia (grant no 451-03-66/2024-03/ 200017, topic number: 1702407).

REFERENCES

[1] A.A. Sallam, M.M. Ahmed, M.A. El-Magd, A. Magdy, H.I. Ghamry, M.Y. Alshahrani, M.F. Abou El-Fotoh, Molecules, 27 (2022) 2117.
[2] V. Vilas-Boas, M. Vinken, Arch. Toxicol., 95 (2021) 27.
[3] Z. Zhang, L. Hu, R. Wang, S. Zhang, L. Fu, M. Li, Q. Xiao, Polymers-basel, 16 (2024) 545.
[4] ACD/ChemSketch (Freeware) version 2023.2.4.
[5] Avogadro: an open-source molecular builder and visualization tool. Version 1.1.1.
[6] Abalone Biomolecular Modelling, Version 1.9.0.

[7] BIOVIA, Dassault Systèmes, DS Visualizer, version 21.1.0.20298, San Diego: Dassault Systèmes, 2020.
[8] M. Kumara, G. Sharmab, C. Misraa, R. Kumarc, B. Singhb,c, O.P. Katareb, K. Razaa, Sci. Eng. 89, (2018) 274.
[9] S. K. Malek, M. A. Gabris, B. H. Jume, R. Baradaran1, M. Aziz, K. J. Bt. Abd Karim, H. R. Nodeh, DARU J. Pharm. Sci. 27 (2019) 9.

MICROCRYSTALLINE BRUSHITE MATERIAL AS EFFICIENT ADSORBENT OF LEAD AND NICKEL FROM WATER

M. Mirković [1], A. Krstić [2], D. Đukić[3], V. Pavlović[4], M. Sari Yilmaz[5], I. Bracanović[1] and A. Kalijadis [1]

[1]*University of Belgrade, Institute of Nuclear Sciences "Vinča" - National Institute of the Republic of Serbia-Department of Materials, 11000 Belgrade, Serbia*
[2]*University of Belgrade, Institute of Nuclear Sciences "Vinča" - National Institute of the Republic of Serbia - Department of Physical Chemistry, 11000 Belgrade, Serbia (aleksandar.krstic@vinca.rs)*
[3]*University of Belgrade, Faculty of Biology, Institute of Botany and Botanical Garden, Takovska 43, 11000 Belgrade, Serbia.*
[4] *University of Belgrade, Faculty of Agriculture, Nemanjina 6, 11080, Belgrade, Serbia*
[5]*Chemical Engineering Department, Yildiz Technical University, 34220 Istanbul, Turkey*

DOI: https://doi.org/10.46793/Phys.Chem24I.333M

ABSTRACT

Main goal of this work was to show adsorption efficiency of pure brushite material for heavy metals removal i.e. Pb^{2+} and Ni^{2+} from polluted water. The brushite material was synthesized by a simple solution-precipitation method, guided by green chemistry principles. The obtained material was investigated by XRD and SEM-EDS methods. The results of adsorption showed that lead removal efficiency goes up to 90%, while for nickel was about 20%. Obtained result showed that synthesized material can be successfully used as adsorbent for lead removal from tailings waters.

INTRODUCTION

Brushite ($CaHPO_4 \cdot 2H_2O$) is intensively investigated as bio material, since it has biocompatible and non-cytotoxic characteristics it is widely used as material for bone tissue regeneration [1] [2] [3]. On the other hand, this material also can be very successfully used as adsorbent material for water purification. Lead and nickel contamination of water and soils causes serious problems when they reach into living organisms and causes serious damage with genotoxic and carcinogenic changes [4]. The metals pass through aquatic life system, part of heavy metal ions can be accumulated by plants, but heavy metals are non-degradable and persist in polluted waters for ages [5]. Since the migration of this ions in water is high, it is necessary to find adequate materials that will provide good adsorption efficiency, especially for lead contamination. As we previously described in our works, calcium phosphate materials shoed very good results for lead, cadmium and malathion removal from polluted waters [6], [7], [8].

METHODS

Brushite material was synthesized by solution precipitation method in a same way as *Mirković et.al*. previously described [7]. X-Ray powder diffraction analysis was used for phase and structural characterization. For diffraction analysis the Rigaku Ultima IV diffractometer equiped with high speed D/Tex detector was used, in angle range 5-60 ° 2θ, step 0.02 and scanning speed 5°/min. The PDF # 720713 card number was used for phase identification. SEM-EDS analysis were engaged for microstructural and semi quantitative analysis of obtained brushite.

For SEM and EDS analysis, scanning electron microscope JEOL JSM-6390, with magnification of 4000x, and accel voltage 30 kV was used. Sample was Au coated prior to analysis. In order to

examine the application of the brushite sample, Ni and Pb ions were used as water contaminats model analyte in kinetics experiments. The adsorption efficiency was examined in the 5 – 1440 minute time interval. The initial concentration of the metal mixture adsorbate solution was 30 mg/dm^3. The experiments were performed at 25° in duplicate. For the quantification of Pb and Ni ions, Thermo Fisher ICAOduo 7400 ICAP spectrometer was used. Nickel and lead was detected and quantified on 221.747 nm and 220.853 nm wavelenght, respectively.

RESULTS AND DISCUSSION

Results of structural and phase properties of synthesized brushite material are presented on powder diffractogram (**Figure 1.**). Results of obtained brushite material show that pure monocrystalline material is successfully obtained. At Figure 1 *hkl* indexes of most intense reflections of brushite are labeled, which confirms that simple precipitation method of synthesis can be successfully used for pure brushite material synthesis. Inserted picture which represents crystal structure of brushite shows structural positions of atoms, and also hydrogen bonds along *b*-axis which linkage neighboring tetrahedral and octahedral in structure. These hydrogen bonds that exist in the structure that attract heavy metals so that they most likely interlock between the tetrahedral and octahedral layers [9].

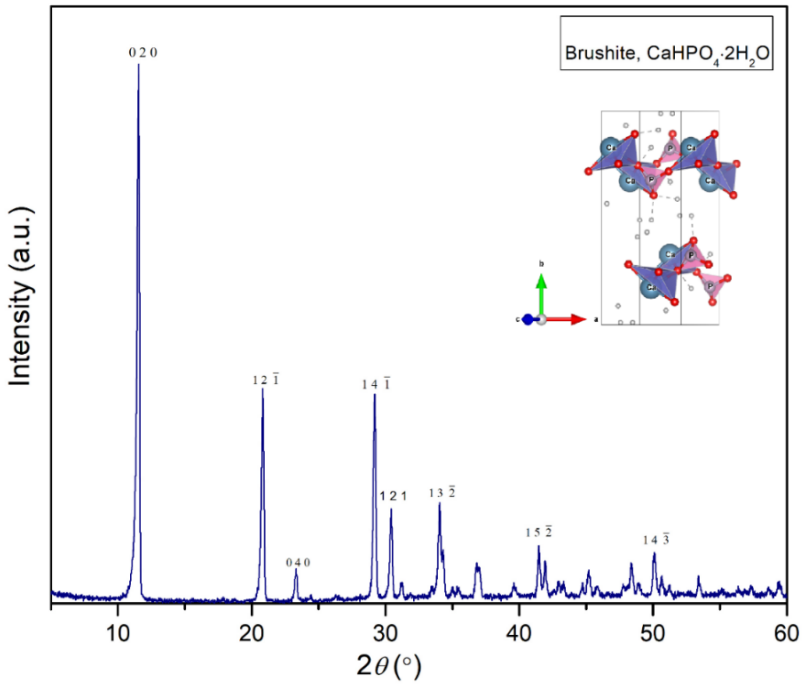


Figure 1. Result of powder diffraction analysis of synthesized brushite (inserted figure shows structure of brushite, blue polyhedron represents Ca positions, pink polyhedron represents P positions, red balls represent oxygen and gray balls represents hydrogen atoms, dash lines represent hydrogen bonds along *b*-axis).

Results of SEM-EDS analysis are presented on Figure 2. Based on SEM results it can be seen that brushite have proper prismatic monoclinic grain shapes.

Approximately sizes of larger grains are about 20 μm, while smaller grains have sizes about 5 μm. Ca/P ratio amounts 1.0 which is which is in full agreement with literature data [10].

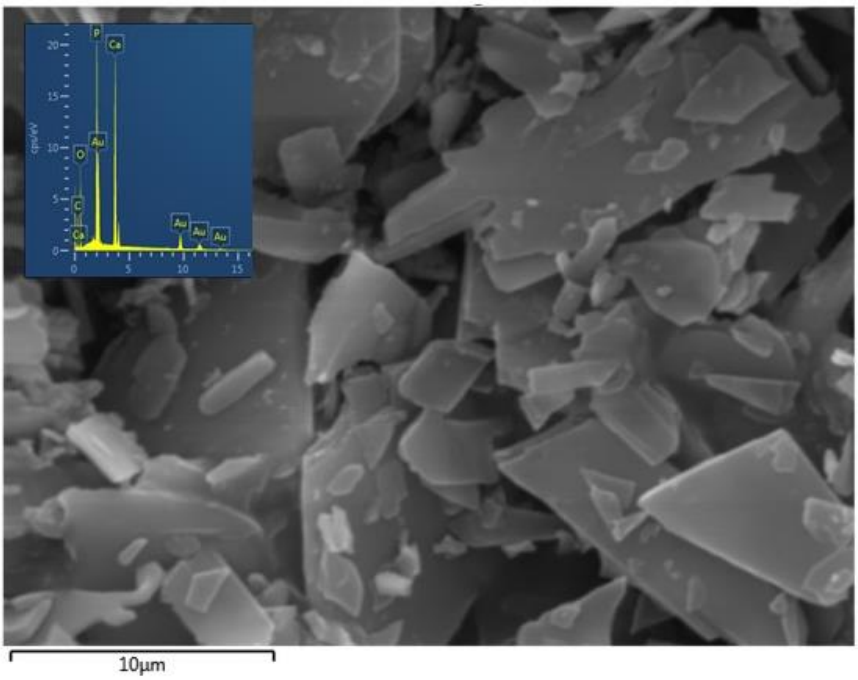


Figure 2. Micrograph of brushite with EDS spectra (inserted figure).

Adsorption results are presented on Figures 3a and 3b. Figure 3a represents adsorption kinetic study for Ni and Pb ions, while Figure 3b represents the adsorption kinetic for Pb ions in the 1-10-minute time interval. Based on presented adsorption results the adsorption graphs of Ni ions and Pb ions are presented in Figure 3a and 3b. As can be observed, in the first 10 minutes, adsorption of Pb ions was fastest and increased up to 93%, after that equilibrium state was reached. In the case of Ni ions, adsorption is slower, and after 1 hour 23% of Ni ions were adsorbed and adsorption process reached a plateau. Figure 3b present Pb ions adsorption in 1-10-minute time interval. As can be noticed, adsorption of Pb ions was very fast and after 3 minutes, 70% of Pb^{2+} were adsorbed, which is more efficient and faster than Ni^{2+} adsorption. This phenomenon can be explained by previously described hydrogen bonds in brushite structure along *b*-axis, where probably lead ions are triggered in the structure occupying a place between tetrahedral and octahedral positions [11].

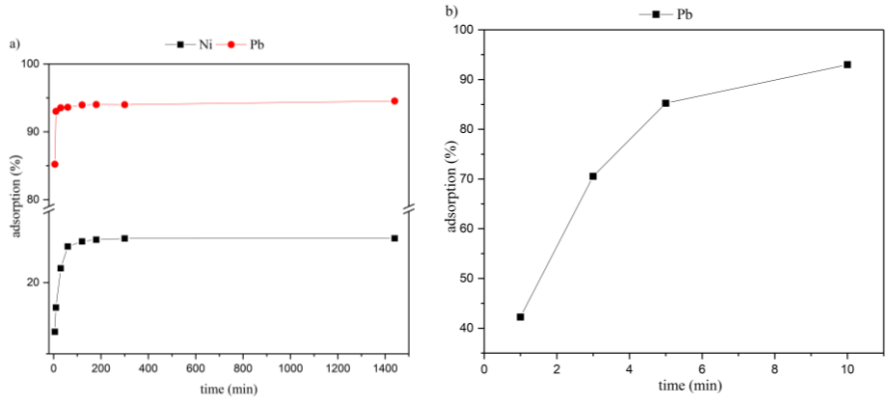


Figure 3. a) The adsorption kinetic study for Ni and Pb, b) Pb ions adsorption in 1-10-minute time interval.

CONCLUSION

The pure monocrystalline brushite material is successfully synthesized from acetate and phosphate solutions using precipitation method. XRD analysis showed that material possess proper structural

order and high crystallinity. Based on SEM micrographs it can be concluded that brushite grains have proper prismatic grains up to 20 μm in size. According to adsorption analysis it can be concluded that this material can be used as lead adsorbent from aqueous solutions since it reaches equilibrium after 10 minutes and have adsorption capacity of 93%. For future investigations and researchers which are related to water purification the development of filter manufacturing technology based on calcium phosphate materials should be taken into account. This material shows excellent structural properties, and obtaining them is very rewarding because it is possible to be synthesize from non-toxic precursors that are, among other things, environmentally and economically friendly.

Acknowledgment
This work was supported by the Ministry of Education, Science and Technological Development of the Republic of Serbia (grant no 451-03-66/2024-03/ 200017, topic number: 1702407).

REFERENCES

[1] M.L. Hasan, B. Kim, A.R. Padalhin, O. Faruq, T. Sultana, B.-T. Lee, Materials Science and Engineering: C 103 (2019) 109775.
[2] Z. Xue, Z. Wang, A. Sun, J. Huang, W. Wu, M. Chen, X. Hao, Z. Huang, X. Lin, S. Weng, Materials Science and Engineering C 111 (2020).
[3] Y. Lukina, S. Kotov, A. Senyagin, L. Bionyshev-Abramov, N. Serejnikova, R. Chelmodeev, A. Tavtorkin, M. Ryndyk, D. Smolentsev, S. Sivkov, T. Safronova, Open Ceramics 17 (2024) 100548.
[4] P. Kanwar, M. Kumar, S. Srivastava, Environmental Technology & Innovation 32 (2023) 103238.
[5] L.T. Haber, L. Erdreicht, G.L. Diamond, A.M. Maier, R. Ratney, Q. Zhao, M.L. Dourson, Regulatory Toxicology and Pharmacology 31 (2000) 210.
[6] D. Djukić, A. Krstić, K. Jakovljević, S. Butulija, L. Andjelković, V. Pavlović, M. Mirković, Sustainability 14 (2022) 4003.
[7] M.M. Mirković, T.D.L. Pašti, A.M. Došen, M.Ž. Čebela, A.A. Rosić, B.Z. Matović, B.M. Babić, RSC Advances 6 (2016) 12219.
[8] M. Mirković, A. Kalijadis, I. Bracanović, A. Krstić, D. Đukić, V. Dodevski, Journal of the Serbian Chemical Society 89 (2024) 231.
[9] S. Mandel, A.C. Tas, Materials Science and Engineering: C 30 (2010) 245.
[10] D. Griesiute, E. Raudonyte-Svirbutaviciene, A. Kareiva, A. Zarkov, CrystEngComm 24 (2022) 1166.
[11] M.K. Ahmed, S.F. Mansour, R. Ramadan, M. Afifi, M.S. Mostafa, S.I. El-dek, V. Uskoković, Journal of Water Process Engineering 34 (2020) 101090.

REAL-TIME PHOTORESPONSIVE CHITOSAN FOR DIRECT LASER WRITING OF MICROSTRUCTURES

B. Murić[1], S. Savić-Šević[1], D. Pantelić[2] and B. Jelenković[1]

[1] *Institute of Physics Belgrade, University of Belgrade, Pregrevica 118,11080 Belgrade, Serbia (muric@ipb.ac.rs)*
[2] *Senzor INFIZ, Institute of Physics, University of Belgrade, Serbia*

DOI: https://doi.org/10.46793/Phys.Chem24I.337M

ABSTRACT

Photoresponsive, nontoxic, elastic chitosan was prepared for rapid, one-step fabrication of various microstructures. Concave or convex microlenses (individual or microlenses arrays), gratings, microchannels, and many other complex microstructures were produced on the chitosan layer by direct laser writing at 488 nm. Any waste material not created during the microstructures formation. The microstructures can be used directly as prepared or contact copied into PDMS without additional chemical processing, for various applications such as: lab on a chip, sensors, cameras, security, etc.

INTRODUCTION

Microoptical components such as positive and negative single microlenses, square or hexagonal microlenses arrays, gratings, microchannels, and various complex microstructures are used in different sensors, medical devices, cameras, labs on a chip, security, and numerous other applications. The microstructures were produced on various photosensitive materials (polymers, composites, photosensitive glasses, etc.) by a range of techniques such as: hot embossing, direct laser writing (DLW), photolithography, droplet process, ink yet process, etc Some of them are mostly complex and expensive techniques that partially use of toxic chemicals [1-4].

Chitosan is biodegradable and biocompatible linear polysaccharide derived by deacetylation of chitin (polysaccharide found in the exoskeleton of crustaceans and insects). Chitosan, as a natural polysaccharide, consisting of β-(1-4)-linked d-glucosamine and N-acetyl-d-glucosamine, and is available in a range of molecular weights and degrees of deacetylation. It is insoluble in water and organic solvents, but dissolves in diluted acidic aqueous solutions depending on pH and deacetylation degree. Chitosan as nontoxic, antibacterial, biocompatible and biodegradable was initially used in pharmacy and biomedicine. However, the need for new natural materials has expanded the applications range of chitosan to bioengineering, agriculture, dentistry, food industry, cosmetics, water filtration, etc [5, 6].

Chitosan, chemically modified with a nontoxic (food grade) compounds, was used for a fast, one-step production of microoptical structures, by direct laser writing (DLW) at 488 nm. Individual positive and negative microlenses or their arrays, gratings, microchannels and various complex microstructures can be produced on the chitosan layer. The microstructures, which do not produce any waste material at all, can be used as such without any additional chemical treatment. They can also be contact copied into dental composite, PDMS and other related materials [7]. Their application areas are diverse, so they can be used for sensors, security, compound eyes, lab on a chip and numerous other applications.

RESULTS AND DISCUSSION

The 2% chitosan solution was prepared by dissolving low molecular weight, 85% deacetylated chitosan supplied from Sigma-Aldrich, in 1% aq. solution of acetic acid (purchased from Sigma Aldrich). The solution was stirred at 50°C for a long time, until a homogeneous solution was obtained. Chemical modification of chitosan was achieved with an aqueous solution composed of glycerol, sucrose, glucose, polysorbate 80, citric acid and sodium benzoate, which act as plasticizers, humectants and preservatives. 0.2 ml of this solution was added per 1 ml of chitosan solution, with stirring. The photosensitivity of chitosan was achieved by adding 0.1 ml of anthocyanin food coloring (E163) also per 1 ml of solution. After complete dissolution the prepared chitosan solution was centrifuged in order to remove all remained impurities. As a result of chemical modification, both mechanical and optical properties of the chitosan layer were changed.

The gravity settling method [8] was used for preparing of chitosan layer dried in the dark overnight, under ordinary environmental conditions (T=25 ^{o}C and RH=50-60%). The layer thickness of 100 μm was obtained for a volume of 2 ml modified chitosan solution. Using a digital micrometer the thickness was determined as the average of six random layer locations measurements. The thickness can be changed varying the quantity and chemical composition of chitosan solution.

The microstructures were produced on the chitosan layer using a homemade laser writing device occupied with a blue laser at 488 nm and 100 mW maximal output power. The precise xy - linear translation stage with step resolution of 25 nm and position repeatability of 2 μm, allows good layer positioning placed on it. The laser beam focused on the layer by the microscope objective (50×0.55NA). Synchronization of laser and coordinate table operation is achieved by software control using standard g-code. By controlling the laser power, exposure time and speed of laser writing the various microstructures were created. Diffraction gratings were recorded line by line using a program that determines the line parameters (number, length and width) from the corresponding image file.

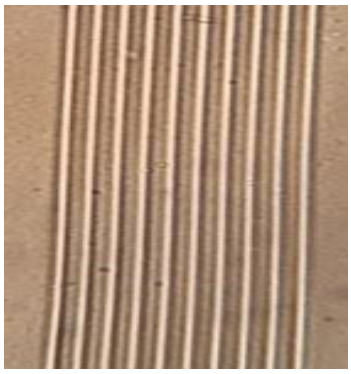


Figure 1. Diffraction gratings recorded on the chitosan layer.

By writing a series of gratings the spatial resolution of 100 lp/mm was found, for the laser power of 35 mW, exposure time of 200 ms, and line width of 0.01 mm. The image of diffraction grating taken by a digital camera through the optical microscope is shown in Fig. 1.

The arrays of convex microlenses were recorded lens by lens using the program that determines the lens parameters (polygon diameter, number of polygonally positioned spots, and distance among neighbors) from the image file. The spherical surface in the polygon center arranged from 8 polygonally positioned spots acts as a good quality positive (convex) microlens. The radius of

curvature and corresponding focal length of microlenses can be controlled by the diameter of a polygon.

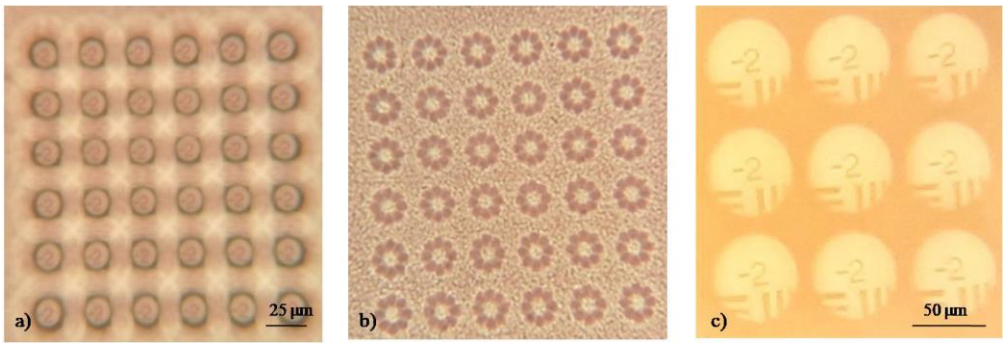


Figure 2. Transmission images of digit "-2" formed by array of 6x6 convex microlenses (a) and by array of 3x3 concave microlenses on the chitosan layer (c). Reflection image of 6 x 6 array convex microlenses on the chitosan layer (b).

The good repeatability of microlenses was obtained. An image of digit "-2" taken by a digital camera through the optical microscope and 6x6 convex microlens array is shown in Fig. 2a (the diameter of polygon was 25 µm, while microlenses were fabricated using 50 mW of laser power and 200 ms exposure time), while the reflection image of 6 x 6 array convex microlenses is shown in Fig. 2b. The concave lens was formed by controlled and local melting of the chitosan layer, following the laser beam profile. An image of digit "-2" taken by a digital camera through the optical microscope and 3x3 concave microlens array is shown in Fig. 2c (lens diameter of 50 µm with 35 mW of laser power and 200 ms exposure time).

By controlled guiding of the laser beam across the surface, microstructures of various shapes (rather complex) can be produced on the chitosan layer. Based on our previous investigations [1], we assume that by varying the laser power, exposure time, writing speed, and layer thickness, the structures with a width and depth of up to several hundred micrometers can also be obtained on the modified chitosan layers. Exposure time can be reduced by using higher laser powers. In most cases, there is no postprocessing, so the microstructures are usable immediately after fabrication. An image of a half of rather complex microchannel structure on a chitosan layer, taken by a digital camera through the optical microscope, is presented in Figure 3. With regard to the cross section of the microchannel, preliminary investigations have shown that it is approximately semicircular in shape.

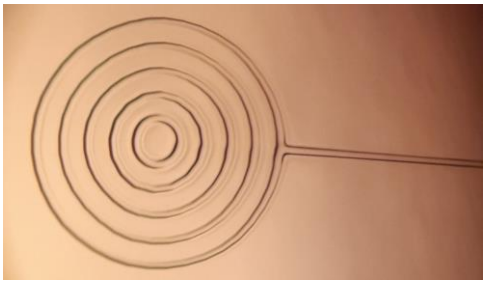


Figure 3. Microchanels (complex structure) recorded on chitosan layer.

CONCLUSION

Chitosan was chemically modified to be ecofriendly, biocompatible, elastic, nontoxic and to allow fast, one-step fabrication of different microoptical structures by direct laser writing (DLW) at 488 nm. The microstructures such as: convex, concave, aspherical microlenses, microchannels, diffraction gratings, etc. can be produced using cheap lasers. The microlenses with good optical and imaging properties were obtained. The elasticity of the chitosan layer is suitable for adaptive optics.

The microstructures can be used immediately, without additionally chemical treatment and waste. They can be used for a variety of applications such as: optical sensors, medical devices, cameras, security, biological structure, etc.

The subject of further research will be profile analysis and more detailed characterization of the obtained microstructures, as well as further improvement of the physicochemical properties of chitosan layer.

Acknowledgment

This paper was supported by the Ministry of Education, Science and Technological Development of the Republic of Serbia.

REFERENCES

[1] B. D. Murić, D. V. Pantelić, D. M. Vasiljević, B. M. Panić, Appl. Opt., 46 (2007) 8527.
[2] H. Jiang, S. Fraser, B. Kaminska, H. Porras, M. Raymond, Adv. Opt. Mater., 7 (2019) 1900237.
[3] B. D. Murić, D. V. Pantelić, D. M. Vasiljević, S. N. Savić-Šević, B. M. Jelenković, Curr. Appl. Phys., 16 (2016) 57.
[4] J. Tang, G. Qiu, X. Cao, Y. Yue, X. Zhang, J. Schmitt, J. Wang, Lab Chip, 20 (2020) 2334.
[5] R. Ye, S. Liu, W. Zhu, Y. Li, L. Huang, G. Zhang, Y. Zhang, Polymers, 15(2023) 2482.
[6] M. Monier, I. Youssef, D.A. Abdel-Latif, React. Func. Polymers, 124 (2018) 129.
[7] J. Xu, J.Ma, J. Lian, Y. Liao, L. Wang, L. Dong, H. Sun, J. Phys. D: Appl. Phys., 55 (2022) 315401
[8] B. Murić, D. Pantelić, D. Vasiljević, B. Panić, Opt. Mater., 30 (2008) 1217.

AN ELECTRON SPIN RESONANCE STUDY OF PRODUCT OBTAINED BY THE PROLONGED AUTOXIDATION OF PYROGALLOL IN THE PRESENCE OF COPPER(II) IONS

M.G. Nikolić [1], D.M. Đorđević [1] and G.M. Nikolić [2]

[1] *University of Niš, Faculty of Sciences and Mathematics, Department of Chemisty. Višegradska 33, 18000 Niš, Serbia.*
[2] *University of Niš, Faculty of Medicine, Department of Chemistry, Bulevar dr Zorana Đinđića 81, 18000 Niš, Serbia. (e-mail: goranhem@yahoo.com)*

DOI: https://doi.org/10.46793/Phys.Chem24I.341N

ABSTRACT
Product obtained by the prolonged autoxidation of pyrogallol in the presence of copper(II) ions was characterized by electron spin resonance (ESR) spectroscopy. The presence of both paramagnetic copper(II) ions and organic free radicals in obtained autoxidation product was deduced from room temperature ESR spectrum which is similar to the ESR spectra of copper(II) ions complexed humic acids. Existence of two distinct types of copper(II) ion binding sites in the autoxidation product was assumed in order to obtain satisfactory computer simulation of copper(II) ions ESR spectrum. Prevalent ionic bonding of copper(II) ions in polymeric matrix with tetrahedral distortion at copper(II) ion binding sites and small to negligible exchange interactions between them was indicated by the parameters obtained from computer simulation of copper(II) ions ESR spectrum. ESR linewidth of organic radical(s) signal was larger and its *g*-value smaller than the values characteristic for humic acids due to the dipolar interactions with paramagnetic copper(II) ions.

INTRODUCTION
Bioinspired polyphenolic polymers and coatings, as well as metal-phenolic networks, are extensively investigated, especially for medical applications due to their antimicrobial properties [1, 2]. Poly(pyrogallol)-based materials are also the subject of this ongoing research [3, 4] and autoxidation presents one convenient way for their preparation. Like many other di- and trihydric simple phenolic compounds, pyrogallol (1,2,3-trihydroxybenzene) is easily susceptible to autoxidation in aqueous solutions and this process is greatly influenced by the solution pH and the presence of metal ions [5-7].

Electron spin resonance (ESR, also known as electron paramagnetic resonance - EPR) spectroscopy can be used as a valuable tool for studying various polymeric materials [8], including polyphenolic polymers [9]. ESR spectroscopy is especially useful for studying polymeric materials containing paramagnetic metal ions like copper(II) ions [8, 10] because it enables the precise characterization of their local environment.

Here we applied ESR spectroscopy for the characterization of product obtained by the prolonged autoxidative polymerization of pyrogallol in weakly alkaline aqueous solution in the presence of copper(II) ions.

EXPERIMENTAL
Materials: Pyrogallol, copper(II) chloride dihydrate ($CuCl_2 \times 2H_2O$), buffer compounds, sodium hydroxide, and hydrochloric acid were all purchased from commercial suppliers (Sigma-Aldrich (USA), Merck (Germany), and Centrochem (Serbia)), were of *p.a.* quality and used without further purification. Demineralised water was used for preparing all aqueous solutions.

Autoxidation product preparation: One gram (7.9 mmol) of pyrogallol was dissolved in 28 mL of freshly prepared phosphate buffer (pH 7.4) in a round-bottomed flask. In order to obtain pyrogallol/Cu(II) ions molar ratio of 10 : 1, exact mass of 0.135 g of $CuCl_2 \times 2H_2O$ was ultrasonically dispersed in 2 mL of phosphate buffer and then added in small portions to stirring pyrogallol solution. A pH value was accurately adjusted to 7.4 by the dropwise addition of 1 M NaOH solution and reaction mixture was continuously stirred in an open flask for 96 hours without direct exposure to sunlight at room temperature (22±2 °C). After 96 hours, pH of reaction mixture was adjusted to ≈2 by adding 1M HCl solution and mixture was left for 72 hours without stirring at room temperature in order to precipitate the reaction product. Reaction mixture was then centrifuged at 4000 rpm for 15 minutes and filtered under vacuum. Collected precipitate was rinsed with 50 mL of deminarelised water and then with 50 mL of 0.01 mL HCl solution. Finally, precipitate was dried for 48 hours at 40 °C before ESR measurements.

ESR measurements: Room temperature ESR spectra were recorded on an X-band EMX spectrometer (Bruker, Germany) with autoxidation product placed in a 2 mm inner diameter quartz tube. Instrumental ESR parameters were: nominal microwave frequency - 9.86 GHz, modulation frequency - 100 kHz, modulation amplitude - 2 G, center field - 3500 G, scan width - 2000 G, time constant - 0.64 ms, conversion time - 81.92 ms, and attenuation 25 dB (0.585 mW nominal microwave power). As an external standard for *g*-value determination, DPPH (g = 2.0036) was used in the field offset calibration routine. WinEPR and SimFonia software (Bruker, Germany) was used for ESR spectra manipulation and simulation.

RESULTS AND DISCUSSION

Experimental ESR spectrum of obtained pyrogallol autoxidation product and computer simulation of copper(II) ions ESR signal are shown in Figure 1.

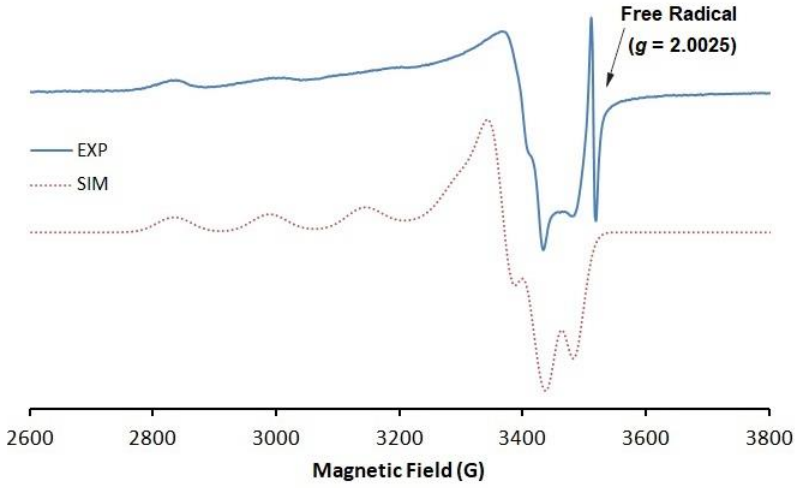


Figure 1. Experimental ESR spectrum of obtained pyrogallol autoxidation product and computer simulation of copper(II) ions ESR signal.

The presence of two distinct spectral contributions can be seen in the experimental ESR spectrum shown in Figure 1.: broad resonance lines originating from the presence of copper(II) ions, and one sharp resonance line at higher value of magnetic field originating from the presence of organic radical(s). Such kind of ESR spectra are characteristic for copper(II) ions complexed humic acid-type polymeric materials [11].

Spectral features originating from the presence of copper(II) ions show similarity to the ESR spectra of polymeric materials where copper(II) ions coordination with only O-donor ligands may

be expected like some polysaccharide-Cu(II) complexes [10, 12]. This implies that our sample contains mononuclear copper(II) centers (S = 1/2) with axial symmetry. Parallel and perpendicular hyperfine coupling constants ($A_{\parallel}$ and $A_{\perp}$, respectively) that characterize interaction of unpaired electron with copper(II) ions nuclei (I = 3/2 for both ^{63}Cu and ^{65}Cu), and parallel and perpendicular *g*-values ($g_{\parallel}$ and $g_{\perp}$, respectively) are principal parameters of such bonding sites. Satisfactory computer simulation of experimental ESR spectrum was obtained by assuming the existence of two types of copper(II) ions bonding sites and is shown in Figure 1. (dotted line). However, the match between the experimental and simulated ESR spectrum is not so good because the distribution of molecular binding parameters in amorphous and polymeric materials differs from polycrystalline solids for which simulation algorithm is optimized [10]. Hyperfine coupling constants and *g*-values obtained by computer simulation enabled us to calculate the geometric parameter G, in-plane sigma bonding parameter α^2, and empirical factor *f* which are all useful for the characterization of copper(II) ions bonding sites local environment [13, 14].

The geometric parameter G was calculated for individual bonding sites by using the equation:

$$G = \frac{g_{\parallel} - 2.0023}{g_{\perp} - 2.0023}$$

and can be used as a measure of the exchange interaction between the copper(II) centers. Exchange interaction is negligible if G > 4, and considerable exchange interaction is indicated if G < 4.

The value of in-plane sigma bonding parameter α^2 was calculated for each species by the following equation:

$$\alpha^2 = \frac{|A_{\parallel}|}{0.036} + (g_{\parallel} - 2.0023) + \frac{3}{7}(g_{\perp} - 2.0023) + 0.04$$

This value may be used to estimate the ionic character of ligand-copper(II) ion bonding and this bond is assumed to be completely ionic if $\alpha^2 = 1$, and completely covalent if $\alpha^2 = 0.5$.

The value of *f* is an empirical index of tetrahedral distortion of copper(II) binding sites and may be calculated as:

$$f = \frac{g_{\parallel}}{|A_{\parallel}|}$$

The *f* value vary from 105 to 135 cm for square planar complexes with small to extreme distortion, and values above 150 cm are observed for tetrahedrally distorted copper(II) complexes.

The ESR parameters determined by spectral simulation, together with the calculated values of G, α^2, and *f* for pyrogallol autoxidation product are given in Table 1.

Table 1. ESR spectral parameters of copper(II) ions in analyzed sample.

Site (fraction)	$g_{\parallel}$	$g_{\perp}$	$A_{\parallel}\times10^{-4}$ (cm^{-1})	$A_{\perp}\times10^{-4}$ (cm^{-1})	G	α^2	*f* (cm)
A (0.57)	2.305	2.092	165.0	7.5	3.38	0.839	139.70
B (0.43)	2.295	2.053	167.0	7.5	5.77	0.818	137.42

Data from Table 1. indicate that both copper(II) bonding sites in our sample have prevalent ionic bonding with significant distortion from planarity. While bonding sites B have negligible exchange

interactions (G > 4), bonding sites A have small but significant exchange interactions (G < 4). These results are similar to the results we have already reported for the products of prolonged autoxidation of simple dihydric phenols in the presence of copper(II) ions [14].

For organic radical(s) ESR signal measured linewidth was 7.8 G, which exceeds the range of linewidths characteristic for ESR signals of various humic acids, and *g*-value was determined to be 2.0025, which is smaller value than the corresponding values measured for humic acid-type polymeric materials and humic acids [11, 15]. These discrepancies may be explained by the dipolar interactions of oxygen-centered radical species with metal ions present in polymer matrix [16].

CONCLUSION

Electron spin resonance (ESR) spectroscopy showed that product of prolonged pyrogallol autoxidation in the presence of copper(II) ions contains both paramagnetic copper(II) ions and organic radical(s) as is the case in copper(II) ions complexed humic acid-type polymeric materials. Computer simulation of copper(II) ions ESR spectrum indicated that two copper(II) ion binding sites are present with prevalently ionic bonding of copper(II) ions in polymeric matrix, significant tetrahedral distortion at copper(II) ion binding sites, and small to negligible exchange interactions between them. Organic radical(s) ESR signal has larger linewidth and smaller *g*-value than the values characteristic for various types of humic acids due to the dipolar interactions with metal ions.

Acknowledgment

This work was supported by the Ministry of Education, Science and Technological Development of the Republic of Serbia (grants no 451-03-65/2024-03/200113 and 451-03-65/2024-03/200124).

REFERENCES

[1] J. Bolaños-Cardet, D. Ruiz-Molina, V. J. Yuste, S. Suárez-García, Chem. Eng. J., 481 (2024) 148674.
[2] Y. Li, Y. Miao, L. Yang, Y. Zhao, K. Wu, Z. Lu, Z. Hu, J. Guo, Adv. Sci., 9 (2022) 2202684.
[3] P. K. Balne, S. Harini, C. Dhand, N. Dwivedi, M. L. S. Chalasani, N. K. Verma, V. A. Barathi, R. Beuerman, R. Agrawal, R. Lakshminarayanan, Mater. Sci. Eng. C, 90 (2018) 673.
[4] Z. Tian, G. Wu, M. Libby, K. Wu, K. J. Jeong, Y. J. Kim, J. Mater. Chem. B, 11 (2023) 3356.
[5] M. Friedman, H. S. Jürgens, J. Agric. Food Chem., 48 (2000) 2101.
[6] A. M. Veselinović, R. S. Nikolić, G. M. Nikolić, Cent. Eur. J. Chem., 10 (2012) 1942.
[7] E. Nkhili, M. Loonis, S. Mihai, H. El Hajji, O. Dangles, Food Funct., 5 (2014) 1186.
[8] K-R. Naveed, L. Wang, H. Yu, R. S. Ullah, M. Haroon, S. Fahad, J. Li, T. Elshaarani, R. U. Khan, A. Nazir, Polym. Chem., 9 (2018) 3306.
[9] L. Panzella, G. D'Errico, G. Vitiello, M. Perfetti, M. L. Alfieri, A. Napolitano, M. d'Ischia, Chem. Commun., 54 (2018) 9426.
[10] S. K. Hoffmann, J. Goslar, I. Ratajczak, B. Mazela, Holzforschung, 62 (2008) 300.
[11] M. F. Barriquello, S. da Costa Saab, N. C. Filho, L. Martin-Neto, J. Braz. Chem. Soc., 21 (2010) 2302.
[12] Ž. Mitić, M. Cakić, G. M. Nikolić, R. Nikolić, G. S. Nikolić, R. Pavlović, E. Santaniello, Carbohydr. Res., 346 (2011) 434.
[13] E. Manoj, M. R. Prathapachandra Kurup, A. Punnoose, Spectrochim. Acta A, 72 (2009) 474.
[14] M. G. Nikolić, N. S. Krstić, D. M. Đorđević, Chem. Naiss., 4 (2022) 56.
[15] A. Watanabe, D. B. McPhail, N. Maie, S. Kawasaki, H. A. Anderson, M. V. Cheshire, Org. Geochem., 36 (2005) 981.
[16] E. Giannakopoulos, K. C. Christoforidis, A. Tsipis, M. Jerzykiewicz, Y. Deligiannakis, J. Phys. Chem. A, 109 (2005) 2223.

THE INFLUENCE OF Mn(II) IONS ON THE FORMATION AND CHARACTERISTICS OF PRODUCTS RESULTING FROM PROLONGED AUTOXIDATION OF CATECHOL IN AQUEOUS SOLUTION

M.G. Nikolić [1], A. Ranđelović [1], D.M. Đorđević [1] and G.M. Nikolić [2]

[1] *University of Niš, Faculty of Sciences and Mathematics, Department of Chemisty. Višegradska 33, 18000 Niš, Serbia*.
[2] *University of Niš, Faculty of Medicine, Department of Chemistry, Bulevar dr Zorana Đinđića 81, 18000 Niš, Serbia*. *(e-mail: goranhem@yahoo.com)*

DOI: https://doi.org/10.46793/Phys.Chem24I.345N

ABSTRACT
The process of autoxidation of catechol in aqueous solution at pH 7.4 in the absence and in the presence of manganese (II) ions was observed for five days. UV-Vis spectra recorded during this period revealed that Mn (II) ions greatly enhance the rate of autoxidation process. The presence of metal ions also resulted in the formation of larger quantity of product. Obtained materials were characterized using FTIR and ESR spectroscopy. FTIR spectra confirmed that polymerization has occurred during autoxidation of catechol in both systems. The ESR data revealed that both autoxidation products contain oxygen-centered radicals. A retention of a low amount of Mn (II) ions in the product was also established from the ESR spectrum. According to the literature, products of catechol autoxidation studied in this paper resemble the characteristics of natural and synthetic humic acid-like substances.

INTRODUCTION
Catechol (benzene-1,2-diol) is a phenolic compound that is naturally present in small quantities, but significant amounts of this compound find their way to the environment via industrial wastewaters [1]. Monomeric phenols are prone to autoxidation in the presence of atmospheric oxygen, so they represent precursors to soil humic substances, and in soil solution can contribute to up to 10% of the total organic carbon [2,3]. Other than the pH of the system, rate and degree of humification are largely affected by the presence of metal ions [4]. Substances formed in this process can sometimes retain metal ions, thus making them not readily available to the soil biota [5].

This paper examines the influence of Mn (II) ions on the process of catechol autoxidation in aqueous solution, as well as impact these metal ions possibly have on characteristics of autoxidation products.

EXPERIMENTAL
Materials and methods: Catechol and manganese (II) chloride dihydrate (*p.a*. grade) were purchased from Merck, Germany and used without further purification. Hydrochloric acid (37%, *p.a*. grade), sodium hydroxide (*p.a.* grade), and potassium bromide (FTIR grade) were purchased from Sigma Aldrich, USA. All solutions were prepared with ultrapure deionised water. UV absorption spectra were recorded in 0.01 M HCl solution using a UV-1800 PC Shimadzu spectrophotometer (Japan) equipped with 1.0 cm quartz cell. IR measurements were carried out on a Bruker Tensor 27 FTIR instrument (Bruker, Germany) with the spectral resolution of 2 cm^{-1}. ESR measurements were performed at room temperature on an X-band EMX spectrometer (Bruker, Germany) using 2 mm quartz tube cell for solid samples. The main ESR settings were as follows:

microwave frequency – 9.85 GHz, attenuation – 25 dB, modulation frequency – 100 kHz, modulation amplitude – 1 G, and time constant – 0.64 msec

Autoxidation product preparation: Catechol (1g, 9.1 mmol) was dissolved in deionized water, and pH was adjusted to 7.4 with 1M NaOH solution. For the second autoxidation product, after dissolving catechol (1g, 9.1 mmol) in deionized water, a small amount of manganese (II) chloride dihydrate (n(catechol):n($MnCl_2 \times 2H_2O$) = 1:10) was added and pH was adjusted to 7.4 with 1M NaOH solution. Total volume of each solution was 30 mL. Solutions were stirred at room temperature (22 °C) in an open round bottom flask without direct exposure to sunlight for five days. After 120 hours, the pH of the solutions was adjusted to approximately 2 by adding 1M HCl and products were allowed to precipitate for 48 h. Obtained dark brown products were vacuum filtered, washed with 100 mL of 0.1M HCl, and dried for 24 h at 60 ˚C.

RESULTS AND DISCUSSION

In order to observe the autoxidation process, UV-Vis spectra of solutions were recorded right after adjusting the pH, and subsequently every 24 hours during the next five days (20 µl aliquot in 10 mL of 0.01 M HCl). The resulting UV-Vis spectra are shown in Figure 1.

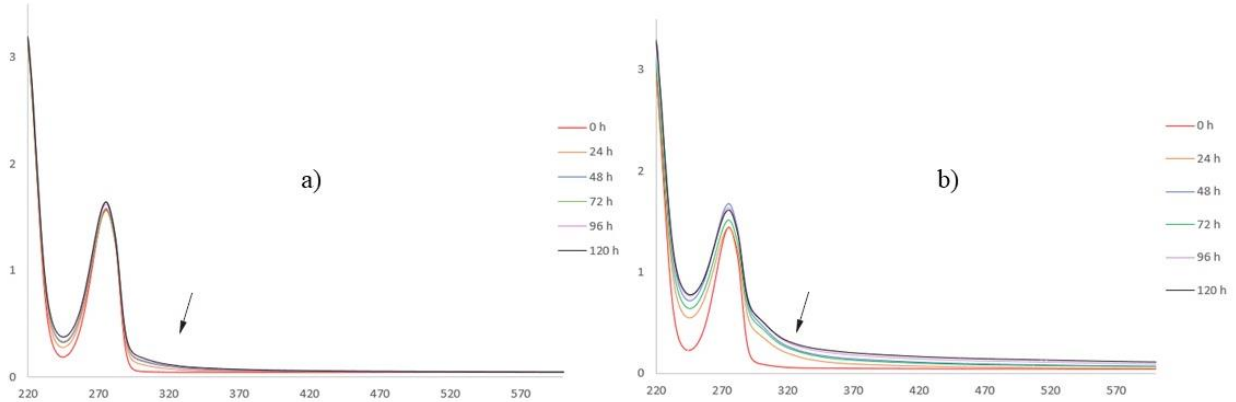


Figure 1. UV-Vis spectra of catechol autoxidation (a) and catechol autoxidation in the presence of Mn (II) ions (b). Arrows point towards the catechol autoxidation band at 320 nm.

Increase in the absorbance at 320 nm in the spectra of catechol autoxidation (Figure 1. a) recorded after 24 h of stirring, along with noticeable browning of the solution, pointed to the formation of products with higher molecular weight [6]. Increase in absorbance, as well as slight widening of the absorption peak that originates from π→π* electron transitions in catechol (276 nm) is most likely the consequence of its overlapping with the absorption peak originating from π→π* electron transitions in 1,2-benzoquinone (245nm), which is known to form quickly under alkaline conditions [7]. This trend continued throughout the duration of the experiment and a minor extent of the observed changes indicates that the autoxidation process is slow.

It is obvious from the UV-Vis spectra of catechol autoxidation in the presence of metal ions (Figure 1. b) that formation of products with higher molecular weight occurs much faster since increase in the absorbance and peak widening is much more noticeable throughout the duration of the experiment. Mn(II) ions initiate autoxidation as soon as pH is adjusted, which can be seen as a slight increase in absorbance at 320 nm in the UV-Vis spectra recorded at 0 h.

According to prior studies, the ratio of absorptivity at 465 and 665 nm (commonly referred to as E_{465}/E_{665} ratio) for humic substances from different sources is <5 and independent of their concentration [8]. For isolated products of catechol autoxidation prepared in this study this ratio is 1.39 and 1.2 respectively, which, along with the characteristic appearance of their UV-Vis spectra strongly suggests that these materials resemble natural and synthetic humic acid- like substances.

Other than the influence that metal ions have on the rate of the autoxidation of catechol, they also affect the quantity of the obtained product. In our experimental settings, the amount of product obtained from autoxidation of catechol influenced by Mn (II) ions was ten times larger compared to the amount isolated from the reaction system without metal ions.

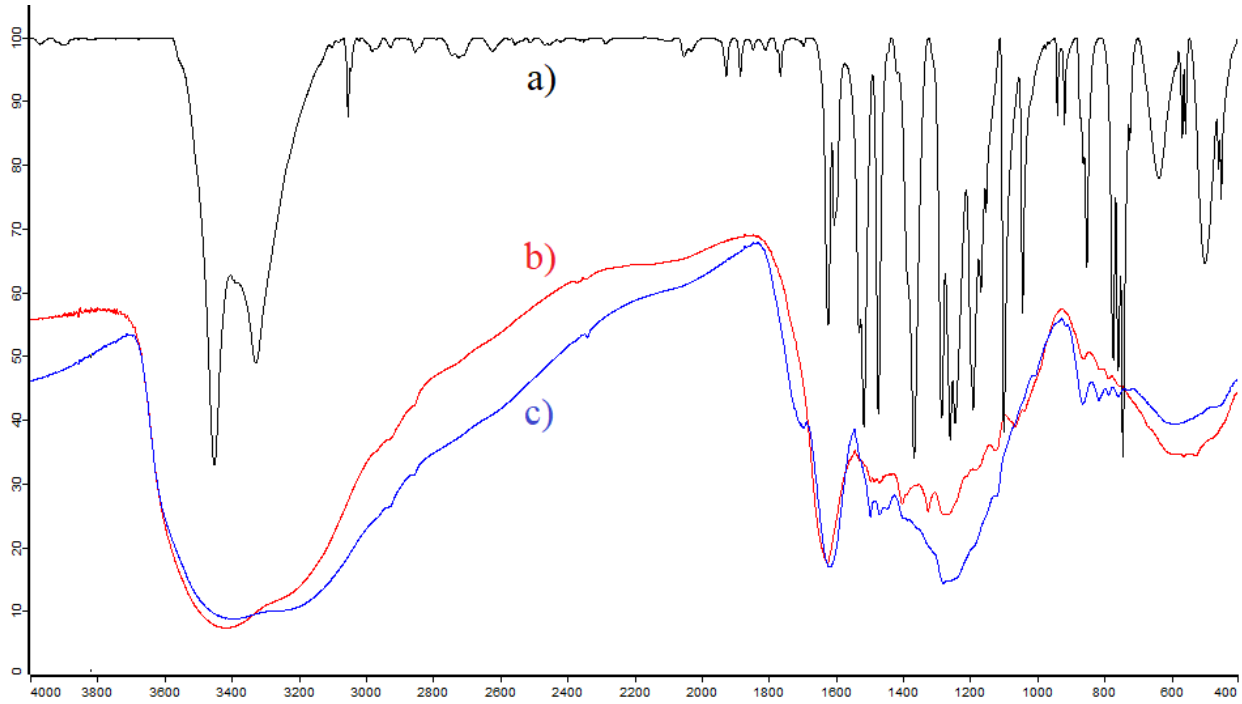


Figure 2. FTIR spectra of catechol (a), product of catechol autoxidation (b), and product of catechol autoxidation in the presence of Mn(II) ions (c).

In the FTIR spectra of products obtained from the autoxidation of catechol in the absence (Figure 2. a) and in the presence of Mn (II) ions (Figure 2. c) the number of individual absorption bands has significantly decreased when compared to the spectra of pure catechol (Figure 2. a). This is due to the broadening of absorption bands, which indicates that polymerization occurred during the autoxidation process and it makes identification of possible new adsorption bands more difficult. Most noticeable is the broadening of the valence vibration bands of the O–H groups, presumably due to the hydrogen bonding in the resulting polymers.

Possible presence of carbonyl groups in the autoxidation product obtained in the presence of Mn (II) ions could also provide an explanation for the increased absorption between 270 and 300 nm in UV-Vis spectra due to overlapping of peaks from $\pi \rightarrow \pi^*$ electrons transitions in catechol and low intensity $n \rightarrow \pi^*$electron transitions in carbonyl group.

The ESR spectrum of catechol autoxidation products formed in the absence of metal ions consisted of only one slightly asymmetrical signal with the linewidth of 3.43 G and *g*-value of 2.0042 (Figure 3. a). In addition to one signal with the linewidth of 3.83 G and *g*-value of 2.0034, the ESR spectrum of catechol autoxidation product formed in the presence of Mn (II) ions also showed six symmetrical low intensity signals (Figure 3. b). Amplitude of these signals, that originate from the Mn (II) ions (S=5/2) retained in the autoxidation product, was very low and only observable when the receiver gain was increased (Figure 3 c), which suggests that the amount of Mn (II) ions in the product is very small. According to the literature, linewidths and *g*-values for signals observed in both spectra are in agreement with the data for oxygen-centered radical species in both natural and synthetic humic acid-like substances [9].

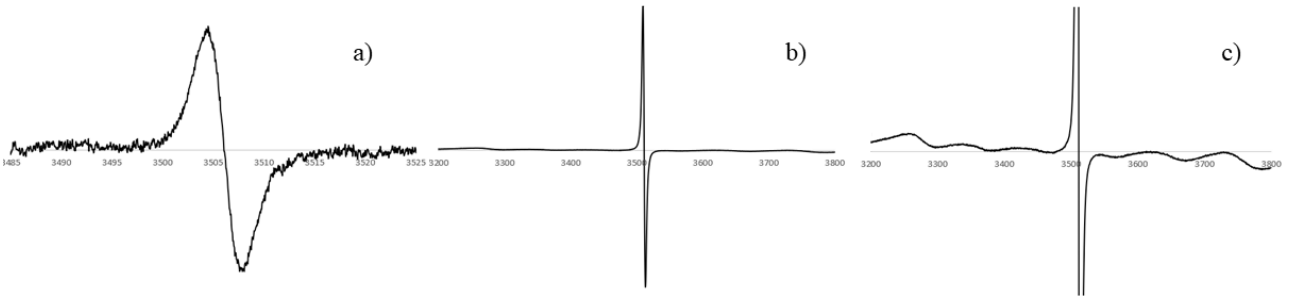


Figure 3. ESR spectra of products of autoxidation of catechol in the absence (a) and in the presence of Mn(II) ions (b and c).

CONCLUSION

UV-Vis spectra recorded during autoxidation of catechol in aqueous solution at pH 7.4 for five days showed that reaction rate noticeably increased in the presence of Mn (II) ions. Metal ions also increase the amount of autoxidation product in observed timeframe. FTIR spectra confirmed that some degree of polymerization occurred in resulting products and indicate the formation of new functional groups. ESR spectra established the presence of oxygen-centered radicals and also revealed that a very small amount of manganese (II) ions is retained in the product of autoxidation. Literature data for natural and synthetic humic acid-like substances is in good agreement with characteristics of obtained products.

Acknowledgment

This work was supported by the Ministry of Education, Science and Technological Development of the Republic of Serbia (grant no 451-03-65/2024-03/200113 and 451-03-65/2024-03/200124).

REFERENCES

[1] M. Matijević, M. N. Stanković, N. S. Krstić, M. G. Nikolić, D. A. Kostić, Rev. Roum. Chim., 65 (2020) 313.
[2] C. Gallet, C. Keller, Soil Biol. Biochem. 31 (1999) 1151.
[3] J. Shan, R. Ji, Y. Yu, Z. Xie, X. Yan, Sci. Rep., 5 (2015) 16000.
[4] G. M. Nikolić, S. C. Živanović, N. S. Krstić, M. G. Nikolić, Russ. J. Phys. Chem. A, 93 (2019) 2656.
[5] S. Hättenschwiler, P. M. Vitousek, Trends Ecol. Evol., 15(2000) 238.
[6] R. M. Duarte, E. B. Santos, A. C. Duarte, Water Res., 37(2003) 4073.
[7] A. Kuboyama, S. Matsuzaki, H. Takagi, H. Arano, Bull. Chem. Soc. Jpn., 47(1974) 1604.
[8] Y. Chen, N. Senesi, M. Schnitzer, Soil Sci. Soc. Am. J., 41 (1977) 352.
[9] V. A. Litvin, B. F. Minaev, G. V. Baryshnikov, J. Mol. Struct., 1086 (2015) 25.

THE SORPTION OF REACTIVE BLUE 19 DYE BY LAYERED DOUBLE HYDROXIDE: EFFECTS OF CONTACT TIME, pH, AND INITIAL CONCENTRATION

M. Kostić, M. Petrović, S. Najdanović, M. Radović-Vučić, N. Velinov, J. Mitrović and A. Bojić

University of Niš, Faculty of Sciences and Mathematics, Department of Chemistry, Višegradska 33, 18000 Niš, Serbia. (mk484475@gmail.com)

DOI: https://doi.org/10.46793/Phys.Chem24I.349K

ABSTRACT

The removal of Reactive Blue 19 (RB19) by Layered double hydroxide (NiFe-LDH) was investigated. The study examined the influence of various sorption parameters, including contact time, initial concentration, and pH. Adsorption isotherm data under optimal conditions indicated that the adsorption of RB19 by NiFe-LDH followed the Langmuir monolayer adsorption model. The sorption capacity of NiFe-LDH was found 414.03 mg g^{-1} at an optimal pH of 3.

INTRODUCTION

Environmental contamination by reactive textile dyes, can have severe and chronic effects on living organisms. Reactive Blue 19 (RB19), also known as the disodium salt of 1-amino-2-sulfo-4-(3-sulfoxy-ethyl-sulfophenyl-1-ylamino)-5,10-anthraquinone, is a very stable and resistant anionic dye. It may be mutagenic and toxic due to the presence of electrophilic vinyl sulfone groups [1]. Therefore, the removal of dyes from water is crucial, and various processes and technologies can be employed for this purpose, including biological treatments, membrane filtration, electrochemical technology, advanced oxidation processes, and sorption processes. Sorption is frequently used because of its high efficiency, economic feasibility, and operational simplicity [2]. In order to remove dyes from water, various sorbents were used, such as carbon nanotubes [3], bentonite [4], hydrolytic and aerobic microorganisms [5], nanocomposite [6], silica gel [7], chitosan [8], and biosorbent [9]. In recent years, layered double hydroxides (LDH), also known as anionic clays or hydrotalcite clays, have been increasingly used for removing dyes from water. LDH can be represented by the general formula $\left[M^{II}_{1-x}M^{III}_{x}(OH)_2\right]^{x+}\left[A^{n-}_{x/n}\right]\times yH_2O$, where M^{II} is a divalent metal cation such as Mg^{2+}, Ca^{2+}, Zn^{2+}, Cu^{2+}, Co^{2+}, Ni^{2+}, etc., and M^{III} is a trivalent metal cation such as Fe^{3+}, Al^{3+}, Ga^{3+}, Cr^{3+}, etc. The electroneutrality of LDHs is achieved by the presence of hydrated organic or inorganic anions, such as CO_3^{2-}, NO_3^-, SO_4^{2-}, OH^-, Cl^-, Br^-, etc., in interlamellar space.

The main aim of this research was the synthesis of layered double hydroxide based on nickel and iron (NiFe-LDH) and investigation of the sorption efficiency by varying different parameters such as contact time, pH solution and initial concentration of RB19. The experimental results of RB19 sorption on NiFe-LDH were analyzed using both Langmuir and Freundlich isotherm models.

METHODS

$FeCl_3{\cdot}H_2O$, $FeCl_2{\cdot}4H_2O$ and $NiCl_2{\cdot}6H_2O$ and RB19 were purchased from Sigma-Aldrich. All solutions were prepared with deionized water (18 MΩ). NiFe-LDH was synthesized by the coprecipitation method. Appropriate amounts of $FeCl_3{\cdot}H_2O$, $FeCl_2{\cdot}4H_2O$ and $NiCl_2{\cdot}6H_2O$ with a molar ratio of Fe(III):Fe(II):Ni(II)=1:1:2 were dissolved in 50 cm^3 of deionized water. The three solutions were mixed in an Erlenmeyer flask with a reflux condenser and heated to 80 °C. After that, slow precipitation was performed by adding 3.0 mol dm^{-3} NaOH dropwise to reach a pH of 10.

The brown precipitate was washed several times with hot deionized water and dried at 80 °C. The obtained LDH was labeled as NiFe-LDH.

The sorption study analyzed the effects of the pH from 2.0 to 10.0 and initial RB19 concentration from 50.0 to 700.0 mg dm^{-3} on the sorption of RB19 by using NiFe-LDH. The concentrations of RB19 in the solution as measured at 569 nm using UV-1800 spectrophotometer (Shimadzu, Japan).

The sorption capacity q_t (mg g^{-1}) was determined using the equation 1:

$$q_t = \frac{c_0 - c_t}{m} \times V \quad (1)$$

where c_0 and c_t are the initial and final concentration of the dye in the solution (mg dm^{-3}), V is the solution volume (dm^3) and m is the mass of the sorbent (g).

The Langmuir model [10] can be expressed by the nonlinear equation 2:

$$q_e = \frac{q_m K_L c_e}{1 + K_L c_e} \quad (2)$$

where q_m (mg g^{-1}) is the maximum sorption capacity, K_L (dm^3 mg^{-1}) is Langmuir equilibrium constant.

The Freundlich model [11] can be expressed by the nonlinear equation 3:

$$q_e = K_F c_e^{\frac{1}{n}} \quad (3)$$

where K_F is Freundlich equilibrium constant (mg g^{-1}) (dm^3 mg^{-1})$^{1/n}$, n is the exponent associated with the intensity of sorption.

RESULTS AND DISCUSSION

Influence of contact time and initial concentration of RB19 on the sorption capacity of the sorbent NiFe-LDH were shown in **Figure 1a**. The results indicate that the sorption capacity increases with increasing of contact time. The initial sorption step was rapid (0 to 40 min), after which the sorption rate slows down, reaching equilibrium fot approximately 90 minutes. This can be attributed to the greater number of available adsorption sites on the sorbent at the beginning of the sorption process and the higher concentration of dye in the initial time period [12]. The amount of RB19 sorbed onto NiFe-LDH increased with the increasing of initial concentration of the pollutant. The increased sorption at higher concentrations of RB19 may be due to the driving force of the concentration gradient, which overcomes the mass transfer resistance.

To determine the optimal pH for dye removal, sorption experiments were carried out in the pH range from 2.0 to 10.0 (Figure **1b**). When the pH increased from 3 to 10 the sorption capacity decreased from 325.7 to 164.8 mg g^{-1}. The sorption capacity obtained at pH 2 is approximately the same as at pH 3. At low pH values, the sulfonic groups in RB19 molecules were dissociated and negatively charged, while the active sites on the sorbent surface were protonated and positively charged, resulting in higher attraction at lower pHs. Conversely, with the increase of pH, the positive charge on the surface of the sorbent decreases (more $-OH^-$ ions were present in solution and compete with the sulfonic groups), leading to a decrease in dye removal efficiency [13]. The optimal pH for sorption of RB19 on NiFe-LDH is 2.0, which was used in all further experiments.

Table 1 and **Figure 1c** present the results of modeling for the Langmuir and Freundlich isotherm models. Notably, the Langmuir model emerges with the higher R^2 value and the value of the experimentally obtained equilibrium sorption capacity is approximately equal to the value obtained from the Langmuir model. Consequently, The Langmuir model is able to accurately describe the alignment with the experimental data. According to the Langmuir isotherm, the adsorption process occurs on homogeneous surfaces where there is no significant attraction between binding ions.

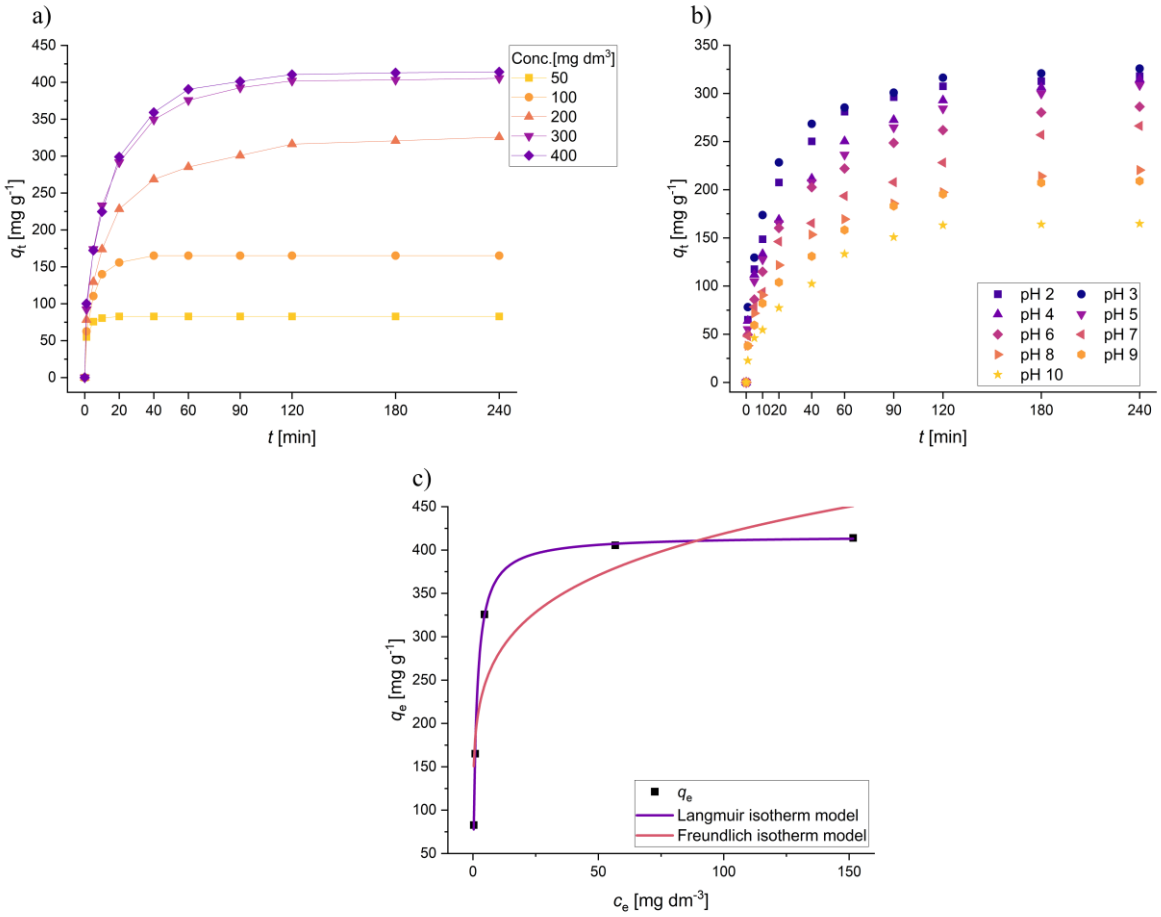


Figure 1. a) Effect of RB19 concentration, b) effect of pH, and c) sorption isotherms.

Table 1. The isotherms parameters for sorption RB19 on NiFe-LDH at 20 °C.

Isotherm parameters						
	$q_{e,exp}$	414.03				
Langmuir	q_m	416.61	K_L	0.765	R^2	0.999
Freundlich	K_F	134.85	n	6.300		0.941

CONCLUSION

The newly developed sorbent NiFe-LDH, synthesized via the coprecipitation method, has demonstrated remarkable efficiency in removing RB19 from aqueous solutions. The results indicate that sorption capacity increases with prolonged contact time, reaching equilibrium at approximately 90 minutes. The optimal pH for maximal RB19 removal is found to be 3.0. The adsorption process of RB19 onto NiFe-LD H aligns well with the Langmuir adsorption isotherm model, exhibiting a maximum adsorption capacity of 414.03 mg g^{-1}. These findings suggest that NiFe-LDH holds promise as an effective sorbent for anthraquinone reactive dye removal from water.

Acknowledgment
This work was supported by the Ministry of Education, Science and Technological Development of the Republic of Serbia (grant no 451-03-66/2024-03/200124 and 451-03-65/2024-03/200124).

REFERENCES

[1] S. S. Moghaddam, M. R. A. Moghaddam, M. Arami, J. Hazard. Mater., 175 (2010) 651.
[2] J. Xiao, H. Zhang, Y. Xia, Z. Li, W. Huang, RSC Adv., 6 (2016) 39861.
[3] S. Karimifard, M. R. A. Moghaddam, Process Saf. Environ. Prot. 99 (2016) 20.
[4] A. Özcan, Ç. Ömeroğlu, Y. Erdoğan, A. S. Özcan, J. Hazard. Mater. 140 (2007) 173.
[5] H. Wang, Q. Li, N. He, Y. Wang, D. Sun, W. Shao, K. Yang, Y. Lu, Sep. Purif. Technol. 67 (2009) 180.
[6] N. A. Fathy, S. E. El-Shafey, O. I. El-Shafey, W. S. Mohamed, J. Environ. Chem. Eng. 1 (2013) 858.
[7] A. Banaei, S. Samadi, S. Karimi, H. Vojoudi, E. Pourbasheer, A. Badiei, Powder Technol. 319 (2017) 60.
[8] N. K. Nga, H. D. Chinh, P. T. T. Hong, T. Q. Huy, J. Polym. Environ. 25 (2016) 146.
[9] M. Shirzad-Siboni, A. Khataee, F. Vafaei, S. W. Joo, Korean J. Chem. Eng. 31 (2014) 1451.
[10] I. Langmuir, J. Am. Chem. Soc. 40 (1918) 1361.
[11] H. M. Freundlich, J. Phys. Chem. 57 (1906) 385.
[12] L. Ai, C. Zhang, L. Meng, J. Chem. Eng. Data 56 (2011) 4217.
[13] X. Li, C. Han, W. Zhu, W. Ma, Y. Luo, Y. Zhou, J. Yu, K. Wei, J. Chem. (2014) 765856.

ELECTROSYNTHESIZED ZnO AS A CATALYST FOR THE CORONA PLASMA DYE DEGRADATION

M. Petrović [1], S. Rančev [2], S. Najdanović [1], M. Kostić [1], M. Radović-Vučić [1], J. Mitrović [1] and A. Bojić [1]

[1] *University of Niš, Faculty of Sciences and Mathematics, Department of Chemistry, 33 Višegradska str., 18000 Niš, Serbia (mk484475@gmail.com)*
[2] *University of Niš, Faculty of Sciences and Mathematics, Department of Physics, 33 Višegradska str., 18000 Niš, Serbia*

DOI: https://doi.org/10.46793/Phys.Chem24I.353P

ABSTRACT
ZnO was synthesized by potentiostatic electrodeposition, characterize by XRD, SEM and EDX, and used as a catalyst for degradation of Reactive Blue 19 (RB 19) dye by non-thermal atmospheric pressure corona plasma discharge. The principle of degradation and the role of the catalyst were presented. ZnO improved the degradation rate by 2.35 times by enhancing decomposition of plasma-generated H_2O_2 into ·OH radical, which was found to be a major degradation reagent.

INTRODUCTION
Advanced oxidation processes (AOPs) are a promising alternative for degradation of reactive dyes in wastewaters, which are difficult to remove by conventional treatments [1]. AOPs involve short-living, highly reactive oxidative species, like hydroxyl radical, ·OH, capable of completely degrading the dye molecule, which are generated by a high energy source. Plasma degradation of organics proceeds via reactive oxidative species generated by the discharge in the gas or liquid phase under the high voltage [1 - 4]. Non-thermal corona discharge has many advantages: operating in open air at atmospheric pressure and ambient temperature, high efficiency, simplicity of construction, low cost, and high energy yield [5]. Recently, the use of catalyst in plasma degradations has been deployed to further improve the processes efficiency. Various materials, mostly semiconductive metal oxides, were tested as the catalysts [1, 3, 6]. ZnO is one of the most deployed photocatalysts due to its unique characteristics, such as direct and wide band gap in the near-UV region, and a large binding energy with availability of excitonic emission processes [1, 2]. That makes it a promising candidate for the plasma degradation processes as well. Electrochemical method was chosen for ZnO synthesis due to its simplicity, excellent parameters control and low cost.

In this paper, ZnO was synthesized by potentiostatic electrodeposition and used as the catalyst in the non-thermal atmospheric pressure pulsating corona plasma degradation of RB 19 dye. The role of the catalyst, as well as the interactions in the gas – liquid system during the plasma discharge in the presence of the catalyst were revealed.

METHODS
$ZnSO_4 \cdot 7H_2O$, H_2SO_4 and RB 19 (Sigma Aldrich) were of reagent grade. The solutions were prepared by dissolving a required amount of powder substance in deionized water. ZnO was synthesized by electrodeposition from 0.50 M $ZnSO_4$ in 0.001 M H_2SO_4 at a constant potential of -0.75 V for 30 minutes in the three - electrode cell with a Ti sheet, SCE and Pt sheet as the working, reference, and auxiliary electrode, respectively, using Amel 510 DC potentiostat (Materials Mates, Italy), controlled by VoltaScope software at 22±1°C, following thermal treatment in furnace in air

at 800°C for 100 minutes. XRD was performed on a Bruker D8 Advance X-ray Diffractometer (Bruker-AXS, Germany) in reflection mode in theta-theta geometry. SEM images were taken by a Hitachi High Technologies SU8030 field emission gun (Tokyo, Japan) at an accelerating voltage of 1 kV. EDX data was taken on the same instrument at 15 kV using a Thermo Scientific System 7 Ultradry EDX detector (Massachusetts, USA). Band gap was determined by electrochemical method, based on their HOMO/LUMO levels. Dye degradation was conducted by the self-made non-thermal atmospheric pressure positive pulsating corona plasma reactor [5] Its power supply consisted of DC pulse generator and high voltage output stage. The corona discharge was created in the close vicinity of the tips of the multipoint anode's needles (stainless steel), in the gas phase (air) over the liquid surface (treated dye solutions) directly exposed to plasma discharge - cathode. The discharge current density, reactor input voltage, and operational frequency were 9.15 μA cm^{-2}, 13.0 kV, and 40 kHz, respectively. Concentration of dye and H_2O_2 formed in the solutions during the plasma treatments (which was determined by iodometric method), were determined using UV-VIS spectrophotometer Shimadzu UV-1650 PC (Japan) at 592 and 425 nm, respectively.

RESULTS AND DISCUSSION

XRD pattern of ZnO catalyst (**Figure 1a**) show well crystalline wurtzite hexagonal (P6_3mc) space group ZnO. The peaks are positioned at 2θ values of 31.51°, 34.40°, 36.01°, 47.46°, 56.52°, 62.64°, 67.79°, and 69.02°, corresponding the crystal planes (100), (002), (101), (102), (110), (103), (200), (112) and (201), respectively. Lattice parameters were $a = b$ = 3.2515897 Å and c =5.2088869 Å. Cell volume and crystal size were 47.69436 $Å^3$ and 65.3 nm, respectively. Angle γ was 120 °. SEM image (Figure 1b) shows that the catalyst mostly consisted of aggregated and singular crystalline material which was approximately 100 - 700 nm in diameter, with some of the aggregates being larger than several μm. Individual grains varied in size and shape, being mostly oval. EDX shows the presence of Zn and O with the average atomic ratio of the elements (%) O : Zn = 52.2 : 47.8 (close to their theoretical ratio). The elements distribution on the examined surface was relatively uniform (the error was within ±4% for each element). The band gap of the catalyst was 3.32 eV.

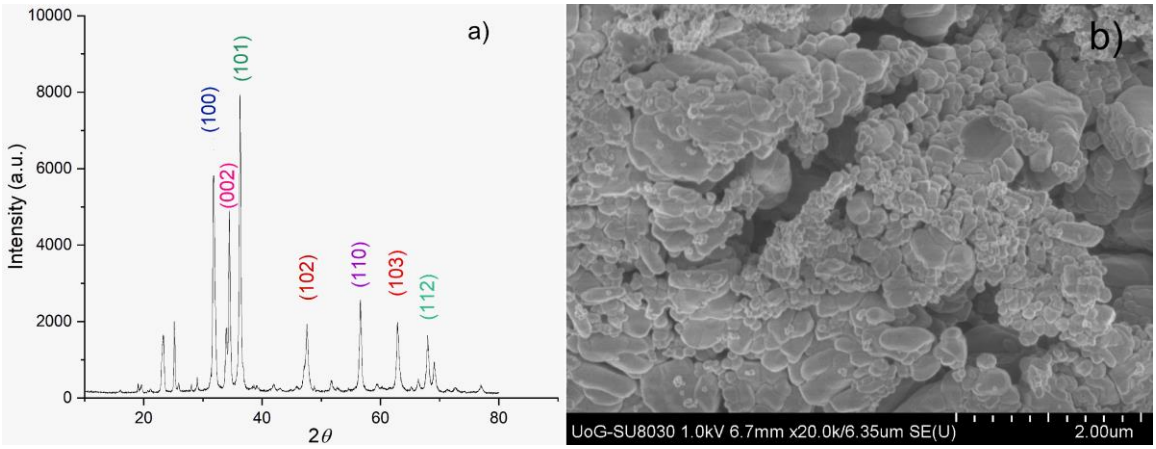


Figure 1. a) XRD pattern and b) SEM image of ZnO catalyst.

Plasma decolorization rate of 50 mg dm^{-3} RB 19 significantly increased in the presence of ZnO catalysts (**Figure 2a**). Complete decolorization was done in about 15 minutes with ZnO, while it took more than 30 minutes without it. The catalyzed reaction rate was 2.35 times higher than non-catalyzed one.

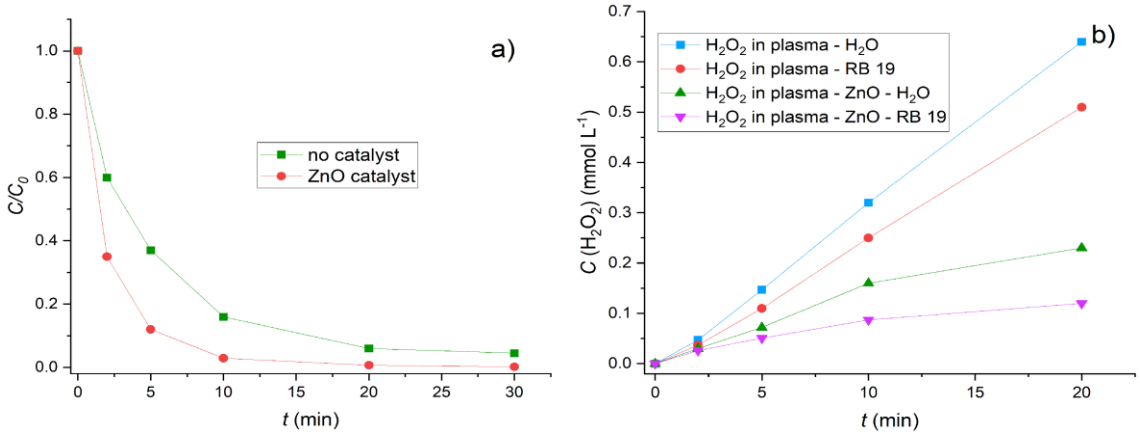


Figure 2. a) decolorization rate of catalyzed and non-catalyzed plasma decolorization of RB 19 and b) H_2O_2 content change in H_2O and RB 19 solution with and without ZnO during plasma treatment.

During the plasma treatment of water, fast electrons, e^- (bearing the energy of up to 15 eV), were generated in gas phase between multipoint anode and liquid surface (cathode) by the electric discharge, accelerated by the electric field and stroke the neutral molecules, such as H_2O and O_2, causing their ionization and formation of short – living reactive species, like ·OH [1 – 4, 7]. Those plasma-generated species underwent many reactions, some of them leading to the formation of H_2O_2, which is represented by the following equations [1, 2]:

$$e^- + H_2O \rightarrow \cdot H + \cdot OH + e^- \quad (1)$$

$$\cdot OH + \cdot OH \rightarrow H_2O_2 \quad (2)$$

H_2O_2 was detected in both plasma treated water and dye solutions, with and without catalyst. Its concentration remained stable hours after the treatments. RB 19 is chemically stable in the presence of H_2O_2, so H_2O_2 alone did not directly react with the dye. H_2O_2 concentration increased linearly in water and in dye solution without ZnO catalysts during the plasma treatment (**Figure 2b**). It also increased with the presence of ZnO, but its concentration was significantly lower than without ZnO (both in water and in dye solution). In both cases, the content of H_2O_2 was lower in corresponding dye solution than in the water. Dye degradation rate was opposite to the H_2O_2 concentration increase rate: it was lower without ZnO (more generated H_2O_2), and higher in the presence of ZnO (less generated H_2O_2). In both cases, dye degradation stopped immediately after the plasma exposure was over, though the H_2O_2 in the solutions remained. It was assumed that H_2O_2 was not consumed in the direct reaction with the dye, but rather as the source of reactive species, generated by plasma, which then degraded the dye. The catalyst enhanced the process of H_2O_2 decomposition (both in water and in the dye solution) and dye degradation under the plasma discharge.

During the plasma treatment, H_2O_2 was being decomposed by the electric discharge, which lead to the formation of •OH radical [6]:

$$H_2O_2 \rightarrow 2 \bullet OH \quad (3)$$

Experiments with the radical scavengers showed that •OH was the main degrading agent (the addition of •OH scavenger IPA caused the decease of degradation rate by more than 90% for both catalyzed and non-catalyzed reaction). It was assumed that the dye was degraded mostly by the •OH radicals generated by plasma decomposition of previously plasma generated H_2O_2. The participation of •OH radicals generated in other processes during the discharge was also possible.

$$RB\ 19 + \bullet OH \rightarrow degradation\ products \quad (4)$$

ZnO alone did not spontaneously react with H_2O_2, nor with the dye in the presence of H_2O_2. However, when exposed to plasma discharge, it rapidly reduced the amount of H_2O_2, both in water in the dye solution, as well as the dye concentration. So, it was assumed that the catalyst was activated by plasma. ZnO particles were constantly present on the liquid surface area due to the mixing caused by plasma-generated ion wind. They were exposed to the strikes of corona generated reactive species accelerated by the strong electric field. Also, the streamers which reached the surface of the solution contained fast electrons of up to 15 eV, which interacted with the suspended catalyst particles. These fast electrons and reactive ions and radicals with the energy higher than the catalyst's band gap, stroke the catalyst and caused its excitation by the creation of the electron (e^-) – holes (h^+) pairs [3, 4]. (the intensity of UV radiation created in the corona discharge was low, so its impact in this case was negligible). Once created, the e^- from the conductive band attacked the plasma-generated H_2O_2 and decomposed it into the •OH radical which further attacked the dye molecules. This process is represented by the equations 5 and 6:

$$Bi_2O_3 \xrightarrow{\Delta E(plasma)} Bi_2O_3{}^* + e^- + h^+ \quad (5)$$

$$e^- + H_2O_2 \rightarrow \bullet OH + OH^- \quad (6)$$

Radical scavengers test showed that h^+ had a minor role in the plasma catalytic degradation as well (the addition of h^+ scavenger Na_2-EDTA reduced degradation rate by about 9%), most likely by direct attack of the H_2O molecules and formation of •OH, which is represented by the equation 7:

$$H_2O + h^+ \rightarrow \bullet OH + H^+ \quad (7)$$

CONCLUSION

Electrosynthesized ZnO catalyst improved the rate of the non-thermal atmospheric pressure corona plasma degradation of the RB 19 dye by more than 2.3 times. The catalyst promoted generation of the •OH radical, a major degradation reagent, by promoting the decomposition of plasma generated H_2O_2, a source of the •OH radical. Excitation of the catalyst was done by the strikes of plasma-generated high-energy species and streamers.

Acknowledgment

This work was supported by the Ministry of Education, Science and Technological Development of the Republic of Serbia (grant no 451-03-66/2024-03/200124 and 451-03-65/2024-03/200124).

REFERENCES

[1] C.A. Aggelopoulos, O. Dolinski, Chemosphere 347 (2024) 140667.
[2] N.Takeuchi, N. Ishibashi, Plasma Sources Sci. Technol. 27 (2018) 045010.
[3] A. Bogaerts et al., J. Phys. D: Appl. Phys. 53 (2020) 443001.
[4] P.J. Bruggeman et al., Plasma Sources Sci. Technol. 25 (2016) 053002.
[5] S. Rančev, M. Petrović, D. Radivojević, A. Bojić, C. Maluckov, M. Radović, Plasma Sci. Technol. 21 (2019) 125501.
[6] M.R. Ghezzar, F. Abdelmalek, M. Belhadj, N. Benderdouche, A. Addou, J. Hazard. Mater. 164 (2009) 1266.
[7] M. Abroyan, A. Eremeev, N.N. Petrov, Sov. Phys. Usp. 10 (1967) 332.

SYNTHESIS AND CHARACTERIZATION OF BASIC BISMUT NITRATE PHOTOCATALYST

S. Najdanović, M. Kostić, M. Petrović, N. Velinov, J. Mitrović and D. Bojić and A. Bojić

University of Niš, Faculty of Sciences and Mathematics, Department of Chemistry, Višegradska 33, 18000 Niš, Serbia. (mk484475@gmail.com)

DOI: https://doi.org/10.46793/Phys.Chem24I.357N

ABSTRACT

The bismuth basic nitrate (BBN) was synthesized by precipitation method from bismuth nitrate as precursor. Precipitation was done at pH 3.5 at room temperature. Characterization was done by Scanning electron microscopy with energy dispersive X-ray spectroscopy (SEM-EDX) and X-ray diffraction (XRD) methods. Morphologically the BBN consisted of plane-like structures with nanometric particles on their surface. Results of XRD analysis show that bismuth basic nitrate with chemical formula $Bi_6O_5(OH)_3(NO_3)_5 \cdot 3H_2O$ crystallizes in the monoclinic space group $P2_1/c$ (14) with a = 17.15200, b = 9.18100, c = 17.75200, β = 127.830 and V = 2207.94. The obtained material showed a certain adsorption activity for textile dye Reactive Blue 19 (RB19), and a very high photocatalytic activity for the same dye. Photocatalytic decolorization of RB19 was achieved in 15 minutes. The findings clearly demonstrated the applicability of BBN for the photocatalytic decolorization of RB19.

INTRODUCTION

Synthetic dyes are widely used in different industries such as textile, paper, leather, food, cosmetics, pharmaceutical and color photography. About 10–20% of dyes are released into wastewater during the dyeing process [1]. Wastewater from these industries which contains colored compounds has caused many serious problems for the environment, human, animal, and plant life, due to their low biodegradability and high toxicity [2,3]. RB19, which belongs to anthraquinone reactive dye is widely used in the textile industry. Because of the presence of electrophilic vinyl sulfone in its structure, RB19 may have mutagenic properties. Therefore, it is very important to develop methods to treat effluents containing RB19 before they are released into wastewater [1,4]. Conventional methods for organic pollutants removal, such as adsorption, coagulation, electrocoagulation and membrane filtration, convert biodegradable materials into sludge. Among conventional methods, the photocatalytic process has advantages such as the complete mineralization of organic pollutants and the absence of secondary pollution production [4].

Bismuth-containing compounds have recently attracted growing attention as photocatalyst due to their rich and versatile crystal chemistry and diversity of chemical compositions, as well as unique physicochemical properties. Among them basic bismuth nitrates (BBN) are of special interest due to the abundant resources, non-toxicity, and rich crystal chemistry. As a precursor for obtaining bismuth based compounds bismuth nitrate pentahydrate ($Bi(NO_3)_3 \cdot 5\ H_2O$) is commonly used [5].
In this work, bismuth basic nitrate $Bi_6O_5(OH)_3(NO_3)_5 \cdot 3H_2O$ was synthesized as an efficient photocatalyst for RB19 decolorization.

METHODS

Synthesis of photocatalyst

BBN photocatalyst was synthesized by the precipitation method using $Bi(NO_3)_3 \cdot 5\ H_2O$ as a precursor. According to the procedure, 1.0 g of bismuth nitrate was dissolved in 10.0 cm^3 of nitric

acid concentration of 2.0 mol dm^{-3}. After that, 30 cm^3 of deionized water was added to the solution and NaOH concentration of 2.0 mol dm^{-3} was added to pH 3.5. The pH was maintained at 3.5 with stirring on a magnetic stirrer for 1.5 h at room temperature. At pH 3.5, a BBN precipitate is formed. The obtained precipitate was washed several times with warm deionized water, separated by centrifugation, and dried in a laboratory dryer for 6 h at 80 ºC. After that, the materials were cooled to room temperature and ground to a powder, after which they were ready for use in photocatalytic processes.

Characterization of the photocatalyst

For low magnification SEM images (x100 up to x15000), samples were attached to aluminum stubs with Leit adhesive carbon tabs. Secondary electron images were collected with a Hitachi High Technologies SU8030 (Tokyo, Japan) field emission gun SEM operated at an accelerating voltage of 1 kV. For high magnification images (x30000 up to x150000), samples were mounted on silicon wafers attached to aluminum stubs. Secondary electron plus back scattered electron images were collected on the same instrument operated at an accelerating voltage of 1 kV. Samples were imaged uncoated. EDX data was collected on the same instrument at an accelerating voltage 20 kV with a Thermo Scientific System 7 Ultradry EDX detector (Massachusetts,USA) at 20kV. Five random areas were analyzed on each sample.

Samples for XRD were packed into Si low background holders and data collected on a Bruker D8 Advance X-ray Diffractometer (Bruker-AXS, Germany) in theta-theta geometry in reflection mode. Cu Kα radiation was used at 40 kV and 40 mA with a LynxEye silicon strip position sensitive detector. Data collection was between 2-70° 2θ, step size of 0.02° and a counting time of 0.5 seconds per step. Data was collected using DIFFRAC plus XRD Commander version 2.6.1 software (Bruker-AXS), qualitative assessment with the aid of EVA version 5 (Bruker-AXS) and the PDF-2 2020 database (ICDD).

Photocatalytic activity determination

The photocatalytic activity of the obtained BBN was evaluated by the decolorization of an aqueous solution of textile dye RB19. The experiments were performed in a batch photoreactor under UV light radiation with light intensity of 1950 μW cm^{-2} and a maximum emission at 253.7 nm, at room temperature. In 50 cm^3 of RB19 solution with a concentration of 25 mg dm^{-3}, a photocatalyst with a concentration of 500 mg dm^{-3} was added. Before irradiation, the suspension was stirred for 30 min to achieve adsorption-desorption equilibrium. At given time intervals, about 4 cm^3 of the suspension was taken out and filtered using a 0.45 μm regenerated cellulose membrane filter (Agilent Technologies, Germany) to get rid of the catalyst powders. The concentration of RB19 in the solution was determined by UV-Visible spectrophotometer (UV-1800, 10 Shimadzu, Japan) at 592 nm.

RESULTS AND DISCUSSION

Characterization of the photocatalyst

The morphology of obtained material is determined by SEM. The SEM images at different magnification are shown in Fig.1. The material consists of different irregular sizes and shape plane like structures. Their dimensions vary from 5 μm to 0.5 μm. Also, on the surface of these structures can be observed some smaller particles with nanometric dimensions, some smaller than 100 nm. Such a micro/nano-structured mixed surface can favor the dye adsorption, and thus photocatalysis, which mainly occurs on the surface of the material.

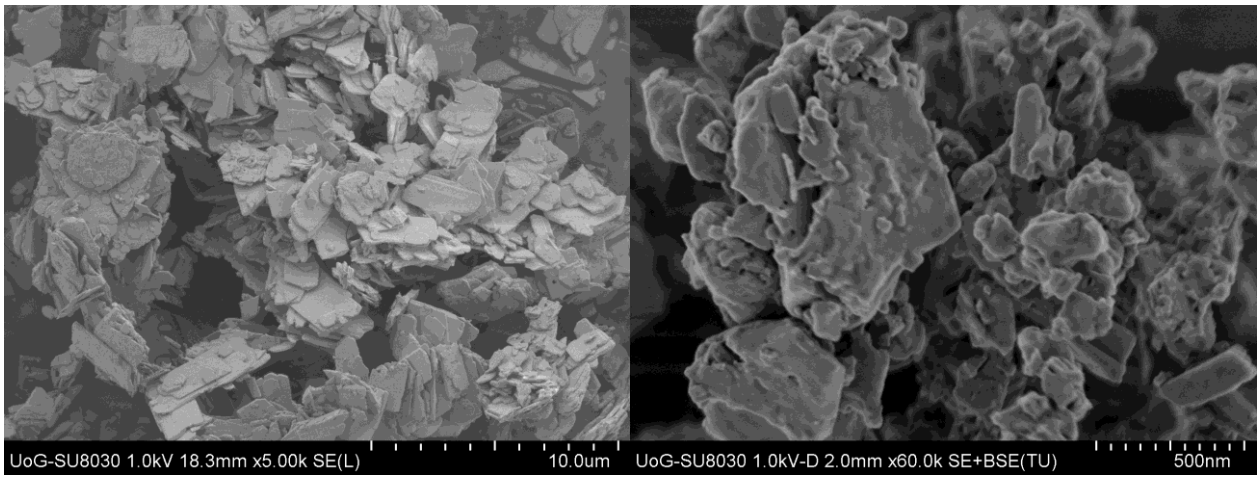


Figure 1. SEM images of obtained material at magnification of x5000 and x60000.

The crystal structure of the material was determined by XRD analysis. As shown in Fig. 2, the observed diffraction peaks of material matched well with the data from JCPDS database (PDF 01-070-1226) and could be indexed to monoclinic $Bi_6O_5(OH)_3(NO_3)_5 \cdot 3H_2O$ with space group $P2_1/c$ (14), a = 17.15200, b = 9.18100, c = 17.75200, β = 127.830 and V = 2207.94.
The observed sharp and intense diffraction peaks of BBN exhibited their excellent crystalline nature and high purity. The sample was crystalline, predominantly $Bi_6O_5(OH)_3(NO_3)_5 \cdot 3H_2O$ with a small amount of an unidentified phase (probably below 5 weight % in abundance).

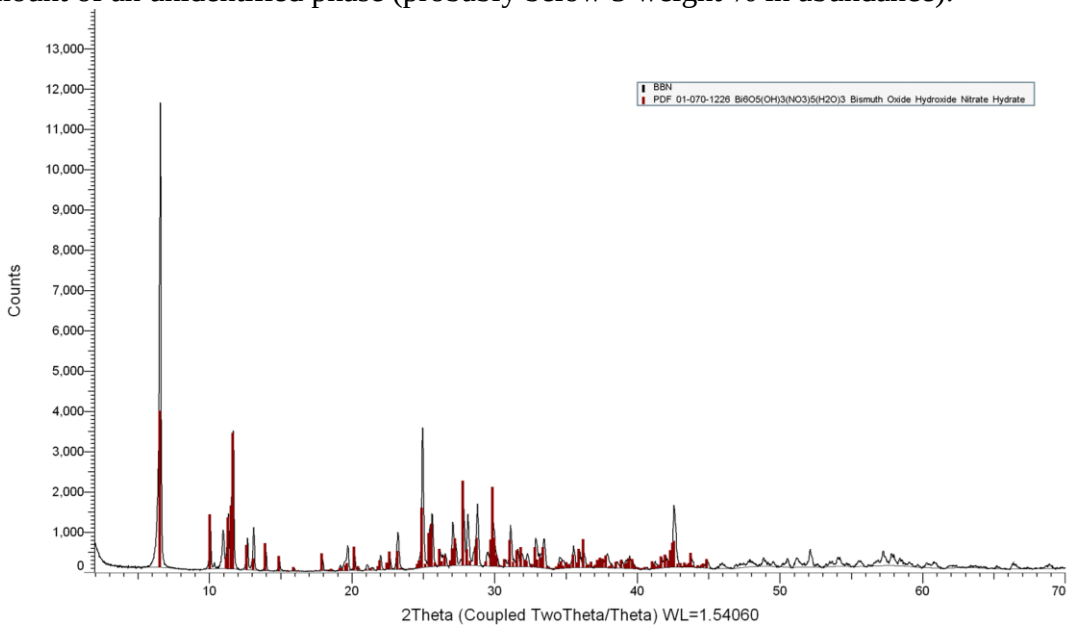


Figure 2. XRD pattern of obtained material.

The results of EDX analysis show the presence of Bi, O and N in weight percentages of 70.9%, 24.6% and 4.5% respectively, which is in good agreement with elemental weight percentages for $Bi_6O_5(OH)_3(NO_3)_5\ 3H_2O$.

Photocatalytic activity of BBN

The photocatalytic activity of the obtained BBN was determined by the decolorization of the textile dye RB19. Before the photocatalytic experiment, the adsorption properties of the material were examined. The results of the adsorption experiment (Fig. 3.) show that BBN has a certain

adsorption activity for RB19. The RB19 concentration decreased from 25.0 mg dm^{-3} to 16.79 mg dm^{-3} in 30 minutes. After the adsorption experiment, the solution was irradiated with UV light. The photocatalytic process is very fast (Fig. 4.). Complete decolorization of the RB19 solution was done in 15 minutes. Therefore, the obtained BBN photocatalyst can be effectively used for the photocatalytic degradation of RB19.

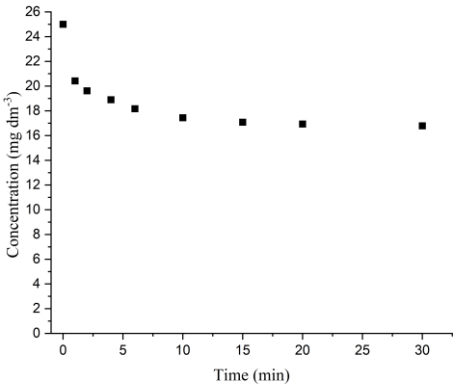


Figure 3. Adsorption efficiency of BBN: c_{RB19} 25.0 mg dm^{-3}, c_{BBN} 500.0 mg dm^{-3}, native pH, temperature 25.0 ± 0.5 ºC.

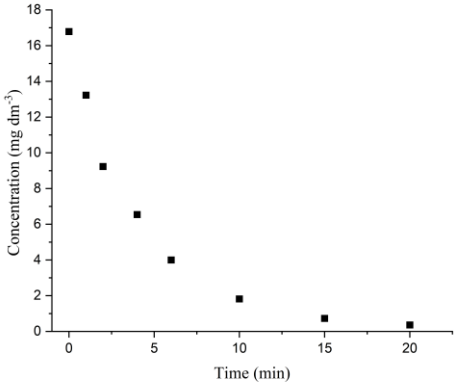


Figure 4. Photocatalytic efficiency of BBN: c_{RB19} 25.0 mg dm^{-3}, c_{BBN} 500.0 mg dm^{-3}, UV light intensity 1950 μW cm^{-2}, temperature 25.0 ± 0.5 ºC.

CONCLUSION

BBN photocatalyst was successfully synthesized by precipitation method from an acidic bismuth nitrate solution at pH 3.5 at room temperature. The obtained BBN powder is fully crystallized monoclinic $Bi_6O_5(OH)_3(NO_3)_5 \cdot 3H_2O$. The morphology of the BBN surface favors dye adsorption, which enables good photocatalytic properties. BBN shows both adsorption and photocatalytic activity for textile dye RB19, with the photocatalytic activity being significantly higher. Overall, given the simple way of synthesis, low cost and environmentally friendly starting materials, high efficiency, BBN could be a promising material for the photocatalytic degradation of RB19 from aqueous solutions.

Acknowledgment

This work was supported by the Ministry of Science, Technological Development and Innovations of the Republic of Serbia (Agreement No 451-03-66/2024-03/200124 and Agreement No 451-03-65/2024-03/200124).

REFERENCES

[1] M. Bilal, T. Rasheed, H.M.N. Iqbal, C. Li, H. Wang, H. Hu, W. Wang, X. Zhang, Chem. Eng. Res. Des., 129 (2018) 384.
[2] M. Bagheri, M. Farhadian, M. Vesali-Naseh, Adv. Powder Technol., 34 (2023) 104088.
[3] S. Cherif, H. Yazid, G. Rekhila, Z. Sadaoui, M. Trari, Optik (Stuttg)., 238 (2021) 166751.
[4] H. Bel Hadjltaief, M.E. Galvez, M. Ben Zina, P. Da Costa, Arab. J. Chem., 12 (2019) 1454.
[5] R. Yan, H. Huang, H.L. Wang, S. Chu, W.F. Jiang, Sep. Purif. Technol., 299 (2022) 121766.

EFFICIENT PRODUCTION OF TWO-DIMENSIONAL PYROPHYLLITE THROUGH LIQUID-PHASE EXFOLIATION

I.R. Milošević, T. Tomašević, J. Vujin, R. Panajotović, J. Pešić and T. Tomašević-Ilić

Institute of Physics Belgrade, University of Belgrade, Laboratory for 2D Materials, Center for Solid State Physics and New Materials, Pregrevica 118, 11080 Belgrade, Serbia. (novovic@ipb.ac.rs)

DOI: https://doi.org/10.46793/Phys.Chem24I.361M

ABSTRACT

2D-Pyrophyllite, a layered material with notable physico-chemical properties, is suitable for various applications, such as electrical insulator, protective coating or lubricant. Liquid-phase exfoliation (LPE) has emerged as a promising, large-scale, low-cost method for obtaining substantial yields of high-quality, basal plane defect-free pyrophyllite flakes in dispersion. Optimizing exfoliation conditions is crucial for achieving these objectives. After adjusting experimental parameters (initial concentration of bulk material, sonication time, solvent type, and centrifugation rate), a stable pyrophyllite dispersion with a high concentration of 98.8 μg/mL was obtained. The LPE method enables the production of high-yield flakes with well-defined shapes, flat surfaces, and regular edges.

INTRODUCTION

Layered materials are compounds characterized by a structure in which atomic layers are bonded together by weak forces, making them easily separable to atomically thin layers. These materials exhibit strong in-plane and weak between layers bonds, typically of the van der Waals type. Some of them are graphene [1], transition metal dichalcogenides (TMDs) [2], elemental analogues to graphene like silicene, germanene etc. [3]. In recent years a new group of earth-abundant, low-cost nanomaterials has emerged. The new group, known as clay minerals, includes two-dimensional (2D) insulating materials based on phyllosilicates (talc, kaolinite, mica, pyrophyllite, vermiculite, etc.). Layered materials in 2D form exhibit unique electronic, mechanical, and chemical properties that differ from their bulk counterparts. To fully realize their potential, layered materials must be exfoliated.

The advancement of these materials has been limited by the absence of a straightforward method to exfoliate them into mono- or few-layer nanosheets in large quantities. One of the developed methods is liquid-phase exfoliation (LPE). This method is simpler and less costly than chemical vapor deposition and provides a higher yield than mechanical exfoliation. In this study, we present a method for obtaining 2D pyrophyllite nanosheet dispersions using ultrasound induced LPE. Optimization of exfoliation conditions (including the initial concentration of bulk material, sonication time, solvent type, and centrifugation rate) are key processes for enhancing the yield, stability, and quality of 2D pyrophyllite dispersions.

The pyrophyllite chemical formula is $Al_2Si_4O_{10}(OH)_2$. Pyrophyllite single layer consists of the $AlO_4(OH)_2$ octahedral sheet which is between two SiO_4 tetrahedral sheets [4]. Pyrophyllite is an abundant, inexpensive material, chemically inert, good electrical and thermal insulator with a high melting point, soft mineral which can withstand large pressures [5]. Pyrophyllite dispersions obtained by LPE method can be used to form films through various methods, such as spray coating, vacuum filtration, or Langmuir–Blodgett assembly (LBA).

METHODS

Liquid-phase exfoliation, a non-covalent exfoliation that uses solvents, is one of the most promising synthesis methods [1, 2, 6]. We have used sonication assisted LPE in ultrasonic bath (Figure 1) where ultrasound induces separation of 2D nanosheets from bulk material in appropriate solvent due to the propagation of ultrasound waves. The starting material for LPE of pyrophyllite was ground pyrophyllite crystal (Hillsborough mine, Orange County, North Carolina, USA). Sonication results in exfoliation of the initial flakes, where the largest were removed by centrifugation. Exfoliation conditions, such as the initial concentration of bulk material, sonication time, solvent type, and centrifugation rate were varied to enhance the yield, stability, and quality of pyrophyllite dispersions. When optimization was achieved, we had a stable dispersion of few-layer defect-free pyrophyllite nanosheets.

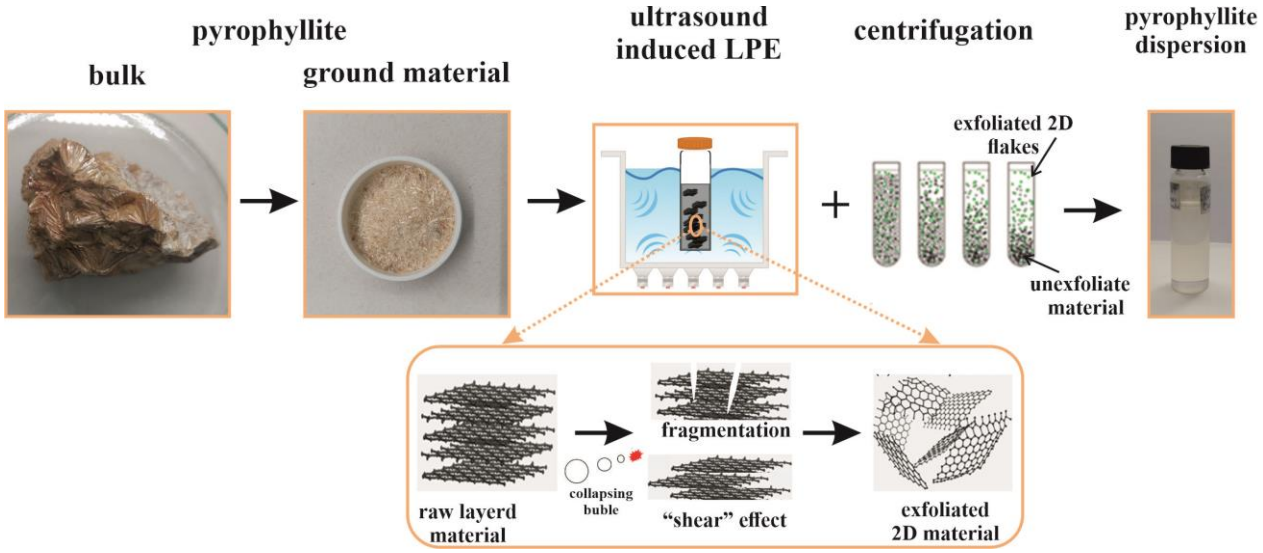


Figure 1. Schematic representation of pyrophyllite liquid-phase exfoliation (LPE).

For optical characterization of nanosheet dispersions, UV–VIS spectra were measured using a Shimadzu 2600i spectrophotometer with quartz cuvettes. Vacuum filtration was used to obtain the mass of exfoliated pyrophyllite flakes, a necessary parameter for calculating the absorption coefficient of pyrophyllite. For filtration of pyrophyllite dispersions Omnipore hydrophilic PTFE membrane filter (0.2 μm pore size) was used. The morphology characterization was done by imaging in the tapping AFM mode with an atomic force microscope, NTEGRA Spectra.

RESULTS AND DISCUSSION

The concentration of the dispersion can be calculated from the Lambert- Beer law ($A/l = \alpha c$, where l is the cell length, and c is the concentration) if the absorption coefficient (α) is known [1, 2, 7]. However, absorption coefficient is unknown for phyrophyllite dispersed in N-methylpyrrolidone (NMP) and Dimethylformamide (DMF). To determine the absorption coefficient firstly concentration after centrifugation must be determined, so we prepared pyrophyllite dispersions in NMP and DMF using ultrasound induced LPE method of initial concentration of 10 mg/mL. The dispersions were diluted two, five and ten times and the corresponding UV-VIS absorption spectra were recorded (Figure 2a) for both solvents. Precisely measured volume (V= 20mL) of both as-prepared (stock) and diluted pyrophyllite dispersions were passed through the PTFE membrane filters of known mass (Figure 2b, inset). Careful measurement of the filtered mass provided the concentration of as prepared-stock and diluted dispersions. The absorbance (660 nm) divided by the

cell length was plotted versus concentration (Figure 2b) showing a linear relationship with measured concentrations, giving absorption coefficients of 15.6 $mLmg^{-1}m^{-1}$ for DMF and 8.5 $mLmg^{-1}m^{-1}$ for NMP. Using these absorption coefficients, we can determine the concentration for all subsequent samples.

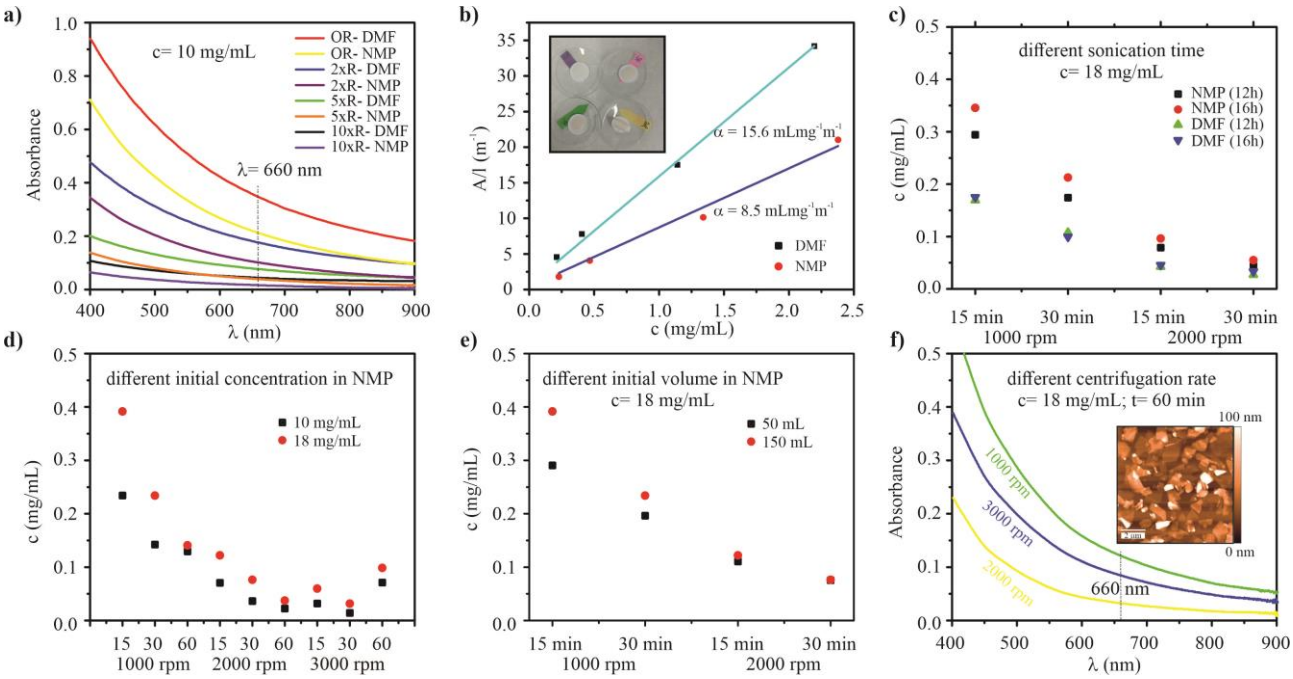


Figure 2. Optical characterization of pyrophyllite dispersions: a) Absorption spectra of pyrophyllite dispersions in NMP and DMF (initial concentration of 10 mg/mL): original stock dispersion after centrifugation (OR), and dispersions diluted 2, 5, and 10 times (2xR, 5xR, 10xR). b) Lambert-Beer plots: optical absorbance (λ= 660 nm) divided by cell length as a function of pyrophyllite concentration (inset: Filters showing the filtered dispersed material for the corresponding diluted dispersions). c) Pyrophyllite concentration calculated from the experimentally obtained absorption coefficient at 660 nm for different sonication times, starting with an initial concentration of 18 mg/mL in NMP and DMF. d) Pyrophyllite concentration calculated from the absorption coefficient at 660 nm for various initial concentrations in NMP. e) Pyrophyllite concentration calculated from the absorption coefficient at 660 nm for different initial volume with a concentration of 18 mg/mL in NMP; f) Absorption spectra for different centrifugation rates with a centrifugation time of 60 minutes (inset: Topography image of 2D pyrophyllite flakes obtained by LPE method on Si/SiO_2).

We varied exfoliation conditions, including the initial concentration of bulk material, sonication time, solvent type, and centrifugation rate, to optimize the yield, stability, and quality of pyrophyllite dispersions. Concentration was calculated using experimentally obtained absorption coefficients from absorbance (660 nm) for different sonication times with an initial concentration of 18 mg/mL in NMP and DMF (Figure 2c). Figure 2c shows that longer sonication times (16h) result in higher yields of dispersed pyrophyllite in both solvents. Also, for the 16h of sonication time NMP gives higher yields of pyrophyllite. Initial concentrations of 18 mg/mL yield higher concentrations across all centrifugation rates and times used. Similarly, larger initial volumes have the same effect, but at higher centrifugation rates, concentrations were equalized (Figure 2e). Dispersions centrifuged at lower rates were less stable, with pyrophyllite flakes aggregating after two weeks. Only about 20% of the dispersed flakes remained in the solvent, while the rest formed sediment. The least aggregation occurred at 3000 rpm compared to 1000 and 2000 rpm.

Additionally, 60 minutes was found to be the optimal centrifugation time for the best dispersion quality (Figure 2f). A stable pyrophyllite dispersion with a concentration of 98.8 μg/mL was obtained by using an initial concentration of 18 mg/mL ground pyrophyllite in NMP, sonicated for 16 hours in 150 mL, and centrifuged for 60 minutes at 3000 rpm.

The topography of the 2D pyrophyllite flakes obtained by the LPE method in NMP is shown in the inset of Figure 2f. The flakes exhibit well-defined shapes, flat surfaces, and regular edges, with varying lateral dimensions and heights. The samples produced by the LPE method consist of a network of flakes typically 5-15 nm in height and around 1 μm in lateral dimensions, as previously reported [8]. Although these flakes are thicker and smaller than those produced by mechanical exfoliation, the LPE method enables large-scale production and can be effectively used for various applications, particularly when combined with film formation techniques such as the Langmuir-Blodgett Assembly method.

CONCLUSION

We have demonstrated that by optimizing the exfoliation parameters in the LPE technique, it is possible to achieve a stable dispersion with a significant yield of high-quality pyrophyllite flakes, which have well-defined shapes, regular edges, and varying lateral dimensions and heights. By determining the absorption coefficient of pyrophyllite in different solvents and adjusting the initial concentration of bulk material, sonication time, and centrifugation rate, pyrophyllite can be dispersed at concentrations up to 98.8 μg/mL in NMP. This dispersion can be used to create thin films through vacuum filtration or the Langmuir-Blodgett Assembly methods, opening new perspectives for the application of pyrophyllite.

Acknowledgment

This research was supported by the Science Fund of the Republic of Serbia, Grant No 7456, 2D Material-based Tiled Network Films for Heritage Protection-2DHeriPro and by the Institute of Physics Belgrade through the grants by the Ministry of Science, Technological Development and Innovation of the Republic of Serbia.

REFERENCES

[1] Y. Hernandez, V. Nicolosi, M. Lotya et al., Nat. Nanotechnol., 3 (2008) 563.
[2] J.N. Colman, M. Lotya, A. O´Neill et al., Science, 331 (2011) 568.
[3] S. Balendhran, S. Walia, H. Nili et al., Small, 11 (2015) 640.
[4] A.I. Mitrović Rajić, Mechanochemical and thermal modification of pyrophyllite for use in electrochemical sensors and membranes, Doctoral Dissertation, Faculty of Physical Chemistry, 2023.
[5] M.A. Ali, H.A.M. Ahmed, H.M. Ahmed, M. Hefni, Appl. Sci., 11 (2021) 11357.
[6] A. Matković, I. Milošević, M. Milićević et al., 2D Mater., 3 (2016) 015002.
[7] M. Lotya, Y. Hernandez, P.J. King et al., J. Am. Chem. Soc., 131 (2009) 3611–3620.
[8] B. Vasić, R. Gajić, I. Milošević et al. Appl. Surf. Sci., 608 (2023) 155114.

ASSESSMENT OF THE INFLUENCE OF FORMULATION PARAMETERS ON THE PHYSICO-CHEMICAL PROPERTIES OF HYPROMELLOSE-BASED FILM-FORMING SOLUTIONS

S. Milinković, A. Ćirić and Lj. Đekić

University of Belgrade, Faculty of Pharmacy,
Vojvode Stepe 450, 11000 Belgrade, Serbia. (sandra.milinkovic@pharmacy.bg.ac.rs)

DOI: https://doi.org/10.46793/Phys.Chem24I.365M

ABSTRACT

There is great interest in development of film-forming systems for dermal (topical or transdermal) drug delivery (FFSDDD) due to their unique property to form a thin, continuous film upon administration to the skin surface, offering numerous advantages compared to conventional topical preparations. The primary research challenge in the FFSDDD development is the formulation of a carrier that represents a polymer solution in a volatile and non-volatile solvents mixture. We examined the influence of the film-forming polymer (hypromellose) concentration and the type and concentration of nonvolatile solvent (propylene glycol or macrogol 400) and volatile solvent (ethanol or isopropanol) on the physicochemical (pH and transmittance) and rheological properties of the film-forming solution (FFS) and the properties of the film formed. FFS containing 2.5% of hypromellose and 1.25% and 5% propylene glycol form films with the most desirable pH, appearance, viscosity, and flexibility, so they can be considered promising dermal drug delivery carriers.

INTRODUCTION

There is a constant need for the development of new formulations as suitable alternatives to conventional liquid and semi-solid dosage forms for dermal drug delivery to overcome the short residence time on the skin and improve the therapeutic efficiency. FFS with film-forming polymers and both volatile and non-volatile solvents allow the formation of a thin film on the skin surface providing a longer retention time and increased concentration of the active ingredient in the film thereby promoting the percutaneous penetration [1] [2].

Although the field of FFS has made considerable progress in recent years, there are still many aspects that need to be explored. This paper aimed to formulate FFS based on hypromellose, a biomass-based semisynthetic, sustainable and biocompatible polymer [3] with solvents approved as pharmaceutical excipients. This offers a compelling advantage over other FFS with synthetic polymers and toxic solvents, which not only meets the industry's trend towards environmentally friendly practices, but also ensures the safety and efficacy of pharmaceutical products for broader consumer satisfaction. The particular focus was to investigate the influence of the polymer concentration, the type and concentration of the volatile solvent and the non-volatile solvent (i.e., film plasticizer) used on the physicochemical (pH and transmittance) and rheological properties of FFS as well as the properties of the films formed *in vitro*.

METHODS

For the preparation of FFS, hypromellose (nominal viscosity 30 mPas at a concentration of 2%) was used in concentrations of 1%, 1.5%, 2% and 2.5%, while purified water, a mixture of water and ethanol in a 1:1 mass ratio (WE11) or a mixture of water and isopropanol in a 3:1 mass ratio (WI31) was used as vehicle. In addition, FFS with 2.5% hypromellose containing 1.25%, 5% and 20% of a

plasticizer (propylene glycol or macrogol 400) were prepared. For the preparation of FFS with plasticizers were used WE11 or WI31. All solvents were of Ph. Eur. grade.

Physicochemical characterization of the prepared FFS included the measurement of transmittance (%T), pH and rheological parameters. To evaluate the transparency of the FFS, %T was measured using an Evolution 300 UV spectrophotometer (Thermo Scientific, USA) at 600 nm. The pH was measured with a HI2223 pH meter (HANNA Instruments, USA) at 20±3 °C. Rheological measurements were performed using a RheolabMC120 rotational rheometer (PaarPhysica, Germany) with an MK 22 cup-plate measuring system at a temperature of 20±0.1 °C and 32±0.1 °C and a controlled shear rate of 0-200 s^{-1} (ascending curve) and 200-0 s^{-1} (descending curve), and the data obtained were used to determine the flow type and viscosity of FFS. The FFS were poured into Petri dishes, at least in triplicate, and dried under ambient conditions to a constant mass. The appearance of the dry films (color, transparency, integrity when detached from a flat surface) was observed and their mass was measured.

RESULTS AND DISCUSSION

Transmittance of all FFS was greater than 90% (Table 1), indicating complete dissolution of hypromellose in all three vehicles used [4]. The pH ranged from 4.47 to 5.66 (Table 1) and it was observed that the pH decreased with the increase in hypromellose concentration. The highest pH values were observed for FFS with ethanol (F2, F5, F8 and F11), followed by FFS with isopropanol (F3, F6, F9 and F12), while the lowest pH values were found for FFS where the only solvent was water (F1, F4, F7 and F10). Since the pH values of the mixture of water and ethanol in a ratio of 1:1 (6.97) [5] and the mixture of water and isopropanol in a ratio of 1:1 (7.2) [6] are very similar, the differences obtained can be explained by differences in the proportion of solvent used.

Table 1. Composition, pH, transmittance (%T) and viscosity (η) of FFS without plasticizer (F1-F12) and mass of obtained films (FM).

Sample	Polymer [%]	Vehicle	pH	%T	η [mPas]		FM [mg]
					20 °C	32 °C	
F1	1	W	4.62±0.00	96.04±0.17	15±15	9±4	61±4
F2	1	WE11	5.64±0.02	96.85±0.20	11±10	9±9	63±2
F3	1	WI31	4.74±0.01	96.37±0.76	12±10	8±6	62±2
F4	1.5	W	4.49±0.00	93.83±0.39	12±8	8±8	91±2
F5	1.5	WE11	5.59±0.01	94.95±0.38	29±7	17±4	91±2
F6	1.5	WI31	4.74±0.00	94.51±0.28	36±8	19±2	93±2
F7	2	W	4.55±0.00	91.86±0.06	27±7	15±3	124±2
F8	2	WE11	5.63±0.00	93.87±0.36	68±7	37±8	123±3
F9	2	WI31	4.80±0.00	93.31±0.49	80±7	40±10	124±3
F10	2.5	W	4.47±0.00	90.43±0.97	47±13	32±3	154±2
F11	2.5	WE11	5.63±0.01	92.52±0.24	128±11	70±9	159±5
F12	2.5	WI31	4.80±0.00	91.41±0.64	163±10	93±11	159±4

Rheological measurements showed that all FFS without plasticizers are Newtonian systems, as their viscosity (Table 1) remained constant when the shear rate changed and did not change over time. An increase in viscosity was observed with increasing hypromellose concentration in both FFS with WE11 (F2, F5, F8 and F11) and FFS with WI31 (F3, F6, F9 and F12). The viscosity of FFS was also influenced by the choice of volatile solvent, so the viscosity of FFS containing isopropanol (F3, F6, F9 and F12) was higher than that of FFS with ethanol (F2, F5, F8 and F11), which can be explained by the higher viscosity of pure isopropanol (2.414 mPas) [7] compared to ethanol (1.2 mPas) [8] and water (1 mPas) [8].

The drying time of FFS with ethanol was the shortest (around 13.5 h), while drying of FFS with water or WI31 took about 20 h. The obtained films were transparent, smooth, non-sticky and showed no signs of cracking when folding (Figure 1a.). Films with ethanol were slightly harder to peel from the glass surface compared to films with isopropanol. Films with a higher proportion of

hypromellose had higher mass values (Table 1). Films with a lower concentration of hypromellose were thin, brittle and more difficult to peel off, and therefore FFS with 2.5% was selected for further tests in the presence of plasticizers.



Figure 1. Photographs of films with 2.5% hypromellose: a) without plasticizer; b) with propylene glycol; c) with macrogol 400.

The addition of propylene glycol and its concentration increase in FFS decreased pH (Table 2), while the pH of FFS with macrogol 400 was higher compared to FFS without plasticizers. No effect of the plasticizers on the transmittance of FFS was observed, indicating that they had no significant influence on the solubility of 2.5% hypromellose in the vehicles used.

Table 2. Composition, pH, transmittance (%T) and viscosity (η) of FFS and mass of obtained films (FM) with a plasticizer (propylene glycol in F13-F18 and macrogol 400 in F19-F24).

Sample	Vehicle	Plasticizer [%]	pH	%T	η [mPas]		FM [mg]
					20 °C	32 °C	
F13	WE11	1.25	5.25±0.01	93.04±0.24	135±7	79±8	175±4
F14	WI31	1.25	4.56±0.01	92.87±0.28	160±6	88±9	182±5
F15	WE11	5	4.82±0.00	94.19±0.36	143±5	79±8	177±11
F16	WI31	5	4.18±0.01	92.86±0.83	168±5	87±10	169±7
F17	WE11	20	4.34±0.00	95.83±0.32	188±6	91±8	668±84
F18	WI31	20	3.78±0.00	95.31±1.31	225±4	96±8	703±56
F19	WE11	1.25	5.70±0.01	93.59±0.15	141±5	73±12	239±3
F20	WI31	1.25	4.88±0.01	93.50±0.15	160±7	83±10	243±4
F21	WE11	5	5.85±0.01	94.22±0.40	150±4	91±8	481±3
F22	WI31	5	5.01±0.00	94.50±0.67	174±6	96±8	479±3
F23	WE11	20	6.37±0.01	89.76±0.58	248±11	156±9	1454±7
F24	WI31	20	5.52±0.03	91.17±0.29	295±9	163±9	1438±5

FFS with plasticizers were also Newtonian systems. The addition of both plasticizers led to an increase in viscosity compared to FFS without plasticizers and also an increase in viscosity was observed as a function of the increasing plasticizer content (Table 2). FFS with macrogol 400 showed higher η values compared to those with propylene glycol, as macrogol 400 is a more viscous (114.5 mPas at 20 °C) compared to propylene glycol (60.61 mPas) [9]. At 32 °C, lower η values were measured for all FFS (without and with plasticizers) (Tables 1 and 2), indicating a potentially better spreadability of FFS at skin surface temperature.

Films with plasticizers (Figures 1b and 1c) had a higher mass than films without plasticizers (Table 2). The mass of macrogol 400 films was higher than that of propylene glycol films, and an increase in film mass was observed with increasing plasticizer concentration, so the highest mass was measured for films with 20% macrogol 400. The increase in film mass with added plasticizers is due to the lower volatility of macrogol 400 [10] and propylene glycol [11] compared to water, ethanol, and isopropanol.

CONCLUSION

Changes in the type and proportion of plasticizer and the type and proportion of organic solvent led to differences in the values obtained for the parameters investigated (pH, %T, η, and film mass). The solubility of hypromellose in the vehicles used was satisfactory in all samples. The pH values of all FFS were acceptable for skin application. All FFS were Newtonian systems. Although water is the most suitable solvent in terms of biocompatibility, the addition of an organic solvent is still necessary to ensure relatively rapid drying of the FFS after application to the skin. From the results obtained, it can be concluded that both ethanol and isopropanol are equally good volatile solvents. FFS with ethanol had a lower viscosity and a shorter drying time, while films with isopropanol were easier to separate from the flat glass surface. The addition of plasticizers had no significant effect on the pH and %T, while the η values were increased. FFS with 2.5% of hypromellose and propylene glycol at lower concentrations (1.25 % and 5 %) form films with the most desirable properties in terms of pH, appearance, and flexibility, suitable for dermal drug delivery. Future research will focus on comprehensive characterization of drug delivery performances of the selected FFSs with active substances with different physicochemical properties, including *in vitro* release studies.

REFERENCES

[1]L. C. Pünnel, D. J. Lunter, Pharmaceutics, 7 (2021) 932.
[2] E. O. Bakhrushina, M. M. Shumkova, F. S. Sergienko, E. V. Novozhilova, N. B. Demina, Saudi Pharmaceutical Journal, 1 (2023) 154-169.
[3] S. Sharma, T. N. Ansari, S. Handa, ACS Sustainable Chemistry and Engineering, 38 (2021) 12719-12728.
[4] A. Ćirić, Đ. Medarević, B. Čalija, V. Dobričić, M. Rmandić, T. Barudžija, A. Malenković, Lj. Đekić, International Journal of Biological Macromolecules 167, (2021) 547-558.
[5] M. Kotrba and L. H. Schilling, Collection Forum, 1-2 (2017) 84-101.
[6] Honeywell/50/50 Isopropyl Alcohol-Water [Internet] [cited 31 May 2024] Available from: https://us.vwr.com/assetsvc/asset/en_US/id/16549067/contents.
[7] F. M. Pang, C. E. Seng, T. T. Teng, M. H. Ibrahim, Journal of Molecular Liquids, 1-2 (2007) 71–78.
[8] M. A. Haidekker, T. P. Brady, D. Lichlyter, E. A. Theodorakis, Bioorganic Chemistry, 6 (2005) 415–425.
[9] M. C. M. Sequeira, M. F. M. Pereira, H. M. N. T. Avelino, F. J. P. Caetano, J. M. N. A. Fareleira, Fluid Phase Equilibria, (2019) 7–16.
[10] ThermoFisher/Macrogol 400 [Internet] [cited 31 May 2024] Available from: https://www.fishersci.se/chemicalProductData_uk/wercs?itemCode=10744381&lang=EN.
[11] PubChem/Propylene glycol [Internet] [cited 31 May 2024] Available from: https://pubchem.ncbi.nlm.nih.gov/compound/1030#section=Vapor-Pressure.
[12] R. D. Robinson, F. R. Toulan, C. B. Stabler, D. Flanagan, H. Feuer, P. Touchet, J. J. La Scala, Evaluation of Low Hazardous Air Pollutant Thermoset Adhesives for the Application of Rubber-to-Metal Bonding on Army Tank Pads and Road Wheels (2011).

INVESTIGATION OF WETTABILITY OF NOVEL CALCIUM ALUMINATE-BASED DENTAL CEMENT

V. Ilić [1], S. Milutinović-Smiljanić [1], V. Biočanin [2], A. Despotović [3], K. Janjetović [3], N. Zogović[3], V. Danilović [1], J. Simonović[1] and Đ. Antonijević [4]

[1] *Department of General and Oral Histology and Embryology, School of Dental Medicine, University of Belgrade, Serbia.*
[2] *Faculty of Somatology in Pančevo, University Business Academy in Novi Sad, Serbia.*
[3] *Institute for Biological Research "Siniša Stanković" – National Institute of the Republic of Serbia, University of Belgrade, Serbia. (ana.despotovic@ibiss.bg.ac.rs)*
[4] *Department of Anatomy, School of Dental Medicine, University of Belgrade, Serbia.*

DOI: https://doi.org/10.46793/Phys.Chem24I.369I

ABSTRACT

The wettability is the tendency of a liquid to disperse or adhere to a solid surface. The aim of research was to evaluate and compare the wettability of newly synthesized calcium aluminate-based dental cement and mineral trioxide aggregate (MTA). Two materials were examined: novel calcium aluminate cement with added zirconium dioxide (CaAl+ZrO_2) and MTA (Cerkamed, Poland). The wettability of disc-shaped samples, produced by mixing and moulding of cement, was calculated through the contact angle between the disc and a drop of the reference liquid (glycerol, diiodomethane), using the ImageJ computer software. No significant difference in wettability was noted between CaAl+ZrO_2 and MTA when glycerol was applied. CaAl+ZrO_2 expressed significantly higher contact angle values compared to MTA ($p<0.05$) when diiodomethane was used. Both tested materials possess similar wettability properties when introduced to glycerol. MTA showed better wettability after the placement of diiodomethane.

INTRODUCTION

Dental materials represent a specific entity due to close contact with human oral tissues. Accordingly, surface characteristics of these materials play a significant role in the success of therapeutic outcomes. One of those properties is wettability, which can be defined as the ability of a liquid to spread or adhere to a solid surface of material. Wettability is usually displayed through contact angle (CA), and materials used in dentistry can be hydrophilic (CA lower than 90 °) or hydrophobic (CA higher than 90 °), regarding their surface properties and clinical application.

Dental cements are materials utilized daily in oral surgery, endodontics, and restorative dentistry, for direct/indirect pulp capping, root and crown perforation therapy, management of internal resorptions, partial pulpectomy, furcation defect treatment, and as a retrograde filling/apical plug material. Dental cements should possess high wettability (lower CA) to easily penetrate irregular spaces, allow the adhesion of reparatory cells, etc. Current ‘gold standard’ dental cement, mineral trioxide aggregate (MTA), possesses numerous benefitial properties (excellent biocompatibility and antimicrobial properties, good radiopacity, etc.), but still exhibits some downsides, like long setting time, difficult manual manipulation, cost, etc. [1]. This fact has encouraged many researchers to develop new dental cements with superior phycicochemical and biological properties. Our research group has created a new calcium aluminate-based dental cements that exhibited satisfying properties, such as porosity, retrograde-filling ability, and biocompatibility, so far [2,3]. The aim of this study is to investigate and compare the wettability of newly synthesized calcium aluminate cement with added zirconium dioxide (CaAl+ZrO_2) with commercially available MTA.

METHODS

Two dental cements were investigated: newly synthesized calcium aluminate cement with added zirconium dioxide ($CaAl+ZrO_2$), and commercially available MTA (Cerkamed, Poland). The synthesis of $CaAl+ZrO_2$ was described in our previous study [3]. However, in this study, our experimental cement, $CaAl+ZrO_2$, was created by replacing 20 % by weight of pure calcium aluminate cement with radiopacifier (ZrO_2). $CaAl+ZrO_2$ was then mixed with distilled water in a 3:1 powder-to-liquid ratio using a stainless-steel spatula on a glass slab (**Fig. 1**). MTA was mixed according to the manufacturer's instruction. Mixed cements were then moulded, and disc specimen

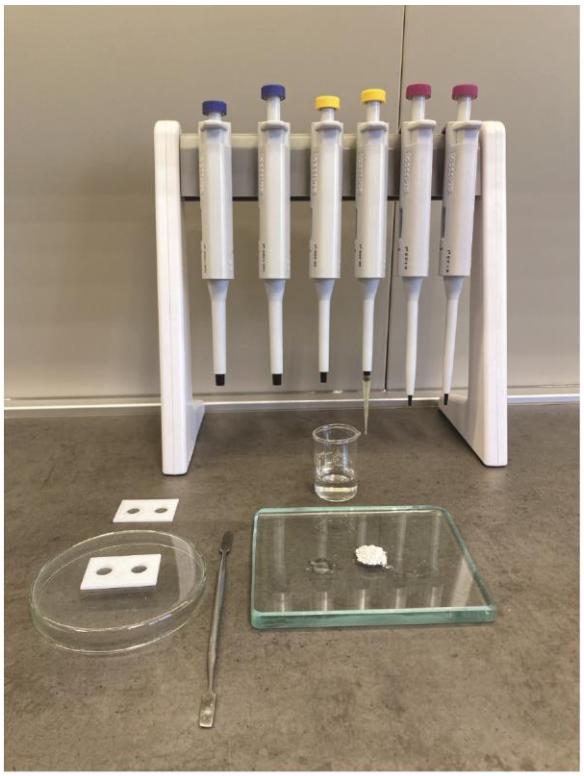


Figure 1. The armamentarium used for the preparation of experimental disc-shaped samples, and the placement of the reference liquid dropplet.

(5 mm wide and 2 mm thick) were obtained for both groups of material (n = 20). All samples were then placed in an incubator (37 ºC, 99 % humidity) and left for 24 h to fully set. Later, specimens were removed from the incubator and placed on a flat horizontal surface. A 33,3% glycerol solution and pure diiodomethane (Sigma-Aldrich, UK) were used as reference liquids. A sessile 2 µl droplet of reference liquid was carefully placed using a pipette on the surface of disc samples and then photographed with a digital HD camera (Camcolms1, Velleman ®) (**Fig. 2**). Obtained images were analyzed using the open-source software ImageJ (National Institute of Health, Bethesda, MA, USA) with a contact angle analyzer (**Fig. 2**).

Statistical analysis was performed using SPSS (v17.0, Chicago, IL, USA). The normality of data distribution was checked using Kolmogorov-Smirnov test. Parametric Student's t-test was utilized for between-group analysis ($p < 0.05$).

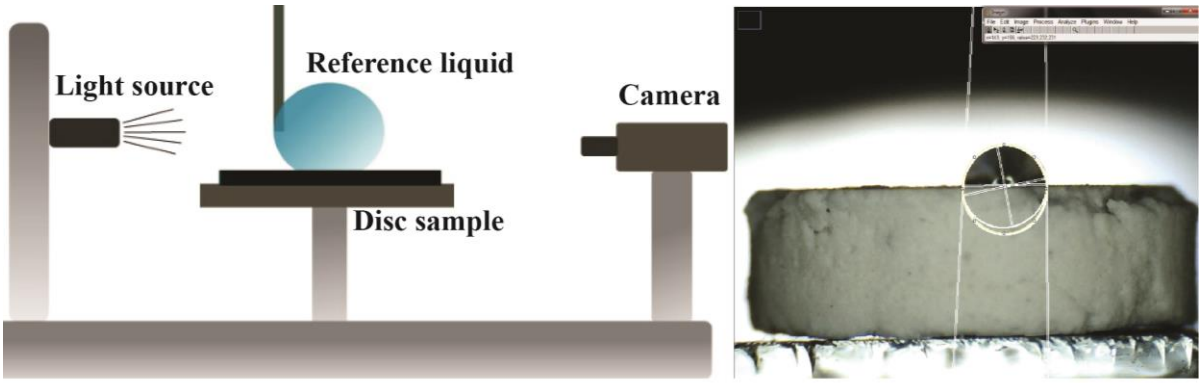


Figure 2. The experiment setup (left), and the computer software ImageJ used for the calculation of contact angle between the cement dics sample surface and the reference liquid dropplet (right).

RESULTS AND DISCUSSION

The results of the wettability assessment are presented in **Figure 3**.

Glycerol is a polar liquid, with a viscosity like human blood [4], making it suitable for the

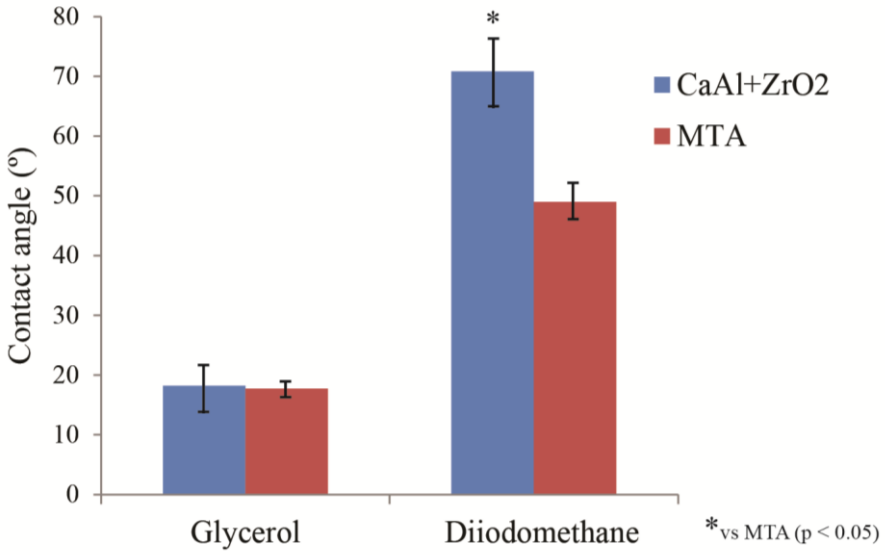


Figure 3. Results of the wettability assessment presented as mean ± SD. MTA - mineral trioxide aggregate; CaAl+ZrO2 - calcium aluminate cement with added zirconium dioxide.

investigation of materials that come in direct contact with blood and tissue. It can be observed that CA values were similar for CaAl+ZrO_2 and MTA when glycerol was applied. Analogous results for the MTA were obtained in a previous study [5], which justifies the selected methodology.

When diiodomethane was applied, CaAl+ZrO_2 demonstrated a significantly higher value of CA compared to MTA (but still lower than 90 °). This finding might be a result of fewer non-polar molecules present on the surface of CaAl+ZrO_2, thus making this cement more hydrophobic (but still hydrophilic) in the presence of non-polar substances, like diiodomethane. Therefore, we assume that this material is less wettable than MTA. Diiodomethane was used due to its zero value of the polar contribution to the surface tension.

Glycerol and diiodomethane are commonly used for the investigation of surface wettability [6]. The method used in this study can be justified by the nature of tested materials that don't possess a liquid phase. Different methodology for various dental materials wettability testing was thoroughly described and performed by our group of researchers [7].

CONCLUSION

Experimental CaAl+ZrO_2 material exhibited similar wettability to MTA when glycerol was applied. On the other hand, CaAl+ZrO_2 showed higher contact angle values when diiodomethane was introduced. The future clinical application of newly created calcium aluminate-based dental cement might be justified after the examination and comparison of its other physicochemical and biological properties. Therefore, more laboratory and clinical studies are needed.

Acknowledgement

This study was supported by the Ministry of Science, Technological Development and Innovation (Grant No. 451-03-66/2024-03/ 200007) and by a bilateral PPP grant provided jointly by the Ministry of Education, Science and Technological Development of the Republic of Serbia and Ministry of Science and Technology of The People's Republic of China (Grant No. 451-02-818/2021-09/20).

REFERENCES

[1] M. Parirokh, M. Torabinejad. J Endod., 36(3) (2010) 400–413.
[2] S. Paraš, O. Janković, D. Trišić, et al. Int Endod J., 52(8) (2019) 1162-1172.
[3] D. Ćetković, C. Zhiyu, N. Vuković, et al. Science of Sintering 2024. OnLine-First Issue 00, Pages: 65-65.
[4] G. H. Yassen, A. H. Sabrah, G. J. Eckert, et al. J Endod., 41 (2015) 956–60.
[5] V. Biočanin, Đ. Antonijević, S. Poštić, et al. J Endod., 44(5) (2018) 816-821.
[6] K. Hashizaki, Y. Hoshii, K. Ikeuchi, et al. Chem Pharm Bull (Tokyo), 69(11) (2021) 1083-1087.
[7] Đ. Antonijević, P. Milovanović, D. Brajković, et al. Appl Surf Sci, 355 (2015) 369–78.

EFFECTS OF NEW LYSINTHETIZED BIOCERAMIC DENTAL MATERIAL ON THE BRAIN TISSUE OF WISTAR RATS

S. Milutinović-Smiljanić [1], V. Ilić [1], A. Despotović [2], J. Simonović [1], V. Biočanin [3], K. Janjetović [2], N. Zogović [2], V. Danilović [1], and Dj. Antonijević [4]

[1] *Department of General and Oral Histology and Embryology, School of Dental Medicine, University of Belgrade, Serbia.*
[2] *Institute for Biological Research "Siniša Stanković" – National Institute of the Republic of Serbia, University of Belgrade, Serbia. (ana.despotovic@ibiss.bg.ac.rs)*
[3] *Faculty of Somatology in Pančevo, University Business Academy in Novi Sad, Serbia.*
[4] *Department of Anatomy, School of Dental Medicine, University of Belgrade, Serbia.*

DOI: https://doi.org/10.46793/Phys.Chem24I.373MS

ABSTRACT

The novel dental material, calcium aluminate with zirconium dioxide (CaAl+ZrO_2) has good physical properties, but its biological effects need to be elucidated. This study aimed to investigate the effects of implanted CaAl+ZrO_2 on rat brain tissue. 24 adult male Wistar rats were implanted intraalveolarly with CaAl+ZrO_2 or control material mineral trioxide aggregate (MTA). The rats were weighed before implantation and before euthanasia. Cage-side observation for neurotoxicity signs was conducted. Animals were sacrificed after 30 and 180 days. Histological specimens of hippocampus revealed that perinuclear vacuolization and neuronal necrosis decreased over time, in both CaAl+ZrO_2 and MTA. 180 days postimplantation, the percentage of necrotic cells and neurons with perinuclear vacuolization was significantly lower in CaAl+ZrO_2 than in MTA group. Intraalveolar implantation of CaAl+ZrO_2 did not induce neurotoxicity signs and significant changes in hippocampal morphology in rats. These results, together with its physicochemical properties, indicate that CaAl+ZrO_2 possesses good biological properties and could be applied in the clinical studies/dentistry.

INTRODUCTION

Dental materials often comprise several toxic components, including allergens, carcinogenic, and teratogenic components, although they are created to be biologically inactive and inert. Mineral trioxide aggregate (MTA) is the most commonly used material in dental practice. Because of its exceptionally good physical and biological properties, it is used in contact with hard and soft tissues as an apical barrier and root-end filling material, pulp capping agent, root canal perforation repair material, etc. [1]. Despite its advantages, the disadvantages of MTA include handling difficulties, long setting time, discoloration, etc. Therefore, there is a need to develop an enhanced formula to overcome these drawbacks. The increasing number of development studies of novel dental materials with applications in the orofacial region has led to an increased consciousness about the biological risks [2]. A new material, calcium aluminate with added zirconium dioxide (CaAl+ZrO_2), with satisfactory or even better physicochemical properties when compared to the MTA, was developed by our research group [3]. Therefore, its potential usage in dentistry can be considered. But, due to the specificity of the oral environment, there is a justified concern about its systematic effects, including brain function. Using rats as animal models (translational approach) is useful because rat brain fundamental organization is more similar to the human brain compared to mice. Also, rats are bigger, exhibit more complex behavior, and live longer [4]. Behavior tests, weighting the brain and histology evaluation are useful for brain examination [1,5]. According to the study of

Andreollo et. al, a third of a human life (18 years) corresponds to 6 months of a rat`s life, so the period of 6 months is chosen for our experiments [6]. Therefore, this study aimed to evaluate the potential neurotoxicity of new calcium aluminate with added zirconium dioxide, implanted in rats in vivo, after a period of 1 and 6 months.

METHODS

Protocols regarding animal use were approved and performed according to the Directive of the Protection of animals useful for scientific purposes of the European Parliament 2010/63/EU. The School of Medicine, University of Belgrade, Ethics Review Board approved the experimental protocol reference number 323-07-10816/2022-05/3.

In this study, adult male outbred Wistar rats were used (n = 24, age 3 months, weight 280 ± 20 g). One week before surgery animals were acclimated and caged separately under laboratory controlled conditions (12 h / 12 h light-dark cycle, temperature 21 °C ± 2, and humidity 65 % ± 10). Rats were fed with standard food pallets (Veterinarski zavod, Subotica, Serbia) and had access to tap water ad libitum. The maxillary first upper molar was extracted from all animals and each socket was filled with MTA (Cerkamed, Poland) or calcium aluminate with added zirconium dioxide ($CaAl+ZrO_2$). Rats were randomly allocated into four groups (n = 6) according to the implanted material and periods of euthanasia: MTA 30 days and MTA 180 days as positive controls, $CaAl+ZrO_2$ 30 days, and $CaAl+ZrO_2$ 180 days. The rats were weighed before implantation and before euthanasia. Cage-side observation for any sign of neurotoxicity was included. Motor activities (the presence of unusual locomotion, tremor, fasciculation, catalepsy, ataxia, or/and prostration), reflexes (myotactic, corneal, light, strartle reflex), the presence of convulsion, ocular signs (exophthalmos, miosis, iritis, ptosis, conjunctivitis, mydriasis), the presence of excessive salivation, piloerection and muscle tone (hypotonia, hypertonia) was observed twice a day. Animals were sacrificed by overdose of thiopentone sodium (150 mg i. p.) after 30 or 180 days. The brain of each animal was removed, rinsed in normal saline, and sampled. The preparations were prepared by routine histological methods and were cut (4 μm) by rotary microtome (Leica SM2000R, Leica Microsystems, Wetzlar, Germany). After de-waxing specimens were stained by Hematoxylin and Eosin (HE). Histological and histomorphometric specimens were analysed at 100× and 400× magnification under a microscope (Leitz Labor Lux S Fluorescence Microscope, Ernst Leitz Wetzlar GMBH, Germany), and three nonoverlapped randomly chosen microscopic fields high power field, 40×) of fixed sizes (220× 280 μm) per rat were captured by a digital camera (Leica DFC295, Germany) and analyzed using software (Leica University Suite, version 4.3, Leica Microsystems, Germany). The region of interest was the Hippocampus, the major part of the Cerebrum, especially Ammon's horn or Cornu Ammonis (CA) and its CA1 and CA2 areas due to their role in social/spatial memory, cognition, neurodegenerative pathology, etc. The quantified parameters used in the evaluation were the percentages of perineural vacuolization of neurons and necrotic neurons regarding the total number of neurons per image and the percentage of the area fraction covered intracerebral hemorrhages, intracerebral blood vessels, and congestion regarding blood vessel area, and the area covered with neuriopil microcavitation regarding total area.

All results were subjected to statistical analysis using SPSS (version 18.0, Inc., Chicago, IL, USA). Non-parametric tests, Friedman, Kruskal-Wallis, and Wilcoxon signed ranks tests were utilized. The level of marginal significance was defined ($p < 0.05$).

RESULTS AND DISCUSSION

No non-physiological clinical signs or behavior changes, changes in motor activities, ocular, or mortality, were observed among all operated animals.

Also, no significant differences in body weight and the weight of the brain compared to the control group were observed, which is very important because the loss of brain weight is one of the major signs of neurodegenerative illnesses [5].

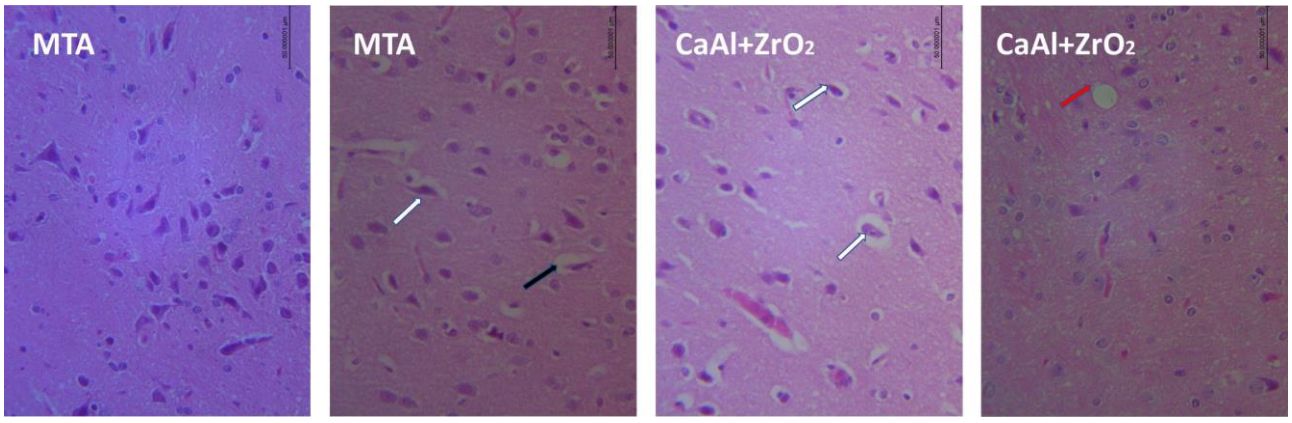


Figure 1. Representative photomicrographs of HE-stained brain sections showing normal histology (scale bar = 100μm, 10× magnification). The first image (from left) shows the normal cytoarchitecture of the CA1 and CA2 region. White arrows indicate perineural vacuolization, black arrow indicates necrotic neuron, and red arrow indicates neuropil microcavitation. MTA - mineral trioxide aggregate; CaAl+ZrO_2 - calcium aluminate cement with added zirconium dioxide.

A histopathological evaluation of the brain did not reveal any gross pathological lesions (**Figure 1**). The percentage of neurons with perineural vacuolization decreased significantly in the CaAl+ZrO_2 180 days group compared to CaAl+ZrO_2 30 days ($p < 0.05$). The same was observed for the MTA 30 vs 180 days groups. However, CaAl+ZrO_2 180 days group exhibited a significantly lower percentage of perineural vacuolization than MTA 180 days. Generally, such small values of neurons with perineural vacuolization indicate that there is occasional incidental finding that does not have pathological meaning.

Although the presence of necrotic neurons in all groups is low, the percentage of necrotic neurons was significantly smaller in the CaAl+ZrO_2 180 days group compared to the MTA 180 days group ($p < 0.001$). Necrosis of neural cells occurs after exposure to neurotoxins like metals and drugs. The nerve cell body is usually angular and shrunken due to cytoplasmic collapse. As neurodegeneration progresses, in rare cases, karyolysis or karyorrhexis are present, and necrotic neurons can not be distinguished from other cells at the light microscopic level. Sometimes glial cells are around necrotic neurons. They could be microglia and astrocytes. The presence of phagocytic microglial cells means neuronophagia which is commonly associated with encephalitis, but because of their small number, we suppose that they are perineural satellite cells which are resident oligodendroglia that often surround normal or defected neurons. It has been shown that in the presence of toxic agents, oxidative stress-dependent glial activation occurs in brain tissue [7], which increases the number of glial cells. At the same time, a toxic circumstance triggers apoptosis, decreasing glial cells number [8]. Further studies and special staining procedures are required to determine changes in the number of glial cells and whether they replace lost neurons.

The presence of neuronal necrosis may play a crucial role in acute and chronic neurodegenerative disorders like stroke, Alzheimer's disease, etc. [9], but such a minor number of necrotic neurons in our results is not as meaningful as well as the previous finding. The findings of the perinuclear vacuolization and neuron necrosis can be observed in **Figure 2**.

No statistically significant differences between MTA and CaAl+ZrO_2 in the percentage of the area fraction covered intracerebral hemorrhages, intracerebral blood vessels, and congestion regarding blood vessel area, and the area covered with neuropil microcavitation for both periods. We found hemorrhage only in one specimen, but that is probably artificial hemorrhage because that brain tissue was not handled carefully.

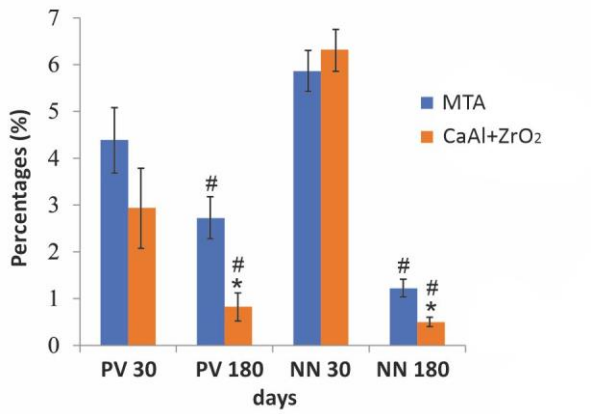


Figure 2. Results of the perinuclear vacuolization (PV) and neuron necrosis (NN) of the brain tissue after the implantation of mineral trioxide aggregate (MTA) and calcium aluminate cement with added zirconium dioxide (CaAl+ZrO_2). * *vs* MTA, # *vs* 30 days ($p<0.05$).

CONCLUSIONS

Based on the results of this study, we can conclude that intraalveolar implantation of CaAl+ZrO_2 did not induce significant effects on brain function and hippocampus morphology in rats. CaAl+ZrO_2 showed similar, or even better, results when compared to the widely used MTA. Nevertheless, further studies on the biological and mechanical properties of the CaAl+ZrO_2 are needed.

Acknowledgment

This study was supported by the Ministry of Science, Technological Development and Innovation (Grant No. 451-03-66/2024-03/ 200007) and by a bilateral PPP grant provided jointly by the Ministry of Education, Science and Technological Development of the Republic of Serbia and Ministry of Science and Technology of The People's Republic of China (Grant No. 451-02-818/2021-09/20).

REFERENCES

[1] M. Torabinejad, M. Parirokh, J Endod. 36 (2010) 190-202.
[2] S. Shahi, M. Özcan, S. Maleki Dizaj, et al. Toxicol. Mech.Methods, 29(5) (2019) 368–377.
[3] D. Ćetković, C. Zhizu, N. Vuković, et al. Science of Sintering 2024, pp 65-65.
[4] A. Agmo, E. Ellingsen. Scand J Psychol, 44 (2003) 293–301
[5] N.A. Aziz, M.A. van der Marck, H. Pijl, et al. J Neurol, 255 (2008) 1872–1880.
[6] N.A. Andreollo, E.F. Santos, M.R. Araújo, L.R. Lopes. Arq Bras Cir Dig.,25(1) (2012) 49-51.
[7] I.D. Akinrinade, E.A. Memudu, O.M. Ugundele. Pathophysyology, 22(2) (2015) 105-115.
[8] R.A.Yokel, J.P. O'Callaghan, Neurotoxicology and teratology, 20(1) (1998) 55–60.
[9] M. Fricker, A.M. Tolkovsky, V. Borutaite, et al. Physiol Rev., 98(2) (2018) 813-880.

WETTABILITY OF LANGMUIR-BLODGETT FILMS FROM SIZE-SELECTED LIQUID PHASE EXFOLIATED GRAPHENE FLAKES

B. Bekić [1], J. Lazarević [1], M. Spasenović[2] and T. Tomašević-Ilić [1]

[1] *University of Belgrade, Institute of Physics, Pregrevica 118, 11080 Belgrade, Serbia. (barbara.bekic@gmail.com)*
[2]*Center for Microelectronic Technologies, Institute of Chemistry, Technology and Metallurgy, University of Belgrade, Njegoševa 12, 11000, Belgrade, Serbia*

DOI: https://doi.org/10.46793/Phys.Chem24I.377B

ABSTRACT

We investigated the wettability of Langmuir-Blodgett films from liquid phase exfoliated graphene. By applying cascade centrifugation, dispersions with size-selected flakes are obtained, and depending on the selected dispersion for film formation, films with different defect density are produced. We determined the wettability of our films by measuring the contact angle (CA). Films with the highest defect density, produced by the self-organization of smaller-sized and thinner graphene flakes, exhibited the highest wettability, with a CA of 77°. Conversely, films produced from dispersions with larger nanosheet dimensions demonstrated a hydrophobic nature, with a CA of 90°. This suggests that the wettability of our films can be adjusted by varying the size of the nanosheets used for film formation. Controlling the defect density and wettability of self-assembled graphene films allows the optimization of their properties for various application, particularly in wearable electronics.

INTRODUCTION

Liquid Phase Exfoliation (LPE) is a widely-used method in obtaining a high yield of two-dimensional nanosheets in solution. It can be applied on a broad range of layered materials, in various liquids, and it is suitable for large-scale production. Followed by iterative centrifugation different rates (cascade centrifugation), obtained particles can be separated, and dispersions with narrow nanosheets size and thickness distributions can be produced [1]. Langmuir-Blodgett (LB) deposition is a simple and versatile method based on the self-organization of nanostructures from solution. It is used to make large surfaces of highly transparent graphene films, with few-nanometer thickness [2]. Our previous works demonstrated the potential of LB graphene films for utilization in sensor technology [3, 4]. Due to the high defect density and an abundance of edges, these films exhibit high reactivity, especially to gases [5]. However, the wettability of these films, as one of the fundamental properties of a material surface, has never been reported. Several factors could affect the wettability of graphene. The contact angle of water droplets on a graphene surface may vary from 33° to 127° depending on thickness, substrate of films, defect type and density, surface roughness, present impurities, production method, etc. [6]. Understanding the wetting behavior of graphene would benefit a diverse array of graphene applications. Graphene with a hydrophobic nature can reduce liquid deposition and prevent contamination of devices, while a hydrophilic surface of graphene could be beneficial for applications in biomaterials and the production of supercapacitor electrodes.

In this work we report tunable wettability of Langmuir-Blodgett films from LPE exfoliated graphene achieved through surface manipulation of our films by varying the size of the graphene nanosheets used in the film formation process. Varying the size of the graphene nanosheets used for

film formation contributes to the production of graphene films with different defect densities, and such to the different wetting behavior.

METHODS

All chemicals were purchased from Sigma Aldrich: graphite powder (product number 332461), sodium cholate (SC), isopropyl alcohol (IPA) and N-Methyl-2-pyrrolidone (product number 328634). Two types of graphene dispersions were prepared: one by LPE from a water-based solution of SC, and one by LPE in NMP, using previously established methodologies [7]. The initial concertation of graphite was 20 mg/ml in both solutions. Centrifugation at 0.7 kg was used to remove the unexfoliated material in NMP-based dispersions, and obtain a solution with broad lateral flake size and thickness distributions. To obtain graphene dispersions with size-selected flakes, cascade centrifugation of the water-based dispersion was applied. After removing unexfoliated material at 0.1 kg, the supernatant was collected and subjected to further centrifugation at 0.5 kg. The resulting sediment was collected in diluted solution of SC, while the supernatant was centrifuged at 1 kg. The process was repeated once more for the centrifugation rate of 5 kg. To aid the deposition at the water–air interface, the aqueous dispersion was transferred to NMP. To this end, the dispersion was centrifuged at 15 kg (99 min) to force the nanosheets to sediment. The aqueous supernatant was discarded, and the sediment was redispersed in IPA. The centrifugation was repeated, and the sediment was redispersed in NMP by 5 minutes of bath sonication. Graphene films were formed at the water-air interface and deposited with the Langmuir-Blodgett method on SiO_2/Si substrates following the previously reported procedure [8].

Raman characterization was performed with a Jobin Yvon T64000 Raman spectrometer using a 514 nm laser line at room temperature and an exposure time of 300 s. The contact angle measurement was performed using the Ossila Contact Angle Goniometer. The deionized water droplet (9 μl) was released on the sample at room temperature, and the recording included 20 frames per second.

RESULTS AND DISCUSSION

Dispersions with the largest and thickest flakes, obtained with centrifugation rates 0.1-0.5 kg (G1), dispersions with nonselected flakes (G2), and dispersions with the smallest and thinnest flakes, obtained with centrifugation rates 1-5 kg (G3) are chosen for film formation. Lateral dimensions, and flake thicknesses were previously established [7], with thickness shown to be approximately 5 and 10 layers, for G1 and G3 respectively.

Figure 1a depicts Raman spectra of graphene films produced from dispersions with different flake sizes: G1, G2, and G3. All spectra feature four pronounced bands: D at ~1355 cm^{-1}, G at ~1582 cm^{-1}, D' at ~1625 cm^{-1}, and the 2D band at ~2715 cm^{-1}, characteristic for Langmuir-Blodgett graphene films. Raman spectra show evident changes of the intensity of the D mode depending on the choice of dispersion, i.e. size of the flakes used for film formation. **Figure 1b** depicts the intensity ratio of the D peak to the G peak, and calculated distance between defects (L_D) for the used laser wavelength [8]. The D/G ratio increases, and the L_D decreases (from 27 to 7 nm), with centrifugation rate. The results indicate a strong dependence of the film defect density on the flake size in dispersion. We also observe that the ratio of the D-peak intensity to the D'-peak intensity in our films is nearly constant at a value of 5.5 ± 0.5 (**Figure1c**), indicating that regardless of the graphene flakes size, edges are the dominant defect type in all films, ruling out vacancies, substitutional impurities, and sp3 defects [9, 10]. These findings point out that the self-organization of nanosheets with a narrow size and thickness distribution at an air-water interface will results in films that are abundant in edge defects.

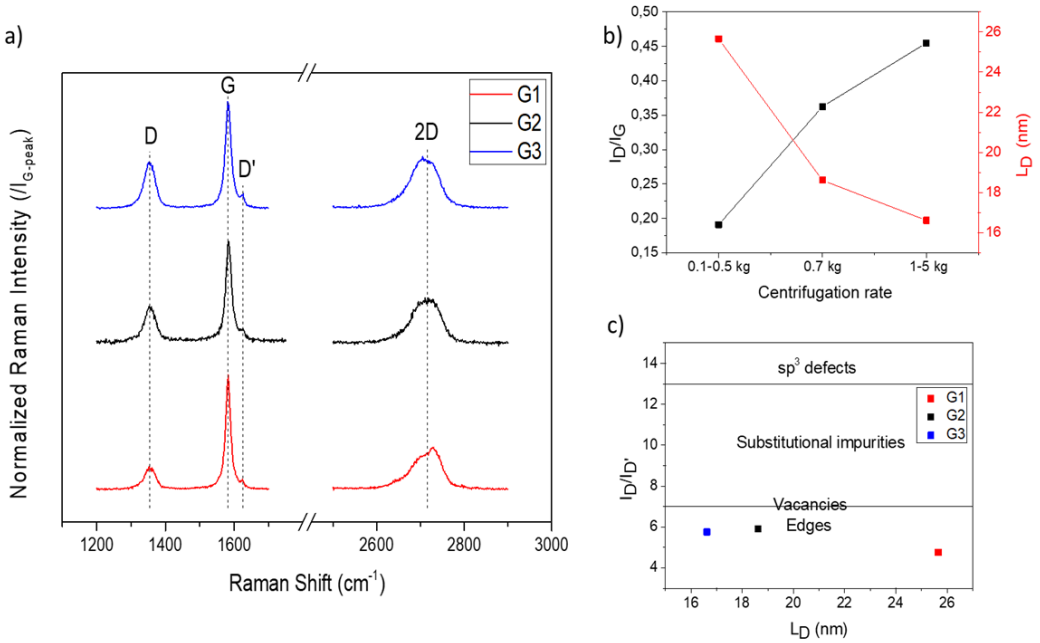


Figure 1. a) Representative Raman spectra of graphene films obtained from dispersion with: nanosheets isolated by centrifugation between 100-500 g (G1), broad lateral size and nanosheets thickness distribution (G2), and smallest nanosheets isolated by centrifugation between 1000-5000g (G3); b) The ratio of the intensities of the D and G modes (black) and distance between defects (red) of the samples; c) The D/D' intensity ratio as a function of the mean carrier path.

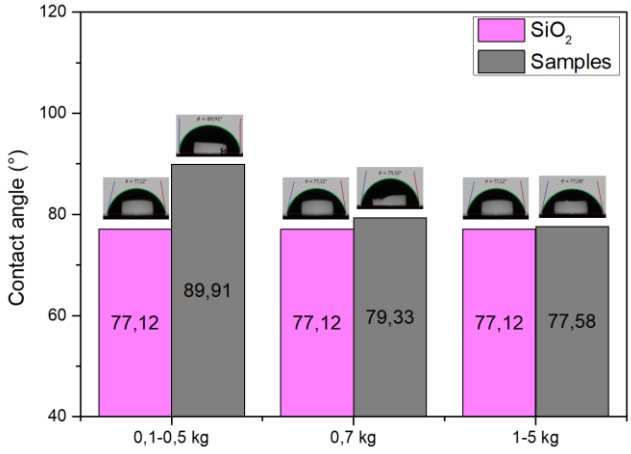


Figure 2. Contact angle measurements of LB graphene films deposited from dispersions with nanosheets isolated by centrifugation between 0.1-0.5 kg (G1), 1-5 kg (G2), and dispersion with dispersions with nonselected flakes (G3) on a SiO2/Si substrate.

Figure 2 depicts contact angle (CA) measurements for LB graphene films deposited from solution with different sizes and thicknesses. Films with the highest defect density, deposited from G3 dispersion, exhibited the highest wettability, with a CA of 77°. Films produced from G1 dispersions, with the lowest defect density, demonstrated a hydrophobic nature, with a CA of 90°. The CA value of 79º for films produced from the G2 dispersion was between values reported for films deposited from G1 and G3 dispersions. This outcome is anticipated since these films were made from a dispersion with a wide range of lateral flake sizes and thicknesses, encompassing nanosheets ranging from monolayers to multilayer graphene. The results are in agreement with

previous studies on the wettability of vertically-oriented few-layer graphene, where graphene with a high density of defects shows a much better wettability, while surfaces with a low defect density show a hydrophobic nature [11]. Defects are favorable for the generation of C=O bonds when the graphene is in contact with water, imparting hydrophilic nature of the surface, and allowing water droplets to easily permeate between the nanosheets. Nevertheless, the wetting transparency of graphene must also be considered as a factor that affects the wetting behavior of our films, since the wettability of the SiO_2/Si substrate does not significantly differ from the wettability of the coated substrate with the thinner graphene nanosheets.

CONCLUSION

The wettability of Langmuir-Blodgett films from liquid-phase exfoliated graphene is reported for the first time. We show that by adjusting the size of the graphene nanosheets used in the film formation process, defect density on the graphene surface can be modulated. This surface manipulation enables the tuning of the wetting properties of self-assembled graphene films, ranging from hydrophilic to hydrophobic. Such control could be advantageous for numerous applications, particularly in the development of skin-interfaced sensors and devices.

Acknowledgment

This work was supported by the Institute of Physics Belgrade through the Grant by the Ministry of Science, Technological Development and Innovations. M. S. acknowledges the Ministry of Science, Technological Development, and Innovation of Republic of Serbia (Contract No: 451-03-66/2024-03/200026).

REFERENCES

[1] C. Backes et al., ACS Nano 10 (2016) 1589–1601.
[2] A. Matkovic et al., 2D Mater. 3 (2016) 015002.
[3] S. Andric et al., Nanotechnology 32 (2021) 025505
[4] S. Andric et al., Sens. Mater. 34 (2022) 3933-3947.
[5] M. Spasenović et al., 2021 IEEE 32nd International Conference on Microelectronics (MIEL), Nis, Serbia, 2021, pp. 25-28.
[6] J. Feng et al., Nanoscale Horiz. 4 (2019) 339-364.
[7] C. Backes et al., ACS Nano 13 (2019) 7050–7061.
[8] T. Tomasevic-Ilic et al., Appl. Surf. Sci. 458 (2018) 446–453.
[9] A. Eckmann et al., Nano Lett. 12 (2012) 3925–3930.
[10] A. Eckmann et al., Phys. Rev. B 88 (2013) 035426.
[11] J. L. Qi et al., Nanoscale 7 (2015) 3675–3682.

THE INTERACTION OF MAGNESIUM SILICATE-BASED EXPERIMENTAL DENTAL CEMENTS WITH BLOOD PLASMA AND L929 CELLS: WETTABILITY AND CELL MORPHOLOGY EVALUATION

Dj. Antonijević [1], A. Despotović[2], V. Ilić[3], D. Ćetković[1], A. Dožić[1], K. Janjetović[2], N. Zogović[2] and S. Milutinović-Smiljanić

[1] *Department of Anatomy, School of Dental Medicine, University of Belgrade, Serbia*
[2] *Institute for Biological Research "Siniša Stanković" – National Institute of the Republic of Serbia University of Belgrade, Serbia (ana.despotovic@ibiss.bg.ac.rs)*
[3] *Department of General and Oral Histology and Embryology, School of Dental Medicine, University of Belgrade, Serbia*

DOI: https://doi.org/10.46793/Phys.Chem24I.381A

ABSTRACT

This study investigates the wettability and biocompatibility of different magnesium silicate-based dental cements. Experimental cements (EC1, EC2, and EC3) were composed of magnesium silicate, calcium silicate, calcium aluminate, strontium carbonate, and zirconium oxide, in different ratios. MTA (Cerkamed) was used as a control. Wettability was investigated using a contact angle analyzer, while morphology and proliferation of L929 murine fibroblast cells were used for assessment of biocompatibility. The contact angle between human plasma and EC2 was the lowest, while the highest was observed for MTA. MTA slightly slowed cell proliferation, whereas EC1, EC2, and EC3, exposed a strong influence on proliferation capacity and cell morphology, and no effect on cell viability, suggesting that cell differentiation may be initiated. These results advocate that proposed dental cements based on magnesium silicate may be a suitable alternative to commercially available calcium silicate cements.

INTRODUCTION

Calcium silicate-based dental cements present one of the most important breakthroughs in the field of dentistry in the last several decades [1]. These materials provided many clinical opportunities, such as preserving the vitality of the tooth and treating some forms of pulpitis (inflammation of the tooth) without nerve extirpation [2]. In addition, the success rate of many clinical procedures such as direct pulp capping, perforation repair and apexification dramatically increased up to 96 % in comparison with the previously 30-60 % success rate using the calcium hydroxide-based treatment options [3, 4].

Many improvements in calcium-silicates were performed in the last decade. The first formulation was a mixture of Portland cement and bismuth oxide. Further improvements included the replacement of Portland cement that contains impurities with pure laboratory-manufactured calcium silicates, as well as the replacement of bismuth oxide that showed cytotoxic effects and induced the discoloration of the tooth with zirconium oxide, tantalum oxide and other radiopacifying agents. Further improvements may include bioactive compounds that have beneficial effect for osteoblasts/fibroblasts proliferation. In this context, it was already proven that strontium-based contrast agents may be a suitable alternative for currently used radiopaque agents. The beneficial effects of magnesium for bone tissue are widely known. The tooth structure resembles the bone tissue and therefore it is stipulated that the incorporation of the magnesium into dental cements may result in positive biological properties. In this context, the present study is designed to test the

properties of several new magnesium silicate-based dental cements. In brief, experimental cements were formulated and tested in contact with L929 murine fibroblasts and human blood plasma.

METHODS

Three experimental cements were synthetized: experimental cement 1 (EC1) containing magnesium silicate, calcium silicate, calcium aluminate, and strontium carbonate, experimental cement 2 (EC2) containing magnesium silicate, calcium silicate, calcium aluminate, and zirconium dioxide, and experimental cement 3 (EC3) containing magnesium silicate, calcium silicate, and strontium carbonate. MTA (Cerkamed, Poland) served as a control group.

Contact angles of the specimens were determined by contact angle analysis using citrated human plasma as reference liquid. The procedure included applying the sessile drop (2 µl in volume) of the reference liquid to a sample using a syringe. The profile of the liquid drops was recorded using a contact angle analyzer and measured by the software program Image J (Version 1.42, National Institute of Health, USA). One drop of reference liquid was applied on each specimen and contact angles were measured at 3 s upon droplet application. The ambient temperature and humidity were 24 ºC and 50 %, respectively.

For *in vitro* biocompatibility analysis cements were manipulated under sterile conditions. 5 mm in diameter and 3 mm thick cements specimens were prepared using pre-sterilized PTFE moulds where cements were placed after mixing. The cements were left to set for 24 h in a humidified atmosphere. Specimens were sterilized by ultraviolet irradiation for 2 h and thereafter immersed in 1 ml complete medium Dulbecco's modified Eagle medium (DMEM; Gibco, Thermo Fisher Scientific, Inc., USA) supplemented with 5 % fetal bovine serum (FBS), 2 mM L-glutamine and penicillin/streptomycin (all from Capricorn Scientific, Germany) to prepare cements extracts. After 24 h of soaking at 37˚C, discs were discarded, and collected supernatants (extracts) were used for cell treatment.

The murine fibroblast L929 cell line (European Collection of Animal Cell Cultures, UK) was cultivated in a complete medium and maintained at 37 °C, in a humidified atmosphere with 5 % CO_2. Cells were prepared for experiments using the conventional trypsinization procedure with trypsin/EDTA and seeded in 96-well flat-bottom plates (5×10^3 cells/well) for the cell morphology assessment. Cells were treated 24 h post-seeding with non-diluted cements' extracts. Morphological changes were evaluated after 48 h of treatment by Bio-rad ZOE fluorescent cell imager (Bio-Rad Laboratories, Hercules, CA, USA) and the bright field live images of L929 cells were taken at random 3 positions within each well at 200× magnification.

Wettability data were expressed as means with standard deviations. The data were tested for normality of distribution by the Kolgomorov-Smirnov test. One-way ANOVA followed by Bonferroni test was used to compare differences in the contact angles among the experimental groups. All calculations were performed using an SPSS ver. 20 statistical software package (IBM, Armonk, USA).

RESULTS AND DISCUSSION

The results of the wettability testing are presented in **Figure 1**. All experimental cements exhibited statistically lower contact angles than commercially available material MTA. The statistically lowest contact angle of the human plasma was detected in EC2, while the highest was found in MTA. There was no statistical difference between contact angles in EC1 and EC3. It is to stress that the lower contact angle of the human blood is more desirable from the clinical point of view. Namely, the lower contact angle reflects the higher hydrophilicity of the cement and consequently increased contact of the cement with surrounding pulpal/periapical tissues. In the case of osteoconductive and dentinoconductive properties of the cement, a higher contact surface results in

superior healing. Furthermore, the difference in contact angle between EC1/EC3 and EC2 goes in favor of EC2. This can be explained by the chemical composition of the manufactured mixtures. The main difference between EC1 and EC3 on one side and EC2 on the other side is the presence of the radiopacifying agent. Radiopacifying agent has to be added to the cement to be visualized on dental radiographs (according to ISO standard 6876) [5]. Indeed, the mixtures EC1 and EC3 contain strontium carbonate, while EC2 contains the zirconium dioxide. Therefore, from the point of view of formulating the most desirable magnesium-based dental cement, it can be stated that it should be used in combination with zirconium dioxide. This goes in line with the choice of contrast agent in Biodentine (Septodont, France) which is nowadays considered as the most valuable formulation of calcium silicate-based dental cement in clinical practice.

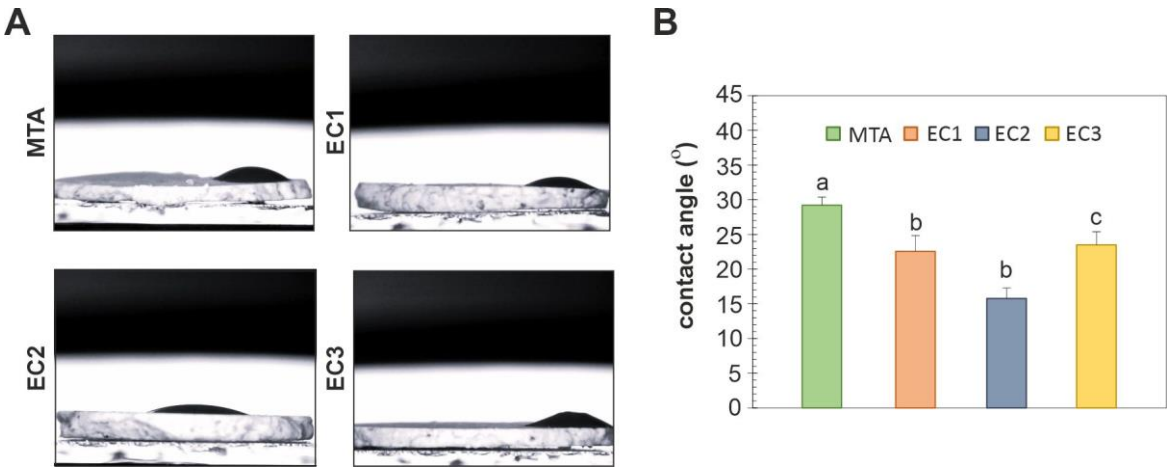


Figure 1. Wettability of the experimental cements. (A) Contact angles of the citrated human blood plasma and cements surfaces. (B) Values of contact angles observed on examined cements. Columns marked with different letters are statistically different from each other (one-way Anova). EC1 - experimental cement 1, EC2 - experimental cement 2, EC3 - experimental cement 3.

Photomicrographs of L929 cells exposed to pure, non-diluted extracts of all investigated cements showed preserved integrity of cell membranes without visible signs of cell death such as cell rounding and detachment from the well surface (**Figure 2**). MTA slightly decreased a number of cells in comparison to cells incubated in a culture medium, probably due to slower cell proliferation. Regardless, cells kept their polygonal shape and reached almost complete confluence after 48 h of treatment. Unlike MTA, extracts of experimental cements (EC1, EC2, EC3) greatly reduced the number of cells after 48 h, with obvious changes in cell morphology. Given the absence of death cells in the extract-treated cultures and preserved morphological features of vital cellular phenotype, it could be speculated that the reduced confluence is a consequence of the decreased proliferative capacity of treated L929 cells. Morphological changes (elongated, spindle-shaped cells) could be related to the process of differentiation since it is known that silicate ions can initiate processes that lead cells to expression of differentiated phenotype [6]. It should be noted that the morphology of cells treated with EC3 extract is different from those treated with EC1 and EC2. All experimental cements contain magnesium silicate and calcium silicate, while onlyEC1 and EC2 contain calcium aluminate. Therefore, it could be speculated that the calcium aluminate content may be the cause of the difference in morphological properties of L929 cells treated with EC1 and EC2 on one side, and cells incubated with EC3 extract on the other side. Observed changes of cell

morphology and preserved cell viability indicate good biocompatibility of composed cements and raises the question of their effect on intracellular processes involved in the cell differentiation, which requires additional research.

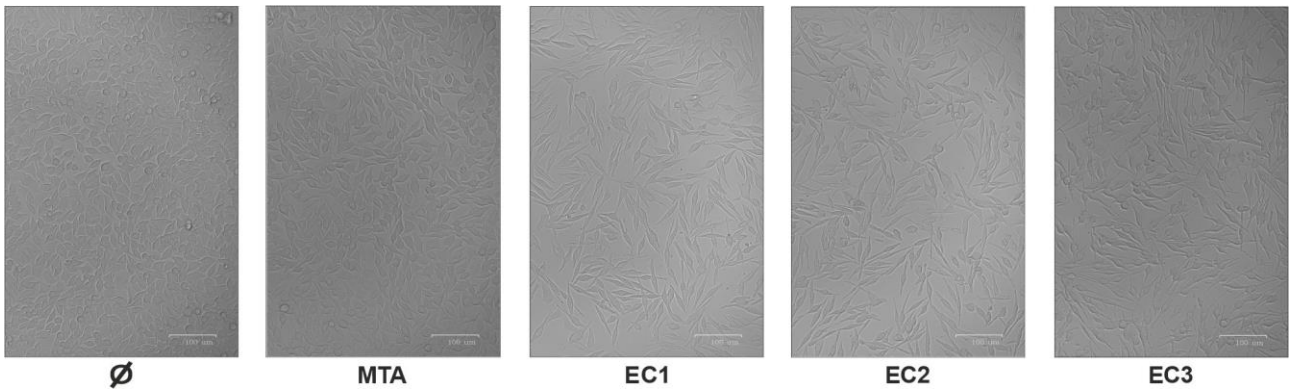


Figure 2. Influence of non-diluted cements' extracts on the morphology of L929 cells. Cells were incubated in cultivation medium (Ø) or in pure (non-diluted) extracts of MTA or experimental cements 1-3 (EC 1-3) for 48 h and morphology was analyzed using bright-field microscopy. Photomicrographs from one representative of three independent experiments are shown.

CONCLUSION

Magnesium silicate dental cements may present suitable alternative to currently available calcium silicate-based cements. These materials showed superior wettability and biocompatibility, regarding contact angle measurement and observation of L929 cell morphology and death. Further analysis of experimental cements properties and provoked intercellular signals bears a great potential to introduce them into clinical use.

Acknowledgment

This study was supported by the Ministry of Science, Technological Development and Innovation (Grant No. 451-03-66/2024-03/200007) and by a bilateral PPP grant provided jointly by the Ministry of Education, Science and Technological Development of the Republic of Serbia and Ministry of Science and Technology of The People's Republic of China (Grant No. 451-02-818/2021-09/20).

REFERENCES

[1] C. Estrela, L.T.A. Cintra, M.A.H. Duarte et al. Braz Dent J., 34(1) (2023) 1-11.
[2] S. Cushley, H.F. Duncan, M.J. Lappin, et al. Int Endod J. (2021) 556-571.
[3] X. Wang, Y. Xiao, W. Song, et al. J Transl Med., 21(1) (2023) 853.
[4] S. Caruso, T. Dinoi, G. Marzo, et al. BMC Oral Health.,18(1) (2018) 54.
[5] International Organization for Standardization. International Standard ISO 6876:2001. 2nd ed. ISO; Geneva, Switzerland: (2001). Dental root canal sealing materials; p. 10.
[6] K. Dashnyam, A. El-Fiqi, J.O. Buitrago, et al. J Tissue Eng.,8 (2017) 1545530549.

POLY(METHYL METHACRYLATE) REINFORCED WITH YTTRIA: MECHANICAL AND MORPHOLOGICAL PROPERTIES

I. Stajčić [1], F. Veljković [1], S. Veličković [1], M. Ćurčić [1], M. Stoiljković [1], V. Radojević [2] and A. Stajčić [3]

[1] *University of Belgrade, VINČA Institute of Nuclear Sciences - National Institute of the Republic of Serbia, Mike Petrovića Alasa 12-14,11000, Belgrade, Serbia*
[2] *University of Belgrade, Faculty of Technology and metallurgy, Karnegijeva 4, 11000 Belgrade, Serbia*
[3] *University of Belgrade, Institute of Chemistry, Technology and Metallurgy, Njegoševa 12, 11000 Belgrade, Serbia. (ivana_r@vin.bg.ac.rs)*

DOI: https://doi.org/10.46793/Phys.Chem24I.385S

ABSTRACT
Although dental poly methyl methacrylate (PMMA) possesses distinctive features such as ease of fabrication, cost-effectiveness, and good physical and mechanical properties, these attributes alone are inadequate to impart the tensile strength and modulus of elasticity necessary for everyday application as denture base material. Thus, modification of PMMA is required for the improvement of mechanical performance. This research is focused on the incorporation of 0.5 wt% and 1.0 wt% of Y_2O_3 (Yttria) into PMMA to improve tensile properties of commonly used two-component denture base. Investigations of mechanical properties have revealed the significant influence of Yttria filler on modulus of elasticity and tensile strength, which were increased by 37.1% and 26.5%, in the composite sample with 1 wt% loading of particles. Results presented in this study revealed the reinforcing potential of Yttria that could find application in other polymers as well.

INTRODUCTION
Poly(methyl methacrylate) (PMMA) is the most commonly used denture base polymer [1-4]. It is a rigid, thermoplastic material that offers excellent biocompatibility and dimensional stability. Denture bases based on PMMA can be easily processed using heat-curing or cold-curing techniques. They provide good esthetics and resistance to oral fluids, making them a reliable choice for complete or partial dentures [5-8]. Dental PMMA is generally supplied as a powder (poly (methyl methacrylate) with colorants and initiators) and a liquid (methyl methacrylate monomer with cross-linking agents and inhibitors) [9]. PMMA is a transparent polymer, and various additives are used to alter its physical properties. These include coloring agents, nylon or acrylic synthetic fibers, and titanium oxide, which serves as an opacifier. To enhance the mechanical and thermal properties of the prostheses, alumina and glass fibers are also incorporated [10]. Despite its advantages, PMMA faces challenges in terms of mechanical properties, prompting studies to enhance its strength, toughness, impact resistance, and hardness. One method to improve the mechanical performance of PMMA involves incorporating fillers to adjust both mechanical and functional characteristics. Various studies have demonstrated enhancements in targeted properties of PMMA by adding fibers or nanoparticles. Silica (SiO_2) and alumina (Al_2O_3) are commonly investigated as reinforcements for PMMA due to their mechanical and antibacterial qualities [11]. Researchers have achieved notable results in improving PMMA properties by adding fillers, such as a 13% increase in hardness with 5 wt% of alumina, and over 100% hardness enhancement with 23% of nanoporous silica. For higher antibacterial properties, silver and gold were also added to PMMA bone cement [12,13]. Recently, mechanical properties of PMMA were significantly

improved with the incorporation of hybrid $SrTiO_3/MnO_2$ nanoparticles, as well as with the use of $SrTiO_3$ in the polymer blend poly(4-styrenesulfonic acid-co-maleic anhydride) sodium salt (PSSMA)/PMMA [14].

In this study, Y_2O_3 (Yttria) was used as a filler dental PMMA-based composite, with different particle loading. Fracture surface morphology and tensile properties were investigated in order to determine the potential for the use of Yttria as a reinforcement for PMMA.

METHODS

Y_2O_3 (Yttria) was purchased from Sigma–Aldrich and two-component dental PMMA from AKRILAT, Serbia. Two-component PMMA consists of liquid part containing monomer methyl methacrylate and powder part with polymer and additives. Yttria powder was mixed with the powder, the liquid monomer was added afterward. Mixture was left for 24 h at room temperature. Overall loadings of particles in composites were 0.5 wt% and 1.0 wt%. Samples were labeled PMMA, PMMA-Y0.5 and PMMA-Y1, depending on Yttria concentration.

FESEM analysis was performed on device Tescan Mira 3 (Brno, Czech Republic). For tensile test, Shimadzu EZ Test LX (Kyoto, Japan) was used, in accordance with the ISO 527-2 standard. The device was equipped with a 500 N load cell, and the applied strain rate was 10 mm/min; the measurements were performed at room temperature.

RESULTS AND DISCUSSION

FESEM analysis presented in Figure 1 showed formation of large Yttria agglomerates, which participated in matrix toughening via crack pinning mechanism. Furthermore, the particles were surrounded with the PMMA, without separation, which indicates good interaction with the matrix.

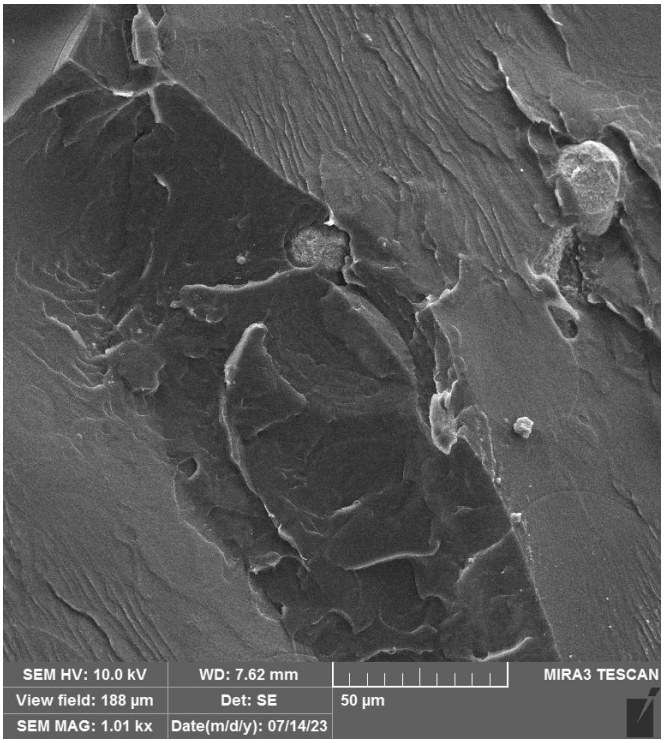


Figure 1. FESEM of PMMA-Y1 fracture surface.

Results from tensile test are shown in Figure 2. As can be seen, tensile strength and modulus of elasticity increased with the incorporation of Yttria particles. Compared to the pure PMMA, modulus of elasticity increased by 17.2% for PMMA-Y0.5 and 37.1% for PMMA-Y1. Tensile strength rose by 21.3% and 26.5% in PMMA-Y0.5 and PMMA-Y1, respectively. These results show that Yttria can contribute significantly to an improvement in mechanical performances of dental PMMA.

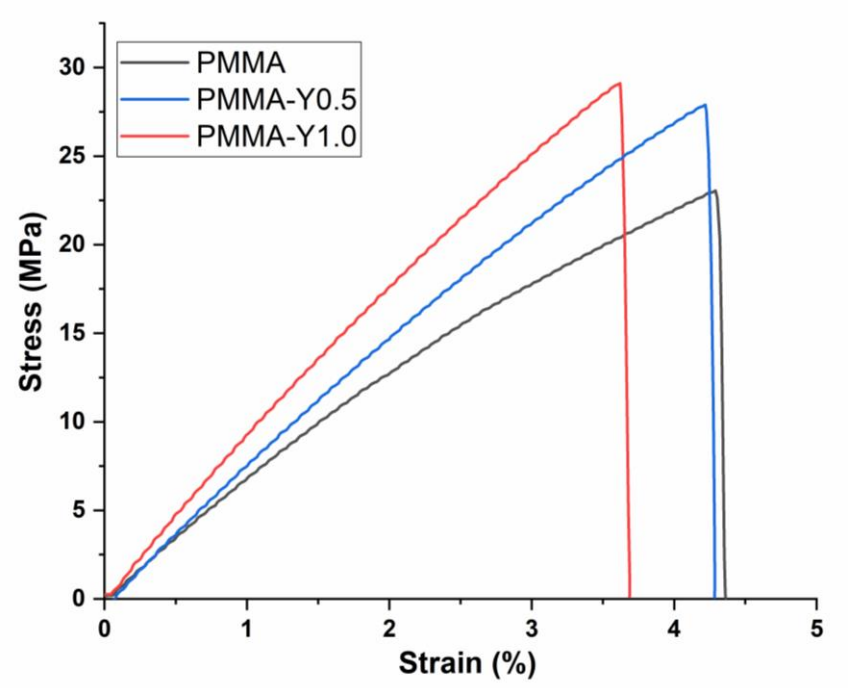


Figure 2. Stress-strain curves for PMMA and composites.

CONCLUSION

This study presented the influence of Y_2O_3 (Yttria) particles on mechanical properties of dental PMMA. Particle concentration in the polymer matrix was 0.5 wt% and 1 wt%. Morphological analysis proved the existence of agglomerates which participated in matrix toughening. Investigation of tensile properties have shown that, with 1 wt% of Yttria, modulus of elasticity and tensile strength can be increased by 37.1% and 26.5% respectively, which revealed the potential for the use of these particles as reinforcements in polymers used in dentistry.

Acknowledgment

This work was financially supported by the Ministry of Science, Technological Development and Innovation of the Republic of Serbia (Grant No. 451-03-66/2024-03/200017, 451-03-66/2024-03/200026 and 451-03-65/2024-03/200135).

REFERENCES

[1] U. Mangal, J.-Y. Seo, J.-H. Ryu, J. Jin, C. Wu, J.-Y. Cha, K.-J. Lee, H.-S. Yu, K.-M. Kim, J.-S. Kwon, S.-H. Choi, J. Mech. Behav. Biomed. Mater. 138 (2023) 105634.
[2] U. S. B. Lakshmi, B. L. Rao, B. R. Prasad, P. V. B. C. Shetty, P. Sekar, Int. J. Oral Health Dent. 8 (2022) 236.
[3] N. W. Elshereksi, F. A. Kundie, A. Muchtar, C. H. Azhari, J. Met. Mater. Miner. 32 (2022) 1.
[4] M. E. Mehdi, A. S. Khaleel, Int. J. Health Sci. (2022) 3621.

[5] S. M. Pituru, M. Greabu, A. Totan, M. Imre, M. Pantea, T. Spinu, A. M. C. Tancu, N. O. Popoviciu, I.-I. Stanescu, E. Ionescu, Materials 13 (2020) 2894.
[6] M. S. Zafar, Polymers 12 (2020) 2299.
[7] C. Abad-Coronel, M. Bravo, S. Tello, E. Cornejo, Y. Paredes, C. A. Paltan, J. I. Fajardo, Polymers 15 (2023) 3773.
[8]H. Kaur, A. Thakur, Mater. Today Proc. 50 (2022) 1619.
[9] H. T. Elhmali, C. Serpa, V. Radojevic, A. Stajcic, M. Petrovic, I. Jankovic-Castvan, I. Stajcic, Fractal Fract. 8 (2024) 314.
[10] N. Dinçkal Yanıkoğlu, R. E. Sakarya, J. Mater. Res. Technol. 9 (2020) 9720.
[11] H. Aghajani Derazkola, A. Simchi, J. Mech. Behav. Biomed. Mater. 79 (2018) 246.
[12] V. Alt, T. Bechert, P. Steinrücke, M. Wagener, P. Seidel, E. Dingeldein, E. Domann, R. Schnettler, Biomaterials 25 (2004) 4383.
[13] E. Y. Taha, M. M. B. Elmahdy, S. M. M. E. Masry, M. E. Elsayed, BMC Oral Health 23 (2023) 153.
[14] H. T. Elhmali, I. Stajcic, M. Petrovic, B. Jankovic, B. Simovic, A. Stajcic, V. Radojevic, Polym. Compos. (2024) pc.28574.

INFLUENCE OF MODIFICATION METHODS ON THE SURFACE CHEMISTRY OF GRAPHENE OXIDE COMPOSITE WITH PERYLENETETRACARBOXYLIC DIANHYDRIDE

M. Pejčić [1], Ž. Mravik [1], M. Grujičić [1], M. Jelić [1], D. Petković [1], J. Rmuš Mravik [1], P. Stolić [2], N. Filipović [3], S. Jovanović [1] and Z. Jovanović [1]

[1] *Laboratory of Physics, Vinča Institute of Nuclear Sciences – National Institute of the Republic of Serbia, University of Belgrade, P.O. Box 522, 11001, Belgrade, Serbia* (zjovanovic@vin.bg.ac.rs)
[2] *Technical Faculty in Bor, University of Belgrade, Bor, Serbia*
[3] *Institute of Technical Sciences of the Serbian Academy of Sciences and Arts, Belgrade, Serbia*

DOI: https://doi.org/10.46793/Phys.Chem24I.389P

ABSTRACT

The influence of different modification methods on the interaction between graphene oxide (GO) and perylenetetracarboxylic dianhydride (PTCDA) through the changes of nanocomposites' surface chemistry *i.e.* changes in the desorption profile using the temperature programmed method (TPD) was investigated. The TPD method allowed better understanding of the type and amount of surface oxygen groups present on the surface of GO and their behaviour when combined with PTCDA. The nanocomposite was prepared by physical mixing initial GO and PTCDA suspensions. One part of resulting suspension was hydrothermally treated for 8h at 180°C. The other part was placed in an oven at 60 °C until completely dry and the resulting powder was thermally treated at T=450°C in Ar atmosphere. The third type of modification was done by ball milling for 20 min, where ball to powder mass ratio was at 10:1. GO and PTCDA (with 15% PTCDA) were initially mixed and homogenized in an agate pestle with mortar for 10 minutes, and then subjected to mechanochemical treatment. The results show that selected methods influence CO and CO_2 desorption profile and the total amount of desorbed functional groups. These changes can be attributed to different nature of interaction between the GO and PTCDA in selected modification methods. Obtained results can be further expanded for engineering of the surface chemistry of graphene oxide-based nanocomposites for various applications.

INTRODUCTION

Graphene oxide (GO) has been extensively studied over the years due to its excellent properties, such as high theoretical surface area, two-dimensional morphology, rich surface chemistry, tunable structure, and electric properties because of which it is being widely applied in energy storage, environmental protection, sensors, etc. Its two-dimensional nature allows the preparation of composites with other low-dimensional materials [1]. In this process, the surface functional groups play an essential role in the application of GO, as they are often the first to interact with the various agents used to functionalize this material [2].

The reduction of GO, *i.e.*, modification of its surface chemistry, is usually achieved by appropriate physical or chemical processes. After this, the material resembles a graphene layer but with a certain amount of residual oxygen and residual or introduced structural defects. There are different ways of modifying GO and its composites; some of them are thermal treatment, milling, and hydrothermal treatment.

This study examines the nanocomposite of GO and perylenetetracarboxylic dianhydrid (PTCDA), which is known for its redox activity [3]. The surface chemistry of GO/PTCDA composite hasn't been studied previously with the TPD method. The chemical properties of these

two systems, rich with oxygen functional groups, make them compatible and interesting subjects for studying how modification by thermal treatment, milling, and hydrothermal treatment influences the interaction between the components and the evolution of surface chemistry. The obtained results show significant differences in CO and CO_2 desorption of studied samples, thus indicating different interaction between the components and surface chemistry caused be selected modification methods.

METHODS

GO and PTCDA nanocomposite (15 wt.% of PTCDA) was prepared as follows: initial aqueous suspension of GO (6.46 mg/ml) was ultrasonicated for 1 hour, after which it was diluted to 1 mg/ml, and then 10 mg/ml of aqueous suspension of PTCDA was added to achieve 15 wt.% relative to GO. The nanocomposite was prepared by physical mixing initial GO and PTCDA suspensions. One part of resulting suspension was hydrothermally treated for 8h at 180°C. The other part was placed in an oven at 60 °C until completely dry and the resulting powder was thermally treated at T=450°C in Ar atmosphere. The third type of modification was done by ball milling for 20 min, where ball to powder mass ratio was at 10:1. GO and PTCDA (with 15% PTCDA) were initially mixed and homogenized in an agate pestle with mortar for 10 minutes, and then subjected to mechanochemical treatment. The functional groups of the prepared nanocomposites were studied using the temperature-programmed desorption (TPD) method. The samples were annealed in a vacuum (base pressure 1×10^{-7} mbar) at a constant heating rate of 10 °C/min, from room temperature to 870 °C. Analysis was performed utilizing homemade equipment, where desorbed gaseous products were detected by a quadrupole mass spectrometer EXTORR XT300.

RESULTS AND DISCUSSION

The change in surface chemistry was monitored by the CO and CO_2 evolution, **Figure 1** (left and right, respectively). The desorption profiles of samples prepared by hydrothermal treatment for 8h at 180 °C (GO/PTCDA_HT), thermal treatment at T=450 ^{o}C in Ar atmosphere (GO/PTCDA_T), milling for 20 min (GO/PTCDA_M) are compared to desorption profiles of initial/non-modified GO and PTCDA.

Each TPD peak corresponds to a distinct oxygen functional group. It can be observed that CO desorption originates from the decomposition of epoxy and alkoxy groups (around 200°C), carbonyl groups transitioning into α-substituted ketones and aldehydes (at approximately 270°C), carboxylic anhydrides (less stable form, roughly 350°C; more stable form, about 550-650°C), phenol (at 600-650°C), and carbonyl/quinone groups (approximately 700°C). Similarly, CO_2 desorption originates from the decomposition of carboxylic groups (at approximately 290°C), carboxylic anhydrides (less stable form, around 350°C; more stable form, about 550-650°C), and lactone groups (at around 700°C) [4, 5].

In the case of GO the peak at ~200 °C, corresponding to alkoxy and epoxy groups, is the most intensive both in CO and CO_2 desorption. The overall desorption profile of GO corresponds to previously described in Ref. [4]. In the case of PTCDA, in CO desorption, peak at 350°C and steep desorption above 700°C are the most noticeable, corresponding to decomposition of carboxylic anhydrides and carbonyl/quinone groups, respectively. In CO_2 desorption the peaks at 350°C and 650°C correspond to carboxylic anhydrides, less and more stable form. The steep desorption starting at 700°C corresponds to decomposition of lactone groups.

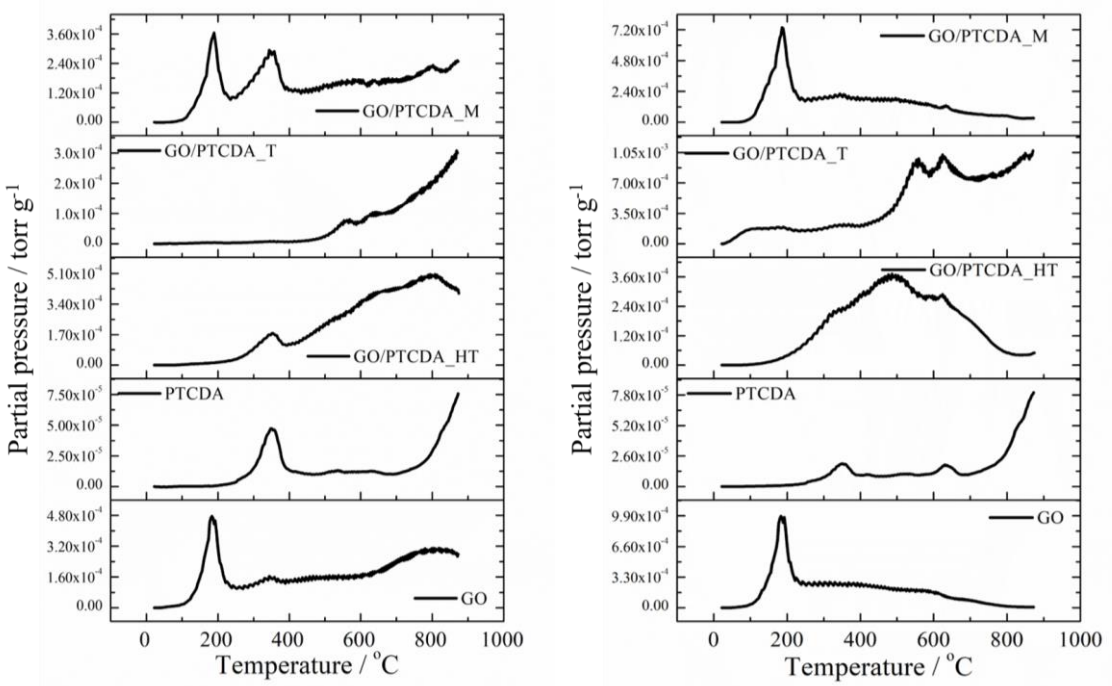


Figure 1. The desorption profiles of prepared samples and initial GO and PTCDA of CO (left) and CO_2 (right).

In the case of nanocomposite modified by hydrothermal treatment (GO/PTCDA_HT), absence of peaks at 200 °C can be noticed both in CO and CO_2 desorption, which is due to removal of epoxy and alkoxy groups. The peak at ~350 °C of carboxylic anhydrides from PTCDA is present in desorption of CO and CO_2. The overall desorption CO and CO_2 profile, above 400°C is similar to desorption profile of initial GO, with slight difference of higher content of carboxylic anhydrides and phenol groups at 500-600°C.

For GO/PTCDA_T sample the removal of functional groups up to 450 °C is evident due to thermal treatment. The two peaks at 550 and 620 °C, in CO and CO_2 desorption, can be noticed that correspond to carboxylic anhydrides, both belonging to its more stable form. Above 700°C the desorption profiles look more similar to the desorption profile of PTCDA.

After milling, there is a slight decrease in alkoxy and epoxy groups, evidenced by lower intensity of peak at ~200 °C. Also, in milled sample peak at ~200 °C appear less symmetric i.e. there is part of epoxy groups that are being desorbed at lower temperature. The same can be observed for the peak at 350 °C of carboxylic anhydrides. The overall CO and CO_2 desorption profile, above 400°C is more similar to desorption profile of initial GO.

Table 1. Amount of oxygen functional groups from initial GO, PTCDA and their nanocomposites after hydrothermal (HT), thermal (T) and mechanochemical (M) modification.

Sample	GO	PTCDA	GO/PTCDA_HT	GO/PTCDA_T	GO/PTCDA_M
Amount of groups (mmol/g)	23.50	1.78	24.53	34.45	19.93

The overview of the total amount of oxygen functional groups in studied samples is presented in **Table 1**. GO shows a substantial amount of 23.50 mmol/g, while PTCDA exhibits a significantly lower value of 1.78 mmol/g. For modified samples, GO/PTCDA_HT had 24.53 mmol/g, GO/PTCDA_T 34.45 mmol/g and GO/PTCDA_M 19.93 mmol/g. The selected methods are known for reduction of graphene oxide [6-8]. Thus, it is interesting to note that the amount of groups in GO/PTCDA nanocomposite is reduced for ~3% in the case of hydrothermal treatment and ~20 % in the case of milling. However, in the case of thermal treatment, the amount of desorbed groups increased for ~35%. These changes can be attributed to different nature of interaction between the GO and PTCDA in selected modification methods.

CONCLUSION

The study highlights the distinct effects of various modification methods on the oxygen functional groups in GO/PTCDA nanocomposite. Hydrothermal and mechanochemical treatments reduced the amount of groups, opposite to thermal treatment which led to increase of the amount of desorbed functional groups. These methods can be used for engineering of the surface chemistry of graphene oxide-based nanocomposites that is important in various applications, including catalysis, sensors, environmental protection, energy storage, etc.

Acknowledgment

This research was supported by the Science Fund of the Republic of Serbia, grant No. 6706, Low-dimensional nanomaterials for energy storage and sensing applications: Innovation through synergy of action – ASPIRE and by the Ministry of Science, Technological Development and Innovation of the Republic of Serbia (contracts No. 451-03-66/2024-03/200017 and 451-03-65/2024-03/200131).

REFERENCES

[1] W. Yu, et al., RSC advances, 10 (2020) 15328-15345.
[2] S. Ray, S., Chapter 2. Application and Uses of Graphene Oxide and Reduced Graphene Oxide. 2015. p. 39-55.
[3] L. Wang, et al., Electrochimica Acta, 340 (2020) 135804.
[4] Z. Jovanović, et al., Electrochimica Acta, 258 (2017) 1228-1243.
[5] P. Solís-Fernández, et al., Journal of Alloys and Compounds, 536 (2012) S532-S537.
[6] H.-H. Huang et al., Scientific Reports, 8 (2018) 6849.
[7] V. Agarwal and P.B. Zetterlund, Chemical Engineering Journal, 405 (2021) 127018.
[8] F. M. Casallas Caicedo et al., Diamond and Related Materials, 109 (2020) 108064.

SELECTIVE ABLATION OF Nb/Ti NANO COMPOSITE WITH SINGLE FEMTOSECOND LASER PULSES

B. Gaković[1], C. Siogka[2], B. Sagbas[3] and S. Petrović[1]

[1] *VINČA Institute of Nuclear Sciences, University of Belgrade, P.O.Box 501, 11000 Belgrade, Serbia (biljagak@vin.bg.ac.rs)*
[2] *Institute of Electronic Structure and Laser (FORTH), Heraklion, Greece*
[3] *Mechanical Engineering Faculty, Yildiz Technical University, Istanbul, Turkey*

DOI: https://doi.org/10.46793/Phys.Chem24I.393G

ABSTRACT
The selective ablation of nano composite thin film with femtosecond laser pulses is presented. The experimental sample, thin film composed of alternating metallic bi-layers of niobium and titanium (Nb/Ti) was deposited on Si substrate by ion-sputtering. A single laser pulses irradiation was performed in air with focused and linearly polarized Gaussian laser beam; single pulse duration 170 fs and wavelength 513 nm. To achieve selective ablation of the one and two nanolayers from the composite, energy of laser pulses was gradually increased from 0.5 to 1.0 J/cm^2. Detailed morphological characterization of the obtained spots on Nb/Ti nanocomposites indicates a well-defined selective ablation of the first one and the two layers for all applied fluences. However, at higher fluences, the central part is additionally modified due to the combination of photomechanical and thermal effects of the laser interaction.

INTRODUCTION

There are numerous applications for thin metallic films of nanometer thicknesses in electronics, nanodevices, catalysis, sensing, and medicine devices [1]. These applications need the procedure to design and fabricate projected structures directly on the thin film surface. Laser pulses, with pulse duration from few femto-seconds to ten pico-seconds, are known as ultra-short laser pulses (USLP). Using them material processing and modification is extremely precise, collateral damage is minimized, and no need for post-processing [2]. Among others, USLPs can be used to remove/ablate one or more surface layers of the nanolayer thin films (NLTF's) precisely and selectively. This ablation is known as selective photomechanical ablation or spallation. Selective ablation can be achieved at specified laser irradiation parameters for a given composition of NLTF [3,4]. In this work, to achieve selective ablation of the particular nanolayer of the (Nb/Ti) composite, the single pulse energy was progressively increased from close to the ablation threshold to a point where selective ablation was compromised. Optical microscopy, scanning electron microscopy (SEM), and optical profilometry, were used to analyse the laser-induced morphology and quantify the ablation depths. Experiments concerning selective ablation of NLTFs using USLPs are important to extend the applications and to verify the current theory in the field of USLP materials interactions.

EXPERIMENT

The NLTF was deposited on Si substrate by ion-sputtering technique. The sample was composed of Nb and Ti bilayers denoted as (Nb/Ti). It is comprised of 15 bilayers of Nb and Ti, with the total thickness of 440 nm (a single layer ~14,7 nm; Nb on the top). Laser irradiation was done in air using an a Yb-fibre laser system. Serial of single pulse irradiation was completed at wavelength of 513 nm, and pulse duration of 170 fs. The pulse energy was constant at a line, and gradually

changed from a raw to the next one (Fig.1.). To be sure that the single pulse energy is constant in one line, five shots were done with the same pulse energy. To compare results of surface modifications with different laser's processing conditions laser fluence is commonly introduced [4]. Laser fluence depends on laser pulse energy and irradiated area. In the case of Gaussian beam, $F = E_p/S$, $S = \pi w^2$, w is the beam radius (at which the beam intensity has fallen to 1/e of its peak). In the experiment, the cross section of the laser beam was slightly elliptical (Fig.2.) so we calculated S of corresponding ellipses. As pulse energy increased, the laser fluence increased gradually from 0.05 to 1.0 J/cm^2, 0.05 at each step. After laser processing, the qualitative and quantitative examination of the morphology on the sample surface were done by optical microscopy, scanning electron microscopy (SEM) and profilometry.

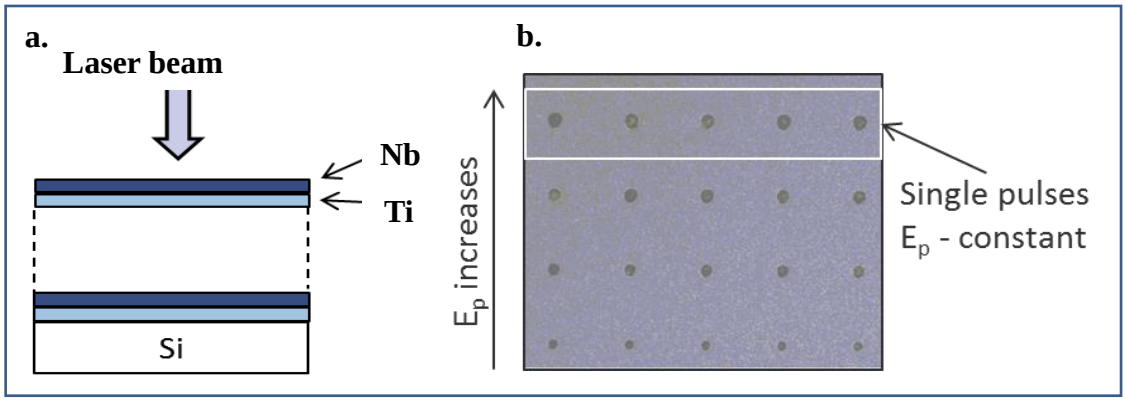


Figure 1. (a) Scheme of the sample cross section and laser beam irradiation. (b) SEM micrograph of the surface of (Nb/Ti) after irradiation with single laser pulses with different energy/fluence.

RESULTS AND DISCUSSION

Our investigation is related to the selective ablation of one surface layer, or a few of them, from the NLTF surface composed of Nb and Ti bilayers. This kind of ablation, which is typical of USLP processing, is referred to photomechanical spallation, spallation in short. Spallation can be found at specific conditions, and it has photomechanical nature. The spallation creates are shallow craters with a flat bottom and a sharp edge-step.

The first inspection of the sample after irradiation was done by optical microscopy. It helps us to conclude at which pulse energy/fluence started ablation of the (Nb/Ti). The morphology of ablated areas was further examined in detail with SEM. We found that at F = 0.05 J/cm^2 the surface of (Nb/Ti) was not in the crater's form, only some corrugation at the irradiated places happened. At the next value i.e., at F = 0.1 J/cm^2, one step ablated area, with sharp edge and flat bottom, appeared (Fig.2.a.). Further increasing of pulse energy/fluence manifested in the same way, only diameters of ablated areas increased. As laser fluence value reached F = 0.3 J/cm^2, one can see (Figs.2.b.1) two circles - two step form of ablation with a flat the first step area and flat central part (Fig.2.b.2). The same kind of ablation remained as values of fluence increased (Figs. 2.c.), only diameters of the ablated areas increased. As laser fluence increased, we registered the third form of ablation - three step ablation that happened at F = 0.9 J/cm^2 (Fig.2.d.). The characteristic of this spot are the flat surface of the first step and sharp edge of the first and second steps. The second step and central area showed different surface morphology. This morphology was similar after irradiation at higher fluences, but the central parts got rougher while the rims of the first and second steps got narrower. From this study we conclude that selective ablation in the form of single step happened as the values of single laser pulse fluences are equal to 0.1 J/cm^2 but less than 0.3 J/cm^2. When fluence

was equal to 0.3 J/cm^2 but less than 0.65 J/cm^2 two step selective ablation happened. To conclude if spallation happed in the above range of laser fluences we performed additional measurements.

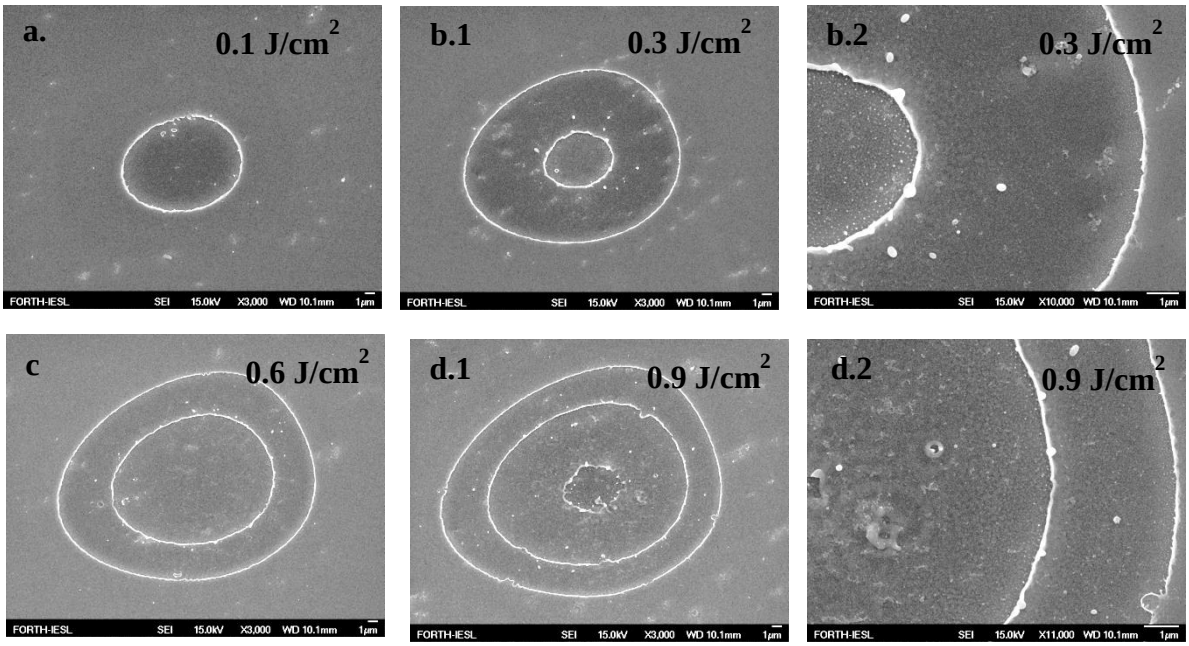


Figure 2. SEM micrographs of the (Nb/Ti) after irradiation with pulse energy-fluence: (a) F = 0.1 J/cm^2, (b.1 and b.2) F = 0.3 J/cm^2, (c) F =0.6 J/cm^2, and (d.1 and d.2) F = 0.9 J/cm^2.

Optical profilometry was used for quantitative examination of the irradiated areas. Cross-sectional measurements revealed the form of the bottom of irradiated area. On Figure 3. one can see that the bottom of the spot produced with F = 0.1 J/cm^2 (Fig.2.a.), is relatively flat. Note that the length of the spot cross section is given in micrometers while the height is in nanometers. Distance h between the lowest point on the cross section of the spot and the NLTF surface was in average h_1=15 nm. This value is very close to the thickness of the first Nb layer of the NLTF composite. From cross-section and inserted picture is visible that the redeposition or elevation of the materials was on the edge of the spot that manifested on SEM picture as a sharp edge.

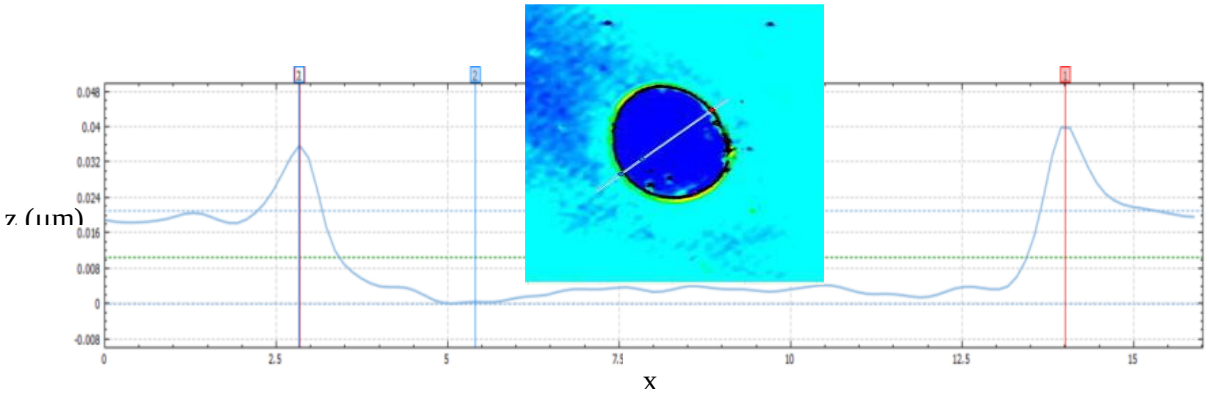


Figure 3. Result of profilometry of the irradiated area (Fig.2.a.). The inserted picture is two-dimensional presentation of the surface. The profile was taken along the white line.

As laser fluence increased diameters of the spots increased but height of h_1~15 nm of the first step remained. In the case of irradiation with laser fluence F = 0.3 J/cm^2 (Figs.2.b.1), the distance between the second step area and the surface of the NLTF was h_2 ~ 33 nm, while h_1 remained the same. The flat bottoms and same steps heights were registered up to F = 0.6 J/cm^2. In this interval,

it can be concluded that ablation comprises Nb, Ti, and part of the next Nb layer. At F = 0.9 J/cm^2 the new morphology, which was registered on SEM pictures (Fig.2.d.2), was confirmed with profilometry. Namely, the second step and center of the spot were uneven. The value of h_1 was again the same but the maximal depth in the center was $h_3 \sim 61$ nm and it was very rough. Effect of fluence of 0.9 J/cm^2 and higher values ablated the NLTF surface in steps but redeposit of the ablated material made the spot profiles more uneven than in the case of lower fluences. From these results, we can conclude that selective ablation/spallation of the surface Nb nano layer, from the rest layers of the NLTF composite, started at 0.1 and ended at 0.25 J/cm^2.

The laser ablation identified as photomechanical ablation-spallation can appear in some materials as response to USLP irradiation. Spallation causes disruptive removal of nanometer thick layer with constant depth, different from gradually increasing crater depths versus laser fluence in the phase explosion regime. The physical mechanism can be explained in short: the fast rate of energy deposition in short-pulse laser irradiation leads to a sharp temperature rise in the highly localized region of the target, the subsurface boiling, and generation of compressive stresses. The interaction of the induced compressive stresses with free surfaces of the target can transform them into tensile stresses of sufficient strength to cause mechanical fracture of bulk material. Multi-layered thin films of different materials exhibit strongly inhomogeneous heating and transient stresses generation because of the existence of inner interfaces [4]. In that case, spallation can be related to an acoustic rarefaction wave. Such a wave usually follows the thermo acoustic compressive one because of its anti-phase reflection from the inner boundary with different (mismatched) acoustic impedances. In our experiment, NLTF constituents are with different acoustic impedance $Z=\rho C$ (ρ and C are the mass densities and sound velocities, respectively). The acoustic's impedances of the constituents are $Z_{Nb} \approx 3.4$ kg/(m^{2}s) and $Z_{Ti} \approx 2.8$ kg/(m^{2}s). This mismatch additionally provides multiple reflections and reverberations at the interfaces with the opposite phases and interfering destructively in the resonant nano-layer. For higher values of fluence the interaction mechanism changes; thermal effects become more pronounced. This is reflected in an increase of roughness of the irradiated surface, especially in the central part (Gaussian peak).

CONCLUSION

In this study, we investigated selective ablation/spallation of the nanolayer thin film, composed of Nb and Ti, irradiated with single femtosecond laser pulses. Selective ablation, i.e., ablation of the single Nb nano layer from the bimetallic composite was confirmed as the laser fluence gradually increased from 0.1 J/cm^2 to 0.25 J/cm^2. The two-steps ablation of the two nano-layers from the surface, i.e. Nb and Ti, and a part of Nb layer beneath, happened at fluence 0.3 - 0.85 J/cm^2.

Acknowledgment

This work was supported by the Ministry of science, technological development and innovation of the Republic of Serbia (project No.451-03-66/2024-03/ 200017). B.Gaković thanks European Cooperation in Science and Technology (COST), action CA 21159, for the STSM grant.

REFERENCES

[1] D. Photiou, et al., Surface & Coatings Technology, 302 (2016) 310–319.
[2] K. Sugioka and Y. Cheng, Light: Science&Application, 1 (2014) el 49.
[3] S. Petrović, G.D. Tsibidis, A. Kovačević, N. Božinović, D. Peruško, A. Mimidis, A. Manousaki, E. Stratakis, European Physical Journal, 75(12) (2021) 304.
[4] S.I. Kudryashov, B. Gaković, P.A. Danilov, S. Petrović, D. Milovanović, A.A. Rudenko, A.A. Ionin, Applied Physics Letters, 112 (2018) 023103.

PHYSICOCHEMICAL EVALUATION OF TiO_2 NANOPARTICLES PREPARED BY PLANT-MEDIATED GREEN SYNTHESIS

D. Stoyanova [1], I. Stambolova [1], P. Markov [1], O. Dimitrov[2], R. Mladenova[3] and M. Shipochka [1]

[1] *Institute of General and Inorganic Chemistry, Bulgarian Academy of Sciences, Acad. G. Bonchev Str., bl. 11, 1113 Sofia, Bulgaria. (dsto@svr.igic.bas.bg)*
[2] *Institute of Electrochemistry and Energy Systems "Academician Evgeni Budevski", Bulgarian Academy of Sciences, Acad. G. Bonchev Str., bl. 10, 1113 Sofia, Bulgaria*
[3] *Institute of Catalysis, Bulgarian Academy of Sciences, Acad. G. Bonchev St., bl. 11, 1113 Sofia, Bulgaria.*

DOI: https://doi.org/10.46793/Phys.Chem24I.397S

ABSTRACT

The present article is devoted to the physicochemical characterization of TiO_2 nanoparticles, prepared by environmentally friendly green synthesis. The precursor solution consists of titanium isopropoxide and *Mentha Spicata* (MS) aqueous extract having three different concentrations. It was hydrothermally treated at 150°C in autoclave. The resulting powder was washed and then treated thermally at 400°C. The particles were characterized by X-ray diffraction (XRD), Energy dispersive X-ray analysis (EDX), Transmission Electron spectroscopy (TEM), and X-ray photoelectron spectroscopy (XPS), Diffuse reflectance spectroscopy (DRS) and Electron paramagnetic resonance (EPR). All powders possess pure anatase phase of spherical shape. It has to be noted the effect of the addition of the plant extract for the modification of optical parameters and lattice structure of TiO_2 nanoparticles. The number of oxygen vacancies increases, while the band gap values decrease slightly upon the increase of MS concentration. Several signals have been registered in all EPR spectra of the powders, which can be ascribed to the presence of oxygen radicals (g=2.000*).* When the MS concentration increases, the intensities of the EPR signals, which correspond to oxygen radicals also increase. The proposed by us *Mentha Spicata* - mediated synthesis is suitable for preparation of biocompatible titanium dioxide materials of defined structure and opical parameters etc., which could be applied in specific areas of medicine, pharmacy, industry, etc.

INTRODUCTION

Recently, the attention of the scientists is focused on the bio synthesis of oxide particles, due to its advantages: rapid, environmentally friendly low cost production of metal and metal oxide particles. It includes participation of different plants, enzymes, bacteria or fungi [1]. The presence of terpenoids, flavonoids, alkaloids etc. organic compounds in different parts of the plants (leafs, roofs, flowers) makes it suitable for green synthesis, due to their stabilizing and capping role. The aggregation of the obtained particles can be prevent by the presence of O–H, C=O, and C–N residues of organic derivatives. They might form bonds with the metal by covering the surface and decreasing agglomeration [2]. *Mentha Spicata* is a plant, which belongs to the family Lamiaceae. It is widely used in medicine, pharmacy etc., due to its excellent antimicrobial and antioxidant properties. Several synthesis parameters (nature and concentration of the plant extract, concentration of the metal salt, the pH, temperature and contact time) affect the quantity and physicochemical characteristics of the obtained particles [3].Titanium dioxide is a non-toxic, insoluble and stable metal oxide, which can be found in three distinct polymorphs: anatase, rutile, and brookite. TiO_2 is extensively used in various industries, due to its excellent optical,

photocatalytic, antimicrobial and anticorrosive properties. Various chemical synthesis methods can be used for the preparation of TiO_2 nanoparticles: precipitation [4], hydrothermal [5], CVD [6], spray pyrolysis [7], green synthesis [8] etc.
The aim of this article is to evaluate the impact of the MS concentration in titanium solution on some physicochemical features of the TiO_2 nanoparticles: phase composition, particles size, optical band gap and the type of the lattice defects. The obtained materials could be applied in specific areas of medicine, industry, etc.

METHODS

Mentha Spicata - mediated green approach combined with hydrothermal treatment, was used in order to obtain titanium dioxide nanoparticles. The MS leaves (origin from Bulgaria) were washed then left to dry up then they were ground into powder using a mortar, and the powder was mixed double-distilled water. The mixture was heated at 60°C. In order to obtain the final extract, the solution then was centrifuged and filtered. Titanium precursor solution was prepared using Ti isopropoxide and complexing agents, dissolved in isopropanol. It was poured into beaker, and then the evaluated quantities of the so-prepared extract MS were added and stirred. The resulting mixture was transferred into an autoclave at 150 °C. The so-obtained precipitates were washed and dried up in an oven, after which they were treated at 400 °C for 3 h. Powders, prepared from solution having 40ml MS, 70ml MS, and 100 ml MS are denoted as M0, M1, and M2, respectively.

The chemical composition of the samples was monitored using energy dispersive spectroscopy (EDS) probe Oxford Ultim Max 40 at four different points. X-ray diffractometer (CuKα radiation; generator voltage 40 kV), equipped with a PW1830 generator and a PW1050 goniometer. The Transmission Electron Microscopy (TEM) investigations were performed on a JEOL 2100 transmission electron microscope and a JEOL 2100 XEDS: Oxford Instruments, X-MAXN 80 T CCD Camera ORIUS 1000, 11 Mp, GATAN. The X-ray photoelectron spectroscopy (XPS) was carried out using AXIS Supra electron-spectrometer (Kratos Analitycal Ltd, AlKα radiation; photon energy of 1486.6 eV). The areas and binding energies (accuracy of ±0.1 eV) of C1s, O1s, Ti2p photoelectron peaks were monitored. The UV-Vis diffuse-reflectance spectra (DRS) have been recorded on Thermo Evolution 300 UV-VIS spectrometer (190 nm - 1100 nm). Electronic paramagnetic resonance spectra (EPR) were recorded at room temperature by a JEOL JES-FA 100 EPR spectrometer operating within the X-band with a standard TE011 cylindrical resonator at a modulation frequency of 100 kHz, microwave power of 3 mW.

RESULTS AND DISCUSSION

The EDX spectrum of *Mentha Spicata* proved the presence of mainly C, O, K, Ca, Mg, Cl and some minor quantities of other elements (Fig. 1).

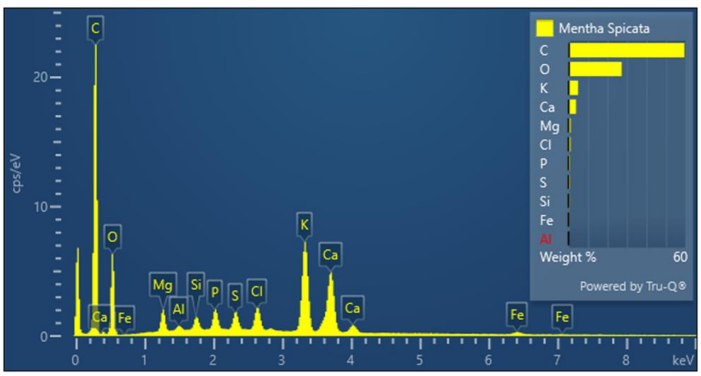
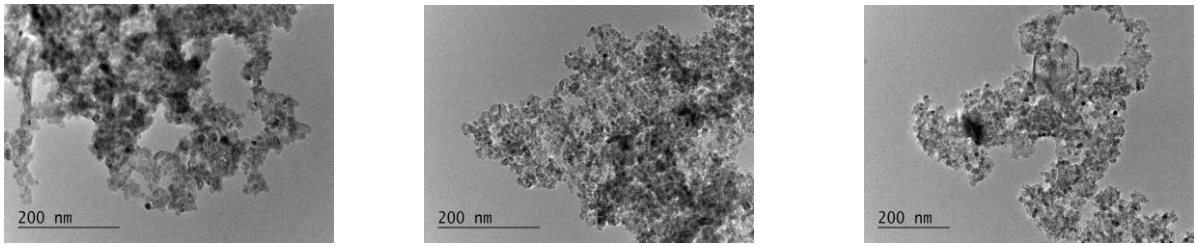


Figure 1. EDX spectrum of *Mentha Spicata.*

The XRD analyses revealed the presence of pure anatase phase in all the samples (it is not shown). The Scherrer's equation was used to calculate the crystallite size for M0, M1 and M2 particles (~11 nm, 9 nm and 10 nm resp.). TEM photographs show that the powders have mostly spherical morphology. The particles sizes are within the range 5-20 nm (Fig. 2).



a b c

Figure 2. TEM photographs of M0(a), M1 (b) and M2 (c) particles.

The chemical compositions of the nanoparticles, evaluated by means of XPS analyses are shown in **Table 1**. Both ratios $O_{total}/O_{lattice}$ increase slightly with the increasing of plant extract quantity in the precursor solution. This fact indicates a increased number of oxygen vacancies inside TiO_2 lattice.

Table 1. XPS chemical composition of the green synthesized TiO_2 powders.

Sample	C, at.%	O, at.%	Ti, at.%	$O_{total}/O_{lattice}$
M0	22.1	54.1	23.8	1.49
M1	20.4	56.8	22.8	1.56
M2	21.7	55.8	22.5	1.85

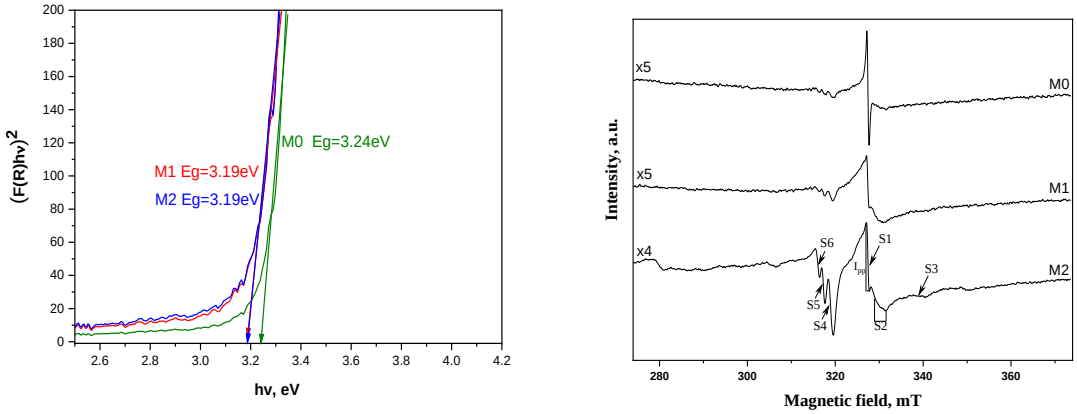


Figure 3 Comparative diagram of $(F(R)h\nu)^2$ as a function of hν (left); EPR spectra (right) of green synthesized TiO_2 powders.

The $Ti2_{3/2}$ and $Ti2p_{1/2}$ peaks and their positions at 457.5 eV and 463.2 eV and the doublet separation between them of ~5.7 eV are characteristic of Ti^{4+} oxidation state (these are not shown). As the biosynthesized particles possess organic residues, which cover the surface and create barrier layer, we did not find a Ti^{3+} signal in the Ti2p XPS spectrum

The optical band gap is estimated using the Tauc equation. From the extrapolation of the linear section of the graph $(h\nu F(R\infty))^{1/n}$ from hν, the values of the optical band gaps were determined

(Figure 3-left). When the MS concentration increases, the band gap values decrease. Figure 3 (right) shows the EPR spectra of the green synthesized particles. The signal S1 at g=2.000 could be attributed to the presence of oxygen radicals [9,10]. The signals at g < 2 can be due to capture of an electron on titanium ions. The broad EPR line (S3) at g = 1.93 indicates formation of Ti^{3+} species on surface sites, while the narrow EPR signal (S2) at $g_{\perp}$ = 1.991 and g//=1.976 probably assigned to inner electron traps (Ti^{3+}) of the particle [9, 11]. The signal S4 at g= 2.054 can be assigned to adsorbed water or absorbed oxygen O_2^- [10, 11]. Chloride ions can react with the hole to form Cl• atoms with EPR signals at g = 2.063(S5) and 1.997, which can be originating from the plant extract (proved by EDX analysis). The signal S6 at g=2.07 can be due to OH• radicals, adsorbed on the TiO_2 surface [9]. When the MS concentration increases, the intensities of these EPR signals, which are contributed to the presence of Ti^{3+} and oxygen radicals increase. Probably the ability of plant compounds constituents to reduce the metal cations is responsible for the presence of Ti^{3+} ions. The physicochemical features of the obtained TiO_2 plant synthesized particles: nanocrystalline anatase structure, increased number of oxygen vacancies and decreased band gap value make them suitable for possible applications in the fields of catalysis or photocatalysis.

CONCLUSION

Titanium dioxide biocompatible nanoparticles were prepared using plant mediated synthesis by means of *Mentha Spicata* aqueous extract. It has to be note the role of the plant extract for the tuning of the optical parameters and lattice structure of the particles. All samples possess well crystallized nanosized anatase phase with spherical-like particles. When the MS concentration increases, the band gap values decrease, while the number of oxygen vacancies inside TiO_2 lattice increase. The proposed by us plant mediated synthesis is suitable for preparation of titania powders having defined structure, optical features etc., which could be applied in specific areas of medicine, industry, etc.

Acknowledgment The authors express their gratitude for support of the contract “Environmentally friendly anticorrosive hybrid coatings” is within the Non-currency Equivalent Exchange Bilateral Cooperation between the Bulgarian Academy of Sciences and the Serbian Academy of Sciences and Fine Arts and the Project KP-06-H69/8 “Novel polymer-hybrid materials containing (bio)synthesized metal oxide particles with improved photocatalytic and antimicrobial potential” of the National Science Fund, Ministry of Education and Science, Bulgaria.

REFERENCES

[1] V. Verma, M. Al-Dossari, J. Singh, M. Rawat, M. G. M. Kordy, M. Shaban, Polym., 14 (2022) 1444.
[2] Y.Kumar, R. Santhosh, M. Hoque, D. Nath, R. Thakur, D. Madhubabu, V. R. Suryavanshi, H.Singhi, J. Ahmed, P. Sarkal., Packag. Technol. Sci. 36 (2023) 715.
[3] A. D. Dwivedi, K. Gopal, Colloids Surf A: Physicochem. Eng. Asp., 369 (2010) 27.
[4] H. Wang, P. Liu, X. Cheng, A. Shui, L. Zeng, Powd. Technol., 188 (2008) 52.
[5] T. Gupta, Samriti, J. Cho, J. Prakash, Materials Today: Chemistry, 20 (2021) 10042.
[6] A. K. Singh, V. Chaudhary, A. K. Singh, S.R.P. Sinha, Synth. Met., 264 (2020) 116389.
[7] A. Ansari, N. M. Nouri, Ceram. Intern., 49 (2023) 57.
[8] H. Ali, S. Dixit, B. O. Almutairi, N. Yadav, J. King Saud Univ. Sci., 35 (2023) 102918.
[9] L.-B. Xiong, J.-L. Li, Y.Yu, J. Nanomater., 831524 (2012) 1.
[10] Y. Nakaoka, Y. Nosaka, J. Photochem. Photobiol.A: Chemis., 110 (1997) 299.
[11] C. P. Kumar, N. O. Gopal, T. C. Wang, M.-Sh. Wong, S. C. Ke, J. Phys. Chem. B, (2006) 110, 5223.

CIP - Каталогизација у публикацији Народна библиотека Србије, Београд

544(082)
621.35(082)
577.3(082)
543.42(082)

INTERNATIONAL Conference on Fundamental and Applied Aspects of Physical Chemistry (17 ; 2024 ; Beograd)

Physical Chemistry 2024 : proceedings. Vol. 1 / 17th International Conference on Fundamental and Applied Aspects of Physical Chemistry, September 23-27, 2024 Belgrade, Serbia ; [organized by The Society of Physical Chemists of Serbia in co-operation with Institute of Catalysis Bulgarian Academy of Sciences ... [et al.]] ; [editors Željko Čupić, Slobodan Anić and Ana Ivanović-Šašić]. - Belgrade : Society of Physical Chemists of Serbia, 2024 (Belgrade : Jovan). - VI, 400 str. : ilustr. ; 29 cm

Na nasl. str.: This conference is dedicated to the 100th anniversary of the birth of Professor Slobodanka Caca Veljković. - Tiraž 50. - Bibliografija uz svaki rad.

ISBN 978-86-82475-45-3
ISBN 978-86-82475-44-6 (niz)

a) Физичка хемија -- Зборници b) Електрохемијско инжењерство -- Зборници v) Биофизичка хемија -- Зборници g) Спектроскопија -- Зборници

COBISS.SR-ID 160310793